Exploring Methods of Magnetic Manipulation in Defective Dicubanes, Dinuclear, and Extended Structures

Author:
Sidney Woodhouse

Supervisor:
Prof. Paul Plieger

A thesis submitted in fulfillment of the requirements for the degree of

Doctor of Philosophy

in

Chemistry

School of Natural Sciences

Massey University

2023

Declaration of Authorship

I, Sidney Woodhouse, declare that this thesis titled, "Exploring Methods of Magnetic Manipulation in Defective Dicubanes, Dinuclear, and Extended Structures" and the work presented in it are my own. I confirm that:

- This work was done wholly or mainly while in candidature for the research degree of PhD in Chemistry at Massey University.
- Where I have consulted the published work of others, this is always clearly attributed.
- Where I have quoted from the work of others, the source is always given. With the exception of such quotations, this thesis is entirely my own work.
- I have acknowledged all main sources of help.
- All work presented in this thesis was completed by the author, except:
  - The magnetic analyses (SQUID) presented in Chapters 3 and 4 and the computational analysis presented in Chapter 3, were collected and analysed through collaboration with Prof. Euan Brechin at the University of Edinburgh, Edinburgh, Scotland and his students Mukesh Singh, Emily Payne, and Alvaro Etcheverry-Berríos.
  - The computational analysis presented in Chapter 4 was performed and analysed by Dr Tyson Dais, Massey University, Palmerston North, New Zealand.
  - The magnetic data reported in Chapter 5 was collected by Sören Schlittenhardt through collaboration with Prof Annie Powell and Dr Christopher Anson, Karlsruhe Institute of Technology, Karlsruhe, Germany. This includes the curve fitting and analysis of **C17**.
  - The magnetic analysis of **C63** presented in Chapter 6 was collected and analysed through collaboration with Professor Takayuki Ishida at the University of Electro-Communications, Tokyo, Japan and his student Rina Takano.

Signed: Sidneyw

Date: 27/07/23

"Be less curious about people and more curious about ideas."

Marie Curie

Abstract

Transition metal (3*d*) and lanthanide (4*f*) coordination clusters form a base for which many fields of research expand from. One field of interest, magnetic materials, has risen in popularity due to the discovery of single molecule magnets (SMMs), which are currently capable of operation up to 80 K. Although this field is highly researched, significant improvements are still required in order for SMMs to be stable enough for implementation into modern technological devices. One fundamental area of interest is the electron sharing pathway between metal ions, which is responsible for the magnetic properties of the molecules. Methods which optimise this to promote ferromagnetic exchange, an intrinsic property of SMMs, are an important focus.

Polynuclear homometallic 3*d* and heterometallic 3*d*3*d*′ and 3*d*4*f* coordination clusters are reported, which explore different ways as to which the exchange pathway angles can be manipulated. Several complexes have undergone magnetic and computational analyses to explore how the different manipulations have affected the exchange pathways. A series of Ni^{II}_4 defective dicubanes composed of both ligand and anion based exchange pathways present a platform for manipulations based on the switching of key donor groups and solvate molecules found in the crystal lattice. The results revealed that the strongest manipulator was the introduction of lattice-bound solvent molecules, capable of hydrogen bonding to the metal ion donor groups.

Moving from a combination of ligand and anion based exchange pathways to those that are solely ligand derived were explored by synthesising a series of homometallic and heterometallic 3*d*3*d*′ dinuclear complexes, and conducting a study which closely looked at how different metal ion combinations affected the magnetic properties. Transmetalation reactions were performed alongside a computational analysis to determine the stabilities of the 3*d*3*d*′ dinuclear complexes, with the most stable being that of the $Cu^{II}Mn^{II}$ complex. Unexpectedly, the Cu^{II}_2 complex was found to have the largest ferromagnetic coupling, indicating the large coordination number for a Cu^{II} ion to be the strongest magnetic manipulator.

Expanding the 3*d*3*d*′ dinuclear series was achieved by the introduction of 4*f* ions with the aim of producing a series of 3*d*4*f* dinuclear complexes, where the use of different metal ions, anions, and coordinated solvent molecules have been structurally analysed to determine the success of the manipulations. It was found that the complexes with smaller exchange angles had a common similarity, that being additional bridging groups between the metal ions.

Finally, a series of clusters ranging from mononuclear to icosanuclear are reported, all of which were unexpected results. These complexes reveal unusual and uncommon properties, such as the coordination of an alkyloxime oxygen.

Acknowledgements

First of all I would like to thank my supervisor, Prof. Paul Plieger for his constant support, guidance, and endless enthusiasm. I would like to thank my co-supervisor Assoc. Prof. Gareth Rowlands for his support and readiness to answer any questions. To all the Plieger group members and honorary members, past and present, thanks for your constant support and willingness to help, couldn't have made it through the last five years without it.

I would like to thank a number of research collaborators who have contributed to this research, Prof. Euan Brechin and his students from the University of Edinburgh for performing both magnetic and computational analyses on several structures; Prof. Annie Powell, Dr Christopher Anson, and Sören Schlittenhardt from Karlsruhe Institute of Technology, for the collection, curve fitting and analysis of magnetic data; Prof. Takayuki Ishida and his students from the University of Electro-Communications, for performing magnetic analysis; Prof. Joseph Lane from the University of Waikato for his advice regarding computational work; and finally Dr Tyson Dais from Massey University, for performing computational analyses and support over the years.

Finally to Mum, Dad, Ben, and the rest of the family, thanks for your endless support and encouragement, I'm almost there!

Publication List

Publications relevant to this thesis

- Woodhouse, S. S., Dais, T. N., Payne, E. H., Singh, M. K., Brechin, E. K., Plieger, P. G. The structural manipulation of a series of Ni_4 defective dicubanes: Synthesis, X-ray structures, magnetic and computational analyses. *Dalton Trans.*, **2021**, **50**(*15*), 5318-5326.

- Woodhouse, S. S., Dais, T. N., Etcheverry-Berríos, A., Brechin, E. K., Lane, J. R., Plieger, P. G. Against the Norm: Non Irving-Williams Transmetalation in Transition Metal Dimers. *Inorg. Chem.*, **2022**, **61**(*44*), 17819-17827.

Additional publications by author

- Woodhouse, S. S., De Silva, D. N. T., Jameson, G. B., Cutler, D. J., Sanz, S., Brechin, E. K., Davies, C. G., Jameson, G. N. L., Plieger, P. G. New salicylaldoximato-borate ligands resulting from anion hydrolysis and their respective copper and iron complexes. *Dalton Trans.*, **2019**, **48**(*31*), 11872-11881.

- Ainscough, E. W., Woodhouse, S. S., Brodie, A. M., Freeman, G. H., Plieger, P. G. Insights into the Chemistry and Structural Features of the Copper(II) 2,2'-Bipyridyl-Thiosulfate System. *Aus. J. Chem.*, **2019**, **73**(*1*), 43-48.

- Woodhouse, S. S., Buchanan, J. K., Dais, T. N., Ainscough, E. W., Brodie, A. M., Freeman, G. H., Plieger, P. G. Structural trends in a series of bulky dialkylbiarylphosphane complexes of Cu^{I}. *Acta Crystallogr. C*, **2021**, **77**(*9*), 513-521.

- Roach, B. D., Forgan, R. S., Kamenetzky, E., Parsons, S., Plieger, P. G., White, F. J., Woodhouse, S. S., Tasker, P. A. From gas phase observations to solid state reality: the identification and isolation of trinuclear salicylaldoximato copper complexes. *Molecules*, **2022**, **27**(*19*), 6421-6443.

Contents

List of Figures

List of Tables

List of Abbreviations

3*d*	First row transition metal
4*f*	Lanthanide
AC	Alternating current
Acac	2,4-Pentanedione
AF	Antiferromagnetic
ATR-IR	Attenuated total reflectance - Infrared spectroscopy
BS	Broken symmetry
CCDC	Cambridge crystallographic database centre
CShM	Continuous shape measurement calculation
DC	Direct current
DFT	Density funtional theory
En	Ethane-1,2-diamine
ESI-MS	Electrospray ionisation - Mass spectrometry
FAAS	Flame atomic absorption spectroscopy
F	Ferromagnetic
Me	Methyl group
NeSI	New Zealand eScience Infrastructure
NMR	Nuclear magnetic resonance
OAM	Orbital angular momentum
o-van	*o*-Vanillin
QTM	Quantum tunnelling of magnetisation
RT	Room temperature
Sal	Salicylaldehyde
SCXRD	Single crystal X-ray diffraction
SMM	Single molecule magnet
SOC	Spin-orbit coupling
SQUID	Superconducting quantum interference device
TA-QTM	Thermally assisted - Quantum tunnelling of magnetisation
^{t}Bu	*tert*-Butyl group
VTVB	Variable-temperature variable-field
XRD	X-ray diffraction
ZFS	Zero field splitting

List of Symbols

α	Flux coupling factor
B	Applied magnetic field
χ	Magnetic susceptibility
χ_{M}	Molar magnetic susceptibility
$\chi_{\mathrm{M}}T$	Temperature dependent molar magnetic susceptibility
D	Anisotropy parameter
E	Energy
H	Magnetic field
I	Current
I_{c}	Critical current
J	Heisenberg exchange coupling constant
K	Kelvin
κ_B	Boltzmann constant
M	Magnetisation
M_S	Spin state quantum number
μ_{B}	Bohr magneton
N_A	Avogadro's number
ϕ	Magnetic flux
S	Total spin
T	Tesla
T	Temperature
T_{B}	Blocking temperature
U_{eff}	Effective barrier for reversal of magnetisation

Chapter 1

Introduction

1.1 Magnetism

The phenomena known as magnetism was first found in crystalline deposits of magnetite, Fe_3O_4, which were found to be naturally magnetised and attracted metallic compounds. The first reported use of magnetism was in the 11th century, with the invention of the compass for navigation. Since then magnetism is more well known, as it has become a popular field of research, with magnetism now utilised in many different applications.[1–3]

The magnetism found in metallic compounds arises from the magnetic moment that is derived from the compound's orbital angular momentum (OAM) and the total spin (S) of the compound, both of which arise from the compound's electrons. Magnetism can be simply defined as an interaction, either attractive or repulsive between two metallic objects, or as more commonly found between a metallic object and an applied magnetic field.[1] When a metallic compound and the applied magnetic field come into contact, the spin of the compound's ground state electrons reorientate in such a way that they become aligned and ordered with the magnetic field. This results in the magnetisation of the object, a property that can be measured. The removal of the magnetic field causes the electrons to rapidly become disordered, quenching the magnetisation of the compound.[4]

Within the field of magnetism, there exists two overall classes: diamagnetism and paramagnetism, which are defined by how their ground state electrons respond to a magnetic field. Each class responds differently, either attractively or repulsively, depending on the electron configuration of the corresponding metal ion(s). Diamagnetic compounds are characterised as having no unpaired electrons, resulting in a net magnetic moment of zero and weakly negative magnetic susceptibility. When in contact with a magnetic field, a repulsive interaction occurs producing no observable magnetisation. Paramagnetic compounds are the opposite in that they are characterised as having unpaired electrons, resulting in both positive magnetic moments and magnetic susceptibility. An attractive interaction arises with a magnetic field as the result of the electrons aligning in the direction of the magnetic field, producing magnetisation.[1,5]

When discussing bulk solids, further classes, ferro-, antiferro-, and ferrimagnetism are introduced due to their temperature dependent nature. These classes contain aspects of both diamagnetism and paramagnetism however instead of the interaction arising solely between a metallic compound and a magnetic field, the interaction is a direct correlation to the alignment of magnetic dipoles (the orientation of the magnetic moment for a given domain) on adjacent metal ions within the bulk solid and

how they collectively respond to a magnetic field. Ferromagnetism is characterised by the dipoles aligning parallel, whereas antiferromagnetism is characterised by antiparallel dipoles. Ferrimagnetism is similar to antiferromagnetism with antiparallel dipoles, however the dipoles are disproportional allowing for spontaneous magnetisation. The directionality of the dipoles can be influenced by bridging atoms and groups, as they can induce a spin polarisation onto an adjacent metal ion.[1,2,6]

1.1.1 Single Molecule Magnetism

Single molecule magnets (SMMs) are a class of magnetic materials, which are defined as discrete compounds that display slow relaxation of magnetisation and magnetic hysteresis, simply described as the retention of magnetisation. SMMs differ from traditional magnetic materials in that they do not have magnetic domains consisting of many interacting molecules, instead the magnetic domains found in SMMs consist of a single, well isolated molecule.[5] This results in molecular based hysteresis derived from metal - ligand interactions and ground spin states.[3,7–9] These properties also result in the slow relaxation of magnetisation, which is appealing for potential application in quantum computing, spintronic devices, and high density information storage.[9–12]

SMMs are defined by three characteristic properties: temperature dependent magnetic susceptibility ($\chi_M T$), the blocking temperature (T_B), and the effective barrier for the reversal of magnetisation (U_{eff}). Magnetic susceptibility, specifically that of temperature dependent magnetic susceptibility indicates how the SMM will interact when in contact with a magnetic field, and the degree to which it will be magnetised.[1,13–15] The magnetic susceptibility of a compound is commonly reported in plots of $\chi_M T$ versus temperature (T) where the direction of the curve is used to indicate the compounds overall magnetic properties (discussed further in Section 1.2.2).

The blocking temperature, T_B, is the maximum temperature at which a SMM will retain magnetisation and display magnetic hysteresis. Above this temperature, the system gains enough energy to overcome the effective barrier and quench the magnetisation through random orientation of the electron spins. The blocking temperature can be determined experimentally from plots of magnetisation (M) versus magnetic field (H), however these results are dependent on the rate at which the magnetisation is measured, a measurement that has not been formally defined within the literature.[16] The blocking temperature is one of the most challenging aspects of SMM research, as for a SMM to be functional, it needs to display hysteresis and retain magnetisation at an operable temperature. This aspect of SMMs has been widely researched since their discovery in the early 1990s.[16–18] Until recently, all SMMs have required liquid helium cooling (4 K) in order to be operable, however in 2018 a breakthrough was made with a SMM reported to have a blocking temperature of 80 K, surpassing the need for liquid helium cooling, only requiring liquid nitrogen cooling (77 K).[19]

The effective barrier for the reversal of magnetisation, U_{eff}, is the total energy required in order for the magnetisation to be quenched, simply put, the energy required in order to 'flip' the orientation of the electrons. The effective barrier is defined as the energy difference between the highest and lowest ground spin states of

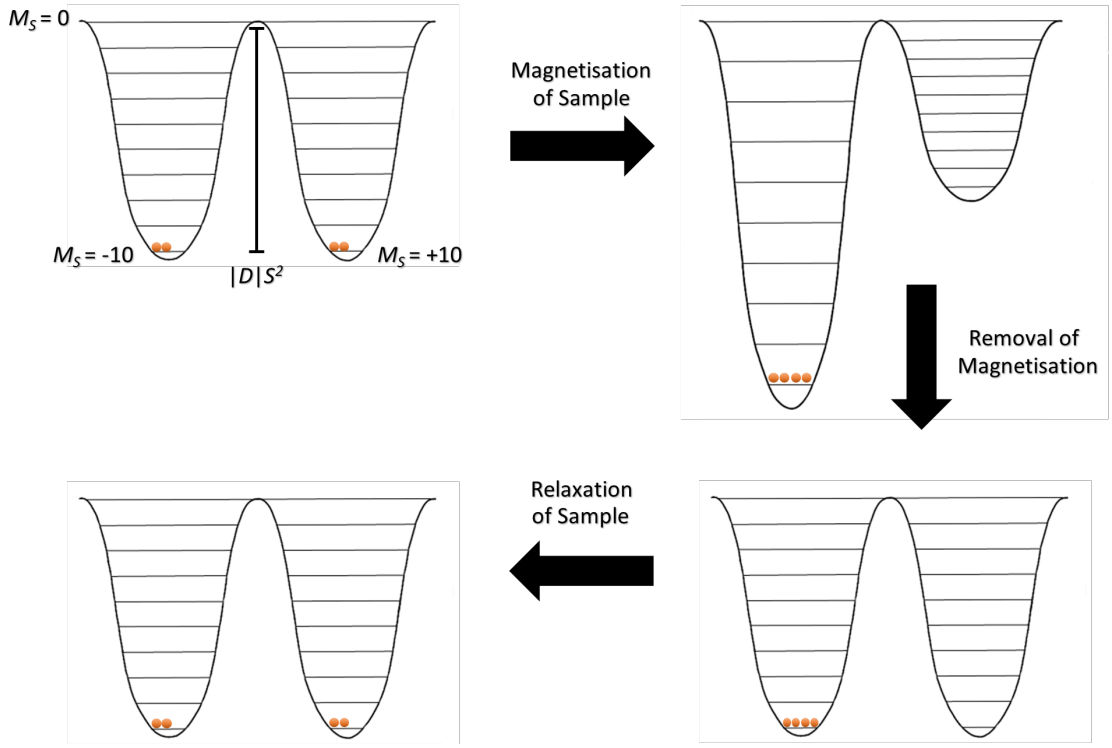

Figure 1.1: Schematic representation of the double well system which occurs when the system undergoes magnetisation and relaxation. The orange circles represent the electrons.

the metal ion.[5,17,20] This can be seen in a simple double well schematic (Figure 1.1), where for a given complex, with a total spin of S, there are as many as $2S+1$ possible spin states. Each of these spin states has a quantum number M_S, when $M_S = +S$, this is considered 'spin up' and when $M_S = -S$, this is considered 'spin down'. When a compound comes into contact with a magnetic field, the wells repopulate as shown by the top right image in Figure 1.1, as the compound is classed as being 'magnetised'. When the magnetic field is removed, if the associated energy isn't greater than the effective barrier, then the compound will remain in a 'magnetised' state. This is known as the retention of magnetisation, or slow relaxation of magnetisation, a characteristic feature of SMMs.[21–23] The strength or height of the effective barrier ($|D|S^2$) is directly related to both the spin, S, of the compound and the aniostropy, D, of the metal ion(s), which for $3d$ ions is derived from the zero-field splitting (ZFS) of the metal ions ground state electrons.[20]

In order for the system to return to a non-magnetised state, the barrier must be overcome. This can occur by several relaxation methods: quantum tunnelling of magnetisation (QTM), thermally assisted - QTM (TA - QTM), Orbach relaxation, and Raman relaxation (Figure 1.2). These relaxation processes are typically found for $4f$ ions/complexes that have an odd number of ground state electrons, known as Kramers ions/complexes. QTM occurs when the ground state electrons effectively tunnel through the barrier from the ground spin state, rather than surpassing the barrier. TA - QTM resembles QTM, however temperature assists by exciting the electrons to an excited spin state level where tunnelling can occur. Raman and Orbach relaxation pathways occur when the inelastic scattering of a photon promotes the relaxation to occur by either a virtual (Raman) or real (Orbach) transition state.[1,20–24]

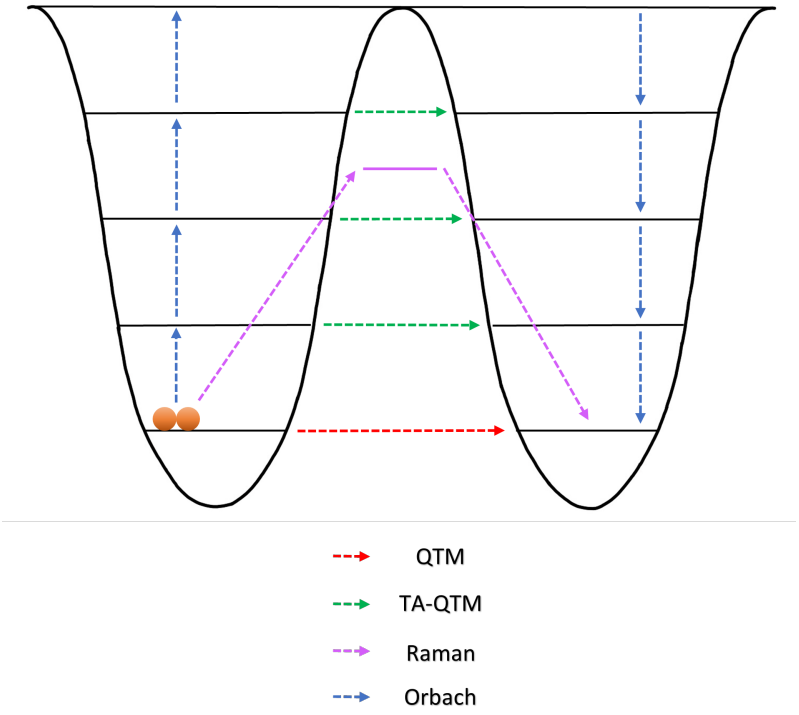

Figure 1.2: Schematic representation of the possible relaxation pathways for a SMM. The orange circles represent electrons.

Throughout the literature, there are many different record breaking SMMs, whether it be for mononuclear SMMs, mixed metal SMMs, or for a specific topology, the one that has the greatest interest however is the SMM with the largest blocking temperature, and subsequently the largest effective barrier. The SMM that currently holds these records was produced in 2018 by Guo *et al*. and consists of a mononuclear Dy^{III} ion coordinated axially by cyclopentadienyl (Cp) derived ligands, Cp^{iPr_5} and Cp* (penta-*iso*-propylcyclopentadienyl and pentamethylcyclopentadienyl respectively) as discussed further in Section 1.3.1 and Figure 1.3. The record blocking temperature was found to be 80 K, and the effective barrier was found to be 2217 K (1541 cm^{-1}).[19]

1.1.2 Exchange and Superexchange

Within metallic clusters, specifically clusters with two or more metal ions, an exchange interaction is defined as the electronic interaction between two metal ions originating from the mutual overlap formed between two partially occupied atomic orbitals.[25] Superexchange pathways, while similar, typically occur when a partially occupied atomic orbital of a metal ion overlaps with a molecular orbital of a bridging group, which facillitates a coupling between adjacent metal ions.[25,26]

For polynuclear clusters, there is an angular dependence for the type of superexchange present within the cluster. Antiferromagnetic exchange occurs when the metal-ligand-metal (M-L-M) angle approaches 180°. Ferromagnetic exchange occurs when the M-L-M angle approaches 90° due to the involvement of a secondary *p* orbital found on the bridging ligand. This allows the donation of electron density from

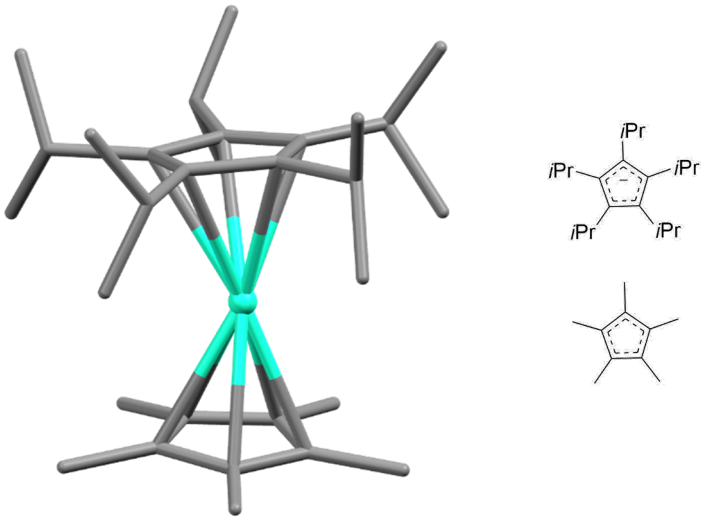

Figure 1.3: Crystal structure and corresponding ligands of the record breaking SMM, $[Cp^{iPr5}Cp^{*}Dy^{III}]^{+}$, produced by Layfield and coworkers.[19] Hydrogen atoms and lattice anions have been omitted for clarity. Colour code: Dy^{III} = aqua and C = grey.

the bridging ligand to be parallel unlike antiferromagnetic exchange where the single bridging ligand donates antiparallel electron density (Figures 1.4 and 1.5). The nature of the superexchange pathway, whether antiferromagnetic or ferromagnetic can be predicted using the Pauli exclusion principle. The principle states that coupled metal ions will exhibit antiferromagnetic exchange if both ions have half-filled orbitals. For ferromagnetic exchange, the principle states that one orbital must be half-filled, and the other fully occupied. When the complex in question does not fit the exact specifications of the generalisation, for example, the complex contains many metal ions and/or superexchange pathways, the prediction breaks down due to the dominant nature of antiferromagnetic exchange.[25,26]

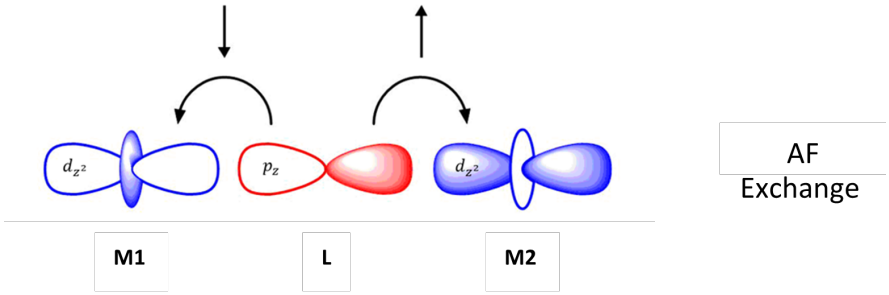

Figure 1.4: Schematic representation of antiferromagnetic (AF) exchange.

1.2 Characterisation Techniques

When it comes to characterisation, there is a large number of different techniques and instruments that can be used to examine the properties, behaviour, interactions, purity, and composition of small molecules. Popular characterisation techniques utilised for the characterisation of small molecules, specifically polynuclear

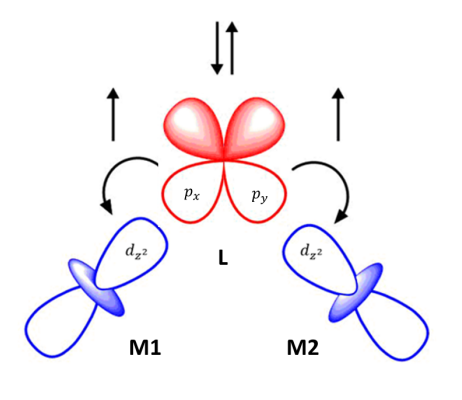

Figure 1.5: Schematic representation of ferromagnetic (F) exchange.

complexes include, nuclear magnetic resonance (NMR), infrared (IR), and ultraviolet - visible (UV/vis) spectroscopy and mass spectrometry (MS). These techniques are commonly used for the identification of organic molecules as they can identify key features of the chemical structure and/or properties, such as functional groups, atomic nuclei, and the absorbance of light, and additionally, in some instances determine purity.[1]

There is also a large range of techniques that are used more for specific forms of characterisation, some of these are flame atomic absorption (FAAS), electron paramagnetic resonance (EPR), and Mössbauer spectroscopy, X-ray diffraction (XRD), SQUID magnetometry, and computational calculations. These techniques are less popular than the ones mentioned above as they are only relevant to specific areas of research. FAAS is a method of elemental analysis that quantitatively determines the concentration of elements contained within the sample.[1,27] FAAS is based off the principle that elements absorb radiation at a specific wavelength, therefore, by using standards of known concentration the absorption of radiation by the elements within the sample can be converted into concentration using the Beer-Lambert law.[1] EPR spectroscopy is a method that investigates paramagnetic materials, compounds with one or more unpaired electrons. EPR provides information about the paramagnetic material, such as properties surrounding the structure, coordination spheres and geometries of the metal ions, oxidation states, and the number of magnetic centres present in the material.[1,28,29] Mössbauer spectroscopy is a characterisation technique that investigates structural properties, electronic, magnetic, and oxidation states of a crystalline solid containing Mossbauer active nuclei.[1,30–32] The most commonly measured Mössbauer nuclei is ^{57}Fe, as it has a sufficient combination of natural abundance, and recoil free fraction.[32]

The characterisation techniques used throughout this research were chosen for a number of reasons including, the information they provided/determined directly related to the goal of this research and a key reason being the availability of instruments. Three key characterisation methods used throughout this research can be found described in detail below.

1.2.1 X-ray Diffraction

XRD is a characterisation technique used extensively by coordination chemists. A compound, either a polycrystalline powder (PXRD) or a single crystal (SCXRD), is irradiated with X-rays causing the electrons of the atoms contained within the compound to scatter the X-rays, resulting in a diffraction pattern.[33] In the particular case of SCXRD, this diffraction pattern can be used together with software to produce a three dimensional spatial arrangement of the atoms within the crystal lattice.

The scattering of the X-rays is directly related to the Bragg equation (equation 1.1), as X-rays scatter at a specific angle, the Bragg angle, 2θ. The Bragg equation is commonly used to determine the distance between lattice planes in a specific crystalline material, this distance is defined as the diffraction parameter, d.[33] Additional parameters used in the Bragg equation are the scattering angle, θ, and the wavelength of the X-rays utilised, λ.[1]

$$2d \sin\theta = n\lambda \tag{1.1}$$

In order to resolve the diffraction pattern(s) and generate a structural representation of the crystalline material, a series of steps are performed. To start, a small series of diffraction patterns are collected to obtain both a crystal system that matches the lattice symmetry and a unit cell for the material. The unit cell describes the lengths, angles, and volume of the cell and is used to determine a collection strategy, the goal is to maximise the completeness and signal to noise ratio of the data whilst minimising the collection time. A 'collection' of the material is then undertaken whereby a large series of diffraction patterns are recorded over a range of different scattering angles, measuring the associated intensity data. The collection data is then integrated, generating a file known as a *hkl* file, which contains various hkl indices, diffraction intensities, estimated standard deviations, and associated structural factors.[33–35] The *hkl* file in conjunction with computer software, can then generate the three dimensional representation of the material.[1] This is where the 'phase problem' (discussed further below) is encountered. Refinement of the model structure is where small changes (placement of atoms) are made to the model in order to produce the best agreement between the calculated and observed structural factors. A visual representation of these steps for SCXRD can be seen in Figure 1.6.

One common problem encountered in XRD, specifically in SCXRD, is the 'phase problem'. Each X-ray wave that it is diffracted during the collection process has the following properties: wavelength, amplitude, and phase. Each diffraction pattern is a measure of intensity, which is directly proportional to amplitude^2, therefore the amplitude of each wave can be determined. The phase of each wave on the other hand is lost during the diffraction process, therefore a fourier transformation (the mathematical relationship between the electron density of the cell and the diffraction intensity) cannot be used to reproduce the corresponding electron density or the real space lattice of the material, as both the amplitude and phase are required.[35] There are a number of methods to overcome this, with the most common for small molecules ($<$ 1000 atoms) being direct methods and Patterson method, both of which require some assumptions such as the composition of the material to mathematically reproduce the missing 'phase' information.[33–36]

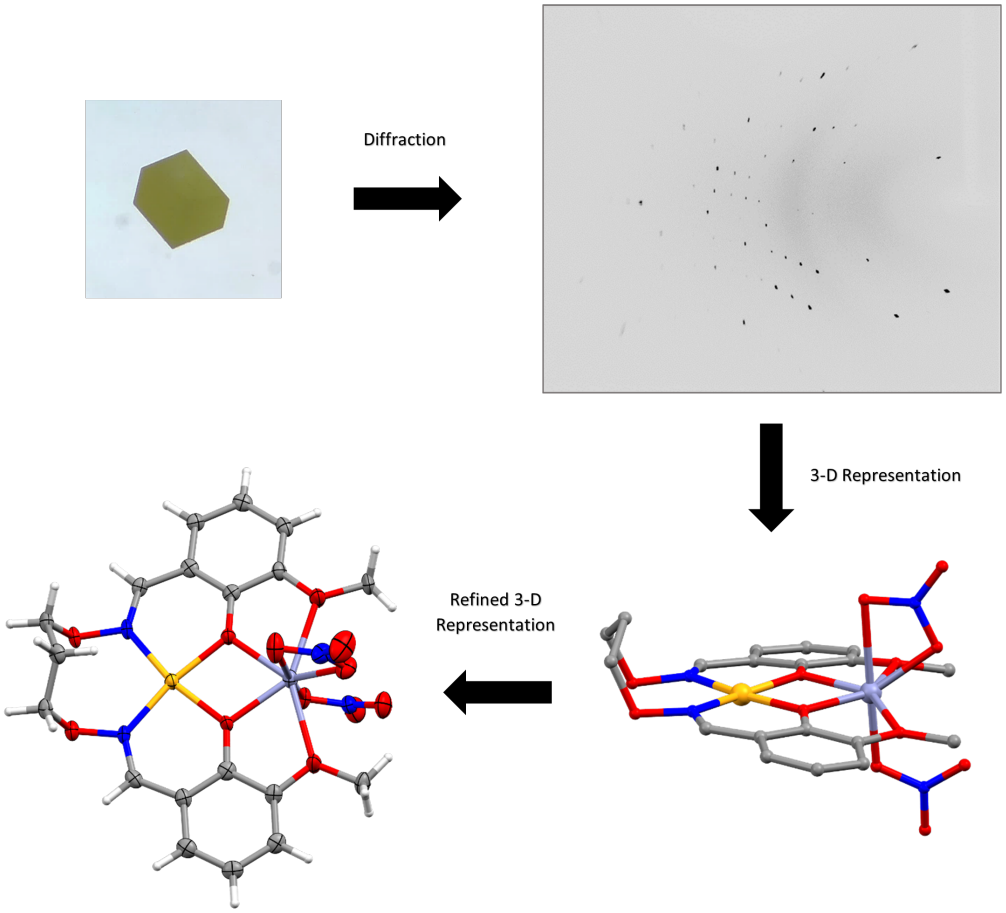

Figure 1.6: Simplified schematic illustrating the process of SCXRD; Top left, selected single crystal; Top right, a resulting diffraction pattern at a specific angle; Bottom right, resulting 3-D representation of the data; Bottom left, final refined 3-D representation of the data.

1.2.2 SQUID Magnetometry

A superconducting quantum interference device, or as more commonly known, a SQUID magnetometer is the most common instrument used to measure magnetic properties, specifically the magnetic susceptibility and/or magnetic moment of a polycrystalline material. By measuring subtle changes in the magnetic flux (Φ) of a material, directly related changes in the magnetic susceptibility/magnetic moment of the material can be measured. This arises from the relationship between Φ and magnetisation (M) (equation 1.2) alongside the flux coupling factor, α (a factor generated by the position and geometry of both the instrument and sample).[1,37–39]

$$\Delta\Phi = \alpha\Delta M \tag{1.2}$$

The measurement process to obtain the magnetic moment of a material begins by passing the material up and down a superconducting coil at constant speed, which generates a current (I), this current is specific to the material as it corresponds to the Φ and is directly applied to the SQUID. A SQUID magnetometer consists of a superconducting loop with at least two parallel Josephson junctions, a region where two superconductors are separated by a section of non-superconducting material (Figure 1.7). Josephson junctions are the result of the Josephson effect prediction made in the 1960s by Brian Josephson and measure changes in voltage, a measurement that can be manipulated to give the magnetic moment of a material. The applied current allows the superconductors electrons to tunnel through the non-superconducting region of the Josephson junction, which continues with no voltage associated (voltage = zero) until the critical current (I_c) of the instrument is reached producing a voltage across the Josephson junction. The voltage output can then be manipulated using software and computational methods to give the magnetic moment of the material.[1,39–42] Depending on the type of measurement being performed (discussed below), the measurement process is repeated multiple times at varying temperature.

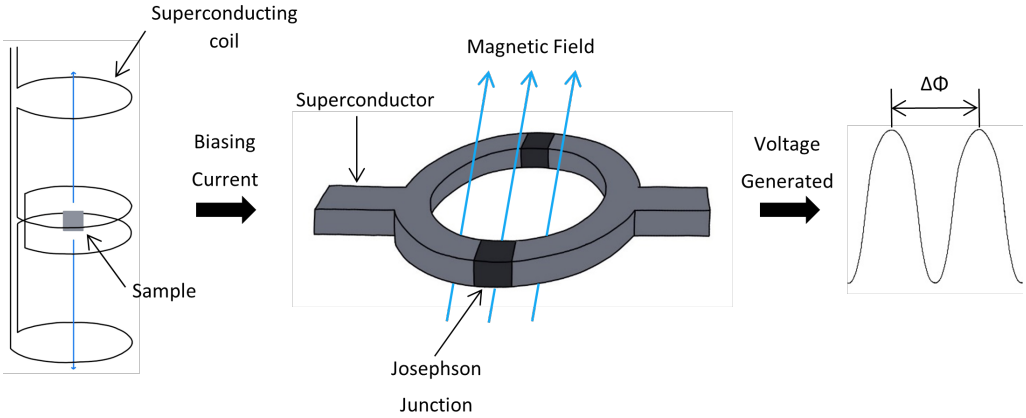

Figure 1.7: Schematic representation of the measurement process using a SQUID magnetometer.

A few of the different plots produced from data obtained from SQUID measurements can be seen in Figure 1.8. Plots a - d show direct current (DC) molar magnetic susceptibility and field dependence magnetisation measurements in an applied magnetic field over a temperature range (300 - 2 K). From these plots the nature of the magnetic susceptibility and spin states can be determined, for example plots

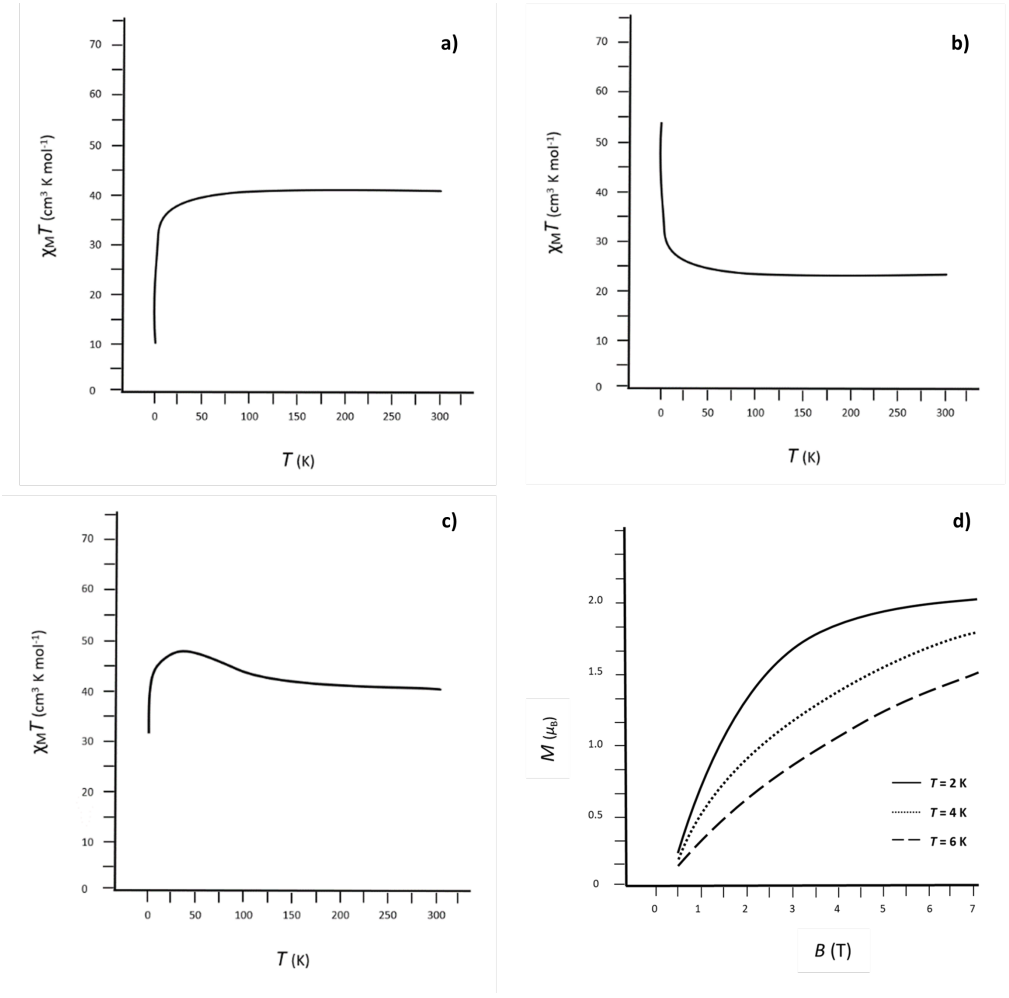

Figure 1.8: Example plots produced from data obtained by a SQUID magnetometer. a) Exhibits dominant AF exchange, b) Exhibits dominant F exchange, c) Exhibits competing AF and F exchange, d) The field-dependence of magnetisation for a given complex at specified temperatures (2, 4, and 6 K).

a and b are indicative of antiferromagnetic and ferromagnetic interactions respectively and plot c exhibits competing antiferromagnetic and ferromagnetic interactions. Plot d shows the field dependence of magnetisation at specified temperatures, used to determine the magnetic properties and any metal centre interaction at low temperatures. To further probe the magnetic properties of a complex, specifically to determine whether the complex behaves as an SMM, alternating current (AC) magnetic susceptibility measurements are performed with and without a magnetic field. AC susceptibilily measurements are a measure of the magnetic dynamic behaviour and from these plots, parameters such as the blocking temperature and effective barrier can be determined. As subtle changes in a material are measured, these samples need to have been prepared and handled carefully so that no impurities, no matter the quantity, are introduced as this can cause inaccurate results.[41]

1.2.3 Computational Analysis

Over the last few years, computational analyses, the most common being density functional theory (DFT), have become increasingly popular to investigate and model

properties such as the electronic structure and transition states but more commonly to corroborate experimental findings. DFT is a computational modelling method used to investigate the electronic structure of systems that consist of atoms, molecules and condensed phases.[43,44] A key premise of DFT is that the energy of a system can be determined solely from the distribution of the systems electron density instead of using many 'costly' wave functions.[1] In terms of this research, DFT calculations were used to perform broken symmetry analyses, geometry optimisations, and to determine thermodynamic properties for a series of complexes.

Broken Symmetry (BS)

Commonly when magnetic characterisation is performed on polynuclear complexes, a computational analysis is subsequently performed. This is to compare key parameters of the complexes magnetic properties, such as the magnetic exchange between metal ion(s), known as the Heisenberg exchange coupling constant, J. Experimentally, J is determined from fitting the magnetic data to a spin Hamiltonian equation, typically based off of the Heisenberg Dirac van Vleck Hamiltonian (Eqn 1.3), where $\hat{S}_A$ and $\hat{S}_B$ denote the spin operators for two metal centres, A and B.

$$\hat{H} = -2J\hat{S}_A\hat{S}_B \tag{1.3}$$

In order to calculate the spin Hamiltonian by general DFT methods, a large amount of computational cost is required in the form of multideterminant calculations which calculate the energy difference between the singlet and triplet states.[43,45] A common way researchers circumvent this is to use a Broken Symmetry (BS) DFT approach, as it has shown to have a lower computational cost while producing comparable results.[46,47] The BS approach uses a single determinant that calculates an in-between spin state ('imaginary' spin state), the BS spin state, which mixes properties of both the singlet and triplet states.[45–47]

As the goal of this analysis is to calculate J, additional schemes are required to connect the energy obtained from the BS calculation and J. There are three common methods used to calculate J from a BS approach, with two methods by Noodleman and Alvarez *et al*. which concern the weak and strong couplings.[48,49] The third method, which is the one used in this research, is by Yamaguchi and coworkers and accounts for both strong and weak couplings (Eqn 1.4), E_{HS} and E_{BS} describe the energies of both the high spin and BS states, and $\langle\hat{S}^2\rangle_{HS}$ and $\langle\hat{S}^2\rangle_{BS}$ describe the expectation values of the spin states.[50]

$$J = -\frac{E_{HS} - E_{BS}}{\langle\hat{S}^2\rangle_{HS} - \langle\hat{S}^2\rangle_{BS}} \tag{1.4}$$

1.3 Coordination Complexes

Throughout the literature there are numerous examples of coordination complexes, ranging from nuclearity of one to 490.[51] Complexes consisting of 3*d* and 4*f* ions, both homometallic and heterometallic (3*d*3*d* and 3*d*4*f*) have become increasingly popular as these metal ions have exciting properties for desired applications, such as catalysis, molecular magnetism, bioinorganic functions, extractive hydrometallurgy, and

photosynthetic pathways with researchers constantly striving to improve upon current models.[11,21,52–58] Other common metal ions found in both homometallic and heterometallic complexes are 2*p*, 4*d*, 5*d*, and 5*f*.

1.3.1 Homometallic Complexes

Over the years, a plethora of different homometallic complexes have been reported with a large proportion consisting of 3*d* or 4*f* ions. Popularity surrounding these metal ions has gone through many ups and downs over the years due to the rise and fall of various research topics. For example, in the 1990s and early 2000s, the popularity surrounding Mn, specifically Mn^{III} and Mn^{IV}, soared due to both the discovery of the first SMM in 1993 by Sessoli and coworkers and the X-ray structure determination of the oxygen-evolving centre, Mn_4Ca^{2+}, of Photosystem II.[59,60]

In 1980, a Mn_{12} cluster consisting of four Mn^{IV} and eight Mn^{III} ions was reported by Lis, who detailed the structural properties and magnetic moment of the complex (obtained by a Gouy balance).[61] Thirteen years later, more extensive magnetic properties of the same complex were reported by Sessoli *et al*. revealing the cluster known as Mn_{12} to be the first SMM.[59] Mn_{12} consists of a central tetrahedron of Mn^{IV} ions bridged by μ_3-oxide groups, surrounded by a ring of Mn^{III} ions with capping H_2O molecules and OAc^- groups bridging between both the Mn^{III} ions and the Mn^{III}/Mn^{IV} ions (Figure 1.9). Over the years, several researchers have produced different variations of Mn_{12}, with the benzoate (Bz^-) version, $[Mn^{IV}_4Mn^{III}_8O_{12}(Bz)_{16}(H_2O)_4]$, produced by Christou and coworkers producing analagous results to the original OAc^- version by Lis.[61,62] Both of these complexes were found to have a total ground spin state of S = 10 and as a result of the large anisotropy derived from the Jahn-Teller distorted Mn^{III} ions, the ground states were split by ZFS resulting in bistable wells (similarly to Figure 1.1) and an effective barrier of 60 - 64 K (86.34 - 92.10 cm^{-1}).[61,62]

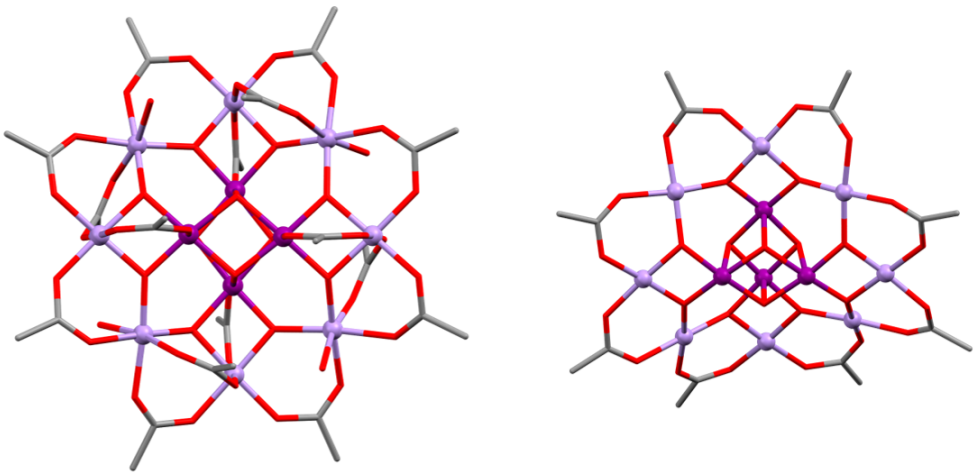

Figure 1.9: Crystal structure of Mn_{12}, $[Mn^{IV}_4Mn^{III}_8O_{12}(OAc)_{16}(H_2O)_4]$ produced by Lis with two different orientations.[61] Hydrogen atoms, lattice solvent molecules, selected bridging OAc^- groups (right), and H_2O molecules (right) have been omitted for clarity. Colour code: Mn^{IV} = dark purple, Mn^{III} = light purple, O = red, and C = grey.

As mentioned for Mn_{12}, the anisotropy of the complex was derived from the Jahn-Teller effect, which is one of the main reasons for the popularity surrounding Mn^{III} ions. The Jahn-Teller effect is commonly seen in d^9, low spin d^7, and high spin d^4 metal ions due to their electron configurations having doubly degenerate states. As this is not energetically favourable, the metal ion will attempt to reduce the energy of the states by distorting the metal geometry along an axis, typically resulting in the elongation of the axial coordinates.[63,64] Many researchers exploit the Jahn-Teller effect to enhance the anisotropy of a complex, specifically for use in magnetic materials or SMMs. One group that successfully exploited the Jahn-Teller effect was the Brechin group, when they successfully produced a Mn^{III}_6 double triangular cluster, $[Mn^{III}_6O_2L_6(Bz(Me)_2)_2(EtOH)_6]$ (L = 2-hydroxyphenylpropanone oxime), a record SMM of its time.[65] This complex consists of two triangles made up of three Mn^{III} ions coordinated to an oximato ligand, bridged by μ_3-oxide and oximato nitrogen and oxygen atoms (Figure 1.10). The two triangles are bridged by two oximato oxygens, with capping EtOH and 3,5-dimethylbenzoyl ($Bz(Me)_2$) molecules. The combined enhanced anisotropy and structural torsion induced by structural bulk and M-N-O-M bridging produced an effective barrier of 86.4 K (60.04 cm^{-1}) and a blocking temperature of 4.5 K. One of the favourable properties of 3*d* ions, which has maintained their popularity as magnetic materials for several decades is their effective orbital overlaps, which allow for metal-ligand interactions and magnetic exchange, both appealing properties for magnetic materials.[7,21]

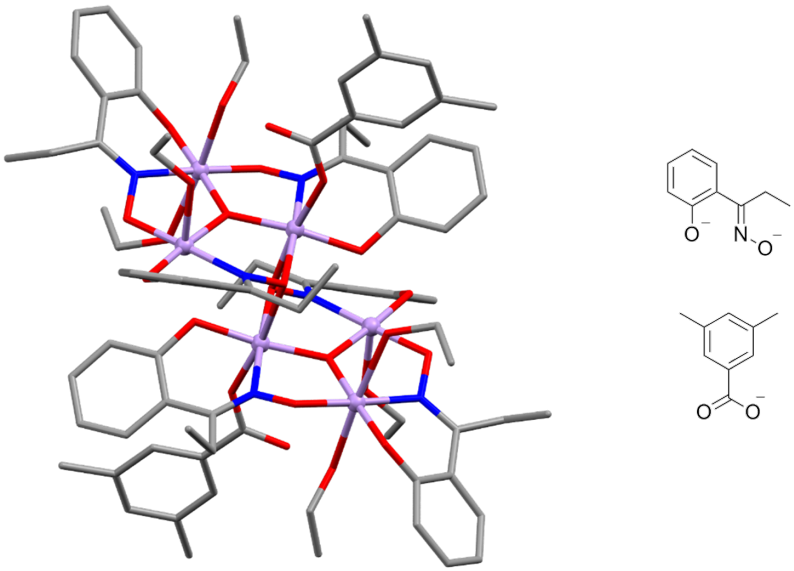

Figure 1.10: Crystal structure of the record SMM, $[Mn^{III}_6O_2L_6(Bz(Me)_2)_2(EtOH)_6]$, produced by the Brechin group, which exploits the Jahn-Teller effect.[65] Hydrogen atoms have been omitted for clarity. Colour code: Mn^{III} = light purple, N = blue, O = red, and C = grey.

Apart from Mn^{III} ions, another popular metal ion in the field of magnetochemistry and SMMs is Co^{II}. The research groups of Banerjee *et al.*, Chandrasekhar *et al.*, Zhu *et al.*, and Buvaylo *et al.* all report mixed valence Co^{II}/Co^{III} based complexes, both dinuclear and tetranuclear, that display SMM properties to varying degrees (Figures 1.11 and 1.12).[66–69] Although all of the complexes are mixed valence, for the purpose of magnetic characterisation they are all considered as mononuclear Co^{II} due to the

low spin and diamagnetic nature of the Co^{III} ions.[66] The star-shaped complex by Zhu *et al*. was found to display SMM properties under no magnetic field, with a reported effective barrier of 109 K.[68] The opposite was found for the complexes by Banerjee *et al*., Chandrasekhar *et al*., and Buvaylo *et al*. as these complexes were all reported to have zero SMM properties under a zero field, due to QTM, however upon applying an external magnetic field they displayed SMM properties.[66,67,69] These complexes are considered field-induced SMMs. A field-induced SMM is a complex that shows no signal when AC magnetic measurements are performed with an applied DC field of zero, an indication of an absence of slow relaxation of magnetisation or in this case, the presence of QTM quenching. However when the AC measurements are performed with a non-zero applied DC field, these complexes show a signal/maxima indicating they do indeed have SMM properties.[66,70,71]

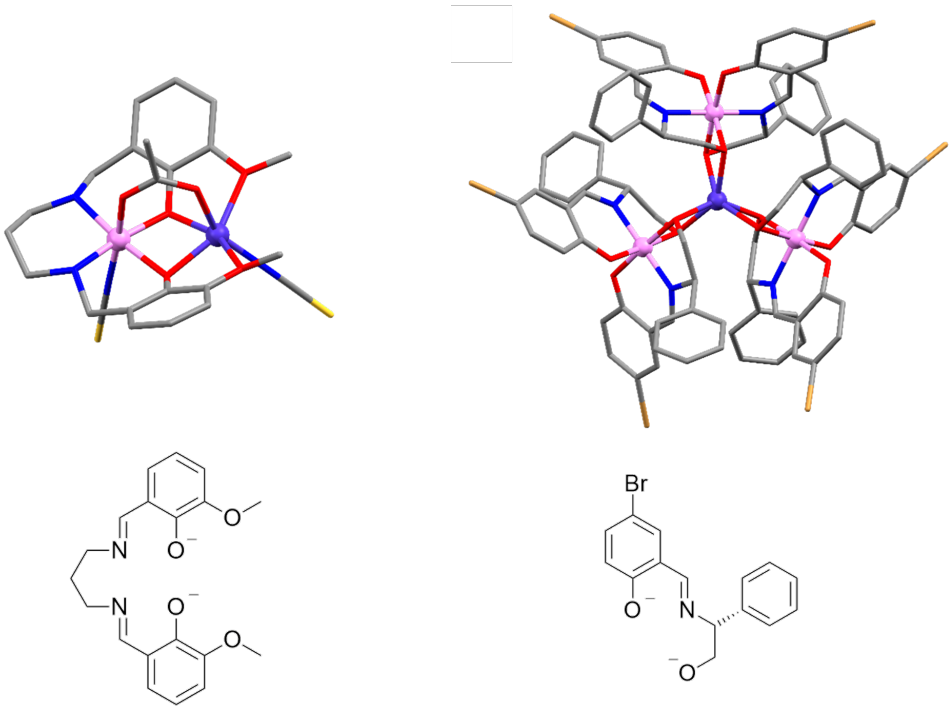

Figure 1.11: Crystal structures of two of the $Co^{II}Co^{III}$ SMMs produced by the Banerjee (left) and Zhu (right) research groups.[66,68] The ligands for both complexes can be found below the corresponding structure. Hydrogen atoms and lattice solvates have been omitted for clarity. Colour code: Co^{III} = pink, Co^{II} = purple, N = blue, O = red, S = yellow, Br = light orange, and C = grey.

Aside from 3*d* based coordination complexes, another popular type of homometallic complexes are 4*f* based ones. The popularity of 4*f* complexes has arisen from the field of magnetochemistry, especially in relation to SMMs, however homometallic 4*f* complexes also have potential for application as luminescent devices,[72] MRI contrast agents,[55] and in fields such as catalysis[53] and bioimaging/sensing.[57]

4*f* based SMMs have gained popularity since 2003 when Ishikawa *et al*. reported the first example.[73] One key property of 4*f* ions is that their magnetic moments arise from the inner shell orbitals, not the outer shell orbitals like 3*d* ions. This produces

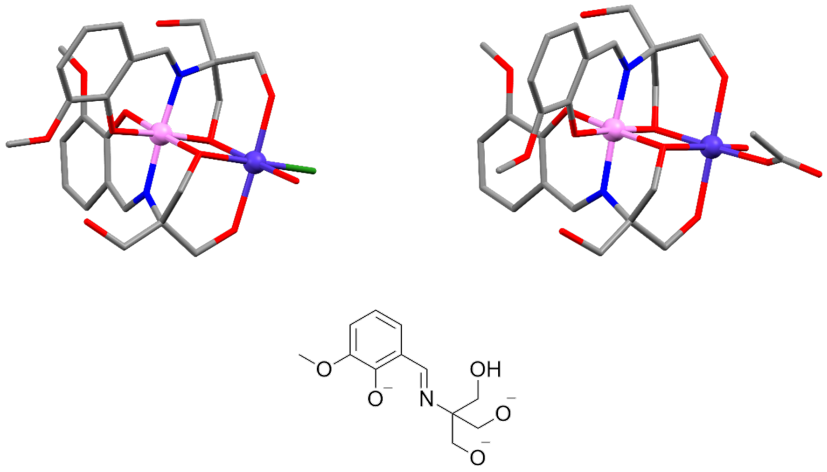

Figure 1.12: Crystal structures of two of the $Co^{II}Co^{III}$ SMMs produced by the Chandrasekhar (left), and Buvaylo (right) research groups.[67,69] The ligand used for both complexes can be found below the structures. Hydrogen atoms and lattice solvates have been omitted for clarity. Colour code: Co^{III} = pink, Co^{II} = purple, N = blue, O = red, Cl = green, and C = grey.

the 'shielding' effect, as the electrons in the outer shells 'shield' the inner shell electrons resulting in no quenching of the OAM. This however results in limited possibilities for the overlap of orbitals of neighbouring ions and weak ligand field interactions. Although the weak metal-ligand interactions are not desirable, it means the anisotropy of the complex is derived solely from the metal ion(s), which can be further enhanced by careful ligand design.[2]

For 4*f* ions, the nature in which bistable ground states are determined does not solely result from ZFS, however it results from the interaction between orbital motion and a magnetic dipole, known as spin-orbit coupling (SOC). For 3*d* ions, the only parameter needed for the splitting of the ground state is *S*, however for 4*f* ions, two additional parameters, *J*, the total angular momentum quantum number, and *L*, the total orbital quantum number, are required to give the ground state splitting as $[2J + 1]M_J$ microstates within the ground term, $^{2S+1}L_J$. When a metal ion has an odd number of ground state electrons, it is referred to as a Kramers ion, for example Dy^{III} has a ground state of 15/2 and will always have a bistable ground state no matter the ligand field symmetry.[74] Non-Kramers ions, for example, Tb^{III} are not guaranteed to have bistable ground states, however, when the anisotropy of the ion is enhanced by the ligand field, a bistable ground state can be achieved. There are two main types of electron distributions found for 4*f* ions, prolate and oblate, as shown in Figure 1.13. Each distribution has a preferred ligand field symmetry and subsequent geometry, which has been shown to enhance the anisotropy of the metal ion. Ions with oblate electron distributions, such as Ce^{III}, Tb^{III}, and Dy^{III} prefer a ligand field and geometry where the ion is coordinated to axial donors, whereas ions with prolate electron distributions, such as Er^{III} and Yb^{III} prefer a ligand field and geometry where the ion is coordinated to equatorial donors (Figure 1.13).[16,21,22,74]

Exploiting the anisotropy of 4*f* ions has been a focus of SMM researchers for several years, with efforts coming to fruition in 2018 with the current record holding SMM for both blocking temperature and effective barrier produced by the Layfield group.[19] The record breaking anisotropy of the mononuclear Dy^{III} complex was achieved by enhancing the ligand field and preserving the OAM and SOC of

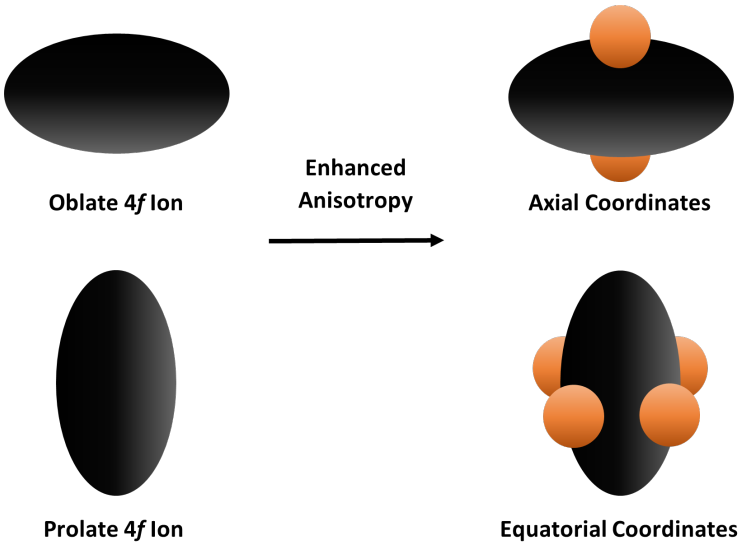

Figure 1.13: Schematic representation of how ligand coordinates can enhance the anisotropy of different orbital shapes found for 4*f* ions.

the Dy^{III} ion, quenching any QTM effects (See Section 1.1.1).[19] The design of this record SMM was built off of the success of the previous record holder that was produced by the same researchers in 2017.[75] The Layfield group utillised Cp derived ligands to coordinate to the Dy^{III} ions axially, enhancing the anisotropy of the ion. The 2017 record SMM (Figure 1.14, left) consisted of Cp^{tBu} (1,3,5-tri-*tert*-butylcyclopentadienyl) ligands, the repulsion of which produced a 'bent' structure with a Cp^{tBu}-Dy^{III}-Cp^{tBu} angle of 152.8°.[75] By creating an asymmetric complex using Cp^* and Cp^{iPr_5} ligands, the Layfield group were able to reduce the repulsion and create a complex with a more linear Cp^{iPr_5}-Dy-Cp^* angle of 162.5°, resulting in increased anisotropy and a new record breaking SMM.[19]

1.3.2 Heterometallic Complexes

There are a broad range of heterometallic coordination complexes found in the literature with 3*d*3*d*', 3*d*4*f*, and 3*d*5*f* to name a few. They are used in applications such as catalysis,[76,77] molecular magnets,[23] magnetic refrigeration,[23,78] biotechnology,[54] and anticancer agents.[79]

One of the largest obstacles faced when producing heterometallic complexes, specfically 3*d*4*f*, is that both 3*d* and 4*f* ions are classed as 'hard acids' and prefer similar donor atoms.[1] This makes the ligand design important as the binding sites need to be substantially different in order for the ligand to coordinate the different metal ions.[20,80–82] There are of course examples throughout the literature, where heterometallic 3*d*4*f* complexes have been produced using ligands with symmetric binding sites, however for the majority of complexes, this is not the case.[83] Common methods used to combat this issue either produce ligands that have rigid size preferential binding sites, and/or use a mixture of donor atoms. It is well reported that 4*f* ions are largely oxophilic, with few cases where the donor atoms are nitrogen, whereas 3*d* ions will coordinate to a larger range of atoms.[20,80–82]

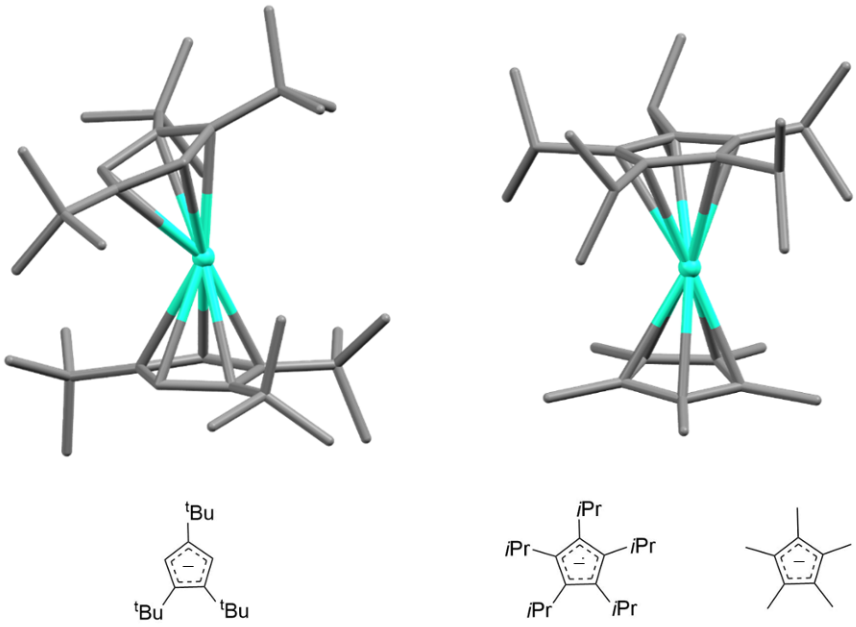

Figure 1.14: Crystal structures and corresponding ligands of the record SMMs, $[(Cp^{tBu})_2Dy^{III}]^+$ (left) and $[Cp^{iPr5}Cp^*Dy^{III}]^+$ (right), produced by Layfield and coworkers.[19,75] Hydrogen atoms and lattice anions have been omitted for clarity. Colour code: Dy^{III} = aqua and C = grey.

One of the more common applications for 3*d*4*f* complexes is magnetic materials or molecular magnets.[9,84] The use of 3*d*4*f* complexes were initially proposed as a response to combat the unfavorable properties of the individual homometallic 3*d* and 4*f* complexes.[9,85,86] It was hoped that by combining the large anisotropy of the 4*f* ions with the metal-ligand interactions and magnetic exchange of the 3*d* ions, QTM effects and the rapid quenching of magnetisation would be reduced.[5,16,17,81] This however was found to not be the case for the majority of examples as similarly to the homometallic 4*f* SMMs, the persistence of QTM effects resulted in negilible SMM properties.[87]

Currently, the 3*d*4*f* SMM with the highest effective barrier is a trinuclear $Co^{II}{}_2Dy^{III}$ complex produced by Tong and coworkers (Figure 1.15).[88] By manipulating the coordination environment of the metal ions, researchers found that the effective barrier height and rate at which QTM relaxed the system could be increased and decreased respectively. Tong and coworkers were able to achieve this remarkable property, an effective barrier of 600 K (416 cm^{-1}), by simple manipulation such as the desolvation of a complex or single-crystal-to-single-crystal transformations. The dehydration of a precursor complex resulted in an alteration of the Co^{II} ion geometry, shifting from distorted octahedral towards a more trigonal prismatic geometry. This subsequently caused the axial coordinates on the Dy^{III} ion to lengthen and elongate along the anisotropic axis or 'easy axis' resulting in greater magnetisation and a greater effective barrier. Although as mentioned previously, the combination of the 3*d*4*f* ions did not prevent the QTM, and no blocking temperature was obtained.

Throughout the literature, heterometallic SMMs are typically of the 3*d*4*f* composition however there are a few examples of heterometallic 3*d*3*d*' SMMs. Similarly to the 3*d*4*f* counterparts, the ligand design is crucial as the desired ions coordinate to

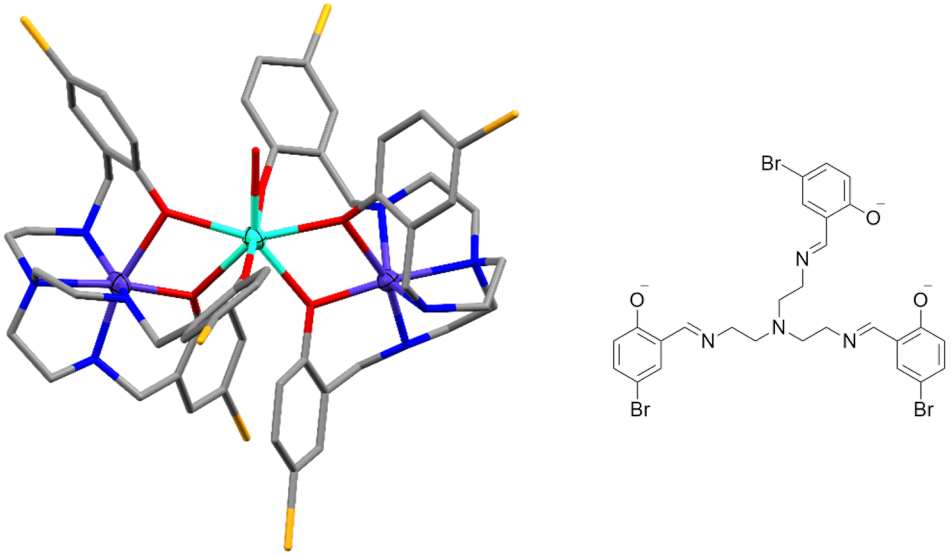

Figure 1.15: Crystal structure of the current record holding 3*d*4*f* SMM, $[Co^{II}_2Dy^{III}L_2(H_2O)][NO_3]$, produced by Tong and coworkers.[88] Hydrogen atoms, and lattice NO_3^- anions have been omitted for clarity. Colour code: Dy^{III} = aqua, Co^{II} = purple, N = blue, O = red, Br = yellow, and C = grey.

similar environments. The solution to this is compartmental ligands, as described above, where the binding pockets are asymmetrical in both donor groups and size, giving preference to one metal ion over the other. The research group of Zhou illustrated this concept when they produced a $Zn^{II}Mn^{II}$ complex (Figure 1.16) with an asymmetric macrocyclic ligand to aid in the binding and cleavage of DNA.[54] Zhou *et al*. compared their heterometallic complex against literature examples of similar homometallic systems and found that their system had a higher rate of cleavage, which was attributed to the combination of the two different metal ions among other things.

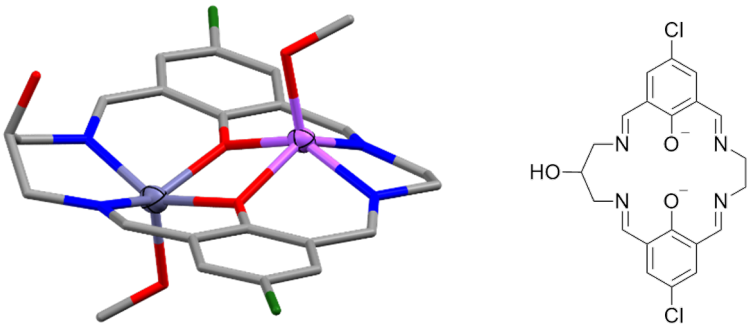

Figure 1.16: Crystal structure of the 3*d*3*d*′ complex, $[Zn^{II}Mn^{II}L(MeOH)_2]\cdot H_2O$, produced by Zhou *et al*. to bind and cleave DNA.[54] Hydrogen atoms and lattice H_2O molecules have been omitted for clarity. Colour code: Mn^{II} = purple, Zn^{II} = light blue, N = blue, O = red, Cl = green, and C = grey.

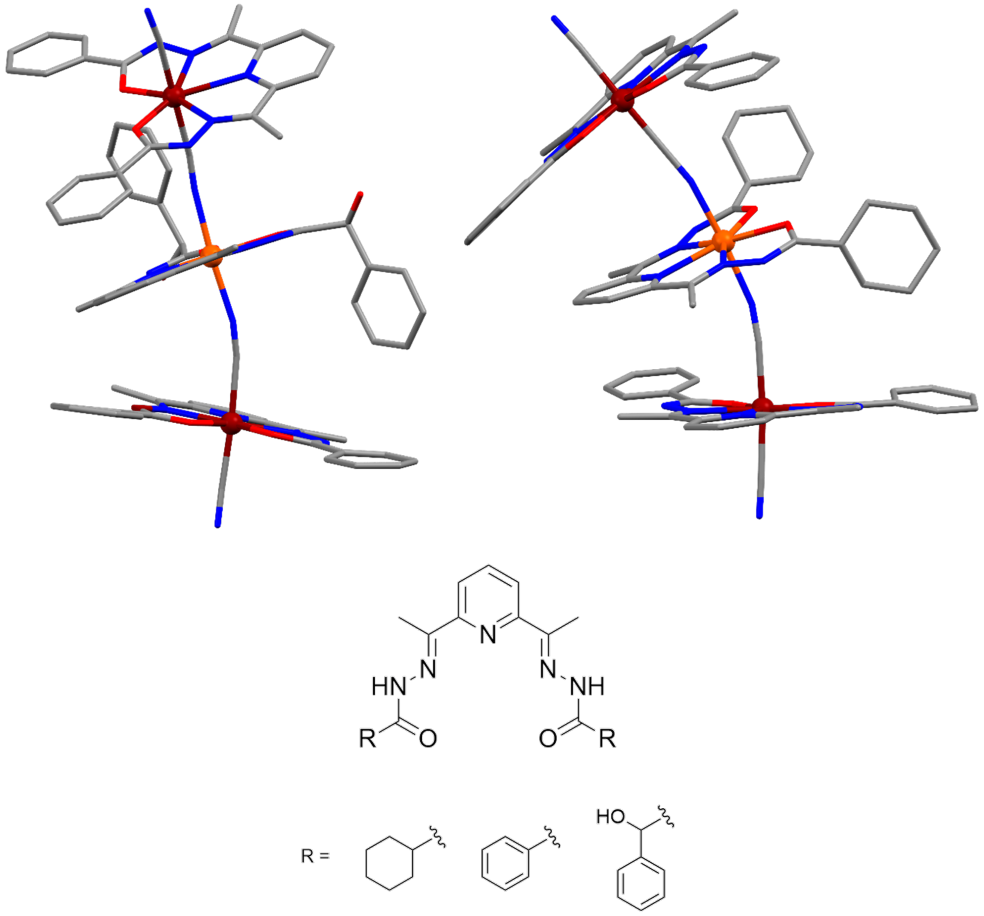

Figure 1.17: Crystal structures of the chain-like $Fe^{II}Cr^{III}_2$ complexes produced by Pichon *et al.*[89] Hydrogen atoms and lattice solvates have been omitted for clarity. Colour code: Cr^{III} = dark red, Fe^{II} = orange, N = blue, O = red, and C = grey.

Another 3*d*3*d*′ SMM example is the trinuclear chain-like $Fe^{II}Cr^{III}_2$ complex produced by Pichon *et al.* (Figure 1.17, left), which was found to have an effective barrier of 35 K.[89] When producing the $Fe^{II}Cr^{III}_2$ SMM, Pichon *et al.* found that the 'straightness' of the CN-Fe linkages was important as an analgous $Fe^{II}Cr^{III}_2$ complex (Figure 1.17, right) produced was 'bent' approximately 20° more than the original complex and resulted in no significant SMM properties. This result resembles what was found by Layfield and coworkers, that by straightening the M-L linkages along or towards the anisotropic axis, the magnetic properties of the complex are enhanced.[19,75,89]

1.3.3 Defective Dicubanes

Throughout the field of coordination chemistry, there is a large number of different topologies, such as catenanes, rotaxanes, knots, helicates, triangles, and squares to name a few, with one topology of interest being cubanes.[90–92] A cubane is a tetranuclear structure where metal ions and μ_3 bridging groups occupy alternating vertices as show in the schematic on the left in Figure 1.18.[93] The defective dicubane topology is a subset of a cubane as it refers to a tetranuclear structure with alternating metal ions and $\mu_{2/3}$ bridging groups however it is composed of two face sharing cubanes, each with an opposite vertice missing (Figure 1.18, right).[94,95]

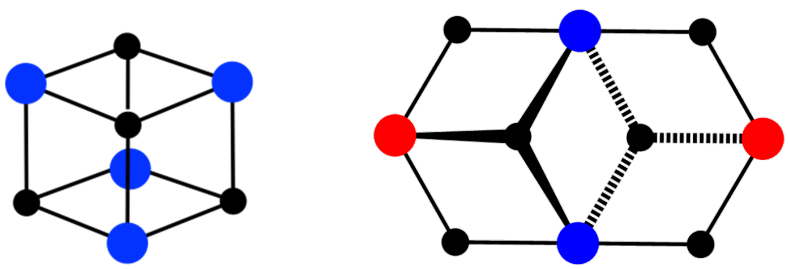

Figure 1.18: Schematic representation of both a cubane (left) and a defective dicubane (right). The coloured circles represent the metal ions (blue circles the 'body' ions and the red circles the 'wingtip' ions for the defective dicubane) and the black circles the bridging groups.

Defective dicubanes are commonly referred to as 'butterfly' structures with the two central metal ions the 'body' and the two outer metal ions the 'wingtips'.[95] This nomenclature is commonly used as the metal ion composition can vary, such as the dicubane can be homometallic, heterometallic, or the oxidation state of the metal ions can vary within the one structure. Specifically for heterometallic/varied oxidation cases, the nomenclature is useful as the different metal ions will always either be in the 'body' or 'wingtip' positions.[96–98] The use of this nomenclature was shown in the research reported by Peng *et al*. where they produced two heterometallic defective dicubanes with similar composition, however they were able to switch the metal ion positions corroborating that the ion pairs are always either in the body or wingtip positions.[99] Peng *et al*. achieved the different ion placements through the use of two common synthetic methods: stepwise and one-pot syntheses (Figure 1.19 bottom and top respectively). Stepwise synthesis for heterometallic complexes involves the coordination of one metal ion prior to coordination of the second metal ion whereas a one-pot synthesis involves adding both metal ions simultaneously.[99]

Defective dicubanes have been utilised in several applications such as catalysis, luminescent devices, and magnetic materials.[100–103] The popularity and appeal of this topology arose from both its possible application in magnetic materials but also the ease at which the exchange pathways and composition can be manipulated.[104,105] The literature has shown that by optimising these exchange angles for ferromagnetic exchange, QTM effects can be reduced and/or effectively quenched, as shown by the research groups of Powell, Tian and Liu.[8,101,106–108] An effective way researchers have found to alter these exchange pathways is to change the composition of the structure, whether it be to change the metal ions, bridging groups, or solvent and anions found in the crystal lattices.[101,106]

Although most defective dicubanes are produced for their luminescence or magnetic properties, there are several examples where the defective dicubanes have been utilised for catalysis.[52,109–111] The Kostakis group have explored the use of defective dicubanes as catalysts for several named reactions, such as the Michael addition and Friedel-Crafts alkylation, with more recent work looking at the metal-promoted Suzuki-Miyaura coupling reaction.[52,109,110] Their chosen defective dicubane had a $Cu^{II}Dy^{III}$ core, which was coordinated to four ligands ((*E*)-2-(2-hydroxy-3-methoxybenzylideneamino)phenol), two MeCN molecules, and two NO_3^- anions (Figure 1.20). The research group tested their defective dicubane in a coupling reaction between

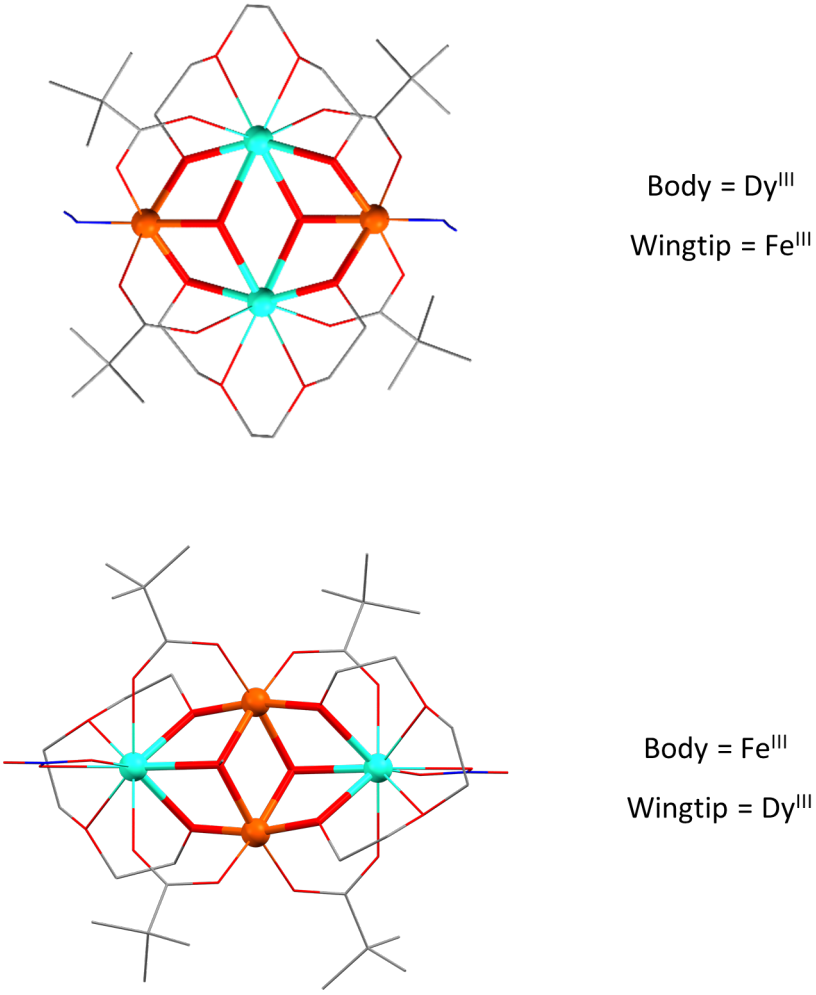

Figure 1.19: Crystal structures of the defective dicubanes, $[Fe^{III}_2Dy^{III}_2(OH)_2(teg)_2(N_3)_2(piv)_4]$ (teg = triethylene glycol, piv = pivalic acid) (top) and $[Fe^{III}_2Dy^{III}_2(OMe)_2(teg)_2(NO_3)_2(piv)_4]$ (bottom), produced by Peng *et al.* illustrating the body/wingtip nomenclature.[99] Hydrogen atoms apart from those attached to donor atoms have been omitted and peripheral ligands and anions shown as wireframe for clarity. Colour code: Dy^{III} = aqua, Fe^{III} = orange, N = blue, O = red, and C = grey.

aryl halides and phenylboronic acids in DME : H_2O (1 : 1) and when compared to other Cu^{II} catalysts, the dicubane produced analogous results with a reduced amount of the Cu based catalyst.

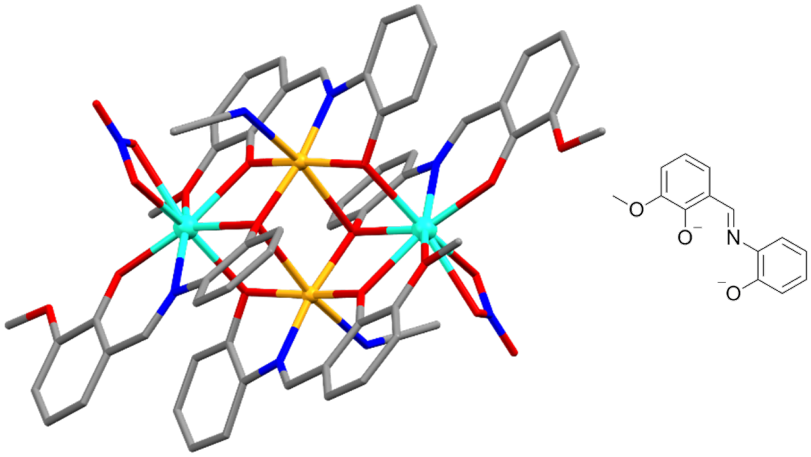

Figure 1.20: Crystal structure of the defective dicubane, $[Cu^{II}_2Dy^{III}_2L_4(NO_3)_2(MeCN)_2] \cdot 2MeCN$, produced by the Kotastkis group for use as a catalyst in a Suzuki-Miyaura reaction.[52] Hydrogen atoms and lattice MeCN molecules have been omitted for clarity. Colour code: Dy^{III} = aqua, Cu^{III} = yellow, N = blue, O = red, and C = grey.

1.3.4 Transmetalation

Transmetalation is an organometallic reaction commonly used in synthetic chemistry. It is an irreversible reaction that covers a range of processes such as the transfer of a ligand from one metal ion to another or the exchange of one or more metal ions in a polymetallic cluster.[1,112,113] These transmetalation processes are commonly seen in catalysis and the synthesis of main group and transition metal complexes.[1,114]

Transmetalation is most commonly seen in catalytic cross-coupling reactions, such as the Suzuki-Miyaura and Sonogashira cross coupling reactions (Figure 1.21). These reactions involve the use of first and second row transition metal catalysts such as Cu^{II} and Pd^{II}, which catalyse the carbon-carbon bond formation between organohalides and alkynes or organoboron species.[115] These reactions occur when the 'ligands' of the two catalytic metals transmetalate, specifically, the two organo species will both 'end up' on the Pd^{II} catalyst as it is the more electropositive metal. A subsequent reductive elimination then gives the new carbon-carbon bond.[1,114,115]

The synthesis of new transition metal complexes by transmetalation is similar to that of the before mentioned catalytic cross coupling reactions, the goal however is not to form new organic compounds but to exchange one or more metal ions.[113] This form of transmetalation is commonly used to synthesise complexes, which have difficult syntheses. In theory, to produce a complex by transmetalation, the initial complex would need to be produced with a more electronegative metal ion as ligands are typically more attracted to electropositive metals. Common methods for transmetalation of transition metal complexes is by routes such as single-crystal-to-single-crystal transformations and *in situ* reactions.[1,114,116,117]

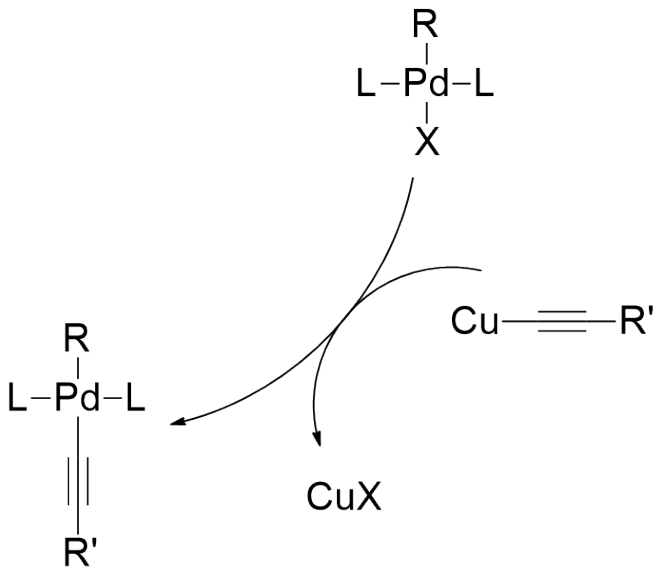

Figure 1.21: Schematic showing the transmetalation step of the Sonogashira catalytic cycle.

The use of transmetalation to produce new transition metal complexes has been demonstrated by the research group of Kleij who reported a series of 3*d* salphen (*N*,*N*′-phenylenebis(salicylidene-imine)) complexes that originated from a Zn^{II} salphen complex, as shown by the Zn^{II} to Ni^{II} example (Figure 1.22).[116] The purpose of this research was to explore the different functions of this ligand framework and how supramolecular and catalytic properties could be switched on and off in solution.

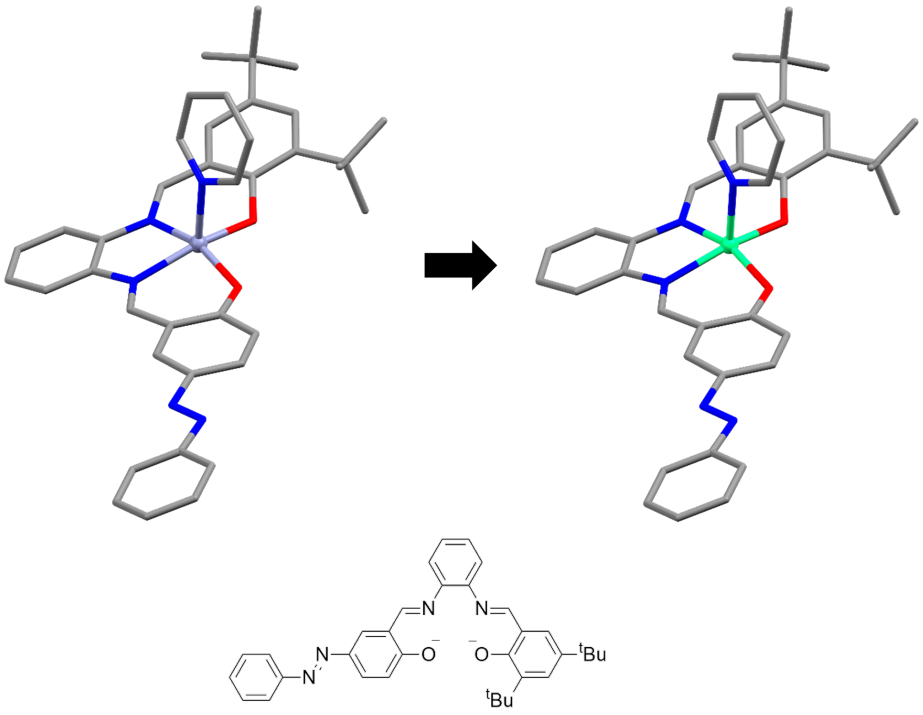

Figure 1.22: Transmetalation reaction used by the research group of Kleij to produce new 3*d* complexes. Hydrogen atoms have been omitted for clarity. Colour code: Zn^{II} = light blue, Ni^{II} = green, N = blue, O = red, and C = grey.

As mentioned above, transmetalation reactions typically follow the general trend of the ligands being attracted to the more electropositive metal ion however this is not always the case for 3*d* complexes as these have additional rules and/or trends of coordination. One such trend of coordination is the relative stability of the complex formed, which is known as the Irving-Williams series: Mn < Fe < Co < Ni < Cu > Zn.[118] The Irving-Williams series describes a stability trend found for 3*d* ions in the +2 oxidation state. The trend suggests that the stability increases across the periodic table, reaching a maximum at Cu^{II}.[118] The trend is supported by a number of explanations with a few key ones being that as you move along the first row of the 3*d* ions, both the ionic radius and crystal field stabilisation energy increase, supporting the increase in stability seen across the row. Although Cu^{II} doesn't fit the trend for having the highest stability, it is thought that octahedral Cu^{II} complexes have increased stability as a result of the Jahn-Teller effect.[1,64,116,117] This doesn't explain the effect for non-octahedral Cu^{II} complexes, however that is a phenomenom not well understood by researchers. Upon discovering the trend, it was found that it was independent of the ligand, however for most ligands the trend holds up as shown in Figure 1.23 and this has been further corroborated throughout the literature.[117,119,120]

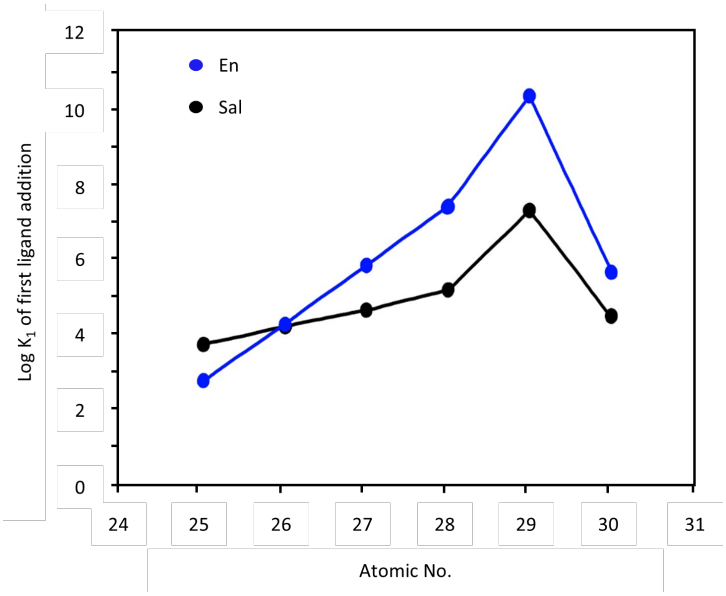

Figure 1.23: Schematic representation of the log K_1 plots for the first addition of ligand (L), ethane-1,2-diamine (En, blue) and salicylaldehyde (Sal, black) to metal ions with a +2 charge.

There are several examples where the Irving-Williams series has been exploited to synthesise new transition metal complexes and macrocycles, which only form through transmetalation or template reactions. An example of this is the Cu^{II} coordination polymer reported by Kumar *et al.* that only forms through a transmetalation reaction of the Zn^{II} complex (Figure 1.24).[117] The transmetalation method used was a single-crystal-to-single-crystal transformation, which allowed for the reaction to be monitored by the crystals changing colour. When the researchers attempted to reproduce this complex initially, they found that the initial complexation reaction with the Zn^{II} salt subsituted for a Cu^{II} salt produced a different Cu^{II} coordination polymer.

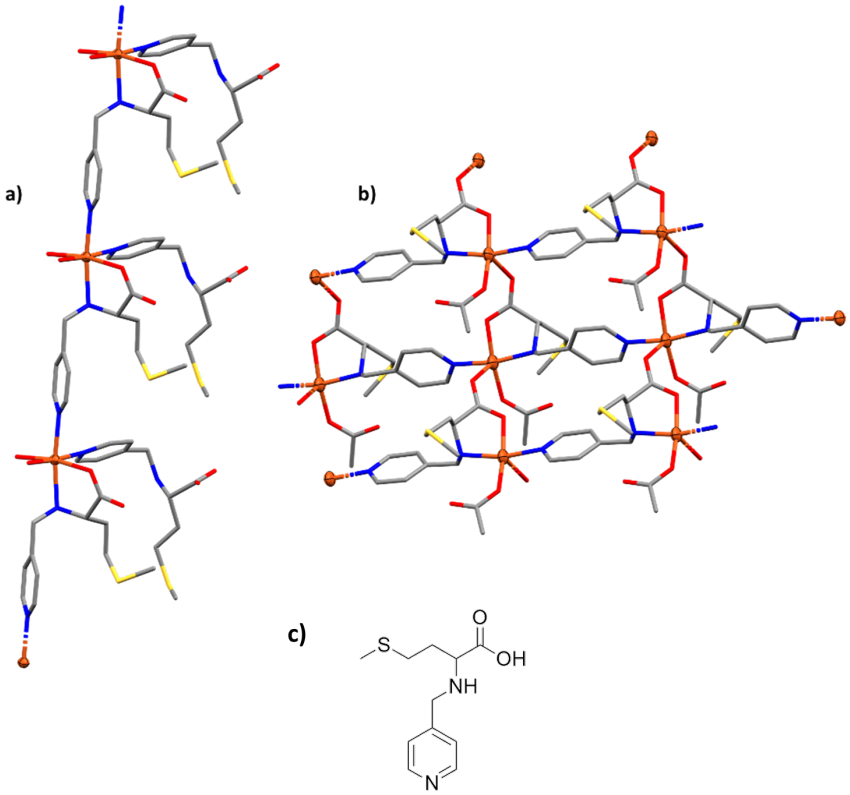

Figure 1.24: Crystal structures of the Cu^{II} polymeric complexes, $[Cu^{II}(L)(HL)(H_2O)_2]_n$ (left) and $[Cu^{II}(L)(CH_3COO)]_n$ (right), produced by Kumar *et al.*[117] The polymer on the left is the result of transmetalation whereas the polymer on the right is the result of an *in situ* reaction. Hydrogen atoms have been omitted for clarity. Colour code: Cu^{III} = orange, N = blue, O = red, S = yellow and C = grey.

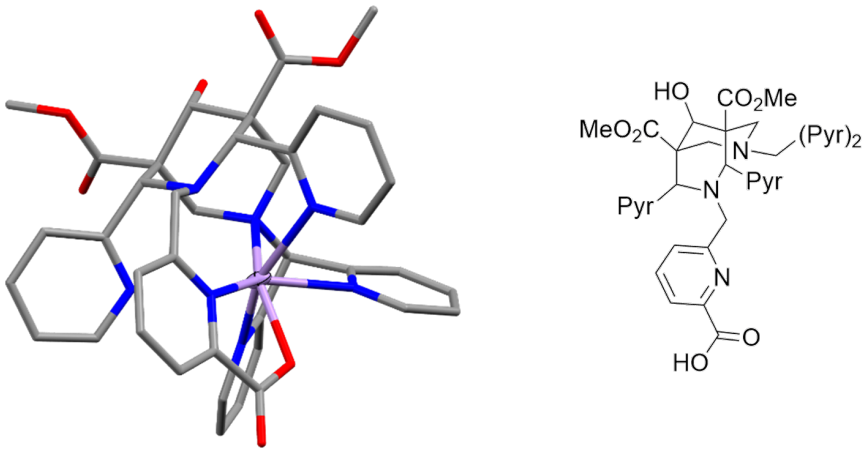

Figure 1.25: Crystal structure of the Mn^{II} complex, $[Mn^{II}L]$, produced by Cieslik *et al.*, which does not follow the Irving-Williams series.[121] Hydrogen atoms have been omitted for clarity. Colour code: Mn^{II} = purple, N = blue, O = red, and C = grey.

As mentioned above, the Irving-Williams series is independent of the ligand being utilised, with the trend holding up for a large majority of complexes. However, several researchers have found that the trend does not apply to their ligand framework. This was seen in the research of Cieslik *et al.* who were trying to achieve a framework that would selectively coordinate Mn^{II} ions in the presence of Zn^{II} ions as 1) they are more abundant in biological enviroments and 2) according to the Irving-Williams series more stable when coordinated.[121] They found that when the corresponding ligand was large, rigid, and could fully encapsulate the metal ion, the relative stability of Mn^{II} versus Zn^{II} was reversed. The ligands they utilised in this research were bispidine derivatives that incorporated ester, acid and pyridyl functional groups (Figure 1.25).[121]

1.4 Salicylaldehyde and its Many Derivatives

Throughout the literature, there are many different examples of ligands used in coordination complexes. Different types of coordination complexes have different requirements for a ligand such as for 4*f* based complexes the donor groups should be predominantly oxygen, whereas for 3*d* based complexes, donor groups such as oxygen, nitrogen, sulfur, phosphorus, chloride, and fluoride are all acceptable.[1] For heterometallic complexes, specifically 3*d*4*f* complexes, the design of the ligands and donor groups is important so that each metal ion has a specific 'pocket' allowing for the heterometallic coordination to be successful.[20,82]

One molecule and its derivatives that have been used as chelating ligands for many years, is salicylaldehyde (Sal). Sal and its derivatives such as salicylaldoxime and saliylaldimine are popular choices for chelating ligands as they are capable of coordinating both 3*d* and 4*f* ions and can form heterometallic complexes when appropriately functionalised. These ligands can also act as starting points for further derivation, such as *o*-alkyloxime ligands (Figure 1.26).

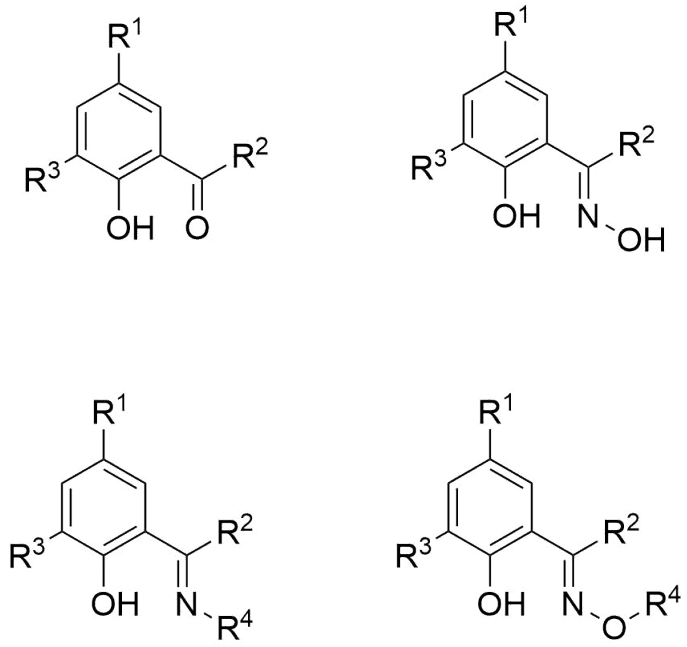

Figure 1.26: Schematic representations of salicylaldehyde (top left) and its derivatives salicylaldoxime (top right), salicylaldimine (bottom left), and *o*-alkyloxime (bottom right).

Sal has been used as a chelating ligand since it was first reported in 1930.[122] Various derivatives of Sal are found throughout the literature with common derivatives featuring methoxy, bromomethyl, ^{t}Bu, methyl, nitro, and amino groups. Coordination complexes utilising Sal derivatives range from simple M_1L_2 systems such as the simple Cr^{III} complex reported by Zhu *et al.* (Figure 1.27) to larger M_xL_x complexes like the 3*d*4*f* complex by Li and coworkers (Figure 1.28).[123,124] As the complex by Zhu *et al.* shows, Sal typically coordinates to metal ions between the deprotonated phenol and the aldehyde, with the phenolate oxygen capable of μ_2 coordination as shown by Li and coworkers (Figures 1.27 and 1.28 respectively).[124] Generally when Sal is involved in 3*d*4*f* complexes, its role is as a coligand, due to salicylaldehyde having no preformed coordination pockets, however, this was not an issue for the $Co^{II}Eu^{III}_2$

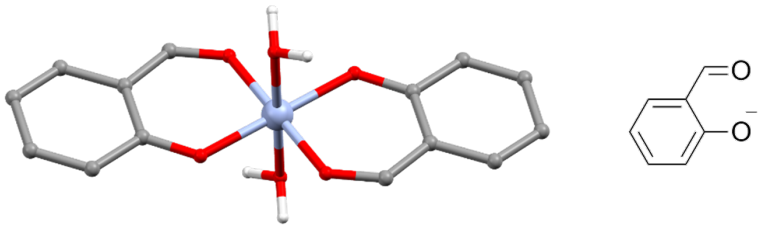

Figure 1.27: Crystal structure of the $[Cr^{III}L_2(H_2O)_2][Cl]$ complex produced by Zhu and coworkers.[123] Hydrogen atoms apart from those attached to donor atoms and lattice anions have been omitted for clarity. Colour code: Cr^{III} = light blue, O = red, C = grey, and H = white.

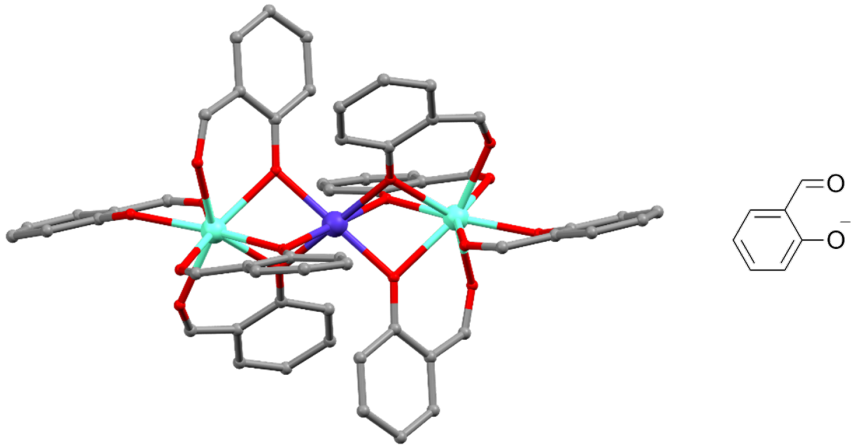

Figure 1.28: Crystal structure of the $[Co^{II}Eu^{III}_2L_8]$ complex produced by Li and coworkers.[124] Hydrogen atoms have been omitted for clarity. Colour code: Eu^{III} = aqua, Co^{II} = purple, O = red, and C = grey.

structure produced by Li and coworkers. The mechanism for how the metal ions coordinate however can not be determined as this example has no associated experimental details.

One of the most common derivatives of Sal found in the literature is *o*-vanillin (3-methoxy-2-hydroxybenzaldehyde, Figure 1.29). *o*-Vanillin (*o*-van) has gained popularity as a chelating ligand due to its ability to coordinate both 3*d* and 4*f* ions in homometallic and heterometallic complexes.[125] The two coordination pockets of *o*-van are distinctly different enough that 3*d* and 4*f* complexes can form. When two units of *o*-van are opposite each other as in Figure 1.29, the two coordination pockets are different in size, with the smaller pocket a better match for the smaller 3*d* cations and capable of forming either a four-, five-, or six-coordinate geometry. The second pocket formed between the phenolate and methoxy oxygens is larger and more suited for the 4*f* ions. It is possible for the 4*f* ions to coordinate between the phenolate and carbonyl oxygens however these structures form different topologies such as triangles, or defective dicubanes to allieviate steric strain.

As shown by the research group of Costes, the use of 3*d*4*f* ions commonly form dimeric complexes when produced at room temperature (RT) as show in Figure 1.30 (left), however when heat was applied to the complex, a new 3*d*4*f* complex was

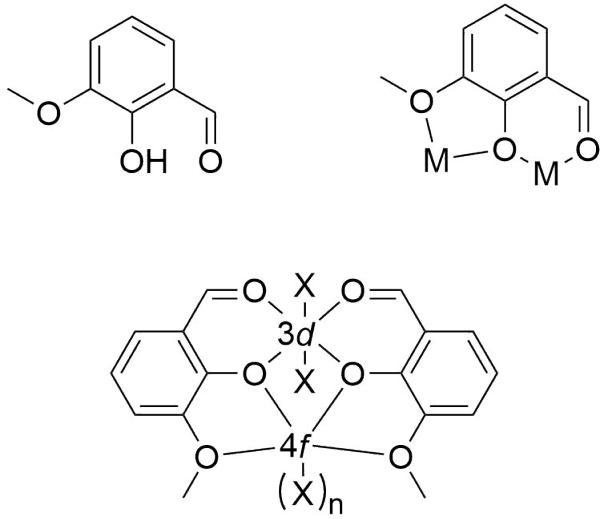

Figure 1.29: Schematic representation of *o*-van shown on the left with the most common coordination mode shown on the right. The schematic at the bottom represents the common form of 3*d*4*f* coordination.

produced (Figure 1.30, right).[126] This new complex was reported to have a defective dicubane core and showed a shift in the coordination pockets, as for two of the four ligands, the 4*f* ions were coordinated to the carbonyl/phenolate pocket, and the 3*d* ions were found to coordinate to the phenolate/methoxy pocket. As discussed above, when the metal ions change which pocket they coordinate to, the resulting strain forces the topology to change to alleviate this, as shown by the new defective dicubane core. Another example where the topology alleviates strain is shown by the M_3L_3 structure (Figure 1.31) produced by Tang *et al*. where a triangular topology was produced to alleviate the strain induced by 4*f* ion coordinating to both pockets of *o*-van.[127]

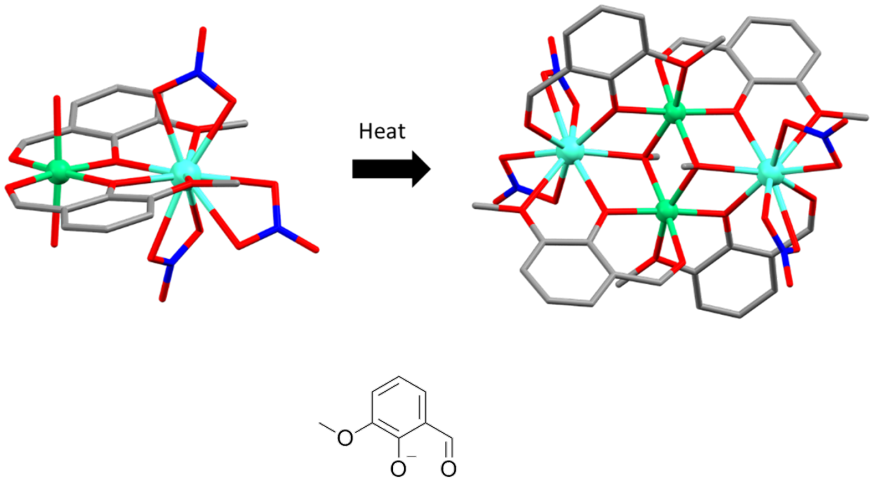

Figure 1.30: Crystal structures of the 3*d*4*f* complexes, $[Ni^{II}Gd^{III}L_2(H_2O)_2(NO_3)_3]$ (left) and $[Ni^{II}{}_2Gd^{III}{}_2L_4(OMe)_2(NO_3)_4]$ (right), produced by Costes and researchers.[126] Hydrogen atoms have been omitted for clarity. Colour code: Gd^{III} = aqua, Ni^{II} = green, N = blue, O = red, and C = grey.

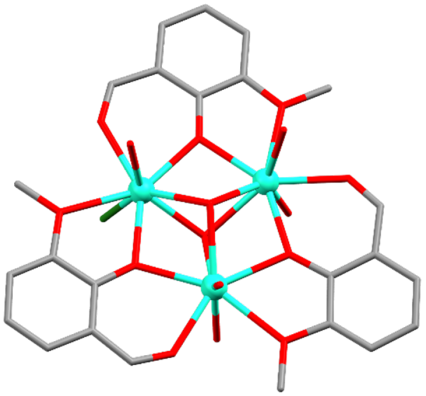

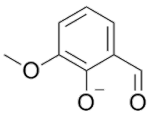

Figure 1.31: Crystal structure of the triangular structure, $[Dy^{III}_3L_3(OH)_3Cl(H_2O)_5][Cl_3]\cdot 4H_2O$, produced by Tang *et al.*[127] Hydrogen atoms and lattice solvent and anion molecules have been omitted for clarity. Colour code: Dy^{III} = aqua, O = red, Cl = green, and C = grey.

1.4.1 Schiff Base Compounds

Schiff base compounds are those which originate from a condensation reaction between a carbonyl group and a primary amine. Throughout the literature, there is a large number of coordination complexes that utilise Schiff base ligands with both homometallic and heterometallic 3*d* and 4*f* ions. Some of the more popular Schiff base ligands are derivatives of salicylaldimine, with 'single', 'double', and 'triple headed' ligands as well as macrocyclic ligands commonly found (Figure 1.32). Similarly to Sal, Schiff base ligands are largely used in magnetochemistry based applications due to the ease at which they can bridge metal ions and promote magnetic exchange.

Double headed salicylaldimine derived ligands are popular due to their compartmental nature, a requirement of heterometallic 3*d*4*f* complexes. An example of this can be seen in the $Cu^{II}Gd^{III}$ dinuclear complex produced by Costes and coworkers, the first reported dinuclear 3*d*4*f* complex to be structurally characterised (Figure 1.33).[128] The ligand utillised was 1,2'-bis((3-methoxysalicylidene)diamino)-2-methylpropane, a derivative of salicylaldimine that utilises *o*-van, and as shown by Figure 1.33 the coordination of the Cu^{II} and Gd^{III} ions resemble that of the *o*-van dinuclear complexes. These compartmental ligands however are more suited for dinuclear 3*d*4*f* complexes as the coordination pockets are more defined for the different metal ions. The Schiff base alkyl bridge introduces additional rigidity to the inner pocket, providing a size selective site that is well matched to the 3*d* ions. Additionally as 4*f* ions are well known to be largely oxophilic, when derivatives such as *o*-van are used, the outer coordination pocket is more appealing for the 4*f* ions as the pocket is solely oxophilic.

Although Schiff bases are one of the more popular types of chelating ligands, they are known to be unstable and can undergo hydrolysis reactions depending on the complexation environment. Generally these hydrolysis reactions occur during a complexation when the environment is acidic, with the Schiff base returning to its aldehyde and amine precursors with these becoming the new ligands.[129] One of the more common methods to combat this is to initially form the desired complex with the aldehyde precursor(s) and then perform the Schiff base reaction on the complex to obtain the desired product.

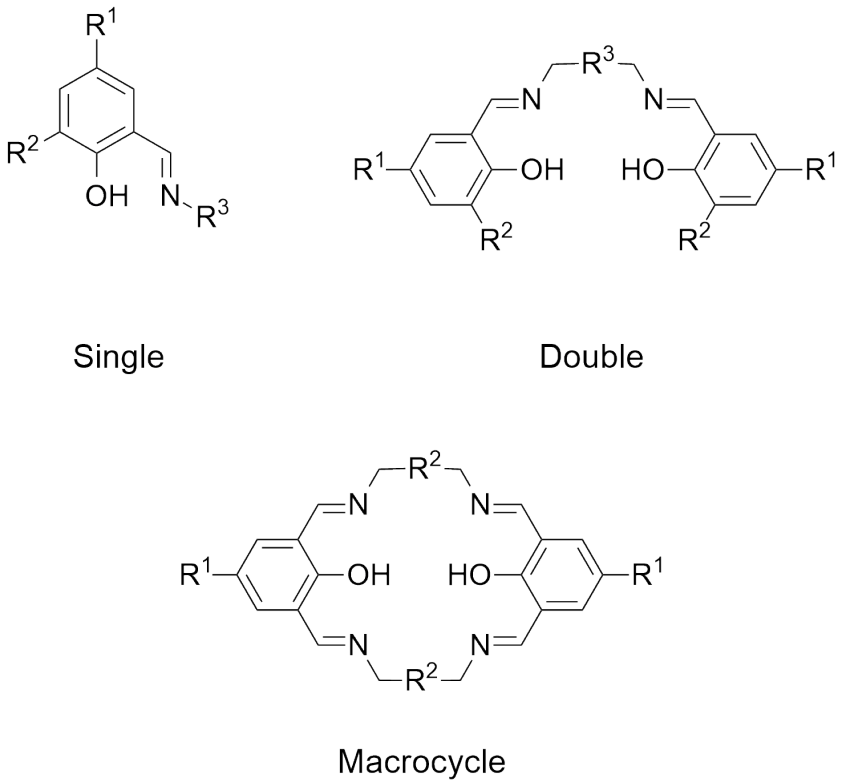

Figure 1.32: Schematic representations of single, double, and macrocyclic salicylimine derived Schiff base ligands.

1.4.2 Oxime Based Compounds

Oximes are an extension of Schiff bases, however instead of a primary amine, an aminooxy group is used. Generally the aminooxy used is hydroxylamine, NH_2OH, to give single headed compounds and double headed compounds which are bridged via the 3-position. Another type of salicylaldoxime derivative is *o*-alkyloximes, these compounds use an aminooxy group, NH_2OR or NH_2ORONH_2, and bridge two aromatic units through the alkyloxime functionality (Figure 1.34, bridged).

Salicylaldoxime derivatives are commonly used in fields such as magnetic materials and extractive hydrometallurgy due to the ligands having multiple binding sites, coordination modes, and the ease at which the phenol readily deprotonates upon interaction with a metal ion. Additionally hydrogen bonding networks within the protonated and deprotonated compounds stabilise the molecules making them more resistant to hydrolysis unlike their Schiff base counterparts.

A large proportion of the literature examples are homometallic 3*d* complexes as a result of the more popular fields of extractive hydrometallurgy and magnetic materials.[7,65,130,131] Commonly salicylaldoxime derivatives have amino functionality added to R^2 in Figure 1.34, partly due to the corresponding complexes produced but also due to the ease at which amino functionality can be added, through reactions such

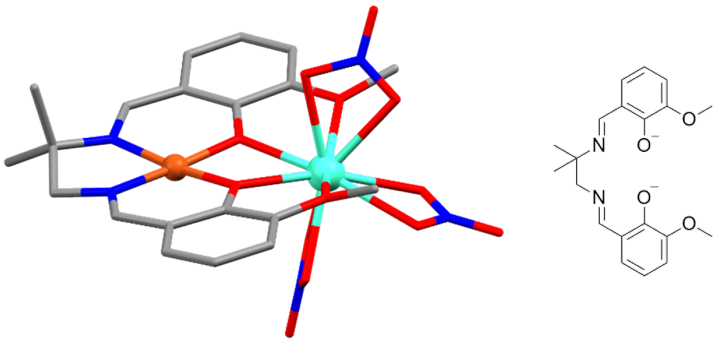

Figure 1.33: Crystal structure of the first structurally characterised 3*d*4*f* dinuclear complex, $[Cu^{II}Gd^{III}L(NO_3)_3] \cdot Me_2CO$, produced by Costes and coworkers.[128] Hydrogen atoms and lattice solvent molecules omitted for clarity. Colour code: Gd^{III} = aqua, Cu^{II} = orange, N = blue, O = red, and C = grey.

as Mannich condensation and amine alkylation. This is demonstrated by the hydrometallurgic research of Tasker and coworkers where by adding a simple secondary amine such as piperidine, the ligand can coordinate to a Cu^{II} cation but also be used to extract anions through hydrogen bonding to protonated amino groups as shown by Figure 1.35.

Literature examples have shown that single headed oximes most commonly coordinate to metal ions in a *trans* conformation, as this reduces any repulsion that would occur between the oxime groups.[130,131] A large proportion of double headed oxime based ligands have lengthy alkyl chains bridging the two units resulting in the production of different complexes such as helicates and mesocates, subsequently causing the ligands to coordinate in a *trans* conformation as shown by Wenzel *et al*. (Figure 1.36). These particular helicates are an extended version of the simple metal extractants produced by Tasker and coworkers, as they have the capability to encapsulate anions in the cavity formed by the helicate through both weak metal ion coordination and hydrogen bonding.[132]

One of the more well known oxime based complexes, is the hexametallic $[Mn^{III}{}_3]_2$ triangular structure, a previous SMM record, synthesised by Brechin and coworkers (Figure 1.10). The ligand they utilised was 2-hydroxyphenylpropanone oxime (Figure 1.10, top right), a single headed oxime with functionalisation off the carbon of the C=N group. Instead of the single headed oximato ligand coordinating to a metal ion in a *trans* conformation, three ligands form a triangle with classical oximato M-N-O-M bridging, imparting structural torsion into the complex.

An extension to Schiff base and oxime compounds are *o*-alkyloximes. An *o*-alkyloxime has the notation R'-C=N-O-R", with a carbon chain replacing the typical OH functionality of an oxime. This extension is interesting for coordination complexes as the added oxygen in the bridge imparts additional electronegativity, which is thought to have an impact on both the N_2O_2 pocket and associated coordination sphere. These compounds akin to both Schiff bases and traditional oxime ligands, can be single headed or double headed, however a large proportion of coordinated compounds found in the literature are at least double headed, with several triple headed, both 1,3 and 1,4 C=N functionalisation (Figure 1.37). The coordination modes are more alike to Schiff bases, in such that the oxygen atom in the bridge rarely coordinates to

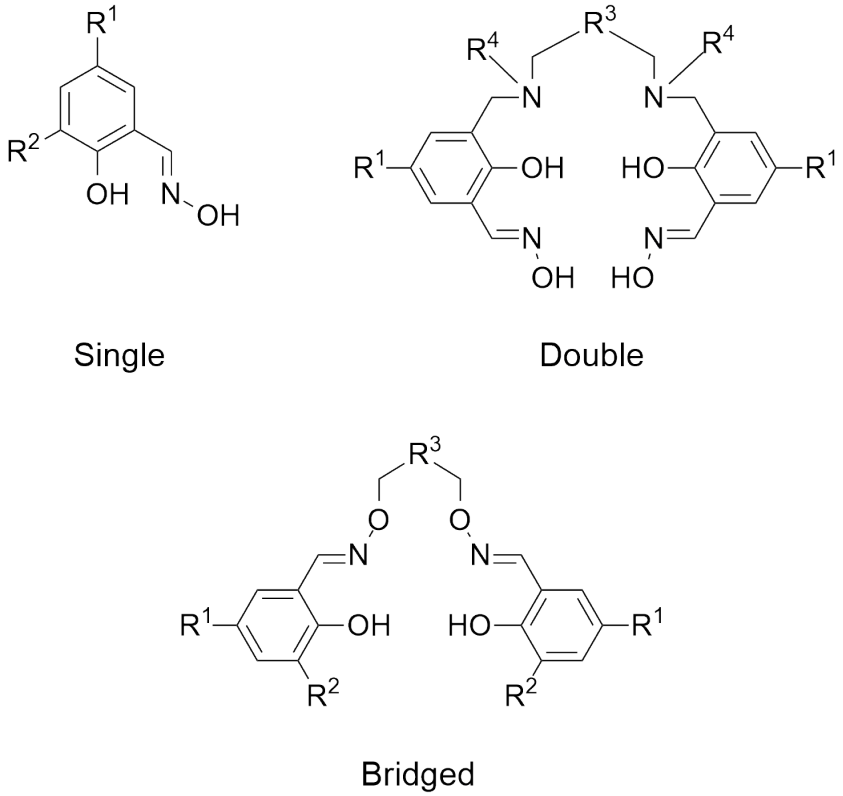

Figure 1.34: Schematic representations of three different types of oxime based compounds; single headed, double headed, and bridged.

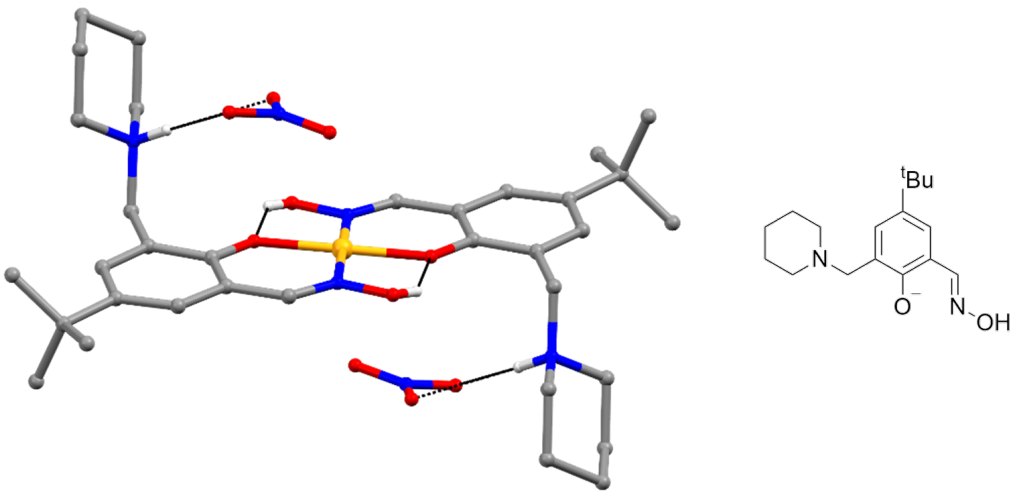

Figure 1.35: Crystal structure of the Cu^{II} extractant, $[Cu^{II}L_2][(NO_3)_2]$, produced by Tasker and coworkers.[130] Non-interacting hydrogen atoms have been omitted for clarity. Hydrogen bonding represented as black dotted lines. Colour code: Cu^{II} = orange, N = blue, O = red, C = grey, and H = white.

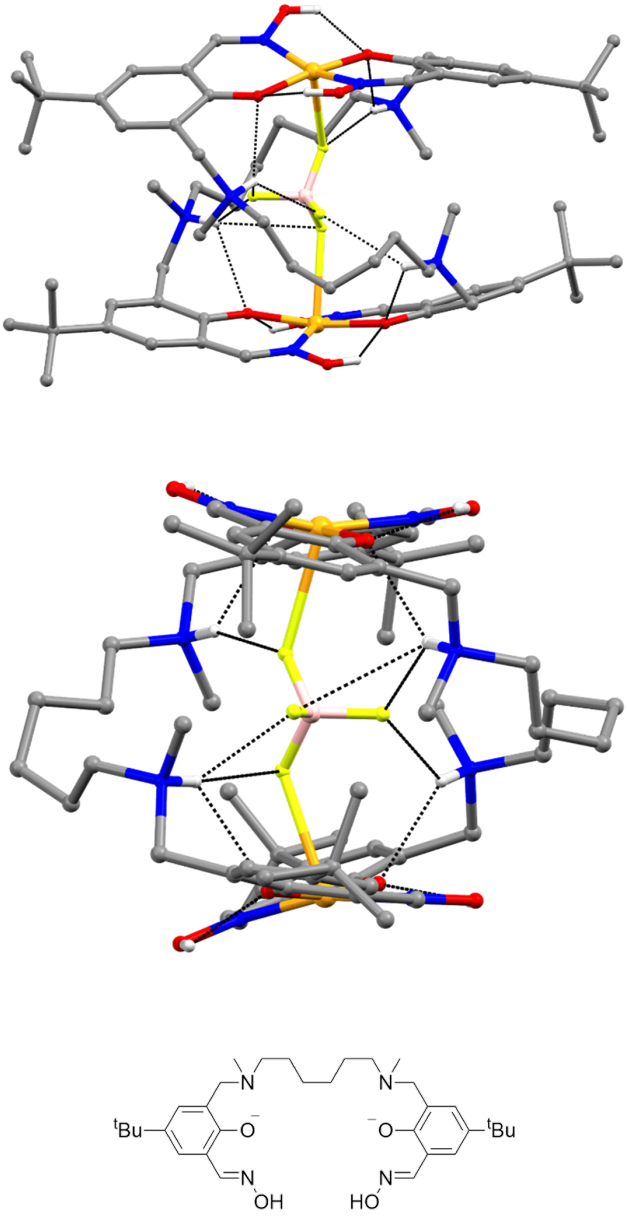

Figure 1.36: Crystal structure of the Cu^{II} helicate, $[BF_4 \subset Cu^{II}_2L_2][(BF_4)_3] \cdot 2MeCN$, produced by Wenzel *et al.*[132] Top view illustrates the metal ion coordination, bottom view shows the cavity of the helicate. Non-interacting hydrogen atoms and lattice anions and solvent molecules have been omitted for clarity; Hydrogen bonding represented as black dotted lines. Colour code: Cu^{II} = orange, N = blue, O = red, B = light pink, F = yellow, C = grey, and H = white.

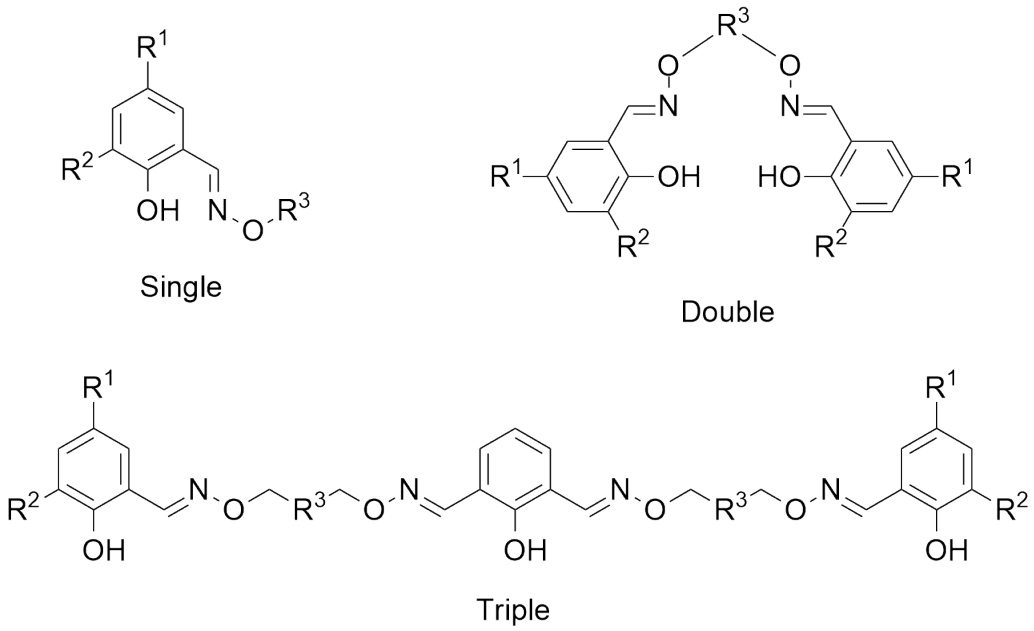

Figure 1.37: Schematic representations of single, double, and triple headed *o*-alkyloxime compounds.

a metal ion however it has been shown in the literature that this is still possible.[133,134]

o-Alkyloximes have been utilised in coordination complexes for applications such as fluorescence,[135,136] catalysis,[137] antimicrobial,[138,139] and magnetic materials.[140] Many examples consist of dinuclear and trinuclear complexes, either homometallic 3*d* or heterometallic 3*d*4*f*. Many of the trinuclear complexes utilise bridging groups such as OAc^- anions to bridge between metal ions as shown by Li *et al*. who produced a series of trinuclear homometallic Ni^{II} and Co^{II} complexes (Figure 1.38).[141] The M_3L_2 complex utilised an asymmetric double headed *o*-alkyloxime derivative, 2-hydroxy-4-methoxy-*O*-[2-[[[(2-hydroxy-5-nitrophenyl)methylene]amino]oxy]ethyl]oxime benzaldehyde (Figure 1.38, bottom), as the ligand. Each ligand is coordinated to one of the Ni^{II} ions in the oxime/phenolate pockets with the central ion coordinated to the four phenolate oxygens and two bridging OAc^- anions.

One of the more simpler topologies is the dinuclear M_2L_1 topology, which utilises the exchange pathway facillitated by the phenolate oxygen. An example of this is shown by the research of Yao *et al*. who produced a series of $Ni^{II}Ln^{III}$ complexes, where all complexes were found to have desirable ferromagnetic exchange however only the $Ni^{II}Dy^{III}$ complex shown in Figure 1.39 displayed SMM properties.[142] The ligand utilised was a popular *o*-alkyloxime derivative found in the literature, 2-hydroxy-3-methoxy-1,1'-(*O*,*O*'-1,2-ethanediyldioxime)-benzaldehyde, where the Ni^{II} ions coordinate in the inner oxime/phenolate pocket and the 4*f* ions in the outer phenolate /methoxy pocket.

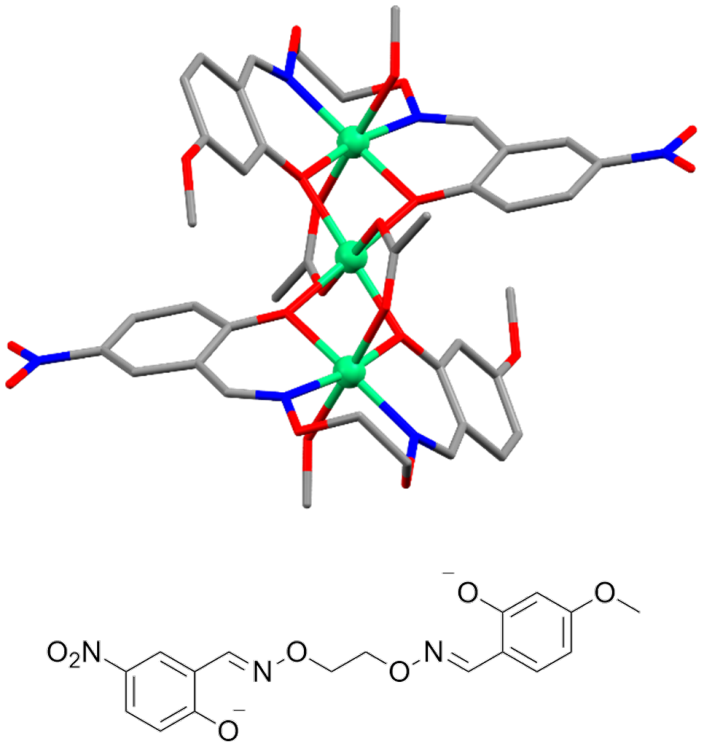

Figure 1.38: Crystal structure of the Ni^{II}_3 trinuclear complex, $[(Ni^{II}L(MeOH)(OAc))_2Ni^{II}] \cdot 2MeOH$, produced by Li *et al.* with the corresponding *o*-alkyloxime ligands shown below.[141] Non-interacting hydrogen atoms and lattice solvent molecules have been omitted for clarity. Colour code: Ni^{II} = green, N = blue, O = red, and C = grey.

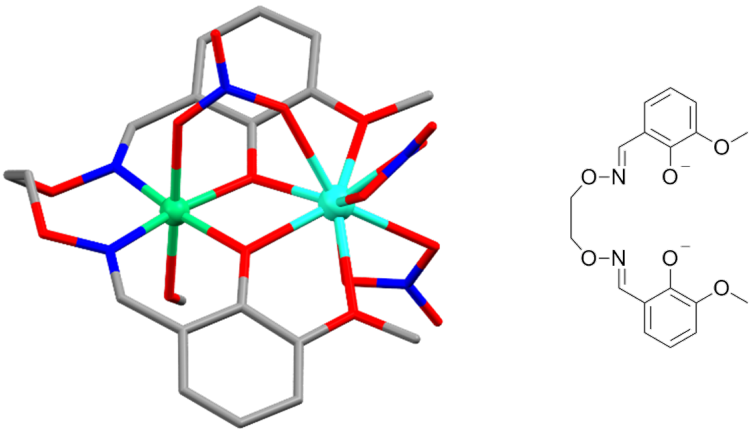

Figure 1.39: Crystal structure of the $Ni^{II}Dy^{III}$ complex, $[Ni^{II}Dy^{III}L(MeOH)(NO_3)_3] \cdot Et_2O$, produced by Yao *et al.*[142] Non-interacting hydrogen atoms and lattice solvent molecules have been omitted for clarity. Colour code: Dy^{III} = aqua, Ni^{II} = green, N = blue, O = red, and C = grey.

1.5 Aims of Research

The overarching theme of this research is to explore the manipulation of magnetism found in polynuclear clusters, by targeting the exchange interactions found between metal ions. The exchange pathways of interest will originate from both defective dicubane and dinuclear topologies, where ligands and/or anions will be utilised as the bridging groups. Two different oxime and *o*-alkyloxime based ligands will be used to produce both homometallic 3*d* and heterometallic 3*d*3*d*′ and 3*d*4*f* complexes. Key manipulations will be to change the bridging groups, metal ion combinations, and metal ion coordinates.

The first series centers on a previously reported Ni^{II}_4 defective dicubane with ferromagnetic exchange, and explores how the exchange pathways, largely made up of anions and coligands, can be manipulated through the incorporation of different metal anions, solvents, and coligands. This series of maniplations looks at the effect of changing the group that has direct influence on the exchange pathways, peripheral groups, and the crystal lattice. Successful complexations will be characterised by SCXRD, ESI-MS, ATR-IR, CHN microanalysis and magnetic and computational analyses to determine the magnetic properties of the complexes and the success of the manipulations.

An investigation into two further series will then be undertaken. These differ from the defective dicubane series in that the exchange pathways originate solely from the ligand itself rather than additional coligands, allowing the effect of different metal ion combinations, both homo- and heterometallic to be explored. The first of the two series explores how different 3*d*3*d*′ combinations affect the ligand geometry and most importantly the angles and distance of the exchange pathways. The second of the two series builds off of the 3*d*3*d*′ series but explores 3*d*4*f* metal ion combinations and how different anions and solvent combinations affect both the ligand geometry and the exchange pathway angles and distance(s). Successful complexations will be characterised by a combination of SCXRD, ESI-MS, ATR-IR, CHN microanalysis and magnetic and computational analyses to determine both the magnetic properties of the complexes and the success of the manipulations.

Chapter 2

Ligand Design and Synthesis

2.1 General Details

All starting materials and solvents were used as purchased from commercial sources, unless otherwise stated. HPLC grade MeOH and absolute EtOH were dried according to the procedure of Lund and Bjerrum and stored over activated 3 Å and 4 Å molecular sieves respectively.[143,144] Alternatively HPLC grade MeOH was stored over activated 3 Å molecular sieves for a week prior to use. All reactions were carried out in acetone-washed, oven-dried glassware under ambient conditions unless otherwise stated. The glassware utilised for crystallisation was either used straight from purchase, or outer vials (previously used solely for Et_2O) were washed with H_2O and MeOH, soaked in a KOH/IPA base bath, rinsed with H_2O, and then air dried. All complexation and crystallisation attempts were performed at RT in ambient conditions, unless otherwise stated.

All organic compounds have been characterised by ^{1}H NMR, ATR-IR, and ESI-MS with new organic compounds characterised by ^{13}C NMR. The metallic complexes have been characterised by a combination of SCXRD, ATR-IR, FAAS, CHN elemental analysis, and magnetic susceptibility measurements. For the complexes that have been characterised by magnetic measurements, the measured material was generated from metal-contaminant free, bulk complexations and was characterised by unit cell checks (several crystals screened from the same bulk material), SCXRD, ATR-IR, ESI-MS, FAAS (**C6**, **C8**, **C10**, and **C12**), and CHN microanalysis. A number of the complexes reported in this research have solely been characterised by SCXRD due to an initial small sample size and issues surrounding reproducibility with bulk synthesis attempts. All complex yields reported are of isolated crystalline material.

^{1}H and ^{13}C NMR spectra were recorded at RT on a Bruker-500 Avance instrument, with the ^{1}H shift of the solvent used as an internal standard. ESI-MS spectra were collected on a Dionex UltiMate 3000 and run in positive ion mode. ATR-IR spectra were collected on a Nicolett 5700 IR using a diamond ATR sampling accessory. FAAS was collected using a GBC XplorAA dual instrument with SpectrAA (Mn), S&J (Cu and Zn), Photron (Ni), and Varian (Co) hollow cathode lamps used. The CHN elemental analysis was collected by the Campbell Microanalytical Laboratory, Chemistry Department, The University of Otago. Selected spectra of new compounds can be found in Appendix A.

Throughout this research a modified version of the Harris method (Appendix A; Section A.6.1) was used to describe the coordination modes of the ligands and anions, with schematics showing the various coordination modes in Figures 2.2, 2.6, 2.8, 2.11, and A.16, - A.19.[145] The metal ion geometries for complexes **C1** - **C66** have been

determined using Consistent Shape Measurement (CShM) calculations performed using the software, SHAPE.[146,147] Details and results of which can be found in Tables A.1 - A.9, B.1, C.3, D.2, D.3, and E.4.

2.2 H_2L1

The known compound, H_2**L1**, utilised for the defective dicubane series was synthesised by a series of reactions: formylation, methyl bromination, amine alkylation, and oximation (Figure 2.1). The structure of compounds **1** (5-*tert*-butyl-2-hydroxybenzaldehyde), **2** (5-*tert*-butyl-3-bromomethyl-2-hydroxybenzaldehyde), **3** (5-*tert*-butyl-3-(*N*-methyl-*N*-(2,2-dimethoxyethyl)amino)methyl-2-hydroxybenzaldehyde), and H_2**L1** (5-*tert*-butyl-3-(*N*-methyl-*N*-(2,2-dimethoxyethyl)amino)methyl-2-hydroxybenzaldehyde oxime) were confirmed by ^{1}H NMR, ATR-IR, and ESI-MS with the synthetic procedures well documented by the Plieger group.[148,149]

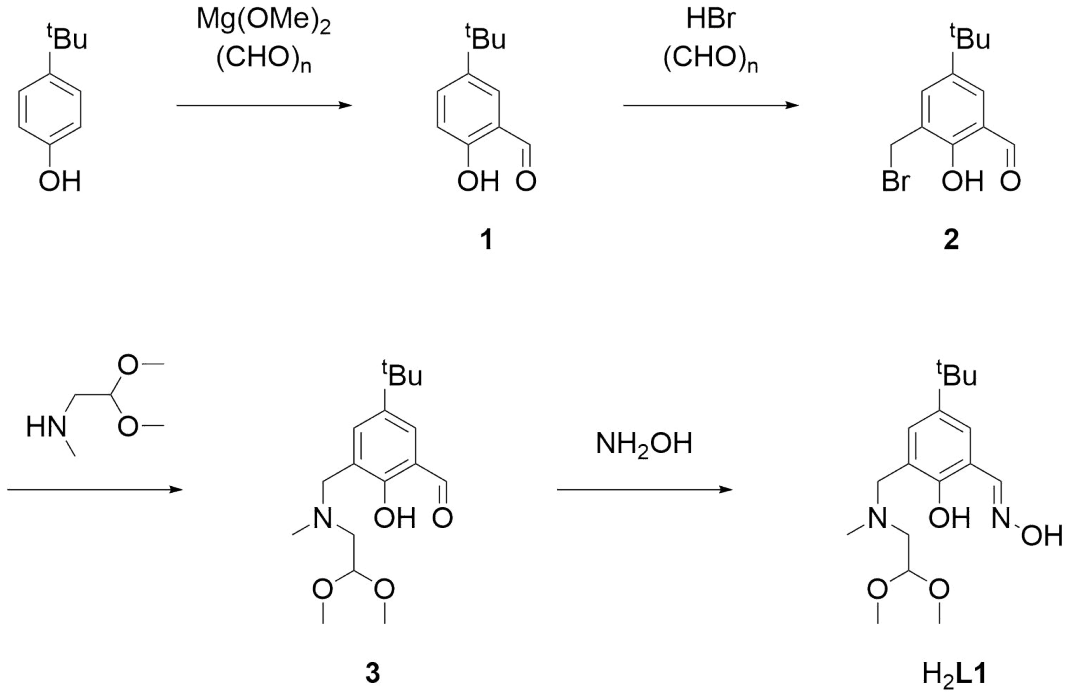

Figure 2.1: The synthetic pathway to produce, H_2**L1**

There are two coordination modes found for H_2**L1** (Figure 2.2) which vary slightly from each other. For coordination mode I, the ligand is present in the form H**L1**$^-$ with one metal ion coordinated to the phenolate oxygen, one methoxy oxygen, and the amino nitrogen with a second metal ion coordinated to the phenolate oxygen and oxime nitrogen. Mode II resembles that of mode I however the ligand is present in the form **L1**$^{2-}$, with an additional metal ion coordinated to the oxime oxygen.

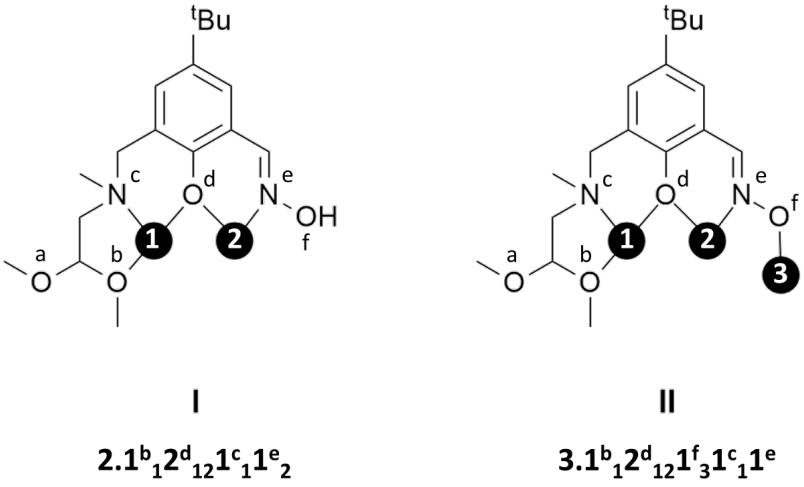

Figure 2.2: Representation of the coordination modes and Harris notation found for the ligands, H**L1**$^{-}$ and **L1**$^{2-}$ in this research. Metal ions are represented as black circles.

2.2.1 Synthesis of H_2L1

5-*tert*-Butyl-2-hydroxybenzaldehyde (1)

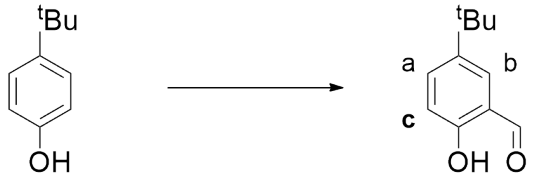

1

Prepared as per the method of Woodhouse *et al.*[149] Dry Mg turnings (14.8 g, 0.609 mol, 0.6 eq.) were added to a stirred solution of dry MeOH/toluene (3 : 7; 200 mL) and $Mg(OMe)_2$ solution (8%; 100 mL), and refluxed under argon overnight, ensuring all Mg had dissolved. The reaction mixture was then added to a stirred solution of 4-*tert*-butylphenol (152 g, 1.01 mol, 1 eq.) in toluene (100 mL) and refluxed for three hours. Toluene (100 mL) was added prior to fractionally distilling off a MeOH/toluene azeotrope under reduced pressure until the reaction mixture appeared to be a thick consistency. Additional toluene (100 mL) was added, followed by a paraformaldehyde slurry (90.4 g, 3.01 mol, 3 eq.) in toluene (200 mL) that was added piecewise over one hour, with volatile by-products removed by vacuum distillation between aliquots. Toluene (200 mL) was added to the reaction mixture and left to stir overnight at 85 °C, producing a thick yellow/brown mixture. A solution of H_2SO_4 (30%; 500 mL) was added dropwise over an hour, then stirred vigorously for a further three hours at 50 °C forming two yellow layers. The aqueous layer was extracted with toluene (3 x 150 mL), and the combined organic layers were washed with a H_2SO_4 solution (10%; 2 x 200 mL) and H_2O (2 x 200 mL), dried over anhydrous $MgSO_4$, filtered, and concentrated *in vacuo* to afford crude **1** (177 g, 0.993 mol) as a brown oil and was found to be sufficiently clean to proceed to the next reaction. A small quantity (5.19 g, 0.0291) of the crude material however was further purified by silica gel column chromatography, eluting with 4 : 1 *n*Hex : EtOAc (R_f = 0.75), affording purified **1** as a dark orange oil (3.04 g, 0.0171 mol, 59%). The ^{1}H NMR spectrum agreed with literature values[149] (500 MHz, $CDCl_3$): δ 10.90 (1H, s, Ar-*OH*), 9.92 (1H, s, *CH*=O), 7.61 (1H, dd, J_1 = 8.8 Hz, J_2 = 2.5 Hz, *c*), 7.54 (1H, d, J = 2.5 Hz, *b*), 6.97 (1H, d, J = 8.8 Hz, *a*), 1.36 (9H, s, ^{t}*Bu*) ppm; ATR-IR: $\overline{\nu}$ = 3191 (O-H), 2963 (C-H), 1658 (C=O), 1484 (C-H), 1394 (C-H), 1362 (O-H), 1230 (Ar-O), 833 (C=C), 732 (Ar) cm^{-1}; ESI-MS: *m/z* 179 $[M+H]^+$.

5-*tert*-Butyl-3-bromomethyl-2-hydroxybenzaldehyde (2)

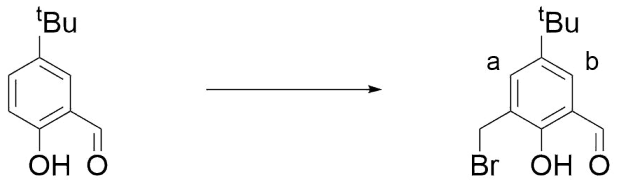

1 **2**

Prepared as per the method of Meier *et al.*[150] **1** (65.0 g, 0.365 mol, 1 eq.), HBr (48%, 150 mL, 2.74 mol, 7.5 eq.), and paraformaldehyde (16.4 g, 0.548 mol, 1.5 eq.) were added together and stirred at 0 °C. Conc. H_2SO_4 (5 mL) was added slowly dropwise to the mixture stirring at 0 °C until a light-yellow colour persisted, the mixture was then refluxed for 20 hours at 70 °C. After cooling to RT, H_2O (200 mL) was added. The aqueous layer was extracted with DCM (3 x 150 mL) and combined organic layers were dried over anhydrous Na_2SO_4, filtered, and concentrated *in vacuo* to produce crude **2** as a brown oil (62.9 g, 0.232 mol). The crude material was recrystallised from hot pentane (10% w/v) to give light yellow block shaped crystals of purified **2** (59.4 g, 0.291 mol, 60%). The ^{1}H NMR spectrum agreed with literature values[150] (500 MHz, $CDCl_3$): δ 11.32 (1H, s, Ar-*OH*), 9.90 (1H, s, *CH*=O), 7.64 (1H, d, J = 2.4 Hz, *b*), 7.51 (1H, d, J = 2.5 Hz, *a*), 4.59 (2H, s, CH_2-Br) 1.34 (9H, s, ^{t}*Bu*) ppm; ATR-IR: $\overline{\nu}$ = 3251 (O-H), 2964 (C-H), 1652 (C=O), 1467 (C-H), 1394 (C-H), 1363 (O-H), 1222 (Ar-O), 826 (C=C), 739 (Ar), 584 (C-Br) cm^{-1}; ESI-MS: *m/z* 206 [M-Br]$^+$.

5-*tert*-Butyl-3-(*N*-methyl-*N*-(2,2-dimethoxyethyl)amino)methyl-2-hydroxybenzaldehyde (3)

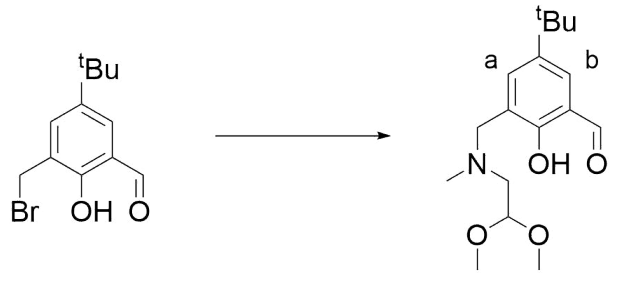

2 **3**

Prepared as per the procedure of Woodhouse *et al.*[149] Solutions of 1,1-dimethoxy-*N*-methyl methanamine (0.940 mL, 7.38 mmol, 1 eq.) and **2** (2.01 g, 7.38 mmol, 1 eq.), both in $CHCl_3$ (40 mL) were added dropwise to a stirred solution of Et_3N (1.03 mL, 7.38 mmol, 1 eq.) in $CHCl_3$ (40 mL). The resulting bright yellow solution was stirred for 24 hours at RT. The solution was washed with H_2O (3 x 50 mL), and the combined organic layers were dried over anhydrous $MgSO_4$, filtered, and concentrated *in vacuo* to afford **3** as a yellow oil (1.89 g, 6.11 mmol, 83%). ^{1}H NMR agreed with literature values[149] (500 MHz, $CDCl_3$): δ 10.33 (1H, s, *CH*=O), 7.62 (1H, d, J = 2.2 Hz, *b*), 7.35 (1H, d, J = 2.2 Hz, *a*), 4.59 (1H, t, J = 5.4 Hz, CH_2-*CH*), 3.77 (2H, s, Ar-CH_2-N), 3.38 (6H, s, O-CH_3), 2.66 (2H, d, J = 5.4 Hz, N-CH_2-CH), 2.37 (3H, s, N-CH_3), 1.30 (9H, s,

^{t}Bu) ppm; ATR-IR: $\overline{\nu}$ = 2957 (C-H), 1678 (C=O), 1652 (C-H), 1395 (C-H), 1364 (O-H), 1124 (C-N), 1073 (C-O) cm^{-1}; ESI-MS: *m/z* 310 $[M+H]^+$.

5-*tert*-Butyl-3-(*N*-methyl-*N*-(2,2-dimethoxyethyl)amino)methyl-2-hydroxybenzaldehyde oxime (H_2L1)

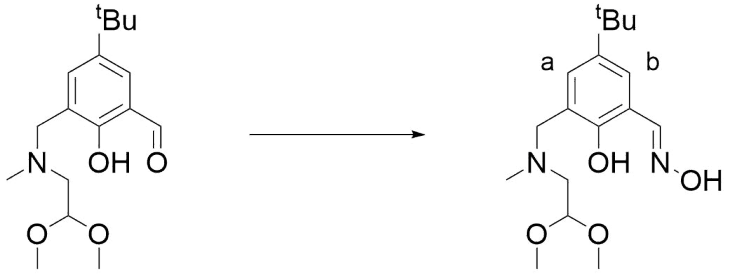

3 H_2**L1**

Prepared as per the procedure of Woodhouse *et al.*[149] A solution of $NH_2OH \cdot HCl$ (0.781 g, 11.2 mmol, 1 eq.) in EtOH (40 mL) was neutralised with a solution of KOH (0.630 g, 11.2 mmol, 1 eq.) in EtOH (40 mL). The filtrate was added slowly dropwise to a solution of **3** (3.47 g, 11.2 mmol, 1 eq.) in EtOH (40 mL). The resulting solution was stirred for 24 hours at RT. The light-yellow solution was concentrated *in vacuo* affording an oil, which was redissolved in $CHCl_3$ (50 mL). This solution was washed with H_2O (3 x 50 mL) and the combined organic layers were dried over anhydrous $MgSO_4$, filtered, and concentrated *in vacuo* affording H_2**L1** as a yellow oil (2.24 g, 6.90 mmol, 62%). ^{1}H NMR agreed with literature values[149] (500 MHz, $CDCl_3$): δ 8.37 (1H, s, *CH*=N), 7.36 (1H, d, J = 2.5 Hz, *b*), 7.13 (1H, d, J = 2.5 Hz, *a*), 4.62 (1H, t, J = 5.2 Hz, CH_2-*CH*), 3.74 (2H, s, Ar-CH_2-N), 3.36 (6H, s, O-CH_3), 2.67 (2H, d, J = 5.2 Hz, N-CH_2-CH), 2.36 (3H, s, N-CH_3), 1.27 (9H, s, ^{t}Bu) ppm; ATR-IR: $\overline{\nu}$ = 3279 (O-H), 2959 (C-H), 1616 (C=N), 1478 (Ar), 1463 (C-H), 1363 (O-H), 1266 (Ar-O), 1126 (C-O), 1070 (C-N), 964 (N-O), 737 (Ar) cm^{-1}; ESI-MS: *m/z* 325 $[M+H]^+$.

2.3 H_2L2

The known *o*-alkyloxime compound, H_2**L2**, utilised for the 3*d*3*d*′ and 3*d*4*f* series was synthesised by three steps, begining with an adapted Gabriel synthesis (condensation followed by hydrolysis) where an acidic hydrolysis replaced the more typical Ing-Manske procedure, followed by a Schiff base condensation to yield the final compound, H_2**L2** (Figure 2.3).[151]

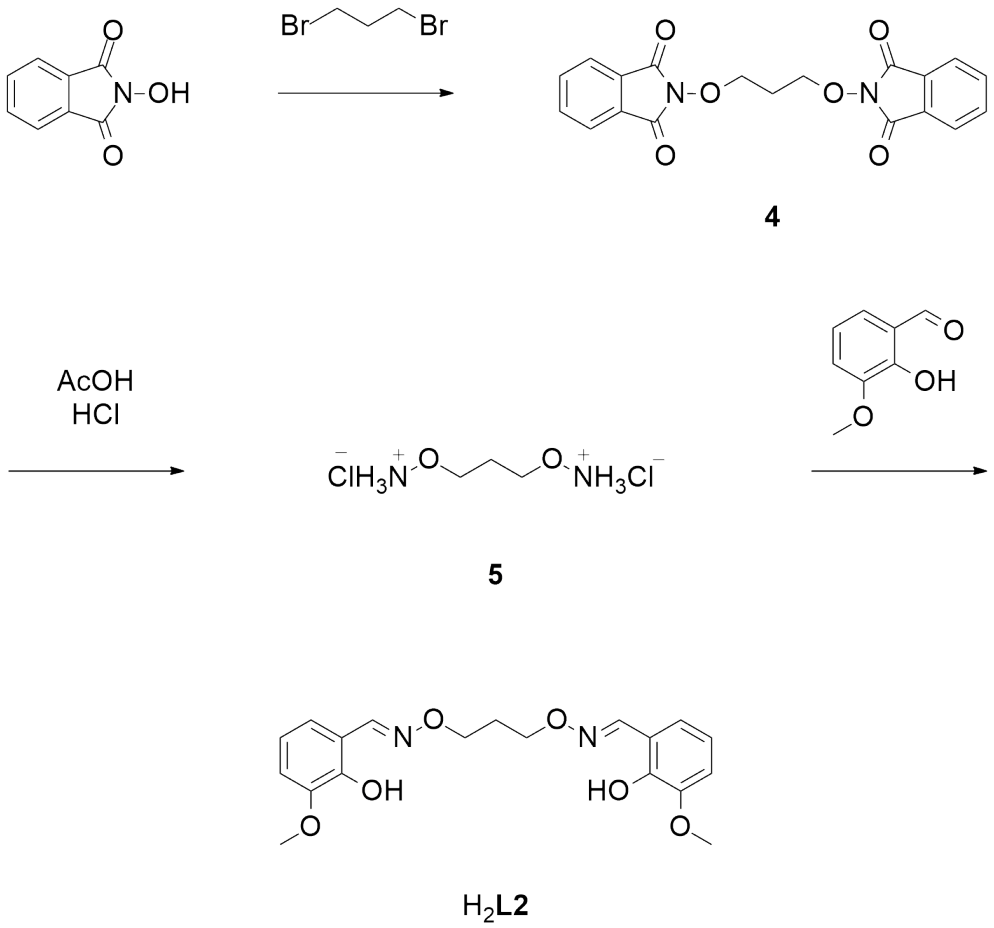

Figure 2.3: Reaction scheme for the synthesis of H_2**L2**

Gabriel syntheses are well established in the literature, with the most common being that of a derivative of H_2**L2** where the propyl bridge is replaced by a ethyl bridge.[152,153] The first step is a simple condensation reaction, with the methods of Covaci *et al*. and Bauer and Suresh adapted for this research.[154,155] It was found that by increasing both the temperature and length of reaction, the yield could be improved from 37% to $\sim$ 63%. The next step is traditionally a hydrolysis reaction by the Ing-Manske procedure utilising hydrazine monohydrate, however due to available resources at the time, an acidic hydrolysis following an adaptation of the procedure by Shirayev *et al*. was performed to give the colourless crystalline product.[156] Finally a Schiff base condensation following an adaptation of the method by Ren *et al*. gave H_2**L2** as a light yellow solid.[157] By optimising the reaction concentration the yield was improved from $\sim$ 40% to $\sim$ 75%.

A crystal structure of H_2**L2** was obtained through a failed complexation attempt (Figure 2.4). The crystal structure shows the compound packs in a v-shape arrangement, with moderate intramolecular hydrogen bonding (X· · ·A, 2.5 - 3.2 Å)[158] found between the phenolate oxygen and adjacent oxime nitrogen, O1· · ·N1, 2.621(3) Å (Figure 2.5).

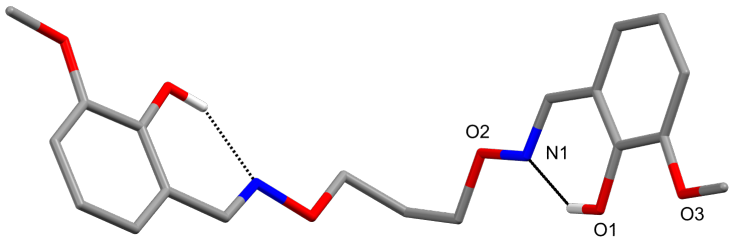

Figure 2.4: Crystal structure of H_2**L2**. Non-interacting hydrogen atoms omitted for clarity and hydrogen bonding represented as black dotted lines. Colour code: N = blue, O = red, C = grey, and H = white.

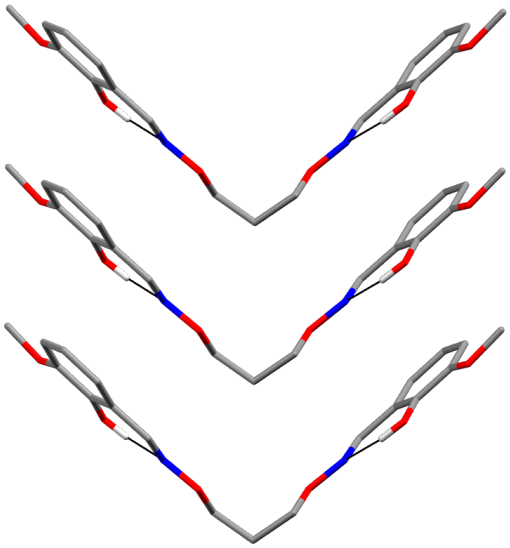

Figure 2.5: Representation of the v-shaped packing of H_2**L2**. Non-interacting hydrogen atoms omitted for clarity and hydrogen bonding represented as black dotted lines. Colour code: N = blue, O = red, C = grey, and H = white.

Within this research there are seven different coordination modes found for H_2**L2** (Figure 2.6). The ligand is found in the deprotonated form of **L2**$^{2-}$ for all seven modes with two - four metal ions coordinated between the alkyloxime nitrogens and phenolate and methoxy oxygens. An unusual form of coordination is found for mode IV with a metal ion coordinated to an alkyloxime oxygen. This type of coordination has only been seen twice before by Dong *et al.* and Yang *et al.*[133,134]

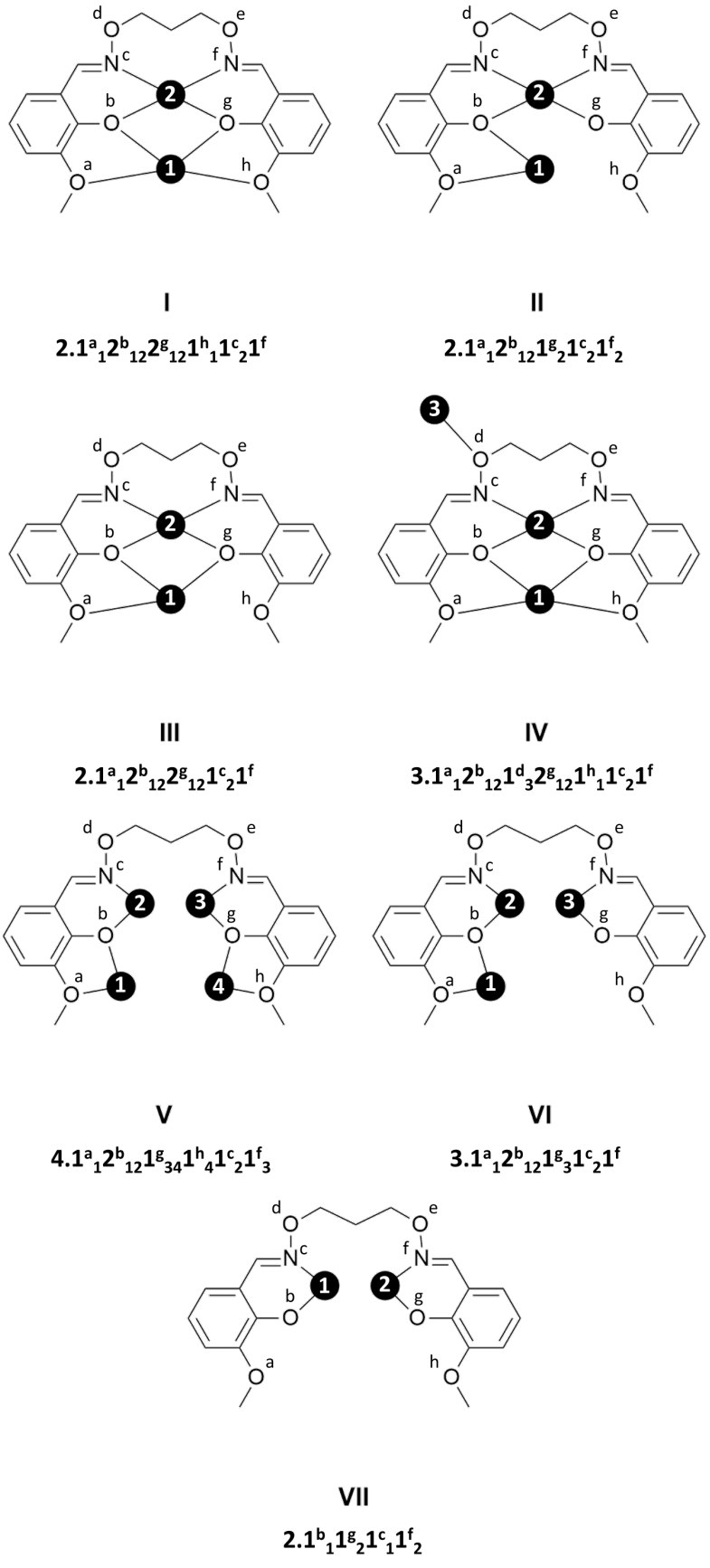

Figure 2.6: Representation of the coordination modes and Harris notation found for **L2**$^{2-}$ in this research. Metal ions are represented as black circles.

2.3.1 Synthetic Procedure for H_2L2

1,3-Bis(phthalimidooxy)propane (4)

4

Adapted from the methods of Covaci *et al.*[154] and Bauer and Suresh.[155] To a solution of *N*-hydroxyphthalimide (4.97 g, 30.7 mmol, 2 eq.) in DMF (50 mL) was added 1,3-dibromopropane (1.60 mL, 15.3 mmol, 1 eq.) and Et_3N (7.50 mL, 53.8 mmol, 3.5 eq.). The dark red mixture was stirred at 70 °C for five days after which a light yellow precipitate formed. The reaction mixture was cooled to RT and filtered. The precipitate was washed with $NaHCO_3$ (10% aq.) until the filtrate became colourless, followed by HCl (10% aq.) until the filtrate became acidic (pH 2), and then finally with H_2O to give crude **4** as a white solid (6.01 g, 16.4 mmol). The crude material was recrystallised from hot DMF to give colourless crystals of purified **4** (3.70 g, 10.1 mmol, 66%). ^{1}H NMR agreed with literature values[154,155] (500 MHz, $CDCl_3$): δ 7.83 (4H, m, *a*), 7.75 (4H, m, *b*), 4.52 (4H, t, J = 6.1 Hz, O-CH_2-CH_2), 2.23 (2H, quintet, J = 6.1 Hz, CH_2-CH_2-CH_2) ppm; ATR-IR: $\overline{\nu}$ = 2915 (C-H), 1730 (C=O), 1612 (Ar), 1499 (N-O), 1468 (O-H), 1124 (C-O), 1081 (C-N), 982 (N-O) cm^{-1}; ESI-MS: *m/z* 398.97 $[M+Na]^+$.

1,3-Bis(aminooxy)propane dihydrochloride (5)

4 **5**

Adapted from the method of Shirayev *et al.*[156] A suspension of **4** (1.00 g, 2.73 mmol, 1 eq.) in conc. HCl (4 mL) and glacial AcOH (6 mL) was heated at 115 °C for three hours. The solvents were removed by short-path distillation leaving a light yellow residue. H_2O (10 mL) was added to the residue and the white precipitate was filtered and washed with aq. HCl (6 M, 6 mL). The combined filtrates were distilled off via short-path distillaiton to give crude **4** as a light yellow crystalline solid (0.644 g, 3.60 mmol). The crude material was recrystallised from hot EtOH to give colourless crystals of purified **5** (0.442 g, 2.47 mmol, 90%). ^{1}H NMR agreed with literature values[156] (500 MHz, D_2O): δ 4.19 (4H, t, J = 6.1 Hz, O-CH_2-CH_2), 2.11 (2H, quintet, J = 6.1 Hz, CH_2-CH_2-CH_2) ppm; ATR-IR: $\overline{\nu}$ = 3405 (N-H), 2877 (C-H), 1502 (N-O), 1449 (C-H), 1190 (C-O), 966 (N-O) cm^{-1}; ESI-MS: *m/z* 107 [M-2HCl].

6,6′-Dimethoxy-2,2′-[(1,3-propylene)dioxybis(nitrilomethylidyne)] diphenol (H_2L2)

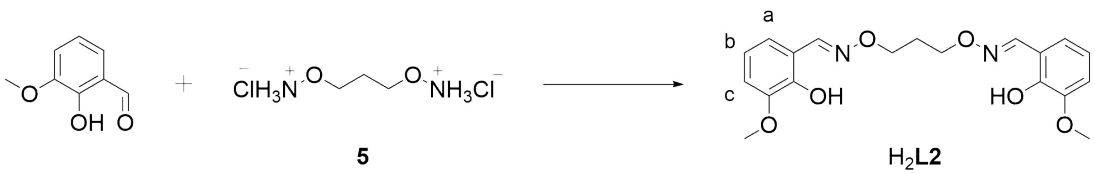

5 H_2**L2**

Adapted from the method of Ren *et al.*[157] To a solution of 3-methoxy-2-hydroxybenzaldehyde (0.850 g, 5.59 mmol, 2 eq.) in dry EtOH (30 mL) was added **5** (0.510 g, 2.79 mmol, 1 eq.) and Et_3N (0.780 mL, 5.59 mmol, 2 eq.). The light yellow solution was stirred at 55 °C for three hours. After cooling to RT, the light yellow precipitate was filtered and washed successively with cold H_2O, EtOH and Et_2O to give H_2**L2** as a light yellow solid (0.832 g, 2.22 mmol, 80%). ^{1}H NMR agreed with literature values[157] (500 MHz, $CDCl_3$): δ 9.87 (2H, s, Ar-O*H*), 8.20 (2H, s, C*H*=N), 6.91 (2H, dd, J_1 = 7.9 Hz, J_1 = 1.4 Hz, *a*), 6.86 (2H, t, J = 7.9 Hz, *b*), 6.81 (2H, dd, J_1 = 7.9 Hz, J_2 = 1.4 Hz, *c*), 4.32 (4H, t, J = 6.3 Hz, O-CH_2-CH_2), 3.91 (6H, s, O-CH_3), 2.16 (2H, quintet, J = 6.3 Hz, CH_2-CH_2-CH_2) ppm; ATR-IR: $\overline{\nu}$ = 3421 (O-H), 2941 (C-H), 1606 (C=N), 1576 (Ar), 1471 (C-H), 1412 (O-H), 1251 (Ar-O), 1066 (C-O), 993 (N-O), 729 (Ar) cm^{-1}; ESI-MS: *m/z* 397 $[M+Na]^+$.

2.4 H_4L3

The compound H_4**L3** utilised in complex **C65**, the $Cu^{II}_{12}Eu^{III}_4$ cluster, was produced as an extension to H_2**L2** to provide more possibilities for μ_2-O coordination. H_4**L3** was synthesised similarly to H_2**L2**, with the same adapted Gabriel synthesis, however an additional nucleophilic substitution reaction was included to synthesise the modified aromatic unit (Figure 2.7). The procedure was adapted from the methods of Smith *et al.* and Jeong *et al.* and gave **6** as a brown oil in 40 - 50% yield.[159,160] Alike H_2**L2**, a Schiff base condensation was the final reaction to obtain H_4**L3** as a dark yellow waxy solid. Optimisation of the temperature and length of reaction of the method used for H_2**L2** afforded H_4**L3** in $\sim$ 90% yield.

This research found two different coordination modes for H_4**L3**, with metal ions coordinated to the alkyloxime nitrogens and phenolate and hydroxy oxygens (Figure 2.8). For both modes, the ligand is found in the form $\mathbf{L3}^{4-}$ with the phenolate and hydroxy oxygens deprotonated. A key difference between the two modes is that for mode I, inner and outer coordination pockets are formed with additional coordinated metal ions on the exterior of the outer pocket. For Mode II, the ligand doesn't form coordination pockets, it coordinates the metal ion in an extended orientation with each aromatic unit coordinating to three metal ions.

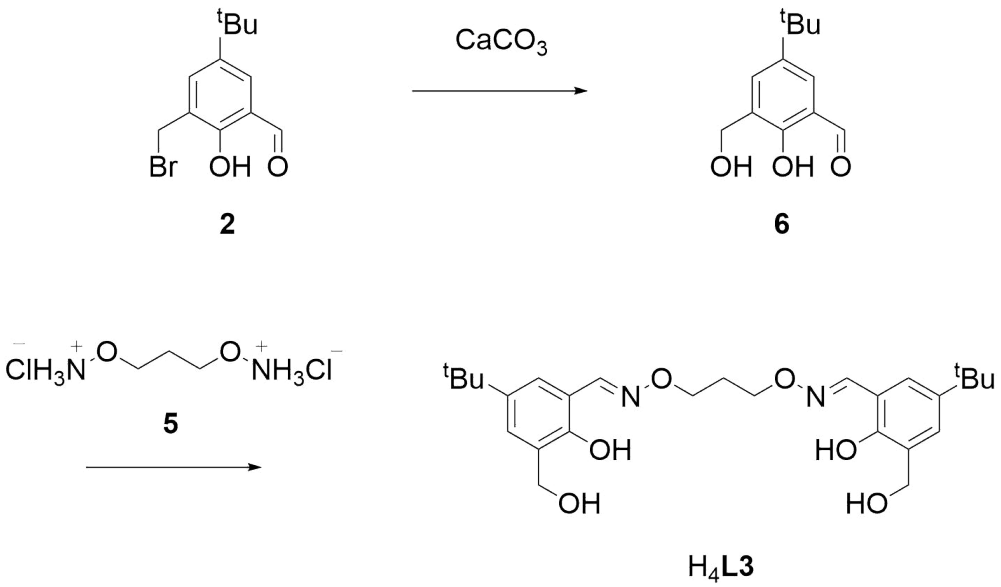

Figure 2.7: Reaction scheme for the synthesis of H_4**L3**

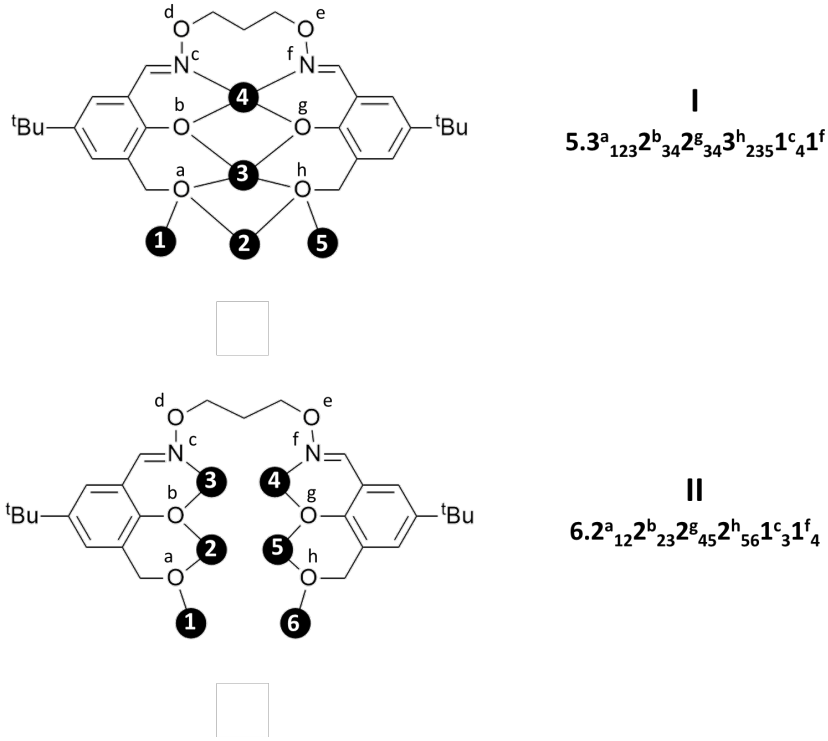

Figure 2.8: Representation of the coordination modes and Harris notation found for **L3**$^{4-}$ in this research. Metal ions are represented as black circles.

2.4.1 Synthetic Procedure for H_4L3

5-*tert*-Butyl-3-hydroxymethyl-2-hydroxybenzaldehyde (6)

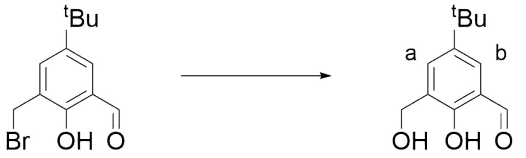

2 **6**

Adapted from the methods of Smith *et al.*[159] and Jeong *et al.*[160] To a stirred solution of **2** (2.04 g, 7.38 mmol, eq.) in dioxane (50 mL) was added a solution of $CaCO_3$ (3.69 g, 36.9 mmol, 5 eq.) in H_2O (50mL) at RT. The light yellow suspension was then refluxed overnight. The suspension was cooled to RT and filtered through celite. The filtrate was reduced *in vacuo* by half to give a yellow solution. The aqueous layer was extracted with DCM (2 x 30 mL) and combined organic layers were dried over anhydrous $MgSO_4$, filtered, and concentrated *in vacuo* to give **6** as a brown oil (0.813 g, 3.90 mmol, 52%). ^{1}H NMR agreed with literature values[159,160] (500 MHz, $CDCl_3$): δ 11.22 (1H, s, Ar-O*H*), 9.91 (1H, s, C*H*=O), 7.62 (1H, d, J = 2.3 Hz, *b*), 7.47 (1H, d, J = 2.3 Hz, *a*), 4.76 (2H, d, J = 5.6 Hz, Ar-CH_2-O), 1.34 (9H, s, ^{t}*Bu*) ppm; ATR-IR: $\overline{\nu}$ = 3278 (O-H), 2955 (C-H), 1649 (C=O), 1618 (Ar), 1454 (C-H), 1323 (O-H), 1218 (Ar-O), 1066 (C-O), 732 (Ar) cm^{-1}; ESI-MS: *m/z* 231 $[M+Na]^+$.

6,6′-Dihydroxymethyl-2,2′-[(1,3-propylene)dioxybis(nitrilomethylidyne)]diphenol (H_4L3)

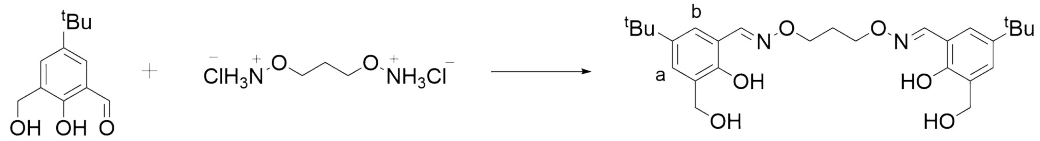

6 **5** H_4**L3**

Adapted from the method of Ren *et al.*[157] To a solution of **6** (0.47 g, 2.40 mmol, 2 eq.) in dry EtOH (20 mL) was added **5** (0.22 g, 1.20 mmol, 1 eq.) and Et_3N (0.33 mL, 2.40 mmol, 2 eq.). The light yellow solution was refluxed overnight. After cooling to RT, the yellow solution was concentrated *in vacuo* to give H_2**L3** as a dark yellow waxy solid (0.544 g, 1.12 mmol, 92%). ^{1}H NMR (500 MHz, $CDCl_3$): δ 10.09 (2H, s, Ar-O*H*), 8.24 (2H, s, C*H*=N), 7.34 (2H, d, J = 2.3 Hz, Ar-*b*), 7.12 (2H, d, J = 2.3 Hz, Ar-*a*), 4.74 (4H, d, J = 5.6 Hz, Ar-CH_2-O), 4.34 (4H, t, J = 6.1 Hz, O$-$CH_2-CH$_2$), 2.19 (2H, qunitet, J = 6.1 Hz, CH$_2-$CH_2-CH$_2$), 1.32 (9H, s, ^{t}*Bu*) ppm; ^{13}C NMR (176 MHz, $CDCl_3$): δ 153.2, 152.1, 142.5, 128.2, 127.7, 126.9, 115.5, 70.9, 62.1, 34.0, 31.4, 28.6 ppm; ATR-IR: $\overline{\nu}$ = 3382 (O-H), 3250 (O-H), 2956 (C-H), 1614 (C=N), 1478 (C-H), 1364 (O-H), 1217 (Ar-O), 1071 (C-O), 953 (N-O), 745 (Ar) cm^{-1}; ESI-MS: *m/z* 508 $[M+Na]^+$.

2.5 H_3L4

Throughout the course of this research, a common similarity found between the complexes was the coordination of phenolate groups in a μ_2 fashion, which provided a pathway for superexchange to occur. As this was shown to be an optimal feature, the design of the compound, H_3**L4**, 6,6′-dimethoxy-2,2′-[(4-*tert*-butylphenol)dimethyloxybis(nitrilomethylidyne)]diphenol (Figure 2.9), was centered around this with the inclusion of an additional phenolate group into the alkyloxime bridge. H_3**L4** was synthesised by a series of four reactions: a dimethylbromination followed by an adapted Gabriel synthesis, this time however using a Ing-Manske hydrolysis, and finally a Schiff base condensation to give H_3**L4** as a light yellow solid.

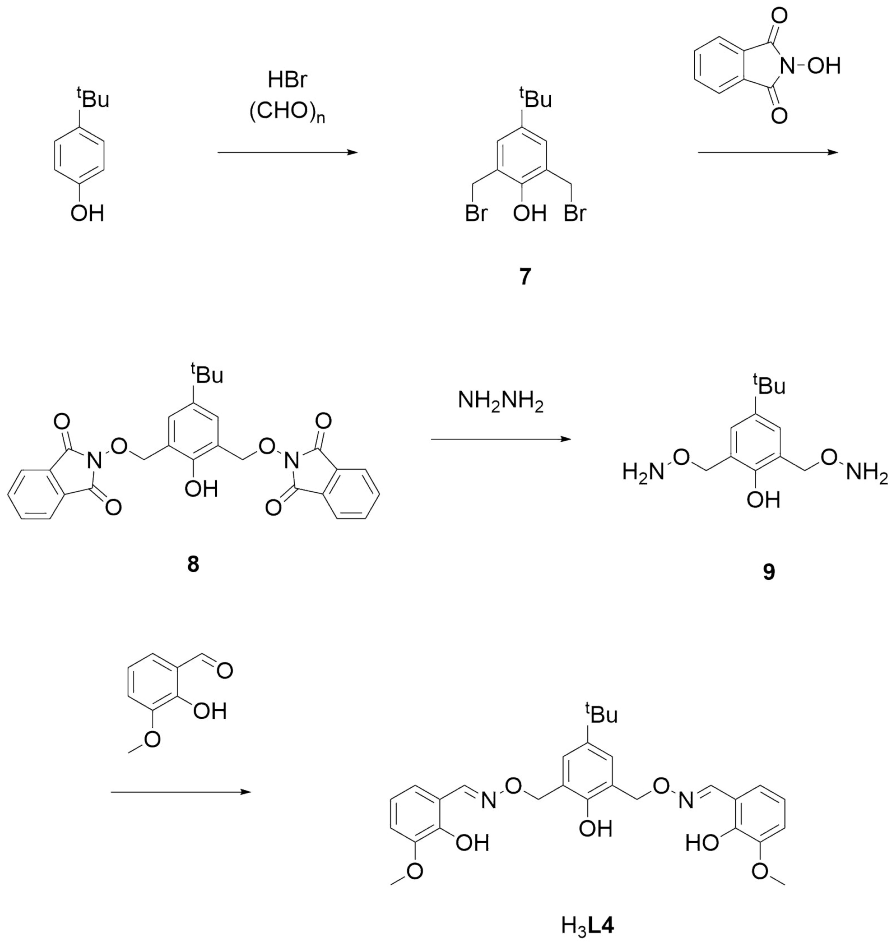

Figure 2.9: Reaction scheme for the synthesis of H_3**L4**

The dimethylbromination reaction followed the procedure of Baker *et al.* to give **7** as a dark yellow oil.[161] Previous work with similar methylbromination reactions showed that recrystallisation of the oily product produced a crystalline material that was nicer to work with. This led to the hot recrystallisation of the dark yellow oil from pentane to give **7** as a light yellow soild in 50% yield. An adapted Gabriel synthesis was performed to obtain the aminooxy bridge, where the condensation reaction followed that of an adapted method by Welch and Seper to give **8** as a white solid in $\sim$ 70% yield.[162] The isolation of **8** was simplified from the method of Welch and Seper as upon sitting at RT overnight, the white product precipitated out. The

second part of the Gabriel synthesis, a hydrolysis reaction, followed an adapted Ing-Manske procedure by Liu *et al.* to give **9** as a light yellow solid in $\sim$ 80% yield.[163] An Ing-Manske procedure was preferred over the acidic hydrolysis used to produce **5** in the effort to limit any side reaction from occuring with the phenolate group. The final reaction utilised a Schiff base condensation, the procedure of which followed an adapted method of Kulchat *et al.* to give H_3**L4** as a light yellow solid in $\sim$ 60% yield.

When analysing the literature, there were several examples of *o*-alkyloxime compounds where a central bridging group has additional oxygen coordinates, with a few examples closely resembling that of H_3**L4** however instead of the central unit being the bridge itself, two separate bridges join the central unit to the outer units (Figure 2.10).[164–166]

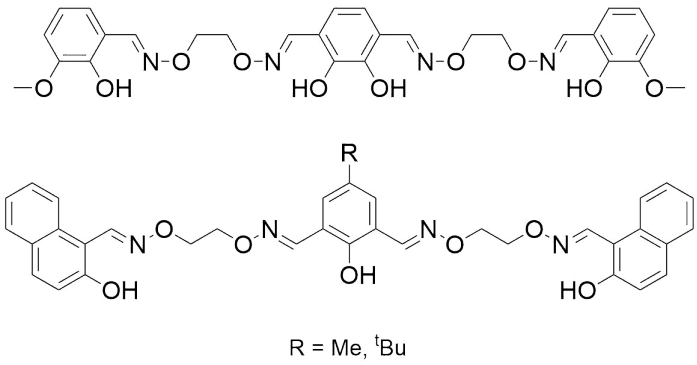

Figure 2.10: Similar oxygen containing central bridging units found in the literature; Top reported by Akine *et al.* and bottom reported by Pan *et al.* and Guo *et al.* for -Me and -^{t}Bu respectively.

During several complexation reactions it was found that H_3**L4** underwent rearrangement, resulting in two new ligands, 3-methoxy-2-hydroxybenzaldehyde oxime (**L5**) and 4-*tert*-butyl-2-(((((2-hydroxy-3-methoxybenzylidene)amino)oxy)methyl)benzyl)-6-*N*,*N*-diethylethanaminium phenolate (**L6**) (Figure 2.11). There are a number of possible pathways for which this rearrangement occurred, including protonation and/or metal ion coordination to produce good leaving groups. The method we are proposing is the coordination of a metal ion and subsequent protonation of an alkyloxime oxygen. As different metal ions coordinate in different fashions, for example a Ni^{II} ion would coordinate between the alkyloxime nitrogen and phenolate oxygen, whereas a Mn^{III} ion requires an additional donor, such as the phenolate oxygen of the bridge, therefore, the mechanism in Figure 2.12 only concerns the protonation part of the proposed mechanism. This method was proposed as the resulting ligand, **L5** has a protonated alkyloxime group and secondly, due to the fact it is less likely for a metal ion to coordinate to an alkyloxime oxygen.

L5 was found to have one coordination mode, with one metal ion coordinated to the oxime nitrogen and phenolate oxygen. **L6** was also found to have a single coordination mode, with a metal ion coordinated to the two phenolate oxygens and the alkyloxime nitrogen. In terms of reproducibility, both ligands **L5** and **L6** can be reproduced through complexation of H_3**L4** with either Cu^{II}/Ni^{II} or Mn^{II} ions respectively.

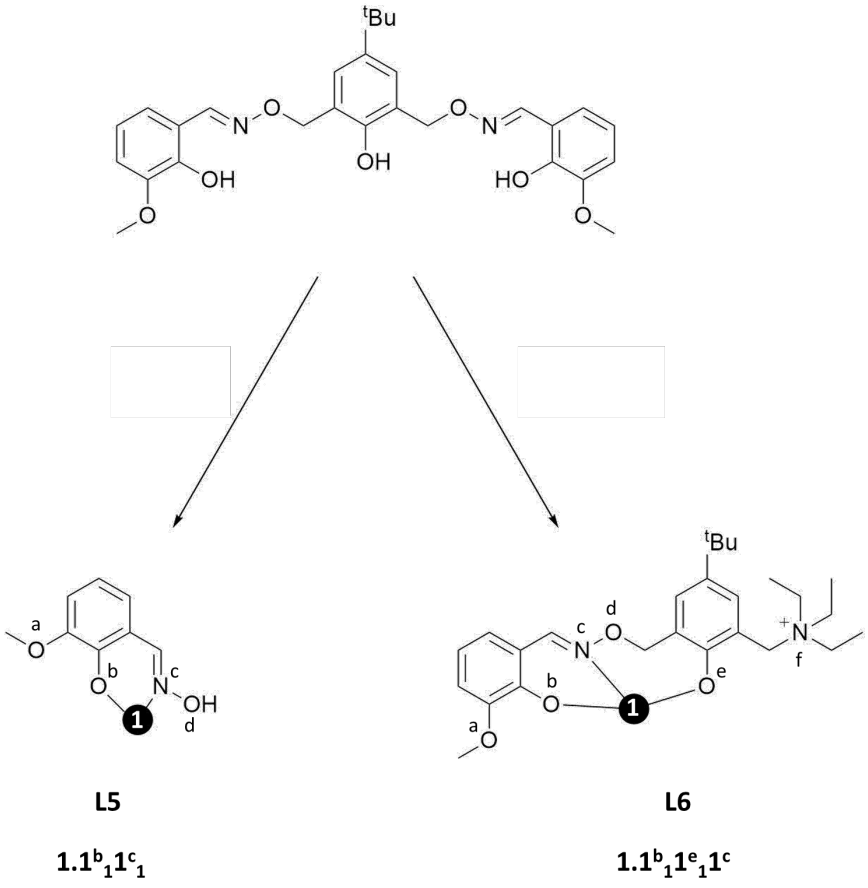

Figure 2.11: Representation of the coordination modes and Harris notation found for the *in situ* ligands, **L5** and **L6** in this research. Metal ions are represented as black circles.

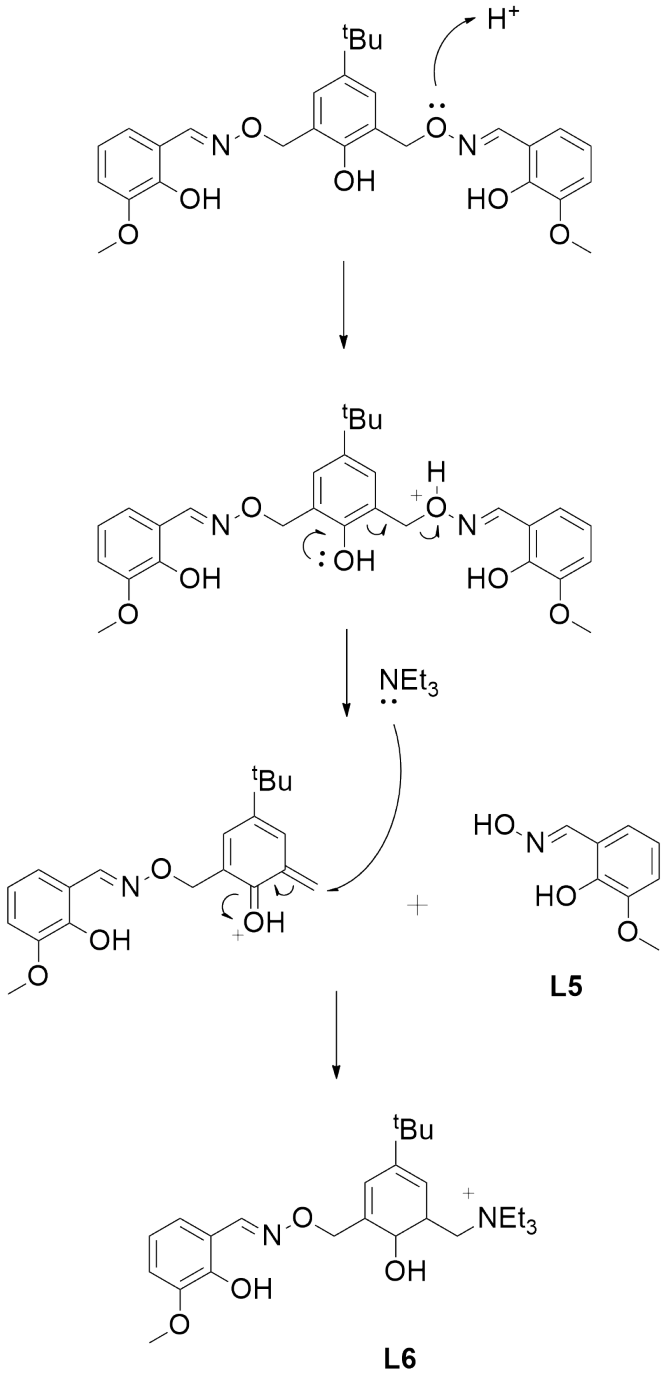

Figure 2.12: Mechanism for the proposed rearrangement of H_3**L4** to produce the ligands **L5** and **L6**.

2.5.1 Synthetic procedure for H_3L4

4-*tert*-Butyl-2,6-dibromomethylphenol (7)

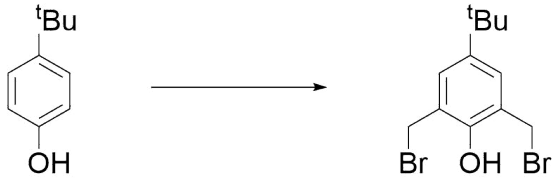

7

Prepared as per the method of Baker *et al.*[161] To a stirred solution of paraformaldehyde (2.55 g, 0.085 mol, 2.5 eq.) in HBr (48% in AcOH; 26 mL, 0.15 mol, 4.4 eq.) at 0 °C was added 4-*tert*-butylphenol (5.10 g, 0.034 mmol, 1 eq.) slowly portionwise. The solution was stirred at 0 °C for one hour, then a further two hours at RT. Ice (100 g) was added to the solution and it was allowed to warm to RT. The aqueous layer was extracted with petroleum ether (60-80; 2 x 30 mL), followed by DCM (2 x 30 mL). The organic layers were combined and dried over anhydrous $CaCl_2$, filtered, and concentrated *in vacuo* to give crude **7** as dark yellow oil (6.30 g, 0.0187 mol). The crude material was recrystallised from hot pentane to give purified **7** as a light yellow solid (5.71 g, 0.0170 mol, 50%). ^{1}H NMR agreed with literature values[161] (500 MHz, $CDCl_3$): δ 7.26 (2H, s, Ar-*H*), 5.49 (1H, s, Ar-O*H*), 4.57 (4H, s, Ar-CH_2-Br), 1.29 (9H, s, ^{t}*Bu*) ppm; ATR-IR: $\overline{\nu}$ = 3498 (O-H), 2958 (C-H), 1491 (Ar), 1462 (C-H), 1364 (O-H), 1208 (Ar-O), 1119 (C-O), 762 (Ar), 566 (C-Br) cm^{-1}; ESI-MS: *m/z* 337 $[M+H]^+$.

4-*tert*-Butyl-2,6-Bis(phthalimidooxymethyl)phenol (8)

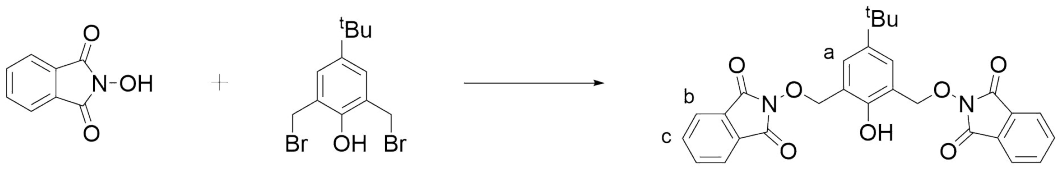

7 **8**

Adapted from the method of Welch and Seper.[162] To a solution of **7** (0.516 g, 1.53 mmol, 1 eq.) in MeCN (8 mL) was added *N*-hydroxyphthalimide (0.506 g, 3.07 mmol, 2 eq.) and Et_3N (0.43 mL, 3.07 mmol, 2 eq.). The orange solution was refluxed for three hours. The light yellow solution was left to sit at RT overnight, producing a white precipitate. The precipitate was filtered and washed with cold MeCN to give **8** as a white solid (0.591 g, 1.18 mmol, 77%). ^{1}H NMR (500 MHz, $CDCl_3$): δ 7.85-7.83 (4H, m, Ar-*b*), 7.75-7.73 (4H, m, Ar-*c*), 7.38 (2H, s, Ar-*a*), 5.31 (4H, s, Ar-CH_2-O), 1.22 (9H, s, ^{t}*Bu*) ppm; ^{13}C NMR (125.7 MHz, $CDCl_3$): δ 163.8, 153.8, 142.8, 134.6, 130.3, 128.9, 123.7, 120.3, 76.8, 34.0, 31.3 ppm; ATR-IR: $\overline{\nu}$ = 3400 (O-H), 2963 (C-H), 1785 (C=O), 1716 (C=O), 1491 (N-O), 1466 (C-H), 1366 (O-H), 1214 (Ar-O), 1185 (C-N), 1080 (C-O), 970 (N-O), 698 (Ar) cm^{-1}; ESI-MS: *m/z* 522 $[M+Na]^+$.

4-*tert*-Butyl-2,6-Bis(aminooxymethyl)phenol (9)

8 **9**

Adapted from the method of Liu *et al.*[163] To a stirred suspension of **8** (0.502 g, 1.00 mmol, 1 eq.) in DCM (2 mL) was added $NH_2NH_2 \cdot H_2O$ (0.26 mL, 2.70 mmol, 2.7 eq.) slowly dropwise. The suspension immediately turned to a yellow solution, which was left to stir at RT overnight. The white precipitate that formed was filtered and the filtrate was poured into Et_2O (20 mL) at 0 °C and stirred for 30 minutes. The light yellow solution was concentrated *in vacuo* to give crude **9** as a yellow solid (0.387 g). The crude material was dried under high vac for 24 hours to give **9** as a light yellow solid (0.202 g, 0.842 mmol, 84%). ^{1}H NMR (500 MHz, $CDCl_3$): δ 7.24 (2H, s, Ar-*H*), 4.77 (4H, s, Ar-CH_2-O), 1.30 (9H, s, ^{t}*Bu*) ppm; ^{13}C NMR (125.7 MHz, $CDCl_3$): δ 153.0, 142.6, 128.6, 124.3, 74.7, 34.1, 31.6 ppm; ATR-IR: $\overline{\nu}$ = 3444 (N-H), 3282 (O-H), 2937 (C-H), 1651 (N-H), 1557 (Ar), 1475 (C-H), 1364 (O-H), 1170 (C-O), 1035 (N-O), 804 (Ar) cm^{-1}; ESI-MS: *m/z* 241 $[M+H]^+$.

6,6′-Dimethoxy-2,2′-[(4-*tert*-Butylphenol)dimethyloxybis(nitrilomethylidyne)]diphenol (H_3L4)

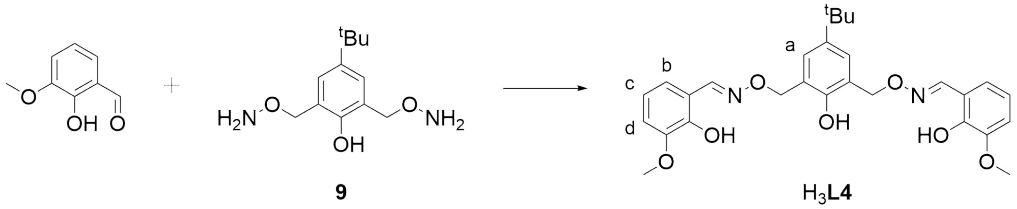

9 H_3**L4**

Adapted from the method of Kulchat *et al.*[167] To a solution of 3-methoxy-2-hydroxybenzaldehyde (0.13 g, 0.84 mmol, 2 eq.) in dry MeOH (5 mL) was added **9** (0.10 g, 0.42 mmol, 1 eq.) and the dark yellow solution was refluxed for three hours. The solution was cooled to RT, followed by cooling in the freezer overnight. The light yellow precipitate that formed was filtered and washed sequentially with cold MeOH and Et_2O to give H_3**L4** as a light yellow solid (0.127 g, 0.25 mmol, 59%). ^{1}H NMR (500 MHz, $CDCl_3$): δ 9.02 (2H, s, Ar-O*H*), 8.26 (2H, s, C*H*=N), 7.54 (1H, s, Ar-O*H*), 7.29 (2H, s, *a*), 6.88 (2H, td, J_1 = 7.27 Hz, J_2 = 1.89 Hz, *c*), 6.86 - 6.82 (4H, m, *ad*), 5.26 (4H, s, Ar-CH_2-O), 3.89 (6H, s, OCH_3), 1.30 (9H, s, ^{t}*Bu*) ppm; ^{13}C NMR (125.7 MHz, $CDCl_3$): δ 152.4, 150.7, 147.9, 146.7, 143.0, 128.6, 123.1, 121.7, 119.5, 116.5, 113.2, 73.6, 56.1, 34.0, 31.5 ppm; ATR-IR: $\overline{\nu}$ = 3412 (O-H), 3152 (O-H), 2957 (C-H), 1609 (C=N), 1575 (Ar), 1463 (C-H), 1362 (O-H), 1258 (Ar-O), 1214 (C-O), 995 (N-O), 728 (Ar) cm^{-1}; ESI-MS: *m/z* 509.16 $[M+H]^+$.

Chapter 3

Defective Dicubanes

This chapter describes a series of Ni^{II}_4 defective dicubanes and explores the way in which magnetism can be manipulated through synthetic modification. This research is an extension to previous work conducted by the Plieger group, which resulted in a Ni^{II}_4 defective dicubane, $[Ni^{II}_4(H\mathbf{L1})_2(OMe)_2(OAc)_2Cl_2] \cdot 3Et_2O$ (Figure 3.1), that exhibited dominant ferromagnetic exchange. Three key exchange interactions were found: J_1, Ni1-O1-Ni2, J_2, Ni1-Cl1-Ni2, and J_3, Ni1-O2-Ni1 (Figure 3.2). The research presented here further investigates how small structural changes can affect the overall magnetic properties in the hope of controlling and promoting ferromagnetic exchange between metal centres. The original dicubane, found to have dominant ferromagnetic exchange, will be the starting point for structural modifications to further improve upon the ferromagnetic exchange.[148,149] The target for the structural modifications were the original three exchange interactions, aiming for Ni-L-Ni angles of 95 - 98°, with modifications occuring on the bridging groups and/or crystal lattice.[168–170] The structural modifications resulted from the use of different solvents and/or metal anions during complexation.

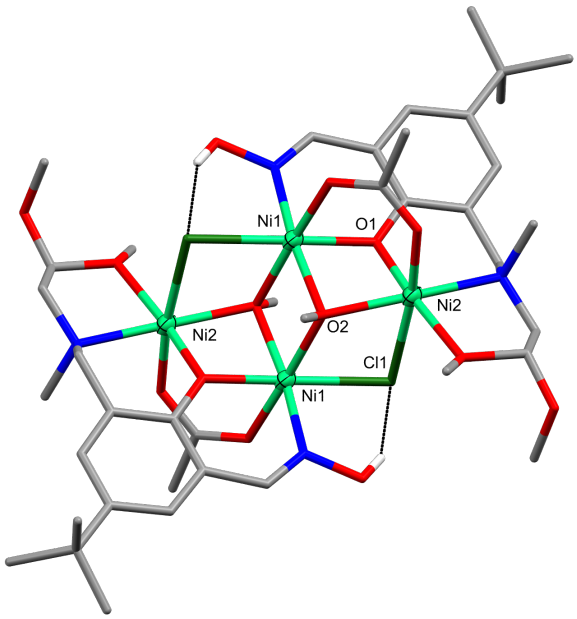

Figure 3.1: Crystal structure of the original Ni^{II}_4 defective dicubane, $[Ni^{II}_4(H\mathbf{L1})_2(OMe)_2(OAc)_2Cl_2] \cdot 3Et_2O$. Non-interacting hydrogen atoms and lattice solvent molecules have been omitted for clarity, hydrogen bonding represented as black dotted lines, and the thermal ellipsoids of the metal ions are shown at 70% probability. Colour code: Ni^{II} = light green, N = blue, O = red, Cl = dark green, C = grey, and H = white.

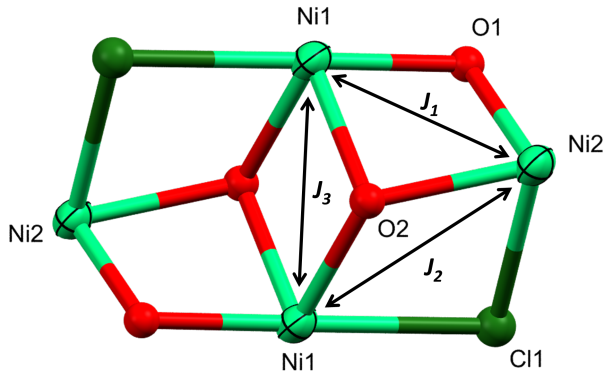

Figure 3.2: The three exchange interactions, J_1, J_2, and J_3, of the original Ni^{II}_4 defective dicubanes. Colour code: Ni^{II} = light green, O = red, and halide = dark green.

3.1 Results and Discussion

The solid state complexes **C1** - **C5** were synthesised by a RT reaction between H_2**L1**, $NiX_2{\cdot}H_2O$ (X = OAc^-, $BF_4{}^-$, Cl^-), and Et_3N in a 1 : 2 : 6 molar ratio. For all complexes, a visible colour change from the yellow ligand solution to a green solution indicated successful coordination. The complexes were isolated by slow vapour diffusion of Et_2O into the reaction solution over a period of three to nine weeks where X-ray quality crystals were obtained. Successful complexations were confirmed by SCXRD, ATR-IR, and CHN microanalysis. Magnetic and computational analyses were performed through a collaboration with Prof. Euan Brechin and his research group at The University of Edinburgh.

Table 3.1: Structural differences in the complexes **C1** - **C5**

	M	Anion	Solvent
C1	Ni^{II}	$OMe^-/Cl^-/OAc^-$	–
C2	Ni^{II}	$OH^-/Cl^-/OAc^-$	–
C3	Ni^{II}	OMe^-/Cl^-	MeOH
C4	Ni^{II}	OMe^-/F^-	MeOH
C5	Ni^{II}	$OMe^-/Cl^-/F^-$	MeOH

3.1.1 Structural Analysis

The complexes **C1** - **C5**, were found to be tetranuclear with a defective dicubane topology, crystallising in either the monoclinic space groups, $P2_1/a$ (**C1**) and $P2_1/c$ (**C3** and **C5**) or the triclinic space group, $P\bar{1}$ (**C2** and **C4**). Representative structures and the metallic cores highlighting the different bridging groups are shown in Figures 3.3 and 3.4 respectively, with full structures of **C1** - **C5** found in Figures B.1 - B.5.

The general structure of **C1** - **C5**, consists of two oxime ligands, H**L1**$^{2-}$, coordinated to four Ni^{II} ions (Mode I, Figure 2.2), with bridging and capping groups such as OMe^-, OH^-, OAc^-, Cl^-, F^-, and MeOH. Each Ni^{II} ion is six-coordinate with an octahedral geometry as determined by CShM (Table B.1), with selected bond lengths and angles found in Table 3.2.[146,147,171] For all complexes, the body ions (Ni1/3) have

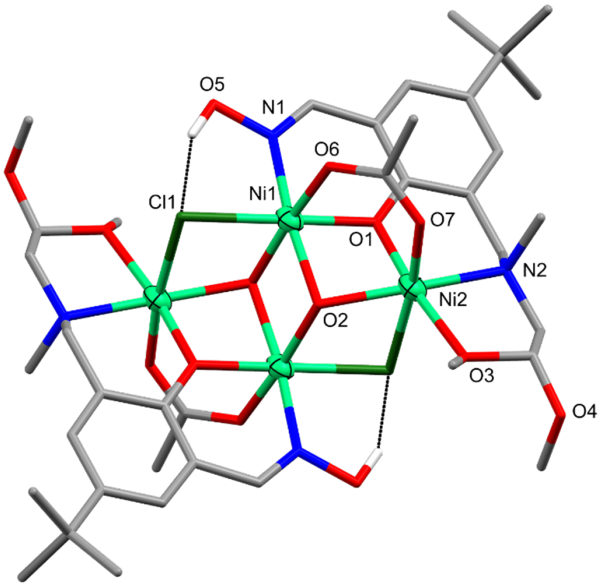

C1 & **C2**

$[Ni^{II}_4(HL1)_2(O)_2(OAc)_2Cl_2]$

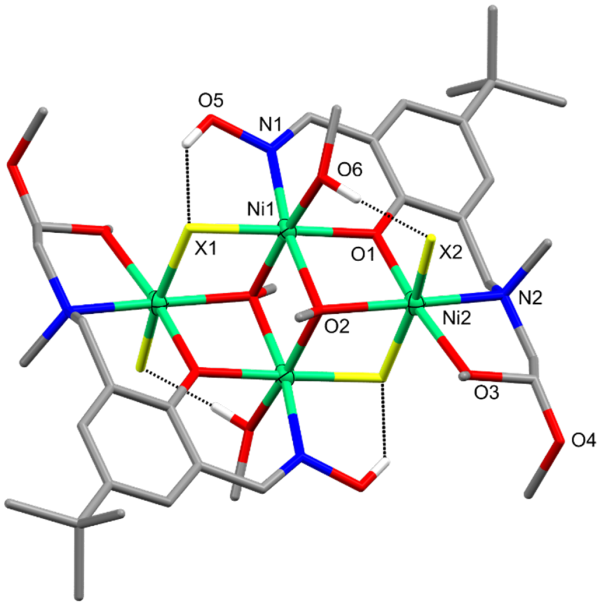

C3 - **C5**

$[Ni^{II}_4(HL1)_2(OMe)_2(MeOH)_2X_4]$

Figure 3.3: Figures of the two different types of Ni^{II}_4 defective dicubanes. Top is representative of **C1** and **C2**, $[Ni^{II}_4(HL1)_2(O)_2(OAc)_2Cl_2]$·solvent (O = OMe^- (**C1**) and OH^- (**C2**)) and bottom is representative of **C3** - **C5**, $[Ni^{II}_4(HL1)_2(OMe)_2(MeOH)_2X_4]$·solvent (X = Cl^- (**C3**), F^- (**C4**), and F^-/Cl^- (60 : 40, **C5**)). Non-interacting hydrogen atoms have been omitted for clarity, hydrogen bonding is represented as black dotted lines, and the thermal ellipsoids of the metal ions are shown at 70% probability. Colour code: Ni^{II} = light green, N = blue, O = red, X = dark green, C = grey, and H = white.

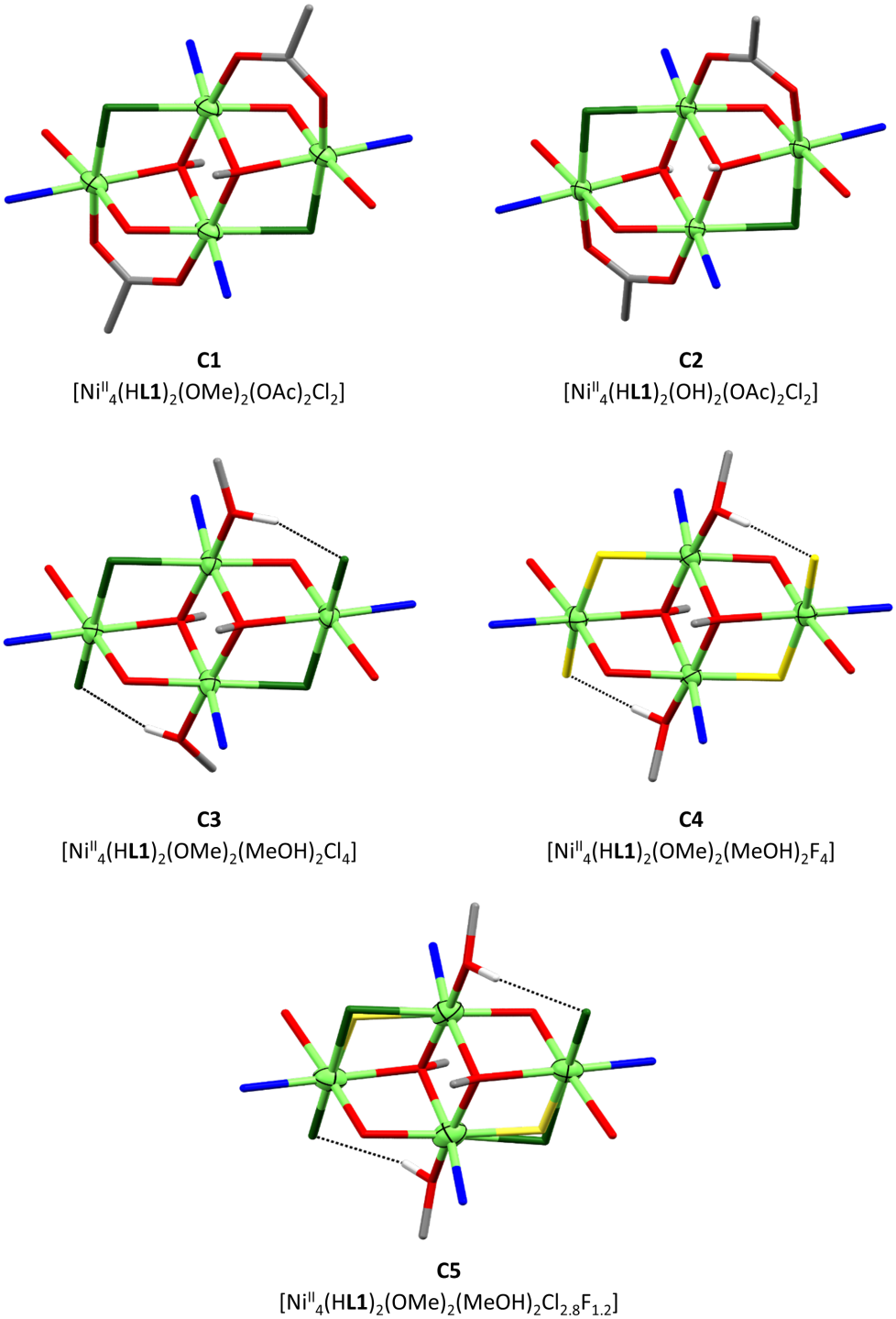

Figure 3.4: The metallic cores of the Ni^{II}_4 defective dicubanes **C1** - **C5** illustrating the structural differences. Non interacting hydrogen atom have been omitted for clarity, hydrogen bonding represented as black dotted lines, and the thermal ellipsoids of the metal ions are shown at 70% probability. Colour code: Ni^{II} = light green, N = blue, O = red, Cl = dark green, F = yellow, C = grey, and H = white.

a donor set of NO_4Cl consisting of a phenolate oxygen, an oxime nitrogen, two μ_3-O groups (OMe^- (**C1**, **C3** - **C5**) and OH^- (**C2**)), one μ_2 halide (Cl^- (**C1** - **C3** and **C5**) and F^- (**C4** and **C5**)), and either an OAc^- (**C1** and **C2**) or a MeOH molecule (**C3** - **C5**). For the wingtip ions (Ni2/4), the donor sets vary between the two different defective dicubane types however for all complexes, the wingtip ions are coordinated to one each of phenolate and methoxy oxygens, an amino nitrogen, a μ_3-O group (OMe^- (**C1** and **C3** - **C5**) or OH^- (**C2**)) and one μ_2 halide (Cl^- (**C1** - **C3** and **C5**) or F^- (**C4** and **C5**)). For **C1** and **C2**, the NO_4Cl donor set is completed by an OAc^- anion. For **C3** - **C5**, the NO_3X_2 donor sets are completed by a capping halide (Cl^- (**C3** and **C5**) or F^- (**C4** and **C5**)). For all complexes, moderate hydrogen bonding is found between the oxime OH groups (O5) and the μ_2 halides (X1), O5$\cdots$X1, 2.657(2) - 3.073(7) Å, additionally for complexes, **C3** - **C5**, moderate hydrogen bonding is found between the capping halide (X2) and MeOH molecules (O6) O6$\cdots$X2, 2.657(2) - 3.018(3) Å.[158] All complexes are found to have solvent molecules, such as MeOH (**C1** and **C4**), MeCN (**C2**), and Et_2O (**C3** and **C5**) in the crystal lattice. The MeOH molecules are found to form moderate hydrogen bonds with the OAc^- anions (O6$\cdots$O8, 2.835(4) Å) in **C1** and between another MeOH molecule (O8$\cdots$O7, 2.729(3) Å) and the capping halides (O7$\cdots$F2, 2.559(2) Å) in **C4**.[158]

As shown by the Figure 3.3, there are two distinct types of defective dicubanes, **C1**/**C2** and **C3** - **C5**. For the complexes **C1** and **C2**, the key difference is the oxygen donors bridging the Ni1-Ni1' pathway (J_3). The use of OMe^- versus OH^- donors has shown to not significantly influence the Ni1-O2-Ni1' angle as both complexes have an angle of 94°(Table 3.3). For the complexes, **C3** - **C5**, the J_2 pathway was exploited, with the use of different halides and/or combination of halides. Complexes **C3** and **C4**, are opposites with the use of Cl^- and F^- anions respectively, which has resulted in the biggest difference in the exchange angles with 86.80° for the Cl^- bridge and 98.14(5)° for the F^- bridge. **C5** has both Cl^- and F^- bridges for this pathway, and as shown in Table 3.3, the Cl^- bridge has decreased in angle whereas the F^- bridge has increased in angle in comparison to **C3** and **C4** respectively. When comparing the two types of dicubanes, the pathway with the greatest difference in angle is J_1, Ni1-O1-Ni2. Although the bridge is via the phenolate for all complexes, **C1**/**C2** has additional OAc^- bridging whereas **C3** - **C5** has interacting (hydrogen bonding) halide and MeOH molecules. From Table 3.3 it can be seen that the OAc^- bridging incorporation into the structure has resulted in a smaller Ni1-O1-Ni2 angle with 94.75(12)° and 94.20(10)° for **C1** and **C2** respectively, while the hydrogen bonded molecules have shown to influence a larger Ni1-O1-Ni2 angle with 100.30°, 98.92(7)°, and 99.64° for **C3** - **C5** respectively.

In addition to the bridging groups, the crystal lattice was targeted with the inclusion of different solvents. One of the biggest differences found was when comparing **C1** with the original Ni^{II}_4 defective dicubane. From a first glance, these two dicubanes appear identical however they have differing lattice bound solvent molecules. **C1** has MeOH molecules, which form hydrogen bonds whereas the original has Et_2O molecules. It was found that the inclusion of an interacting lattice bound solvent did not greatly influence the exchange angles, however it did greatly affect the packing of the unit cell. This can be seen in the intermolecular Ni1-Ni1' distances within and between planes. The Ni1-Ni1' distance within a plane for **C1** is 10.91 Å whereas for the original it is 13.86 Å. Between planes the Ni1-Ni1' distance is 10.15 Å for **C1** and 9.94 Å for the original.

Table 3.2: Selected bond lengths (Å) and angles (°) of the complexes **C1** - **C5** from crystal structure determination

	C1	**C2**	**C3***	**C4**	**C5***
Ni1-Cl1	2.428(1)	2.477(1)	2.407	–	2.296
Ni1-O1	2.006(3)	2.021(2)	2.008	1.997(2)	2.012
Ni1-O2	2.058(3)	2.034(2)	2.082	2.049(2)	2.058
Ni1-O6/11	2.071(3)	2.045(3)	2.090	2.120(2)	2.103
Ni1-N1	2.054(3)	2.042(3)	2.050	1.996(2)	2.014
Ni1-O2	2.071(3)[a]	2.079(2)[b]	2.078	2.043(2)[c]	2.060
Ni1-F1	–	–	–	2.077(1)	2.107
Ni2-O1	2.006(3)[a]	2.004(2)[b]	2.030	2.010(2)[c]	2.030
Ni2-O2	2.063(3)	2.019(2)	2.080	2.061(2)	2.091
Ni2-O7	2.021(3)	2.041(3)	–	–	–
Ni2-O3/5	2.163(3)	2.139(2)	2.179	2.151(2)	2.174
Ni2-N2	2.096(4)	2.083(3)	2.096	2.084(2)	2.090
Ni2-Cl1	2.474(1)	2.515(1)	2.476	–	2.485
Ni2-Cl3	–	–	2.374	–	2.360
Ni2-F1	–	–	–	2.080(1)	2.043
Ni2-F2	–	–	–	2.000(1)	–
Ni1-O2-Ni1/3	98.24(11)[a]	99.85(9)[b]	95.65	95.18(7)[c]	94.96
Ni1-O1-Ni2/4	94.75(12)[a]	94.20(10)[b]	100.30	98.92(7)[c]	99.64
Ni1-Cl1-Ni2	85.60(4)	83.51(3)	86.80	–	84.82
Ni1-F1-Ni2	–	–	–	98.14(5)	102.10
Ni1-O2-Ni2	107.82(14)	110.21(11)	106.95	99.88(7)	102.26
Ni2-O2-Ni1/3	91.13(11)[a]	92.02(9)[b]	96.80	95.64(7)[c]	96.04
Ni1···Ni1/3	3.122(1)[a]	3.147(1)[b]	3.083(2)	3.021(1)[c]	3.035(1)
Ni1···Ni2	2.952(1)	2.949(1)	3.100	3.046(1)	3.088
Ni2···Ni2/4	5.465(2)[a]	5.439(1)[b]	5.675(2)	5.400(1)[c]	5.540(1)

* Averaged values; Non-averaged values can be found in Tables B.3 and B.2

[a] 1-X, 1-Y, -Z; [b] 1-X, 1-Y, 1-Z; [c] -X, 1-Y, 1-Z

Table 3.3: Bond angles of the three key exchange pathways (J_1 - J_3) for complexes **C1** - **C5** from crystal structure determination

	J_1 Ni1-O1-Ni2 (°)	J_2 Ni2-X1-Ni1′ (°)	J_3 Ni1-O2-Ni1′ (°)
C1	94.75(12)	85.60(4)	98.24(11)
C2	94.20(10)	83.51(3)	99.85(9)
C3*	100.30	86.80	95.65
C4	98.92(7)	98.14(5)	95.18(7)
C5*	99.64	84.82[a] 102.10[b]	94.96

* Averaged values; Non-averaged values found in Table B.2

[a] Ni1-Cl-Ni2; [b] Ni1-F-Ni2

3.1.2 Magnetic Analysis

Magnetic characterisation has been performed on complexes **C1** - **C3** and **C5**. The magnetic characterisation was performed at The University of Edinburgh through collaborative work with Prof. Euan Brechin and his research group.[149] For complexes **C1**, **C3**, and **C5**, variable-temperature, solid-state DC magnetic susceptibility data in the temperature range T = 290 - 2 K was collected on a Quantum Design MPMS XL-5 SQUID magnetometer equipped with a 7 T DC magnet. For the complex **C2**, magnetic susceptibility and magnetisation measurements in the temperature range T = 300 - 2 K was collected on a Quantum Design PPMS Dynacool VSM magnetometer in the field range, B = 0.1 - 9 T. Samples were mounted in gelatine capsules and either embedded in eicosane or restrained by the addition of a small quantity of either eicosane or hexadecane. The magnetic measurements for both series had their observed paramagnetic susceptibilities corrected for diamagnetic contributions using Pascal's constants.

For complexes **C1** - **C3** and **C5** DC molar magnetic susceptibilities, χ_M, were measured on polycrystalline samples in an applied magnetic field of B = 0.1 T over the temperature ranges of 290 - 2 K (**C1**, **C3**, and **C5**) and 300 - 2 K (**C2**). The experimental results are shown in Figures 3.5a and 3.6a in the form of a $\chi_M T$ versus T plot. At 290 K the $\chi_M T$ values for **C1**, **C3**, and **C5** were found to be 5.48, 5.25, and 4.91 cm^3 K mol^{-1} respectively. The values resemble what was expected for four uncorrelated Ni^{II} ions at 290 K (S_{Ni} = 1, $\chi_M T$ = 5.06 cm^3 K mol^{-1}, and g_{Ni} = 2.25), with the values for **C1** and **C3** slightly above and **C5** slightly below. For **C2**, the $\chi_M T$ value at 300 K was found to be 4.61 cm^3 K mol^{-1}, slightly above what was expected for four uncorrelated Ni^{II} ions at 300 K (S_{Ni} = 1, $\chi_M T$ = 4.41 cm^3 K mol^{-1}, and g_{Ni} = 2.10). For **C1** - **C3**, the $\chi_M T$ value rises upon cooling to reach a maxima of 10.72 (T = 3.7 K), 5.06 (T = 50 K), and 5.62 (T = 18 K) cm^3 K mol^{-1} respectively. Further cooling causes the $\chi_M T$ values to rapidly fall to 9.87 (**C1**), 0.55 (**C2**) and 4.42 (**C3**) cm^3 K mol^{-1} at 2 K. As these susceptibility values are lower than expected for a ferromagnetically coupled $[Ni^{II}_4]$ unit (S = 4; 12.66 cm^3 K mol^{-1}), it is assumed that there are competing ferro- and antiferromagnetic exchange interactions present, along with ZFS effects and antiferromagnetic intermolecular interactions. For **C5**, the experimental susceptibility data is indicative of dominating antiferromagnetic exchange interactions, as evidenced by the $\chi_M T$ value remaining constant upon initial cooling to approximately 77 K, where it rapidly falls to a $\chi_M T$ value of 1.58 cm^3 K mol^{-1} at 2 K. As the complex **C5** has a large degree of disorder in the Cl^-/F^- bridges, the magnetisation data shown in Figures 3.5a and 3.5d has not been fitted.

To obtain a greater definition of the magnetic properties at low temperatures, variable-temperature variable-field (VTVB) magnetisation measurements were performed in the temperature ranges of 3 - 6 K (**C1**, **C3**, and **C5**) and 2 - 10 K (**C2**) and magnetic field ranges of 0.5 - 7 T (**C1**, **C3**, and **C5**) and 0.5 - 9 T (**C2**) as shown in Figures 3.5b - 3.5d and 3.6b. For complexes, **C1**, **C3**, and **C5** the magnetisation reaches a maxima at a temperature of 3 K and field of 7 T to give 8.77, 7.02, and 7.02 μ_B respectively. For **C2**, the magnetisation data rises rapidly in a near linear fashion reaching a maxima at a temperature of 2 K and field of 9 T to give a value of 5.62 μ_B.

The susceptibility and magnetisation data and exchange interactions for complexes

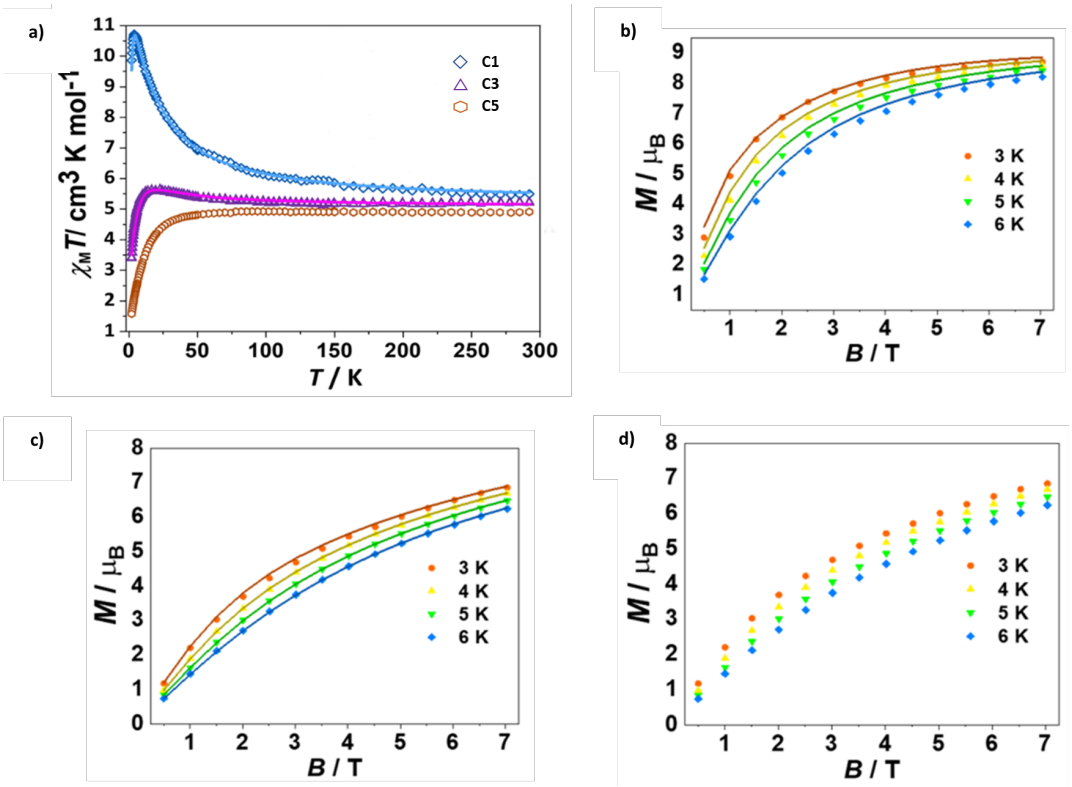

Figure 3.5: (a) $\chi_M T$ vs T for **C1**, **C3**, and **C5** in the temperature (T) range 290 - 2 K and magnetic field (B) of 0.1 T. Field dependence of the magnetisation (M) measured in the T = 3 - 6 K and B = 0.1 - 7 T temperature and field ranges for complexes **C1** (b), **C3** (c), and **C5** (d). The solid lines for (a) - (c) are the corresponding fit of the experimental data. The data for **C5** (brown hexagons in plots (a) and (d)) has not been fitted due to the large degree of disorder present in the complex.

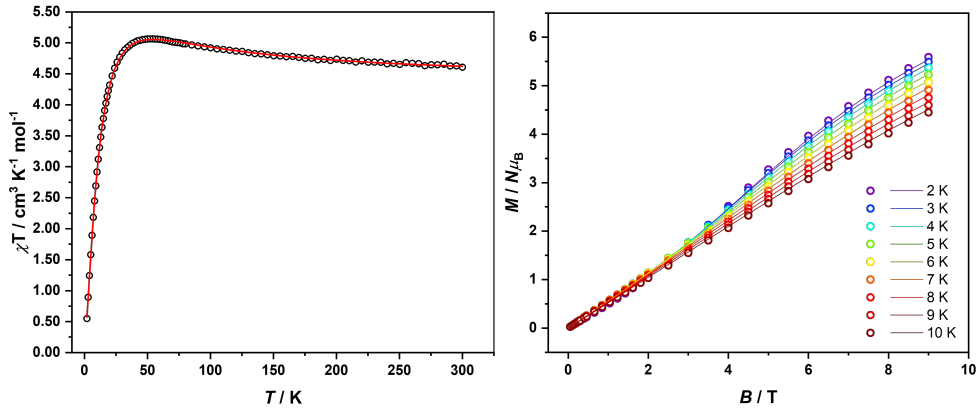

Figure 3.6: (a) $\chi_M T$ vs T for **C2** in the temperature (T) range 300 - 2 K and magnetic field (B) of 0.1 T. (b) Plot of magnetisation (M) versus field measured in the T = 2 - 10 K and B = 0.5 - 9.0 T temperature and field ranges. The solid lines represent the simultaneous fit of the susceptibility and magnetisation data using spin-Hamiltonian (Equation 3.2).

C1 and **C3** were fitted simultaneously using the program PHI with the spin-Hamiltonian (Equation 3.1), where the summation indices i and j label consecutive metal centres, D is the uniaxial single-ion anisotropy parameter of Ni^{II}, $\hat{S}$ is a spin operator, S is the total spin, and J is the isotropic exchange interaction parameter.[172] In order to determine the exchange interactions between the Ni^{II} ions, a model using three different exchange couplings was employed. The three couplings used were the two wing-body interactions (J_1, Ni-O-Ni and J_2, Ni-X-Ni) and the body-body interaction (J_3, Ni-O-Ni) as illustrated in Figure 3.2. These interactions are typical for a [M_4] butterfly and are a reflectance of the significantly different exchange angles present (the fitted values can be found in Table 3.4). The experimental values found for the exchange interactions and anisotropy parameters for **C1** and **C3** are consistent with similar Ni^{II} based defective dicubanes found in the literature.[173–176]

$$\hat{H} = \sum_i D_i \left(\hat{S}_{z,i}^2 - \frac{1}{3} S_i(S_i+1) \right) + \mu_B B \sum_i g_i \hat{S}_i - 2 \sum_{i,j<1} J_{i,j} \hat{S}_i \cdot \hat{S}_j \tag{3.1}$$

The susceptibility and magnetisation data for **C2** were simultaneously fitted to the spin-Hamiltonian, Equation 3.2 (where the first part is a Heisenberg exchange term, the second part collects the anisotropy terms of the Ni^{II} ions, and the third part is the Zeeman term), employing the same model as **C1** and **C3** with three different exchange interactions. This affords the best fit parameters J_1 = +11.2 cm^{-1}, J_2 = +1.96 cm^{-1}, and J_3 = -8.17 cm^{-1} and D_{Ni} = +4.30 cm^{-1}, with g_{Ni} fixed to 2.1. Using the isotropic-only part of the spin-Hamiltonian (Equation 3.2) this leads to an S = 0 ground state with several low-lying excited states.

$$\hat{H} = -2 \sum_{i<j} J_{ij} \hat{S}_i \cdot \hat{S}_j + \sum_i \hat{S}_i \cdot D_i \cdot \hat{S}_j + \mu_B \overrightarrow{B} \cdot \sum_i g_i \hat{S}_i \tag{3.2}$$

Previous reports of O-bridged Ni^{II} complexes have revealed a correlation between the Ni-O-Ni angle and the sign and magnitude of the magnetic exchange.[149,168,177–183] As the Ni-O-Ni angle increases, the larger the antiferromagnetic contribution becomes, with the switch from ferromagnetic to antiferromagnetic occurring at approximately 98°. The exchange in **C2** follows this exchange with J_1 which is mediated via a syn, syn-carboxylate and a Ni-$\mu_{2/3}$-$O_{phenolate/OH^-}$-Ni moiety with bridging angles of 94.19° and 92.33°, respectively, and would therefore be expected to promote weak ferromagnetic exchange. For J_2 the weak ferromagnetic contribution is likely due to an orbital counter complementarity effect arising from the Ni-μ_3-O_{OH^-}-Ni bridge (110.67°) and the Ni-μ_2-Cl-Ni bridge (83.52°). J_3 is mediated by two μ_3-O_{OH^-} groups with a Ni-O-Ni angle of 100.19°, resulting in a weak antiferromagnetic exchange. The calculated ZFS of the Ni^{II} ions is consistent with that observed octahedral Ni^{II} ions in similar coordination spheres.[149,184–188]

Table 3.4: Fitted experimental magnetic exchange (J_1, J_2, and J_3) and anisotropy parameters (g and D_{Ni}) for **C1** - **C3**.

	J_1(cm^{-1})	J_2(cm^{-1})	J_3(cm^{-1})	g	D_{Ni}(cm^{-1})
C1	+7.94	-1.31	+6.67	2.28	-3.99
C2	+11.2	+1.96	-8.17	2.10	+4.30
C3	-0.27	-0.17	+4.73	2.25	-15.10

As discussed in the previous subsection, the inclusion of interacting, in this case hydrogen bonding, lattice solvent molecules in **C1**, greatly altered the way in which the unit cell packs. The effect of these differences on the magnetic properties of the complexes can be seen in the **C1**/original defective dicubane comparison $\chi_M T$ vs T plot (Figure 3.7). For both complexes, the $\chi_M T$ rises upon cooling, however different maxima are reached, 5.12 cm^3 K mol^{-1} for the original dicubane compared to **C1** which reaches 10.72 cm^3 K mol^{-1}. This shows that the magnetic properties of the original have been greatly improved by the inclusion of an interacting solvent molecule.[149] This has previously been seen in the literature, with an example by Zenno *et al*. who found that hydrating their sample resulted in enhanced magnetic properties, which was attributed to hydrogen bonding between a lattice bound H_2O molecule and a Cl^- anion, which resulted in the Cl^- anion lengthening enhancing the Jahn-Teller nature of the metal ion.[189] Similarly to the results by Zenno *et al*., Ge *et al*. found that by exchanging the lattice solvent from benzene to $CHCl_3$ they could introduce different intermolecular interactions, which resulted in an enhancement of the magnetic properties.[190]

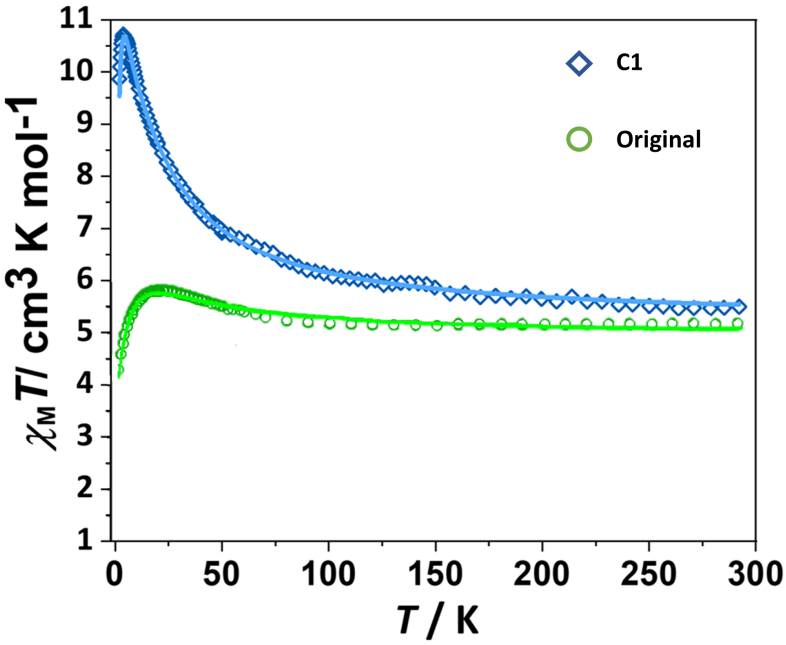

Figure 3.7: Comparison of $\chi_M T$ vs T for **C1** and the original defective dicubane, both in the temperature (T) range, 290 - 2 K and magnetic field (B) of 0.1 T.

3.1.3 Computational Analysis

In order to corroborate the structural and magnetic properties of the complexes **C1**, **C3**, and **C5**, a computational analysis was performed to confirm the validity of the experimental results. The analysis was again performed at The University of Edinburgh through collaborative work with Prof. Euan Brechin.[149]

The software, Gaussian 16, was used to estimate the magnetic exchange parameters, J_1 - J_3, for **C1**, **C3**, and **C5**.[149,191] DFT calculations in conjunction with a BS approach (discussed further in Section 1.2.3) has been employed for this chapter as it has been shown in the literature that this method reliably estimates the magnetic exchange

parameters to a high level of accuracy.[48,192–194] The B3LYP hybrid functional was utilised for all atoms with a TZV basis set for Ni^{II}, Zn^{II}, Cl, F, O, and N and a 6-31G* basis set for C and H.[195–201] For **C5**, the disorder in the μ_2-Cl^-/F^- bridges was considered to only be F^- bridged, as the Cl^- bridging was more similar to **C3** than the F^- bridges were to **C4**.

Eight different spin configurations were used to estimate the three exchange couplings, as illustrated in Figure 3.2. The different spin configurations consisted of one high spin model where all four Ni^{II} ions are spin up (S = 4), four models where one Ni^{II} ion has its spin down (S = 2), and finally, three models where two Ni^{II} ions are spin down (S = 0), as shown in Table B.4. For these spin configurations, pairwise exchange interaction calculations were performed, where two paramagnetic Ni^{II} ions were replaced by Zn^{II} ions. In addition to this, overlap intergral calculations were performed using the Heisenberg-Dirac-Van Vleck Hamiltonian (equation 3.3) to determine the overlap between the non-orthogonal singly occupied molecular orbitals of the Ni^{II} ions, in order to further analyse the magnetic exchange parameters of complexes **C1**, **C3**, and **C5**.[202,203]

$$\begin{aligned}\hat{H} = &-2J_1(\hat{S}_{Ni1}\cdot\hat{S}_{Ni2}+\hat{S}_{Ni3}\cdot\hat{S}_{Ni4})\\ &-2J_2(\hat{S}_{Ni1}\cdot\hat{S}_{Ni4}+\hat{S}_{Ni2}\cdot\hat{S}_{Ni3})\\ &-2J_3(\hat{S}_{Ni1}\cdot\hat{S}_{Ni3})\end{aligned} \tag{3.3}$$

In order to estimate the exchange coupling values (J_1, J_2, and J_3), DFT calculations have been performed on the full X-ray structures of complexes **C1**, **C3**, and **C5** (Table 3.5). The J_1 exchange interaction, which is mediated via μ_3-$O_{methoxy}$, μ_2-$O_{phenolate}$, and μ_2-O_{OAc^-} groups for **C1** with an average Ni-$\mu_{2/3}$O-Ni angle of 93.0°(Table B.5), is estimated to be moderately ferromagnetic (+9.2 cm^{-1} (**C1**)). Overlap calculations suggest one moderate overlap for **C1** ($\langle Ni(1)d_{z^2}|p_{x/y/z}|Ni(2)d_{z^2}\rangle$ = 0.041, Table B.6) and three small/orthogonal magnetic orbital overlaps resulting in ferromagnetic exchange. Previous studies on polymetallic Ni^{II} complexes highlight the importance of the Ni-$\mu_{2/3}$O-Ni angle on the magnetic exchange coupling value: the larger the angle, the larger the antiferromagnetic contribution, with the crossover between ferro- and antiferromagnetic being ∼97 - 98°.[168,177,178,183] In addition to this, it has been shown previously that the presence of a bridging phenolate group in tandem with a bridging carboxylate group exhibits a counter-complementary effect, often resulting in a ferromagnetic interaction.[204] The J_1 magnetic exchange interaction for complexes **C3** and **C5**, mediated by μ_3-O_{OMe^-} and μ_2-$O_{phenolate}$ bridging groups with average Ni-$\mu_{2/3}$O-Ni angles of 98.6° and 97.8°, respectively (Table B.5), shows weak antiferromagnetic exchange (-2.3 cm^{-1} (**C3**) and -0.3 cm^{-1} (**C5**)). One strong ($\langle Ni(1)d_{z^2}|p_{x/y/z}|Ni(2)d_{x^2-y^2}\rangle$ = 0.061 (**C3**) and $\langle Ni(1)d_{x^2-y^2}|p_{x/y/z}|Ni(2)d_{x^2-y^2}\rangle$ = 0.050 (**C5**), Table B.6) and three small/orthogonal magnetic orbital overlaps result in weak antiferromagnetic exchange.

The J_2 exchange interaction is mediated by μ_3-$O_{methoxo}$ and μ_2-Cl/F groups with average Ni–$\mu_{2/3}$(O/Cl/F)–Ni angles of 96.7°(**C1**), 96.8°(**C3**), and 102.4°(**C5**), (Table B.5), resulting in weak antiferromagnetic interactions in **C1** (-0.8 cm^{-1}), a weak ferromagnetic interaction for complex **C3** (+2.1 cm^{-1}), and a moderate antiferromagnetic interaction in complex **C5** (-7.7 cm^{-1}). Overlap calculations suggest one strong interaction

Table 3.5: DFT computed magnetic exchange interactions for **C1**, **C3**, and **C5**. The non-bolded values refer to calculations on the full molecules whereas the bolded values refer to dimeric models.

	J_1(cm^{-1})	J_2(cm^{-1})	J_3(cm^{-1})
C1	+9.7/**+9.2**	-0.3/**-0.8**	+0.3/**+1.3**
C3	-2.9/**-2.3**	+1.8/**+2.1**	+9.1/**+9.7**
C5	-2.2/**-0.3**	-5.9/**-7.7**	+7.2/**+10.7**

for **C1** ($\langle \mathrm{Ni}(2)d_{x^2-y^2}|p_{x/y/z}|\mathrm{Ni}3)(d_{x^2-y^2}\rangle = 0.055$, Table B.6), leading to a small antiferromagnetic interaction. For **C3**, only one moderate interaction ($\langle \mathrm{Ni}(2)d_{x^2-y^2}|p_{x/y/z}|\mathrm{Ni}(3)d_{x^2-y^2}\rangle = 0.035$, Table B.6) is observed, resulting in a small ferromagnetic interaction between the Ni^{II} centres. Although the average structural parameters for **C1** and **C3** are similar, there is a significant difference in sign and magnitude of the magnetic coupling (-0.8 cm^{-1} and +2.1 cm^{-1}, respectively). The Ni–μ_2Cl–Ni angle is 85.6°(**C1**) and 86.7°(**C3**) whereas the Ni–μ_3O–Ni angle is 107.8°(**C1**) and 107.0°(**C3**). In agreement with previously published magneto-structural studies, the change in the Ni–O–Ni angle gives a more dominant shift to antiferromagnetic coupling, compared to the small increased ferromagnetic contribution due to narrowing of the Ni–Cl–Ni angle, as supported by overlap calculations.[183] For **C5**, one strong and one moderate magnetic orbital overlap ($\langle \mathrm{Ni}(2)d_{x^2-y^2}|p_{x/y/z}|\mathrm{Ni}(3)d_{z^2}\rangle = 0.061$ and $\langle \mathrm{Ni}(2)d_{z^2}|p_{x/y/z}|\mathrm{Ni}(3)d_{z^2}\rangle = 0.036$, Table B.6) results in a moderate antiferromagnetic interaction. Note that **C5** contains the more electronegative F-bridging group with a smaller average Ni–F distance resulting in a much stronger antiferromagnetic interaction compared to the Cl$^-$ analogue.

The J_3 exchange interaction is mediated by two μ_3-O$_{methoxy}$ groups with average Ni–μ_3O–Ni angles of 98.2°, 95.7°, and 95.0°, respectively for **C1**, **C3**, and **C5**. This results in weak ferromagnetic exchange in **C1** (+1.3 cm^{-1}) and moderate ferromagnetic exchange for complexes **C3** (+9.7 cm^{-1}) and **C5** (+10.7 cm^{-1}). Overlap calculations suggest the presence of one moderate overlap interaction for **C1** ($\langle \mathrm{Ni}(1)d_{x^2-y^2}|p_{x/y/z}|\mathrm{Ni}(3)d_{x^2-y^2}\rangle = 0.044$, Table B.6), which leads to a small ferromagnetic interaction. For **C3** and **C5**, none of the magnetic orbitals are interacting (Table B.6), affording a relatively large ferromagnetic exchange interaction.

The spin density plots for **C1**, **C3**, and **C5** (Figure 3.8 and Table B.7) suggest a spin delocalisation mechanism with the spin density on the Ni^{II} ions in the range 1.661 - 1.717, which is as expected since the unpaired electrons reside in the e$_g$ orbitals.[205,206] Of all the bridging atoms, the largest spin density is detected on the μ_3-O$_{methoxo}$ atoms (0.162 - 0.168). The spin density on the μ_2-Cl bridging atoms (0.099 - 0.112) is greater than that on the μ_2-F bridging atoms (0.068 - 0.074), since the 3*p* orbitals of Cl are energetically closer to the 3*d* orbitals of the Ni^{II} ions.

Two complexes, **C1** and **C3** have both been characterised by magnetic and computational analyses. The DFT calculated *J* values were found to be in good agreement with the experimental values (Table 3.6) as the sign and order of magnitude of the calculated exchange interactions were consistent with the experimental findings. One minor outlier to the agreement between the computed and experimental values was the J_2 value for **C3**, as the experimental magnetic exchange value was found to be weakly antiferromagnetic with a value of -0.17 however the computed

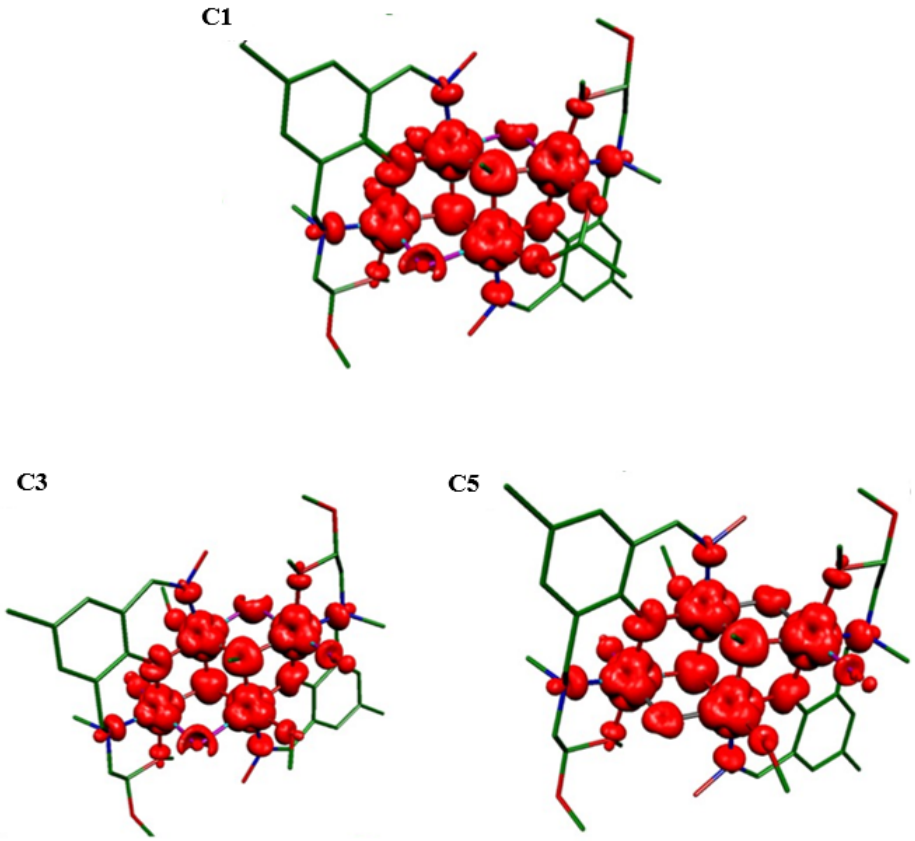

Figure 3.8: Spin density plots for the high spin states of **C1**, **C3**, and **C5**. Hydrogen atoms have been removed for clarity. The iso-density surface shown corresponds to a value of 0.005 $e^-/bohr^3$.

value was found to be weakly ferromagnetic with a value of +1.8. This is thought to result from the differences in the exchange angles (μ_2-Cl versus μ_3-OMe) and the degree to which they contribute to the magnetic exchange. As mentioned above, larger exchange angles, specifically the J_2 pathway mediated by a μ_3-OMe group has been shown to provide a more dominant shift towards antiferromagnetic exchange compared to the ferromagnetic contribution provided by the reduction of the μ_2-Cl group.[183] Although the experimental magnetic exchange for **C5** was not fitted, the magnetic susceptibility data was indicative of dominant antiferromagnetic exchange, which is consistent with the DFT computed values of -2.2 and -5.9 for the J_1 and J_2 pathways. The computed value found for the J_3 value was found to be positive, indicating ferromagnetic exchange. This result however fits with the exchange pathway angle of 94.96°.

Table 3.6: Fitted experimental/DFT computed magnetic exchange (J_1, J_2, and J_3) for the complexes **C1** and **C3**.

	J_1(cm^{-1})	J_2(cm^{-1})	J_3(cm^{-1})
C1	+7.94/+9.7	-1.31/-0.3	+6.67/+1.3
C3	-0.27/-2.9	-0.17/+1.8	+4.73/+9.1

3.2 Literature Analysis

When comparing **C1** with the literature, there are many examples of μ_3-OMe bridging with several examples of OAc^- bridging in dicubanes, specifically Ni^{II}_4 dicubanes. An example of this is shown by the Ni^{II}_4 dicubane reported by Oyarzabal *et al.* (Figure 3.9), which has two exchange pathways that resemble that of **C1**.[207]

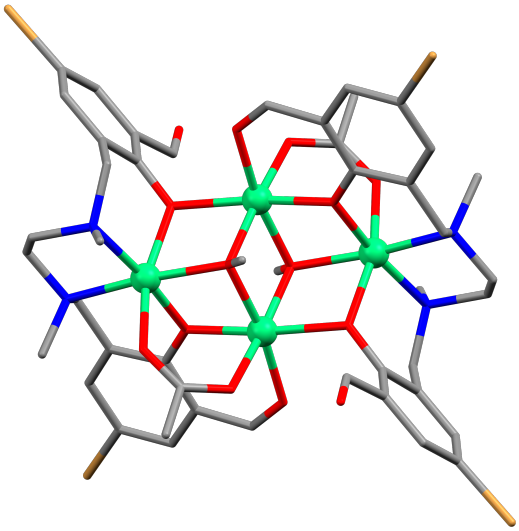

Figure 3.9: Crystal structure of the Ni^{II}_4 defective dicubane, $[Ni^{II}_4\mathbf{L}_2(OMe)_2(OAc)_2]$, produced by Oyarzabal *et al.*[207] Colour code: Ni^{II} = light green, N = blue, O = red, Br = light orange, and C = grey.

The ligand utilised by Oyarzabal *et al.* was a symmetrical bridged salicylaldamine derivative, *N*,*N*'-bis(2-hydroxy-3-formyl-5-bromo-benzyl)-ethylenediamine which introduced an additional phenolate group to mediate exchange between the metal ions. This key difference is shown in Figure 3.9, with two body - wing interactions mediated by a μ_2-phenolate group instead of the μ_2-Cl interaction as seen in **C1**.[207] With the inclusion of a different bridging group for the J_2 pathway, it was thought that the angles of the other two exchange pathways would also differ significantly, however this was not found to be the case (Table 3.7).

Table 3.7: Bond angles/Exchange parameters of the three exchange pathways (J_1 - J_3) for complexes **C1** and **C2** and the structure by Oyarzabal *et al.*

	J_1 Ni1-O-Ni2 (°/cm^{-1})	J_2 Ni2-X-Ni1' (°/cm^{-1})	J_3 Ni1-O-Ni1' (°/cm^{-1})
C1	94.76(12)/+7.94	85.60(4)[a]/-1.31	98.24(11)/+6.67
[M]*	94.83()/+4.2	99.68()[b]/-4.8	97.22()/+11.5

*Oyarzabal *et al.*[207]

[a] Ni1-Cl-Ni2; [b] Ni1-O-Ni2

With **C1** and the structure by Oyarzabal *et al*. having comparable exchange angles and parameters, the $\chi_M T$ vs. T plot results were unexpected. At RT (290 and 300 K for **C1** and Oyarzabal *et al*. respectively) the $\chi_M T$ values are comparable with 5.48 and 5.03 cm^3 K mol^{-1} respectively for **C1** and Oyarzabal *et al*. where upon cooling both values increase however the maxima achieved are significantly different, 10.72 (T = 3.7 K) and 5.31 (T = 36 K) cm^3 K mol^{-1} respectively. Further cooling sees both values decrease rapidly to give 9.87 (T = 2 K) and 3.46 (T = 5 K) cm^3 K mol^{-1} respectively. These results show that both complexes have competing ferro- and antiferromagnetic interactions with the ferromagnetic interactions dominant, but what is more interesting is that the competing interactions along with ZFS effects and antiferromagnetic intermolecular interactions are stronger in the structure by Oyarzabal *et al*. significantly reducing the magnetic properties compared to that of **C1**.

3.3 Conclusions

The reaction between ligand, H_2**L1**, and Ni^{II} metal salts, $Ni(X)_2 \cdot H_2O$ (X = OAc^-, Cl^-, $BF_4{}^-$), has resulted in the formation of five new tetranuclear Ni^{II} defective dicubanes ($[Ni_4(H$**L1**$)_2(OMe)_2(OAc)_2Cl_2]\cdot$2MeOH (**C1**), $[Ni_4(H$**L1**$)_2(OH)_2(OAc)_2Cl_2]\cdot$2MeCN (**C2**), $[Ni_4(H$**L1**$)_2(OMe)_2(MeOH)_2Cl_4]\cdot Et_2O$ (**C3**), $[Ni_4(H$**L1**$)_2(OMe)_2(MeOH)_2F_4]\cdot$4MeOH (**C4**), and $[Ni_4(H$**L1**$)_2(OMe)_2(MeOH)_2Cl_{2.8}F_{1.2}]\cdot Et_2O$ (**C5**). The Ni^{II} ions are bridged by a series of phenolate, OMe^-, OH^-, Cl^-, and F^- groups originating from the Ni^{II} metal salt used. Despite the similarities in the formulae and general structural topology of **C1** - **C5** there are significant geometric differences that result in rather different magnetic properties (**C1** - **C3**, and **C5**). Perhaps the most striking example comes from a comparison of **C1** and the original dicubane where different solvation leads to different packing in the extended structure which in turn leads to different intramolecular Ni-X-Ni angles and thus different magnetic exchange interactions. A computational study performed on the complexes **C1** and **C3** was found to be in good agreement with experimental findings as the sign and order of magnitude of the exchange values with consistent with the experimental findings. This study highlights the subtle intricacies involved in controlling intramolecular geometries and hence the sign and magnitude of magnetic coupling constants, particularly those relating to non-coordinating species such as anions/cations and solvent of crystallisation.

Complex Preparation and Characterisation

To a solution of H_2**L1** (1 eq.) was added a solution of $NiX_2 \cdot H_2O$. The bright green solution was stirred at RT for 10 minutes followed by the addition of Et_3N (6 eq.). The dark green solution was stirred for a further 10 minutes at RT. Isolation of the complex was achieved by the diffusion of Et_2O into the reaction solution. Green X-ray quality crystals were produced after a period of three to eight weeks.

$[Ni^{II}_4(HL1)_2(OMe)_2(OAc)_2Cl_2] \cdot 2MeOH$ (**C1**): H_2**L1** (0.200 g, 0.616 mmol, 1 eq.) in MeOH (20 mL), $Ni(OAc)_2 \cdot 4\,H_2O$ (0.153 g, 0.616 mmol, 1 eq.) and $NiCl_2 \cdot 6\,H_2O$ (0.146 g, 0.616 mmol, 1 eq.), both in MeOH (15 mL), and Et_3N (0.520 mL, 3.70 mmol, 6 eq.). Green prism shaped crystals were produced after three weeks. Yield (0.140 g, 19%); ATR-IR: $\bar{\nu}$ = 3255

(O-H), 2944 (C-H), 1639 (C=O), 1575 (C=N), 1487 (Ar), 1472 (C-H), 1417 (O-H), 1219 (Ar-O), 1131 (C-O), 1027 (C-N) 990 (N-O), 717 (Ar) cm^{-1}; elemental analysis calcd. (%) for $C_{40}H_{66}N_4O_{14}Cl_2Ni_4$: C 42.42, H 5.87, N 4.95; found: C 42.82, H 6.07, N 4.83.

$[Ni^{II}_4(HL1)_2(OH)_2(OAc)_2Cl_2] \cdot 2MeCN$ (C2): H_2**L1** (0.0648 g, 0.1 mmol, 1 eq.) in MeCN (10 mL), $Ni(OAc)_2 \cdot 4\,H_2O$ (0.0498 g, 0.1 mmol, 1 eq.) and $NiCl_2 \cdot 6\,H_2O$ (0.0476 g, 0.1 mmol, 1 eq.), both in MeCN (2 mL), and Et_3N (0.168 mL, 0.6 mmol, 6 eq.). Green platelet shaped crystals were produced after four weeks. Yield (0.0403 g, 34%); ATR-IR: $\overline{\nu}$ = 3655 (O-H), 3238 (O-H), 2947 (C-H), 1639 (C=O), 1572 (C=N), 1489 (Ar), 1463 (C-H), 1336 (O-H), 1221 (Ar-O), 1132 (C-O), 1061 (C-O), 1033 (C-N), 986 (N-O), 719 (Ar) cm^{-1}; elemental analysis calcd. (%) for $C_{42}H_{68}N_6O_{14}Cl_2Ni_4$: C 42.51, H 5.78, N 7.08; found: C 42.52, H 6.03, N 6.80.

$[Ni^{II}_4(HL1)_2(OMe)_2(MeOH)_2Cl_4] \cdot Et_2O$ (C3): H_2**L1** (0.0530 g, 0.163 mmol, 1 eq.) in MeOH (10 mL), $NiCl_2 \cdot 6\,H_2O$ (0.0775 g, 0.326 mmol, 2 eq.) in MeOH (20 mL), and Et_3N (0.140 mL, 0.979 mmol, 6 eq.). Green platelet shaped crystals were produced after three weeks. Yield (0.030 g, 15%); ATR-IR: $\overline{\nu}$ = 3637 (O-H), 3291 (O-H), 2966 (C-H), 1609 (C=N), 1479 (Ar), 1462 (C-H), 1330 (O-H), 1221 (Ar-O), 1128 (C-O), 1052 (C-O), 1024 (C-N), 986 (N-O), 718 (Ar) cm^{-1}; elemental analysis calcd. (%) for $C_{38}H_{68}N_4O_{12}Cl_4Ni_4$: C 39.70, H 5.96, N 4.87; found: C 40.62, H 5.36, N 4.15.

$[Ni^{II}_4(HL1)_2(OMe)_2(MeOH)_2F_4] \cdot 4MeOH$ (C4): H_2**L1** (0.234 g, 0.616 mmol, 1 eq.) in MeOH (10 mL), $Ni(BF_4)_2 \cdot 6\,H_2O$ (0.419 g, 1.23 mmol, 2 eq.) in MeOH (10 mL), and Et_3N (0.520 mL, 3.70 mmol, 6 eq.). Green block shaped crystals were produced after eight weeks. Yield (0.0655 g, 9%); ATR-IR: $\overline{\nu}$ = 3585 (O-H), 3352 (O-H), 2954 (C-H), 1608 (C=N), 1511 (Ar), 1468 (C-H), 1361 (O-H), 1215 (Ar-O), 1125 (C-O), 1052 (C-O), 1027 (C-N), 992 (N-O), 713 (Ar) cm^{-1}; elemental analysis calcd. (%) for $C_{38}H_{68}N_4O_{12}F_4Ni_4 \cdot 5H_2O$: C 38.96, H 6.36, N 5.05; found: C 39.03, H 6.33, N 5.32.

$[Ni^{II}_4(HL1)_2(OMe)_2(MeOH)_2Cl_{2.8}F_{1.2}] \cdot Et_2O$ (C5): H_2**L1** (0.100 g, 0.308 mmol, 1 eq.) in MeOH (5 mL), $Ni(BF_4)_2 \cdot 6\,H_2O$ (0.105 g, 0.308 mmol, 1 eq.) and $NiCl_2 \cdot 6\,H_2O$ (0.0732 g, 0.308 mmol, 1 eq.), both in MeOH (7.5 mL), and Et_3N (0.260 mL, 1.85 mmol, 6 eq.). Green platelet shaped crystals were produced after three weeks. Yield (0.070 g, 19%); ATR-IR: $\overline{\nu}$ = 3159 (O-H), 2947 (C-H), 1610 (C=N), 1559 (Ar), 1463 (C-H), 1218 (Ar-O), 1127 (C-O), 1038 (C-O), 1020 (C-N), 924 (N-O), 715 (Ar) cm^{-1}; elemental analysis calcd. (%) for $C_{42}H_{78}N_4O_{13}Cl_{2.8}F_{1.2}Ni_4$: C 41.90, H 6.53, N 4.65; found: C 41.80, H 6.64, N 4.44.

Chapter 4

3*d*3*d*′ Dinuclear Complexes

This chapter describes a series of 3*d*3*d*′ dinuclear complexes that expand on the theme of manipulating magnetism through structural modification. Taking the results of the defective dicubane series, where the majority of the exchange interactions originated from co-ligands, this 3*d*3*d*′ series was designed so that the exchange interactions originated solely from the ligand itself. The ligand chosen for this research was 6,6′-dimethoxy-2,2′-[(1,3-propylene)dioxybis(nitrilomethylidyne)]diphenol, H_2-**L2**, as it contained several favourable properties: pre-designed coordination pockets (M1 and M2, Figure 4.1) and phenolate and alkyloxime groups to promote ferromagnetic exchange and provide stability.[81,129,148] The target for structural modification are the two exchange pathways, M1-O1-M2 and M1-O2-M2, where instead of the structural modifications occurring on the bridging groups, the structural modifications will occur on the metal ions with the introduction of mixed metal combinations and the use of transmetalation reactions.

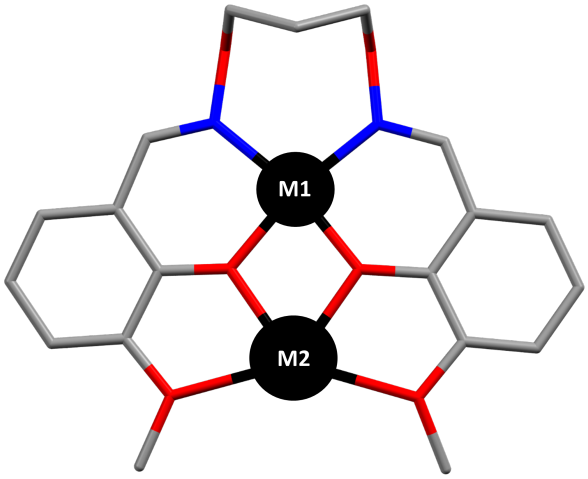

Figure 4.1: Schematic representation of the coordination pockets present for **L2**$^{2-}$. Black circles represent metal ions coordinated in the coordination pockets, M1 and M2.

4.1 Results and Discussion

The solid state complexes **C6** - **C13** were synthesised by RT reactions between H_2**L2**, $M(OAc)_2{\cdot}H_2O$ (M = Co^{II}, Cu^{II}, Mn^{II}, Ni^{II}, and Zn^{II}), and $M(NO_3)_2{\cdot}H_2O$ (M = Co^{II}, Cu^{II}, Mn^{II}, Ni^{II}, and Zn^{II}) in a 1 : 1 : 1 molar ratio. For all complexes, a visible

Table 4.1: Structural differences in the complexes **C6** - **C13**

	M1	M2	Anion	Solvent
C6	Cu^{II}	Co^{II}	NO_3^-	–
C7	Cu^{II}	Cu^{II}	NO_3^-	–
C8	Cu^{II}	Mn^{II}	NO_3^-	–
C9	Cu^{II}	Zn^{II}	NO_3^-	–
C10	Co^{II}	Mn^{II}	NO_3^-	MeOH
C11	Mn^{II}	Mn^{II}	NO_3^-	MeOH
C12	Ni^{II}	Mn^{II}	NO_3^-	MeOH
C13	Zn^{II}	Mn^{II}	NO_3^-	MeOH

colour change from the pale yellow ligand solution confirmed successful coordination. The complexes were isolated by slow vapour diffusion of Et_2O into the reaction solution where X-ray quality crystals were obtained after a period of one to four weeks. Successful complexations were confirmed by SCXRD, FAAS (**C6**, **C8**, **C10**, and **C12**, Section C.1), ATR-IR, ESI-MS, and CHN microanalysis. Magnetic analysis was performed through a collaboration with Prof. Euan Brechin at The University of Edinburgh. Computational analysis was performed by Dr Tyson Dais at Massey University using the New Zealand eScience Infrastructure (NeSI) high performance computing facilities.

4.1.1 Structural Analysis

The complexes, **C6** - **C13**, were found to be discrete dinuclear complexes, either crystallising in the monoclinic space group, $P2_1/n$ (**C6**, **C7**, **C8**, and **C9**) or the triclinic space group, $P\bar{1}$ (**C10**, **C11**, **C12**, and **C13**). For all complexes, the whole structure can be found within the asymmetric unit, with representative structures of the isostructural complexes shown in Figures 4.2 and 4.3. The general structure consists of one unit of **L2** coordinated to two *3d* ions, M1 and M2 (inner and outer pockets respectively, Figure 4.1), which are either homometallic (**C7** and **C11**) or heterometallic (**C6**, **C8** - **C10**, **C12**, and **C13**). Select heterometallic complexes have been characterised by FAAS to determine the 1 : 1 metal ion ratios (Section C.1), with bond length analyses and the crystallographic software, Olex2 used to determine position.[208]

For complexes **C6** - **C9**, M1 is four-coordinate with a distorted square planar geometry or 'seesaw' geometry, with τ_4 values of 0.17 (**C8**) and 0.18 (**C6**, **C7**, and **C9**).[209] The N_2O_2 donor set consists of two alkyloxime nitrogens and two phenolate oxygens. For **C10** - **C13**, M1 is six-coordinate with an octahedral geometry (CShM, Table C.3) and a N_2O_4 donor set which resembles that of **C6** - **C9** but with an additional two MeOH coordinates.[146,147,171]

For all complexes, M2 is seven-coordinate with a distorted capped trigonal prismatic geometry (CShM, Table C.3) and O_7 donor set, consisting of two phenolate oxygens, two methoxy oxygens, and two NO_3^- anions, one bidentate and the other monodentate (Selected bond lengths and angles can be found in Table 4.2).[146,147,210] For the complexes, **C8** and **C10** - **C13**, the second oxygen atom of the monodentate NO_3^- anion is weakly coordinated with bond lengths of 2.486, 2.531, 2.526, 2.565, and 2.495 Å respectively ($M\text{-}_{ONO_3}$ bond lengths in the literature are reported in the

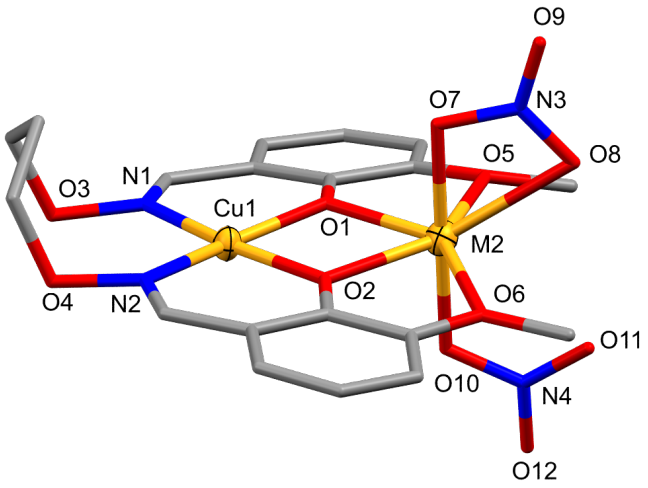

Figure 4.2: Representative structure of complexes, **C6** - **C9**, $[Cu^{II}M2^{II}\mathbf{L2}(NO_3)_2]$ (M2 = Co^{II} (**C6**), Cu^{II} (**C7**), Mn^{II} (**C8**), and Zn^{II} (**C9**)). Hydrogen atoms omitted for clarity and the thermal ellipsoids of the metal ions are shown at 70% probability. Colour code: $Cu^{II}/M2^{II}$ = dark yellow, N = blue, O = red, and C = grey.

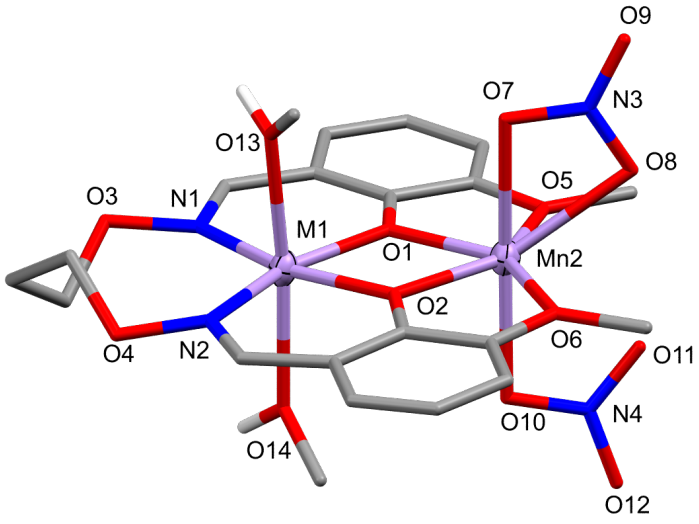

Figure 4.3: Representative structure of complexes, **C10** - **C13**, $[M1^{II}Mn^{II}\mathbf{L2}(MeOH)_2(NO_3)_2]$ (M1 = Co^{II} (**C10**), Mn^{II} (**C11**), Ni^{II} (**C12**) and Zn^{II} (**C13**)). Non-interacting hydrogen atoms omitted for clarity and the thermal ellipsoids of the metal ions are shown at 70% probability. Colour code: $M1^{II}/Mn^{II}$ = light purple, N = blue, O = red, C = grey, and H = white.

range of 1.996 to 2.480 Å).[211–213] This difference can be seen visually when comparing the angle (M2-O10-N4) at which the monodentate NO_3^- anion is coordinated to M2 (Figure 4.4).

Moderate intermolecular hydrogen bonding is found in **C10** - **C13** between the coordinated MeOH molecules (O13 and O14) and NO_3^- anions (O7 and O12) above and below the molecular plane, as shown in Figure 4.5.[158] When only considering one complex, the above-plane hydrogen bonding (2.771(3) - 2.910(5) Å) occurs between O13 (MeOH) and the coordinated oxygen, O7 (NO_3^-), whereas the below-plane hydrogen bonding (2.770(3) - 2.788(6) Å) occurs between O14 (MeOH) and a non-coordinated oxygen, O12 (NO_3^-). This difference is assumed to be largely attributed to both the packing of the unit cell and the M2-O10-N4 angle of the NO_3^- anion, as the larger the angle, the closer the free oxygen, O12, is to the adjacent molecule, as is the case for the below-plane interaction.

The most noticeable structural difference between the complexes is the structural arrangement of the alkyloxime bridge as shown in Figure 4.6. For the complexes where M1 is four-coordinate (**C6** - **C9**), the nitrogen and oxygen atoms of the alkyloxime bridge sit almost planar with the metal ions and aromatic rings, with the alkyl part of the bridge sitting almost perpendicular. For the complexes where M1 is octahedral (**C10** - **C13**), the coordination geometry causes the alkyl part of the bridge to zig-zag above and below the plane of the metal ions/aromatic rings resulting in small differences in the angles surrounding the M1 ions between the two different M1 geometries with the greatest difference being the N1-M1-N2 angle (An average of 101.98 and 112.15 Å for the perpendicular and zig-zag bridges respectively). The structural differences in the bridge however don't influence the O1-M1-O2 angle as the angles are all within experimental error of one and another. Other angles such as M1-N-O and N-O-C of the alkyloxime bridge are also within experimental error of each other. It is assumed that the difference in the bridges has occurred due to the steric hinderence caused by the capping MeOH molecules. If the bridge were structurally arranged as it is in the four-coordinate M1 complexes, then the central carbon of the bridge and its hydrogen atoms would be too close in proximity to the top MeOH molecule (Figure 4.6, top).

The complexes, **C6** - **C13**, have been characterised by ESI-MS, with similar fragmentation patterns found for the complexes. The spectra indicate that when in solution, specifically methanolic solution, the complexes do not remain intact with the loss of NO_3^- and MeOH coordinates as the complexes are present as either $[M\text{-}NO_3]^+$ (**C6** - **C9** and **C11**) or $[M\text{-}NO_3\text{-}2MeOH]^+$ (**C10**, **C12**, and **C13**) instead of the more typical $[M+H]^+$ (Table C.4). This is thought to be due to the fact that less energy is required to remove a NO_3^- anion and/or MeOH molecules than it is to protonate the system.[214] Additionally, [**L2**+M1]$^+$ and [**L2**+Na]$^+$ peaks are present in the spectra.

ATR-IR spectroscopy has been used to compare the complexes, **C6** - **C13** with the free ligand, H_2**L2** (Table C.5). As the results from SCXRD have indicated, the ligand coordinates to the metal ions via the alkyloxime nitrogen and phenolate and methoxy oxygen atoms, therefore it is expected that there will be shifts of the C=N, Ar-O, and C-O stretches indicating coordination. For all complexes, the C=N stretches can be seen to shift from 1606 to approximately 1604 cm^{-1}, the Ar-O stretches shift from 1251 to approximately 1243 cm^{-1} and the C-O stretches shifted from 1066 to approximately 1100 cm^{-1}. All complexes have two coordinated NO_3^- anions, which can be

Table 4.2: Selected bond lengths (Å) and angles (°) of the complexes **C6** - **C13** from crystal structure determination

	C6	**C7**	**C8**	**C9**	**C10**	**C11**	**C12**	**C13**
M1-O1	1.930(2)	1.935(3)	1.932(3)	1.931(3)	2.053(2)	2.107(2)	2.018(2)	2.073(4)
M1-O2	1.941(2)	1.920(2)	1.939(3)	1.936(3)	2.029(2)	2.101(2)	2.029(2)	2.081(4)
M1-N1	1.968(3)	1.970(3)	1.978(3)	1.973(4)	2.151(3)	2.234(2)	2.115(3)	2.192(5)
M1-N2	1.965(3)	1.977(3)	1.973(3)	1.956(4)	2.148(3)	2.236(2)	2.113(3)	2.204(5)
M1-O13	–	–	–	–	2.125(2)	2.240(2)	2.111(2)	2.208(4)
M1-O14	–	–	–	–	2.120(2)	2.232(2)	2.109(2)	2.202(4)
M2-O1	2.102(2)	2.123(2)	2.200(3)	2.092(3)	2.156(2)	2.172(2)	2.165(2)	2.169(4)
M2-O2	2.070(2)	2.157(2)	2.195(3)	2.085(3)	2.165(2)	2.176(2)	2.162(3)	2.166(4)
M2-O5	2.398(3)	2.415(2)	2.377(3)	2.417(3)	2.350(2)	2.409(2)	2.336(2)	2.395(4)
M2-O6	2.370(3)	2.416(2)	2.380(3)	2.435(3)	2.378(2)	2.363(2)	2.369(2)	2.349(4)
M2-O7	2.220(3)	1.952(3)	2.315(3)	2.385(4)	2.313(3)	2.303(2)	2.306(3)	2.315(4)
M2-O8	2.102(3)	2.417(3)	2.288(3)	2.063(5)	2.361(2)	2.356(2)	2.382(3)	2.372(4)
M2-O10	2.029(3)	1.926(3)	2.207(3)	2.018(3)	2.240(2)	2.244(2)	2.219(3)	2.262(4)
M2$\cdots$O11	3.084(3)	2.844(3)	2.486(4)	2.978(4)	2.531(3)	2.527(2)	2.565(4)	2.495(5)
M1-O1-M2	105.13(11)	106.01(10)	107.16(12)	105.06(13)	104.84(9)	103.57(8)	105.93(10)	104.53(17)
M1-O2-M2	105.94(11)	105.22(10)	107.11(12)	105.14(13)	105.33(9)	103.62(8)	105.63(10)	104.40(17)
M1$\cdots$M2	3.203(1)	3.243(7)	3.329(7)	3.194(1)	3.336(1)	3.362(6)	3.340(1)	3.356(1)

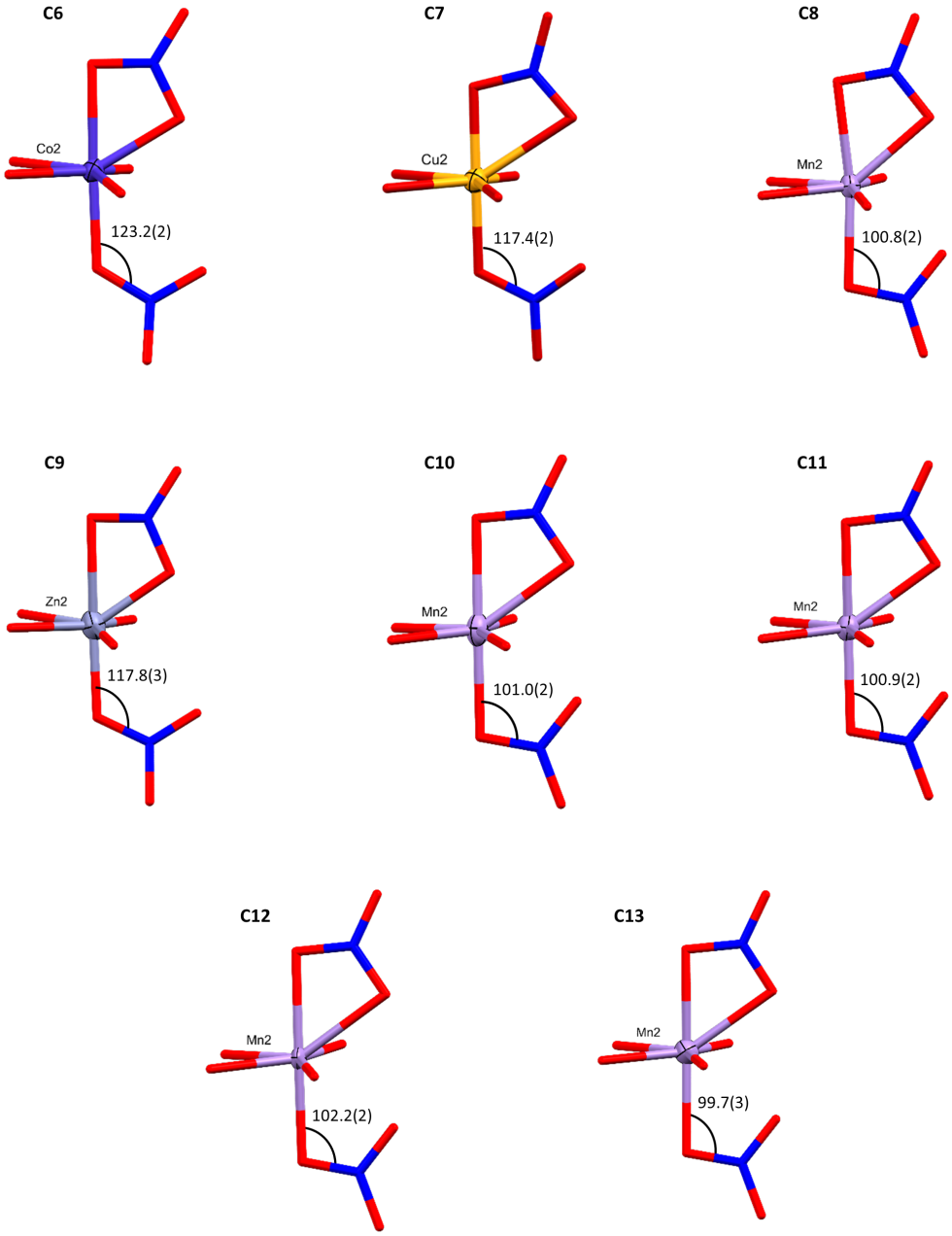

Figure 4.4: Schematic showing the differences in the NO_3^- anion coordination angle to the M2 ions for complexes **C6** - **C13**. Thermal ellipsoids of the metal ions are shown at 70% probability. Colour code: Cu^{II} = dark yellow, Mn^{II} = light purple, Co^{II} = dark purple, Zn^{II} = light purple, N = blue, and O = red.

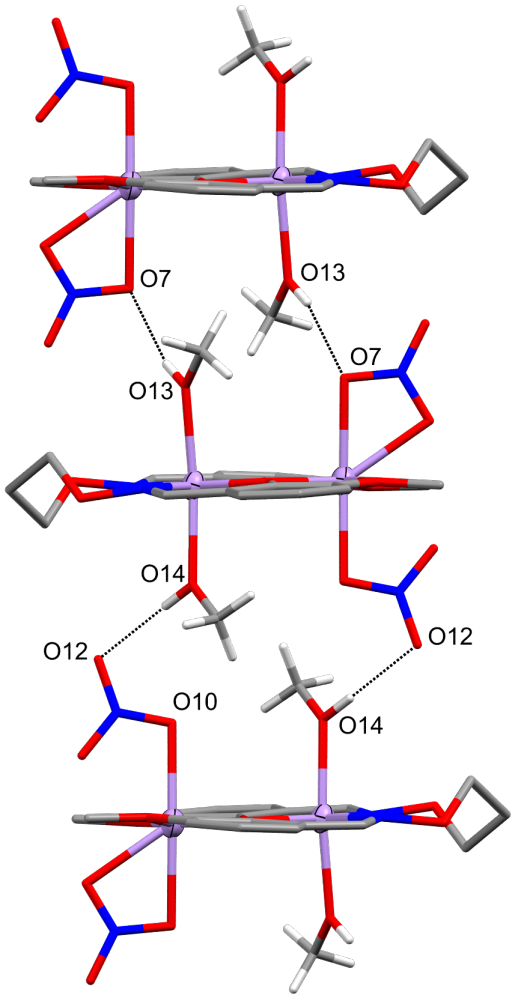

Figure 4.5: The hydrogen bonding network found for complexes **C10** - **C13**. Hydrogen atoms apart from those of the MeOH molecules have been omitted for clarity, hydrogen bonding represented as black dotted lines, and the thermal ellipsoids of the metal ions are shown at 70% probability. Colour code: M^{II} = light purple, N = blue, O = red, C = grey, and H = white.

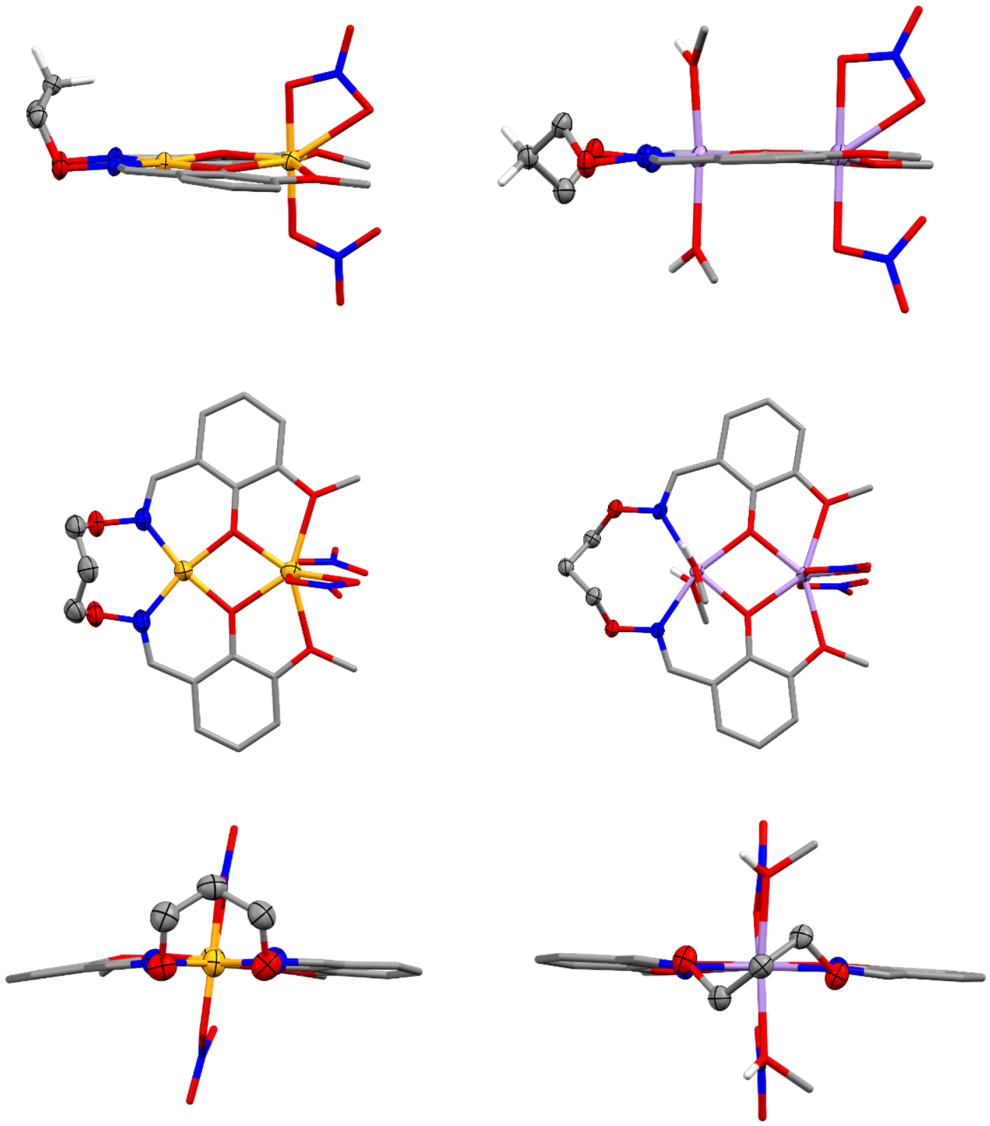

Figure 4.6: The structural differences between the alkyloxime bridges of the $Cu^{II}M2^{II}$ (left; **C6** - **C9**) and $M1^{II}Mn^{II}$ dinuclear complexes (right; **C10** - **C13**). Hydrogen atoms omitted for clarity, metal ions and alkyloxime bridges shown as ellipsoids (70% probability) for ease of view. Colour code: M^{II} = dark yellow (left) and light purple (right), N = blue, O = red, C = grey, and H = white.

seen in the spectra with stretches at approximately 1463, 1298, 1038, and 816 cm^{-1}. Previous research in the literature has found that the coordination of anions, which are capable of coordinating in various modes such as NO_3^- or OAc^-, can be determined by the difference between asymmetric and symmetric stretches.[215,216] For NO_3^- anions, bidentate coordination is found when the range between the stretches at approximately 1463 and 1298 cm^{-1} is $\sim$ 180 cm^{-1} whereas for mondentate coordination the range is $\sim$ 120 cm^{-1}.[215–218] Values of 174, 161, 168, 174, 165, 165, 166, and 166 cm^{-1} were found for **C6** - **C13** respectively indicating mixed coordination, which is in agreement with the SCXRD results.

4.1.2 Transmetalation

The first example of transmetalation in this research occurred when attempting to form a larger mixed metal cluster, subsequently producing the first heterometallic 3*d*3*d*' dinuclear complex (**C8**). After finding the most reliable method to synthesise both **C8** and the other heterometallic complexes (1 : 1 ratio of OAc^- : NO_3^- metal salts) we wanted to determine whether transmetalation could be used to structurally modify the dinuclear complexes and determine the relative stabilities and metal ion preferences of the coordination pockets.

The general method used for the transmetalation reactions was to "soak" several crystals of the starting complex in 2.0 mL of a 0.025 $molL^{-1}$ $M^{II}(NO_3)_2 \cdot xH_2O$ methanolic solution of the desired metal ion to be transmetalated. The 'soaks' were then left for approximately 24 hours, where the crystals dissolved, and for some samples, the methanolic solution changed colour. These solutions were filtered and then set up for Et_2O vapour diffusion, similarly to all other complexation reactions. X-ray quality crystals were produced between periods of 24 hours to three weeks. The initial two transmetalations (**C7** and **C11** to **C8**) were repeated in bulk and characterised by both SCXRD and FAAS (**C7** and **C11** to **C8**, **CuMn1** and **CuMn2** respectively; Table C.2) to confirm the 1 : 1 metal ratio. The remaining transmetalation reactions were characterised by SCXRD and bond length analysis.

A series of transmetalations were set up with the dinuclear complexes, with results found in Table 4.3. It was found that the successful transmetalation reactions involved either $Cu(NO_3)_2 \cdot 3\,H_2O$ or $Mn(NO_3)_2 \cdot 4H_2O$ solutions clearly indicating that Cu^{II} was the most stable in the inner pocket and Mn^{II} the most stable in the outer pocket, further suggesting that **C8** had the greatest overall stability.

As transmetalation reactions are often said to be irreversible processes, this was confirmed by attempting the transmetalation reactions on **C8**. Crystals of **C8** were soaked in 0.025 mol/L methanolic solutions of both $Mn(NO_3)_2 \cdot 4H_2O$ and $Cu(NO_3)_2 \cdot 3H_2O$, following the general method. The result for both reactions was the isolation of **C8** only, showing transmetalation is indeed irreversible for this particular system.

When considering these results from a structural view, they make sense as the smaller Cu^{II} ion was more stable in the smaller coordination pocket and the larger Mn^{II} ion was more stable in the larger coordination pocket. Additionally, the four-coordinate geometry of the Cu^{II} ion retains the structural stability of the inner pocket, whereas the octahedral geometry of the Mn^{II} ion caused the N1-Mn-N2 angles to significantly increase, decreasing the stability of the pocket. If we consider these results using

Table 4.3: Transmetalation results for **C6** - **C13**

Initial Complex	Metal Solution	Result
C6 - $Cu^{II}Co^{II}$	$Mn(NO_3)_2{\cdot}4H_2O$	**C8** - $Cu^{II}Mn^{II}$
C7 - $Cu^{II}Cu^{II}$	$Mn(NO_3)_2{\cdot}4H_2O$	**C8** - $Cu^{II}Mn^{II}$
C8 - $Cu^{II}Mn^{II}$	$Cu(NO_3)_2{\cdot}3H_2O$	**C8** - $Cu^{II}Mn^{II}$
	$Mn(NO_3)_2{\cdot}4H_2O$	**C8** - $Cu^{II}Mn^{II}$
C9 - $Cu^{II}Zn^{II}$	$Mn(NO_3)_2{\cdot}4H_2O$	**C8** - $Cu^{II}Mn^{II}$
C10 - $Co^{II}Mn^{II}$	$Cu(NO_3)_2{\cdot}3H_2O$	**C8** - $Cu^{II}Mn^{II}$
C11 - $Mn^{II}Mn^{II}$	$Cu(NO_3)_2{\cdot}3H_2O$	**C8** - $Cu^{II}Mn^{II}$
C12 - $Ni^{II}Mn^{II}$	$Cu(NO_3)_2{\cdot}3H_2O$	**C8** - $Cu^{II}Mn^{II}$
C13 - $Zn^{II}Mn^{II}$	$Cu(NO_3)_2{\cdot}3H_2O$	**C8** - $Cu^{II}Mn^{II}$

an Irving-Williams lens, the prediction would be that **C7** would be expected to be the most stable. Clearly, the larger coordination pocket and preference for seven-coordinate geometry favours Mn^{II} ions over Cu^{II} ions in the outer pocket.

4.1.3 Magnetic Analysis

For the complexes **C6** - **C13**, two different magnetic analyses have been performed, the first analysis was performed on complexes **C6** - **C8** and **C10** - **C12** as these complexes have two magnetically active metal ions. The second was performed on complexes **C9** and **C13** as these complexes are effectively single-ion complexes due to the presence of non-magnetically active Zn^{II} ions.

Magnetic measurements performed on the complexes, **C6** - **C8** and **C10** - **C12** were performed at the University of Edinburgh through collaborative work with Prof. Euan Brechin.[151] DC molar magnetic susceptibility and magnetisation measurements in the temperature range T = 300 - 2 K were performed on microcrystalline samples and collected using a Quantum Design PPMS Dynacool VSM magnetometer in the applied field range, B = 0.1 - 9 T. Samples were mounted in gelatine capsules and restrained by the addition of a small quantity of either eicosane or hexadecane. The magnetic measurements for both series had their observed paramagnetic susceptibilities corrected for diamagnetic contributions using Pascal's constants. The experimental results are shown in Figures 4.7 and 4.8 as the $\chi_M T$ product versus T, where $\chi_M = M/B$ and M is the magnetisation.

Upon cooling the $\chi_M T$ of **C7** slowly increases from 0.94 cm^3 K mol^{-1} at T = 300 K to a maximum value of 1.11 cm^3 K mol^{-1} at T = 36 K, before decreasing to 0.90 cm^3 K mol^{-1} at 2 K. This behaviour is indicative of a ferromagnetic interaction between the two Cu^{II} ions, with the low T decrease assigned to antiferromagnetic intermolecular interactions, consistent with the packing of the molecules in the extended structure and the close contacts between the NO_3^- molecules on one complex and the alkyloxime ligand on its neighbour (O(NO_3)$\cdots$(H)C, $\sim$ 3.1 Å, Figure C.5). To better define the low temperature magnetic properties of **C7**, VTVB magnetisation measurements were performed in the temperature and field ranges T = 2 - 10 K and B = 0.5 - 9.0 T, respectively (Figure 4.9). The VTVB magnetisation data of **C7** rises

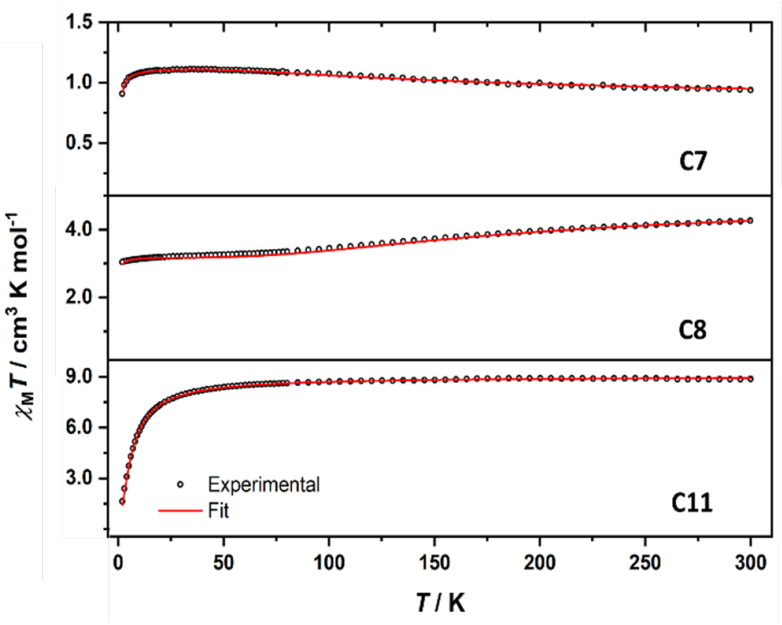

Figure 4.7: Plot of the $\chi_M T$ product versus T for **C7**, **C8**, and **C11** in an applied field, B = 0.1 T over the T = 300 - 2 K temperature range. The solid lines represent the fit of the experimental data (circles) using spin-Hamiltonian (Equation 4.1), as discussed in the text.

rapidly with increasing field, with the maximum value at T = 2 K and B = 9.0 T being 2.12 μ_B. Both the susceptibility and magnetisation data are therefore consistent with the stabilisation of an S = 1 ground state. The susceptibility and magnetisation data were simultaneously fitted to isotropic spin-Hamiltonian (Equation 4.1) affording the best-fit parameters J = +63.0 cm^{-1} and g_{Cu} = 2.12. The fit requires inclusion of an intermolecular interaction term zJ = -0.10 cm^{-1}, consistent with the extended structure. A thorough search of the literature has revealed **C7** to have the largest ferromagnetic coupling for a Schiff-based derived Cu^{II}_2 complex. The ferromagnetic exchange observed is unexpected based on previous magneto-structural correlations of O-bridged dinuclear Cu^{II} complexes which consider only the Cu-O-Cu angles.[219–223] The Cu-O-Cu angles in **C7** are 105° and 106° and would be expected to promote strong antiferromagnetic interactions based on this model and similar Cu^{II} dinuclear complexes found in the literature.[224–227] As discussed by Ruiz and coworkers, other structural factors such as complex asymmetry, metal ion geometry, O-Cu-O-Cu torsion angles, and the out-of-plane shift of the phenolate units can contribute to the magnetic properties of the complex.[228] Upon comparing **C7** with similar Cu^{II}_2 complexes in the literature,[224,225,227] the bond lengths and angles, O-Cu-O-Cu torsion angles, and the out-of-plane shift of the phenolate units are all fairly consistent with no significant outlier for **C7**, therefore it is believed that the unexpected ferromagnetic coupling of **C7** is to be contributed to both the complex asymmetry and the metal ion geometries, specifically the seven-coordinate geometry of Cu2.[229]

$$\hat{H} = -2\sum_{i<j} J_{ij}\hat{s}_i \cdot \hat{s}_j \tag{4.1}$$

For **C8** the $\chi_M T$ product at T = 300 K is 4.25 cm^3 K mol^{-1}, somewhat lower than the value of 4.83 cm^3 K mol^{-1} expected for a dinuclear $Cu^{II}Mn^{II}$ complex assuming g_{Mn} = 2.00 and g_{Cu} = 2.20. Upon cooling the $\chi_M T$ product slowly decreases and then plateaus at a value of 3.24 cm^3 K mol^{-1} at T = 50 K. Below 50 K the $\chi_M T$ value decreases once more reaching a value of 3.05 cm^3 K mol^{-1} at 2 K. This behaviour is indicative of a weak antiferromagnetic interaction between the two metal ions and an S = 2 ground state, with the low T (< 50 K) decrease in $\chi_M T$ being attributed to intermolecular antiferromagnetic interactions ($O(NO_3)\cdots(H)C$, $\sim$ 3.3 Å), which are similar to those found in **C7**. This is corroborated by the VTVB data which saturates at a value of 4.18 μ_B at 2 K and B = 9.0 T (Figure 4.9). A simultaneous fit of the susceptibility and magnetisation data afforded the best-fit parameters J = -34.8 cm^{-1}, g_{av} = 2.06 and zJ = -0.01 cm^{-1}, consistent with similar compounds reported in the literature.[230–232]

For **C11** the $\chi_M T$ product at T = 300 K is 8.84 cm^3 K mol^{-1}, close to the value of 8.75 cm^3 K mol^{-1} expected for two uncorrelated S = 5/2 Mn^{II} ions with g = 2.00. Upon cooling the $\chi_M T$ product decreases slowly to a value of 8.71 cm^3 K mol^{-1} at 100 K and then more rapidly to 1.64 cm^3 K mol^{-1} at 2 K. This behaviour is indicative of a weak antiferromagnetic interaction between the two Mn^{II} ions. The VTVB magnetisation data of **C11** is consistent with this interpretation, initially increasing slowly at lower fields before saturating at a value of 9.95 μ_B at T = 2 K and B = 9.0 T, where the large, applied field overcomes the weak exchange (Figure 4.9). A simultaneous fit of the susceptibility and magnetisation data to (Equation 4.1) affords the best fit parameters J = -0.45 cm^{-1} and g_{Mn} = 2.03, in agreement with similar compounds in the literature.[233–235]

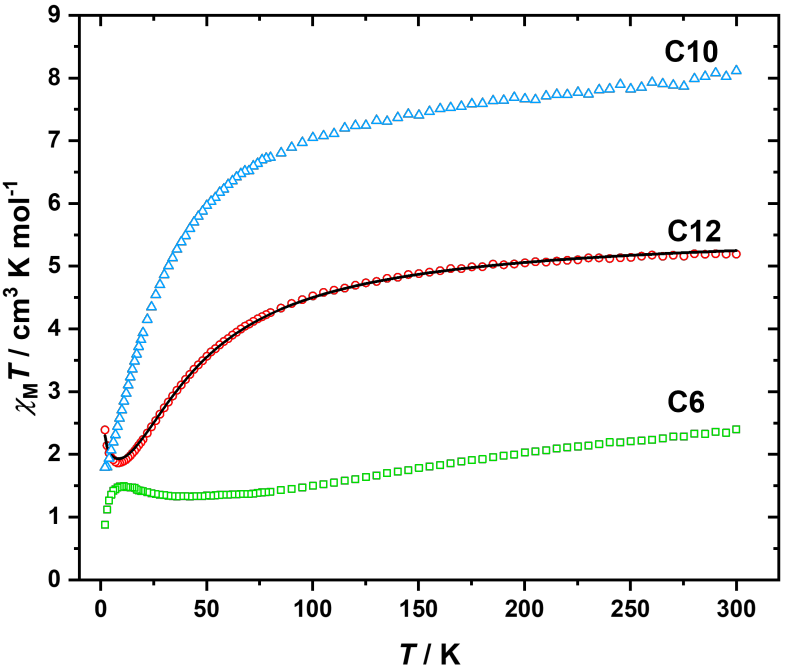

Figure 4.8: Plot of $\chi_M T$ product versus T for **C6**, **C10**, and **C12** in an applied field B = 0.1 T in the T = 300 - 2 K range. The solid line for **C12** is a fit of the experimental data using spin-Hamiltonian (Equation 4.2), as explained in text.

The $\chi_M T$ products of **C6** and **C10** at T = 300 K (2.40 and 8.11 cm^3 K mol^{-1}, respectively) are somewhat larger than the values expected (2.25 and 6.25 cm^3 K mol^{-1}; S_{Cu} = 1/2, S_{Co} = 3/2, S_{Mn} = 5/2, and g = 2.00) for the dinuclear complexes assuming no interaction between the metal ions. Upon cooling, the $\chi_M T$ product of **C6** decreases continuously to a value of 1.33 cm^3 K mol^{-1} at T = 42 K, before rising sharply to a value of 1.49 cm^3 K mol^{-1} at T = 11 K, before decreasing again to a value of 0.88 cm^3 K mol^{-1} at T = 2 K. The VTVB magnetisation data (Figure 4.9) of **C6** rises rapidly with increasing field, saturating at a maximum value of 2.04 μ_B at 2 K and 9 T. Upon cooling, the $\chi_M T$ product of **C10** slowly drops to a value of 7.05 cm^3 K mol^{-1} at 100 K, whereupon it decreases much more rapidly to a value of 1.79 cm^3 K mol^{-1} at 2 K. At T = 2 K (Figure 4.9), the magnetisation data for **C10** increases rapidly with increasing field and tends towards saturating at a value of 3.71 μ_B at B = 7.5 T. At higher fields there is a small inflection in the data, where M appears to rise more rapidly, reaching 4.04 μ_B at B = 9.0 T. At higher temperatures, M rises more linearly with increasing B.

Quantitative interpretation of the magnetic properties of **C6** and **C10** is complicated by the large anisotropy normally associated with Co^{II} ions, specifically for seven-coordinate ions in the case of **C6**, with ZFS parameters typically in the range $|D|$ = 30 - 60 cm^{-1} whose value is highly dependent on both the nature of the donor atoms present and the symmetry around the metal ion.[236,237] Isotropic exchange interactions are usually not relevant in such cases (and thus spin-Hamiltonian, Equation 4.2, is not relevant) and both g and J anisotropy must be determined. Therefore, only a qualitative discussion of the data for **C6** and **C10** is possible. In both cases the initial decrease of $\chi_M T$ upon cooling is due to the presence of SOC and low-symmetry ligand field effects of the Co^{II} ion. For **C6**, the increase in $\chi_M T$ between 11 - 42 K is indicative of ferromagnetic exchange between the two metal ions, with the decrease in $\chi_M T$ between 2 - 11 K ascribed to antiferromagnetic intermolecular interactions, consistent with the X-ray structure. The rapid rise and saturation of the magnetisation data with increasing field corroborates this picture. For **C10** the continual decrease of $\chi_M T$ and non-saturation of the M versus B data is indicative of the presence of weak antiferromagnetic exchange.

At 300 K the $\chi_M T$ product of **C12** is 5.19 cm^3 K mol^{-1}, lower than the expected value of 5.93 cm^3 K mol^{-1} for uncorrelated Ni^{II} and Mn^{II} ions (S_{Ni} = 1, g_{Ni} = 2.15; S_{Mn} = 5/2, g_{Mn} = 2.0). Upon cooling, the value of $\chi_M T$ slowly decreases to a value of 5.00 cm^3 K mol^{-1} at 200 K, then more rapidly to a value of 1.86 cm^3 K mol^{-1} at 8 K, before sharply increasing to 2.39 cm^3 K mol^{-1} at 2 K. This behaviour is indicative of an antiferromagnetic interaction between the two metal centres, with the low T increase assigned to ferromagnetic intermolecular interactions, consistent with the packing of the molecules in the crystal and the short-contacts between neighbouring complexes. To better define the low temperature magnetic properties of **C12**, VTVB magnetisation measurements were performed in the temperature and field ranges T = 2 - 10 K and B = 0.5 - 9 T, respectively (Figure 4.9). The VTVB magnetisation data of **C12** rises rapidly with increasing field, reaching a maximum value of 2.88 μ_B at 2 K and 9 T. Both the susceptibility and magnetisation data are therefore consistent with the stabilisation of an S = 3/2 ground state. The susceptibility and magnetisation data were simultaneously fitted to a spin-Hamiltonian (Equation 4.2; the first part is a Heisenberg exchange term and the second part a Zeeman term) affording the best fit parameters J = -6.43 cm^{-1}, g_{Ni} = 2.15, and g_{Mn} = 2.02. The fit requires the inclusion of an intermolecular interaction term, zJ = +0.06 cm^{-1}, consistent

with the extended structure. The sign and magnitude of the antiferromagnetic exchange observed for **C12** is in agreement with previously established magnetostructural correlations for O-bridged $Ni^{II}Mn^{II}$ compounds where the J value decreases with increasing Ni-O-Mn angle, with a crossing angle of ∼98°.[187,188,238] For **C12**, the Ni-O-Mn angles are both ∼105° and therefore were expected to display weak antiferromagnetic exchange.

$$\hat{H} = -2\sum_{i<j} J_{ij}\hat{S}_i \cdot \hat{S}_j + \mu_B \overrightarrow{B} \cdot \sum_i g_i \hat{S}_i \tag{4.2}$$

Table 4.4: Best-fit parameters for the complexes **C7**, **C8**, **C11**, and **C12**

	J (cm^{-1})	g_M	zJ (cm^{-1})
C7	+63.0	2.12	-0.10
C8	-34.8	2.06*	-0.01
C11	-0.45	2.03	–
C12	-6.43	2.09*	+0.06

* Averaged values

For the complexes **C9** and **C13**, magnetic susceptibility measurements (χ_M) and the effective magnetic moment (μ_{eff}) of the complexes were measured on polycrystalline samples using a Sherwood Scientific magnetic susceptibility balance. Measurements were performed on powdered polycrystalline material packed into a sample tube and collected at RT (294 K). The samples were embedded in polyethylene glycol (PEG; avg. molecular weight of 4000) due to a small sample size. The susceptibility data was corrected for any diamagnetic contributions from the PEG, sample, and sample tube using Pascal's constants.

The μ_{eff} of the complexes was calculated using Equation 4.3, where κ_B is the Boltzmann constant, N_A is Avogadro's number, β is the Bohr magneton, and T is the temperature (294.15 K).[239] The χ_M results shown in Table 4.5 reveal that both **C9** and **C13** are paramagnetic with positive χ_M values of 1.16x10^{-3} cm^3 mol^{-1} and 1.38x10^{-3} cm^3 mol^{-1}. The $\chi_M T$ and μ_{eff} values found for **C9**, 0.342 cm^3 K mol^{-1} and 1.65 μ_B resemble what is found in the literature for salicylaldoxime derived mononuclear Cu^{II} complexes.[148,240,241] In the literature, high-spin Mn^{II} mononuclear compounds are reported to have μ_{eff} values in the range 5.00 - 5.55 μ_B, as the μ_{eff} value found for **C13**, 1.80 μ_B, is considerably lower than 5.00 μ_B it is assumed the Mn^{II} ion is low spin.[242,243]

$$\mu_{eff} = \sqrt{\frac{3\kappa_B}{N_A\beta^2}(\chi_M T)} \tag{4.3}$$

Table 4.5: Magnetic susceptibility results for the complexes **C9** and **C13**

	χ_M (cm^3 mol^{-1})	$\chi_M T$ (cm^3 K mol^{-1})	μ_{eff} (μ_B)
C9	1.16x10^{-3}	0.342	1.65
C13	1.38x10^{-3}	0.405	1.80

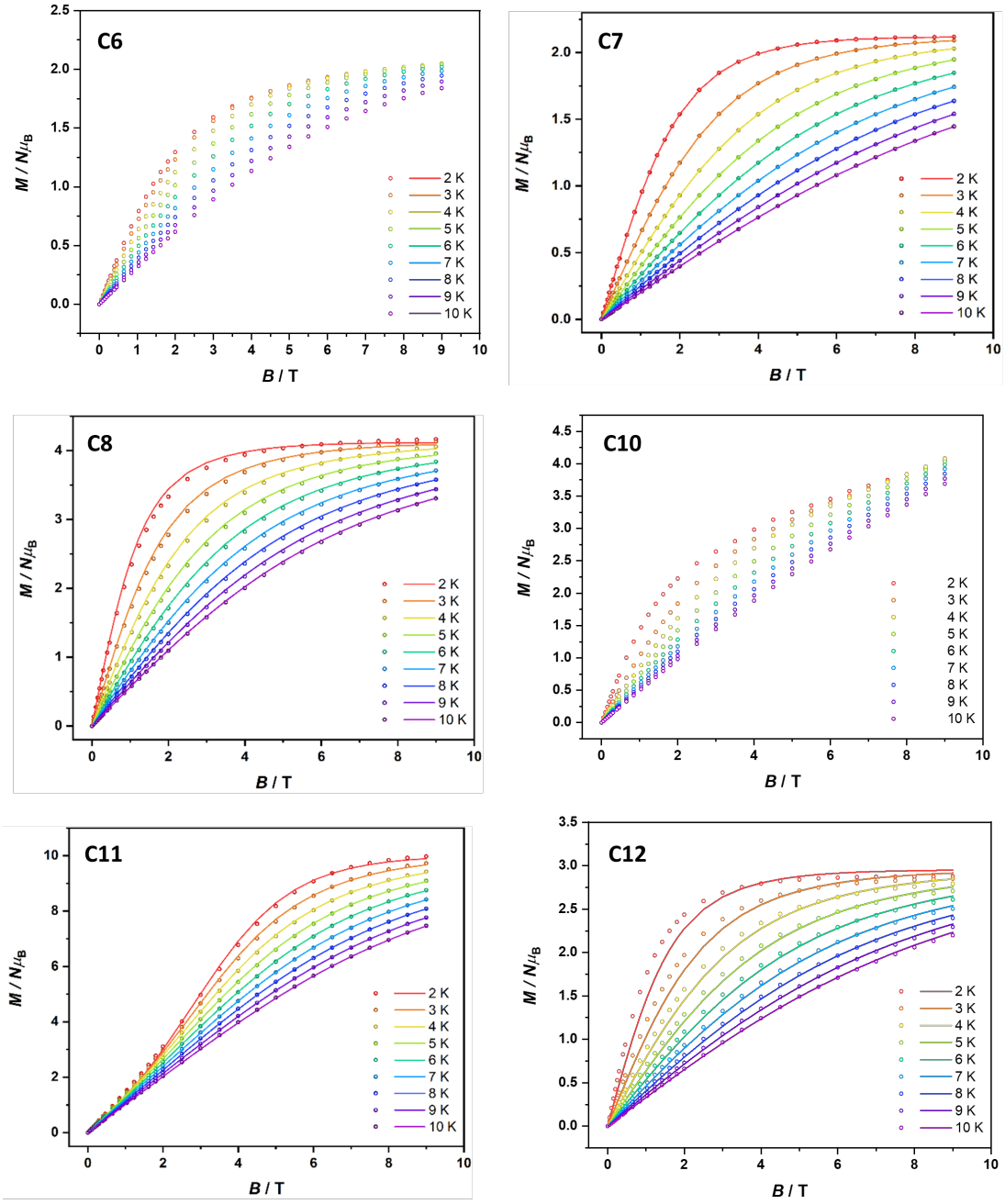

Figure 4.9: Plot of the M vs. B for **C6** - **C8** and **C10** - **C12** in the T = 2 - 10 K range with B = 0.5 - 7 T. The solid line is a fit of the experimental data using spin Hamiltonians, Equations 4.1 (**C7**, **C8**, and **C11**) and 4.2 (**C6**, **C10**, and **C12**). Complexes **C6** and **C10** have not been fitted as discussed in text.

4.1.4 Computational Analysis

A DFT study was performed on the complexes **C7**, **C8**, and **C11** to determine the relative binding energies, based on the calculated Gibbs free energy, of the complexes to establish a trend in the energetic stability of the complexes. These three complexes were chosen based on the transmetalation results. BS-DFT calculations have additionally been performed as a comparison with the experimental magnetic measurements on the complexes **C7**, **C8**, and **C11**.[151] All calculations were performed by a Plieger group member, Dr Tyson Dais using ORCA v5.02.[244,245] Geometry optimisations, starting from the crystal structure coordinates, were completed on an in-house Linux workstation with frequency calculations completed using the NeSI high-performance computing cluster.

Geometry optimisation and frequency calculations were completed for the **C11** complex using the PBE,[246] BP86,[247–249] B3LYP,[195] TPSSh,[250] and M06-2x[191,251] functionals. The PBE and BP86 functionals consistently calculated frequencies $\sim$ 20 cm^{-1} too low while the M06-2x functional consistently overestimated frequencies by $\sim$ 100 cm^{-1}, relative to the experimental ATR-IR data. B3LYP and TPSSh both gave reasonably accurate frequencies for the important functional groups; however TPSSh and M06-2x were considered too computationally expensive, as such B3LYP was chosen to carry out the binding energy calculations. Grimme's third generation dispersion correction with Becke-Johnson damping (D3BJ)[252,253] was also applied to the B3LYP, TPSSh, and M06-2x calculations, however it led to convergence issues in the frequency calculations. All calculations were performed with the B3LYP functional under the unrestricted Kohn-Sham (UKS) formalism,[249] using the Def2-TZVP basis set for all atoms and tight convergence (TightOpt) criteria using the RIJCOSX approximation with Def2/J auxiliary basis.[199,254,255] For consistency with the experimental methods used, methanolic solvation was accounted for by means of the Conductor-like Polarizable Continuum Model (CPCM), as implemented in ORCA, using CPCM(MeOH).[256] Relative binding energies were calculated by taking the difference in final Gibbs free energy between the products (complex + H_2O molecules) and starting components (H_2**L2**, $3d{\cdot}xH_2O$, $3d'{\cdot}xH_2O$, $2NO_3$, + solvents, where $x = 5$ for $d =$ Cu and $x = 6$ for $d =$ Mn; Table C.6).

The resulting binding energies for **C7**, **C8**, and **C11** were found to corroborate the experimental results observed during the transmetalation reactions with a trend of **C8** $>$ **C7** $>$ **C11** (**C8**, -127.1349 kcal mol^{-1}; **C7**, -125.7668 kcal mol^{-1}; **C11**, -91.7206 kcal mol^{-1}). From these results we can confidently say that Cu^{II} ions are the most stable in the M1 pocket, with further confirmation provided by the literature, where several examples show that Cu^{II} ions strongly coordinate to N_2O_2 pockets.[56,257–259]

Upon optimising the crystal structures of **C7**, **C8**, and **C11** it was revealed that the nature of the propylene bridge, whether perpendicular ($Cu^{II}M2^{II}$) or zig-zagged ($M1^{II}Mn^{II}$) was retained, further confirming that this structural confirmation is in fact a result of steric strain introduced by the coordinated MeOH molecules in the $M1^{II}Mn^{II}$ complexes.

The sign and magnitude of the magnetic couplings between metal ions in each dimer have been estimated using the DFT BS approach[48,193] according to the Yamaguchi method.[47,260] These calculations utilised the same level of theory as in the geometry and frequency calculations. It was found that for the complexes, **C7**, **C8**, and **C11**,

the sign and order of magnitude of the calculated J couplings were consistent with the experimentally determined values (Tables 4.6 and 4.7). For all three complexes, the calculated J coupling values are larger than experimentally determined, however the calculated values are still considered to be of the same magnitude. Plots of the magnetic orbitals of **C7**, **C8**, and **C11** can be found in Figures C.6 - C.12.

Table 4.6: J-coupling values for the complexes **C7**, **C8**, and **C11** calculated using the BS DFT approach

	J (cm^{-1})	$E_{HS} - E_{BS}$ (cm^{-1})	$< S^2 >_{HS}$	$< S^2 >_{BS}$
C7	123.78	-123.84	2.0049	1.0044
C8	-85.09	428.26	12.0059	6.9730
C11	-2.09	52.156	30.0067	5.0013

Table 4.7: Fitted experimental/DFT computed magnetic exchange (J) for the complexes **C7**, **C8**, and **C11**.

	Expt. J (cm^{-1})	**Calcd. J (cm^{-1})**
C7	+63.0	+123.78
C8	-34.8	-85.09
C11	-0.45	-2.09

4.2 Literature Analysis

Throughout the literature, there are many examples of 3*d* based complexes where at least two metal ions are bridged by a phenolate group. By refining the search (CCDC v1.20, 02/08/22) to complexes containing Schiff base or oxime based ligands gave 1274 and 135 hits respectively, clearly showing how much smaller the field of oxime based complexes is. Of the 135 hits, only 13 were discrete dinuclear complexes and of those 13, only six were closely related to the research in this chapter, with none of them containing NO_3^- anions.[135,136,261–263] In addition to this, of the 135 hits only four were heterometallic, all with a nuclearity of three.[166,264,265] The most common type of structure found with 84 submissions was trinuclear M_3L_2 structures.

A number of Schiff base counterparts to the complexes **C6** - **C13** are found in the literature, with an example by Branzea and coworkers who produced a number of dinuclear 3*d*3*d*' complexes that they then went on to bridge with various anions to form polymers.[213,266] Two of the dinuclear complexes are heterometallic $Cu^{II}M^{II}$ (M = Co^{II} and Mn^{II}), which resemble that of complexes **C6** and **C8** however the ligand utilised is the Schiff base counterpart of H_2**L2**, *N*,*N*'-propylene-bis-(3-methoxysalcilideneiminato). Initially it was thought that there would not be a large difference between the two types of complexes, with minor differences in bridging angles due to the differences in the bridge. This was found to be the case, with almost neglible differences as shown in Table 4.8, however the biggest difference was found to be the coordination of the second NO_3^- anion between the two $Cu^{II}Mn^{II}$ complexes. Magnetic characterisation wasn't performed on the discrete dinuclear complexes however it was performed on the $Cu^{II}Mn^{II}$ polymers where the dinuclear units were bridged by pyrazole-3,5-dicarboxylic acid, trimesic acid, and $[Ni(CN)_4]$. Interestingly, the

Table 4.8: Selected bond lengths (Å) and bond angles (°) of literature examples vs. complexes **C6** and **C8**

	C6	**[CuCo(L)$(NO_3)_2$]**[a]	**C8**	**[CuMn(L)$(NO_3)_2$]**[a]
Bridge Type	Alkyloxime	Imine	Alkyloxime	Imine
M1···M2	3.2031(7)	3.198	3.329(7)	3.322
M1-O1-M2	105.13(11)	105.55	107.16(12)	107.44
M1-O2-M2	105.94(11)	106.22	107.11(12)	107.51
M2-O_{NO_3}[b]	2.220(3)	2.257	2.315(3)	2.343
M2-O_{NO_3}[b]	2.102(3)	2.094	2.288(3)	2.267
M2-O_{NO_3}[c]	2.029(3)	2.094	2.207(3)	2.191
M2···O_{NO_3}	3.084(3)	3.068	2.486(6)	2.640
M2-O-N_{NO_3}[c]	123.2(2)	123.42	100.8(2)	106.95

[a]Branzea *et al.*;[213] [b]Bidentate NO_3; [c]Monodentate NO_3

$\chi_M T$ vs T curves closely resembled that of **C8**, with room temperature values of 4.20, 3.85, and 3.93 $cm^3\,K\,mol^{-1}$ for pyrazole-3,5-dicarboxylic acid, trimesic acid, and $[Ni(CN)_4]$ respectively. These values are lower than expected for a $Cu^{II}Mn^{II}$ pair of uncoupled ions, similarly to what was found for **C8** however the RT values are lower than the 4.25 $cm^3\,K\,mol^{-1}$ obtained for **C8**. A J coupling value of -34.8 cm^{-1} was obtained for **C8** where values of J = -48.9, -64.7, and -60.4 cm^{-1} were obtained for the pyrazole-3,5-dicarboxylic acid, trimesic acid, and $[Ni(CN)_4]$ polymers respectively.[213,266]

4.3 Conclusion

A series of dinuclear homo- and heterometallic complexes, **C6 - C13**, have been synthesised by a 1 : 1 : 1 reaction of ligand, H_2**L2**, $M(OAc)_2 \cdot H_2O$, and $M(NO_3)_2 \cdot H_2O$. All complexes have been characterised by a combination of SCXRD, FAAS, ESI-MS, ATR-IR, CHN microanalysis, and magnetic and computational analyses. Through the use of transmetalation, it was found that **C8** was the most stable complex, a result that was somewhat unexpected as the canonical Irving-Williams monoatomic stability trend would suggest **C7** to be the most stable. DFT based binding energy calculations confirmed that **C8** was in fact more stable than **C7** by 1.37 kcal mol^{-1} or approximately 2.3 times thermal energy. Magnetic characterisation found that complexes **C8** and **C10 - C12** to have antiferromagnetic couplings and exchange parameters of J = -34.8 cm^{-1} (**C8**), J = -0.45 cm^{-1} (**C11**), and J = -6.43 cm^{-1} (**C12**). Unexpectedly, both **C6** and **C7** were found to have ferromagnetic couplings between the metal ions with an exchange parameter of J = +63.0 cm^{-1} found for **C7**, the largest ferromagnetic coupling for a Schiff base derived dinuclear $Cu^{II}{}_2$ complex reported in the literature. Its thought the unusual seven-coordinate geometry of the Cu^{II} ion was a driving factor for the ferromagnetic coupling and lessened experimental stability. This seven-coordinate Cu^{II} phenomena has introduced the potential to explore unusual coordination environments and their associated magnetic properties in the future.

Complex Preparation and Characterisation

To a solution of H_2**L2** (1 eq.) in $CHCl_3$ was added solutions of $M(OAc)_2 \cdot H_2O$ (1 eq.) and $M(NO_3)_2 \cdot H_2O$ (1 eq.), both in MeOH and stirred at RT for five minutes. Isolation of the complex was achieved by the diffusion of Et_2O into the reaction solution. X-ray quality crystals were obtained after a period of one to four weeks.

[$Cu^{II}Co^{II}$L2$(NO_3)_2$] (**C6**): H_2**L2** (0.0150 g, 0.04 mmol, 1 eq.) in $CHCl_3$ (4 mL), $Cu(OAc)_2 \cdot H_2O$ (0.0080 g, 0.04 mmol, 1 eq.), and $Co(NO_3)_2 \cdot 6H_2O$ (0.0117 g, 0.04 mmol, 1 eq.) both in MeOH (0.8 mL). Brown block shaped X-ray quality crystals were produced after two weeks. Yield (0.0160 g, 65%); ATR-IR: $\overline{\nu}$ = 2924 (C-H), 1607 (C=N), 1594 (Ar), 1555 (N-O), 1462 (NO_3), 1429 (C-H), 1288 (NO_3), 1246 (Ar-O), 1098 (C-O), 1038 (NO_3), 960 (N-O), 809 (NO_3), 743 (Ar) cm^{-1}; ESI-MS: *m/z* 555 $[M\text{-}NO_3]^+$; elemental analysis calcd. (%) for $C_{19}H_{20}N_4O_{12}CuCo$: C 36.88, H 3.26, N 9.05; found C 36.91, H 3.32, N 8.71.

[Cu^{II}_2L2$(NO_3)_2$] (**C7**): H_2**L2** (0.0378 g, 0.101 mmol, 1 eq.) in $CHCl_3$ (4 mL), $Cu(OAc)_2 \cdot H_2O$ (0.0200 g, 0.100 mmol, 1 eq.), and $Cu(NO_3)_2 \cdot 3H_2O$ (0.0242 g, 0.100 mmol, 1 eq.) both in MeOH (0.8 mL). Brown platelet shaped X-ray quality crystals were produced after three weeks. Yield (0.0314 g, 50%); ATR-IR: $\overline{\nu}$ = 2928 (C-H), 1605 (C=N), 1593 (Ar), 1552 (N-O), 1456 (NO_3), 1431 (C-H), 1295 (NO_3), 1244 (Ar-O), 1099 (C-O), 1039 (NO_3), 959 (N-O), 821 (NO_3), 744 (Ar) cm^{-1}; ESI-MS: *m/z* 559 $[M\text{-}NO_3]^+$; elemental analysis calcd. (%) for $C_{19}H_{20}N_4O_{12}Cu_2$: C 36.60, H 3.23, N 8.99; found: C 36.72, H 3.22, N 8.82.

[$Cu^{II}Mn^{II}$L2$(NO_3)_2$] (**C8**): H_2**L2** (0.0378 g, 0.101 mmol, 1 eq.) in $CHCl_3$ (4 mL), $Cu(OAc)_2 \cdot H_2O$ (0.0200 g, 0.100 mmol, 1 eq.), and $Mn(NO_3)_2 \cdot 4H_2O$ (0.0251 g, 0.100 mmol, 1 eq.) both in MeOH (0.8 mL). Green platelet shaped X-ray quality crystals were produced after three weeks. Yield (0.0401, 65%); ATR-IR: $\overline{\nu}$ = 2925 (C-H), 1607 (C=N), 1594 (Ar), 1554 (N-O), 1433 (C-H), 1463 (NO_3), 1298 (NO_3), 1244 (Ar-O), 1098 (C-O), 1038 (NO_3), 973 (N-O), 816 (NO_3), 745 (Ar) cm^{-1}; ESI-MS: *m/z* 551 $[M\text{-}NO_3]^+$, 458 $[L+Cu+Na]^+$, 397 $[L+Na]^+$; elemental analysis calcd. (%) for $C_{19}H_{20}N_4O_{12}CuMn \cdot H_2O$: C 36.06, H 3.50, N 8.85; found: C 35.71, H 3.06, N 8.66.

[$Cu^{II}Zn^{II}$L2$(NO_3)_2$] (**C9**): H_2**L2** (0.0150 g, 0.04 mmol, 1 eq.) in $CHCl_3$ (4 mL), $Cu(OAc)_2 \cdot H_2O$ (0.0080 g, 0.04 mmol, 1 eq.), and $Zn(NO_3)_2 \cdot 6H_2O$ (0.0119 g, 0.04 mmol, 1 eq.) both in MeOH (0.8 mL). Green block shaped X-ray quality crystals were produced after one week. Yield (0.0193 g, 77%); ATR-IR: $\overline{\nu}$ = 2942 (C-H), 1606 (C=N), 1597 (Ar), 1557 (NO_3), 1464 (NO_3), 1430 (C-H), 1290 (NO_3), 1249 (Ar-O), 1105 (C-O), 1036 (NO_3), 969 (N-O), 810 (NO_3), 744 (Ar) cm^{-1}; ESI-MS: *m/z* 564 $[M\text{-}NO_3]^+$; elemental analysis calcd. (%) for $C_{19}H_{20}N_{4012}CuZn \cdot 1.5H_2O$: C 34.98, H 3.55, N 8.59; found: C 34.72, H 3.21, N 8.17.

[$Co^{II}Mn^{II}$L2$(MeOH)_2(NO_3)_2$] (**C10**): H_2**L2** (0.0151 g, 0.04 mmol, 1 eq.) in $CHCl_3$ (4 mL), $Co(OAc)_2 \cdot 4H_2O$ (0.0098 g, 0.04 mmol, 1 eq.), and $Mn(NO_3)_2 \cdot 4H_2O$ (0.0099 g, 0.04 mmol, 1 eq.) both in MeOH (0.8 mL). Orange block shaped X-ray quality crystals were produced after two weeks. Yield (0.0152 g, 56%); ATR-IR: $\overline{\nu}$ = 3374 (O-H), 2943 (C-H), 1605 (C=N), 1557 (N-O), 1468 (NO_3), 1436 (C-H), 1303 (NO_3), 1242 Ar-O), 1102 (C-O), 1081 (C-O), 1041 (NO_3), 979 (N-O), 818 (NO_3), 737 (Ar) cm^{-1}; ESI-MS: *m/z* 548 $[M\text{-}2MeOH\text{-}NO_3]^+$; elemental analysis calcd. (%) for $C_{21}H_{28}N_4O_{14}CoMn$: C 37.40, H 4.19, N 8.31; found C 37.21, H 4.18, N 8.29.

[Mn^{II}_2L2$(MeOH)_2(NO_3)_2$] (**C11**): H_2**L2** (0.0373 g, 0.100 mmol, 1 eq.) in $CHCl_3$ (10 mL), $Mn(OAc)_2 \cdot 4H_2O$ (0.0248 g, 0.100 mmol, 1 eq.), and $Mn(NO_3)_2 \cdot 4H_2O$ (0.0255 g, 0.100 mmol, 1 eq.) both in MeOH (2 mL). Light brown block shaped X-ray quality crystals were produced

after four weeks. Yield (0.0382 g, 57%); ATR-IR: $\overline{\nu}$ = 3362 (O-H), 2942 (C-H), 1604 (C=N), 1598 (Ar), 1555 (N-O), 1463 (NO_3), 1436 (C-H), 1295 (NO_3), 1242 (Ar-O), 1094 (C-O), 1083 (C-O), 1042 (NO_3), 969 (N-O), 809 (NO_3), 736 (Ar) cm^{-1}; ESI-MS: *m/z* 608 $[M\text{-}NO_3]^+$; elemental analysis calcd. (%) for $C_{21}H_{28}N_4O_{14}Mn_2$: C 37.63, H 4.21, N 8.36; found: C 37.90, H 4.38, N 8.13.

$[Ni^{II}Mn^{II}$L2(MeOH)$_2$(NO$_3$)$_2]$ (**C12**): H_2**L2** (0.0187 g, 0.05 mmol, 1 eq.) in $CHCl_3$ (5 mL), $Ni(OAc)_2{\cdot}4H_2O$ (0.0124 g, 0.05 mmol, 1 eq.), and $Mn(NO_3)_2{\cdot}4H_2O$ (0.0123 g, 0.05 mmol, 1 eq.) both in MeOH (1.0 mL). Green platelet shaped X-ray quality crystals were produced after three weeks. Yield (0.0269 g, 80%); ATR-IR: $\overline{\nu}$ = 3374 (O-H), 2943 (C-H), 1605 (C=N), 1596 (Ar), 1557 (N-O), 1467 (NO_3), 1435 (C-H), 1301 (NO_3), 1242 (Ar-O), 1102 (C-O), 1083 (C-O), 1042 (NO_3), 979 (N-O), 817 (NO_3), 737 (Ar) cm^{-1}; ESI-MS: *m/z* 548 $[M\text{-}NO_3\text{-}2MeOH]^+$; elemental analysis calcd. (%) for $C_{21}H_{28}N_4O_{14}NiMn{\cdot}H_2O$: C 36.44, H 4.37, N 8.10; found: C 36.71, H 4.17, N 8.35.

$[Zn^{II}Mn^{II}$L2(MeOH)$_2$(NO$_3$)$_2]$ (**C13**): H_2**L2** (0.0150 g, 0.04 mmol, 1 eq.) in $CHCl_3$ (4 mL), $Zn(OAc)_2{\cdot}2H_2O$ (0.0088 g, 0.04 mmol, 1 eq.), and $Mn(NO_3)_2{\cdot}4H_2O$ (0.010 g, 0.04 mmol, 1 eq.) both in MeOH (0.8 mL). Yellow block shaped X-ray quality crystals were produced after three weeks. Yield (0.0097 g, 36%); ATR-IR: $\overline{\nu}$ = 3366 (O-H), 2942 (C-H), 1604 (C=N), 1598 (Ar), 1557 (N-O), 1464 (NO_3), 1436 (C-H), 1298 (NO_3), 1241 (Ar-O), 1102 (C-O), 1083 (C-O), 1041 (NO_3), 967 (N-O), 817 (NO_3), 736 (Ar) cm^{-1}; ESI-MS: *m/z* 554 $[M\text{-}NO_3\text{-}2MeOH]^+$; elemental analysis calcd. (%) for $C_{21}H_{28}N_4O_{14}ZnMn$: C 37.05, H 4.15, N 8.23; found C 37.10, H 4.20, M 8.13.

Chapter 5

3*d*4*f* Dinuclear Complexes

This chapter describes a series of 3*d*4*f* dinuclear complexes that extend from the success of both the defective dicubane and 3*d*3*d*′ dinuclear series by incorporating different aspects of each. This series takes the next step from the 3*d*3*d*′ series by retaining the same ligand, 6,6′-dimethoxy-2,2′-[(1,3-propylene)dioxybis(nitrilomethylidyne)]diphenol, H_2**L2** and exchange pathways, M1-O1-M2 and M1-O2-M2, but structurally modifying the pathways by introducing 4*f* ions with varying ionic radii. Instead of directly modifying the bridging groups, the peripheral coordinates will be modified by the use of different anions and solvents, similarly to what was shown in the defective dicubane series. Various structural modifications and properties, such as transmetalation, polymorphism, and isomorphism will be explored.

5.1 General Results

The solid state complexes **C14** - **C49** were synthesised from RT reactions between H_2**L2**, $3dX_2{\cdot}H_2O$ (3*d* = Cu^{II}, Co^{II}, Ni^{II}, and Zn^{II}; X = OAc^-, $NO_3{}^-$, and Cl^-), and $4fX_3{\cdot}H_2O$ (4*f* = La^{III}, Ce^{III}, Eu^{III}, Gd^{III}, Tb^{III}, Dy^{III}, Ho^{III}, Er^{III}, Yb^{III}; X = OAc^-, $NO_3{}^-$, and Cl^-) in a 1 : 1 : 1 molar ratio. Successful coordination was indicated by the colour of the solution visibly changing with each addition of metal salt. The complexes were isolated by the slow vapour diffusion of Et_2O into the reaction solution with X-ray quality crystals obtained over a period of one to nine weeks. Successful complexations were confirmed by characterisation methods such as SCXRD, ATR-IR, and ESI-MS, with select complexes (**C17**, **C21**, and **C37**) further confirmed by CHN microanalysis. Due to both an initial small sample size and reproducibility issues, the complexes **C25**, **C27**, **C30** - **C32**, **C40**, and **C41** have solely been characterised by SCXRD. Magnetic measurements were performed on complexes **C17**, **C21**, and **C37** at the Institute of Nanotechnology, Karlsruhe Institute of Technology through collaboration with Prof. Annie Powell and Dr. Christopher Anson.

5.2 Cu^{II}4*f* Complexes

The complexes **C14** - **C40** discussed in this section refer to the Cu^{II}4*f* dinuclear structures where the 4*f* ions are coordinated to either $NO_3{}^-$ or Cl^- anions. Key differences between the complexes can be found in Table 5.1.

Table 5.1: Coordination differences in the complexes **C14 - C40**

	M1	M2	Anion	Solvent
C14	Cu^{II}	Dy^{III}	NO_3^-	–
C15	Cu^{II}	Er^{III}	NO_3^-	–
C16	Cu^{II}	Ho^{III}	NO_3^-	–
C17	Cu^{II}	Gd^{III}	NO_3^-	–
C18	Cu^{II}	Eu^{III}	NO_3^-	–
C19	Cu^{II}	Tb^{III}	NO_3^-	–
C20	Cu^{II}	Yb^{III}	NO_3^-	–
C21	Cu^{II}	Dy^{III}	NO_3^-	–
C22	Cu^{II}	Eu^{III}	NO_3^-	–
C23	Cu^{II}	Gd^{III}	NO_3^-	–
C24	Cu^{II}	La^{III}	NO_3^-	H_2O
C25	Cu^{II}	La^{III}	NO_3^- / $[Cu^{I}(MeCN)_4]^+$	–
C26	Cu^{II}	La^{III}	NO_3^-	–
C27	Cu^{II}	La^{III}	NO_3^-	MeOH
C28	Cu^{II}	Ce^{III}	NO_3^-	MeOH
C29	Cu^{II}	Ce^{III}	NO_3^-	H_2O
C30	Cu^{II}	Ce^{III}	NO_3^-	MeOH
C31	Cu^{II}	Ce^{III}	NO_3^-	MeOH
C32	Cu^{II}	Ce^{III}	NO_3^-	MeOH
C33	Cu^{II}	Eu^{III}	NO_3^-	MeOH
C34	Cu^{II}	Dy^{III}	Cl^-	H_2O/MeOH
C35	Cu^{II}	Eu^{III}	Cl^-	H_2O/MeOH
C36	Cu^{II}	Tb^{III}	Cl^-	H_2O/MeOH
C37	Cu^{II}	Er^{III}	Cl^-	H_2O
C38	Cu^{II}	Ho^{III}	Cl^-	H_2O
C39	Cu^{II}	Ho^{III}	Cl^- / $[CuCl_4]^{2-}$	H_2O
C40	Cu^{II}	Ce^{III}	Cl^-	H_2O

5.2.1 Structural Analysis - NO_3^- Coordinates

The complexes **C14** - **C20** were found to be discrete dinuclear complexes, all crystallising in the monoclinic space group, $P2_1/n$. The whole structure can be found within the asymmetric unit as shown by Figures 5.1, 5.2, and 5.3. The structure consists of one deprotonated alkyloxime ligand, $\mathbf{L2}^{2-}$ coordinated to one Cu^{II} ion (Cu1; M1) and one 4*f* ion (M2) resembling that of Mode I (Figure 2.6).[145] Cu1 is four-coordinate with a distorted square planar geometry as determined by CShM (Table D.2), however when considering the τ_4 values of the complexes (range of 0.15 - 0.17), the values are closer to that of a 'seesaw' geometry.[146,147,209,267] The N_2O_2 donor set, consists of two phenolate oxygens and two alkyloxime nitrogens. M2 is 10-coordinate which as shown by CShM measurements (Table D.3) has very similar values for bicapped square antiprismatic (**C14** - **C16**; Figure 5.1) and sphenocorona geometries (**C17** - **C19**; Figure 5.2), attributed to the small differences in the angles and bond lengths of the NO_3^- coordinates.[146,147,268,269] The O_{10} donor set for M2 consists of two phenolate and methoxy oxygens and three bidentate NO_3^- anions. For **C20**, M2 varies slightly as one of the NO_3^- anions is monodentate, leading to a nine-coordinate Yb^{III} ion with a capped square antiprismatic geometry (Figure 5.3).[146,147,270]

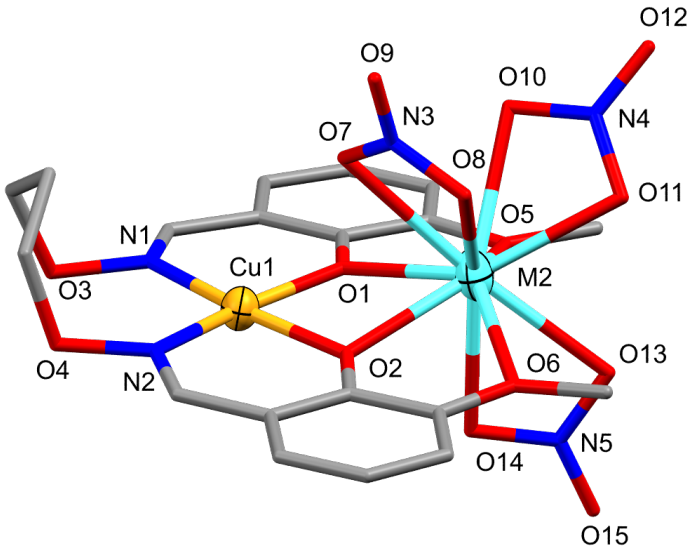

Figure 5.1: Representative structure of $[Cu^{II}M2^{III}\mathbf{L2}(NO_3)_3]$ (M2 = Dy^{III} (**C14**), Er^{III} (**C15**), and Ho^{III} (**C16**)). Hydrogen atoms have been omitted for clarity and thermal ellipsoids of the metal ions are shown at 70% probability. Colour code: Cu^{II} = dark yellow, $M2^{III}$ = aqua, N = blue, O = red, and C = grey.

Due to the similarities of **C14** - **C20**, it was presumed the M1···M2 distances and M1-O-M2 angles would all be within a small range of each other, with the subtle difference a result of the different ionic radii (Table 5.1). This presumption was found to be true for all except **C17**, as the complex was found to have a larger M1···M2 separation (3.547(1) versus 3.360(1) - 3.439(1)) subsequently resulting in a larger M1-O1-M2 exchange angle (109.11(16) versus 104.58(16) - 105.60(2)), which was attributed to the NO_3^- anion coordination.

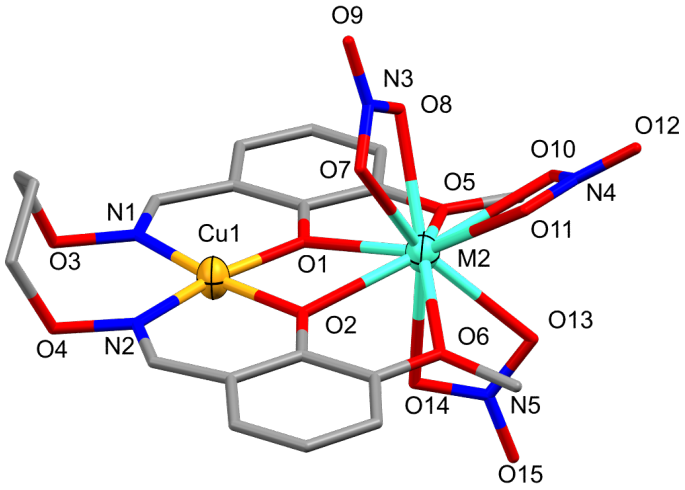

Figure 5.2: Representative structure of $[Cu^{II}M2^{III}\mathbf{L2}(NO_3)_3]$ (M2 = Gd^{III} (**C17**), Eu^{III} (**C18**), and Tb^{III} (**C19**)). Hydrogen atoms have been omitted for clarity and thermal ellipsoids of the metal ions are shown at 60% probability. Colour code: Cu^{II} = dark yellow, $M2^{III}$ = aqua, N = blue, O = red, and C = grey.

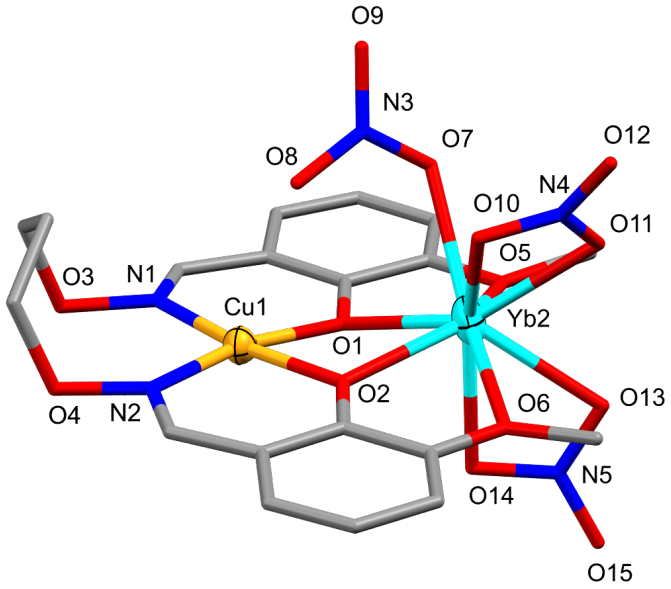

Figure 5.3: Full molecular structure of $[Cu^{II}Yb^{III}\mathbf{L2}(NO_3)_3]$ (**C20**). Hydrogen atoms have been omitted for clarity and thermal ellipsoids of metal ions shown at 60% probability. Colour code: Cu^{II} = dark yellow, Yb^{III} = aqua, N = blue, O = red, and C = grey.

After the initial collection of the complexes, subsequent bulk synthesis attempts were made in order to perform full characterisation. For each remake, the crystals were screened and a structure was collected to determine the success. It was found that for a number of complexes, polymorphic and/or isomorphic structures were formed. A polymorphic complex resembles that of an original complex with the same composition however with a different unit cell and/or space group. This can result in varied connectivity and/or a different number of molecules in the asymmetric unit. This differs from isomorphic complexes, which have the same or similar structural appearance, atom placements, space group, and unit cell but with the replacement of one or more atoms.[1] It has been shown in the literature that polymorphs themselves produce unique magnetic properties therefore bulk samples need to contain only one polymorph to achieve cohesive results. Commonly PXRD is the method used to confirm only one complex is present.[216,271] Three of the above complexes, **C14**, **C17**, and **C18** all had at least one other polymorph produced during bulk synthesis, with many different polymorphs produced for complexes **C14** and **C17**. The most common polymorph found had two molecules per asymmetric unit, as shown by the complexes **C21** - **C23** (Figures 5.4 and D.1).

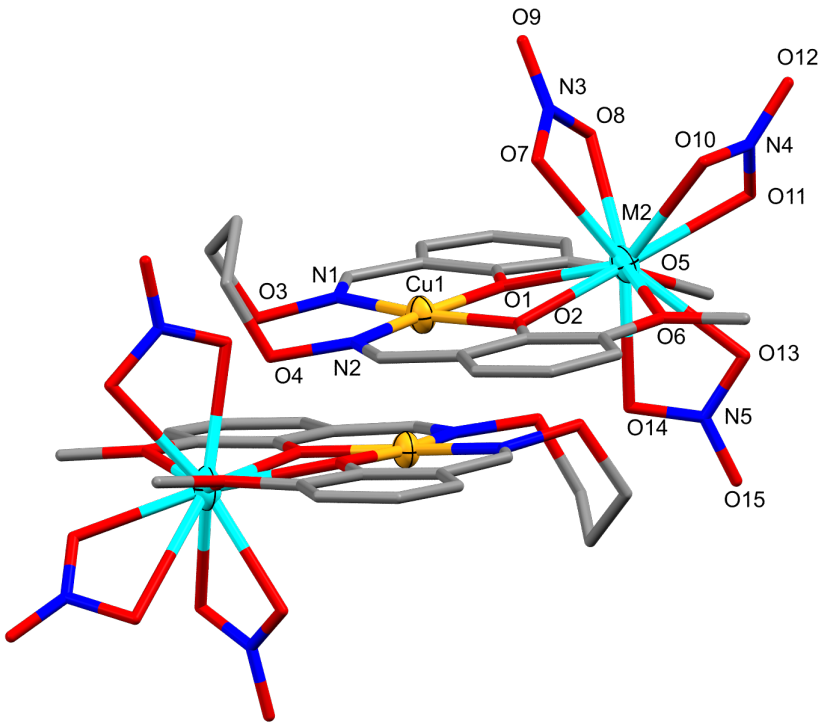

Figure 5.4: Representative structure of $[Cu^{II}M2^{III}\mathbf{L2}(NO_3)_3]_2$ (M2 = Dy^{III} (**C21**), Eu^{III} (**C22**), and Gd^{III} (**C23**)). Hydrogen atoms have been omitted and only one unit numbered for clarity. Thermal ellipsoids of the metal ions are shown at 70% probability. Colour code: Cu^{II} = dark yellow, $M2^{III}$ = aqua, N = blue, O = red, C = grey.

The complexes **C21** - **C23**, closely resemble **C14** - **C19** with one unit of **L2** coordinated to both a Cu^{II} ion (M1) and a 4*f* ion (M2), resembling Mode I (Figure 2.6).[145] Cu1 is four-coordinate with a square planar geometry (CShM, Table D.2) or distorted see-saw geometry (τ_4 values of 0.15 and 0.16) and a N_2O_2 donor set consisting of two alkyloxime nitrogens and two phenolate oxygens.[146,147,209,267] M2 is 10-coordinate

with a sphenocorona geometry (CShM, Table D.3) and an O_{10} donor set consisting of two phenolate oxygens, two methoxy oxygens, and three bidentate NO_3^- anions.[146,147,268]

The creation of the polymorphs and following isomorphic series are phenomena not entirely understood however it is believed the crystallisation conditions have been a large contributor.[272] All crystallisations were performed using the same method of Et_2O vapour diffusion however the environment the crystallisations were performed in was not always identical. For example, the crystallisations were always performed at RT however RT and the temperature shift from day to night can vary significantly depending on the time of year, with other environmental factors such as humidity and the hydration of the metal salt and/or solvent affecting the reproducibility.

The two following series are thought to be the result of kinetic versus thermodynamic products and or the subtle changes in the method and/or reagents, with the first a $Cu^{II}La^{III}$ series where it is believed the differences in composition arose from the different lengths of crystallisation. The complexes **C24** - **C27** were found to crystallise in the triclinic space group, $P\bar{1}$. The four complexes share the similarity of $\mathbf{L2}^{2-}$ coordinated to both Cu^{II} and La^{III} ions (Mode I, Figure 2.6), however apart from the metal ions, the complexes have significant structural differences.[145] The complex **C24** was found to be a dinuclear complex, with the entire structure found within the asymmetric unit as shown in Figure 5.5. Cu1 is four-coordinate with a distorted square planar geometry (CShM value of 2.601, Table D.2).[146,147,267] As indicated by the CShM value, **C24** has a larger degree of distortion for Cu1 than found for the other complexes, thought to be attributed to both the larger 4*f* ion and the introduction of intermolecular hydrogen bonding. The N_2O_2 donor set consists of two phenolate oxygens and two alkyloxime nitrogens, with an additional weakly coordinated monodentate NO_3^- anion (2.567(4) Å; Cu-ONO_2 bond lengths found in the literature range between 1.996 to 2.480 Å).[211–213] La1 is 10-coordinate with a metabidiminished icosahedron geometry (CShM, Table D.3) and O_{10} donor set consisting of two phenolate and methoxy oxygens, one H_2O molecule, and three NO_3^- anions, two bidentate and one monodentate.[146,147,268] Two moderate intermolecular hydrogen bonds are found between the H_2O molecule O16 and the oxygen atoms of two NO_3^- anions, O9 (O16$\cdots$O9, 2.855(5) Å) and O12 (O16$\cdots$O12, 2.860(5) Å), of two adjacent complexes.[158] For **C24**, the SQUEEZE procedure was implemented using the crystallographic software, Olex2, to remove diffuse solvent in the crystal lattice. The result was removal of 30 electrons per asymmetric unit which equates to three H_2O molecules (30 e^-).[208,273]

Due to the inclusion of the H_2O coordinate, the weak coordination between Cu^{II} and the monodentate NO_3^- anion, and the large degree of distortion, it was assumed this would result in significantly different M1-O-M2 angles. It was found however that the average M1-O-M2 angle (105.48°) for **C24** was within the range found for both the $Cu^{II}La^{III}$ and other 3*d*4*f* dinuclear complexes with coordinated NO_3^- anions, 99.69° - 109.11°. A number of reasons could explain this, with it most likely attributed to the intermolecular hydrogen bonding drawing the M2 ions further out of the pocket, increasing both the M1$\cdots$M2 distance and M1-O-M2 angles.

Table 5.2: Selected bond lengths (Å) and angles (°) of the complexes **C14** - **C23** from crystal structure determination

	C14	**C15**	**C16**	**C17**	**C18**	**C19**	**C20**	**C21***	**C22***	**C23***
Cu1-O1	1.944(6)	1.964(5)	1.957(3)	1.946(4)	1.944(5)	1.947(4)	1.949(4)	1.950	1.953	1.960
Cu1-O2	1.949(5)	1.945(6)	1.944(3)	1.956(4)	1.964(4)	1.953(4)	1.958(3)	1.945	1.958	1.942
Cu1-N1	1.968(7)	1.976(7)	1.978(3)	1.978(5)	1.973(6)	1.975(6)	1.971(4)	1.977	1.977	1.981
Cu1-N2	1.972(6)	1.967(7)	1.976(3)	1.977(5)	1.987(5)	1.978(4)	1.983(4)	1.981	1.976	1.975
M2-O1	2.334(5)	2.281(5)	2.303(2)	2.396(4)	2.361(4)	2.339(4)	2.290(3)	2.342	2.425	2.368
M2-O2	2.316(5)	2.284(6)	2.313(3)	2.416(4)	2.368(4)	2.329(3)	2.264(3)	2.382	2.385	2.405
M2-O5	2.477(6)	2.503(6)	2.520(3)	2.497(4)	2.510(5)	2.488(4)	2.415(4)	2.423	2.501	2.478
M2-O6	2.477(6)	2.444(6)	2.472(3)	2.526(4)	2.547(5)	2.532(4)	2.492(4)	2.463	2.482	2.470
M2-O7	2.730(8)	2.668(7)	2.673(3)	2.437(6)	2.603(5)	2.604(4)	2.362(4)	2.438	2.486	2.452
M2-O8	2.450(7)	2.404(6)	2.425(3)	2.430(5)	2.482(5)	2.457(4)	3.264(4)[a]	2.434	2.469	2.442
M2-O10	2.470(8)	2.449(6)	2.466(3)	2.545(7)	2.516(5)	2.492(4)	2.405(4)	2.409	2.503	2.483
M2-O11	2.396(6)	2.369(6)	2.383(3)	2.508(7)	2.441(4)	2.423(4)	2.319(4)	2.671	2.539	2.535
M2-O13	2.478(7)	2.462(6)	2.470(3)	2.492(5)	2.525(5)	2.517(4)	2.399(4)	2.499	2.533	2.508
M2-O14	2.459(6)	2.434(6)	2.458(3)	2.480(4)	2.504(5)	2.467(4)	2.398(4)	2.459	2.504	2.498
Cu1-O1-M2	104.70(2)	104.90(2)	105.03(11)	109.11(16)	105.60(19)	105.04(16)	104.58(16)	108.77	107.38	108.85
Cu1-O2-M2	105.20(2)	105.50(3)	105.10(11)	107.99(16)	104.73(19)	105.22(14)	105.24(14)	107.44	108.78	108.05
Cu1···M2	3.395(3)	3.372(2)	3.387(1)	3.547(1)	3.439(1)	3.409(1)	3.360(1)	3.497	3.539	3.528

* Averaged values; Non-averaged values found in Table D.5

[a] M2···O8

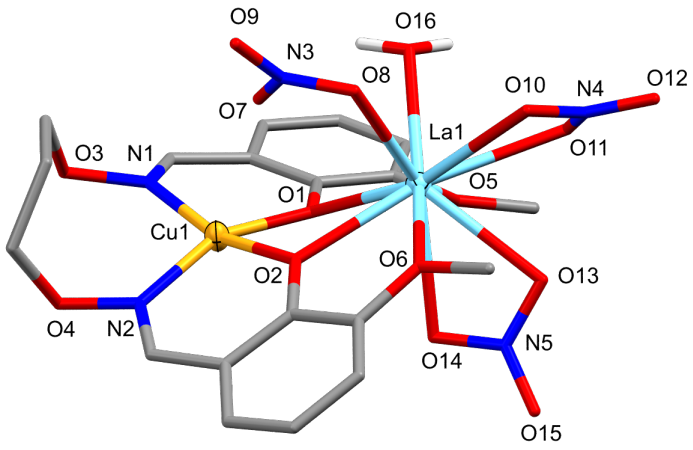

Figure 5.5: Full molecular structure of $[Cu^{II}La^{III}$**L2**$(H_2O)(NO_3)_3]$, **C24**. Non-interacting hydrogen atoms have been omitted for clarity and the thermal ellipsoids of the metal ions are shown at 70% probability. Colour code: Cu^{II} = dark yellow, La^{III} = aqua, N = blue, O = red, C = grey, and H = white.

The complex **C25** (Figures 5.6 and D.2) is a single dinuclear complex, resembling that of **C24** however with one key difference, La1 is 12-coordinate instead of 10. Cu1 is four-coordinate with a square planar (CShM, Table D.2) or distorted seesaw (τ_4 = 0.14) geometry and as typical of the other four-coordinate M1 ions, the donor set consists of two phenolate oxygens and two alkyloxime nitrogens.[146,147,267] La1 as mentioned above is dodecanuclear with an icosahedron geometry (CShM, Table D.3) and an O_{12} donor set consisting of two phenolate oxygens, two methoxy oxygens, and four bidentate NO_3^- anions.[146,147,274,275] Due to the extra bidentate NO_3^- anion, a $[Cu^I(MeCN)_4]^+$ complex is found in the crystal lattice to balance the -1 charge. The asymmetric unit for **C25** consists of two $Cu^{II}La^{III}$ units, two $[Cu^I(MeCN)_4]^+$ units, and one MeCN molecule (Figure D.2). This complex was initially set up as a bulk crystallisation of **C24**, however the crystallisation was left undisturbed for an extended period of time compared to the original sample. The formation of this complex is not entirely understood however there are several reports of complexes with $[Cu^I(MeCN)_4]^+$ anions found in the crystal lattice.[276–279] The groups of Lopez-Dellamury *et al.* and Moreno Pineda *et al.* found that $[Cu^I(MeCN)_4]^+$ anions formed when Cu^{II} salts such as OAc^- and $O_2C^tBu^-$ in MeCN were in the presence of free carboxylic acids. Although it can not be known if this was the cause for the formation of **C25**, it is an example of how these types of complexes can form.

The complex, **C26**, was found to be a dimeric complex, with bridging between two 4*f* ions. The asymmetric unit contains half of the complete structure as shown in Figure 5.7 with the full structure shown in Figure 5.8. Cu1 has a square planar geometry (CShM, Table D.2) with the typical N_2O_2 donor set consisting of two phenolate oxygens and two alkyloxime nitrogens.[146,147,267] Additonally, O7 is weakly coordinated to Cu1 with a bond length of 2.499 Å. La1 is 11-coordinate with a capped pentagonal antiprismatic geometry (CShM) and an O_{11} donor set.[146,147,274,275] The donor set is similar to that of the previous dinuclear complexes, with two phenolate oxygens, two methoxy oxygens, and two bidentate NO_3^- anions, with two additional bridging NO_3^- anions, one bidentate and the other monodentate (2.1_12_{12} Harris coordination mode, Figure A.18).[145] For both **C25** and **C26**, the different structural features such as the 12-coordinate La1 ion and the bridging between two La^{III} ions would in theory result in interesting magnetic properties however due to a lack of 4*f* orbital

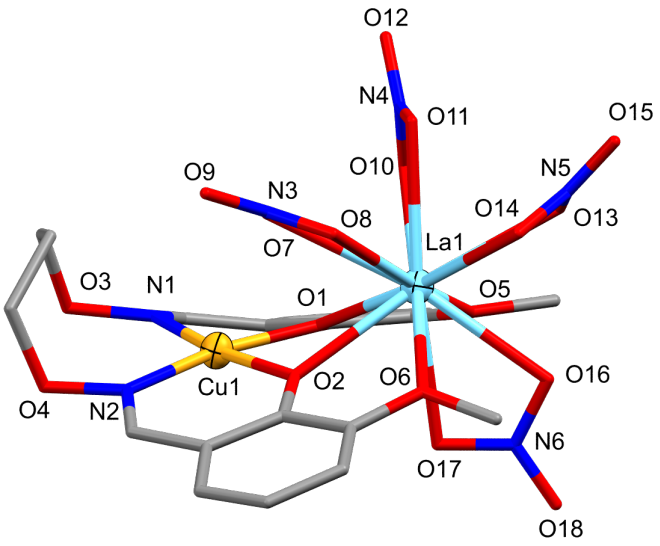

Figure 5.6: Full molecular structure of $([Cu^{I}(MeCN)_4][Cu^{II}La^{III}\mathbf{L2}(NO_3)_4])_2 \cdot MeCN$, **C25**. One $Cu^{II}La^{III}$ unit of **C25**, two units of $[Cu^{I}(MeCN)_4]^{+}$, one MeCN solvate, and hydrogen atoms have been omitted for clarity. Thermal ellipsoids of the metal ions are shown at 70% probability. Colour code: Cu^{II} = dark yellow, La^{III} = aqua, N = blue, O = red, and C = grey.

electrons for the La^{III} ions, the magnetic properties in this structure are solely derived from the Cu^{II} ions.[280]

The final complex in the $Cu^{II}La^{III}$ series, **C27**, differs from the rest in that this structure was produced by transmetalation rather than resulting from a different length of crystallisation. This structure is the result of a transmetalation reaction where **C17** ($Cu^{II}Gd^{III}$) was soaked in a $La(NO_3)_3{\cdot}6H_2O$ methanolic solution (further discussed in Section 5.2.3). The complex, **C27** was found to be a single dinuclear complex where Cu1 is five-coordinate with a vacant octahedral geometry (CShM, Table D.2) and a N_2O_3 donor set consisting of two phenolate oxygens, two alkyloxime nitrogens, and one MeOH molecule.[146,147,281] La1 is 10-coordinate with a metabidiminished icosahedron geometry (CShM, Table D.3) and an O_{10} donor set consisting of two phenolate and methoxy oxygens, one MeOH molecule, and three NO_3^- anions, two bidentate and one monodentate.[146,147,268] Moderate intermolecular hydrogen bonding is found between the MeOH molecules (O7 and O17) and NO_3^- anions (O10 and O16) on structures above and below the molecular plane with O7$\cdots$O10, 2.877 Å and O17$\cdots$O16, 2.889 Å.[158]

When looking at the $Cu^{II}La^{III}$ series in comparison with the previous $Cu^{II}4f$ complexes (**C14 - C23**), it can be seen that the $Cu^{II}La^{III}$ single dinuclear complexes have a larger degree of distortion present in both the metal ion geometries and the ligands (Figure 5.10 and Tables D.2 and D.3). This was thought to be the result of both a larger $4f$ ion and the presence of intermolecular interactions however when looking at **C26**, the dimeric complex (Figures 5.8 and 5.10), it can be seen that the complex is significantly more planar than the other structures. As all structures have the same M2 ion (La1), the most feasible explanation for this is that the intermolecular interactions are inducing the distortion.

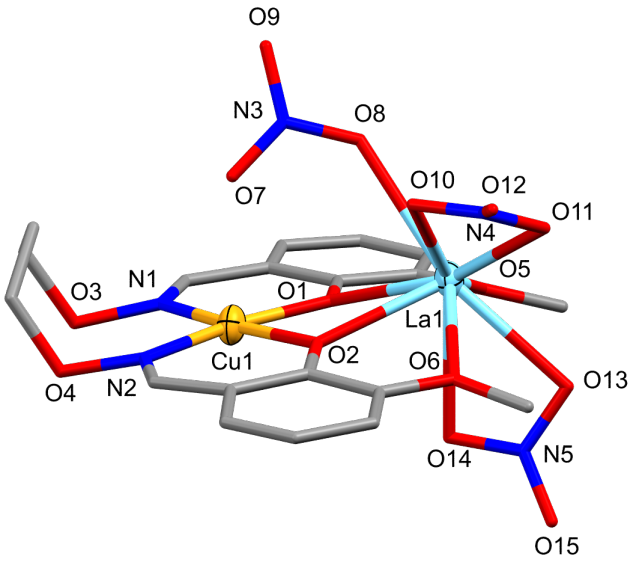

Figure 5.7: Asymmetric unit of $[Cu^{II}_2La^{III}_2(\mathbf{L2})_2(NO_3)_6]$, **C26**. Hydrogen atoms have been omitted for clarity and the thermal ellipsoids of the metal ions are shown at 70% probability. Colour code: Cu^{II} = dark yellow, La^{III} = aqua, N = blue, O = red, and C = grey.

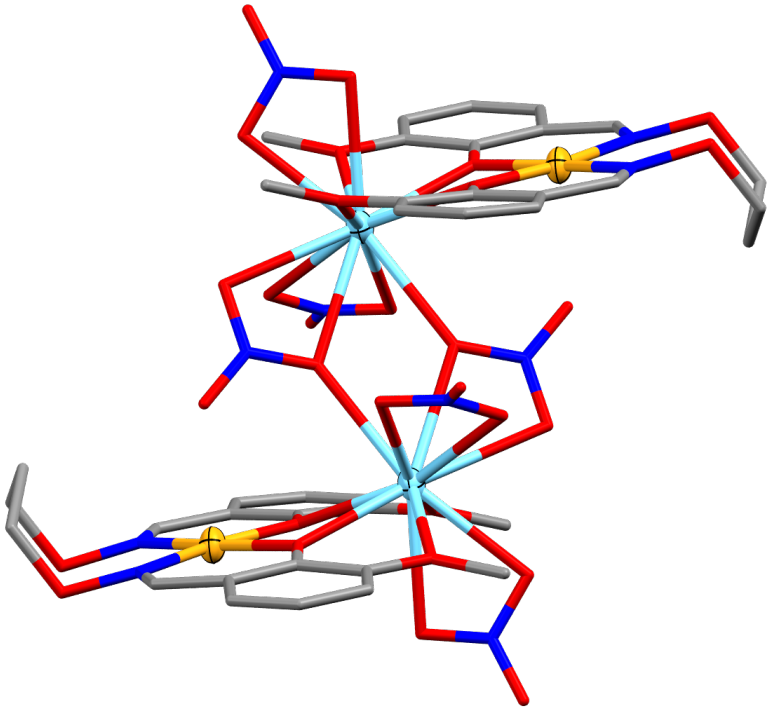

Figure 5.8: Full molecular structure of **C26**. Hydrogen atoms have been omitted for clarity and the thermal ellipsoids of the metal ions are shown at 70% probability. Colour code: Cu^{II} = dark yellow, La^{III} = aqua, N = blue, O = red, and C = grey.

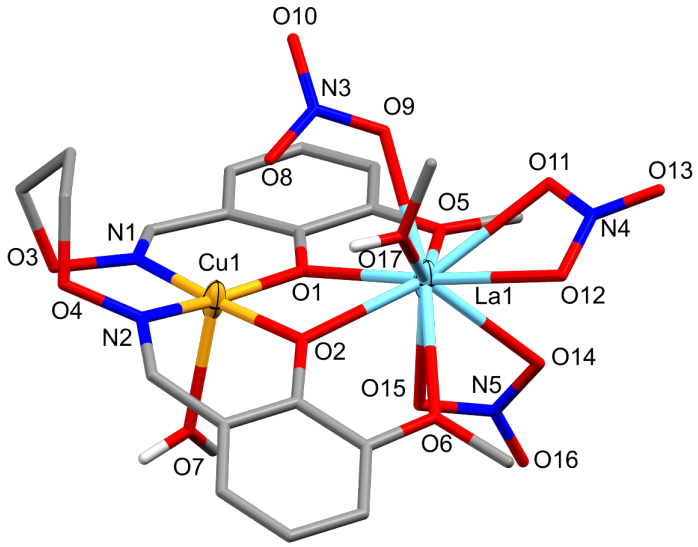

Figure 5.9: Full molecular structure of $[Cu^{II}La^{III}$**L2**$(MeOH)_2(NO_3)_3]$, **C27**. Non-interacting hydrogen atoms have been omitted for clarity and the thermal ellipsoids of the metal ions are shown at 70% probability. Colour code: Cu^{II} = dark yellow, La^{III} = aqua, N = blue, O = red, C = grey, and H = white.

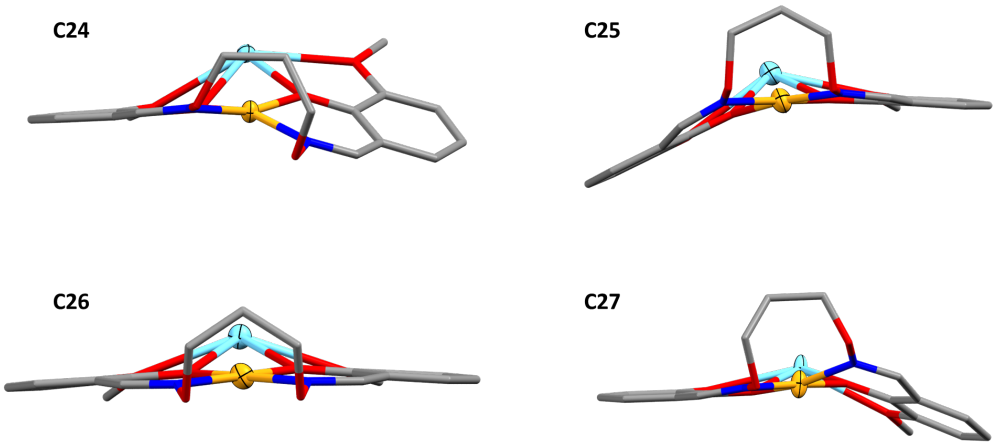

Figure 5.10: Schematic showing the different degrees of ligand distortion for the $Cu^{II}La^{III}$ series, **C24** - **C27**. Hydrogen atoms and metal ion coordinates have been omitted for clarity and the thermal ellipsoids of the metal ions are shown at 70% probability. Colour code: Cu^{II} = dark yellow, La^{III} = aqua, N = blue, O = red, and C = grey.

Initial attempts at producing a metal ion combination can result in many different complexations with subtle differences to allow for the best combination of metal ions, anions, solvent, and coligands to be determined. Previously, it has been found that similar combinations will result in the same structure as it is the most stable however this was initially not the case for the $Cu^{II}Ce^{III}$ series (**C28** - **C32**). The similar complexation combinations resulted in various complexes (Figures 5.11 - 5.16), which have similar compositions but varied connectivity. The complexes **C28** - **C32** are dinuclear complexes where one unit of $\mathbf{L2}^{2-}$ is coordinated to one Cu^{II} ion (M1) and one Ce^{III} ion (M2) with a Harris coordination mode, Mode I (Figure 2.6).[145] For complexes **C28** and **C30**, Cu1 is five-coordinate with a square pyramidal geometry (CShM, Table D.2) and N_2O_3 donor set whereas for **C29**, **C31**, and **C32** Cu1 is four-coordinate with a square planar geometry (CShM, Table D.2) and a N_2O_2 donor set.[146,147,267,281] The donor sets all consist of two phenolate oxygens and two alkyloxime nitrogens, with an extra oxygen coordinate for **C28** and **C30**, a MeOH molecule and a bridging NO_3^- anion ($2.1_1 1_2$ Harris coordination mode, Figure A.18) respectively.[145] For **C29**, **C31**, and **C32**, Cu1 is weakly coordinated to a monodentate NO_3^- anion (2.515, 2.525 and 2.513 Å respectively), coordinated to Ce1 either on the same structure or an adjacent one. For all five complexes, Ce1 is 10-coordinate with either a distorted metabidiminished icosahedral geometry (**C28** - **C30** and **C32**) or a distorted augmented tridiminished icosahedral geometry (**C31**) as determined by CShM (Table D.3).[146,147,268] Ce1 has an O_{10} donor set consisting of two phenolate oxygens, two methoxy oxygens, three NO_3^- anions (two bidentate and one monodentate), and one solvent molecule, MeOH for **C28** and **C30** - **C32** and H_2O for **C29**. For complexes **C30** and **C32**, solvent molecules are found in the crystal lattice, one $CHCl_3$ molecule and one Et_2O molecule respectively. Moderate intermolecular hydrogen bonding is found in the complexes **C28** - **C31** between the coordinated solvent molecules and NO_3^- anions on structures adjacent and above and below the molecular plane; O7···O10, 2.892 Å and O17···O16, 2.953 Å for **C28**, O16···O9, 2.864(6) Å and O16···O12, 2.884(5) Å for **C29**, O16···O13, 2.812(7) Å for **C30**, and 016···09, 2.697(7) Å and 2.690(6) Å for **C31**.[158] The SQUEEZE procedure was implemented for **C29** using the crystallographic software, Olex2, to remove diffuse solvent in the crystal lattice. The result was removal of 30 electrons per asymmetric unit which equates to three H_2O molecules (30 e^-).[208,273]

As mentioned above, it has been found for the $Cu^{II}Ce^{III}$ series that in general the difference in the complexation composition results in small structural differences. This however was found to be incorrect when comparing **C28** and **C29**, as both complexes are derived from $Cu(OAc)_2{\cdot}H_2O$ and $Ce(NO_3)_3{\cdot}6H_2O$ salts. One key difference between the syntheses is the length of crystallisation, one week versus two respectively. It was shown in the $Cu^{II}La^{III}$ series that different crystallisation periods can result in different structures however those periods differed significantly. This again leads to the non-identical environment issue discussed earlier, with factors such as humidity, and/or moisture content resulting in different structures. This repeating issue has resulted in several non-reproducible complexes as the exact enviromental conditions could not be replicated. Attempts were made to try and combat this issue and produce a reproducible environment for the complexes **C28** - **C32**. To combat the large temperature shift during the day, the crystallisations were kept in boxes, both polystyrene and cardboard to create an identical temperature environment. Secondly, for complexes **C28** and **C30**, the crystallisations were set up in duplicates with one of each in dry MeOH and the other in regular lab grade MeOH to see whether the presence of H_2O coordinates were a direct result of 'wet' solvent. It was hoped

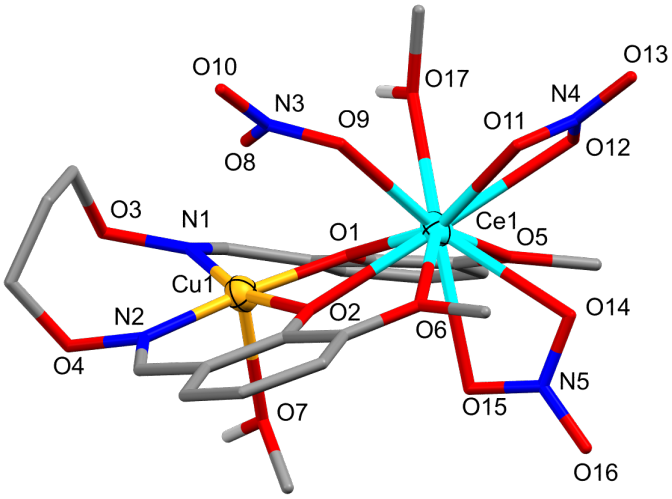

Figure 5.11: Full molecular structure of $[Cu^{II}Ce^{III}$**L2**$(MeOH)_2(NO_3)_3]$, **C28**. Non-interacting hydrogen atoms have been omitted for clarity and the thermal ellipsoids of the metal ions are shown at 50% probability. Colour code: Cu^{II} = dark yellow, Ce^{III} = aqua, N = blue, O = red, C = grey, and H = white.

that by creating a similar environment to the original crystallisations, the resulting structures would be that of **C28** - **C32** however SCXRD analyses revealed that the crystallisations of **C28** and **C30** - **C32** were that of **C28**, the crystallisation of **C29** however successfully produced **C29**. Although this was not the desired outcome, it showed that **C28** is the most stable complex of the $Cu^{II}Ce^{III}$ series. Additionally, it was found that **C28** could be produced via transmetalation. When crystals of **C17** ($Cu^{II}Gd^{III}$) were soaked in a methanolic solution of $Ce(NO_3)_3{\cdot}6H_2O$ the resulting structure was that of **C28** (further discussed in Section 5.2.3).

A key structural difference for **C30** is the coordination of the NO_3^- anions with a NO_3^- anion bridging between M1 and M2. It was thought the bridging NO_3^- would cause the structure and specifically the metal ion geometries to become more distorted than the other $Cu^{II}Ce^{III}$ dimers. This however did not occur, with the geometry distortions comparable to the other structures and the M1-O-M2 angles and M1$\cdots$M2 distance within the range found for the series (Table 5.3). This is thought to be attributed to the fact that the other Cu^{II} centres have weakly coordinated NO_3^- anions.

The complex **C31** is another example of varied connectivity for the $Cu^{II}Ce^{III}$ series as shown in the asymmetric unit and full structure (Figures 5.14 and 5.15 respectively). The asymmetric unit shows a third NO_3^- anion in the crystal lattice however when the full structure is grown, it can be seen that the anion is coordinated to an above-plane unit (Figure 5.15). The composition for this structure resembles that of **C28** and **C29** with $Cu(OAc)_2{\cdot}H_2O$ and $Ce(NO_3)_3{\cdot}6H_2O$ however NH_4Cl was added to this complexation in a 1 : 1 : 3 ratio respectively. This composition mixture was an attempt at producing a $Cu^{II}Ce^{III}$ dinuclear structure with coordinated Cl^- anions as an alternative to using $CeCl_3{\cdot}7H_2O$. When attempts were made to reproduce **C31**, an equimolar ratio of metal salts, ligand, and NH_4Cl resulted in that of **C28**, as mentioned above. This again shows the importance of the complexation and

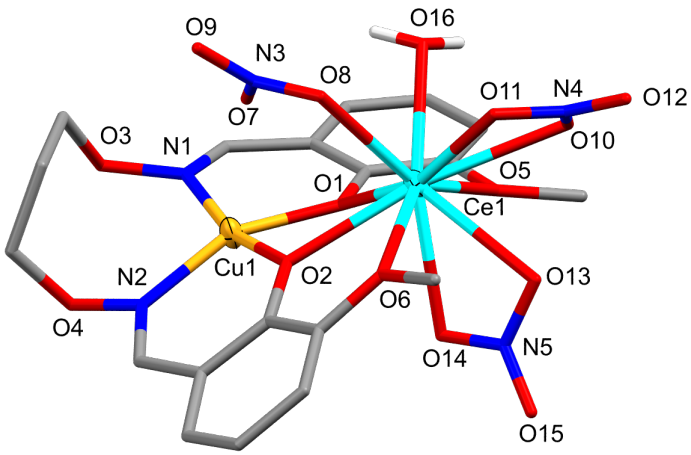

Figure 5.12: Full molecular structure of $[Cu^{II}Ce^{III}\mathbf{L2}(H_2O)(NO_3)_3]$, **C29**. Non-interacting hydrogen atoms have been omitted for clarity and the thermal ellipsoids of the metal ions are shown at 70% probability. Colour code: Cu^{II} = dark yellow, Ce^{III} = aqua, N = blue, O = red, C = grey, and H = white.

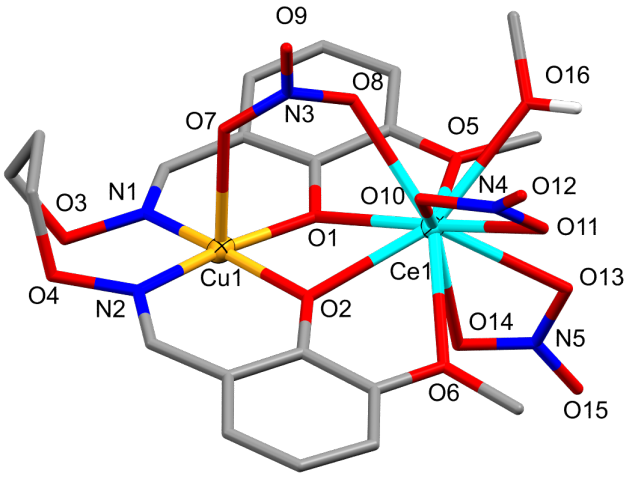

Figure 5.13: Full molecular structure of $[Cu^{II}Ce^{II}\mathbf{L2}(MeOH)(NO_3)_3]\cdot CHCl_3$, **C30**. Non-interacting hydrogen atoms and one $CHCl_3$ solvate have been omitted for clarity. The thermal ellipsoids of the metal ions are shown at 70% probability. Colour code: Cu^{II} = dark yellow, Ce^{III} = aqua, N = blue, O = red, C = grey, and H = white.

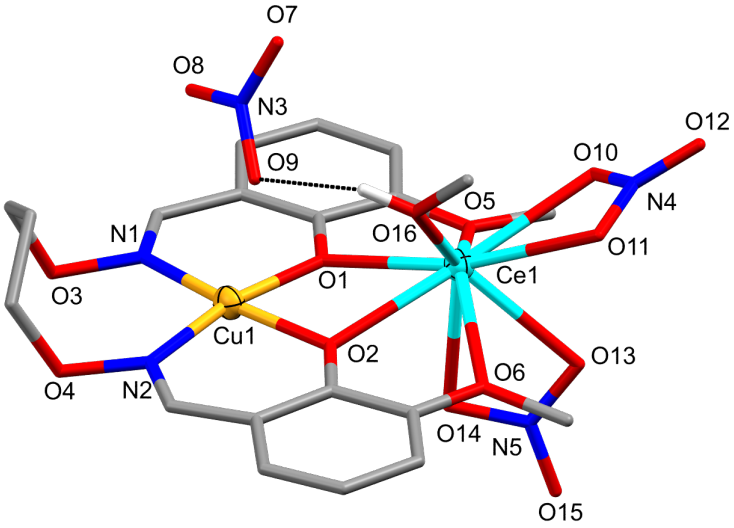

Figure 5.14: Asymmetric unit of the structure $[Cu^{II}Ce^{III}$**L2**$(MeOH)(NO_3)_3]$, **C31**. Non-interacting hydrogen atoms and one half complex have been omitted for clarity. Hydrogen bonding represented as black dotted lines, and the thermal ellipsoids of the metal ions are shown at 50% probability. Colour code: Cu^{II} = dark yellow, Ce^{III} = aqua, N = blue, O = red, C = grey, and H = white.

crystallisation environment, as using a different ratio of NH_4Cl resulted in a different structure. This reaction has been repeated with an excess of NH_4Cl however no crystalline material has been produced to date.

As an alternative to the $Cu(OAc)_2{\cdot}H_2O$, $Ce(NO_3)_3{\cdot}6H_2O$, NH_4Cl synthesis, the opposite in terms of composition ($Cu(OAc)_2{\cdot}H_2O$, $CeCl_3{\cdot}7H_2O$, and NH_4NO_3) was used resulting in **C32**. When comparing the structures, **C32** closely resembles that of **C29** and **C30** however with a coordinated MeOH instead of a H_2O coordinate in the case of **C29** or a bridging NO_3^- anion instead of a monodentate coordinated anion alike **C30**, causing the complexes to pack differently as a result of the varied intermolecular interactions. The difference in packing however has not produced differences in the structural properties such as the M1-O-M2 angles and M1$\cdots$M2 distances. This result was unexpected as for the defective dicubane series reported in Chapter 3, it was found that subtle changes in the composition such as a different lattice bound solvent or coordinated solvent molecule and differences in the packing of the complexes resulted in significant differences in the M-X-M bridging angles.

Throughout the period of this research, many complexations were set up utilising H_2**L2** and for the most part the ligand was stable. One exception to this was a complexation reaction where H_2**L2**, $Cu(OAc)_2{\cdot}H_2O$, $Eu(NO_3)_3{\cdot}6H_2O$, and Et_3N were used in a 1 : 1 : 1 : 1 molar ratio. The resulting structure obtained was a dinuclear $Cu^{II}Eu^{III}$ complex however the ligand had cleaved to its precursor, *o*-van. This was unexpected as the literature had shown that both the alkyloxime type ligands are more stable then their salen counterparts and typically imine hydrolysis occurs under acidic conditions.[129,282] Attempts were made to reproduce this result however the non-cleaved complex, **C18**, was obtained. It is still not entirely understood why the ligand cleaved in this particular reaction however as this structure provided a comparison to determine the effect of the propylene bridge, further attempts were

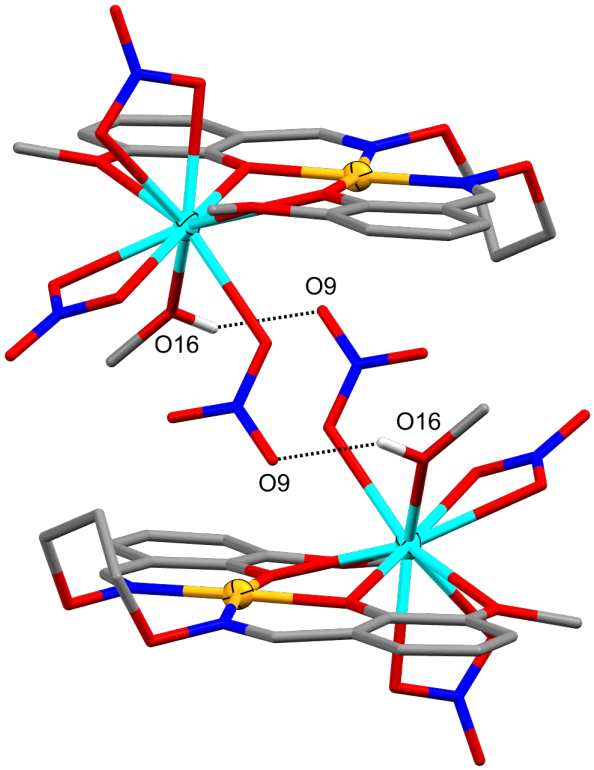

Figure 5.15: Full molecular structure of **C31**. Non-interacting hydrogen atoms and the second complex have been omitted for clarity. Hydrogen bonding represented as black dotted lines, and the thermal ellipsoids of the metal ions are shown at 50% probability. Colour code: Cu^{II} = dark yellow, Ce^{III} = aqua, N = blue, O = red, C = grey, and H = white.

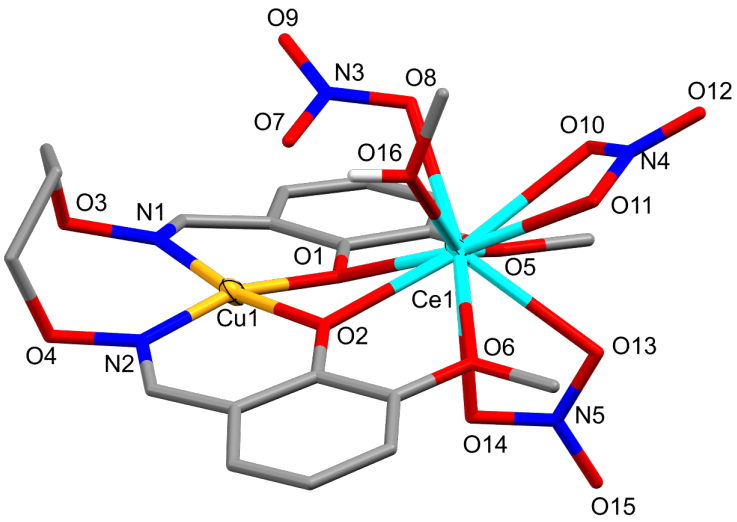

Figure 5.16: Full molecular structure of $[Cu^{II}Ce^{III}\mathbf{L2}(MeOH)(NO_3)_3] \cdot Et_2O$, **C32**. Non-interacting hydrogen atoms and one Et_2O solvate have been omitted for clarity. The thermal ellipsoids of the metal ions are shown at 70% probability. Colour code: Cu^{II} = dark yellow, Ce^{III} = aqua, N = blue, O = red, C = grey, and H = white.

Table 5.3: Selected bond lengths (Å) and angles (°) of the complexes **C24 - C32** from crystal structure determination

	C24	**C25***	**C26**	**C27**	**C28**	**C29**	**C30**	**C31***	**C32**
Cu1-O1	1.923(3)	1.949	1.951(2)	1.962(3)	1.949(3)	1.931(4)	1.964(5)	1.966	1.952(3)
Cu1-O2	1.942(3)	1.944	1.977(2)	1.945(3)	1.954(3)	1.947(4)	1.951(5)	1.963	1.965(3)
Cu1-N1	1.980(4)	1.970	1.999(3)	1.964(3)	2.003(4)	1.983(4)	1.970(6)	1.984	1.983(5)
Cu1-N2	1.939(4)	1.972	1.976(3)	2.011(3)	1.966(5)	1.946(4)	2.005(6)	1.978	1.963(4)
Cu1-O7	–	–	–	–	–	–	2.373(5)	–	–
Cu1-O17	–	–	–	2.308(3)	2.329(4)	–	–	–	–
M2-O1	2.492(3)	2.494	2.527(2)	2.502(3)	2.410(3)	2.458(4)	2.520(5)	2.489	2.497(4)
M2-O2	2.521(3)	2.538	2.506(2)	2.438(3)	2.483(3)	2.489(4)	2.439(5)	2.495	2.443(3)
M2-O5	2.697(3)	2.755	2.644(2)	2.638(3)	2.686(4)	2.685(4)	2.594(5)	2.604	2.657(4)
M2-O6	2.694(3)	2.760	2.705(2)	2.691(3)	2.634(3)	2.682(4)	2.665(5)	2.598	2.649(4)
M2-O7	3.031(4)	2.622	–	2.564(3)	2.558(4)	2.560(4)	2.489(5)	2.591	2.516(4)
M2-O8	2.588(3)	2.742	2.705(2)/2.672(2)[a]	–	–	–	–	–	–
M2-O9	–	–	2.752(2)[a]	–	–	–	–	–	–
M2-O10	2.610(3)	2.614	2.641(2)	2.614(3)	2.632(4)	2.676(4)	2.567(5)	2.593	2.569(4)
M2-O11	2.702(3)	2.721	2.589(2)	2.643(3)	2.586(5)	2.573(4)	2.586(5)	2.595	2.615(4)
M2-O13	2.612(3)	2.657	2.577(2)	2.623(3)	2.597(4)	2.593(4)	2.585(5)	2.577	2.615(4)
M2-O14	2.605(3)	2.633	2.645(2)	2.664(3)	2.643(4)	2.574(4)	2.619(5)	2.588	2.648(4)
M2-O16	2.522(3)	2.636		2.574(3)	2.564(4)	2.513(4)	–	2.536	2.598(4)
M2-O17	–	2.682	–	–	–	–	–	–	–
Cu1-O1-M2	105.48(12)	104.20	107.63(9)	104.26(12)	107.29(14)	105.59(15)	104.20(2)	107.73	103.27(15)
Cu1-O2-M2	103.79(13)	103.85	107.52(9)	107.17(11)	104.40(14)	103.93(15)	107.60(2)	107.60	104.79(14)
Cu1···M2	3.531(1)	3.534	3.630(1)	3.540(2)	3.521(1)	3.510(1)	3.554(1)	3.612	3.505(1)
M2···M2	–	–	4.774(1)	–	–	–	–	–	–

* Averaged values; Non-averaged values found in Table D.5

[a] 1-X, 1-Y, 1-Z

Table 5.4: Selected bond lengths (Å) and angles (°) of the complex **C33** from crystal structure determination

C33					
Cu1-O1	1.913(10)	Cu1-O2	1.886(12)	Cu1-O3	1.942(11)
Cu1-O4	1.945(11)	Cu1-O16	2.336(16)	Eu1-O1	2.405(10)
Eu1-O2	2.392(10)	Eu1-O5	2.584(11)	Eu1-O6	2.609(12)
Eu1-O7	2.503(11)	Eu1-O8	2.459(11)	Eu1-O10	2.485(12)
Eu1-O11	2.583(13)	Eu1-O13	2.525(11)	Eu1-O14	2.457(12)
Cu1-O1-Eu1	107.40(5)	Cu1-O2-Eu1	108.90(5)	Cu1···Eu1	3.492(2)

made to reproduce the structure. Instead of using H_2**L2**, the ligand chosen was *o*-van and a $Cu^{II}Eu^{III}$ complexation was set up base free resulting in the complex **C33** (Figure 5.17), which resembled that of the original cleaved complex. The complex **C33** was found to be a dinuclear complex consisting of two units of *o*-van coordinated to a Cu^{II} ion (M1) and a Eu^{III} ion (M2). Cu1 is five-coordinate with a vacant octahedral geometry (CShM, Table D.2) and an O_5 donor set consisting of two phenolate oxygens, two carbonyl oxygens, and one MeOH molecule (50% occupancy).[146,147,281] There is weak coordination (2.550(13) Å) between Cu1 and an NO_3^- anion, O15, of an above-plane unit. Eu1 is 10-coordinate with a tetradecahedron geometry (CShM, Table D.3) and an O_{10} donor set consisting of two phenolate oxygens, two methoxy oxygens, and three bidentate NO_3^- anions.[146,147,268]

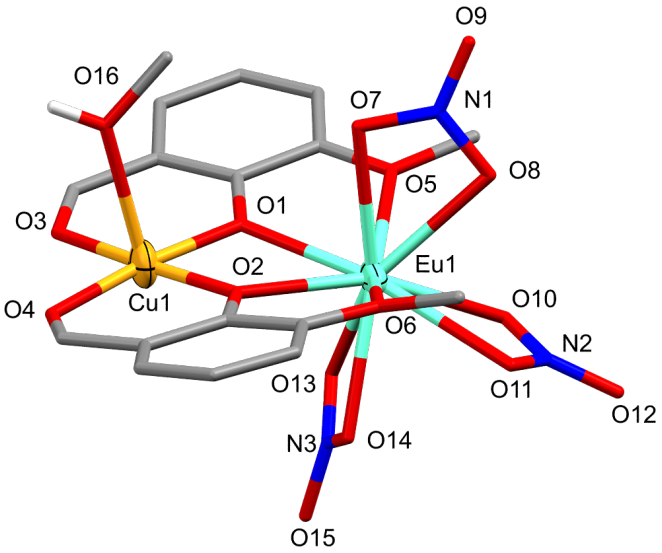

Figure 5.17: Full molecular structure of $[Cu^{II}Eu^{III}(o{-}van)_2(MeOH)(NO_3)_3]$, **C33**. Hydrogen atoms apart from those attached to donor atoms have been omitted for clarity. Thermal ellipsoids of the metal ions are shown at 50% probability. Colour code: Cu^{II} = dark yellow, Eu^{III} = aqua, N = blue, O = red, C = grey, and H = white.

Within this section, there are three different dinuclear $Cu^{II}Eu^{III}$ structures, **C18**, **C22**, and **C33**. The first two complexes are polymorphs of one another, therefore it was assumed that these complexes would have the closest Cu-O-Eu angles and Cu···Eu

Table 5.5: Key differences between the different $Cu^{II}Eu^{III}$ dinuclear complexes from crystal structure determination

Complex	$3d\cdots4f$ (Å)	Cu1-O1-Eu1 (°)	Cu1-O2-Eu1 (°)
C18	3.439(2)	105.60(2)	104.73(19)
C22*	3.539	107.38	108.80
C33	3.492(2)	107.40(5)	108.90(5)

* Averaged values; Non-averaged values can be found in Table D.5

distances, however this was not found to be true. When comparing the two polymorphs with **C33**, the cleaved complex, it can be seen that **C22** (the polymorph with two structures per asymmetric unit) is the closest in both angles and distance. This is believed to be a direct result of the two structures per asymmetric unit as this has caused the Eu^{III} ion to be closer to the ligand plane, reducing the steric interaction between the units but as a consequence, extending the $Cu\cdots Eu$ distance and Cu-O-Eu angles.

5.2.2 Structural Analysis - Cl^- Coordinates

The complexes **C34** - **C40** were found to be discrete dinuclear complexes utilising the deprotonated ligand, **L2**$^{2-}$, coordinated to both Cu^{II} (M1) and 4*f* ions (M2) with a Harris coordination mode, Mode I (Figure 2.6 and Appendix A).[145] The general structure for these complexes are similar with differing Cl^- coordination patterns and coordinated solvents. The complexes **C35** - **C37** were found to crystallise in either the monoclinic space group, $P2_1/c$ (**C34**) or the triclinic space group, $P\bar{1}$ (**C35** and **C36**), with the whole structure found in the asymmetric unit for all (Figure 5.18). Cu1 is five-coordinate with a square pyramidal geometry (CShM, Table D.2) and N_2O_2Cl donor set consisting of two phenolate oxygens, two alkyloxime nitrogens and one Cl^- anion.[146,147,281] M2 is eight-coordinate with a distorted biaugmented trigonal prismatic geometry (CShM, Table D.3) and O_6Cl_2 donor set consisting of two phenolate oxygens, two methoxy oxygens, two Cl^- anions, and two solvent molecules, one MeOH and one H_2O (Figure 5.18).[146,147,283] For **C34**, the two Cl^- anions coordinated to M2 are both disordered over two sites, with Cl2 a 50 : 50 ratio and Cl3 a 65 : 35 ratio. Moderate intramolecular hydrogen bonding is found between the Cl^- anion (Cl1) coordinated to M1 and the coordinated solvent molecules (O7 and O8), $O7\cdots Cl1$ 3.049(4) - 3.178(9) Å and $O8\cdots Cl1$ 3.002(5) - 3.083(8) Å.[158]

The complexes **C37** and **C38** were found to crystallise in the triclinic space group, $P\bar{1}$, with the entire structure found in the asymmetric unit. The isostructural complexes resemble that of **C34** - **C36** however they only have one coordinated solvent molecule leading to a seven-coordinate M2 ion. Cu1 is five-coordinate with a square pyramidal geometry and N_2O_2Cl donor set consisting of two phenolate oxygens, two alkyloxime nitrogens, and one Cl^- anion.[146,147,281] M2 is seven-coordinate with a pentagonal bipyramidal geometry and an O_5Cl_2 donor set consisting of two phenolate oxygens, two methoxy oxygens, two Cl^- anions, and one H_2O molecule (Figure 5.19).[146,147,210] Similarly to the previous complexes, moderate intramolecular hydrogen bonding is found between Cl1 and the H_2O molecule (O7), $O7\cdots Cl1$, 2.998(3) Å (**C37**) and 3.006(5) Å (**C38**).[158]

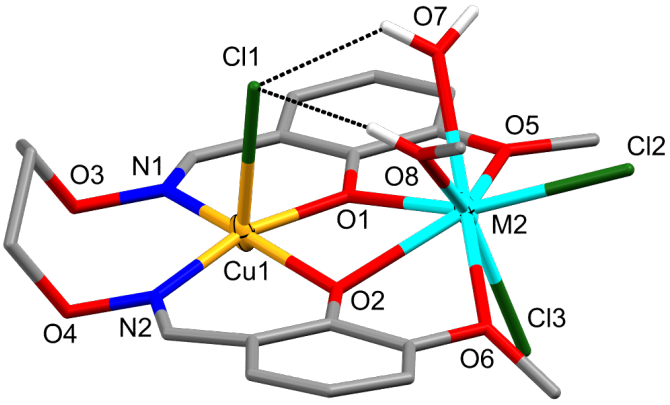

Figure 5.18: Representative structure of $[Cu^{II}M2^{III}\mathbf{L2}(H_2O)(MeOH)Cl_3]$ (M2 = Dy^{III} (**C34**), Eu^{III} (**C35**), and Tb^{III} (**C36**)). Non-interacting hydrogen atoms have been omitted for clarity, hydrogen bonding represented as black dotted lines, and thermal ellipsoids of the metal ions are shown at 70% probability. Colour code: Cu^{II} = dark yellow, $M2^{III}$ = aqua, N = blue, O = red, Cl = green, C = grey, and H = white.

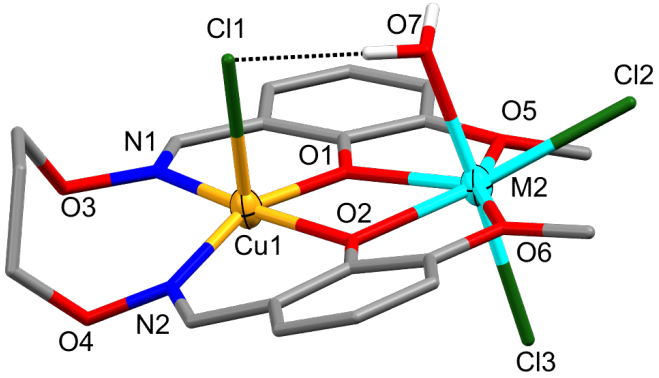

Figure 5.19: Representative structure of the complexes $[Cu^{II}Er^{III}\mathbf{L2}(H_2O)Cl_3]$ (M2 = Er^{III} (**C37**) and Ho^{III} (**C38**)). Non-interacting hydrogen atoms have been omitted for clarity, hydrogen bonding represented as black dotted lines, and thermal ellipsoids of the metal ions are shown at 50% probability. Colour code: Cu^{II} = dark yellow, $M2^{III}$ = aqua, N = blue, O = red, Cl = green, C = grey, and H = white.

Table 5.6: Selected bond lengths (Å) and angles (°) of the complexes **C34** - **C38** from crystal structure determination

	C34	**C35**	**C36**	**C37**	**C38**
Cu1-O1	1.980(8)	1.978(5)	1.970(4)	1.962(2)	1.966(3)
Cu1-O2	1.958(8)	1.985(5)	1.981(4)	1.971(2)	1.968(3)
Cu1-N1	1.981(9)	1.999(6)	2.000(5)	1.998(3)	1.994(4)
Cu1-N2	2.005(10)	1.990(6)	1.977(5)	1.980(2)	1.975(4)
Cu1-Cl1	2.665(4)	2.666(2)	2.671(2)	2.668(1)	2.660(2)
M2-O1	2.317(8)	2.343(5)	2.332(4)	2.291(2)	2.298(3)
M2-O2	2.357(8)	2.378(5)	2.350(4)	2.285(2)	2.297(3)
M2-O5	2.495(8)	2.521(5)	2.513(4)	2.411(2)	2.418(3)
M2-O6	2.473(9)	2.527(5)	2.508(4)	2.452(2)	2.460(3)
M2-O7	2.411(10)	2.441(5)	2.410(4)	2.302(2)	2.298(4)
M2-O8	2.424(8)	2.428(5)	2.393(4)	–	–
M2-Cl2	2.634(3)	2.662(2)	2.630(2)	2.595(1)	2.600(1)
M2-Cl3	2.617(3)	2.739(2)	2.714(1)	2.557(1)	2.576(2)
Cu1-O1-M2	106.30(3)	106.20(2)	105.74(16)	107.89(9)	107.83(13)
Cu1-O2-M2	105.50(4)	104.73(19)	104.69(16)	107.80(8)	107.80(13)
Cu1$\cdots$M2	3.444(3)	3.463(1)	3.437(1)	3.444(1)	3.451(2)

The complex **C39**, differs further from the previous Cl^- capped complexes in that three structures are found within the asymmetric unit, two $Cu^{II}Tb^{III}$ units and one $[Cu^{II}Cl_4]^{2-}$ unit (Figures 5.20 and 5.21). This complex was found to crystallise in the monoclinic space group, $P2_1/c$ and resulted from an attempt to reproduce the dinuclear $Cu^{II}Tb^{III}$ complex, **C36**. The formation of **C39** is not entirely understood as the syntheses for the two complexes closely resembled one another, 1 : 1 : 1 molar ratio of H_2**L2** : $Cu(OAc)_2{\cdot}H_2O$: $TbCl_3{\cdot}6H_2O$. The two $Cu^{II}Tb^{III}$ units resemble each other however have differing M2 coordinates, bond lengths, angles, and distances can be found in Table 5.7. Cu1 and Cu2 are both four-coordinate with a square planar geometry (CShM, Table D.2) and typical N_2O_2 donor set consisting of two phenolate oxygens and two alkyloxime nitrogens.[146,147,267] Tb1 and Tb2 are both eight-coordinate with biaugmented trigonal prism and triangular dodecahedral geometries respectively (CShM, Table D.3), the donor set for Tb1 was found to be O_7Cl consisting of two phenolate oxygens, two methoxy oxygens, three H_2O molecules, and one Cl^- anion.[146,147,283] The donor set (O_8) for Tb2 resembles that of Tb1 however has four H_2O molecules instead of three and a Cl^- anion. To balance the combined +5 charge of the two units, three Cl^- anions and one $[Cu^{II}Cl_4]^{2-}$ unit are found in the crystal lattice. Additionally, one MeOH molecule and one H_2O molecule are found in the lattice, both positionally disordered over two positions, 60 : 40 and 50 : 50 respectively. For both $Cu^{II}Tb^{III}$ units, the central carbon of the propylene bridge is positionally disordered over two sites with a 60 : 40 occupancy ratio for both units. Within this complex, there is a large amount of moderate hydrogen bonding both intramolecular and intermolecular, the details of which can be found in Table 5.8.[158] Within the literature, $[Cu^{II}Cl_4]^{2-}$ anions are commonly found cocrystallised with charged organic molecules, there are however a few examples where $[Cu^{II}Cl_4]^{2-}$ anions are found cocrystalised with 3*d* complexes with the $[(Ni^{II}K^{I}\mathbf{L})_2]$ (L = *N*,*N*′-ethylenedi(3-methoxysalicylicylideneiminato)) complex by Costes *et al*. a close comparison.[224,284–286]

Table 5.7: Selected bond lengths (Å) and bond angles (°) of the complex **C39** from crystal structure determination

C39					
Cu1-O1	1.960(4)	Cu1-O2	1.954(4)	Cu1-N1	1.975(5)
Cu1-N2	1.993(5)	Cu2-O10	1.953(4)	Cu2-O11	1.953(4)
Cu2-N3	1.976(5)	Cu2-N4	1.981(5)	Tb1-O1	2.347(4)
Tb1-O2	2.340(4)	Tb1-O5	2.450(4)	Tb1-O6	2.428(5)
Tb1-O7	2.295(5)	Tb1-O8	2.369(4)	Tb1-O9	2.352(5)
Tb1-Cl1	2.689(2)	Tb2-O10	2.330(3)	Tb2-O11	2.335(4)
Tb2-O14	2.399(4)	Tb2-O15	2.416(4)	Tb2-O16	2.329(4)
Tb2-O17	2.395(4)	Tb2-O18	2.375(4)	Tb2-O19	2.346(4)
Cu1-O1-Tb1	108.72(19)	Cu1-O2-Tb1	109.21(17)	Cu2-O10-Tb2	109.04(16)
Cu2-O11-Tb2	108.84(17)	Cu1···Tb1	3.508(1)	Cu2···Tb2	3.495(1)

The complex **C40** was found to be a dimeric complex with bridging between the two 4*f* ions. The complex was found to crystallise in the triclinic space group, $P\bar{1}$, with half of the structure found in the asymmetric unit and the full structure symmetry generated (Figures 5.22 and 5.23 respectively). Cu1 is four-coordinate with a square planar geometry and typical N_2O_2 donor set consisting of two phenolate oxygens

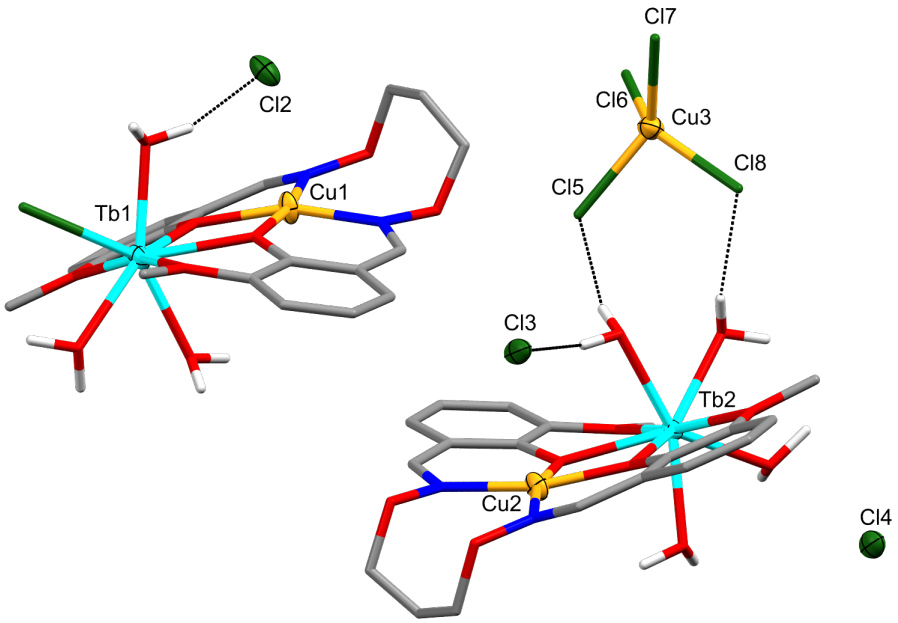

Figure 5.20: Asymmetric unit of $[Cu^{II}Tb^{III}\mathbf{L2}(H_2O)_xCl_y]_2[Cu^{II}Cl_4][Cl_3]$ (x = 3 and 4, y = 1 and 0 respectively), **C39**. Hydrogen atoms apart from those attached to donor atoms and lattice solvate have been omitted for clarity. Hydrogen bonding represented as black dotted lines and the thermal ellipsoids of the metal ions and lattice Cl^- anions are shown at 50% probability. Colour code: Cu^{II} = dark yellow, Tb^{III} = aqua, N = blue, O = red, Cl = green, C = grey, and H = white.

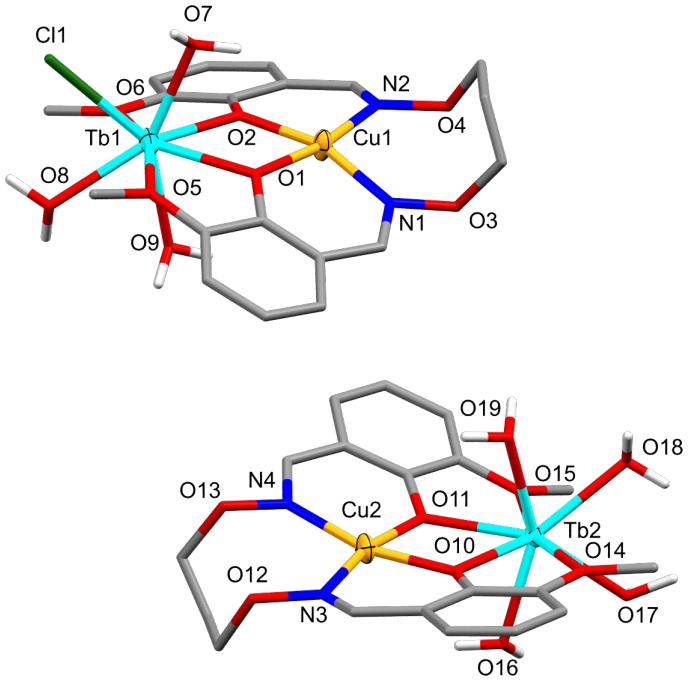

Figure 5.21: Labelled $Cu^{II}Tb^{III}$ units of **C39**. Hydrogen atoms apart from those attached to donor atoms and lattice solvates and anions have been omitted for clarity. Thermal ellipsoids of the metal ions are shown at 50% probability. Colour code: Cu^{II} = dark yellow, Tb^{III} = aqua, N = blue, O = red, Cl = green, C = grey, and H = white.

Table 5.8: Hydrogen bonding distances (Å) of the complex **C39** from crystal structure determination

C39			
O7[a] · · ·O4	2.901(7)	O7[a] · · ·Cl2	2.936(5)
O8· · ·O20	2.761(12)	O8[b] · · ·Cl1	3.102(5)
O9· · ·O20	2.584(10)	O9· · ·Cl2	3.018(5)
O16· · ·O12[c]	2.923(6)	O16· · ·Cl3	2.987(4)
O17· · ·Cl4[d]	3.054(4)	O18· · ·Cl4[d]	3.036(4)
O18· · ·Cl8	3.128(4)	O19[c] · · ·Cl3	3.036(4)
O19· · ·Cl5	3.030(5)	O20· · ·Cl6[e]	3.022(9)

[a] 1-X, -1/2+Y, 1/2-Z; [b] 1-X, 3-Y, -Z; [c] -X, -1/2+Y, 1/2-Z
[d] -X, 2-Y, 1-Z; [e] +X, 5/2-Y, -1/2+Z

and two alkyloxime nitrogens.[146,147,267] Ce1 is nine-coordinate with a muffin geometry and O_5Cl_4 donor set consisting of two phenolate and methoxy oxygens, one H_2O molecule and four Cl^- anions, two of which are bridging.[146,147,270] One of the Cl^- anions, Cl3 has half occupancy, which together with the +1 charge of the structure is balanced by 3 Cl^- anions (1.5 per asymmetric unit) found in the crystal lattice. The lattice Cl^- anions are heavily disordered, with one Cl^- disordered over four positions (Figure D.4). Moderate intramolecular hydrogen bonding is found between a H_2O coordinate (O7) and a Cl^- anion (Cl1) of the other unit, O7· · ·Cl1 3.080(7) Å.[158]

When comparing the M1-O-M2 angles and M1· · ·M2 distances between the Cl^- capped structures, it can be seen that the average M1-O-M2 angles are significantly smaller for **C40** than for **C34** - **C39**: 102.60° for **C40** versus 105.20° - 109.21° for **C34** - **C39**. Although the M1-O-M2 angles are significantly smaller, the M1· · ·M2 distance of 3.454(1) Å is within the range found for **C34** - **C39**, 3.437(1) - 3.508(2) Å. This is thought to result from the bridging between two units as the M2 ion is pulled out of the ligand plane. This result however was not found for the $Cu^{II}La^{III}$ dimer bridged by NO_3^- anions, indicating that the decrease in the exchange angle is correlated to bridging by a single atom. The magnetic properties for **C40** from a structural standpoint have exciting potential with the direct bridging between the Ce^{IV} ions and the smaller M1-O-M2 angles, however due to the fact that the Ce ions are in the +4 oxidation state, they have no 4*f* orbital electrons resulting in diamagnetic ions. Attempts to remake bulk quantities of this structure have been unsuccessful to date.

Table 5.9: Selected bond lengths (Å) and bond angles (°) of the complex **C40** from crystal structure determination

C40					
Cu1-O1	1.959(6)	Cu1-O2	1.947(6)	Cu1-N1	1.958(7)
Cu1-N2	1.993(7)	Ce1-O1	2.458(6)	Ce1-O2	2.451(6)
Ce1-O5	2.689(7)	Ce1-O6	2.714(8)	Ce1-O7	2.463(6)
Ce1-Cl1	2.941(2)	Ce1-Cl2	2.890(2)	Ce1-Cl2[a]	2.891(2)
Ce1-Cl3	2.824(5)	Cu1-O1-Ce1	102.30(2)	Cu1-O2-Ce1	102.90(2)
Ce1-Cl2-Ce1[a]	104.67(6)	Cu1· · ·Ce1	3.454(1)	Ce1· · ·Ce1[a]	4.577(1)

[a] 1-X, 2-Y, -Z

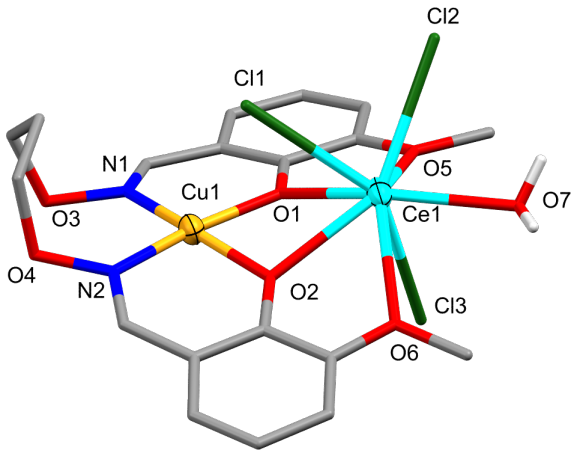

Figure 5.22: Asymmetric unit of $[Cu^{II}_2Ce^{IV}_2(\mathbf{L2})_2(H_2O)_2Cl_5][Cl_3]$, **C40**. Hydrogen atoms apart from those attached to donor atoms and lattice Cl^- anions have been omitted for clarity. Thermal ellipsoids of the metal ions shown at 40% probability. Colour code: Cu^{II} = dark yellow, Ce^{IV} = aqua, N = blue, O = red, Cl = green, C = grey, and H = white.

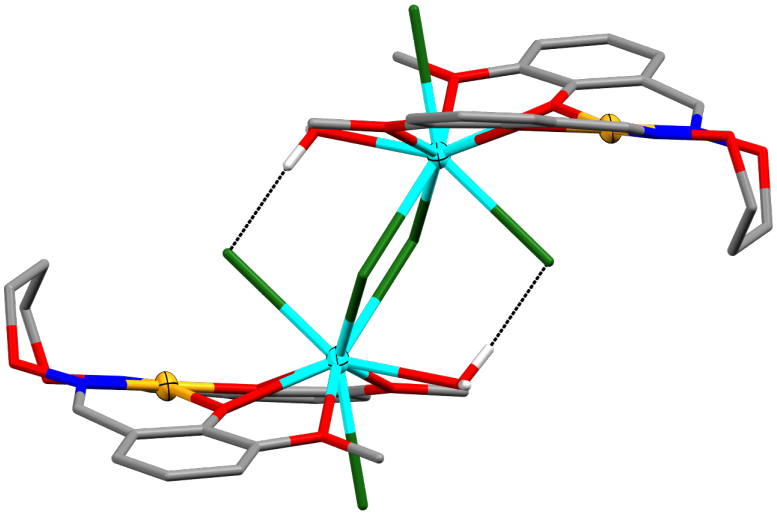

Figure 5.23: Full molecular structure of **C40**. Non-interacting hydrogen atoms and lattice Cl^- anions have been omitted for clarity. Hydrogen bonding represented as black dotted lines and thermal ellipsoids of the metal ions are shown at 40% probability. Colour code: Cu^{II} = dark yellow, Ce^{IV} = aqua, N = blue, O = red, Cl = green, C = grey, and H = white.

5.2.3 Transmetalation

Following on from the success of the 3*d*3*d*' transmetalations, transmetalation reactions were performed on selected Cu^{II}4*f* complexes to investigate the stability of the outer 4*f* ions and whether conversion between dinuclear structures and dimers is possible. The complex chosen to transmetalate was the $Cu^{II}Gd^{III}$ complex, **C17**, as this complex had a short crystallisation period.

The method used for the 3*d*3*d*' complexes was adopted for the Cu^{II}4*f* series, with several crystals of **C17** soaked in 2.0 mL of a 0.025 $molL^{-1}$ $M^{III}(NO_3)_3{\cdot}xH_2O$ methanolic solution of the desired metal ion to be transmetalated. The 'soaks' were then left for approximately 24 hours, where the crystals dissolved, and for some samples, the solution changed colour. The solutions were filtered and set up for Et_2O vapour diffusion. X-ray quality crystals were produced after a period of 24 hours to three weeks and were characterised by SCXRD and bond length analyses.

The first series involved 'soaking' **C17** in solutions of the available 4*f*$(NO_3)_3$ metal salts: $Ce(NO_3)_3{\cdot}6H_2O$, $Dy(NO_3)_3{\cdot}6H_2O$, $Eu(NO_3)_3{\cdot}6H_2O$, and $La(NO_3)_3{\cdot}6H_2O$. The results of these were fairly successful with $Ce(NO_3)_3{\cdot}6H_2O$ and $Eu(NO_3)_3{\cdot}6H_2O$ transmetalations resulting in the complexes **C28** and **C22** respectively (Table 5.10). The $La(NO_3)_3{\cdot}6H_2O$ transmetalation resulted in a new dinuclear $Cu^{II}La^{III}$ complex, **C27**. The transmetalation involving $Dy(NO_3)_3{\cdot}6H_2O$ was unsuccessful and did not result in any crystalline material suggesting the M2 pocket is size preferential, with a preference for the larger 4*f* ions.

Table 5.10: Transmetalation results for selected Cu^{II}4*f* complexes

Initial Complex	Metal Solution	Result
C17 - $Cu^{II}Gd^{III}$	$Ce(NO_3)_3{\cdot}6H_2O$	**C28** - $Cu^{II}Ce^{III}$
C17 - $Cu^{II}Gd^{III}$	$Eu(NO_3)_3{\cdot}6H_2O$	**C22** - $Cu^{II}Eu^{III}$
C17 - $Cu^{II}Gd^{III}$	$La(NO_3)_3{\cdot}6H_2O$	**C27** - $Cu^{II}La^{III}$
C17 - $Cu^{II}Gd^{III}$	$Mn(NO_3)_2{\cdot}4H_2O$	**C8** - $Cu^{II}Mn^{II}$
C20 - $Cu^{II}Yb^{III}$	$Mn(NO_3)_2{\cdot}4H_2O$	**C8** - $Cu^{II}Mn^{II}$
C21 - $Cu^{II}Dy^{III}$	$Mn(NO_3)_2{\cdot}4H_2O$	**C8** - $Cu^{II}Mn^{II}$
C26 - $Cu^{II}{}_2La^{III}{}_2$	$Mn(NO_3)_2{\cdot}4H_2O$	**C8** - $Cu^{II}Mn^{II}$
C29 - $Cu^{II}Ce^{III}$	$Mn(NO_3)_2{\cdot}4H_2O$	**C8** - $Cu^{II}Mn^{II}$
C17 - $Cu^{II}Gd^{III}$	$Zn(NO_3)_2{\cdot}6H_2O$	**C9** - $Cu^{II}Zn^{II}$

Unlike the 3*d*3*d*' series, the structures produced via transmetalation had different connectivity and coordination patterns than the initial complex, **C17** which was a dinuclear complex with a four-coordinate Cu^{II} ion and a 10-coordinate Gd^{III} ion coordinated to three bidentate NO_3^- anions. The structures produced for the $Ce(NO_3)_3{\cdot}6H_2O$ and $La(NO_3)_3{\cdot}6H_2O$ transmetalations (**C28** and **C27** respectively) differed by five-coordinate Cu^{II} ions, both with an additional MeOH coordinate. The M2 ions also differed, this time by the inclusion of a MeOH molecule, resulting in one of the NO_3^- anions having monodentate coordination to retain the 10-coordinate geometry. The general structure for the $Eu(NO_3)_3{\cdot}6H_2O$ transmetalation remained the same as **C17** however the asymmetric unit changed to have two structures instead

of the one.

As the 3*d*3*d*' dinuclear series found that the $Cu^{II}Mn^{II}$ complex, **C8**, was the most stable, a series of transmetalations, this time using $Mn(NO_3)_2{\cdot}4H_2O$ were set up to determine whether **C8** had the greatest stability overall. The selected $Cu^{II}4f$ complexes (**C17**, **C20**, **C21**, **C26**, and **C29**) ranged in terms of 4*f* coordinates, extended structure, and size (dinuclear versus dimer). For all five transmetalations it was found that the resulting complex was that of **C8** indicating just how stable Mn^{II} ions are in the outer pocket (Table 5.10). This result was somewhat surprising as the mini series of $Cu^{II}Gd^{III}$ to $Cu^{II}M^{III}$ transmetalations suggested the larger ions were more stable. Concurrently with the $Mn(NO_3)_2{\cdot}4H_2O$ transmetalations, several other 3*d* $(NO_3)_2{\cdot}4H_2O$ salts were used for transmetalation attempts: $Co(NO_3)_2{\cdot}6H_2O$, $Cu(NO_3)_2{\cdot}3H_2O$, $Ni(NO_3)_2{\cdot}6H_2O$, and $Zn(NO_3)_2{\cdot}6H_2O$. Out of these transmetalations, only the $Zn(NO_3)_2{\cdot}6H_2O$ one produced crystalline material, which was found to be that of **C9**.

5.2.4 Magnetic Analysis

As a result of both reproducibility issues and a number of unforseen events, magnetic characterisation was only performed on the complexes, **C17**, **C21**, and **C37**. Magnetic measurements were performed by Sören Schlittenhardt at the Karlsruhe Institute of Technology, Karlsruhe Germany through collaborative work with Prof. Annie Powell and Dr Christopher Anson. Variable-temperature, solid-state DC magnetic susceptibility data was collected in the temperature range 300 - 1.8 K. Measurements were collected on powdered polycrystalline samples using a Quantum Design MPMS-XL SQUID magnetometer equipped with magnets capable of applying field up to 7 T. The applied field used was 0.1 T. The samples were embedded in eicosane and the data was corrected for the diamagnetic contributions of the eicosane, the sample and the sample holder based on Pascal's constants. The data for **C17** was fitted to Equation 5.1 by Dr Christopher Anson. The remaining data for **C21** and **C37** however was not fitted.

$$\hat{H} = -2J_{ij}\hat{S}_i \cdot \hat{S}_j \tag{5.1}$$

Upon cooling the $\chi_M T$ value of **C17** increases from 8.31 cm^3 K mol^{-1} at 300 K (comparable to the value, 8.25 cm^3 K mol^{-1}, expected for magnetically isolated Cu^{II} and Gd^{III} ions) to a maximum of 9.82 cm^3 K mol^{-1} at 6 K before rapidly decreasing to 9.78 cm^3 K mol^{-1} at 2 K (Figure 5.24).[287] This behaviour is indicative of ferromagnetic exchange between the Cu^{II} and Gd^{III} ions, with the slight decrease at low temperature thought to be a result of either antiferromagnetic intermolecular interactions or saturation effects. The susceptibility data was fitted to the spin-Hamiltonian (Equation 5.1) to give the parameters J = +2.94 cm^{-1}, g_{Gd} = 2.0, and g_{Cu} = 1.86. When comparing the g_{Cu} value with both the magnetic results of **C7** and **C8** and similar literature examples, the value found for **C17** is lower than expected (2.1 - 2.2) however due to the sample sitting around for an extended period of time it is possible that the sample absorbed moisture.[128,288] By accounting for this and changing the formula weight to include one H_2O molecule, a more realistic g_{Cu} = 2.05 was obtained. When comparing **C17** with literature examples, the $\chi_M T$ values obtained at both 300 K and low T are comparable to similar Schiff base complexes.[128,288] One difference however is

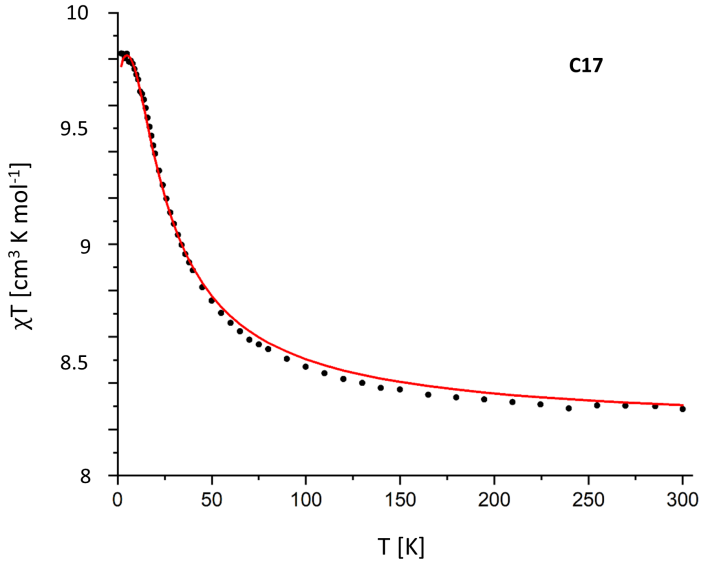

Figure 5.24: Plot of $\chi_M T$ versus T for the complex **C17** in an applied magnetic field of B = 0.1 T over a temperature range of 300 - 2 K. The black circles represent the experimental data with the solid red line the fit of the data using the spin-Hamiltonian, Equation 5.1.

the J coupling value as it is significantly lower than the values found by Costes *et al.* (6.8 and 7.0 cm^{-1}) and Wen *et al.* (4.38 and 6.59 cm^{-1}).[128,288]

The $\chi_M T$ value for **C21** at 300 K was found to be 14.9 cm^3 K mol^{-1}, which is slightly above the expected value of 14.5 cm^3 K mol^{-1} for magnetically isolated Cu^{II} and Dy^{III} ions.[287] Upon cooling, the $\chi_M T$ value decreases to a minimum of 12.0 cm^3 K mol^{-1} at 14 K before increasing to 12.2 cm^3 K mol^{-1} at 2 K (Figure 5.25). Although this behaviour is typically indicative of antiferromagnetic exchange between the metal ions, it can be attributed to a depopulation of the Stark sublevels of the Dy^{III} ions, with the increase of the $\chi_M T$ value at low temperatures an indication of a ferromagnetic interaction between the Cu^{II} and Dy^{III} ions.[287,289–291] Similar complexes in the literature have performed further magnetic characterisation with variable-temperature AC susceptibility measurements to determine the SMM properties of the complex. A few examples report the presence of SMM behaviour (frequency dependent signal both in-phase and out-of-phase) under a zero DC field however most examples report an absence of SMM properties, typically attributed to QTM.[289,292,293] By applying a static DC field, the QTM effects are surpressed and the presence of SMM behaviour can be detected. This is what is known as a field-induced SMM.[287,289–291]

For **C37**, the $\chi_M T$ value at 300 K was found to be 11.2 cm^3 K mol^{-1}, slightly less than the 11.9 cm^3 K mol^{-1} expected for non-interacting Cu^{II} and Er^{III} ions.[291] Upon cooling, the $\chi_M T$ value decreases to 9.8 cm^3 K mol^{-1} at 45 K where the value rapidly decreases to 5.9 cm^3 K mol^{-1} at 2 K (Figure 5.26). This behaviour is fairly indicative of dominant antiferromagnetic interactions, consistent with the large M1-O-M2 angles of 107.89(9)° and 107.80(8)°. Within the literature, similar $Cu^{II}Er^{III}$ dinuclear structures typically have NO_3^- coordinates, with $\chi_M T$ patterns resembling both ferro- and antiferromagnetic coupling between the metal ions.[291,294,295] There are

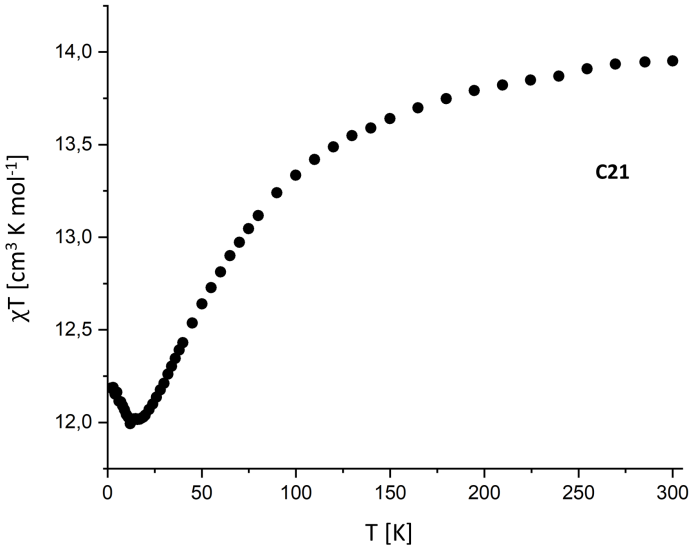

Figure 5.25: Plot of $\chi_M T$ versus T for the complex **C21** in an applied magnetic field of B = 0.1 T over a temperature range of 300 - 2 K. The black circles represent the experimental data.

a few $Cu^{II}Er^{III}$ examples in the literature where variable-temperature AC susceptibility measurements have been performed to determine whether the complexes have SMM properties or not.[294–296] The majority of the examples reported that the complexes had no easy-axis anisotropy (a direction to which the complex can spontaneously be magnetised) or SMM properties, which some of the researchers attributed to QTM.[294–297]

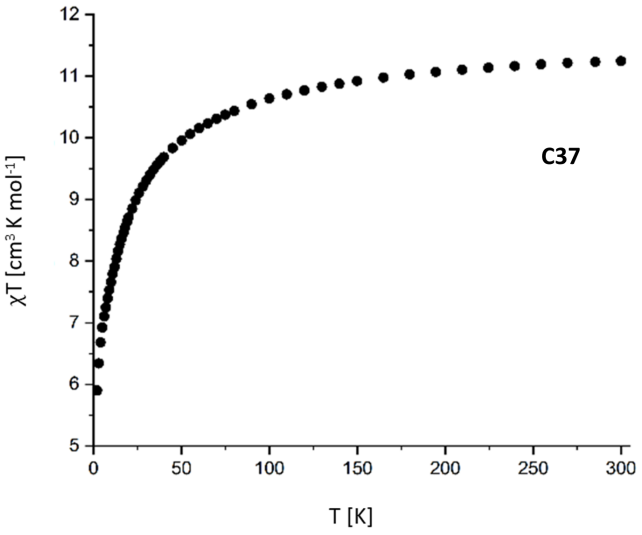

Figure 5.26: Plot of $\chi_M T$ versus T for the complex **C37** in an applied magnetic field of B = 0.1 T over the temperature range of 300 - 2 K. The black circles represent the experimental data.

5.3 $Co^{II}4f$ Complexes

The complexes reported in this Section refer to the $Co^{II}4f$ dinuclear complexes with NO_3^- and Cl^- coordinates. Key differences between the complexes can be seen in Table 5.11 with other selected bond lengths and angles found in Tables 5.12 and 5.13.

Table 5.11: Structural differences in the complexes **C41** - **C46**

	M1	M2	Anion	Solvent
C41	Co^{II}	Eu^{III}	NO_3^-/OAc^-	–
C42	Co^{II}	Er^{III}	Cl^-	H_2O
C43	Co^{II}	Eu^{III}	Cl^-	H_2O
C44	Co^{II}	Dy^{III}	Cl^-	H_2O/MeOH
C45	Co^{II}	Er^{III}	Cl^-	H_2O/MeOH
C46	Co^{II}	Eu^{III}	Cl^-	H_2O/MeOH

5.3.1 Structural Analysis - NO_3^- Coordinates

Within the $Co^{II}4f$ series, only one complex, **C41** was found to have NO_3^- coordinates. This structure was found to be a dimer, differing from the other dimers, **C26** and **C40**, as the bridging occurs between the M1 and M2 ions instead of solely between the M2 ions. The complex was found to crystallise in the monoclinic space group, $P2_1/c$, with half of the structure found in the asymmetric unit as shown in Figure 5.27 and the full structure symmetry generated (Figure 5.28). Co1 is six-coordinate with an octahedral geometry (CShM, Table D.2) and N_2O_4 donor set consisting of two phenolate oxygens, two alkyloxime nitrogens, and two bridging anions, one NO_3^- and the other OAc^- ($2.1_11_21_1$ and 2.1_11_2 Harris coordination modes respectively, Figures A.18 and A.17).[145–147,171] Eu1 is nine-coordinate with a spherical capped square antiprismatic geometry (CShM, Table D.3) and O_9 donor set consisting of two phenolate oxygens, two methoxy oxygens, one bridging OAc^- anion (2.1_11_2 Harris coordination mode, Figure A.17), and two bidentate NO_3^- anions, where one is bridging ($2.1_11_21_1$ Harris coordination mode, Figure A.18).[145–147,270]

When comparing **C41** with the other NO_3^- capped complexes, **C14** - **C33**, there are two very noticeable structural differences, the first being the large distortion of the ligand, most obvious in the propylene bridge and aromatic rings. Looking at the Co1 and Eu1 geometries, slight distortion can be seen with CShM values of 1.140 and 2.250 respectively however in comparison to other similar metal ion geometries (Tables D.2 and D.3) they are fairly consistent. It is believed this is the result of both the two different types of brigding (NO_3^- and OAc^-) between Co1 and Eu1 and the zig-zag nature of the propylene bridge, as these have introduced a large amount of steric strain. This level of distortion isn't seen in the other dimeric complexes **C26** and **C40**, as shown in Figure 5.29, however these complexes are bridged solely between the M2 ions removing the steric interactions between the molecular planes of the two units, additionally their M1 ions are four-coordinate removing the added propylene bridge strain.

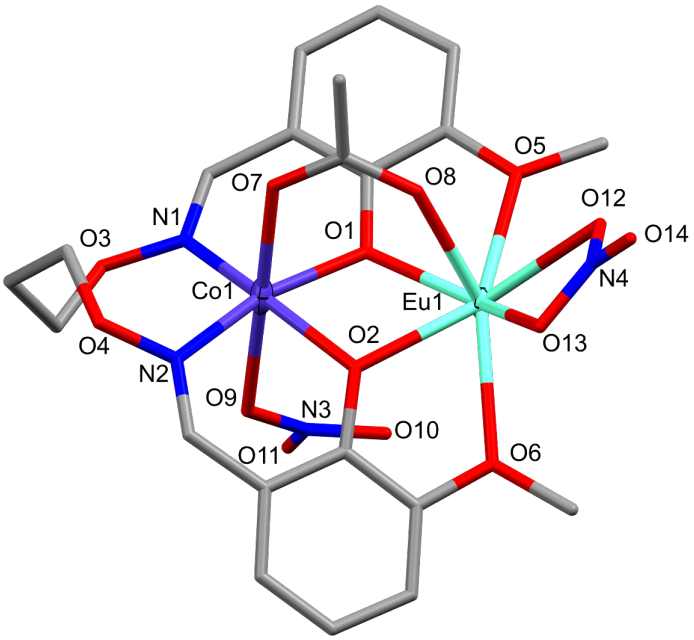

Figure 5.27: Asymmetric unit of $[Co^{II}_2Eu^{III}_2(\mathbf{L2})_2(OAc)_2(NO_3)_4]$, **C41**. Hydrogen atoms have been omitted for clarity and the thermal ellipsoids of the metal ions are shown at 70% probability. Colour code: Co^{II} = dark purple, Eu^{III} = aqua, N = blue, O = red, and C = grey.

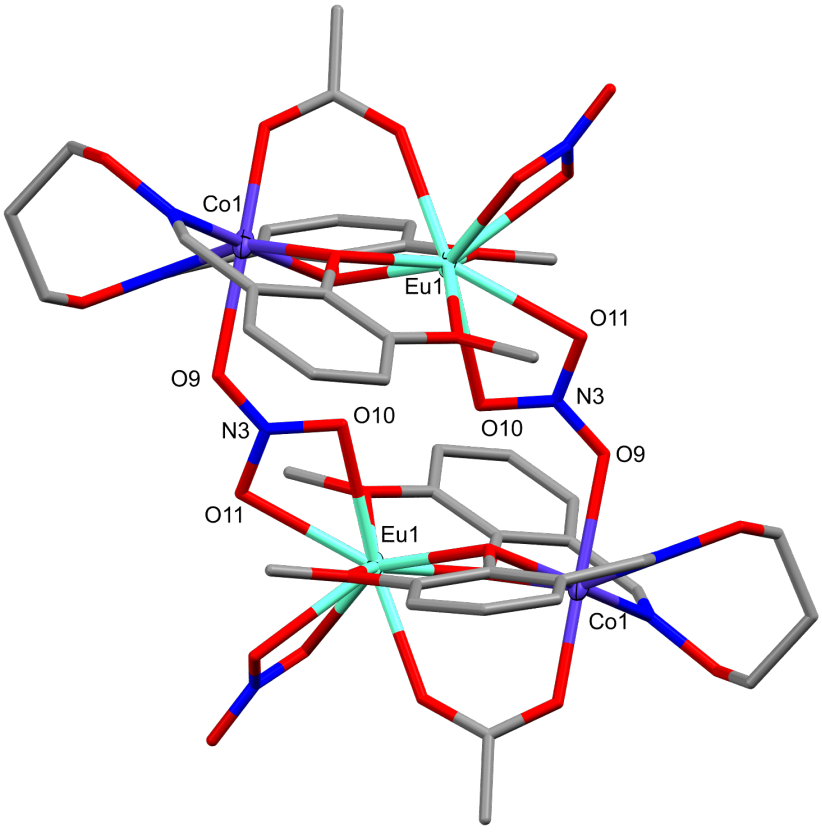

Figure 5.28: Full molecular structure of **C41**. Hydrogen atoms have been omitted for clarity and the thermal ellipsoids of the metal ions are shown at 70% probability. Colour code: Co^{II} = dark purple, Eu^{III} = aqua, N = blue, O = red, and C = grey.

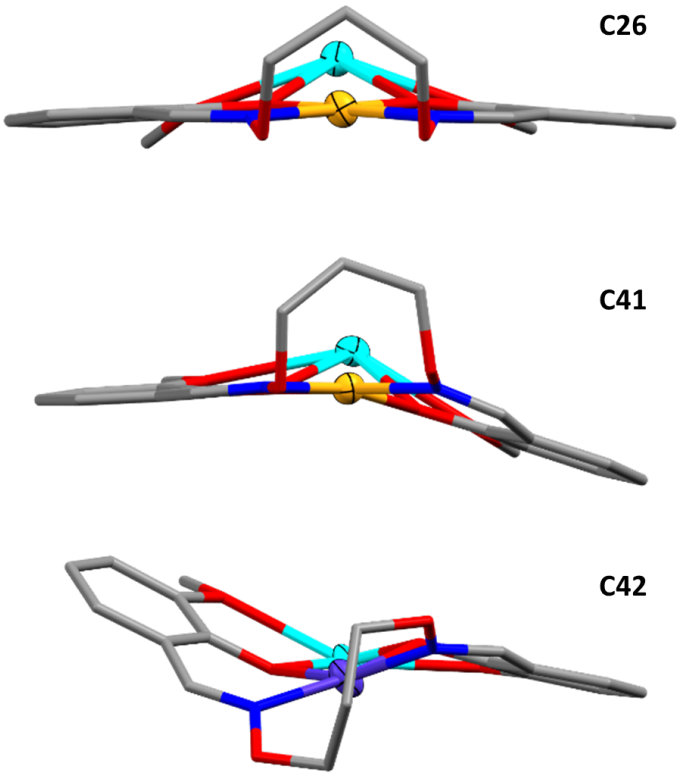

Figure 5.29: Schematic showing the different degrees of ligand distortion found for the dimeric complexes, **C26**, **C40**, and **C41**. The schematic shows the asymmetric units with metal ion coordinates and hydrogen atoms omitted for clarity. Thermal ellipsoids of the metal ions are shown at 70% (**C26** and **C41**) and 40% (**C40**) probability. Colour code: Cu^{II} = dark yellow, Co^{II} = dark purple, $M_2{}^{III}$ = aqua, N = blue, O = red, and C = grey.

The second difference is both the M1-O-M2 angles and M1···M2 distance, which for **C41** are greatly reduced: M1-O-M2 angles of 99.69(15)° and 102.96(16)° and a M1···M2 distance of 3.390(1). The cause for this is most likely derived from both the ligand distortion and the bridging between Co1 and Eu1.

Table 5.12: Selected bond lengths (Å) and bond angles (°) of the complex **C41** from crystal structure determination

C41					
Co1-O1	2.097(4)	Co1-O9	2.266(5)	Eu2-O8	2.360(4)
Co1-O2	2.027(4)	Eu2-O1	2.334(4)	Eu2-O10[a]	2.570(4)
Co1-N1	2.126(5)	Eu2-O2	2.300(4)	Eu2-O11[a]	2.525(4)
Co1-N2	2.104(5)	Eu2-O5	2.515(4)	Eu2-O12	2.494(4)
Co1-O7	2.043(5)	Eu2-O6	2.538(4)	Eu2-O13	2.485(4)
Co1-O1-Eu2	99.69(15)	Co1-O2-Eu2	102.96(16)	Co1···Eu2	3.390(1)
Co1···Eu2[a]	5.787(1)				

[a] 1-X, 1-Y, 1-Z

5.3.2 Structural Analysis - Cl^- Coordinates

The following five complexes, **C42 - C46**, are dinuclear complexes where $\mathbf{L2}^{2-}$ is coordinated to both a Co^{II} ion and a 4*f* ion (Mode I, Figure 2.6).[145] The structures differ by their coordination patterns and the solvent molecules coordinated. For complexes, **C42 - C45**, Co1 is five-coordinate with either a spherical square pyramidal geometry (**C42** and **C43**; Figure 5.30) or a vacant octahedral geometry (**C44 - C45**; Figure 5.31) as determined by CShM (Table D.2).,[146,147,281] The N_2O_2Cl donor set consists of two alkyloxime nitrogens, two phenolate oxygens, and one Cl^- anion, with a weakly coordinated Cl^- anion (Cl3) for all complexes (the weakly coordinated distances range from 2.587(2) Å - 2.717(2) Å; Co-Cl distances in similar literature complexes range from 2.212 - 2.573 Å).[298–302] M2 is eight-coordinate with either a square antiprismatic geometry (**C42** and **C43**) or a triangular dodecahedral geometry (**C44** and **C45**) as determined by CShM (Table D.3).[146,147,283] The four complexes have O_7Cl donor sets consisting of two phenolate oxygens, two methoxy oxygens, one Cl^- anion, and three solvent molecules, three H_2O for **C42** and **C43** and two MeOH and one H_2O for **C44** and **C45**. Moderate intramolecular hydrogen bonding is found for all complexes between the H_2O molecule (O9) and the lattice Cl^- anion (Cl3), O9···Cl3, 3.014(3) - 3.043(4) Å. Complexes **C42** and **C43** have additional moderate intramolecular hydrogen bonding between the H_2O molecule (O7) and the coordinated Cl^- anion (Cl1), O7···Cl1, 2.974(6) and 2.973(5) Å respectively. For **C44** and **C45**, additional hydrogen bonding is found between the coordinated MeOH molecule (O7) and lattice solvent (one MeOH and one H_2O) molecules (O10 and O11), O7···O10 2.589(8) and 2.590(5) Å respectively and O7···O11 2.549(15) and 2.574(17) Å respectively.[158]

The complex, **C46** (Figure 5.32), resembles that of complexes **C42 - C45** however the connectivity is varied, with a different arrangement of anions and solvent molecules. Co1 is six-coordinate with an octahedral geometry (CShM, Table D.2) and N_2O_3Cl donor set consisting of two alkyloxime nitrogens, two phenolate oxygens, one Cl^-

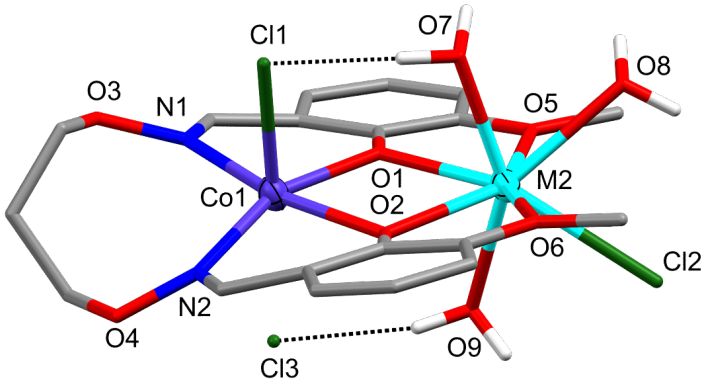

Figure 5.30: Representative structure of $[Co^{II}M2^{III}\mathbf{L2}(H_2O)_3Cl_2][Cl]$ (M2 = Er^{III} (**C42**) and Eu^{III} (**C43**)). Hydrogen atoms apart from those attached to donor atoms have been omitted for clarity, hydrogen bonding represented as black dotted lines, and the thermal ellipsoids of the metal ions are shown at 70% probability. Colour code: Co^{II} = dark purple, $M2^{III}$ = aqua, N = blue, O = red, C = grey, and H = white.

anion, and one MeOH molecule.[146,147,171] Eu1 is eight-coordinate with a largely distorted triangular dodecahedral geometry (CShM value of 5.742; Table D.3) and an O_6Cl_2 donor set consisting of two phenolate oxygens, two methoxy oxygens, two Cl^- anions, and two solvent molecules, one MeOH and one H_2O.[146,147,283] Moderate intramolecular hydrogen bonding is found between the H_2O molecule (O9) and the Cl^- anion (Cl3), O9···Cl3, 3.069(5) Å with intermolecular hydrogen bonding found between the MeOH molecules (O7 and O8) and the Cl^- anions (Cl1 and Cl2) of above-plane and adjacent units respectively, O7···Cl1 3.073(5) Å and O8···Cl2 3.157(5) Å.[158]

The literature has shown that $Co^{II}4f$ complexes, especially those incorporating Dy^{III} and Tb^{III} ions, have interesting magnetic properties as the magnetism originates from the large anisotropies of both the Co^{II} and 4*f* ions.[86,303,304] Out of the six structures reported in this section, **C44** the $Co^{II}Dy^{III}$ dinuclear complex, has the most desirable magnetic properties, as similar literature examples have reported SMM properties when AC susceptibility measurements were performed under a static DC field.[287,303,305] Although the other five complexes do not have magnetically interesting 4*f* ions, the literature has reported several mononuclear Co^{II} complexes as having SMM behaviour therefore the complexes **C41** - **C43**, **C45**, and **C46** could themselves have interesting magnetic properties resulting from the Co^{II} ions.[306,307]

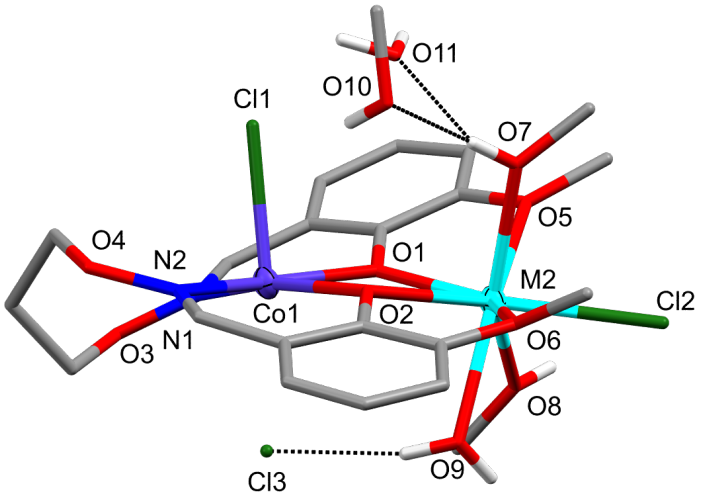

Figure 5.31: Representative structure of $[Co^{II}M2^{III}\mathbf{L2}(H_2O)(MeOH)_2Cl_2][Cl]\cdot H_2O\cdot MeOH$ (M2 = Dy^{III} (**C44**) and Er^{III} (**C45**)). Hydrogen atoms apart from those attached to donor atoms have been omitted for clarity, hydrogen bonding represented as black dotted lines, and the thermal ellipsoids of the metal ions are shown at 70% probability. Colour code: Co^{II} = dark purple, $M2^{III}$ = aqua, N = blue, O = red, C = grey, and H = white.

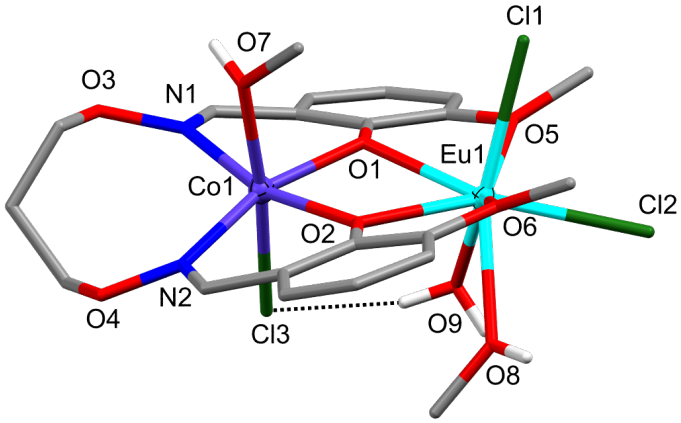

Figure 5.32: Full molecular structure of $[Co^{II}Eu^{III}\mathbf{L2}(H_2O)(MeOH)_2Cl_3]$, **C46**. Hydrogen atoms apart from those attached to donor atoms have been omitted for clarity, hydrogen bonding represented as black dotted lines, and thermal ellipsoids of the metal ions are shown at 70% probability. Colour code: Co^{II} = dark purple, Eu^{III} = aqua, N = blue, O = red, C = grey, and H = white.

Table 5.13: Selected bond lengths (Å) and angles (°) of the complexes **C42** - **C46** from crystal structure determination

	C42	**C43**	**C44**	**C45**	**C46**
Co1-O1	2.057(6)	2.056(4)	2.067(5)	2.076(3)	2.063(5)
Co1-O2	2.108(5)	2.113(4)	2.072(5)	2.070(3)	2.060(4)
Co1-N1	2.116(8)	2.104(5)	2.147(6)	2.146(4)	2.151(5)
Co1-N2	2.115(7)	2.119(5)	2.101(6)	2.110(4)	2.177(5)
Co1-O7	–	–	–	–	2.133(5)
Co1-Cl1	2.416(2)	2.439(2)	2.440(2)	2.428(1)	–
Co1-Cl3	–	–	–	–	2.487(2)
M2-O1	2.276(5)	2.343(4)	2.264(5)	2.239(3)	2.407(4)
M2-O2	2.255(5)	2.313(4)	2.342(5)	2.322(3)	2.333(4)
M2-O5	2.420(6)	2.484(4)	2.509(5)	2.496(3)	2.520(5)
M2-O6	2.418(6)	2.485(4)	2.496(5)	2.491(3)	2.482(4)
M2-O7	2.336(6)	2.417(4)	2.421(6)	2.348(3)	–
M2-O8	2.368(6)	2.434(4)	2.417(5)	2.391(3)	2.477(4)
M2-O9	2.343(5)	2.413(4)	2.349(5)	2.310(3)	2.403(4)
M2-Cl1	–	–	–	–	2.729(2)
M2-Cl2	2.718(2)	2.754(2)	2.660(2)	2.644(1)	2.705(2)
Co1-O1-M2	108.20(2)	106.99(15)	108.70(19)	108.83(13)	105.90(17)
Co1-O2-M2	107.10(2)	106.12(15)	105.69(19)	105.97(12)	108.73(18)
Co1$\cdots$M2	3.511(1)	3.540(1)	3.522(1)	3.510(1)	3.574(1)

5.4 $Zn^{II}4f$ and $Ni^{II}4f$ Complexes

The complexes discussed below, **C47** - **C49**, were found to be $Zn^{II}4f$ and $Ni^{II}4f$ dinuclear complexes with NO_3^- and Cl^- coordinates. Alike the other complexes in this chapter, the deprotonated ligand, **L2**$^{2-}$ is coordinated to both 3*d* and 4*f* ions (Mode I, Figure 2.6).[145] Key differences between these complexes can be seen in the Table 5.14.

Table 5.14: Structural differences in the complexes **C47** - **C49**

	M1	M2	Anion	Solvent
C47	Zn^{II}	Dy^{III}	NO_3^-/OAc^-	–
C48	Ni^{II}	Dy^{III}	$NO_3^-/Acac^-$	H_2O
C49	Ni^{II}	Eu^{III}	Cl^-	H_2O

5.4.1 Structural Analysis - NO_3^- Coordinates

The complex **C47** was found to be a dinuclear $Zn^{II}Dy^{III}$ complex, which was found to crystallise in the triclinic space group, $P\bar{1}$. The whole structure is found in the asymmetric unit as shown in Figure 5.33. Zn1 is five-coordinate with a spherical square pyramidal geometry (CShM, Table D.2) and N_2O_3 donor set consisting of two alkyloxime nitrogens, two phenolate oxygens, and one bridging OAc^- anion (2.1_11_2 Harris coordination mode, Figure A.17).[145–147,281] Dy1 is nine-coordinate with a spherical capped square antiprismatic geometry (CShM, Table D.3) and an O_9 donor set consisting of two phenolate oxygens, two methoxy oxygens, two bidentate NO_3^- anions, and one bridging OAc^- anion (2.1_11_2 Harris coordination mode, Figure A.17).[145–147,270]

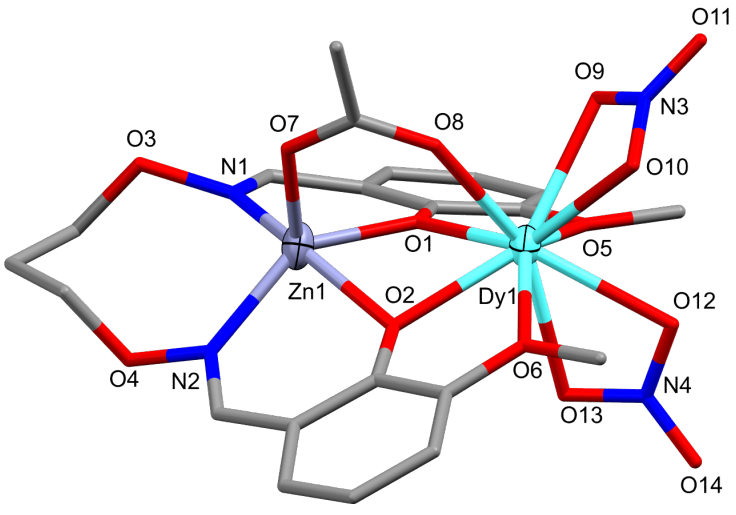

Figure 5.33: Full molecular structure of [$Zn^{II}Dy^{III}$**L2**(OAc)$(NO_3)_2$], **C47**. Hydrogen atoms have been omitted for clarity and the thermal ellipsoids of the metal ions are shown at 40% probability. Colour code: Zn^{II} = light purple, Dy^{III} = aqua, N = blue, O = red, and C = grey.

Attempts to remake **C47** have been unsuccessful, however the magnetic properties of the complex can be predicted using similar complexes found in the literature as a guide. The groups of Zheng *et al.*, Upadhyay *et al.*, Zhang *et al.*, and Panja *et al.*

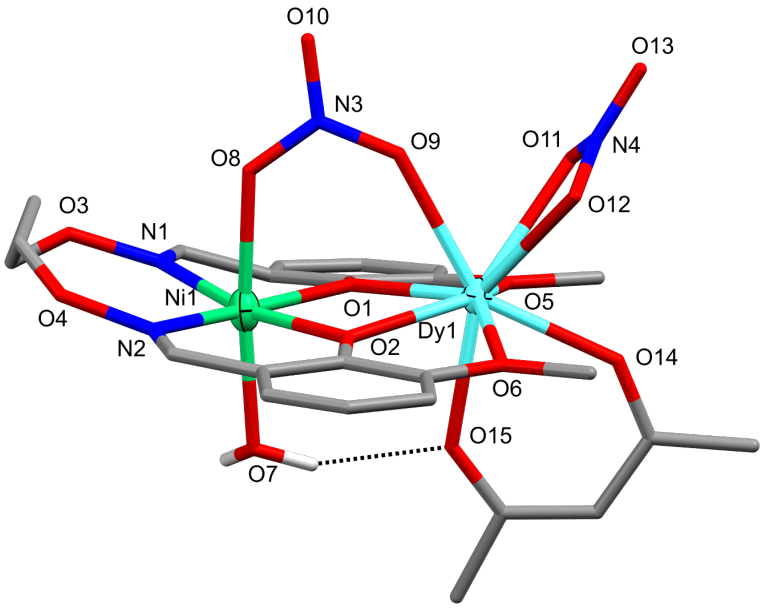

Figure 5.34: Full molecular structure of $[Ni^{II}Dy^{III}$**L2**$(H_2O)(acac)(NO_3)_2]\cdot$MeOH, **C48**. Hydrogen atoms apart from those attached to donor atoms and the disordered bridge have been omitted for clarity. hydrogen bonding represented as black dotted lines and the thermal ellipsoids of the metal ions are shown at 60% probability. Colour code: Ni^{II} = green, Dy^{III} = aqua, N = blue, O = red, C = grey, and H = white.

have reported the magnetic properties of analogous $Zn^{II}Dy^{III}$ complexes, which differ from **C47** by the Schiff base/alkyloxime ligand used.[289,292,293,308] The groups all found that upon cooling, the $\chi_M T$ values gradually decreased as the result of antiferromagnetic interactions and both the single-ion anisotropy and depopulation of the Stark energy levels of the Dy^{III} ion. To further probe the magnetics, three groups, Upadhyay *et al.*, Zhang *et al.*, and Panja *et al.* performed variable temperature AC magnetic susceptibility measurements. It was found that with a zero DC field there was no out-of-phase signal but under an applied DC field, a signal was achieved indicating the presence of slow relaxation of magnetisation and SMM properties. From these literature results, it can be predicted that the interaction between the Zn^{II} and Dy^{III} ions in **C47** will be antiferromagnetic, which is also in line with the M1-O-M2 angles of 101.57(12)° and 102.97(12)°. There is great potential for **C47** to have SMM properties, albeit as a field-induced SMM.

The complex **C48** was found to be a dinuclear $Ni^{II}Dy^{III}$ complex that crystallised in the monoclinic space group, $P2_1/n$. For this complex, the entire structure can be found within the asymmetric unit (Figure 5.34). Ni1 is six-coordinate with an octahedral geometry (CShM, Table D.2) and N_2O_4 donor set consisting of two alkyloxime nitrogens, two phenolate oxygens, one H_2O molecule, and one bridging NO_3^- anion ($2.1_1 1_2$ Harris coordination mode, Figure A.18).[145–147,171] Dy1 is nine-coordinate with a muffin geometry and an O_9 donor set consisting of two phenolate oxygens, two methoxy oxygens, one bidentate $acac^-$ anion, and two NO_3^- anions, one bidentate and the other bridging ($2.1_1 1_2$ Harris coordination mode, Figure A.18).[145–147,270]

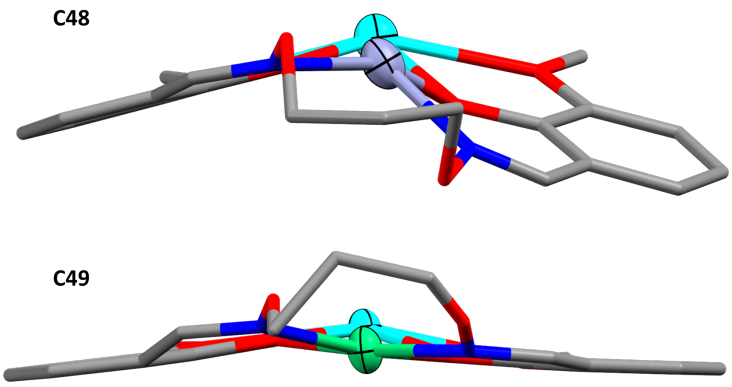

Figure 5.35: Schematic showing the different distortion found in complexes **C47** and **C48**. Metal ion coordinates, hydrogen atoms and the disordered bridge (**C48**) have been omitted for clarity. Thermal ellipsoids of metal ions are shown at 40% (**C47**) and 60% (**C48**) probability. Colour code: Zn^{II} = light purple, Ni^{II} = green, Dy^{III} = aqua, N = blue, O = red, and C = grey.

There is a large amount of disorder found in this structure, with a large portion of the propylene bridge (N1-O3-$(CH_2)_3$-O4) disordered over two positions with a 50 : 50 occupancy ratio. Moderate hydrogen bonding is found in the complex between the H_2O molecule (O7) and one of the $acac^-$ oxygens (O15), O7· · ·O15, 2.899(5) Å and between a lattice MeOH molecule (O16) and an oxygen of the bidentate NO_3^- (O12), O16· · ·O12, 2.800(5) Å.[158] Although magnetic characterisation wasn't performed on this complex, the potential magnetic properties are appealing as throughout the literature there are several examples where the combination of Ni^{II} and Dy^{III} ions exhibited SMM properties, both with and without an applied DC field.[142,287,309,310]

When comparing the different bridging in **C47** and **C48**, it can be seen that the OAc^- bridging in **C47** induces a greater deal of distortion to the molecular plane of the complex (Figure 5.35). The cause for this is not entirely understood as the geometry of OAc^- and NO_3^- anions are very similar however its thought that for **C48** the inclusion of both an extra M1 coordinate and intramolecular hydrogen bonding are responsible for the more planar structure.

Table 5.15: Selected bond lengths (Å) and angles (°) of the complexes **C47** and **C48** from crystal structure determination

	C47	**C48**
M1-O1	2.036(3)	2.027(3)
M1-O2	2.100(3)	2.011(3)
M1-N1	2.099(4)	2.056(9)
M1-N2	2.064(4)	2.054(4)
M1-O7	1.974(3)	2.096(4)
M1-O8	–	2.115(3)
M2-O1	2.307(3)	2.298(3)
M2-O2	2.288(3)	2.306(3)
M2-O5	2.566(3)	2.519(3)
M2-O6	2.517(3)	2.527(3)
M2-O8	2.301(3)	–
M2-O9	2.448(4)	2.454(3)
M2-O10	2.433(4)	–
M2-O11	–	2.520(3)
M2-O12	2.445(3)	2.515(3)
M2-O13	2.455(3)	–
M2-O14	–	2.272(3)
M2-O15	–	2.339(3)
M1-O1-M2	102.97(12)	104.12(11)
M1-O2-M2	101.57(12)	104.39(11)
M1$\cdots$M2	3.402(1)	3.416(1)

5.4.2 Structural Analysis - Cl^- Coordinates

The final complex in this chapter, **C49** is a $Ni^{II}Eu^{III}$ dinuclear complex, which is isostructural to complexes **C42** and **C43**. The complex was found to crystallise in the triclinic space group, $P\bar{1}$, with the whole structure found in the asymmetric unit (Figure 5.36). Ni1 is five-coordinate with a vacant octahedral geometry (CShM, Table D.2) and a N_2O_2Cl donor set, consisting of two alkyloxime nitrogens, two phenolate oxygens, and one Cl^- anion.[146,147,281] Ni1 is also weakly coordinated to a lattice Cl^- anion (Cl3) with a distance of 2.562(4) Å (Ni-Cl distances in similar complexes range from 2.200 - 2.498 Å).[311–313] Eu1 is eight-coordinate with a square antiprismatic geometry (CShM, Table D.3) and an O_7Cl donor set consisting of two phenolate oxygens, two methoxy oxygens, one Cl^- anion, and three H_2O molecules.[146,147,283] Moderate hydrogen bonding is found between the H_2O molecules, O7 and O9 and the Cl^- anions, Cl1 and Cl3 respectively, O7···Cl1, 2.977(10) and O9···Cl3, 3.042(9).[158]

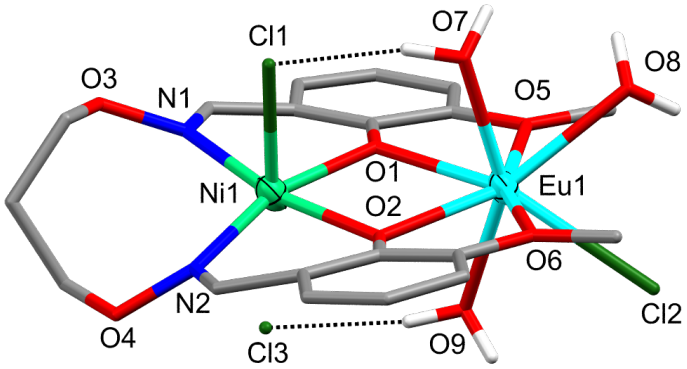

Figure 5.36: Full molecular structure of $[Ni^{II}Eu^{III}\mathbf{L2}(H_2O)_3Cl_2][Cl]$, **C49**. Hydrogen atoms apart from those attached to donor atoms have been omitted for clarity, hydrogen bonding represented as black dotted lines, and the thermal ellipsoids of the metal ions are shown at 70% probability. Colour code: Ni^{II} = green, Eu^{III} = aqua, N = blue, O = red, C = grey, and H = white.

When comparing **C49** with the isostructural complexes **C42** and **C43** there is minimal differences in the complexes with bond lengths and angles within error of each other. The three complexes also have the same degree of distortion indicating the combination of Cl^- and H_2O coordinates and hydrogen bonding are the driving force for the distortion. The potential magnetic properties for this complex do not have the same appeal as the previous Ni^{II} complex (**C48**) as Eu^{III} is not as well known as Dy^{III} for its magnetic properties.

Table 5.16: Selected bond lengths (Å) and bond angles (°) of the complex **C49** from crystal structure determination

		C49			
M1-O1	2.057(5)	M1-N1	2.077(6)	M1-Cl1	2.422(2)
M1-O2	2.077(5)	M1-N2	2.087(6)	M2-O1	2.328(4)
M2-O2	2.312(4)	M2-O7	2.412(5)	M2-O9	2.426(5)
M2-O5	2.486(5)	M2-O8	2.430(5)	M2-Cl2	2.763(2)
M2-O6	2.479(5)	M1-O1-M2	106.97(19)	M1-O2-M2	106.90(19)
M1···M2	3.528(1)				

5.5 Structural Comparisons

When comparing the complexes **C14** - **C49**, it can be seen that the complexes, which have solvent coordinates have a larger degree of ligand distortion. This can be seen clearly between the complexes **C14** - **C23**, which have solely NO_3^- coordinates versus **C24** which has an added solvent coordinate. The complexes **C14** - **C23** have fairly planar ligands, whereas there is a large degree of ligand distortion for **C24** thought to be induced by the introduction of hydrogen bonding, both intramolecular and intermolecular, drawing the metal ion/s and adjacent donor atoms out of the molecular plane. It was also found that the complexes that had NO_3^- anions and solvent coordinates versus those with Cl^- anions and solvent coordinates had a greater degree of ligand distortion, which was thought to result from additional steric strain induced by both the larger anions and the bidentate coordination. Lastly, as expected the five- and six-coordinate M1 ions have induced larger degrees of ligand distortion than the four-coordinate M1 ions. This is believed to result from the arrangement of the propylene bridge as the larger number of coordinates causes the bridge to adopt a zig-zag arrangement, increasing the N1-M1-N2 angle.

For the majority of the complexes, the M1-O-M2 angles are found to be in the range of 104° - 109° with a few outliers. It was found that the complexes **C40**, **C41**, and **C47** had M1-O-M2 angles smaller than the range mentioned above, 102.30(2)° and 102.90(2)° for **C40**, 99.69(15)° and 102.96(16)° for **C41**, and 102.97(12)° and 101.57(12)° for **C47**. One thing these three complexes have in common is that they all have some form of bridging, with complexes **C40** and **C41** having bridging between two units and **C47**, bridging between the M1 and M2 ions. It was thought that these complexes with smaller M1-O-M2 angles would subsequently have smaller M1$\cdots$M2 distances, however this was found to not be true as the M1$\cdots$M2 range found for **C14** - **C49** was 3.36 Å - 3.63Å and the complexes **C40**, **C41**, and **C47** had distances of 3.454(1), 3.309(1), and 3.402(1) Å respectively.

Looking at the ESI-MS data for the 3*d*4*f* series, it can be seen that all of the complexes with solely NO_3^- coordinates, such as **C14** - **C23** are present as $[M\text{-}NO_3]^+$ whereas the complexes with NO_3^- and coordinated solvent are found as $[M\text{-}NO_3\text{-solvent}]^+$, resembling the results found for the 3*d*3*d*'dinuclear series. This is in contrast to the results found for the Cl^- capped complexes where there is greater variability, with $[M\text{-}Cl]^+$, $[M\text{-}Cl\text{-solvent}]^+$, $[M\text{-solvent}]^+$, and $[M]^+$ all found. Similarly, to the 3*d*3*d*' series, peaks corresponding to $[\mathbf{L2}+Na]^+$ and $[\mathbf{L2}+M1]^+$ are found. ATR-IR characterisation was performed on all reproducible complexes (Table D.8) and found, similarly to the 3*d*3*d*' series, that the coordination of the ligand to the metal ions caused the typical ligand stretches, C=N, Ar-O, and C-O, to shift to 1600 - 1611 cm^{-1}, 1219 - 1251 cm^{-1}, and 1066 - 1101 cm^{-1} respectively. For the complexes with solvent coordinates, O-H stretches can be found in the range 3201 - 3400 cm^{-1}. The complexes with NO_3^- coordinates, are found to have symmetric and asymmetric stretches at approximately 1463, 1284, 1028, and 817 cm^{-1}. As discussed for the 3*d*3*d*' series, the range between the NO_3^- stretches at approximately 1463 and 1298 cm^{-1} is characteristic of the type of coordination. The general range found for the 3*d*4*f* series is approximately 175 - 181 cm^{-1}, which is consistent with bidentate coordination.[215–218]

5.6 Literature Analysis

Looking at the literature, there are many examples of 3*d*4*f* complexes where at least two metal ions are bridged by phenolate groups. By refining the comparison search (CCDC v1.20, 22/09/22) to complexes containing an alkyloxime ligand, 107 hits were obtained. Further refining to an alkyloxime ligand with a propylene bridge revealed no results, with the 107 hits all ethylene bridged. Out of the 107 results, 37 were dinuclear, with the remaining complexes trinuclear, dimers, polymers, or larger extended structures. The 3*d* and 4*f* metal ions commonly used were examined, with 82 of the 107 results containing Zn^{II} ions as the 3*d* metal ion source. The 4*f* ions were more distributed with the most common being La^{III} with 23 hits, closely followed by Dy^{III}, Tb^{III}, Gd^{III}, and Eu^{III} with 14, 12, 12, and 10 hits respectively. As shown throughout this chapter, Cu^{II} ions have been the most successful as the 3*d* ion source for this research, which in contrast to the literature is surprising considering only four complexes containing at least one Cu^{II} ion has been reported.[314,315] Another interesting result was that the most common coordinated entities were NO_3^- and OAc^- anions and solvents such as MeOH, H_2O, DMF, and MeCN.

It has been well discussed throughout the literature that the symmetry surrounding the metal ions, specifically 4*f* ions is crucial to whether easy-axis or easy-plane anisotropy is present. Kajiwara and coworkers produced two $Cu^{II}Tb^{III}$ dinuclear complexes using the ligands 2-methoxy-6-((3-methoxypropylimino)methyl)phenol (1) and 2-methoxy-6-((2-ethoxyethylimino)methyl)phenol (2) (Figure 5.37).[316] Although the structural differences in these ligands look minor, the way in which they coordinate has affected the orientation of the bidentate NO_3^- anions, resulting in the complex on the right (2) switching from easy-axis anisotropy to easy-plane anisotropy as the plane of one of the NO_3^- anions now intersects both metal ions. This results in the loss of any SMM behaviour.

For complexes, **C14** - **C33**, the symmetry of the 4*f* coordinates was found to be more alike to complex 1 by Kajiwara *et al.* as the plane of the NO_3^- anion did not align along the crystallographic 2-fold axis, or proposed 'easy axis'. It was found that the plane of the NO_3^- anion intersected a plane of Cu-O1-4*f*-O2 at angles of 50.70 - 51.97° for complexes **C14** - **C33**. It is thought that the reason for the difference between the similar dimers of this work and the work of Kajiwara *et al.* is due to the differences in the planarity of the aromatic rings, with the aromatic ring planes of complexes **C14** - **C33** intersecting at angles ranging from 4.75 - 6.01° whereas the structures of Kajiwara *et al.* have intersecting aromatic rings at degrees of 38.44° and 35.50° for 1 and 2 respectively. The reason for the lack of planarity in the structures of Kajiwara *et al.* is the octahedral coordination around the Cu^{II} ion, whereas for the complexes in this work, the Cu^{II} ions are four- and five-coordinate, which distort the ligand to a lesser degree than for six-coordinate ions.[316]

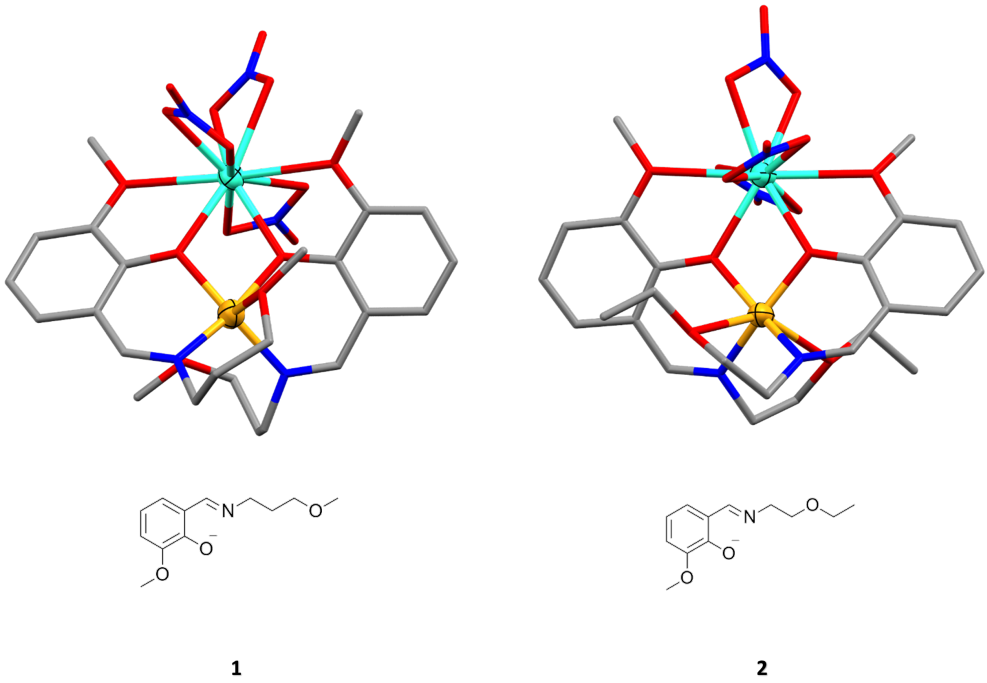

1 2

Figure 5.37: Crystal structures of the $Cu^{II}Tb^{III}$ complexes produced by Kajiwara *et al.*[316] illustrating the different NO_3^- anion orientations, with corresponding ligands below. Hydrogen atoms and lattice solvent molecules omitted for clarity. Colour code: Cu^{II} = dark yellow, Tb^{III} = aqua, N = blue, O = red, C = grey.

5.7 Conclusion

An extensive series of heterometallic Cu^{II}, Co^{II}, Ni^{II}, and $Zn^{II}4f$ dinuclear complexes have been synthesised by a RT reaction between H_2**L2**, $MX_2{\cdot}H_2O$, and $MX_3{\cdot}H_2O$ in a 1 : 1 : 1 ratio. The complexes, apart from a few due to reproducibility issues, have been characterised by SCXRD, ESI-MS, and ATR-IR with the select complexes **C17**, **C21**, and **C37** further characterised by CHN microanalysis and magnetic analysis. Transmetalation reactions were performed on select complexes (**C17**, **C20**, **C21**, **C26**, and **C29**) to determine whether there was a trend in complex stability of the 4*f* ions and 3*d* versus 4*f* ions. The results indicated that 4*f* ions larger than the Gd^{III} ion were more stable in the outer pocket, however when all transmetalated complexes were in the presence of $Mn(NO_3){\cdot}4H_2O$, **C8**, the $Cu^{II}Mn^{II}$ complex was produced. The transmetalation reaction between **C26** and $Mn(NO_3){\cdot}4H_2O$ indicated that interconversion between a dimer and a dinuclear structure was possible as the dimer, **C26** was transmetalated to the dinuclear complex, **C8**. Magnetic characterisation found that both **C17** and **C21** have ferromagnetic exchange between the Cu^{II} and 4*f* ions with a *J* exchange parameter of +2.94 cm^{-1} for **C17**. For **C37**, it was found that dominant antiferromagnetic exchange is present between the metal ions, consistent with the large M1-O-M2 angles. When comparing the 3*d*4*f* series, it was found that the complexes **C40**, **C41**, and **C47** all had additional forms of bridging between the metal ions, which resulted in smaller M1-O-M2 angles. Although these particular complexes have not be magnetically characterised to date, they introduce a potential pathway to explore the effects and associated magnetic properties of different forms of metal ion bridging in the future.

Complex Preparation and Characterisation

To a solution of ligand (1 eq.) in $CHCl_3$ was added solutions of $CuX_2{\cdot}H_2O$ (1 eq.) and $MX_3{\cdot}H_2O$ (1 eq.), both in MeOH and stirred at RT for five minutes. Isolation of the complex was achieved by the diffusion of Et_2O into the reaction solution, with X-ray quality crystals obtained after a period of one to 10 weeks.

[$Cu^{II}Dy^{III}$L2$(NO_3)_3$] (**C14**): H_2**L2** (0.0037 g, 0.010 mmol, 1 eq.) in $CHCl_3$ (1 mL), $Dy(NO_3)_3{\cdot}6H_2O$ (0.0046 g, 0.010 mmol, 1 eq.), $Cu(OAc)_2{\cdot}H_2O$ (0.0020 g, 0.010 mmol, 1 eq.), and NH_4NO_3 all in MeOH (0.2 mL). Brown prism shaped X-ray quality crystals were produced after three weeks. Yield (0.0027 g, 35%); ATR-IR: $\overline{\nu}$ = 2952 (C-H), 1602 (C=N), 1562 (Ar), 1533 (N-O), 1470 (NO_3), 1437 (C-H), 1291 (NO_3), 1230 (Ar-O), 1098 (C-O), 1032 (NO_3), 957 (N-O), 815 (NO_3), 744 (Ar) cm^{-1}; ESI-MS: *m/z* 722 $[M\text{-}NO_3]^+$.

[$Cu^{II}Er^{III}$L2$(NO_3)_3$] (**C15**): H_2**L2** (0.0038 g, 0.010 mmol, 1 eq.) in $CHCl_3$ (1 mL), $ErCl_3{\cdot}6H_2O$ (0.0038 g, 0.010 mmol, 1 eq.), and $Cu(NO_3)_2{\cdot}3H_2O$ (0.0024 g, 0.010 mmol, 1 eq.) both in MeOH (0.2 mL). Brown platelet shaped X-ray quality crystals were produced after three weeks. Yield (0.0030 g, 38%); ATR-IR: $\overline{\nu}$ = 2948 (C-H), 1607 (C=N), 1562 (Ar), 1463 (NO_3), 1438 (C-H), 1286 (NO_3), 1225 (Ar-O), 1093 (C-O), 1027 (NO_3), 955 (N-O), 821 (NO_3), 740 (Ar) cm^{-1}; ESI-MS: *m/z* 666 $[M\text{-}2NO_3]^+$.

[$Cu^{II}Ho^{III}$L2$(NO_3)_3$] (**C16**): H_2**L2** (0.0038 g, 0.010 mmol, 1 eq.) in $CHCl_3$ (1 mL), $HoCl_3{\cdot}6H_2O$ (0.0038 g, 0.010 mmol, 1 eq.), $Cu(OAc)_2{\cdot}H_2O$ (0.0020 g, 0.010 mmol, 1 eq.), and NH_4NO_3 (0.0024 g, 0.030 mmol, 3 eq.), all in MeOH (0.2 mL). Brown platelet shaped crystals were produced after three weeks. Yield (0.0041 g, 52%); ATR-IR: $\overline{\nu}$ = 2955 (C-H), 1611 (C=N), 1558

(Ar), 1463 (NO_3), 1435 (C-H), 1285 (NO_3), 1228 (Ar-O), 1096 (C-O), 1027 (NO_3), 955 (N-O), 817 (NO_3), 742 (Ar) cm^{-1}; ESI-MS: *m/z* 725 $[M\text{-}NO_3]^+$.

$[Cu^{II}Gd^{III}L2(NO_3)_3]$ (**C17**): H_2**L2** (0.0480 g, 0.128 mmol, 1 eq.) in $CHCl_3$ (4.8 mL), $Gd(NO_3)_3 \cdot 6H_2O$ (0.0596 g, 0.128 mmol, 1 eq.) and $Cu(OAc)_2 \cdot H_2O$ (0.0255 g, 0.128 mmol, 1 eq.), both in MeOH (2.6 mL). Dark green block shaped crystals were produced after one week. Yield (0.0706 g, 45%); ATR-IR: $\overline{\nu}$ = 2955 (C-H), 1603 (C=N), 1561 (Ar), 1464 (NO_3), 1435 (C-H), 1284 (NO_3), 1227 (Ar-O), 1098 (C-O), 1029 (NO_3), 955 (N-O), 817 (NO_3), 744 (Ar) cm^{-1}; ESI-MS: *m/z* 718 $[M\text{-}NO_3]^+$; elemental analysis calcd. (%) for $C_{19}H_{20}N_5O_{15}CuGd$: C 29.29, H 2.59, N 8.99; found: C 29.49, H 2.71, N 8.89.

$[Cu^{II}Eu^{III}L2(NO_3)_3]$ (**C18**): H_2**L2** (0.0372 g, 0.020 mmol, 1 eq.) in $CHCl_3$ (5 mL), $Eu(NO_3)_3 \cdot 6H_2O$ (0.0446 g, 0.020 mmol, 1 eq.), and $Cu(OAc)_2 \cdot H_2O$ (0.020 g, 0.020 mmol, 1 eq.) both in MeOH (1 mL). Dark green block shaped X-ray quality crystals were produced after three weeks. Yield (0.0495 g, 64%); ATR-IR: $\overline{\nu}$ = 2954 (C-H), 1603 (C=N), 1561 (Ar), 1464 (NO_3), 1447 (C-H), 1283 (NO_3), 1226 (Ar-O), 1099 (C-O), 1028 (NO_3), 955 (N-O), 817 (NO_3), 743 (Ar) cm^{-1}; ESI-MS: *m/z* 711 $[M\text{-}NO_3]^+$.

$[Cu^{II}Tb^{III}L2(NO_3)_3]$ (**C19**): H_2**L2** (0.0224 g, 0.060 mmol, 1 eq.) in $CHCl_3$ (3 mL), $TbCl_3 \cdot 6H_2O$ (0.0224 g, 0.060 mmol, 1 eq.), and $Cu(NO_3)_2 \cdot 3H_2O$ (0.0145 g, 0.060 mmol, 1 eq.) both in MeOH (0.6 mL). Red/brown block shaped X-ray quality crystals were produced after one week. Yield (0.0106 g, 23%); ATR-IR: $\overline{\nu}$ = 2941 (C-H), 1606 (C=N), 1575 (Ar), 1471 (NO_3), 1424 (C-H), 1249 (NO_3), 1225 (Ar-O), 1093 (C-O), 1065 (NO_3), 968 (N-O), 835 (NO_3), 728 (Ar) cm^{-1}; ESI-MS: *m/z* 718 $[M\text{-}NO_3{}^-]^+$.

$[Cu^{II}Yb^{III}L2(NO_3)_3]$ (**C20**): H_2**L2** (0.0075 g, 0.010 mmol, 1 eq.) in $CHCl_3$ (1 mL), $Yb(OAc)_3 \cdot 6H_2O$ (0.0084 g, 0.010 mmol, 1 eq.), and $Cu(NO_3)_2 \cdot 3H_2O$ (0.0048 g, 0.010 mmol, 1 eq.) both in MeOH (0.2 mL). Yellow/brown block shaped X-ray quality crystals were produced after three weeks. Yield (0.0111 g, 70%); ATR-IR: $\overline{\nu}$ = 2949 (C-H), 1600 (C=N), 1559 (Ar), 1515 (N-O), 1463 (NO_3), 1435 (C-H), 1289 (NO_3), 1228 (Ar-O), 1096 (C-O), 1030 (NO_3), 955 (N-O), 815 (NO_3), 741 (Ar) cm^{-1}; ESI-MS: *m/z* 733 $[M\text{-}NO_3{+}H]^+$.

$[Cu^{II}Dy^{III}L2(NO_3)_3]$ (**C21**): H_2**L2** (0.0475 g, 0.127 mmol, 1 eq.) in $CHCl_3$ (4.8 mL), $Dy(NO_3)_3 \cdot 6H_2O$ (0.0580 g, 0.127 mmol, 1 eq.) and $Cu(OAc)_2 \cdot H_2O$ (0.0254 g, 0.127 mmol, 1 eq.), both in MeOH (2.6 mL). Green/brown platelet shaped crystals were produced after two weeks. Yield (0.0676 g, 68%); ATR-IR: $\overline{\nu}$ = 2954 (C-H), 1601 (C=N), 1562 (Ar), 1532 (N-O), 1468 (NO_3), 1437 (C-H), 1290 (NO_3), 1229 (Ar-O), 1098 (C-O), 1031 (NO_3), 956 (N-O), 815 (NO_3), 744 (Ar) cm^{-1}; ESI-MS: *m/z* 722 $[M\text{-}NO_3]^+$; elemental analysis calcd. (%) for $C_{19}H_{20}N_5O_{15}CuDy$: C 29.09, H 2.59, N 8.99; found: C 29.23, H 2.68, N 8.88.

$[Cu^{II}Eu^{III}L2(NO_3)_3]$ (**C22**): H_2**L2** (0.0038 g, 0.010 mmol, 1 eq.) in $CHCl_3$ (1 mL), $Eu(NO_3)_3 \cdot 6H_2O$ (0.0045 g, 0.010 mmol, 1 eq.), and $Cu(OAc)_2 \cdot H_2O$ (0.0020 g, 0.010 mmol, 1 eq.) both in MeOH (0.2 mL). Dark green block shaped X-ray quality crystals were produced after one week. Yield (0.0057 g, 74%); ATR-IR: $\overline{\nu}$ = 2952 (C-H), 1611 (C=N), 1561 (Ar), 1463 (NO_3), 1435 (C-H), 1285 (NO_3), 1227 (Ar-O), 1098 (C-O), 1029 (NO_3), 955 (N-O), 817 (NO_3), 742 (Ar) cm^{-1}; ESI-MS: *m/z* 711 $[M\text{-}NO_3]^+$.

$[Cu^{II}Gd^{III}L2(NO_3)_3]$ (**C23**): H_2**L2** (0.0075 g, 0.02 mmol, 1 eq.) in $CHCl_3$ (2 mL), $Gd(NO_3)_3 \cdot 6H_2O$ (0.0090 g, 0.02 mmol, 1 eq.) and $Cu(OAc)_2 \cdot H_2O$ (0.0040 g, 0.02 mmol, 1 eq.), both in MeCN (0.4 mL). Dark brown platelet shaped crystals were produced after one week. Yield (0.0042 g, 27%); ATR-IR: $\overline{\nu}$ = 2929 (C-H), 1611 (C=N), 1559 (Ar), 1530 (N-O), 1463 (NO_3), 1435

(C-H), 1286 (NO_3), 1228 (Ar-O), 1096 (C-O), 1030 (NO_3), 956 (N-O), 814 (NO_3), 743 (Ar) cm^{-1}; ESI-MS: *m/z* 716 $[M\text{-}NO_3]^+$.

$[Cu^{II}La^{III}L2(H_2O)(NO_3)_3]$ (**C24**): H_2**L2** (0.0037 g, 0.010 mmol, 1 eq.) in $CHCl_3$ (1 mL), $La(NO_3)_3{\cdot}6H_2O$ (0.0044 g, 0.010 mmol, 1 eq.) and $Cu(OAc)_2{\cdot}H_2O$ (0.0020 g, 0.01 mmol, 1 eq.), both in MeCN (0.2 mL). Green block shaped crystals were produced after two weeks. Yield (0.0064 g, 82%); ATR-IR: $\overline{\nu}$ = 3400 (O-H), 2955 (C-H), 1600 (C=N), 1556 (Ar), 1463 (NO_3), 1435 (C-H), 1282 (NO_3), 1220 (Ar-O), 1093 (C-O), 1028 (NO_3), 959 (N-O), 816 (NO_3), 742 (Ar) cm^{-1}; ESI-MS: *m/z* 697 $[M\text{-}NO_3\text{-}H_2O]^+$.

$[Cu^{II}(MeCN)_4][Cu^{II}La^{III}L2(NO_3)_4]{\cdot}$MeCN (**C25**): H_2**L2** (0.0372 g, 0.020 mmol, 1 eq.) in $CHCl_3$ (5 mL), $La(NO_3)_3{\cdot}6H_2O$ (0.0433 g, 0.020 mmol, 1 eq.) and $Cu(OAc)_2{\cdot}H_2O$ (0.0195 g, 0.020 mmol, 1 eq.), both in MeCN (1 mL). Dark green block shaped crystals were produced after 10 weeks.

$[Cu^{II}_2La^{III}_2(L2)_2(NO_3)_6]$ (**C26**): H_2**L2** (0.0748 g, 0.10 mmol, 1 eq.) in $CHCl_3$ (10 mL), $La(NO_3)_3{\cdot}6H_2O$ (0.0866 g, 0.10 mmol, 1 eq.) and $Cu(OAc)_2{\cdot}H_2O$ (0.0400 g, 0.10 mmol, 1 eq.), both in MeCN (2 mL). Dark green block shaped crystals were produced after four weeks. Yield (0.0080 g, 11%); ATR-IR: $\overline{\nu}$ = 3356 (O-H), 2954 (C-H), 1609 (C=N), 1562 (Ar), 1524 (N-O), 1464 (NO_3), 1430 (C-H), 1351 (O-H), 1286 (NO_3), 1243 (Ar-O), 1101 (C-O), 1032 (NO_3), 954 (N-O), 819 (NO_3), 743 (Ar) cm^{-1}; ESI-MS: *m/z* 699 $[0.5M\text{-}NO_3]^+$.

$[Cu^{II}La^{III}L2(MeOH)_2(NO_3)_3]$ (**C27**): To a solution of $La(NO_3)_3{\cdot}6H_2O$ (0.0217 g, 0.05 mmol) in MeOH (2 mL) was added a few (four - five) crystals of **C17** and the solution was left to sit at RT overnight after which the crystals had dissolved. Isolation of the complex was achieved by the diffusion of Et_2O into the filtered reaction solution with green block-shaped X-ray quality crystals obtained after two weeks.

$[Cu^{II}Ce^{III}L2(MeOH)_2(NO_3)_3]$ (**C28**): H_2**L2** (0.0037 g, 0.010 mmol, 1 eq.) in $CHCl_3$ (1 mL), $Ce(NO_3)_3{\cdot}6H_2O$ (0.0043 g, 0.010 mmol, 1 eq.), and $Cu(OAc)_2{\cdot}H_2O$ (0.0020 g, 0.010 mmol, 1 eq.) both in MeOH (0.2 mL). Dark green block shaped X-ray quality crystals were produced after one weeks. Yield (0.0064 g, 77%); ATR-IR: $\overline{\nu}$ = 3399 (O-H), 2953 (C-H), 1605 (C=N), 1557 (Ar), 1463 (NO_3), 1435 (C-H), 1312 (O-H), 1286 (NO_3), 1222 (Ar-O), 1097 (C-O), 1031 (NO_3), 962 (N-O), 818 (NO_3), 739 (Ar) cm^{-1}; ESI-MS: *m/z* 698 $[M\text{-}NO_3\text{-}2MeOH]^+$.

$[Cu^{II}Ce^{III}L2(H_2O)(NO_3)_3]$ (**C29**): H_2**L2** (0.0375 g, 0.10 mmol, 1 eq.) in $CHCl_3$ (5 mL), $Ce(NO_3)_3{\cdot}6H_2O$ (0.0434 g, 0.10 mmol, 1 eq.), and $Cu(OAc)_2{\cdot}H_2O$ (0.0200 g, 0.10 mmol, 1 eq.) both in MeOH (1 mL). Dark green block shaped X-ray quality crystals were produced after two weeks. Yield (0.0511 g, 62%); ATR-IR: $\overline{\nu}$ = 3352 (O-H), 2954 (C-H), 1600 (C=N), 1564 (Ar), 1556 (N-O), 1463 (NO_3), 1435 (C-H), 1352 (O-H), 1281 (NO_3), 1244 (Ar-O), 1093 (C-O), 1028 (NO_3), 960 (N-O), 815 (NO_3), 742 (Ar) cm^{-1}; ESI-MS: *m/z* 700 $[M\text{-}H_2O\text{-}NO_3]^+$.

$[Cu^{II}Ce^{III}L2(MeOH)(NO_3)_3]{\cdot}CHCl_3$ (**C30**): H_2**L2** (0.0038 g, 0.010 mmol, 1 eq.) in $CHCl_3$ (1 mL), $Ce(NO_3)_3{\cdot}6H_2O$ (0.0043 g, 0.010 mmol, 1 eq.), and $Cu(NO_3)_2{\cdot}3H_2O$ (0.0024 g, 0.010 mmol, 1 eq.) both in MeOH (0.2 mL). Dark Green block shaped X-ray quality crystals were produced after one week.

$[Cu^{II}_2Ce^{III}_2(L2)_2(MeOH)_2(NO_3)_6]$ (**C31**): H_2**L2** (0.0038 g, 0.010 mmol, 1 eq.) in $CHCl_3$ (1 mL), $Ce(NO_3)_3{\cdot}6H_2O$ (0.0043 g, 0.010 mmol, 1 eq.), $Cu(OAc)_2{\cdot}H_2O$ (0.0020 g, 0.010 mmol, 1 eq.), and NH_4Cl (0.0016 g, 0.030 mmol, 3 eq.), all in MeOH (0.2 mL). Dark green block

shaped crystals were produced after one week.

[$Cu^{II}Ce^{III}$L2(MeOH)$(NO_3)_3$]·Et_2O (**C32**): H_2**L2** (0.0038 g, 0.010 mmol, 1 eq.) in $CHCl_3$ (1 mL) was added $CeCl_3 \cdot 6H_2O$ (0.0037 g, 0.010 mmol, 1 eq.), $Cu(OAc)_2 \cdot H_2O$ (0.0020 g, 0.010 mmol, 1 eq.), and NH_4NO_3 (0.0024 g, 0.030 mmol, 3 eq.) all in MeOH (0.2 mL). Green platelet shaped crystals were produced after two weeks.

[$Cu^{II}Eu^{III}$(*o*−van)(MeOH)$(NO_3)_3$] (**C33**): *o*-Van (0.0031 g, 0.020 mmol, 1 eq.) in $CHCl_3$ (2 mL), was added $Cu(OAc)_2 \cdot H_2O$ (0.0040 g, 0.020 mmol, 1 eq.) and $Eu(NO_3)_3 \cdot 6H_2O$ (0.0089 g, 0.020 mmol, 1 eq.), both in MeOH (0.4 mL). The green solution was stirred at RT for five minutes. Isolation of the complex was achieved by the diffusion of Et_2O into the reaction solution. Green block shaped crystals were produced after three weeks. Yield (0.0041 g, 28%); ATR-IR: $\overline{\nu}$ = 3373 (O-H), 2953 (C-H), 1634 (C=O), 1554 (Ar), 1468 (NO_3), 1437 (C-H), 1340 (O-H), 1291 (NO_3), 1219 (Ar-O), 1096 (C-O), 951 (N-O), 735 (Ar) cm^{-1}; ESI-MS: *m/z* 641 [M-NO_3-MeOH]$^+$.

[$Cu^{II}Dy^{III}$L2(H_2O)(MeOH)Cl_3] (**C34**): H_2**L2** (0.0225 g, 0.060 mmol, 1 eq.) in $CHCl_3$ (3 mL), $DyCl_3 \cdot 6H_2O$ (0.0226 g, 0.060 mmol, 1 eq.) and $Cu(OAc)_2 \cdot H_2O$ (0.0120 g, 0.060 mmol, 1 eq.), both in MeOH (0.6 mL). Dark green platelet shaped crystals were produced after four weeks. Yield (0.0230 g, 51%); ATR-IR: $\overline{\nu}$ = 3201 (O-H), 2935 (C-H), 1603 (C=N), 1561 (Ar), 1464 (C-H), 1372 (O-H), 1227 (Ar-O), 1092 (C-O), 1034 (C-O), 953 (N-O), 738 (Ar) cm^{-1}; ESI-MS: *m/z* 668 [M-Cl-MeOH-H_2O]$^+$.

[$Cu^{II}Eu^{III}$L2(H_2O)(MeOH)Cl_3] (**C35**): H_2**L2** (0.0150 g, 0.040 mmol, 1 eq.) in $CHCl_3$ (2 mL), $EuCl_3 \cdot 6H_2O$ (0.0146 g, 0.040 mmol, 1 eq.) and $Cu(OAc)_2 \cdot H_2O$ (0.0080 g, 0.040 mmol, 1 eq.), both in MeOH (0.4 mL). Brown block shaped crystals were produced after two weeks. Yield (0.0084 g, 28%); ATR-IR: $\overline{\nu}$ = 3349 (O-H), 2959 (C-H), 1608 (C=N), 1559 (Ar), 1470 (C-H), 1321 (O-H), 1249 (Ar-O), 1093 (C-O), 1065 (C-O), 968 (N-O), 729 (Ar) cm^{-1}; ESI-MS: *m/z* 711 [M-MeOH]$^+$.

[$Cu^{II}Tb^{III}$L2(H_2O)(MeOH)Cl_3] (**C36**): H_2**L2** (0.0037 g, 0.010 mmol, 1 eq.) in $CHCl_3$ (1 mL), $TbCl_3 \cdot 6H_2O$ (0.0037 g, 0.010 mmol, 1 eq.) and $Cu(OAc)_2 \cdot H_2O$ (0.0020 g, 0.010 mmol, 1 eq.), both in MeOH (0.2 mL). Brown platelet shaped crystals were produced after one week. Yield (0.0061 g, 81%); ATR-IR: $\overline{\nu}$ = 3313 (O-H), 2946 (C-H), 1608 (C=N), 1563 (Ar), 1439 (C-H), 1372 (O-H), 1228 (Ar-O), 1096 (C-O), 960 (N-O), 747 (Ar) cm^{-1}; ESI-MS: *m/z* 665 [M-Cl-H_2O-MeOH]$^+$.

[$Cu^{II}Er^{III}$L2$(H_2O)Cl_3$] (**C37**): H_2**L2** (0.0513 g, 0.137 mmol, 1 eq.) in $CHCl_3$ (4.8 mL), $ErCl_3 \cdot 6H_2O$ (0.0523 g, 0.137 mmol, 1 eq.) and $Cu(OAc)_2 \cdot H_2O$ (0.0274 g, 0.137 mmol, 1 eq.), both in MeOH (2.6 mL). Yellow block shaped crystals were produced after seven weeks. Yield (0.0421 g, 42%); ATR-IR: $\overline{\nu}$ = 3215 (O-H), 2953 (C-H), 1608 (C=N), 1563 (Ar), 1465 (C-H), 1368 (O-H), 1227 (Ar-O), 1093 (C-O), 954 (N-O), 742 (Ar) cm^{-1}; ESI-MS: *m/z* 674 [M-H_2O]$^+$; elemental analysis calcd. (%) for $C_{19}H_{22}N_2O_7Cl_3CuEr$: C 31.37, H 3.05, N 3.85; found: C 31.45, H 3.24, N 3.72.

[$Cu^{II}Ho^{III}$L2$(H_2O)Cl_3$] (**C38**): H_2**L2** (0.0038 g, 0.010 mmol, 1 eq.) in $CHCl_3$ (1 mL), $HoCl_3 \cdot 6H_2O$ (0.0038 g, 0.010 mmol, 1 eq.) and $Cu(OAc)_2 \cdot H_2O$ (0.0020 g, 0.01 mmol, 1 eq.), both in MeOH (0.2 mL). Yellow platelet shaped crystals were produced after two weeks. Yield (0.0019 g, 26%); ATR-IR: $\overline{\nu}$ = 3228 (O-H), 2944 (C-H), 1602 (C=N), 1563 (Ar), 1470 (C-H), 1368 (O-H), 1228 (Ar-O), 1095 (C-O), 960 (N-O), 738 (Ar) cm^{-1}; ESI-MS: *m/z* 669 [M-Cl-H_2O]$^+$.

[$Cu^{II}Tb^{III}$L2$(H_2O)_4$][$Cu^{II}Tb^{III}$L2$(H_2O)_3$Cl][$Cu^{II}Cl_4$][Cl_3] (**C39**): H_2**L2** (0.0037 g, 0.010 mmol, 1 eq.) in $CHCl_3$ (1 mL), $TbCl_3 \cdot 6H_2O$ (0.0037 g, 0.010 mmol, 1 eq.) and $Cu(OAc)_2 \cdot 6H_2O$ (0.0020 g, 0.010 mmol, 1 eq.), both in MeOH (0.2 mL). Light brown platelet shaped crystals were produced after two weeks. Yield (0.0037 g, 22%); ATR-IR: $\overline{\nu}$ = 3242 (O-H), 2954 (C-H), 1602 (C=N), 1558 (Ar), 1461 (C-H), 1357 (O-H), 1221 (Ar-O), 1088 (C-O), 965 (N-O), 740 (Ar) cm^{-1}; ESI-MS: *m/z* 665 $[0.5M\text{-}3Cl\text{-}CuCl_4\text{-}MeOH\text{-}H_2O]^+$.

[$Cu^{II}_2Ce^{IV}_2$(L2)$_2(H_2O)_2Cl_6$] (**C40**): H_2**L2** (0.0378 g, 0.10 mmol, 1 eq.) in $CHCl_3$ (4 mL), $CeCl_3 \cdot 7H_2O$ (0.0373 g, 0.10 mmol, 1 eq.) and $CuCl_2 \cdot 2H_2O$ (0.0170 g, 0.10 mmol, 1 eq.), both in MeOH (0.8 mL). Brown platelet shaped crystals were produced after eight weeks.

[$Co^{II}_2Eu^{III}_2$(L2)$_2(OAc)_2(NO_3)_4$] (**C41**): H_2**L2** (0.0037 g, 0.010 mmol, 1 eq.) in $CHCl_3$ (1 mL), $Eu(NO_3)_3 \cdot 6H_2O$ (0.0045 g, 0.010 mmol, 1 eq.) and $Co(OAc)_2 \cdot 2H_2O$ (0.0025 g, 0.010 mmol, 1 eq.), both in MeOH (0.2 mL). Red block shaped crystals were produced after six weeks.

[$Co^{II}Er^{III}$L2$(H_2O)_3Cl_2$][Cl] (**C42**): H_2**L2** (0.0037 g, 0.010 mmol, 1 eq.) in $CHCl_3$ (1 mL), $ErCl_3 \cdot 6H_2O$ (0.0038 g, 0.010 mmol, 1 eq.) and $Co(OAc)_2 \cdot 4H_2O$ (0.0025 g, 0.01 mmol, 1 eq.), both in MeOH (0.2 mL). Orange prism shaped crystals were produced after three weeks. Yield (0.0052 g, 68%); ATR-IR: $\overline{\nu}$ = 3319 (O-H), 2953 (C-H), 1602 (C=N), 1562 (Ar), 1464 (C-H), 1355 (O-H), 1215 (Ar-O), 1096 (C-O), 977 (N-O), 734 (Ar) cm^{-1}; ESI-MS: *m/z* 758 $[M]^+$.

[$Co^{II}Eu^{III}$L2$(H_2O)_3Cl_2$][Cl] (**C43**): H_2**L2** (0.0075 g, 0.020 mmol, 1 eq.) in $CHCl_3$ (2 mL), $EuCl_3 \cdot 6H_2O$ (0.0074 g, 0.020 mmol, 1 eq.) and $Co(OAc)_2 \cdot 4H_2O$ (0.0050 g, 0.020 mmol, 1 eq.), both in MeOH (0.4 mL). Orange platelet shaped crystals were produced after two weeks. Yield (0.0105 g, 70%); ATR-IR: $\overline{\nu}$ = 3394 (O-H), 2945 (C-H), 1602 (C=N), 1562 (Ar), 1464 (C-H), 1355 (O-H), 1215 (Ar-O), 1096 (C-O), 977 (N-O), 734 (Ar) cm^{-1}; ESI-MS: *m/z* 709 $[M\text{-}Cl]^+$.

[$Co^{II}Dy^{III}$L2$(H_2O)(MeOH)_2Cl_2$][Cl]·MeOH·H_2O (**C44**): H_2**L2** (0.0297 g, 0.080 mmol, 1 eq.) in $CHCl_3$ (4 mL), $DyCl_3 \cdot 6H_2O$ (0.0302 g, 0.080 mmol, 1 eq.) and $Co(OAc)_2 \cdot 4H_2O$ (0.0199 g, 0.080 mmol, 1 eq.), both in MeOH (0.8 mL). Green/brown platelet shaped crystals were produced after four weeks. Yield (0.0351 g, 53%); ATR-IR: $\overline{\nu}$ = 3386 (O-H), 2975 (C-H), 1602 (C=N), 1562 (Ar), 1466 (C-H), 1355 (O-H), 1215 (Ar-O), 1096 (C-O), 1056 (C-O), 977 (N-O), 733 (Ar) cm^{-1}; ESI-MS: *m/z* 732 $[M\text{-}2MeOH\text{-}2H_2O]^+$.

[$Co^{II}Er^{III}$L2$(H_2O)(MeOH)_2Cl_2$][Cl]·MeOH·H_2O (**C45**): H_2**L2** (0.0375 g, 0.020 mmol, 1 eq.) in $CHCl_3$ (5 mL), $ErCl_3 \cdot 6H_2O$ (0.0382 g, 0.020 mmol, 1 eq.) and $Co(OAc)_2 \cdot 4H_2O$ (0.0249 g, 0.01 mmol, 1 eq.), both in MeOH (1 mL). Yellow platelet shaped crystals were produced after three weeks. Yield (0.0198 g, 64%); ATR-IR: $\overline{\nu}$ = 3386 (O-H), 2951 (C-H), 1602 (C=N), 1575 (Ar), 1463 (C-H), 1354 (O-H), 1215 (Ar-O), 1095 (C-O), 1056 (C-O), 978 (N-O), 733 (Ar) cm^{-1}; ESI-MS: *m/z* 723 $[M\text{-}3MeOH\text{-}H_2O]^+$.

[$Co^{II}Eu^{III}$L2$(H_2O)(MeOH)_2Cl_3$] (**C46**): H_2**L2** (0.0300 g, 0.10 mmol, 1 eq.) in $CHCl_3$ (5 mL), $EuCl_3 \cdot 6H_2O$ (0.0366 g, 0.10 mmol, 1 eq.) and $Co(OAc)_2 \cdot 4H_2O$ (0.0249 g, 0.10 mmol, 1 eq.), both in MeOH (1 mL). Yellow platelet shaped crystals were produced after three weeks. Yield (0.0311 g, 40%); ATR-IR: $\overline{\nu}$ = 3374 (O-H), 2942 (C-H), 1606 (C=N), 1575 (Ar), 1471 (C-H), 1354 (O-H), 1251 (Ar-O), 1093 (C-O), 1065 (C-O), 968 (N-O), 729 (Ar) cm^{-1}; ESI-MS: *m/z* 771 $[M+H]^+$.

[$Zn^{II}Dy^{III}$L2$(OAc)(NO_3)_2$] (**C47**): H_2**L2** (0.0037 g, 0.010 mmol, 1 eq.) in $CHCl_3$ (1 mL), $Dy(NO_3)_3 \cdot 6H_2O$ (0.0046 g, 0.010 mmol, 1 eq.) and $Zn(OAc)_2 \cdot 2H_2O$ (0.0022 g, 0.01 mmol, 1 eq.), both in MeOH (0.2 mL). Colourless platelet shaped crystals were produced after six

weeks. Yield (0.0034 g, 44%); ATR-IR: $\overline{\nu}$ = 2940 (C-H), 1641 (C=O), 1606 (C=N), 1575 (Ar), 1471 (C-H), 1353 (O-H), 1249 (Ar-O), 1093 (C-O), 968 (N-O), 728 (Ar) cm^{-1}; ESI-MS: *m/z* 438 $[M\text{-}Dy\text{-}2NO_3\text{-}OAc]^+$.

$[Ni^{II}Dy^{III}L2(H_2O)(acac)(NO_3)_2]\cdot MeOH$ (**C48**): H_2**L2** (0.0748 g, 0.10 mmol, 1 eq.) in $CHCl_3$ (10 mL), $Dy(NO_3)_3\cdot 6H_2O$ (0.0914 g, 0.10 mmol, 1 eq.) and $Ni(acac)_2\cdot 6H_2O$ (0.0586 g, 0.10 mmol, 1 eq.), both in MeOH (2 mL). Green block shaped crystals were produced after eight weeks. Yield (0.0076 g, 19%); ATR-IR: $\overline{\nu}$ = 3255 (O-H), 2947 (C-H), 1611 (C=N), 1585 (Ar), 1523 (N-O), 1467 (NO_3), 1435 (C-H), 1366 (O-H), 1290 (NO_3), 1238 (Ar-O), 1096 (C-O), 1035 (NO_3), 975 (N-O), 810 (NO_3), 745 (Ar) cm^{-1}; ESI-MS: *m/z* 755 $[M\text{-}NO_3\text{-}H_2O]^+$.

$[Ni^{II}Eu^{III}L2(H_2O)_3Cl_2][Cl]$ (**C49**): H_2**L2** (0.0038 g, 0.010 mmol, 1 eq.) in $CHCl_3$ (1 mL), $EuCl_3\cdot 6H_2O$ (0.0037 g, 0.010 mmol, 1 eq.) and $Ni(OAc)_2\cdot 4H_2O$ (0.0025 g, 0.010 mmol, 1 eq.), both in MeOH (0.2 mL). Orange block shaped crystals were produced after four weeks. Yield (0.0060 g, 81%); ATR-IR: $\overline{\nu}$ = 3382 (O-H), 2986 (C-H), 1605 (C=N), 1563 (Ar), 1463 (C-H), 1372 (O-H), 1216 (Ar-O), 1085 (C-O), 978 (N-O), 733 (Ar) cm^{-1}; ESI-MS: *m/z* 744 $[M+H]^+$.

Chapter 6

Other Work

Throughout the duration of this research, several unexpected complexes were produced. Although these complexes do not fit into the other chapter themes of defective dicubanes and dinuclear complexes, they are worthy additions to the overall theme of manipulating magnetism and in their own right are interesting. For several of these complexes, a suitable and reliable synthetic pathway was not achieved and therefore several examples reported below are to date, non-reproducible.

6.1 Ni^{II} Clusters

6.1.1 Ni^{II}_3 Clusters

The complexes **C50** and **C51** are trinuclear Ni^{II}_3 clusters synthesised from RT reactions between H_2**L1**, $Ni(acac)_2{\cdot}6H_2O$, and Et_3N in a 1 : 1.5 : 6 molar ratio. A colour change from the pale yellow solution of the dissolved ligand to a dark green solution indicated successful coordination. Isolation of the complexes was achieved by the slow evaporation of the reaction solution over a period of nine weeks (**C50**) and vapour diffusion of Et_2O into the reaction solution over a period of four weeks (**C51**).

The complex, **C50** was synthesised concurrently with the defective dicubanes series, complexes **C1** - **C5**. The complex was a result of experimenting with various metal anions, solvents, coligands, and crystallisation methods. When attempting to remake **C50**, the same complexation procedure was followed however the method of crystallisation was altered to Et_2O vapour diffusion, as this method had shown to be more reliable at producing high quality crystalline material, resulting in the complex, **C51**. A representative structure of the two complexes can be seen in Figure 6.1 (Note the numbering of the atoms correlates to **C51**) with complete structures found in Figures E.1 and E.3.

The trinuclear Ni^{II}_3 complexes were both found to crystallise in monoclinic space groups, $P2_1/n$ and $C2/c$ respectively for **C50** and **C51**. For **C50**, the whole structure is found within the asymmetric unit, whereas half of the structure is found for **C51**. Both complexes consist of two deprotonated ligands, $\mathbf{L1}^{2-}$ coordinated to three Ni^{II} ions (Mode II, Figure 2.2).[145] Each of the three Ni^{II} ions have an octahedral geometry (CShM, Table E.4) with a NO_5 donor set for the two outer ions (Ni1 and Ni3 in **C50** and Ni1 in **C51**) consisting of one phenolate, one oximato, and one methoxy oxygen, one amino nitrogen, and a bidentate $acac^-$ anion.[146,147,171] Ni2 for both complexes has a N_2O_4 donor set, consisting of two phenolate oxygens, two oximato nitrogens, and two solvent molecules, one MeOH and one H_2O for **C50** and two MeOH molecules for **C51**. The difference in solvent molecules was assumed to

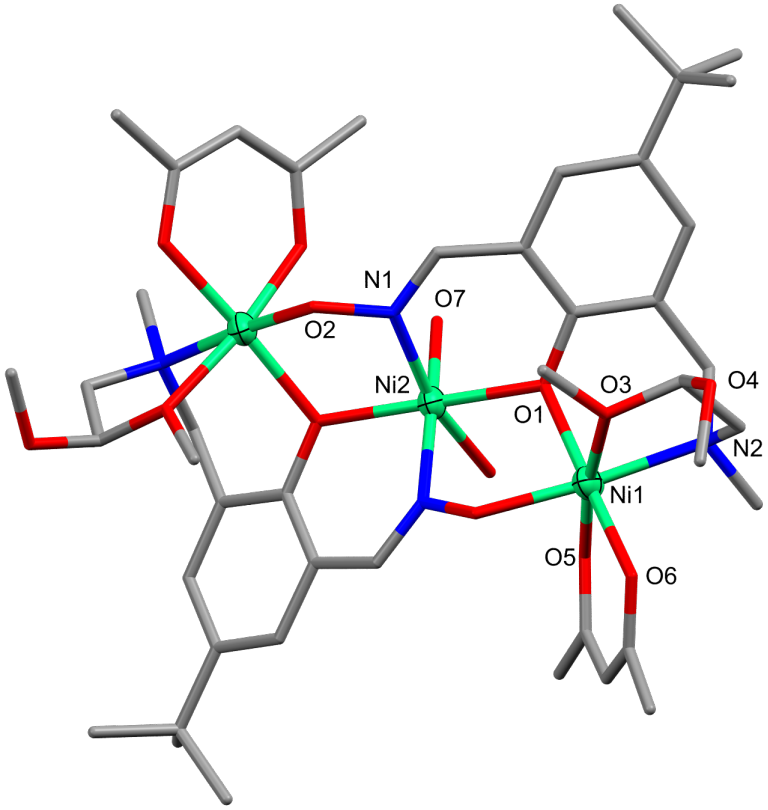

Figure 6.1: Representative structure of $[Ni^{II}_3(\mathbf{L1})_2(H_2O)_n(MeOH)_m(acac)_2]\cdot MeOH$ (n = 1 (**C50**) and 0 (**C51**), m = 1 (**C50**) and 2 (**C51**)). Hydrogen atoms and lattice MeOH molecules have been omitted for clarity and the thermal ellipsoids of the metal ions are shown at 70% probability. Colour code: Ni^{II} = light green, N = blue, O = red, and C = grey.

be a result of the method used for isolation of the complex. For both complexes there is moderate intramolecular hydrogen bonding found between the coordinated solvent molecules (O7 and O14) and $acac^-$ anions (O5 and O12), O7· · ·O5, 2.681(4) Å and 014· · ·O12, 2.630(4) Å for **C50** and 07· · ·O5, 2.629(3) Å for **C51**.[158] For both complexes, MeOH molecules are found in the crystal lattice, with three for **C50**, which form additional moderate hydrogen bonds with each other (017· · ·O16, 2.659(7) Å) and both oximato oxygens (016· · ·O2, 2.601(5) Å and 015· · ·O9, 2.594(5) Å) and two non-interacting MeOH molecules for **C51**. Intermolecular hydrogen bonding is found in **C50**, between the MeOH (O14) and H_2O (O7) molecules coordinated to Ni2 and their opposite counterparts on an above-plane unit, O7· · ·O14 2.951(5) Å (Figure E.2).[158] The SQUEEZE procedure was implemented for both **C50** and **C51** using the crystallographic software, Olex2 to remove diffuse solvent in the crystal lattice. For **C50**, the result was the removal of 24 electrons per asymmetric unit equating to 2.5 H_2O molecules (25 e^-) and for **C51**, the result was the removal of 15 electrons per asymmetric unit which equates to 1.5 H_2O molecules (15 e^-).[208,273]

When comparing the two complexes structurally, there are small differences between the bond lengths and distances of the two complexes, however this was not found for the Ni-X-Ni exchange angles, the exchange angles were found to be 112° for both complexes. The differences were found between bond distances closely associated with the solvent coordinates corroborating the findings of the defective dicubane series that subtle differences in the coordinates can significantly affect the bond lengths and distances. It is thought the exchange pathway angles were not greatly affected, as compared to the defective dicubane series, as the solvent coordinates do not bridge multiple metal ions. Another structural difference between the two complexes **C50** and **C51** is that the lattice bound MeOH molecules for **C50** form hydrogen bond networks whereas the lattice bound MeOH molecules in **C51** do not form any type of interaction. If these results were to follow that of the defective dicubane series, the magnetic properties of the complexes could be significantly different with the magnetic properties of **C50** greatly enhanced by the interacting lattice solvent molecules, this however would need to be analysed at a later date.

Table 6.1: Selected bond lengths (Å) and angles (°) of complexes **C50** and **C51** from crystal structure determination

	C50	**C51**
Ni1-O1	2.065(3)	2.059(3)
Ni1-O2/9	2.032(3)	2.005(3)*
Ni1-O3	2.128(3)	2.151(3)
Ni1-O5	2.032(3)	2.027(3)
Ni1-O6	2.034(3)	2.038(3)
Ni1-N2	2.112(4)	2.115(4)
Ni2-O1	2.010(3)	2.017(3)
Ni2-O7	2.136(3)	2.113(3)
Ni2-O8	2.014(3)	–
Ni2-O14	2.149(3)	–
Ni2-N1	2.053(4)	2.031(4)
Ni2-N3	2.049(4)	–
Ni3-O2/9	2.008(3)	–
Ni3-O8	2.055(3)	–
Ni3-O10	2.161(3)	–
Ni3-O12	2.068(3)	–
Ni3-O13	1.996(3)	–
Ni3-N4	2.137(4)	–
Ni1-O1-Ni2	112.83(15)	112.63(14)
Ni2-O8-Ni3	112.32(14)	–
Ni1···Ni2	3.395(2)	3.392(1)
Ni2···Ni3	3.380(1)	–
Ni1···Ni1/3	6.483(2)	6.551(2)*

* 1-X, +Y, 3/2-Z

6.1.2 Ni^{II}_4 Cluster

Initial attempts at producing a $Ni^{II}Eu^{III}$ dinuclear complex involved two complexations simultaneously set up, one base free and the other in the presence of Et_3N. The base free complexation resulted in **C49**, a dinuclear $Ni^{II}Eu^{III}$ complex whereas the Et_3N containing complexation resulted in **C52**. The complex **C52** was found to be a tetranuclear defective dicubane, similarly to complexes **C1** - **C5** however utilising the deprotonated ligand, $\mathbf{L2}^{2-}$ (Mode II, Figure 2.6).[145] The defective dicubane was found to crystallise in the triclinic space group, $P\bar{1}$, with half of the structure found in the asymmetric unit. The full structure is shown in Figure 6.2. The structure consists of four Ni^{II} ions each with an octahedral geometry (CShM; Table E.4), with a O_5Cl donor set for Ni1 consisting of one μ_2-phenolate oxygen, one methoxy oxygen, two μ_3-OMe^-, one MeOH molecule, and one μ_2-Cl^- anion.[146,147,171] Ni2 has a N_2O_3Cl donor set consisting of two alkyloxime nitrogens, two μ_2-phenolate oxygens, one μ_3-OMe^-, and one μ_2-Cl^- anion.

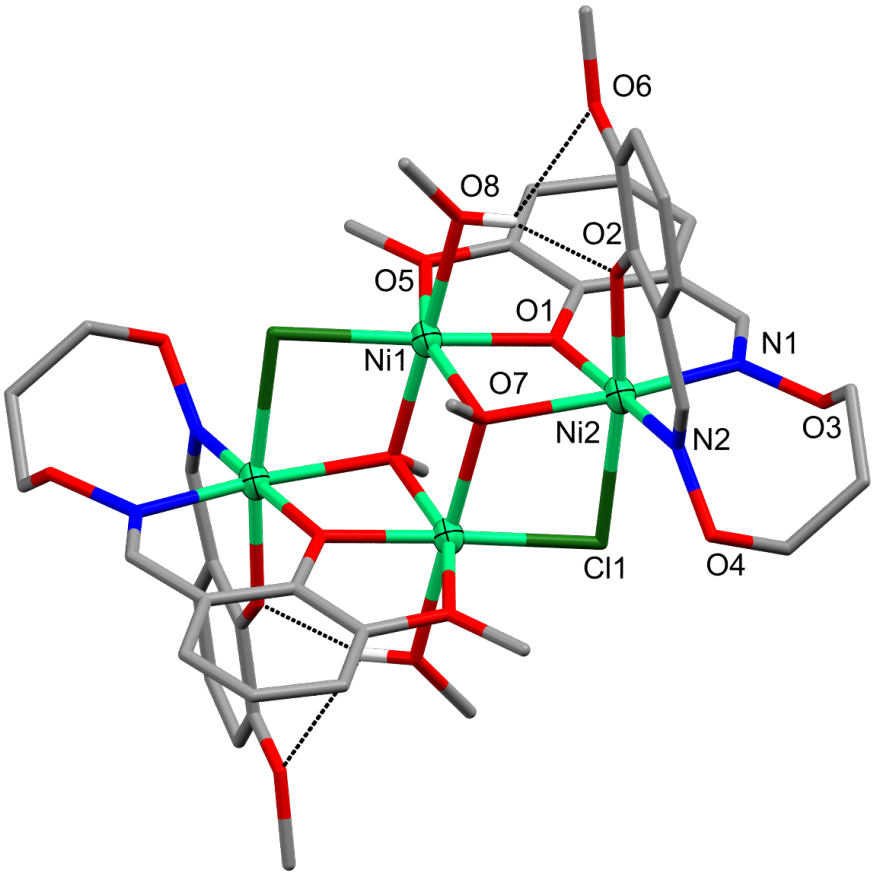

Figure 6.2: Full molecular structure of $[Ni^{II}_4(\mathbf{L2})_2(OMe)_2(MeOH)_2Cl_2]\cdot 2CHCl_3$, **C52**. Non-interacting hydrogen atoms and lattice $CHCl_3$ molecules have been omitted for clarity, hydrogen bonding represented as black dotted lines, and thermal ellipsoids of metal ions shown at 70% probability. Colour code: Ni^{II} = light green, N = blue, O = red, Cl = dark green, C = grey, and H = white.

Moderate hydrogen bonding is found in the complex between the coordinated MeOH molecules (O8) and both the monodentate phenoxo oxygen (O2) and free methoxy oxygen (O6), O8· · ·O2 (2.670(4) Å) and O8· · ·O6 (3.085(4) Å).[158] Within the crystal

lattice, there are two $CHCl_3$ molecules found. The SQUEEZE procedure was implemented using the crystallographic software, Olex2 to remove diffuse solvent found in the crystal lattice. The result was the removal of 20 electrons per asymmetric unit which equates to two H_2O molecules (20 e^-).[208,273]

Apart from the use of different ligands, another large difference between the defective dicubane series (**C1** - **C5**) and **C52** is the way in which the ligands coordinate to the metal ions. For all complexes, the ligands are found on the peripheral of the defective dicubane core with phenolate oxygens bridging between the body and wingtip ions. For **C1** - **C5**, the ligand, H**L1**$^-$ coordinates in such a fashion that the oximato nitrogen is coordinated to the body ions, allowing for moderate hydrogen bonding to occur between the oximato oxygen and bridging Cl^- anions.[158] For **C52** the ligand, **L2**$^{2-}$ coordinates such that the alkyloxime nitrogens are coordinated to the wingtip ions. This difference is thought to result from the difference in both the oxime-based ligands and the donor group pattern as for all complexes the bulk of the ligand is found on the periphery of the wingtip ion, which for H**L1**$^-$ is the amino sidearm and for **L2**$^{2-}$ is the alkyloxime bridgehead. Previous defective dicubane research perfomed in the Plieger group found that differences in the spacing of donor groups coordinated to the wingtip ion, for example the amino nitrogen and methoxy oxygen (five-membered ring) for **C1** - **C5** and the alkyloxime nitrogens (eight-membered ring) for **C52**, can greatly affect the Ni-X-Ni bridging angles.[148] When comparing **C52** to **C3**, the structurally closest complex of the defective dicubane series, the Ni-X-Ni bridging angles are found to be fairly consistent, with no large differences as shown in Table 6.3. This result was unexpected as the eight-membered ring for **C52** had less steric strain associated than the five-membered ring, however steric strain is most likely induced by the perpendicular coordination of the second aromatic unit of **L2**$^{2-}$.

Table 6.2: Selected bond lengths (Å) and angles (°) of the complex **C52** from crystal structure determination

C52			
Ni1-O1	1.985(3)	Ni2-O1	2.009(3)
Ni1-O5	2.196(3)	Ni2-O2	2.024(3)
Ni1-O7	2.046(3)	Ni2-O7^a	2.141(3)
Ni1-O7^a	2.058(3)	Ni2-N1	2.139(3)
Ni1-O8	2.085(3)	Ni2-N2	2.060(4)
Ni1-Cl1	2.349(1)	Ni2-Cl1^a	2.450(1)
Ni1-O7-Ni1^a	93.92(11)	Ni1-O7-Ni2	97.08(11)
Ni1-O1-Ni2	103.99(12)	Ni1-Cl1-Ni2^a	87.96(4)
Ni1-O7^a-Ni2^a	105.54(12)	Ni1$\cdots$Ni1^a	2.999(1)
Ni2$\cdots$Ni1^a	3.334(1)	Ni1$\cdots$Ni2	3.147(1)
Ni2$\cdots$Ni2^a	5.748(1)		

^{a}1-X, 1-Y, 1-Z

Table 6.3: Selected bond angles (°) of the complexes **C3** and **C52**

	C3*	**C52**
Ni1-O_{OMe}-Ni1[a]/3	95.64	93.92(11)
Ni1-O_{Phen}-Ni2	100.35	103.99(12)
Ni2-Cl-Ni1/3[a]	86.79	87.96(4)
Ni2-O_{OMe}-Ni1[a]/3	106.91	105.53(12)

* Averaged values; Non-averaged values, Table B.2

[a] 1-X, 1-Y, 1-Z

6.1.3 Ni^{II}_7 Cluster

The complex **C53** was found to be a heptanuclear Ni^{II}_7 double cubane, utilising three units of the deprotonated ligand, $\mathbf{L2}^{2-}$ (mode VII, Figure 2.6).[145] Each of the three ligands are coordinated diagonally across the double cubane, with the propylene bridge in a zig-zag arrangement producing a paddlewheel-like rotation of the ligands (Figure E.4). This complex resulted from an attempt to produce a $Ni^{II}Gd^{III}$ dinuclear complex from BF_4^- and NO_3^- metal salts respectively. To date a reproducible synthesis has not been achieved, with attempts following both the intial procedure and a newly developed procedure that reflects the structure composition have both been unsuccessful at producing any material.

The complex was found to crystallise in the monoclinic space group, $P2_1/n$, with the full structure found in the asymmetric unit (Figures 6.3 and 6.4). The metallic core resembles that of a double cubane, where two cubanes are rotated vertically 180° and share a vertice, Ni1. All seven Ni^{II} ions have an octahedral geometry (CShM, Table E.4), with a O_6 donor set for Ni1 consisting of six μ_3-OH^- anions.[146,147,171] The remaining six metal ions, Ni2 - Ni7, have NO_5 donor sets consisting of a phenolate oxygen, an alkyloxime nitrogen, a MeOH molecule, a OMe^- anion, and two OH^- anions. Moderate intermolecular hydrogen bonding is found between the MeOH molecules and both the phenolate oxygens (2.693(4) - 2.736(4)) and the methoxy oxygens (3.045(4) - 3.186(4)) with additional hydrogen bonding between the OH^- anions and alkyloxime oxygens (3.024(4) - 3.126(4)).[158] Within the crystal lattice, one Et_2O molecule can be found, with the SQUEEZE procedure implemented using the crystallographic software, Olex2, to remove diffuse solvent found in the crystal lattice. The result was the removal of 33 electrons per asymmetric unit which equates to one MeOH molecule (18 e^-) and 1.5 H_2O molecules (15 e^-).[208,273]

Within the literature there is an analogous Ni^{II}_7 cluster, $[Ni^{II}_7(\mathbf{L})_3(OH)_6(OEt)_2(EtOH)_2]$ produced by the group of Dong *et al*.[317] Key differences between the two complexes are the atom positions *ortho* and *para* to the phenolate group of the ligands and the use of OEt^- anions and EtOH molecules instead of OMe^- anions and MeOH molecules. Despite these small differences in the ligand and coligands, they do not result in any great differences between the complexes bond lengths and angles. The fluorescent properties of the complex by Dong *et al*. were reported, with excitation at 378 nm resulting in a photoluminescence emission at 469 nm. As **C53** is closely related to the structure by Dong *et al*., it is thought that **C53** could have fluorescent properties however due to limited material this was not tested.

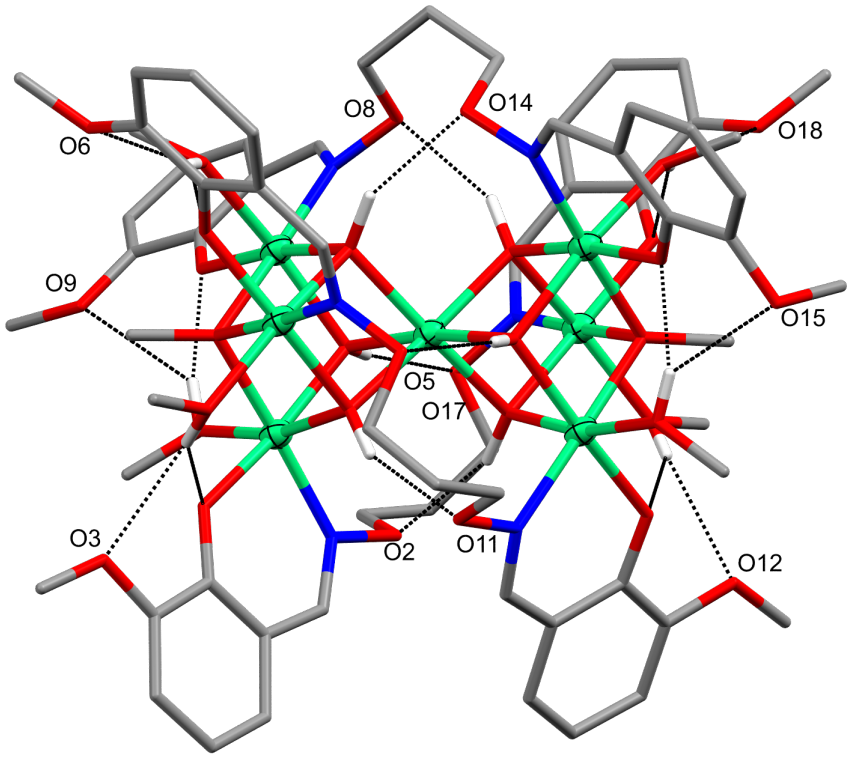

Figure 6.3: Full molecular structure of $[Ni^{II}_7(\mathbf{L2})_3(OH)_6(OMe)_2(MeOH)_2]\cdot Et_2O$, **C53**. Non-interacting hydrogen atoms and lattice solvates have been omitted for clarity, hydrogen bonding represented as black dotted lines, and the thermal ellipsoids of the metal ions are shown at 70% probability. Colour code: Ni^{II} = light green, N = blue, O = red, C = grey, and H = white.

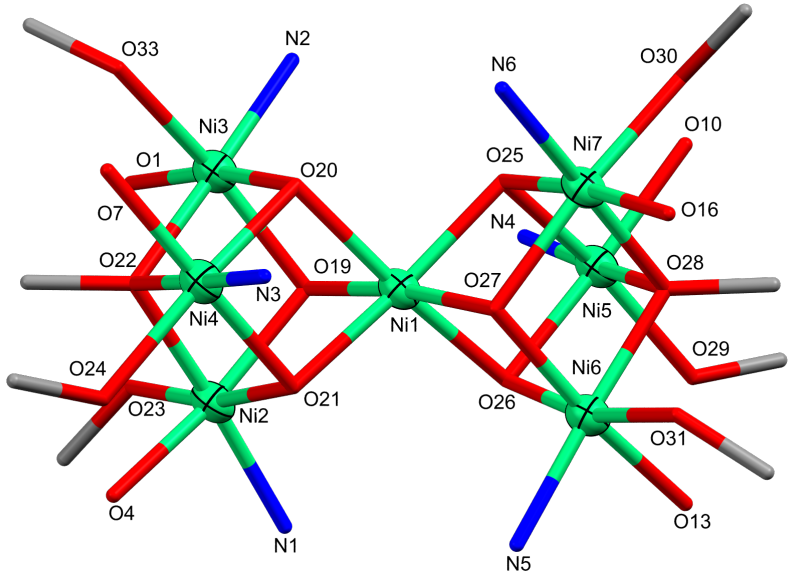

Figure 6.4: Figure showing the metallic core of **C53**. Hydrogen atoms have been omitted for clarity and the thermal ellipsoids of the metal ions are shown at 70% probability. Colour code: Ni^{II} = light green, N = blue, O = red, and C = grey.

Table 6.4: Selected bond lengths (Å) and angles (°) of the complex **C53** from crystal structure determination

			C53		
Ni1-O19	2.062(3)	Ni3-O20	2.072(3)	Ni5-O29	2.111(3)
Ni1-O20	2.069(3)	Ni3-O22	2.041(3)	Ni5-N4	2.065(3)
Ni1-O21	2.049(3)	Ni3-O33	2.138(3)	Ni6-O13	2.037(3)
Ni1-O25	2.050(3)	Ni3-N2	2.048(4)	Ni6-O26	2.045(3)
Ni1-O26	2.070(3)	Ni4-O7	2.032(3)	Ni6-O27	2.067(3)
Ni1-O27	2.076(3)	Ni4-O20	2.038(3)	Ni6-O28	2.063(3)
Ni2-O4	2.011(3)	Ni4-O21	2.074(3)	Ni6-O31	2.139(3)
Ni2-O19	2.055(3)	Ni4-O22	2.056(3)	Ni6-N5	2.050(3)
Ni2-O21	2.048(3)	Ni4-O24	2.122(3)	Ni7-O16	2.035(3)
Ni2-O22	2.058(3)	Ni4-N3	2.045(3)	Ni7-O25	2.072(3)
Ni2-O23	2.101(3)	Ni5-O10	2.053(3)	Ni7-O27	2.034(3)
Ni2-N1	2.060(3)	Ni5-O25	2.039(3)	Ni7-O28	2.053(3)
Ni3-O1	2.040(3)	Ni5-O26	2.067(3)	Ni7-O30	2.093(3)
Ni3-O19	2.047(3)	Ni5-028	2.052(3)	Ni7-N6	2.061(3)
Ni1-O19-Ni2	97.18(11)	Ni1-O26-Ni5	96.89(11)	Ni3-O20-Ni4	97.98(12)
Ni1-O19-Ni3	99.01(11)	Ni1-O26-Ni6	98.85(11)	Ni3-O22-Ni4	98.42(12)
Ni1-O20-Ni3	97.95(11)	Ni1-O27-Ni6	97.96(11)	Ni5-O25-Ni7	98.42(12)
Ni1-O20-Ni4	97.98(12)	Ni1-O27-Ni7	97.70(11)	Ni5-O26-Ni6	97.93(12)
Ni1-O21-Ni2	97.83(11)	Ni2-O19-Ni3	97.24(11)	Ni5-O28-Ni6	97.83(12)
Ni1-O21-Ni4	97.47(12)	Ni2-O21-Ni4	97.39(12)	Ni5-O28-Ni7	97.93(12)
Ni1-O25-Ni5	98.42(11)	Ni2-O22-Ni3	97.33(12)	Ni6-O27-Ni7	97.67(12)
Ni1-O25-Ni7	97.31(11)	Ni2-O22-Ni4	97.64(12)	Ni6-O28-Ni7	97.19(12)
Ni1···Ni2	3.088(1)	Ni1···Ni7	3.095(1)	Ni3···Ni7	5.485(1)
Ni1···Ni3	3.125(1)	Ni2···Ni3	3.078(1)	Ni4···Ni5	6.182(1)
Ni1···Ni4	3.100(1)	Ni2···Ni4	3.097(1)	Ni5···Ni6	3.102(1)
Ni1···Ni5	3.096(1)	Ni2···Ni6	5.325(1)	Ni5···Ni7	3.096(1)
Ni1···Ni6	3.125(1)	Ni3···Ni4	3.102(1)	Ni6···Ni7	3.087(1)

6.2 3*d*3*d*'3*d* Trinuclear Clusters

The complexes **C54** and **C55** were found to be trinuclear heterometallic $M^{II}{}_2Zn^{II}$ complexes, which resulted from attempts to produce the dinuclear combinations of $Co^{II}Zn^{II}$ and $Ni^{II}Zn^{II}$. The complexes were synthesised by RT reactions between H_2**L2**, $M(OAc)_2{\cdot}H_2O$ (M = Co^{II} and Ni^{II}), and $Zn(NO_3)_2{\cdot}6H_2O$ in a 1 : 1 : 1 molar ratio. A colour change from the pale yellow ligand solution to either a pink (**C54**) or light green (**C55**) solution confirmed successful coordination. The complexes were isolated by slow vapour diffusion of Et_2O into the reaction solution where X-ray quality crystals were obtained. As is generally the case, when remaking and/or bulking complexes, the stoichiometry is made to reflect the composition of the complex. For these two complexes that would result in a 2 : 2 : 1 molar ratio of H_2**L2**, $M(OAc)_2{\cdot}H_2O$, and $Zn(NO_3)_2{\cdot}6H_2O$ however when this was attempted there was no resulting crystalline material. Upon remaking the complexes for a second time, a 1 : 1 : 1 molar ratio was used and this resulted in **C54** in four weeks and a few crystals of **C55** in 18 weeks. Although the initial crystallisations of **C54** and **C55** crystallised in the same time period, it is presumed that the extended crystallisation of the remake of **C55** is due to differences in solubility.

The complex **C54** was found to crystallise in the monoclinic space group, $P2_1/c$ whereas **C55** crystallised in the triclinic space group, $P\bar{1}$. For both complexes the whole structure can be found in the asymmetric unit as represented in Figure 6.5. The complexes are composed of two deprotonated alkyloxime ligands, **L2**$^{2-}$, which are coordinated to three metal ions (Mode III, Figure 2.6). The two M^{II} ions are found in the M1 pocket of each ligand with the Zn^{II} ion found between the two M2 pockets. All of the metal ions are six-coordinate with distorted octahedral geometries (CShM, Table 6.5).[146,147,171] For **C54**, Co1 was found to be more distorted than the other metal ions (CShM values of 6.295, 4.806, and 4.814 for Co1, Co3, and Zn2 respectively), thought to be the result of the ligand distortion induced by the coordination of the metal ions and the angle at which the $NO_3{}^-$ anion coordinates. The M1 and M3 ions have a N_2O_4 donor set consisting of two phenolate oxygens, two alkyloxime nitrogens, and a bidentate $NO_3{}^-$ anion. Zn2 has an O_6 donor set consisting of four phenolate oxygen atoms, two from each ligand, and two methoxy oxygen atoms, one from each ligand. For **C54**, the SQUEEZE procedure was implemented using Olex2 to remove diffuse solvent in the crystal lattice. The result was the removal of 54 electrons (e^-) per asymmetric unit which equates to 5.5 H_2O molecules (55 e^-).[208,273]

Similar to the other 3*d* complexes where the metal ion in the inner pocket is octahedral, the propylene bridge has a zig-zag appearance rather than perpendicular to the alkyloxime nitrogen and oxygen atoms. Again this is thought to be due to steric hinderance, due to not only the bidentate $NO_3{}^-$ anion, but also the close proximity of the non-coordinated methoxy group of the other ligand.

These trinuclear complexes were an unexpected result as the dinuclear structures, **C10** ($Cu^{II}Zn^{II}$) and **C13** ($Zn^{II}Mn^{II}$), had previously been obtained. The mechanism for the formation of the trinuclear complexes versus the dinuclear complexes is not entirely understood, however several factors such as coordination pocket preference and coordination of the metal ions and anions/solvents play a role. One theory is that the ligand coordinates to the Co^{II} ion first, with the $NO_3{}^-$ anion completing

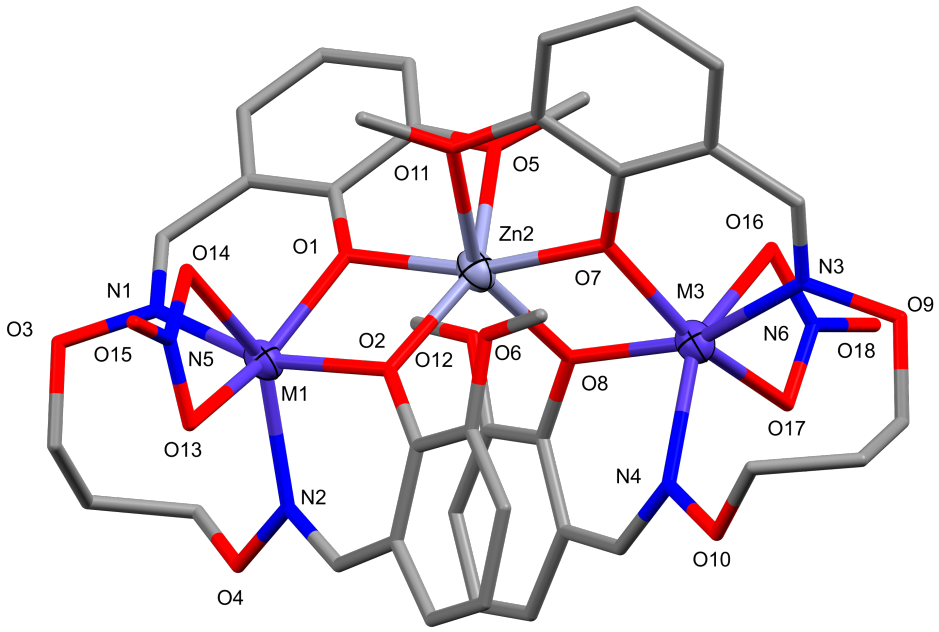

Figure 6.5: Representative structure of $[M^{II}_2Zn^{II}(\mathbf{L2})_2(NO_3)_2]$ (M = Co^{II} (**C54**) and Ni^{II} (**C55**)). Hydrogen atoms have been omitted for clarity and the thermal ellipsoids of the metal ions are shown at 70% probability. Colour code: M^{II} = dark purple, Zn^{II} = light purple, N = blue, O = red, and C = grey.

the donor set. The coordination of the NO_3^- anion induces the large ligand distortion increasing the size of the M2 pocket. The widening of the pocket results in the Zn^{II} ion only coordinating to one of the two methoxy oxygens, allowing a second $[Co^{II}\mathbf{L2}(NO_3)]$ unit to coordinate to the Zn^{II} ion. As shown in Table 6.6, for **C10**, the dinuclear $Cu^{II}Zn^{II}$ complex, the coordination of the Cu1 ion is stronger than the coordination of the Zn2 ion with shorter phenolate bonds (O1 and O2) whereas for the trinuclear structures, M1/3 has weaker coordination than found for **C10** however the coordination of Zn2 is stronger.

As mentioned in the 3*d*3*d*' series (Chapter 4), the most common type of structure utilising an alkyloxime ligand in the literature (CCDC v1.20, 02/08/22) was M_3L_2 clusters. For the majority of these complexes, the ligands do not have functionalised 3-positions (H_2**L2** has a methoxy group in the 3-position) and therefore utilise anions to bridge between the inner and outer metal ions. This leaves the central ion with a donor set of four phenolate oxygens and two bridging anions, with OAc^- the most common anion found. There are two examples where the ligand is functionalised with a methoxy group at the three-position, with the coordination of the central ion reflecting what was found for **C54** and **C55**, these structures however were found to be homometallic Ni^{II}_3 and Co^{II}_3.

Table 6.5: Selected bond lengths (Å) and angles (°) of the complexes **C54** and **C55** from crystal structure determination

	C54	**C55**
M1-O1	1.987(2)	2.000(2)
M1-O2	2.042(2)	2.003(2)
M1-N1	2.132(3)	2.058(3)
M1-N2	2.112(3)	2.089(3)
M1-O13	2.154(2)	2.190(2)
M1-O14	2.282(2)	2.087(2)
Zn2-O1	2.019(2)	1.990(2)
Zn2-O2	2.033(2)	2.022(2)
Zn2-O5	2.251(2)	2.322(2)
Zn2-O7	2.018(2)	1.995(2)
Zn2-O8	2.044(2)	2.037(2)
Zn2-O11	2.272(2)	2.348(2)
M3-O7	1.981(2)	1.983(2)
M3-O8	2.046(2)	2.006(2)
M3-N3	2.114(3)	2.047(3)
M3-N4	2.111(3)	2.083(3)
M3-O16	2.310(2)	2.206(2)
M3-O17	2.110(2)	2.085(2)
M1-O1-Zn2	105.08(9)	101.94(8)
M1-O2-Zn2	102.55(9)	100.78
Zn2-O7-M3	105.15(9)	104.10(9)
Zn2-O8-M3	101.89(9)	101.79(8)
M1···Zn2	3.180(1)	3.101(1)
Zn2···M3	3.175(1)	3.137(1)
M1···M3	5.953(1)	5.899(1)

Table 6.6: Selected bond lengths (Å) of the complexes **C10**, **C54**, and **C55** from crystal structure determination

	C10	**C54**	**C55**
M1-O1	1.931(3)	1.987(2)	2.000(2)
M1-O2	1.936(3)	2.042(2)	2.003(2)
M1-N1	1.973(4)	2.132(3)	2.058(3)
M1-N2	1.956(4)	2.112(3)	2.089(3)
Zn2-O1	2.092(3)	2.019(2)	1.992(2)
Zn2-O2	2.085(3)	2.033(2)	2.022(2)
Zn2-O5	2.417(3)	2.251(2)	2.322(2)
Zn2-O6/11	2.435(3)	2.272(2)	2.348(2)
Zn2-O7	–	2.018(2)	1.995(2)
Zn-O8	–	2.044(2)	2.037(2)
M1···Zn2	3.194(1)	3.180(1)	3.101(1)
M3···Zn2	–	3.175(1)	3.137(1)

6.3 Polymers and More

After finding that the $Cu^{II}Gd^{III}$ complex, **C17**, could be produced in a relatively short period of time, further complexations were attempted using **C17** as a starting platform to extended structures by the addition of various anions and coligands. One coligand used was Na oxalate and when added in excess, the result was three different complexes (**C56** - **C58**) from one complexation. The complexes were synthesised by a RT reaction between **C17** and $Na_2C_2O_4$ in a 1 : 7 molar ratio. Isolation of the complexes was achieved through the use of different crystallisation methods: slow evaporation of the complexation solution (**C56** and **C58**) and Et_2O vapour diffusion (**C57**). X-ray quality crystals were obtained over a period of one to seven weeks. All complexes were found to be heterometallic, with **C56** and **C57** polymeric structures and **C58** a dinuclear structure. The complexes were found to crystallise in either the monoclinic space groups, $P2_1/n$ (**C56**) or $P2_1/c$ (**C58**) or the triclinic space group, $P\bar{1}$ (**C57**).

When only considering one repeating unit ot **C56** (Figure 6.6a), one deprotonated ligand, $\mathbf{L2}^{2-}$ is coordinated to both a Cu^{II} ion and a Gd^{III} ion (Mode I, Figure 2.6), with the unit resembling that of the dinuclear series. Cu1 is five-coordinate with a vacant octahedral geometry (CShM, Table E.4) and a N_2O_3 donor set consisting of two alkyloxime nitrogens, two phenolate oxygens, and one MeOH molecule.[146,147,281] Gd1 is nine-coordinate with a spherical capped square antiprism geometry (CShM, Table E.4) and O_9 donor set consisting of two phenolate oxygens, two methoxy oxygens, a monodentate NO_3^- anion, and two bidentate oxalate (Ox^{2-}) anions, which bridge above-plane and below-plane as shown by Figures 6.6b and 6.6c.[146,147,270] Moderate intramolecular hydrogen bonding is found between the Ox^{2-} anion (O12) that bridges above-plane and the coordinated MeOH molecule (O7), O7···O12, 2.703(12) Å.[158] The SQUEEZE procedure was implemented using the crystallographic software, Olex2, to remove diffuse solvent in the crystal lattice, resulting in the removal of 18 electrons per asymmetric unit, which equates to one MeOH molecule ($18e^-$).[208,273]

The second polymeric structure, **C57** consists of one deprotonated ligand, $\mathbf{L2}^{2-}$ coordinated to both a Cu^{II} ion and a Na^{I} ion (Mode IV, Figure 2.6), again resembling that of the dinuclear series when considering one unit (Figure 6.7a).[145] The coordination of $\mathbf{L2}^{2-}$ in this structure where the alkyloxime oxygen is coordinated to a metal ion is uncommon, as mentioned in Section 2.3, only having been reported twice previously.[133,134] Cu1 is four-coordinate with a square planar geometry (CShM, Table E.4) and typical N_2O_2 donor set consisting of two alkyloxime nitrogens and two phenolate oxygens, additionally Cu1 is weakly coordinated to a monodentate NO_3^- anion (2.463(4) Å) and a phenolate oxygen (2.511(3) Å) from above- and below-plane units.[146,147,267] Na1 is seven-coordinate with a distorted pentagonal bipyramidal geometry (CShM, Table E.4) and an O_7 donor set consisting of two phenolate oxygens, two methoxy oxygens, two monodentate NO_3^- anions, and an above-plane alkyloxime oxygen.[146,147,210] Within the crystal lattice there is one MeOH molecule (O10) per asymmetric unit, which is found to form hydrogen bonds with the bridging NO_3^- anion (O9), O10···O9 3.064(7) Å.

The different bridging groups in the polymeric complexes **C56** and **C57** have resulted in different arrangements and stacking of the dinuclear units. For **C56**, the polymer has a zig-zag appearance with the dinuclear units alternating left and right

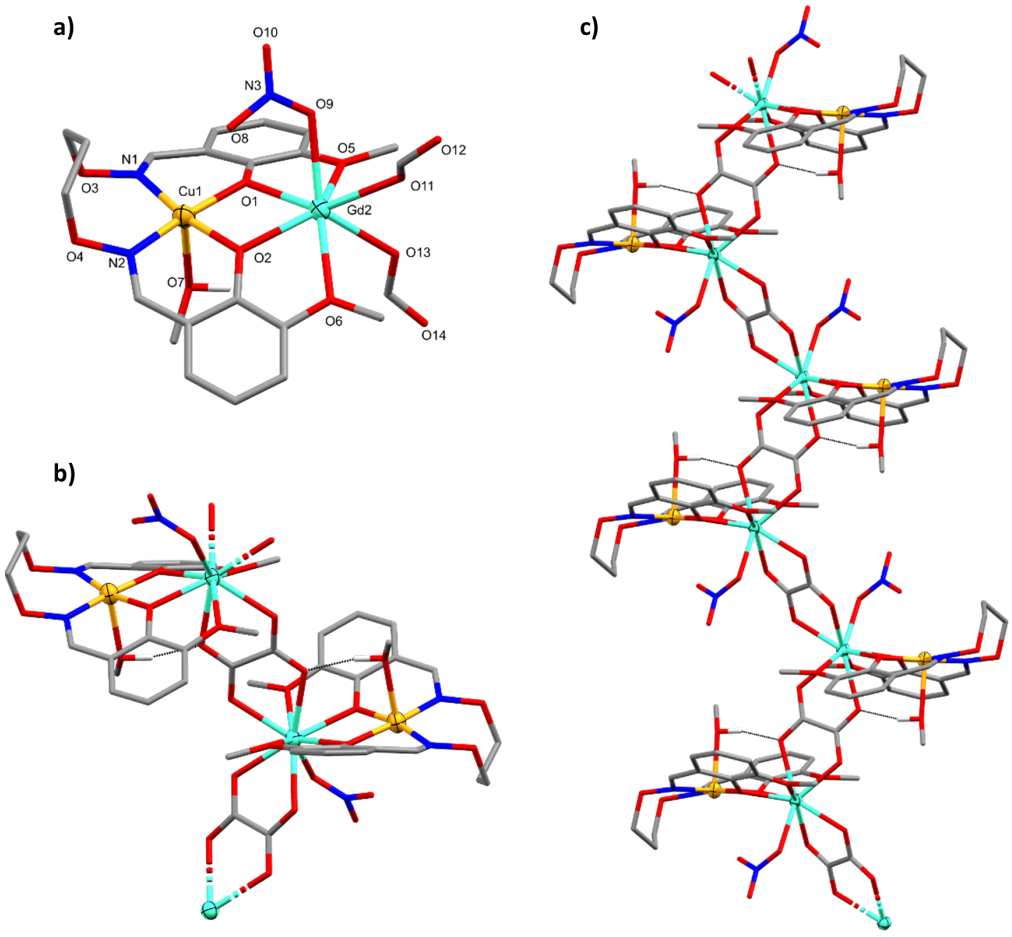

Figure 6.6: Asymmetric unit (a), two units (b), and extended polymeric network (c) of the complex ∞[$Cu^{II}Gd^{III}$**L2**(MeOH)(NO_3)($Ox)_2$], **C56**. Non-interacting hydrogen atoms have been omitted for clarity, hydrogen bonding represented as black dotted lines, and the thermal ellipsoids of the metal ions are shown at 50% probability. Colour code: Cu^{II} = dark yellow, Gd^{III} = aqua, N = blue, O = red, C = grey, and H = white.

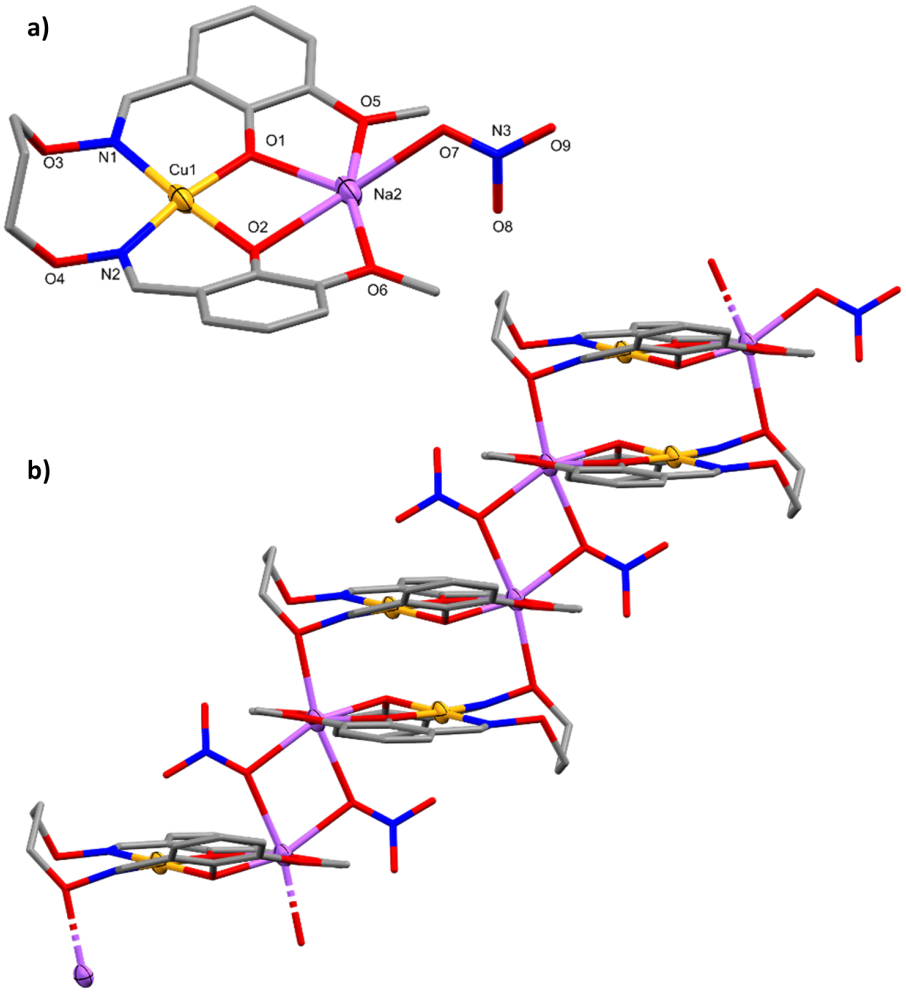

Figure 6.7: Asymmetric unit (a) and the extended polymeric structure (b) of the complex ∞[$Cu^{II}Na^{I}$**L2**(NO_3)]·MeOH, **C57**. Hydrogen atoms and lattice MeOH molecules have been omitted for clarity and the thermal ellipsoids of the metal ions are shown at 50% probability. Colour code: Cu^{II} = dark yellow, Na^{I} = purple, N = blue, O = red, and C = grey.

whereas the stacking for **C57** was found to be an off-centered type of zig-zag with alternating bridges of NO_3^- anions and alkyloxime oxygens. If the bridges were solely NO_3^- anions, the stacking of **C57** would resemble that of **C56** with an alternating zig-zag however the alkyloxime oxygen bridges interrupt this arrangement with two units on top of each other.

The complex, **C58** was found to be a dinuclear structure, similarly to the complexes reported in Chapters 4 and 5. The complex resembles that of **C58** with one unit of $\mathbf{L2}^{2-}$ coordinated to both a Cu^{II} ion and a Na^{I} ion (Mode I, Figure 2.6) as shown in Figure 6.8. Cu1 is four-coordinate with a square planar geometry (CShM, Table E.4) and typical N_2O_2 donor set of two alkyloxime nitrogens and two phenolate oxygens.[146,147,267] Na1 is six-coordinate with a distorted pentagonal pyramidal geometry (CShM, Table E.4) and O_6 donor set consisting of two phenolate oxygens, two methoxy oxygens, and two H_2O molecules.[146,147,171] One NO_3^- anion is found in the crystal lattice to balance the overall charge of the complex. Although **C58** and the polymeric complex **C57** are very similar in terms of asymmetric unit, it is thought the inclusion of H_2O into the crystallisation environment for **C58** (a consequence of slow evaporation and the solution being open to the air for an extended period of time) hindered the polymer formation.

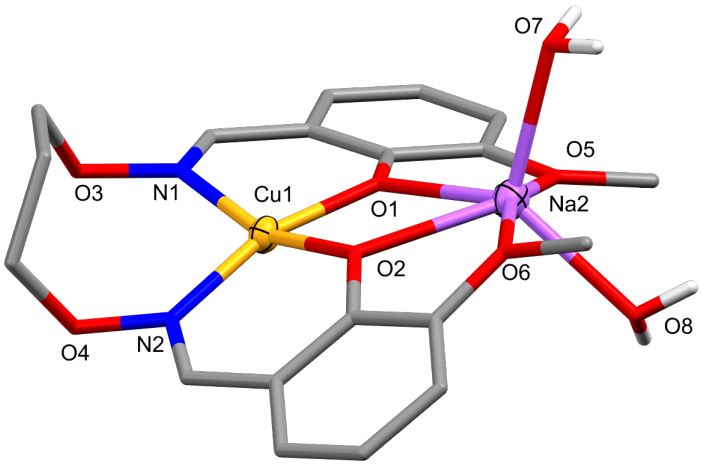

Figure 6.8: Full molecular structure of $[Cu^{II}Na^{I}\mathbf{L2}(H_2O)_2][NO_3]$, **C58**. Hydrogen atoms, apart from those of donor atoms and the lattice NO_3^- anion have been omitted for clarity. Thermal ellipsoids of the metal ions are shown at 70% probability. Colour code: Cu^{II} = dark yellow, Na^{I} = purple, N = blue, O = red, C = grey, and H = white.

For all three complexes, the aromatic rings are found to be non-planar with respect to each other, with intersecting planes at 45.2°, 23.5°, and 37.3° for **C57** - **C59** respectively. This is thought to be the result of steric strain induced by the bridging groups for the polymers **C56** and **C57**, with additional strain induced by the weakly coordinated oxygens for **C57**. The non-planarity for **C58** is not entirely understood, as there should be minimal steric strain induced by the H_2O coordinates. Comparing the alkyloxime nitrogen, phenolate and methoxy oxygen distances with **C8** and **C17**, more planar complexes it can be seen that the smaller metal ions fit better in the M2 pocket.

Table 6.7: Selected bond lengths (Å) and angle (°) of the complexes **C56** - **C58** from crystal structure determination

	C56	**C57**	**C58**
Cu1-O1	1.942(7)	1.928(3)	1.912(2)
Cu1-O2	1.958(8)	1.970(3)	1.913(2)
Cu1-N1	1.952(9)	2.020(4)	1.993(2)
Cu1-N2	2.002(10)	1.986(4)	1.953(2)
Cu1-O7	2.358(9)	–	–
M2-O1	2.352(7)	2.353(4)	2.370(2)
M2-O2	2.334(7)	2.388(3)	2.407(2)
M2-O4	–	2.455(4)[c]	–
M2-O5	2.492(7)	2.478(4)	2.492(2)
M2-O6	2.513(7)	2.406(4)	2.462(2)
M2-O7	–	2.389(4)/ 2.502(4)[b]	2.292(2)
M2-O8	–	–	2.336(2)
M2-O9	2.455(8)	–	–
M2-O11	2.393(7)	–	–
M2-O12	2.412(8)[a]	–	–
M2-O13	2.405(7)	–	–
M2-O14	2.478(8)[b]	–	–
Cu1-O1-M2	106.10(3)	104.98(15)	108.05(8)
Cu1-O2-M2	106.20(3)	102.35(14)	106.57(8)
M2-O7-M2[b]	–	101.77(13)	–
Cu1···M2	3.441(2)	3.405(2)/ 3.835(2)[c]	3.475(1)
M2···M2	6.201(1)[a] / 6.320(1)[b]	3.796(4)	–

[a]1-X, 2-Y, 1-Z; [b]1-X, 1-Y, 1-Z; [c]-X, 1-Y, 1-Z

6.4 Large Clusters

6.4.1 Acetate Cluster

Throughout this research, many attempts were made to synthesise a dinuclear complex with Cu^{II} and Ni^{II} metal salts to complete the 3*d*3*d*′ series. One complexation/crystallisation attempt produced a few green block-like crystals which were found to be the large OAc^- appended polymeric cluster, **C59**. The polymer resulted from the RT reaction between H_2**L2**, $Cu(NO_3)_3{\cdot}3H_2O$, and $Ni(OAc)_2{\cdot}4H_2O$ in a 1 : 1 : 1 molar ratio. The complex was isolated by Et_2O vapour diffusion with X-ray quality crystals obtained after nine weeks. Further attempts to remake **C59** following the original ligand containing method and a second method where the complexation reflected the complex composition (no ligand was present in the crystal structure) have been unsuccessful at producing **C59**. The ligand containing remake successfully produced crystals however they were found to be that of **C62**, discussed in the following section.

The polymeric cluster, **C59** was found to crystallise in the rhombohedral space group, $R\bar{3}c$. The asymmetric unit consists of two Cu^{II} ions, two Ni^{II} ions, and one Na^{I} ion coordinated to H_2O molecules, OH^-, and OAc^- anions with an additional Na^{I} ion found in the crystal lattice (Figure 6.9a). When only considering one unit of the polymer (Figure 6.9b), the metallic core consists of a Cu^{II}_{12} cuboctahedron with one Ni^{II} ion found at each vertice of the cuboctahedron (eight in total). Two Na^{I} ions are found on the exterior of the cuboctahedron, *para* to one another, with the lattice Na^{I} ion found in the void created by the cuboctahedron. Cu1 and Cu2 are both five-coordinate with a vacant octahedron geometry (CShM, Table E.4) with O_5 donor sets consisting of four OH^- anions and one bridging OAc^- anion.[146,147,281] Ni1 (Ni ions adjacent to the coordinated Na^{I} ions) and Ni2 are both six-coordinate with an octahedral geometry (CShM, Table E.4) and O_6 donor sets consisting of three OH^- anions and either three bridging OAc^- anions (Ni1) or one bridging OAc^- anion and two H_2O molecules. Na1, similarly to the Ni^{II} ions is six-coordinate with an octahedral geometry (CShM, Table E.4) and an O_6 donor set consisting of three bridging OAc^- anions and three bridging oxide anions.[146,147,171] Within the structure there are two different coordination modes found for the OAc^- anions, with a 2.1_12_1 Harris cooridnation mode for the bridging between the Cu^{II} and Ni^{II} ions and a $3.2_{12}1_3$ Harris cooridnation mode for the bridging between the Cu^{II}, Ni^{II}, and Na^{I} ions.[145] As shown in Figure 6.9c, the polymer forms a linear chain with each alternating cuboctahedron unit arranged in such a fashion that the view along the *c* axis (looking along the Na^{I} axis, straight through the void), creates a type of six-point star as shown in Figure 6.10.

Intramolecular hydrogen bonding is found in the complex between the H_2O molecules (O7 and O6) and bridging OAc^- anions (O3 and O9). Strong hydrogen bonding (X···A, 2.2 - 2.5 Å)[158] is found between O7···O9, 2.489(11) Å with moderate hydrogen bonding found between O6···O3, 2.626(10) Å. The SQUEEZE procedure was implemented for **C59** using the crystallographic software, Olex2, to remove disorder in the crystal lattice. The result was removal of 64 electrons per asymmetric unit which equates to three MeOH molecules (54 e^-) and one H_2O molecule (10 e^-).[208,273]

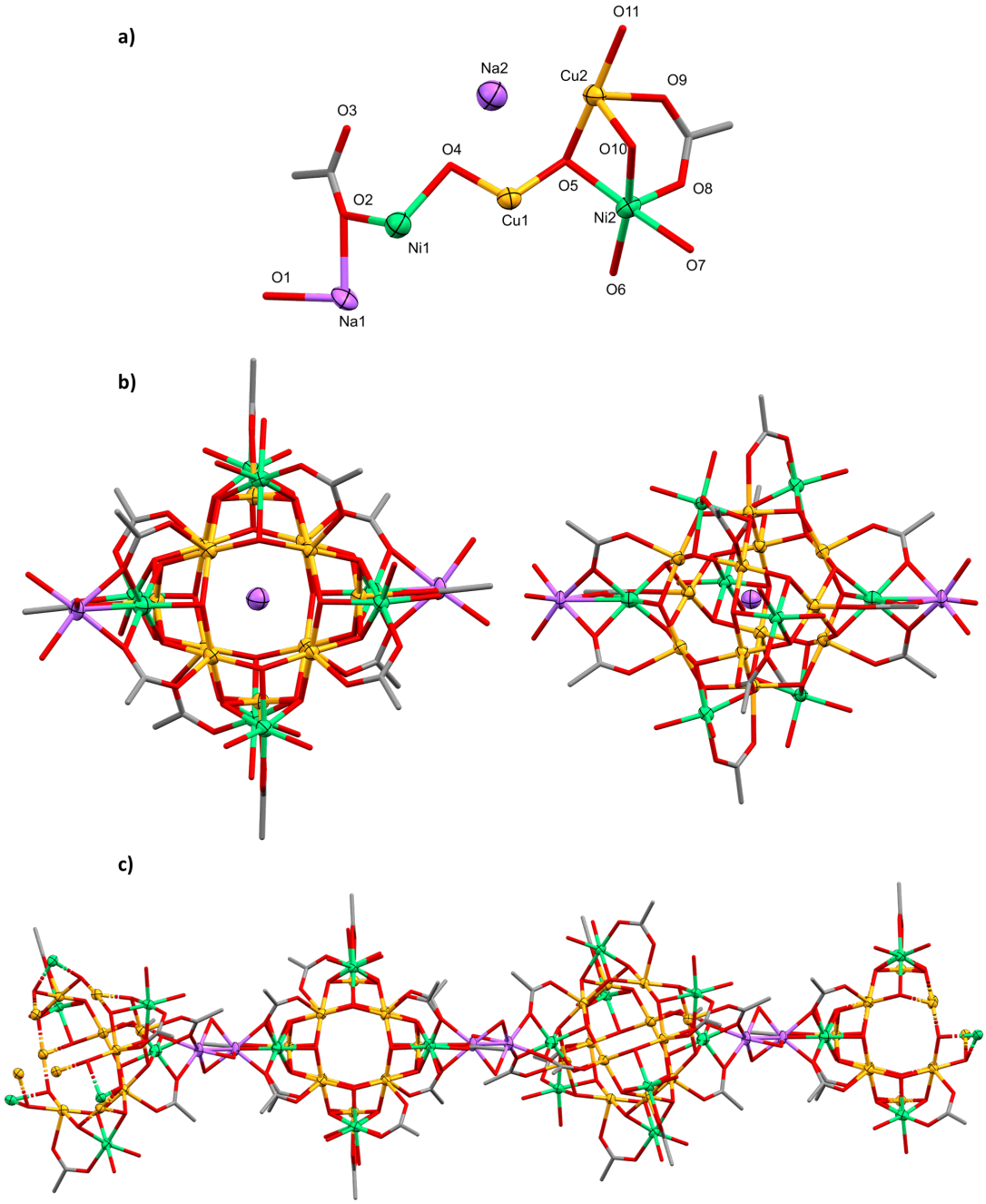

Figure 6.9: Asymmetric unit (a), two views of a single unit (b), and the extended polymeric structure of $\infty[Na^{I}][Cu^{II}_{2}Ni^{II}_{2}Na^{I}O(H_2O)_2(OH)_4(OAc)_2]$, **C59**. Hydrogen atoms and lattice Na^{I} ions (c) have been omitted for clarity. Thermal ellipsoids of the metal ions are shown at 70% probability. Colour code: Cu^{II} = yellow, Ni^{II} = green, Na^{I} = purple, O = red, and C = grey.

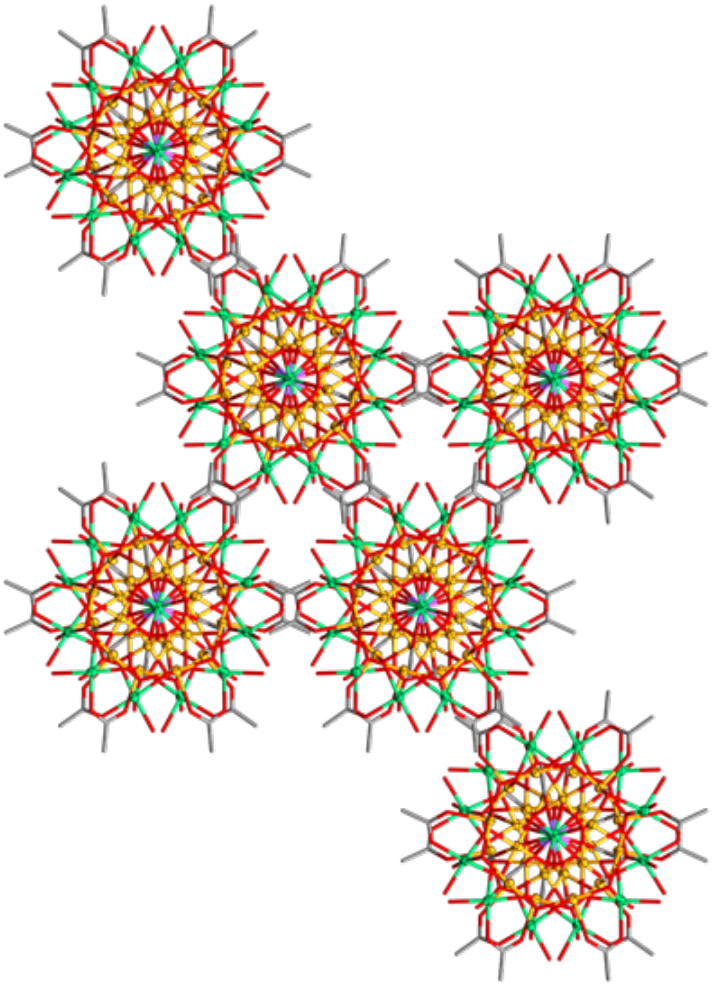

Figure 6.10: Unit cell packing of **C59** along the *c* axis. Hydrogen atoms have been omitted for clarity and the thermal ellipsoids of the metal ions are shown at 70% probability. Colour code: Cu^{II} = yellow, Ni^{II} = green, Na^{I} = purple, O = red, and C = grey.

Table 6.8: Selected bond lengths (Å) and angles (°) of the complex **C59** from crystal structure determination

C59					
Cu1-O3[a]	2.288(7)	Ni1-O2	2.050(7)	Ni2-O10	2.080(6)
Cu1-O4	1.976(6)	Ni1-O2[a]	2.050(7)	Ni2-O11[b]	2.109(6)
Cu1-O4[a]	1.985(6)	Ni1-O2[d]	2.050(7)	Na1-O1	2.022(12)
Cu1-O5	1.966(6)	Ni1-O4	2.071(6)	Na1-O1[a]	2.022(11)
Cu1-O11[b]	1.974(6)	Ni1-O4[a]	2.072(6)	Na1-O1[d]	2.022(11)
Cu2-O5	1.985(6)	Ni1-O4[d]	2.072(7)	Na1-O2	2.118(8)
Cu2-O9	2.283(8)	Ni2-O5	2.069(6)	Na1-O2[a]	2.118(8)
Cu2-O10	1.990(6)	Ni2-O6	2.050(6)	Na1-O2[d]	2.118(8)
Cu2-O10[c]	1.979(6)	Ni2-O7	2.056(7)	Cu1-O4-Cu1[d]	127.50(3)
Cu2-O11	1.977(6)	Ni2-O8	2.032(6)	Cu1-O4-Ni1	93.20(3)
Cu1[d]-O4-Ni1	92.90(2)	Cu1[c]-O11-Ni2[c]	96.60(2)	Cu2[c]-O10-Ni2	97.30(3)
Cu1-O5-Cu2	118.90(3)	Cu2-O5-Ni2	94.20(2)	Cu2-O11-Ni2[c]	96.40(3)
Cu1-O5-Ni2	98.20(2)	Cu2[b]-O10-Cu2	121.99(3)	Ni1-O2-Na1	82.70(3)
Cu1[c]-O11-Cu2	117.60(3)	Cu2-O10-Ni2	93.80(2)	Na1-Na1[e]	69.70(5)
Cu1···Cu1[a]	3.552(2)	Cu2···Cu2[b]	3.471(1)	Ni1···Na1	2.754(6)
Cu1···Cu2	3.402(2)	Cu2···Ni1	5.986(3)	Ni2···Ni2[f]	10.258(3)
Cu1···Cu2[b]	3.379(2)	Cu2···Ni2	2.971(2)	Ni2···Na1	7.742(4)
Cu1···Ni1	2.940(2)	Cu2···Na1	8.383(5)	Na1···Na1[f]	15.225(11)
Cu1···Ni2	3.050(2)	Ni1···Ni1[f]	9.717(6)	Na1···Na1[g]	2.312(11)
Cu1···Na1	5.276(5)	Ni1···Ni2	5.864(2)		
Cu2···Cu1[d]	4.895(2)	Ni1···Ni2[f]	8.089(3)		

[a]1-Y, +X-Y, +Z; [b]1/3-Y+X, -1/3+X, 2/3-Z; [c]1/3+Y, 2/3-X+Y, 2/3-Z; [d]1+Y-X, 1-X, +Z

[e]1/3+Y, 1/3+X, 7/6-Z; [f]4/3-X, 2/3-Y, 2/3-Z; [g]4/3-X, 2/3-X+Y, 7/6-Z

6.4.2 $Cu^{II}_{12}Eu^{III}_{4}$ Cluster

Similarly to the previous large complex, the heterometallic $Cu^{II}_{12}Eu^{III}_{4}$ cluster, **C60** came about when attempting to produce dinuclear complexes using H_4**L3**. The complex **C60**, was synthesised by a RT reaction between H_4**L3**, $Cu(OAc)_2 \cdot H_2O$, $Eu(NO_3)_3 \cdot 6H_2O$, and Et_3N in a 1 : 1 : 1 : 2 molar ratio. Isolation of the complex was achieved by Et_2O vapour diffusion with a few X-ray quality crystals produced after approximately 8.5 months. To date a suitable synthetic method has not been developed, with subsequent attempts to form both the original complexation and the crystal composition having been unsuccessful. Within the asymmetric unit, half of the complex is found with the full structure shown in Figure 6.11. The large cluster was found to crystallise in the monoclinic space group, $C2/m$ and consists of four units of the deprotonated ligand, $\mathbf{L3}^{4-}$ (Harris coordination Modes I and II; Figure 2.8)[145] coordinated to 12 Cu^{II} ions and four Eu^{III} ions forming a pseudo bowl-like shape (Figures 6.11 and 6.12).

The composition of **C60** consists of 12 Cu^{II} ions, where two ions, Cu1 and Cu4, are four-coordinate with a square planar geometry with the remaining five-coordinate, with a spherical square pyramidal geometry (CShM, Table E.4).[146,147,267,281] The donor sets vary among the ions, Cu1 has a typical N_2O_2 donor set consisting of two alkyloxime nitrogens and two phenolate oxygens, with an additional weakly coordinated H_2O molecule. Cu4 has an O_4 donor set consisting of one phenolate oxygen, one hydroxy oxygen, and two OH^- anions, with a weakly coordinated OAc^- anion. Cu8 reflects that of Cu1 however the H_2O molecule is coordinated giving a N_2O_3 donor set. Cu2 and Cu7 have O_5 donor sets consisting of two phenolate oxygens, two hydroxy oxygens and one bridging OAc^- anion. Cu5 similarly has an O_5 donor set however conisting of one phenolate oxygen, one hydroxy oxygen, one bridging OAc^- anion and two OH^- anions. Lastly, Cu3 and Cu6 have NO_4 donor sets consisting of one phenolate oxygen, one hydroxy oxygen, one alkyloxime nitrogen, and two OH^- anions. For the Eu^{III} ions there are two different geometry/donor set combinations with Eu1 and Eu3 eight-coordinate, with a square antiprismatic geometry and Eu2 nine-coordinate with a muffin geometry (CShM, Table E.4).[146,147,270,283] All of the Eu^{III} ions have oxygen donors with O_8 and O_9 donor sets, which for Eu1 and Eu3 consists of two hydroxy oxygens, two OH^- anions, and four bridging OAc^- anions. For Eu2 the donor set consists of two hydroxy oxygens, one OH^- anions, two bridging OAc^- anions and two bidentate $NO_3{}^-$ anions.

As mentioned above, there are two different modes for which the ligand coordinates to the metal ions, with the two outer most ligands coordinating in the same fashion as Mode I and the inner ligands coordinating alike Mode II (Figure 2.8). There are two different coordination modes found for the OAc^- anions with 2.1_11_2 and $3.2_{12}1_3$ (Figure A.17).[145] Solvent molecules are found in the crystal lattice with one H_2O molecule on the periphery of the bowl-like structure with one Cl^- anion and two MeOH molecules found within the cavity of the bowl-like structure. Moderate intramolecular hydrogen bonding is found between the OH^- anions (O13, O14, O16, and O17) and both the alkyloxime oxygens (O5 and O8), O13$\cdots$O5 2.929(12) Å and O17$\cdots$O8 2.820(9) Å and lattice Cl^- anion (Cl1), O14$\cdots$Cl1 3.105(6) Å and O16$\cdots$Cl1 3.079(6) Å.[158] For **C60**, the SQUEEZE procedure was implemented using the crystallographic software, Olex2, to remove diffuse solvent in the crystal lattice. The result was removal of 217 electrons per asymmetric unit which equates to four MeOH molecules, three Et_2O molecules, and two H_2O molecules (218 e^-).[208,273]

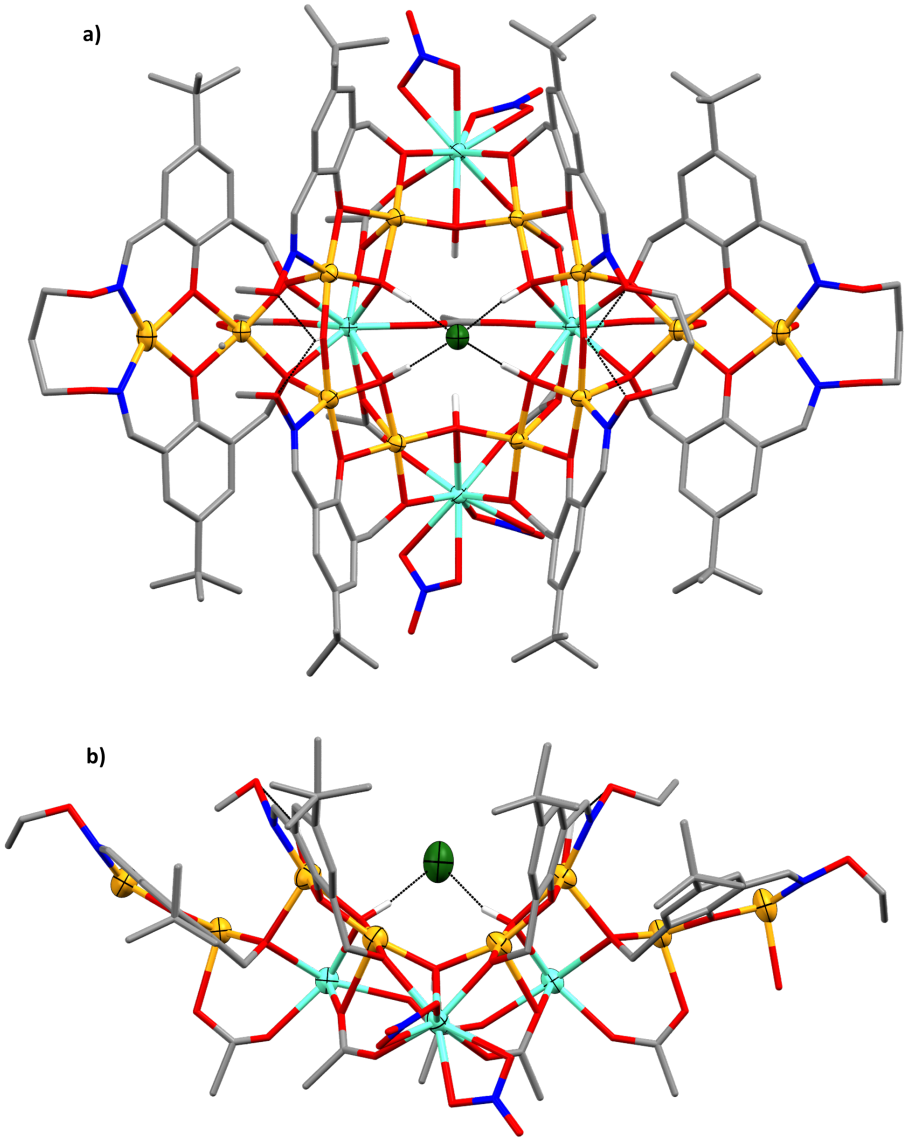

Figure 6.11: Full molecular structure of $[Cu^{II}_{12}Eu^{III}_{4}(\mathbf{L3})_4(H_2O)(OH)_8(OAc)_7(NO_3)_4][Cl]\cdot H_2O\cdot 2MeOH$, **C60** viewed top down (a) and side on (b). Non-interacting hydrogen atoms and lattice solvent molecules have been omitted for clarity, hydrogen bonding represented as black dotted lines, and the thermal ellipsoids of the metal ions and Cl^- anion are shown at 50% probability. Colour code: Cu^{II} = yellow, Eu^{III} = aqua, N = blue, O = red, Cl = dark green, C = grey, and H = white.

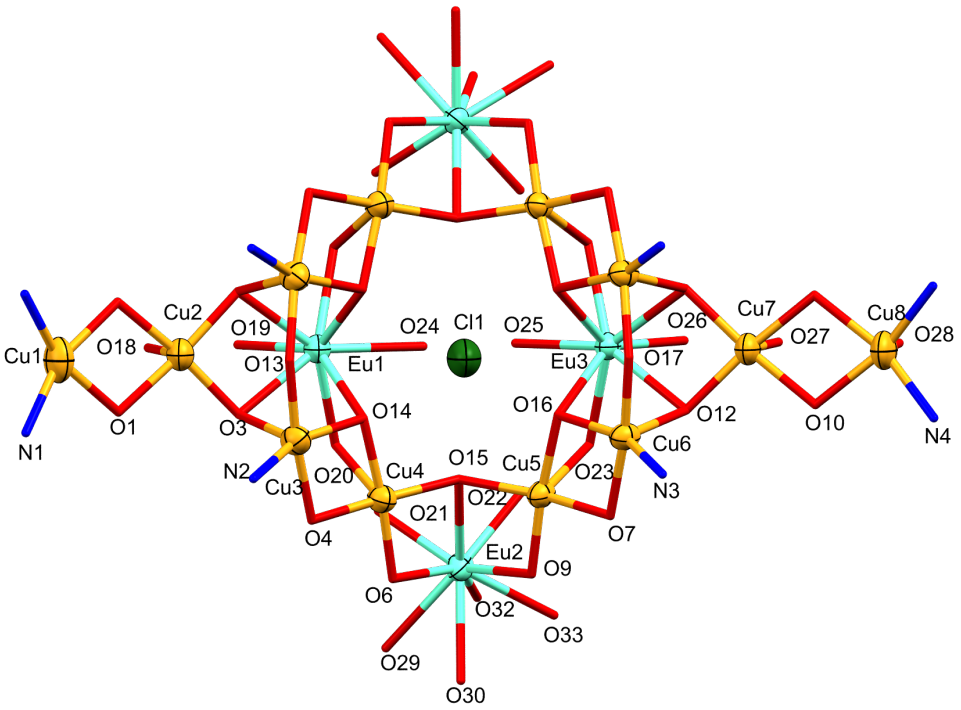

Figure 6.12: Labelled metallic core of **C60**. Hydrogen atoms have been omitted for clarity and the thermal ellipsoids of the metal ions are shown at 50% probability. Colour code: Cu^{II} = yellow, Eu^{III} = purple, N = blue, O = red, and C = grey.

Table 6.9: Selected bond lengths (Å) and angles (°) of the complex **C60** from crystal structure determination

C60					
Cu1-O1	1.962(6)	Cu5-O16	1.925(5)	Eu1-O24	2.410(7)
Cu1-N1	1.972(13)	Cu5-O23	2.450(5)	Eu2-O6	2.365(5)
Cu2-O1	1.944(6)	Cu6-O7	1.945(5)	Eu2-O9	2.283(5)
Cu2-O3	1.905(5)	Cu6-O12	2.287(5)	Eu2-O15	2.526(5)
Cu2-O18	2.385(14)	Cu6-O16	2.006(4)	Eu2-O21	2.349(5)
Cu3-O3	2.290(5)	Cu6-O17	1.902(3)	Eu2-O22	2.377(5)
Cu3-O4	1.957(6)	Cu6-N3	1.938(6)	Eu2-O29	2.545(7)
Cu3-O13	1.907(3)	Cu7-O10	1.959(6)	Eu2-O30	2.526(8)
Cu3-O14	1.995(5)	Cu7-O12	1.921(5)	Eu2-O32	2.526(5)
Cu3-N2	1.932(8)	Cu7-O27	2.308(9)	Eu2-O33	2.594(6)
Cu4-O4	1.980(5)	Cu8-O10	1.970(6)	Eu3-O12	2.492(5)
Cu4-O6	1.895(5)	Cu8-O28	2.345(13)	Eu3-O16	2.427(4)
Cu4-O14	1.950(5)	Cu8-N4	1.955(10)	Eu3-O23	2.438(5)
Cu4-O15	1.957(5)	Eu1-O3	2.475(5)	Eu3-O25	2.370(6)
Cu5-O7	1.998(5)	Eu1-O14	2.433(5)	Eu3-O26	2.361(7)
Cu5-O9	1.881(5)	Eu1-O19	2.335(10)	Cu1-O1-Cu2	102.60(3)
Cu5-O15	1.962(5)	Eu1-O20	2.424(5)	Cu2-O3-Cu3	110.99(3)
Cu2-O3-Eu1	99.70(2)	Cu4-O14-Eu1	115.90(2)	Cu5-O16-Eu3	115.50(2)
Cu3-O13-Cu3[a]	144.50(5)	Cu4-O6-Eu2	104.40(2)	Cu6-O17-Cu6[a]	142.20(4)
Cu3-O4-Cu4	98.90(2)	Cu4-O15-Eu2	96.99(2)	Cu6-O12-Cu7	121.80(2)
Cu3-O14-Cu4	98.60(2)	Cu5-O7-Cu6	98.50(2)	Cu6-O12-Eu3	93.50(2)
Cu3-O3-Eu1	95.10(2)	Cu5-O16-Cu6	98.90(2)	Cu6-O16-Eu3	103.30(2)
Cu3-O14-Eu1	104.70(2)	Cu5-O9-Eu2	104.97(2)	Cu7-O10-Cu8	103.90(3)
Cu4-O15-Cu5	128.30(3)	Cu5-O15-Eu2	94.30(2)	Cu7-O12-Eu3	97.70(2)
Cu1···Cu2	3.049(2)	Cu4···Eu2	3.378(1)	Cu7···Eu3	3.344(2)
Cu2···Cu3	3.463(2)	Cu5···Cu6	2.987(1)	Eu1···Eu2	5.970(1)
Cu2···Eu1	3.367(2)	Cu5···Eu2	3.313(1)	Eu1···Eu3	6.417(1)
Cu3···Cu4	2.991(1)	Cu5···Eu3	3.690(1)	Eu2···Eu2[a]	9.889(1)
Cu3···Eu1	3.517(1)	Cu6···Cu7	3.682(2)	Eu2···Eu3	6.041(1)
Cu4···Cu5	3.527(1)	Cu6···Eu3	3.485(1)		
Cu4···Eu1	3.724(1)	Cu7···Cu8	3.093(2)		

[a] +X, 1-Y, +Z

6.5 3 $d^{II}Na^{I}$ Clusters

6.5.1 $Ni^{II}Na^{I}$ Clusters

The three $Ni^{II}Na^{I}$ clusters, **C61** - **C63** have resulted from different complexation attempts. The complex, **C61** was the result of another attempt at producing an extended structure of **C17** similarly to the polymers reported previously, **C62** was an attempt to remake the large $Cu^{II}Ni^{II}Na^{I}$ cluster reported in the previous section, and finally **C63** resulted from attempts to remake **C61**, however with a varied ratio of $Ni(OAc)_2{\cdot}4H_2O$: NaOAc. The three structures were found to be either tetranuclear (**C61** and **C62**) or decanuclear (**C63**), utilising two or four units of **L2** respectively with Harris coordination modes alike Mode VI (**C61** and **C62**) and Mode V (**C63**).[145] For both **C61** and **C62** the whole structure can be found in the asymmetric unit (representative structure in Figure 6.13 and full structures in Figures E.1 and E.3) whereas for **C63**, half of the structure can be found in the asymmetric unit as shown in Figure 6.14 with the whole structure shown in Figure 6.15.

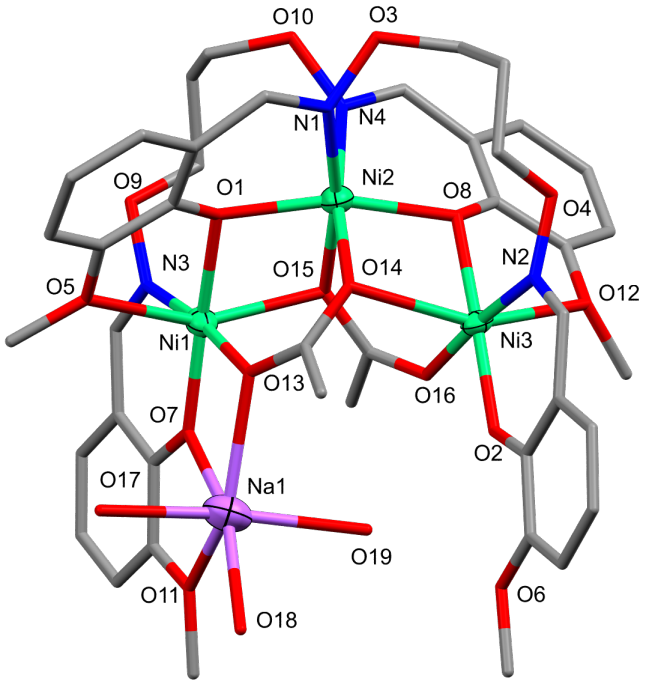

Figure 6.13: Representative structure of $[Ni^{II}_3Na^{I}(\mathbf{L2})_2X_3(OAc)_2]$ (X = one NO_3^- and one H_2O (**C61**) and three MeOH (**C62**)). Hydrogen atoms and lattice solvates (**C61**) and anions (**C62**) have been omitted for clarity. Thermal ellipsoids of the metal ions are shown at 60% probability. Colour code: Ni^{II} = light green, Na^{I} = purple, N = blue, O = red, and C = grey.

All three structures were found to crystallise in the triclinic space group, $P\bar{1}$, with the three Ni^{II} ions for all complexes, Ni1 - Ni3, each adopting a six-coordinate, octahedral geometry (CShM, Table E.4).[146,147,171] The donor sets vary with a NO_5 donor set for Ni1 and Ni3 consisting of two phenolate oxygens, one alkyloxime nitrogen, a methoxy oxygen, and two OAc^- anions and for Ni2, the N_2O_4 donor set consists of two phenolate oxygens, two alkyloxime nitrogens, and two OAc^- anions. The largest structural differences between the complexes is the geometry and coordination of the Na^{I} ion/s. The singular Na^{I} ions for **C61** and **C62** are six-coordinate with

distorted trigonal prismatic and distorted octahedral geometries (CShM, Table E.4) respectively.[146,147,171] The O_6 donor sets consist of a phenolate oxygen, a methoxy oxygen, a bidentate OAc^- anion, and three oxygen atoms (a bidentate NO_3^- anion and H_2O molecule for **C61** and three MeOH molecules (O17 and O18 are both 50% occupancy) for **C62**). The four Na^I ions for **C63** are found to be significantly different due to both the coordination mode of the NO_3^- anion and the disordered NO_3^-/OH^- (75 : 25) bridging. Na1 is found to be seven-coordinate with a very distorted capped trigonal prism geometry (CShM value of 18.618, Table E.4) and O_7 donor set consisting of a phenolate oxygen, a methoxy oxygen, an OAc^- anion, and two bidentate NO_3^- anions (one NO_3^- has 75% occupancy).[146,147,210] For Na2, the geometry and donor set varys depending on the disordered bridge. Na2 is five-coordinate with either a distorted trigonal bipyramidal geometry (NO_3 bridging; CShM, Table E.4) or a highly disorded spherical square pyramidal geometry (OH bridging; CShM value of 12.543, Table E.4).[146,147,281] The O_5 donor set for Na2 consists of one phenolate oxygen, one methoxy oxygen, one OAc^- anion and either a NO_3^- or OH^- anion (75 : 25). When comparing **C61**/**C62** and **C63**, the coordination modes of the OAc^- anions vary slightly due to the different number of Na^I coordinates. For **C61**/**C62** the OAc^- anions coordinate in both a $3.2_{12}1_3$ and $4.2_{12}2_{34}$ fashion, whereas for **C63** both OAc^- anions are coordinated in a $4.2_{12}2_{34}$ fashion (Figure A.17).[145]

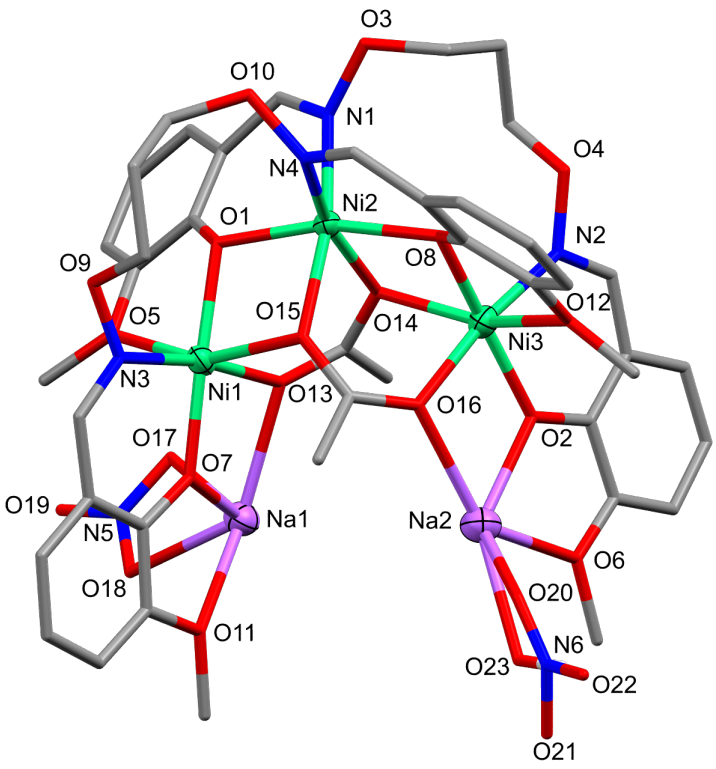

Figure 6.14: Asymmetric unit of $[Ni^{II}_6Na^{I}_4(\mathbf{L2})_4(OH)_{0.5}(OAc)_4(NO_3)_{3.5}]$, **C63**. Non-interacting hydrogen atoms have been omitted for clarity and the thermal ellipsoids of the metal ions are shown at 50% probability. Colour code: Ni^{II} = light green, Na^{I} = purple, N = blue, O = red, C = grey, and H = white.

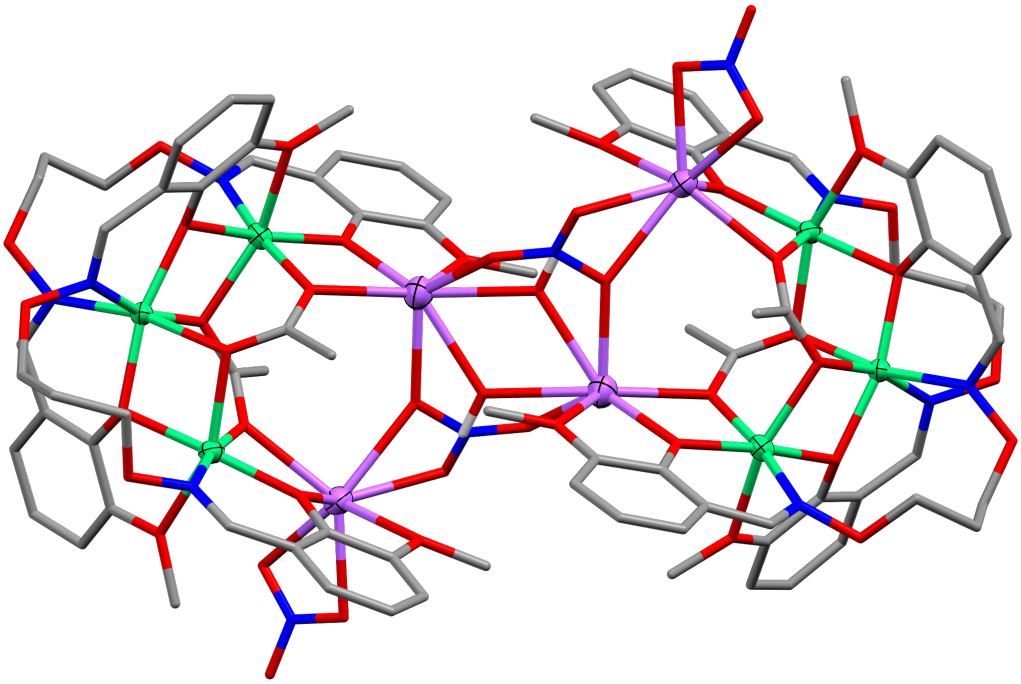

Figure 6.15: Full molecular structure of $[Ni^{II}_6Na^{I}_4(\mathbf{L2})_4(OH)_{0.5}(OAc)_4(NO_3)_{3.5}]$, **C63**. Non-interacting hydrogen atoms have been omitted for clarity and the thermal ellipsoids of the metal ions are shown at 50% probability. Colour code: Ni^{II} = light green, Na^{I} = purple, N = blue, O = red, C = grey, and H = white.

For **C61**, two H_2O molecules (O21 and O22) are found in the crystal lattice, with moderate hydrogen bonding found between the lattice H_2O molecules and a NO_3^- anion (O21···O18, 2.824(5) Å), an OAc^- anion (O22···O16, 2.818(4) Å), and the co-ordinated H_2O molecule (O19···O21, 2.820(5) Å).[158] For **C62**, one Cl^- anion is found in the crystal lattice to balance the +1 charge of the structure. Moderate hydrogen bonding is found for **C62** between the MeOH molecules (C18 and C19), the lattice Cl^- anion (Cl1), and a phenolate oxygen (O2), O18···Cl1 3.089(6) Åand O19···O2 2.959(4) Å. For **C61** and **C62**, the SQUEEZE procedure was implemented using the crystallographic software, Olex2, to remove diffuse solvent in the crystal lattice. The result was removal of 21 electrons per asymmetric unit for **C61** equating to two H_2O molecules (20 e^-) and 14 electrons per asymmetric unit for **C62**, which equates to 0.75 MeOH molecule (14 e^-).[208,273]

Table 6.10: Selected bond lengths (Å) for the complexes **C61** - **C63** from crystal structure determination

	C61	**C62**	**C63**
Ni1-O1	1.983(2)	1.998(2)	2.015(3)
Ni1-O5	2.276(3)	2.227(3)	2.139(3)
Ni1-O7	1.914(2)	1.933(3)	1.966(3)
Ni1-O13	2.023(3)	2.055(3)	2.089(4)
Ni1-O15	2.367(2)	2.235(3)	2.147(3)
Ni1-N3	1.985(3)	2.003(3)	2.024(4)
Ni2-O1	2.043(2)	2.013(2)	1.993(3)
Ni2-O8	2.045(2)	2.031(2)	1.997(3)
Ni2-O14	2.061(2)	2.072(3)	2.149(3)
Ni2-O15	2.113(2)	2.122(2)	2.120(3)
Ni2-N1	2.107(3)	2.103(3)	2.093(4)
Ni2-N4	2.080(3)	2.084(3)	2.103(4)
Ni3-O2	1.923(2)	1.943(3)	1.964(4)
Ni3-O8	1.991(2)	2.007(2)	1.995(3)
Ni3-O12	2.324(2)	2.309(3)	2.169(3)
Ni3-O14	2.418(2)	2.372(3)	2.122(3)
Ni3-O16	1.977(2)	1.993(3)	2.102(4)
Ni3-N2	1.964(3)	1.964(3)	2.025(5)
Na1-O7	2.282(3)	2.325(3)	2.304(4)
Na1-O11	2.462(4)	2.415(4)	2.487(4)
Na1-O13	2.387(3)	2.427(3)	2.423(4)
Na1-O17	2.411(4)	2.359(6)	2.458(5)
Na1-O18	2.467(4)	2.385(6)	2.387(5)
Na1-O19	2.251(4)	2.369(4)	–
Na1-O21	–	–	2.501(8)
Na1-O22	–	–	2.554(6)
Na2-O2	–	–	2.252(4)
Na2-O6	–	–	2.393(5)
Na2-O16	–	–	2.457(4)
Na2-O20	–	–	2.281(7)
Na2-O21	–	–	2.302(8)
Na2-O23	–	–	2.477(18)
Na2-O23*	–	–	2.402(17)

*1-X,1-Y,1-Z

Table 6.11: Selected bond angles (°) and distances (Å) for the complexes **C61** - **C63** from crystal structure determination

	C61	**C62**	**C63**
Ni1-O1-Ni2	103.38(10)	102.44(11)	102.47(13)
Ni1-O15-Ni2	89.51(9)	91.69(10)	94.18(12)
Ni1-O7-Na1	106.22(12)	107.04(13)	106.45(16)
Ni1-O13-Na1	99.08(11)	99.59(11)	98.54(14)
Ni2-O8-Ni3	103.76(10)	103.41(11)	102.83(15)
Ni2-O14-Ni3	89.93(9)	90.69(10)	93.89(13)
Ni3-O2-Na2	–	–	107.23(18)
Ni3-O16-Na2	–	–	96.09(15)
Ni1···Ni2	3.159(1)	3.127(1)	3.125(1)
Ni1···Ni3	4.859(1)	4.780(1)	4.753(1)
Ni1···Na1	3.363(2)	3.432(2)	3.426(2)
Ni1···Na2	–	–	5.414(3)
Ni1···Ni3*	–	–	11.034(1)
Ni2···Ni3	3.175(1)	3.169(1)	3.121(1)
Ni2···Na1	5.521(2)	5.555(2)	5.685(2)
Ni2···Na2	–	–	5.651(2)
Ni2···Ni2*	–	–	14.900(2)
Ni3···Na1	5.298(2)	5.230(2)	5.542(2)
Ni3···Na2	–	–	3.399(2)
Na1···Na2	–	–	4.514(3)
Na1···Na2*	–	–	5.829(3)
Na1···Na2*	–	–	9.548(4)

*1-X,1-Y,1-Z

Magnetic Analysis

Magnetic measurements on the complex, **C63** were performed at The University of Electro-Communications, Tokyo, Japan, through collaborative work with Prof. Takayuki Ishida. Variable-temperature, solid-state DC magnetic susceptibility data was carried out with a Quantum Design MPMS-XL7 SQUID magnetometer over the temperature range 300 - 2 K using a static field of 0.05 T. A field of 0.5 T was used to measure the susceptibility of the sample with small magnetic moments. Measurements were corrected with diamagnetic blank data from the empty sample holder. The diamagnetic contribution of the sample itself was estimated using Pascal's constants. To avoid any possible field alignment effects, the polycrystalline sample was fixed with a small amount of eicosane.

Upon cooling, the $\chi_M T$ value remains constant from 7.8 cm^3 K mol^{-1} at 300 K until 100 K where the $\chi_M T$ value rapidly increases to 13.0 cm^3 K mol^{-1} at 5 K before rapidly decreasing to 10.1 cm^3 K mol^{-1} at 2 K (Figure 6.16). The maximum value was found to slightly exceed the value, 12.0 cm^3 K mol^{-1}, expected for magnetically isolated Ni^{II} ions. This behaviour is indicative of ferromagnetic coupling between the Ni^{II} ions with the decrease of the $\chi_M T$ value at low temperature attributed to either antiferromagnetic intermolecular interactions or ZFS. The low temperature magnetic properties were further investigated with variable field measurements performed at 1.8 K. The results of which are consistent with the presence of six unpaired electrons from six $S = 1$ centres.

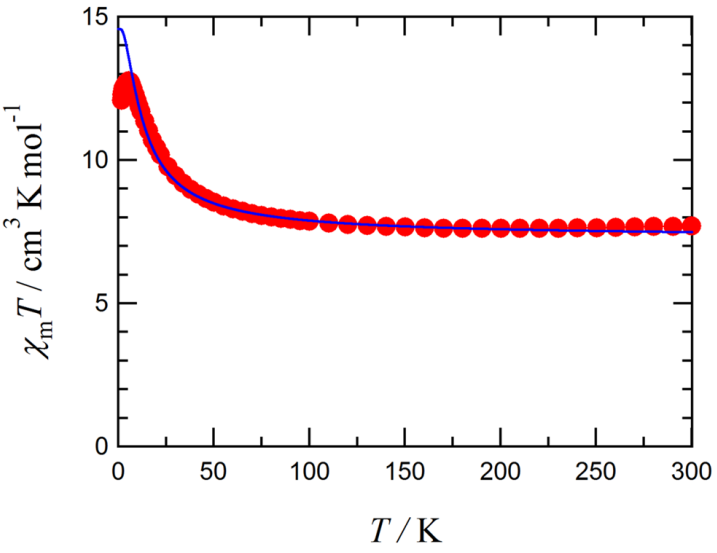

Figure 6.16: $\chi_M T$ vs T plot for **C63** in an applied field of $B = 0.05$ T over the temperature range $T = 300$ - 2 K. The solid line represents the fit of the experimental data using the spin-Hamiltonian, Equation 6.1.

The susceptibility and magnetisation data were simultaneously fitted to the spin-Hamiltonian (Equation 6.1), based on a linear symmetrical model, giving the values $2J/K_B = 5.06(9)$ K and $g_{Ni} = 2.206(3)$ (Figure 6.17). To avoid any analytical contamination due to the possible antiferromagnetic intramolecular interactions as described above, the curve fitting was performed using the data from 10 K to 300 K.

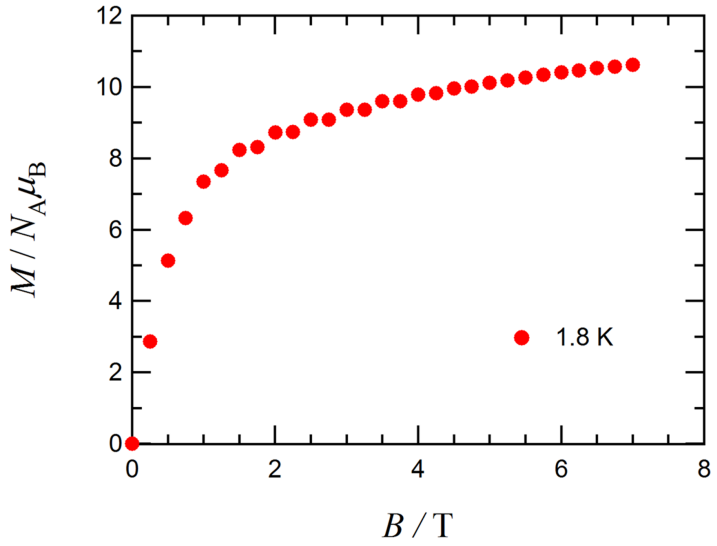

Figure 6.17: Plot of magnetisation versus field for **C63** at 1.8 K over the applied field range of B = 0 - 7 T.

$$\hat{H} = -2J(S_1 \cdot S_2 + S_2 \cdot S_3) \tag{6.1}$$

6.5.2 $Cu^{II}Na^{I}$ Cluster

The $Cu^{II}Na^{I}$ cluster, **C64** resulted from an attempt to produce a Cu^{II} version of **C63**. The cluster was synthesised from the RT reaction between H_2**L2**, $Cu(OAc)_2{\cdot}H_2O$, $Na(NO_3)_2$, and Et_3N in a 1 : 1 : 1 : 1 ratio, with isolation of the complex achieved by Et_2O vapour diffusion into the methanolic complexation solution. The complex was found to crystallise in the triclinic space group, $P\bar{1}$, with half of the complex found in the asymmetric unit (Figure 6.18), the complete structure can be seen in Figure 6.19. The cluster consists of four units of $\mathbf{L2}^{2-}$ coordinated to eight Cu^{II} ions and eight Na^{I} ions (Mode V, Figure 2.6).[145]

The eight Cu^{II} ions are four-coordinate with a square planar geometry (CShM, Table E.4) and NO_3 donor set consisting of an alkyloxime nitrogen, a phenolate oxygen, an μ_2-oxide anion and an OAc^- anion.[146,147,267] The Cu^{II} ions are weakly coordinated to an oxygen atom of the lattice NO_3^- anions found above and below the structure (2.459(5) - 2.643(5) Å), with additional weak coordination between Cu2, Cu3, and the μ_2-oxide anions of opposing ligand planes (2.523(4) and 2.488(3) Å respectively). Na1, Na3, and Na4 were all found to be six-coordinate with distorted trigonal prismatic geometries for Na1 and Na3 and a distorted octahedral geometry (CShM, Table E.4) for Na4.[146,147,171] Each Na^{I} ion has an O_6 donor set consisting of a phenolate oxygen, a methoxy oxygen, an OAc^- anion, a solvent molecule (1 : 1 mixture of MeOH : H_2O for Na1 and Na3 and H_2O molecule for Na4), and bridging NO_3^- anion/s, two monodentate for Na1 and one bidentate each for Na3 and Na4. Na2 was found to be five-coordinate with a distorted spherical square pyramidal geometry (CShM, Table E.4) and an O_5 donor set consisting of a phenolate oxygen, a methoxy oxygen, an OAc^- anion, a bridging NO_3^- anion, and a H_2O molecule.[146,147,281] One Harris coordination mode is found for the OAc^- anions, $4.2_{12}2_{34}$, and two modes for the NO_3^- anions, $3.1_11_22_{23}$ and $2.2_{12}1_2$ (Figures A.17 and A.18).[145]

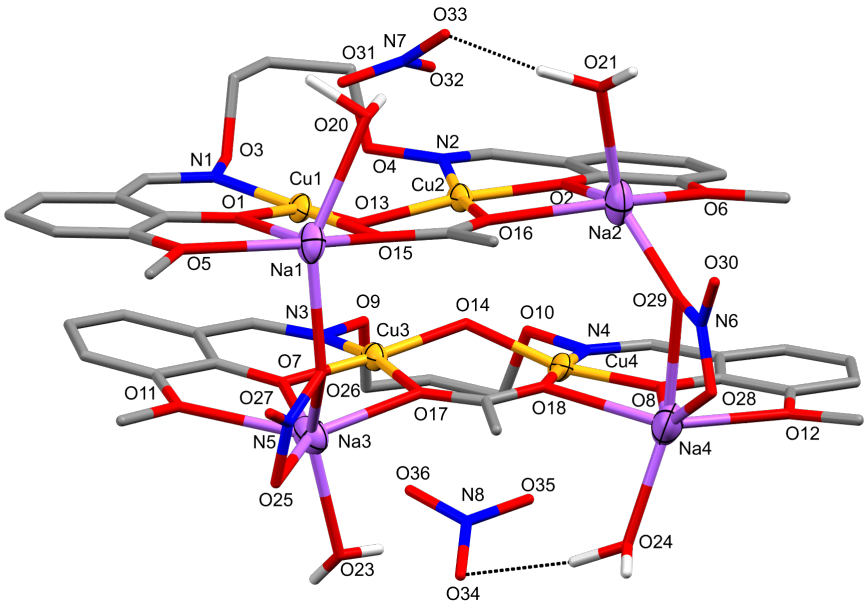

Figure 6.18: Asymmetric unit of $[Cu^{II}_8Na^{I}_8O_4(\mathbf{L2})_4(H_2O)_6(MeOH)_2(OAc)_4(NO_3)_4][(NO_3)_4]$, **C64**. Non-interacting hydrogen atoms and disordered MeOH coordinates have been omitted for clarity, hydrogen bonding represented as black dotted lines, and the thermal ellipsoids of the metal ions are shown at 50% probability. Colour code: Cu^{II} = yellow, Na^{I} = purple, N = blue, O = red, C = grey, and H = white.

Moderate intramolecular hydrogen bonding is found in the complex between the coordinated solvent molecules (O19, O21, and O22) and lattice NO_3^- anions (O31, O33, and O34), O19· · ·O31 2.933(17) Å, O21· · ·O33 2.987(13) Å, and O22· · ·O34 2.827(17) Å.[158] The SQUEEZE procedure was implemented using the crystallographic software, Olex2, to remove diffuse solvent in the crystal lattice. The result was removal of 208 electrons per asymmetric unit which equates to four MeOH molecules, three Et_2O molecules, and one H_2O molecule (208 e^-).[208,273]

As **C64** was produced to be an analogue of **C63**, it was thought the two complexes would have similar structural properties however when comparing the two, they have significant differences. Both complexes consist of two M_xL_2 subunits, which are bridged by NO_3^- anions however for **C63** two overlapping ligands coordinate to three Ni^{II} ions and two Na^{I} ions. The complex **C64** differs in that the two ligands form parallel sheets with each ligand coordinated to two Cu^{II} ions and two Na^{I} ions, with both NO_3^- bridging and weak coordination holding the ligand units together. These differences in the subunits is thought to result from the geometry preferences of the metal ions as the Cu^{II} ions adopt a four-coordinate geometry and the Ni^{II} ions adopt a six-coordinate geometry. Although the metal ions have different geometries, the ligand was found to coordinate alike Mode V (Figure 2.6), for both complexes.[145] The exchange pathways were found to have similarities with the M^{II}-X-M^{II} bridges mediated by OAc^- anions, the M^{II}-X-Na^{I} bridges mediated by phenolate oxygens and OAc^- anions, and the Na^{I}-X-Na^{I} bridges mediated by NO_3^- and OAc^- anions. The differences in the remaining exchange pathways are again thought to be a result of the different geometries and ligand orientations, the Ni^{II}-X-Ni^{II} bridges in **C63** are mediated by phenolate oxygens, whereas the Cu^{II}-X-Cu^{II} bridges in **C64** are mediated by oxide anions.

Table 6.12: Selected bond lengths (Å) and angles (°) of the complex **C64** from crystal structure determination

C64					
Cu1-O1	1.894(4)	Cu4-O14	1.893(4)	Na3-O7	2.287(5)
Cu1-O13	1.899(3)	Cu4-O18	1.989(5)	Na3-O11	2.455(6)
Cu1-O15	1.987(4)	Cu4-N4	1.959(6)	Na3-O17	2.409(4)
Cu1-N1	1.951(5)	Na1-O1	2.298(5)	Na3-O22	2.300[a]
Cu2-O2	1.909(4)	Na1-O5	2.410(4)	Na3-O25	2.458(6)
Cu2-O13	1.913(4)	Na1-O15	2.435(4)	Na3-O26	2.425(5)
Cu2-O16	1.990(4)	Na1-O19	2.410[a]	Na4-O8	2.243(7)
Cu2-N2	1.973(5)	Na1-O26	2.390(5)	Na4-O12	2.426(6)
Cu3-O7	1.915(4)	Na2-O2	2.258(6)	Na4-O18	2.418(5)
Cu3-O14	1.905(4)	Na2-O6	2.425(5)	Na4-O24	2.326(7)
Cu3-O17	1.999(4)	Na2-O16	2.399(4)	Na4-O28	2.356(11)
Cu3-N3	1.984(5)	Na2-O21	2.367(10)	Na4-O29	2.479(10)
Cu4-O8	1.893(4)	Na2-O29	2.207(7)		
Cu1-O13-Cu2	126.50(2)	Cu2-O16-Na2	99.67(17)	Cu4-O8-Na4	107.40(2)
Cu1-O1-Na1	107.85(17)	Cu3-O14-Cu4	127.50(2)	Cu4-O18-Na4	98.07(18)
Cu1-O15-Na1	99.88(16)	Cu3-O7-Na3	106.67(19)	Na1-O26-Na3	130.10(2)
Cu2-O2-Na2	107.41(19)	Cu3-O17-Na3	99.65(17)	Na2-O29-Na4	122.99(4)
Cu1···Cu2	3.404(1)	Cu3···Cu4	3.406(1)	Na1···Na4[b]	9.557(4)
Cu1···Cu3	3.700(1)	Cu3···Na3	3.378(3)	Na2···Na4	4.121(5)
Cu1···Na1	3.397(2)	Cu3···Cu2[b]	14.804(1)	Na2···Na3[b]	11.054(4)
Cu1···Cu4[b]	13.691(1)	Cu4···Na4	3.340(3)	Na3···Na4	6.510(4)
Cu2···Cu4	3.671(1)	Cu4···Cu1[b]	13.691(1)	Na3···Na2[b]	11.054(4)
Cu2···Na2	3.365(2)	Na1···Na2	6.519(3)	Na4···Na1[b]	9.557(4)
Cu2···Cu3[b]	14.804(1)	Na1···Na3	4.365(4)		

[a] Averaged values

[b] 2-X, 1-Y, 2-Z

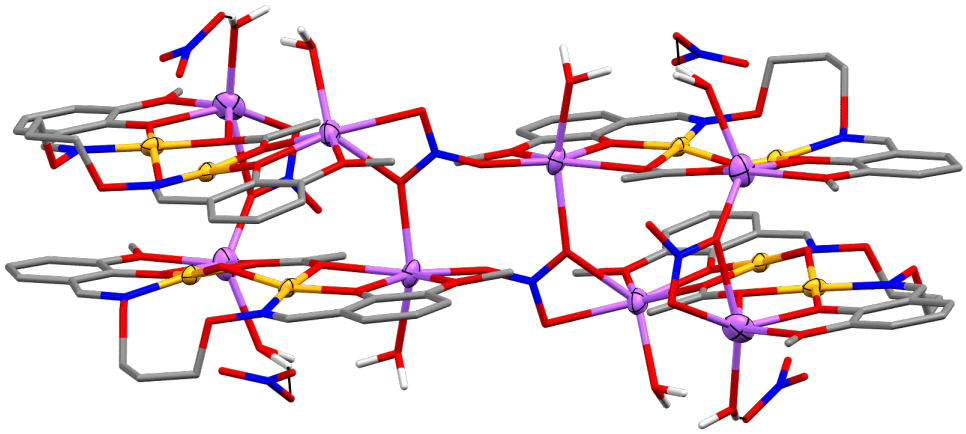

Figure 6.19: Full molecular structure of $[Cu^{II}_8Na^{I}_8O_4(\mathbf{L2})_4(H_2O)_6(MeOH)_2(OAc)_4(NO_3)_4][(NO_3)_4]$, **C64**. Non-interacting hydrogen atoms and disordered MeOH coordinates have been omitted for clarity, hydrogen bonding represented as black dotted lines, and the thermal ellipsoids of the metal ions are shown at 50% probability. Colour code: Cu^{II} = yellow, Na^{I} = purple, N = blue, O = red, C = grey, and H = white.

6.6 Mononuclear Complexes

The mononuclear complexes **C65** and **C66** resulted from intial complexation attempts for the ligand, H_3**L4**, as this ligand had no direct comparisons in the literature, many test complexations were performed to determine whether typical dinuclear complexes or larger clusters would form. As mentioned in Section 2.5, the ligand however did not remain intact during complexation. The complexes were synthesised by RT reactions between H_3**L4**, $MX_2{\cdot}H_2O$ ($Ni(OAc)_2{\cdot}4H_2O$ (**C65**) or $Mn(NO_3)_2{\cdot}4H_2O$ (**C66**)), $Gd(NO_3)_3{\cdot}6H_2O$, and Et_3N in a 1 : 1 : 1 : 1 molar ratio. The complexes were isolated by both slow evaporation of the complexation solution (**C65**) and vapour diffusion of Et_2O into the complexation solution (**C66**). The crystallisations were left undisturbed for an extended period of time, with the structures of the X-ray quality crystals collected after a period of approximately 10 months. Attempts to reproduce **C65** were successful with a RT reaction between H_3**L4**, $Ni(OAc)_2{\cdot}4H_2O$, and Et_3N in a 1 : 1 : 2 molar ratio. The complex was isolated by vapour diffusion of Et_2O into the reaction solution, with X-ray quality crystals produced after approximately two weeks. Attempts to reproduce **C66**, following the initial procedure have been unsuccessful at producing crystalline material however brown precipitate of the complex was obtained after five weeks.

The complexes **C65** and **C66** were found to crystallise in the monoclinic space groups, $P2_1/n$ and $P2_1/c$ respectively. For **C65**, half of the structure can be found in the asymmetric unit with the remainder generated by inversion symmetry through the Ni^{II} ion (Figure 6.20) whereas for **C66**, two units of the structure can be found in the asymmetric unit (Figure 6.21). Both complexes consist of one metal ion coordinated to two units of a new cleaved ligand, for **C65**, the cleaved ligand is **L5** whereas for **C66**, the cleaved ligand is that of **L6** (Figure 2.11).[145] For **C65**, **L5** is coordinated to a four-coordinate Ni^{II} ion with a square planar geometry (CShM, Table E.4).[146,147,267] The Ni^{II} ion sits in a classical N_2O_2 pocket with the donor groups consisting of two phenolate oxygens and two alkyloxime nitrogens. Strong intramolecular hydrogen bonding (X$\cdots$A, 2.2 - 2.5 Å)[158] is found between the alkyloxime oxygen

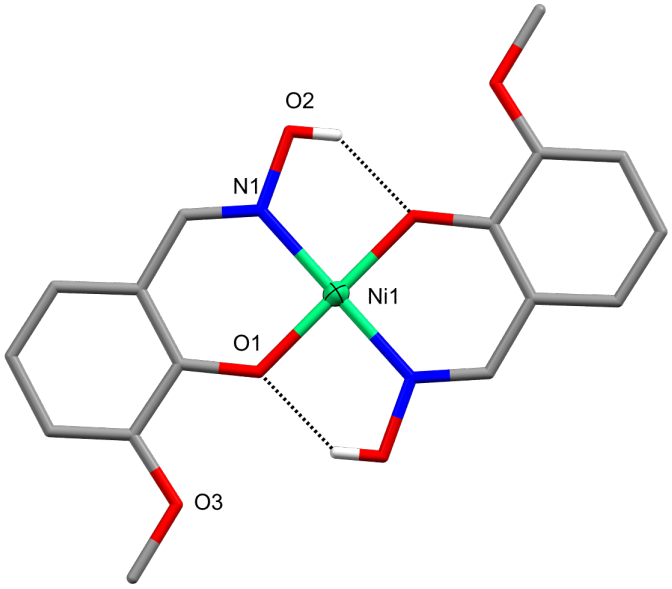

Figure 6.20: Full molecular structure of [Ni^{II}(**L5**)$_2$], **C65**. Non-interacting hydrogen atoms have been omitted for clarity, hydrogen bonding represented as black dotted lines, and the thermal ellipsoid of the metal ion is shown at 70% probability. Colour code: Ni^{II} = light green, N = blue, O = red, C = grey, and H = white.

(O2) and the phenolate oxygen (O1), O2· · ·O1 2.498(1) Å. For **C66**, **L6** is coordinated to a six-coordinate Mn^{III} ion with an octahedral geometry (CShM, Table E.4) and N_2O_4 donor set resembling that of **C65** but with an additional two phenolate oxygens.[146,147,171] Within the crystal lattice, one MeOH molecule and one NO_3^- anion are found for each unit. Moderate intermolecular hydrogen bonding for **C66** between the MeOH molecule (O12) and the NO_3^- anion (O10), O12· · ·O10 2.693(6) Å.[158] Disorder is found in the complex, with one of the two ^{t}Bu groups rotationally disordered for each unit and the SQUEEZE procedure was implemented to remove disorder in the crystal lattice. The result was the removal of 93 electrons per asymmetric unit which equates to two Et_3O molecules (84 e^-) and one H_2O molecule (10 e^-).[208,273]

The mechanism for which these complexations are formed, as mentioned earlier (Figure 2.12), is thought to result from the coordination of a metal ion and subsequent protonation of the alkyloxime oxygen, causing a rearrangement to occur and one of the alkyloxime groups to leave, forming **L5**. When this occurs in the presence of excess Et_3N, the lone pair on the nitrogen attacks and a rearrangement occurs to produce the ligand, **L6**.

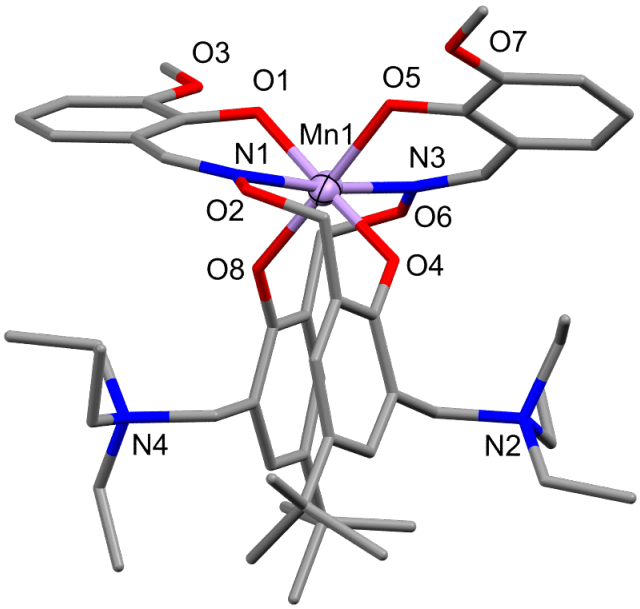

Figure 6.21: Full molecular structure of $[Mn^{III}(\mathbf{L6})_2][NO_3]\cdot MeOH$, **C66**. Hydrogen atoms and the lattice MeOH molecule and NO_3^- anion have been omitted for clarity. The thermal ellipsoid of the metal ion is shown at 70% probability. Colour code: Mn^{III} = purple, N = blue, O = red, and C = grey.

Table 6.13: Selected bond lengths (Å) of the complexes **C65** and **C66** from crystal structure determination

	C65	**C66**
M1-O1	1.829(1)	1.927(3)
M1-O4	–	1.909(3)
M1-O5	–	1.919(3)
M1-O8	–	1.921(3)
M1-N1	1.873(1)	2.328(4)
M1-N3	–	2.307(4)

6.7 Conclusion

A series of complexes ranging from nuclearity of one to large extended clusters and polymers (**C50** - **C66**) have unexpectedly been produced through reactions of ligand (H_2**L1**, H_2**L2**, H_4**L3**, and H_3**L4**), $M(OAc)_2{\cdot}H_2O$, and $M(NO_3)_2{\cdot}H_2O$ in various molar ratios. The complexes, apart from a few due to reproducibility issues, have been characterised by SCXRD, ESI-MS, and ATR-IR with the complex **C63** further characterised by CHN microanalysis and magnetic analysis. A few of the highlights of this chapter are the unusual and uncommon properties of a few of the unexpected complexes. One of the more unusual types of bridging found is the alkyloxime oxygen coordination to a Na^I ion in the polymer **C57**, the structure which is one of three different structures produced from a single complexation reaction between **C17** and Na oxalate, where the alkyloxime oxygen bridging has caused the polymer to have a staircase appearance. Another unexpected result was the bowl-like $Cu^{II}{}_{12}Eu^{III}{}_4$ cluster, **C60**, which provided an example of the bridging capability of the ligand H_4**L3**. This chapter highlights the ligand, H_2**L2** and its capability to produce different and interesting complexes in addition to the extensive dinuclear series. The use of different metal ion combinations such as $Ni^{II}{}_2$, $Co^{II}Zn^{II}$, $Ni^{II}Zn^{II}$, $Cu^{II}Ni^{II}$, and $Ni^{II}Na^I$ have resulted in trinuclear, tetranuclear, decanuclear, and polymeric structures, which highlights the versatility of this simple ligand system.

Complex Preparation and Characterisation

$[Ni^{II}{}_3(L1)_2(H_2O)(MeOH)(acac)_2]{\cdot}3MeOH$ (**C50**): To a solution of H_2**L1** (0.202 g, 0.616 mmol, 1 eq.) in MeOH (10 mL) was added a solution of $Ni(acac)_2{\cdot}2H_2O$ (0.276 g, 0.924 mmol, 1.5 eq.) in MeOH (10 mL). The bright green solution was stirred at RT for 10 minutes, followed by the addition of Et_3N (0.520 mL, 3.70 mmol, 6 eq.). The solution was stirred for a further 30 minutes at RT. Isolation of the complex was achieved by slow evaporation of the reaction solution. Green block shaped X-ray quality crystals were produced after nine weeks. Yield (0.138 g, 19%); ATR-IR: $\overline{\nu}$ = 3328 (O-H), 2951 (C-H), 1594 (C=N), 1515 (Ar), 1460 (C-H), 1392 (O-H), 1259 (C-N), 1221 (Ar-O), 1042 (C-O), 1019 (C-O), 924 (N-O), 723 (Ar) cm^{-1}; ESI-MS: *m/z* 1018 $[M\text{-}4MeOH\text{-}H_2O]^+$.

$[Ni^{II}{}_3(L1)_2(MeOH)_2(acac)_2]$ (**C51**): To a solution of H_2**L1** (0.0065 g, 0.01 mmol, 1 eq.) in MeOH (2 mL) was added a solution of $Ni(acac)_2{\cdot}2H_2O$ (0.0088 g, 0.015 mmol, 1.5 eq.) in MeOH (0.4 mL). The bright green solution was stirred at RT for 10 minutes, followed by the addition of Et_3N (0.017 mL, 0.12 mmol, 6 eq.). The solution was stirred for a further 30 minutes at RT. Isolation of the complex was achieved by vapour diffusion of Et_2O into the reaction solution. Light green needle shaped crystals were produced after three weeks. Yield (0.0002 g, 2%); ESI-MS: *m/z* 1021 $[M\text{-}2MeOH]^+$.

$[Ni^{II}{}_4(L2)_2(OMe)_2(MeOH)_2Cl_2]{\cdot}2CHCl_3$ (**C52**): To H_2**L2** (0.0038 g, 0.010 mmol, 1 eq.) in $CHCl_3$ (1 mL) was added $Ni(OAc)_2{\cdot}4H_2O$ (0.0050 g, 0.02 mmol, 2 eq.) in MeOH (0.2 mL). Isolation of the complex was achieved by the diffusion of Et_2O into the reaction solution. Green block shaped crystals were produced after two weeks. Yield (0.0017 g, 13%); ATR-IR: $\overline{\nu}$ = 3412 (O-H), 2948 (C-H), 1604 (C=N), 1544 (Ar), 1471 (C-H), 1364 (O-H), 1214 (Ar-O), 1084 (C-O), 966 (N-O), 734 (Ar) cm^{-1}; ESI-MS: *m/z* 1137 $[M\text{-}2CHCl_3\text{-}Cl]^+$.

[Ni^{II}_7(L2)$_3$(OH)$_6$(OMe)$_2$(MeOH)$_2$]·2Et_2O (**C53**): To H_2**L2** (0.0025 g, 0.0067 mmol, 0.67 eq.) in $CHCl_3$ (1 mL) was added $Gd(NO_3)_3·6H_2O$ (0.0045 g, 0.01 mmol, 1 eq.) in MeOH (0.2 mL) and the light yellow solution was stirred at RT for five minutes. A solution of $Ni(BF_4)_2·6H_2O$ (0.0034 g, 0.01 mmol, 1 eq.) in MeOH (0.2 mL) was added and the pale green solution was stirred at RT for a further five minutes. Isolation of the complex was achieved by the diffusion of Et_2O into the reaction solution. A few green block shaped crystals were produced after six weeks.

[$Co^{II}_2Zn^{II}$(L2)$_2$(NO_3)$_2$] (**C54**): To a solution of H_2**L2** (0.0113 g, 0.03 mmol, 1 eq.) in $CHCl_3$ (3 mL), was added solutions of $Co(OAc)_2·4H_2O$ (0.0075 g, 0.03 mmol, 1 eq.), and $Zn(NO_3)_2·6H_2O$ (0.0089 g, 0.03 mmol, 1 eq.) both in MeOH (0.6 mL) and stirred at RT for one hour. Isolation of the complex was achieved by the diffusion of Et_2O into the reaction solution. Orange block shaped X-ray quality crystals were produced after four weeks. Yield (0.0012 g, 11%); ATR-IR: $\overline{\nu}$ = 2943 (C-H), 1602 (C=N), 1558 (Ar), 1465 (NO_3), 1437 (C-H), 1285 (NO_3), 1213 (Ar-O), 1093 (C-O), 969 (N-O), 810 (NO_3), 738 (Ar) cm^{-1}; ESI-MS: *m/z* 862 $[M\text{-}Zn\text{-}2NO_3]^+$.

[$Ni^{II}_2Zn^{II}$(L2)$_2$(NO_3)$_2$] (**C55**): To a solution of H_2**L2** (0.0113 g, 0.03 mmol, 1 eq.) in $CHCl_3$ (3 mL), was added solutions of $Ni(OAc)_2·4H_2O$ (0.0075 g, 0.03 mmol, 1 eq.), and $Zn(NO_3)_2·6H_2O$ (0.0089 g, 0.03 mmol, 1 eq.) both in MeOH (0.6 mL) and stirred at RT for one hour. Isolation of the complex was achieved by the diffusion of Et_2O into the reaction solution. A few green block shaped X-ray quality crystals were produced after 18 weeks.

∞[$Cu^{II}Gd^{III}$L2(MeOH)(NO_3)(ox)$_2$] (**C56**): To a brown suspension of **C17** (0.0776 g, 0.10 mmol, 1 eq.) in MeOH (10 mL) was added $Na_2(C_2O_4)$ (0.0957 g, 0.70 mmol, 7 eq.) portionwise. The light yellow suspension was stirred at RT overnight after which the suspension was filtered. Isolation of the complex was achieved by the slow evaporation of the reaction solution. Yellow block shaped X-ray quality crystals were achieved after a period of one week. Yield (0.0067 g, 8%); ATR-IR: $\overline{\nu}$ = 3442 (O-H), 2941 (C-H), 1631 (C=O), 1560 (Ar), 1472 (NO_3), 1453 (C-H), 1354 (O-H), 1278 (NO_3), 1225 (Ar-O), 1094 (NO_3), 1033 (C-O), 956 (N-O), 810 (NO_3), 742 (Ar) cm^{-1}; ESI-MS: *m/z* 771 $[M+H]^+$.

∞[$Cu^{II}Na^{I}$L2(NO_3)]·MeOH (**C57**): To a brown suspension of **C17** (0.0776 g, 0.10 mmol, 1 eq.) in MeOH (10 mL) was added $Na_2(C_2O_4)$ (0.0957 g, 0.70 mmol, 7 eq.) portionwise. The light yellow suspension was stirred at RT overnight after which the suspension was filtered. Isolation of the complex was achieved by the diffusion of Et_2O into 1.4 mL of the reaction solution. A few yellow/brown block shaped X-ray quality crystals were achieved after a period of three weeks. Yield (0.0004 g, 7%); ATR-IR: $\overline{\nu}$ = 34.12 (O-H), 2919 (C-H), 1604 (C=N), 1545 (Ar), 1452 (NO_3), 1436 (C-H), 1307 (NO_3), 1237 (Ar-O), 1075 (NO_3), 984 (N-O), 811 (NO_3), 745 (Ar) cm^{-1}; ESI-MS: *m/z* 458 $[M\text{-}NO_3\text{-}MeOH]^+$.

[$Cu^{II}Na^{I}$L2(H_2O)$_2$][NO_3] (**C58**): To a brown suspension of **C17** (0.0776 g, 0.10 mmol, 1 eq.) in MeOH (10 mL) was added $Na_2(C_2O_4)$ (0.0957 g, 0.70 mmol, 7 eq.) portionwise. The light yellow suspension was stirred at RT overnight after which the suspension was filtered. Isolation of the complex was achieved by the slow evaporation of the reaction solution. Dark green block shaped X-ray quality crystals were achieved after a period of seven weeks. Yield (0.0090 g, 16%); ATR-IR: $\overline{\nu}$ = 3418 (O-H), 2935 (C-H), 1604 (C=N), 1547 (Ar), 1455 (C-H), 1316 (O-H), 1220 (Ar-O), 1103 (C-O), 958 (N-O), 748 (Ar) cm^{-1}; ESI-MS: *m/z* 458 $[M\text{-}2H_2O\text{-}NO_3]^+$.

∞[Na^{I}][$Cu^{II}_2Ni^{II}_2Na^{I}$O(H_2O)$_2$(OH)$_4$(OAc)$_2$] (**C59**): To a solution of H_2**L2** (0.0038 g, 0.01 mmol, 1 eq.) in $CHCl_3$ (1 mL) was added $Ni(OAc)_2·4H_2O$ (0.0025 g, 0.01 mmol, 1 eq.) and $Cu(NO_3)_2·H_2O$ (0.0024 g, 0.01 mmol, 1 eq.), both in MeOH (0.2 mL) and the brown/green

solution was stirred at RT for five minutes. Isolation of the complex was achieved by the diffusion of Et_2O into the reaction solution. A few green block shaped crystals were obtained after nine weeks.

[$Cu^{II}_{12}Eu^{III}_4$(L3)$_4$(H_2O)(OH)$_8$(OAc)$_7$(NO_3)$_4$][Cl]·H_2O·2MeOH (**C60**): To a solution of H_4**L3** (0.0049 g, 0.10 mmol, 1 eq.) in $CHCl_3$ (1 mL) was added Et_3N (0.003 mL, 0.02 mmol, 2 eq.) and the solution was stirred at RT for five minutes. To this was added $Eu(NO_3)_3·6H_2O$ (0.0045 g, 0.01 mmol, 1 eq.) followed by $Cu(OAc)_2·H_2O$ (0.0020 g, 0.01 mmol, 1 eq.), both in MeOH (0.2 mL) and the green solution was stirred at RT for five minutes. Isolation of the complex was achieved by the diffusion of Et_2O into the reaction solution. A few green block shaped crystals were obtained after 33 weeks.

[$Ni^{II}_3Na^{I}$(L2)$_2$(H_2O)(OAc)$_2$(NO_3)]·H_2O (**C61**): To H_2**L2** (0.0038 g, 0.01 mmol, 1 eq.) in $CHCl_3$ (2 mL), was added a solution of $Ni(OAc)_2·4H_2O$ (0.0025 g, 0.01 mmol, 1 eq.) in MeOH (0.4 mL) and the green solution was stirred at RT for approximately one hour. Et_3N (0.01 mL, 0.07 mmol, 7 eq.) was added and the bright green solution was further stirred at RT for 10 minutes. A solution of **C17** (0.0078 g, 0.01 mmol, 1 eq.) in 3 : 2 $CHCl_3$/MeOH (2 mL) was added slowly dropwise and the dark brown solution was stirred overnight at RT. Isolation of the complex was achieved by the diffusion of Et_2O into the filtered reaction solution. A few green block shaped X-ray quality crystals were produced after three weeks. Yield (0.0010 g, 8%); ATR-IR: $\overline{\nu}$ = 3456 (O-H), 2943 (C-H), 1605 (C=N), 1549 (Ar), 1467 (NO_3), 1438 (C-H), 1362 (O-H), 1288 (NO_3), 1216 (Ar-O), 1083 (NO_3), 1046 (C-O), 972 (N-O), 829 (NO_3), 742 (Ar) cm^{-1}; ESI-MS: *m/z* 1105 $[M\text{-}Na\text{-}H_2O]^+$.

[$Ni^{II}_3Na^{I}$(L2)$_2$($MeOH$)$_3$(OAc)$_2$] (**C62**): To H_2**L2** (0.0038 g, 0.01 mmol, 1 eq.) in $CHCl_3$ (1 mL), was added solutions of $Ni(OAc)_2·4H_2O$ (0.0025 g, 0.01 mmol, 1 eq.), $Cu(OAc)_2·H_2O$ (0.0020 g, 0.01 mmol, 1 eq.), and NaOAc (0.0009 g, 0.01 mmol, 1 eq.) all in MeOH (0.2 mL). Isolation of the complex was achieved by the diffusion of Et_2O into the filtered reaction solution. A few green block shaped X-ray quality crystals were produced after three weeks. Yield (0.0011 g, 10%); ATR-IR: $\overline{\nu}$ = 3349 (O-H), 2943 (C-H), 1604 (C=N), 1550 (Ar), 1465 (C-H), 1395 (O-H), 1215 (Ar-O), 1045 (C-O), 968 (N-O), 741 (Ar) cm^{-1}; ESI-MS: *m/z* 1125 $[M\text{-}MeOH]^+$.

[$Ni^{II}_6Na^{I}_4$(L2)$_4$(OH)$_{0.5}$(OAc)$_4$(NO_3)$_{3.5}$] (**C63**): To H_2**L2** (0.0749 g, 0.20 mmol, 1 eq.) in $CHCl_3$ (20 mL) was added $Ni(OAc)_2·4H_2O$ (0.0496 g, 0.20 mmol, 1 eq.) in MeOH (4 mL). The green solution was stirred at RT for 10 minutes. A solution of $NaNO_3$ (0.0171 g, 0.20 mmol, 1 eq.) in MeOH (4 mL) was added and the green solution was stirred at RT for 10 minutes, followed by Et_3N (0.056 mL, 0.40 mmol, 2 eq.) and further stirred at RT for 10 minutes. Isolation of the complex was achieved by the diffusion of Et_2O into the reaction solution. Green block shaped crystals were produced after five weeks. Yield (0.0734 g, 15%); ATR-IR: $\overline{\nu}$ = 2943 (C-H), 1606 (C=N), 1579 (Ar), 1549 (N-O), 1467 (NO_3), 1437 (C-H), 1288 (NO_3), 1240 (Ar-O), 1085 (C-O), 1047 (NO_3), 973 (N-O), 830 (NO_3), 742 (Ar) cm^{-1}; ESI-MS: *m/z* 977 [0.5M-2Na-OAc-0.25OH-1.75NO_3]$^+$; elemental analysis calcd. (%) for $C_{84}H_{92.5}N_{11.5}O_{43}Na_4Ni_6$: C 42.12, H 3.89, N 6.72; found: C 41.97, H 3.67, N 6.79.

[$Cu^{II}_8Na^{I}_8O_4$(L2)$_4$(H_2O)$_6$($MeOH$)$_2$(OAc)$_4$(NO_3)$_4$][(NO_3)$_4$] (**C64**): To H_2**L2** (0.0075 g, 0.020 mmol, 1 eq.) in $CHCl_3$ (2 mL) was added $Cu(OAc)_2·H_2O$ (0.0040 g, 0.020 mmol, 1 eq.) in MeOH (0.4 mL) and the brown solution was stirred at RT for one hour. To this was added Et_3N (0.003 mL, 0.020 mmol, 1 eq.) and the dark brown solution was stirred at RT for 10 minutes, followed by $NaNO_3$ (0.0017 g, 0.020 mmol, 1 eq.) in MeOH (0.4 mL) and the light yellow suspension was stirred at RT overnight. Isolation of the complex was achieved by the diffusion of Et_2O into the filtered reaction solution. Green block shaped crystals were

produced after one week. Yield (0.0062 g, 10%); ATR-IR: $\overline{\nu}$ = 3477 (O-H), 2943 (C-H), 1608 (C=N), 1548 (Ar), 1468 (NO_3), 1455 (C-H), 1348 (O-H), 1243 (NO_3), 1217 (Ar-O), 1103 (C-O), 1047 (NO_3), 964 (N-O), 828 (NO_3), 736 (Ar) cm^{-1}; ESI-MS: *m/z* 1305 [0.5M-2NO_3-MeOH-OAc-3H_2O]$^+$.

[Ni^{II}(L5)$_2$] (**C65**): To a solution of H_3**L4** (0.0051 g, 0.01 mmol, 1 eq.) in $CHCl_3$ (1 mL), was added Ni(OAc)$_2$·4H_2O (0.0025 g, 0.01 mmol, 1 eq.) in MeOH (0.2 mL) and the solution was stirred at RT for five minutes. Et_3N (0.03 mL, 0.02 mmol, 2 eq.) was added and the solution was further stirred at RT for five minutes. Isolation of the complex was achieved by the diffusion of Et_2O into the filtered reaction solution. X-ray quality crystals were achieved after two weeks. Yield (0.0003 g, 8%); ATR-IR: $\overline{\nu}$ = 3490 (O-H), 2931 (C-H), 1600 (C=N), 1557 (Ar), 1470 (C-H), 1332 (O-H), 1218 (Ar-O), 1080 (C-O), 968 (N-O), 734 (Ar) cm^{-1}; ESI-MS: *m/z* 413 [M+Na]$^+$.

[Mn^{III}(L6)$_2$][NO_3]·MeOH (**C66**): To a solution of H_3**L4** (0.0051 g, 0.01 mmol, 1 eq.) in $CHCl_3$ (1 mL), was added solutions of Mn(NO_3)$_2$·4H_2O (0.0025 g, 0.01 mmol, 1 eq.), Gd(NO_3)$_3$·6H_2-O (0.0045 g, 0.01 mmol, 1 eq.) both in MeOH (0.2 mL) and the solution was stirred at RT for 10 minutes. Et_3N (0.03 mL, 0.03 mmol, 3 eq.) was added and the solution was stirred at RT overnight. Isolation of the complex was achieved by the vapour diffusion of Et_2O into the filtered reaction solution. Brown precipitate was collected after five weeks. Yield (0.0012 g, 12%); ATR-IR: $\overline{\nu}$ = 3439 (O-H), 2990 (C-H), 1600 (C=N), 1552 (Ar), 1467 (NO_3), 1451 (C-H), 1362 (O-H), 1311 (C-N), 1248 (NO_3), 1217 (Ar-O), 1084 (NO_3), 1035 (C-O), 975 (N-O), 828 (NO_3), 741 (Ar) cm^{-1}; ESI-MS: *m/z* 938 [M-MeOH-NO_3]$^+$.

Chapter 7

Conclusions and Future Work

This research has explored different methods to which the exchange pathways found in polynuclear clusters can be manipulated. These methods have involved changing the bridging anions and/or groups, lattice solvates, metal ion combinations, and finally changing the peripheral coordinated anions and/or solvent molecules. The topologies of interest for this research were defective dicubanes, dinuclear, and extended structures and networks with a total of 66 complexes produced. Four different ligands systems have been produced, all of which focus on oxime derived groups, with each ligand system building from lessons learnt from the last to increase the potential to promote ferromagnetic exchange.

The ligand, H_2**L1**, a single headed oxime-based ligand with an oxygen containing amino side arm was known to coordinate 3*d* ions, producing homometallic polynuclear clusters. Five Ni^{II}_4 defective dicubanes (**C1** - **C5**) were synthesised during this research which explore the manipulation of three key exchange pathways. Two methods of manipulation were used for this series, the switching of the exchange pathway donor atoms and the incorporation of various solvate molecules into the crystal lattice. DC molar magnetic susceptibility measurements were performed on the complexes **C1** - **C3** and **C5** revealing **C1**, **C2**, and **C3** to have competing ferro- and antiferromagnetic interactions, with the complex **C5** found to have dominant antiferromagnetic exchange between the metal ions. Comparing the magnetic properties of the complexes, it can be seen that the inclusion of the OH^- bridging in **C2** greatly influenced ferromagnetic exchange for the J_1 and J_2 pathways compared to the OMe^- bridging in **C1**, the closest comparison, however this type of bridging (OH^-) produced large antiferromagnetic exchange for the J_3 pathway. This Chapter highlights how subtle differences can result in significantly different magnetic properties most strikingly seen between the original defective dicubane and **C1**, with the key differences being the solvent molecules found in the crystal lattice. For the original dicubane, the starting platform for the manipulations, Et_2O molecules are found in the crystal lattice whereas for **C1**, MeOH molecules are found with the key point of difference being that the MeOH molecules 'interact' (hydrogen bond) with the donor groups of the exchange pathways, resulting in shortened bond lengths and smaller exchange pathway angles ultimately producing greater ferromagnetic exchange. As shown, the best manipulator was the introduction of a hydrogen bonding solvent into the crystal lattice.

Chapter 4 discusses a series of homo- and heterometallic 3*d*3*d*' dinuclear complexes (**C6** - **C13**), which utilise the alkyloxime ligand, H_2**L2**, chosen for its two distinct coordination pockets. These complexes explore the way in which the metal ion combination affects both the exchange pathway angle and the overall magnetic properties of the complex. It was found that for the most part the exchange angles are within

experimental error of each other with the Mn^{II}_2 complex found to have the smallest M1-O-M2 angles and the $Cu^{II}Mn^{II}$ complex the largest. The overall stability of the complexes (**C7**, **C8**, and **C11**) was investigated by a combination of computational methods and transmetalation reactions to determine whether complex stability corresponded to interesting magnetic properties. Transmetalation reactions were performed in conjuction with the aforementioned computational analysis, which revealed that when in the presence of either $Cu(NO_3)_2{\cdot}3H_2O$ or $Mn(NO_3)_2{\cdot}4H_2O$ methanolic solutions, the complexes **C6**, **C7**, and **C9 - C13** all produced the $Cu^{II}Mn^{II}$ dinuclear complex, **C8**. This was further corroborated by computational analysis which confirmed **C8** to have the largest binding energy. DC molar magnetic susceptibility measurements were performed on complexes **C6 - C8** and **C10 C12** revealing complexes **C6**, **C8**, and **C10 - C12** to have antiferromagnetic exchange between the metal ions with *J* coupling parameters of -34.8, -0.45, and -6.43 cm^{-1} for **C8**, **C11**, and **C12** respectively. Due to the large and complicated anisotropy of the Co^{II} ions in **C6** and **C10**, the data was not fitted. The magnetic analysis revealed that **C7** had large ferromagnetic exchange (J = +63.0), an unusual result as typically Cu^{II}_2 dinuclear complexes with large exchange angles ($\sim 105°$) have antiferromagnetic exchange. It is thought the unusual seven-coordinate geometry of the outer Cu^{II} ion was a driving factor for the ferromagnetic exchange.

Following on from the success of the 3*d*3*d*′ series, a series of 3*d*4*f* dinuclear complexes (**C14 - C49**) were produced, which utilised H_2**L2**. This series further investigates the effect of metal ion combination by incorporating 4*f* ions. This series also explores different anion and solvent coordinates and how they effect the structural properties. DC molar magnetic susceptibility measurements were performed on the complexes **C17**, **C21**, and **C37** revealing that both **C17** and **C21** have ferromagnetic exchange between the Cu^{II} and 4*f* ions with a *J* exchange parameter of +2.94 cm^{-1} found for **C17**. For **C37**, it was found that dominant antiferromagnetic exchange was present between the metal ions, consistent with the large M1-O-M2 angles of 107°. Expanding from the transmetalation reactions performed in Chapter 4, a select series of transmetalation reactions were performed starting from the $Cu^{II}Gd^{III}$ dimer, **C17**. It was indicated that the larger metal ions, such as La^{III}, Ce^{III}, and Eu^{III}, were favoured, as the complexes **C22**, **C27**, and **C28** were successfully produced. The stability of the outer pocket was experimentally tested by transmetalating the complexes, **C17**, **C20**, **C21**, **C26**, and **C29**, with $Mn(NO_3)_2{\cdot}4H_2O$, which revealed the $Cu^{II}Mn^{III}$ complex, **C8** to have the greatest stability as all transmetalation reactions resulted in the formation of **C8**. When comparing the structures, it can be seen that the complexes with a Cu^{II} ion in the inner pocket have less structural distortion around the inner pocket than the six-coordinate metal ions, a feature also seen in the 3*d*3*d*′ series.

For a large majority of the structures, the M1-O-M2 exchange angles and M1$\cdots$M2 distances are all within experimental error of one another, which suggests the ligand has considerable control of the binding environments of the metal ions. It was found that additional interactions, such as increased bridging between the metal ions, was required to disturb the ligand geometry and decrease the M1-O-M2 exchange angle(s). In addition to the exchange angle analysis, it was found that the complexes with solvent coordinates and subsequently hydrogen bonding had larger M1-O-M2 exchange angles and M1$\cdots$M2 distances as the metal ions are drawn out of the pocket in order for the intra- and intermolecular hydrogen bonding networks to form.

The final chapter, Chapter 6, explores the complexes that were unexpectedly produced during the duration of this research, ranging from mononuclear complexes to large extended clusters and polymers. One of the most intriguing structures produced in this chapter is the $Cu^{II}{}_{12}Eu^{III}{}_{4}$ cluster, **C60**, which is the only example of the ligand, H_4**L3**. This structure is a bowl-like cluster which surrounds a Cl^- anion found in the crystal lattice. The use of H_4**L3** has provided an additional donor atom to bridge between metal atoms, this is seen by the large nuclearity of the complex as well as the large amount of exchange pathways present. To date a suitable synthetic method has not been achieved with attempts to elucidate whether the Cl^- anion was essential to the formation of the structure proved inconclusive.

When attempting to produce extended networks, the polymeric complexes **C56** and **C57** and dinuclear complex **C58** were produced from a single complexation reaction between **C17** and Na oxalate with the use of different crystallisation methods and time periods. The $Cu^{II}Gd^{III}$ polymer, **C56**, has a zig-zag appearance with alternating dinuclear units bridged by Ox^{2-} groups. The second polymer of this group is a $Cu^{II}Na^{I}$ polymer which has an unusual staggered appearance due to the two different types of bridging groups: $NO_3{}^-$ anions and alkyloxime oxygens. The coordination of the alkyloxime oxygen to the metal ion is an uncommon type of coordination with only a few examples reported in the literature. The final complex in this series is a $Cu^{II}Na^{I}$ dinuclear structure that resembles the single unit of the $Cu^{II}Na^{I}$ polymer however due to the coordination of solvent molecules, the polymer formation was stunted.

This research has explored the way in which magnetic properties of a complex can be manipulated by the use of different bridging groups, lattice molecules, and metal ion combinations and coordinates. The use of simple oxime based ligands has resulted in complexes with defective dicubane and dinuclear topologies providing a solid platform for manipulations. This thesis provides a number of different directions for future research to investigate different types of manipulations that enhance or affect the exchange pathways and/or magnetic properties. The defective dicubanes, investigated in Chapter 3, provide a pathway to further explore subtle differences in the crystal lattice by methods of dehydration, hydration, and the use of different complexation and crystallisation solvents. An interesting project would be to look at single-crystal-to-single-crystal transformations surrounding dehydration, hydration, and the introduction of different solvents into the crystal lattice. The 3*d*3*d*′ dinuclear series found unusual results with the ferromagnetic exchange present in the $Cu^{II}{}_2$ complex, **C7**. It is thought that the unusual seven-coordinate geometry of the outer Cu^{II} ion was a driving factor for the ferromagnetic exchange. This phenomena has created a direction for future research to investigate how unusual coordination geometries affect the magnetic properties of a complex. Another direction from this chapter of research would be to further investigate the dinuclear complexes by both transmetalation and computational methods to establish a stability series for the complete 3*d*3*d*′ dinuclear series. Additionally, future work for this chapter would be to complete the series, for example synthesise dinuclear complexes with $Co^{II}Zn^{II}$, $Ni^{II}Zn^{II}$, $Co^{II}Ni^{II}$, and $Cu^{II}Ni^{II}$ metal ion combinations and look into expanding the series to incude Fe^{II}.

The future work relating to Chapter 5 has a lot of potential, starting with an investigation into reproducing the series of complexes which have been non-reproducible

to date. Another pathway would be to investigate the magnetic properties of all of the 3*d*4*f* complexes, with a closer look at the effect of different 3*d* ions such as Co^{II} and Ni^{II} ions as these metal ions are known to have increased anisotropy compared to Cu^{II} ions. Another direction this research could follow would be to further examine the structural properties of the dinuclear complexes, both by investigating the use of additional bridging to reduce the exchange angle as this provides a method to examine how different types of bridging affect the magnetic properties. Secondly, by more closely examining the stability of the outer pocket with 4*f* ions, similarly to the computational study performed in Chapter 4. The research found in Chapter 6 provides a number of directions for future research, starting with the polymeric complexes **C56** and **C57** as they provide a pathway to research polymer formation using different starting complexes, such as the 3*d*3*d*' dinuclear complexes and different bridging groups such as azide, chloride, and 1,2-benzenedicarboxylic acid. It would be interesting to see whether bridging through an alkyloxime oxygen also occurs when using different metal ions and/or bridging groups. Additionally, it could be investigated whether the $Cu^{II}Na^{I}$ polymer, **C57** could be converted into the single dinuclear $Cu^{II}Na^{I}$ complex, **C58**. The complex **C60** provides a direction to explore the different exchange pathways and the magnetic properties of the cluster, additionally providing an exciting introduction to the ligand H_4**L3** and its potential for extended bridging between metal ions. Similarly to the 3*d*4*f* dinuclear series, several complexes are non-reproducible to date, providing a pathway for future reseach into finding reproducible synthetic methods.

Appendix A

Additional Design and Synthesis Data

A.1 Selected Spectra

Figures A.1 - A.15 show the ^{1}H NMR, ^{13}C NMR and ATR-IR spectra of the new compounds: **8**, **9**, H_4**L3**, and H_3**L4** reported in this research.

A.2 Associated Spectra of 8

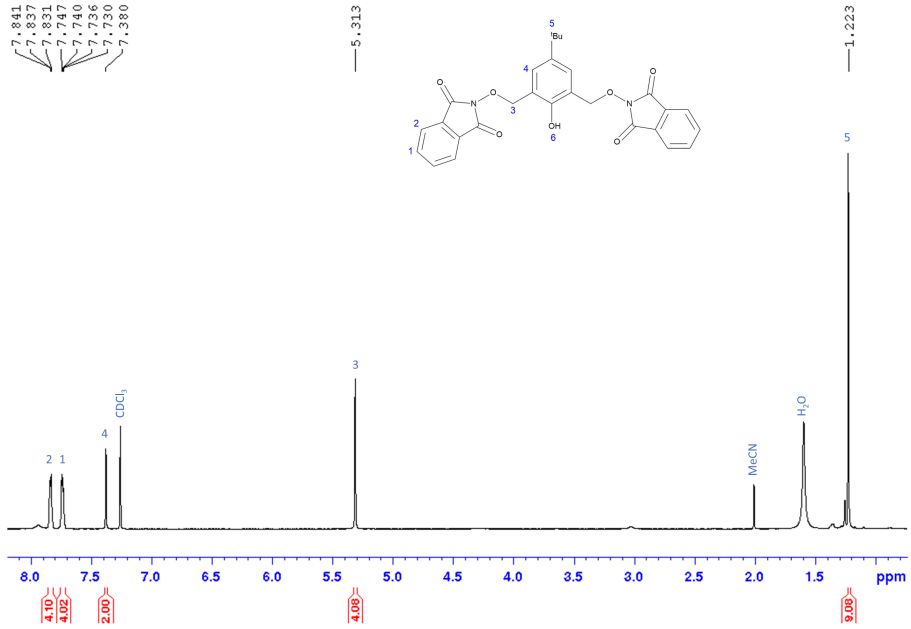

Figure A.1: ^{1}H NMR spectra of **8**

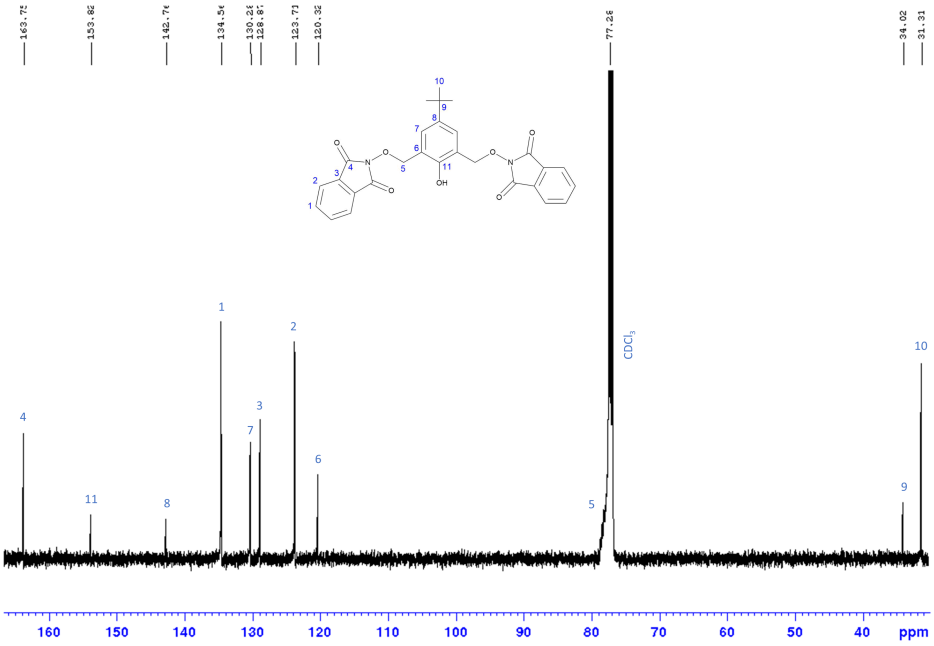

Figure A.2: ^{13}C NMR spectra of **8**

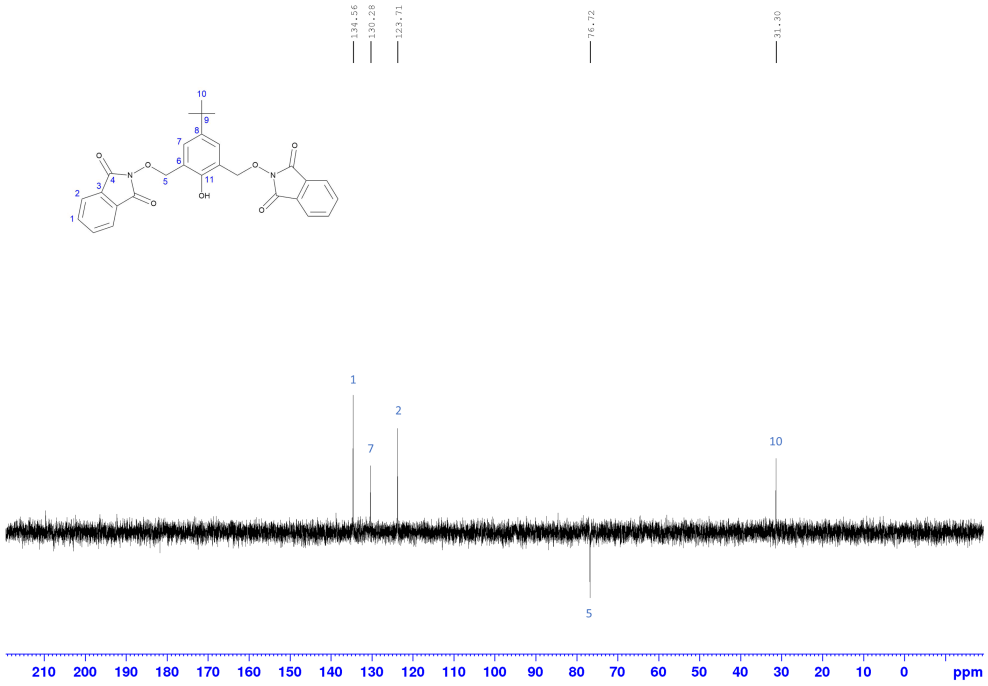

Figure A.3: ^{13}C DEPT NMR spectra of **8**

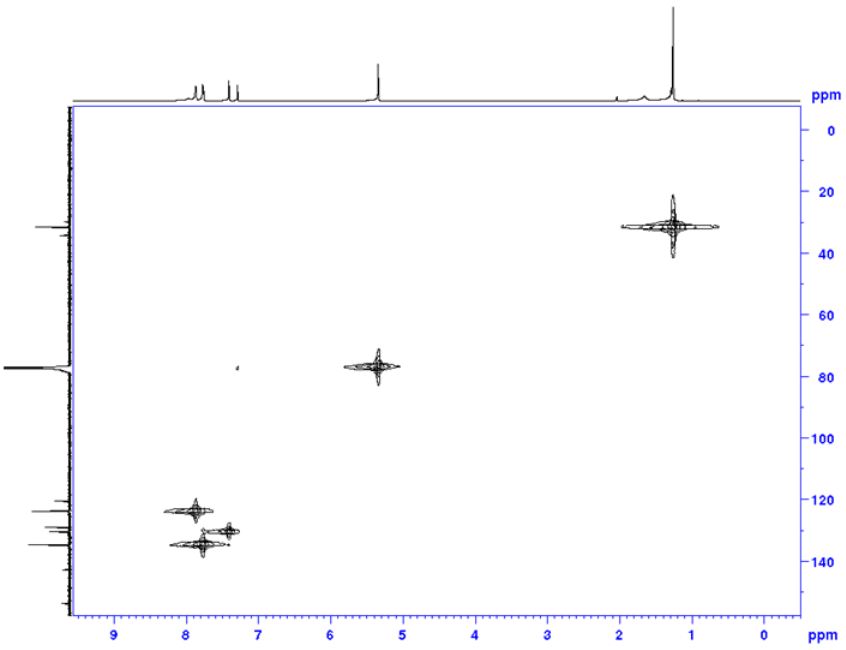

Figure A.4: ^{13}C HMQC NMR spectra of **8**

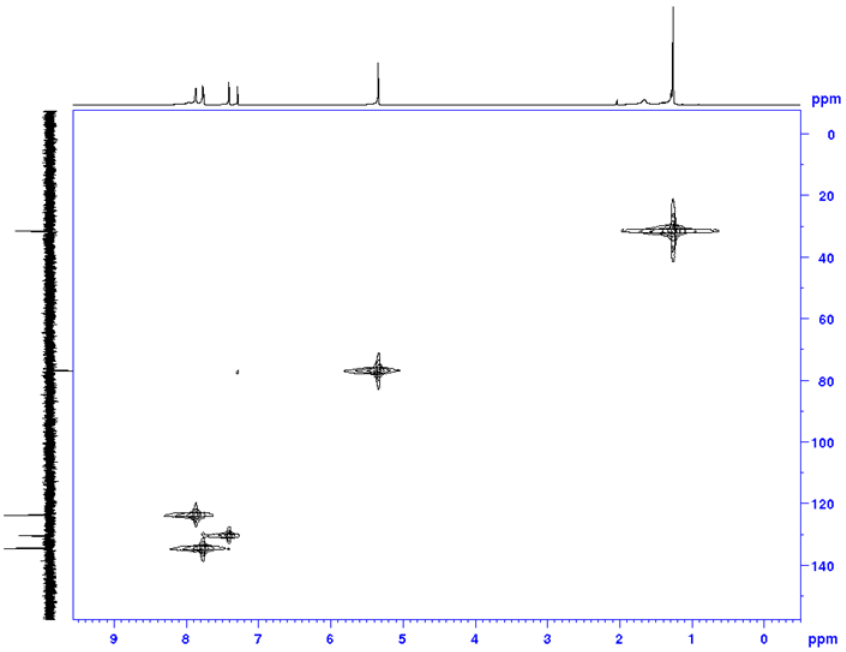

Figure A.5: ^{13}C HMQC NMR spectra of **8**

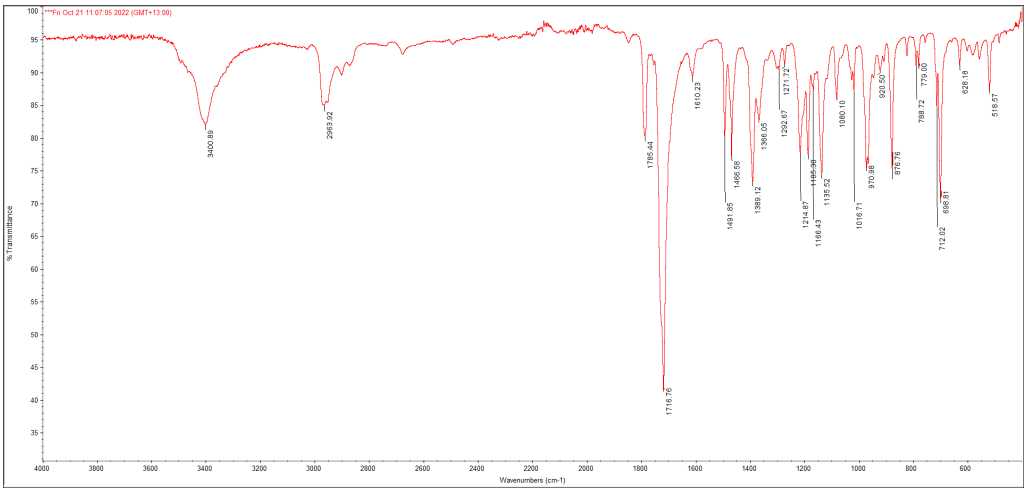

Figure A.6: ATR-IR spectra of **8**

A.3 Associated Spectra of 9

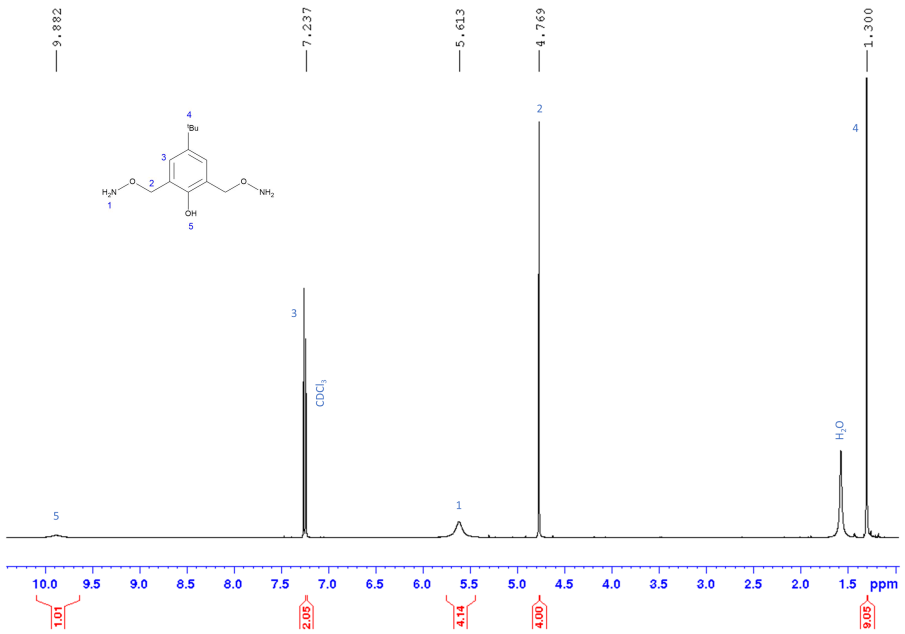

Figure A.7: ^{1}H NMR spectra of **9**

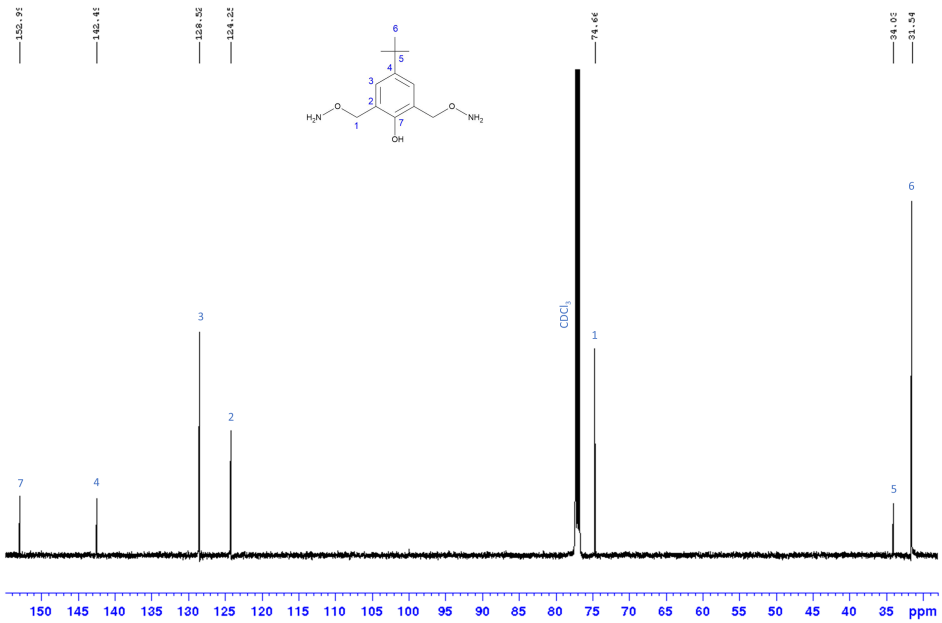

Figure A.8: ^{13}C NMR spectra of **9**

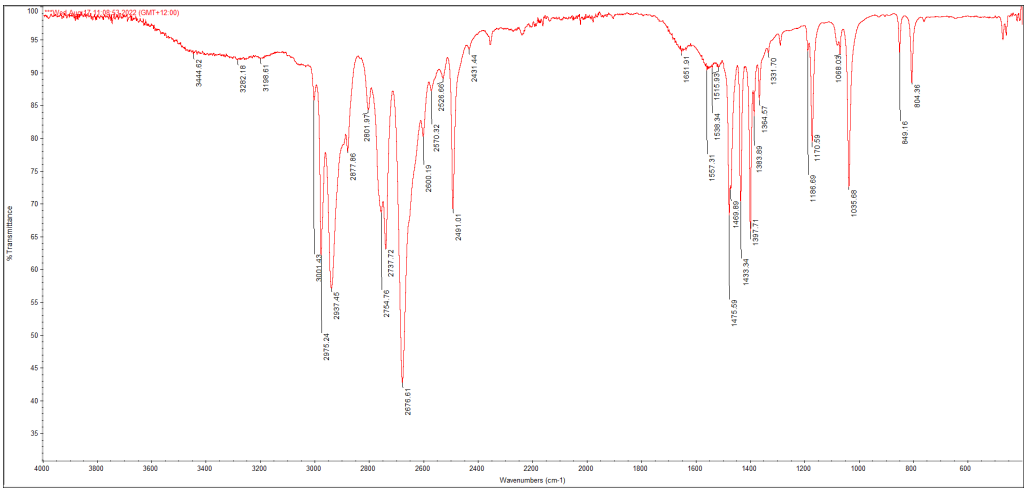

Figure A.9: ATR-IR spectra of **9**

A.4 Associated Spectra of H_4L3

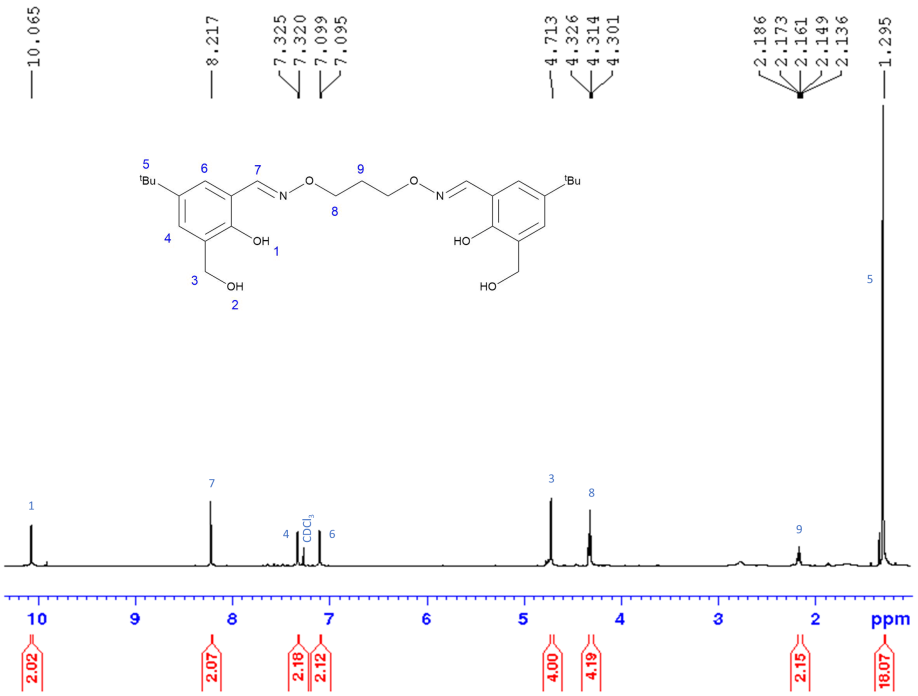

Figure A.10: ^{1}H NMR spectra of H_4**L3**

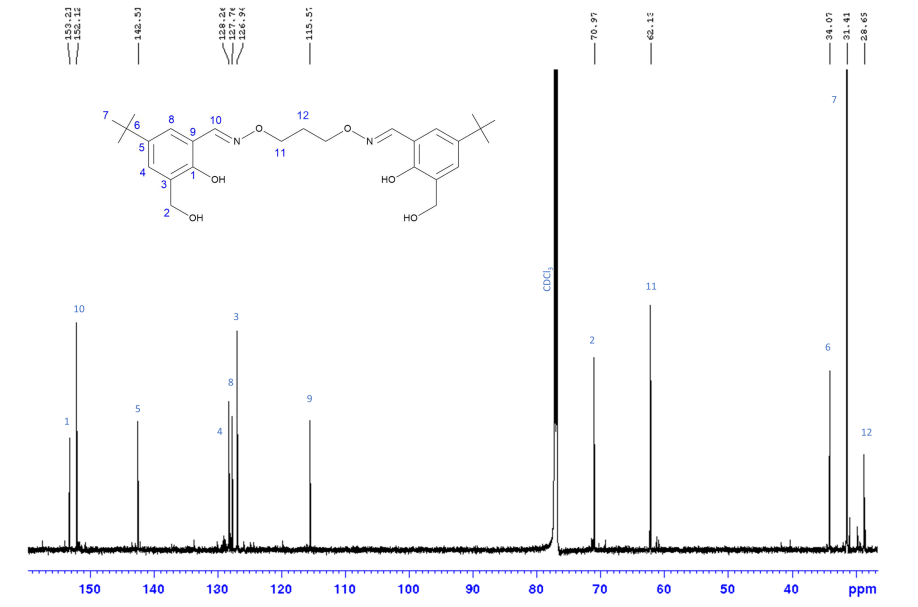

Figure A.11: ^{13}C NMR spectra of H_4**L3**

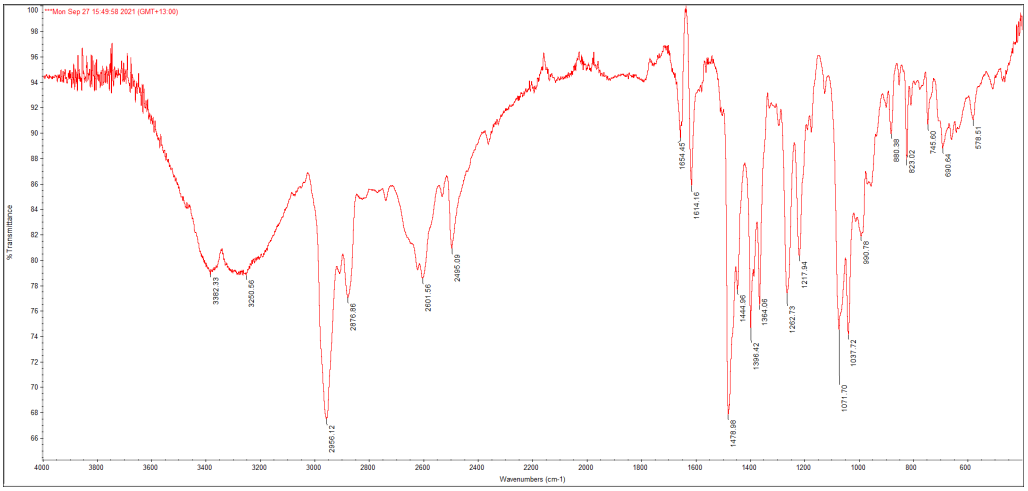

Figure A.12: ^{1}H NMR spectra of H_4**L3**

A.5 Associated Spectra of H_3L4

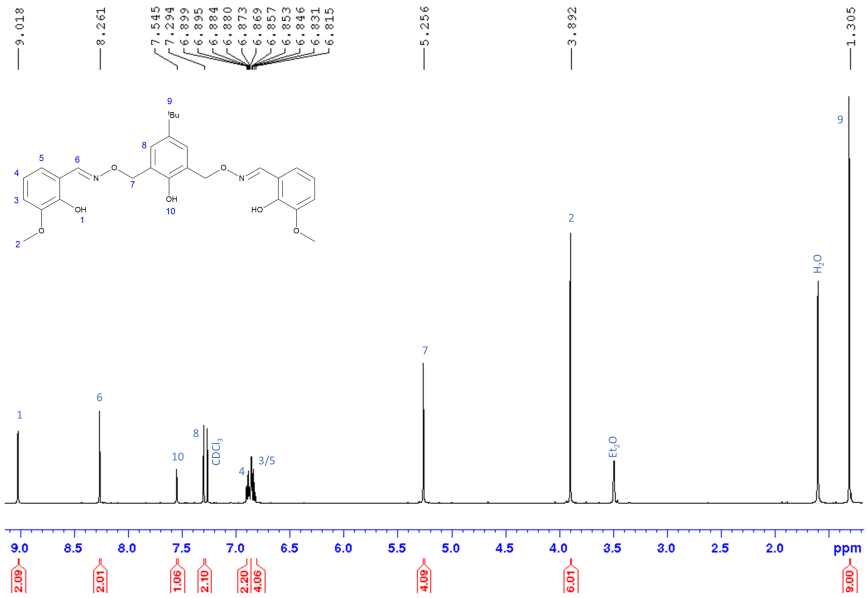

Figure A.13: ^{1}H NMR spectra of H_3**L4**

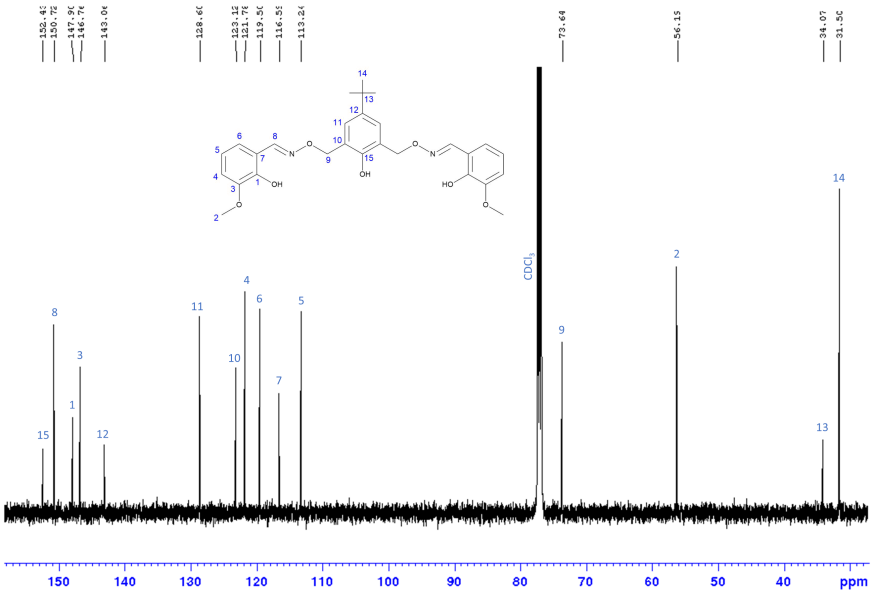

Figure A.14: ^{13}C NMR spectra of H_3**L4**

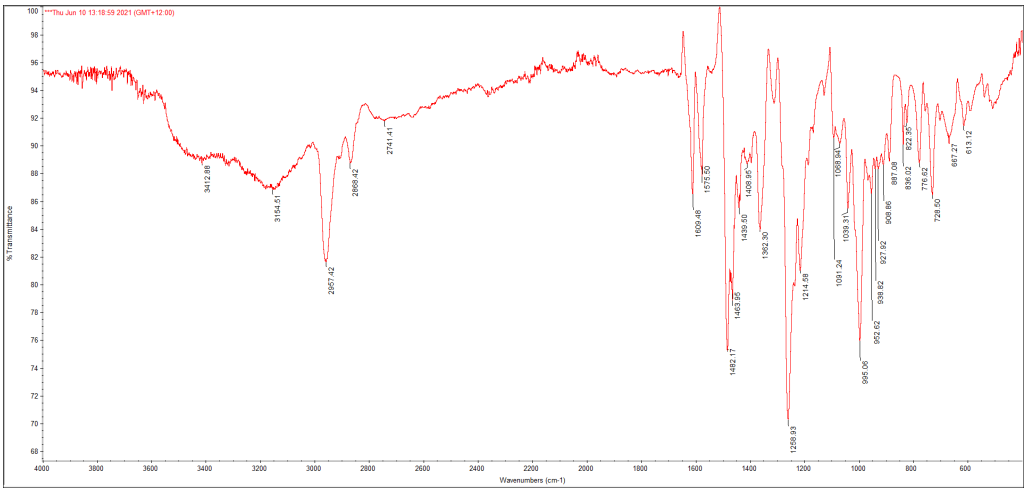

Figure A.15: ATR-IR spectra of H_3**L4**

A.6 Geometric Notation

A.6.1 Harris Notation

As mentioned in Chapter 2, a modified version of the Harris notation has been used to denote the coordination modes of the ligands and anions found in the complexes **C1 - C66**. The Harris notation was derived by Harris[145] during his PhD research at The University of Edinburgh in 1999 and describes the coordination of ligands and anions by a simple numerical code. The notation is most commonly seen in the literature when describing the coordination of polynuclear ligands[318–320] and phosphonate anions.[321–323] The notation has been modified for use in this work by including an additional identifying letter for each donor atom of the ligands. The numerical code, $X.Y^{a}{}_{Z}$, is as follows: X the first number denotes the total number of coordinated metal ions, Y^{a} denotes each donor atom, Y is a number which describes the number of metal ions coordinated to the specific donor atom, with the modified label, a, describing the specific donor atom. The donor atoms are listed from left to right, and in order of highest atomic number, e.g. O is listed before N. Each metal ion is denoted a number, left to right, and is described in the numerical code as Z. An example can be seen in the Figure A.16, where the ligand, $\mathbf{L2}^{2-}$, has a numerical code $2.1^{a}{}_{1}2^{b}{}_{12}2^{g}{}_{12}1^{h}{}_{1}1^{c}{}_{2}1^{f}{}_{2}$. The various different coordination modes described in this research are shown in the Figures 2.2, 2.6, 2.8, 2.11, and A.17 - A.19.

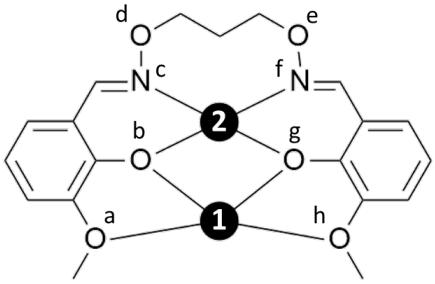

$\mathbf{2.1^{a}{}_{1}2^{b}{}_{12}2^{g}{}_{12}1^{h}{}_{1}1^{c}{}_{2}1^{f}}$

Figure A.16: Example use of the modified Harris notation used in this research.

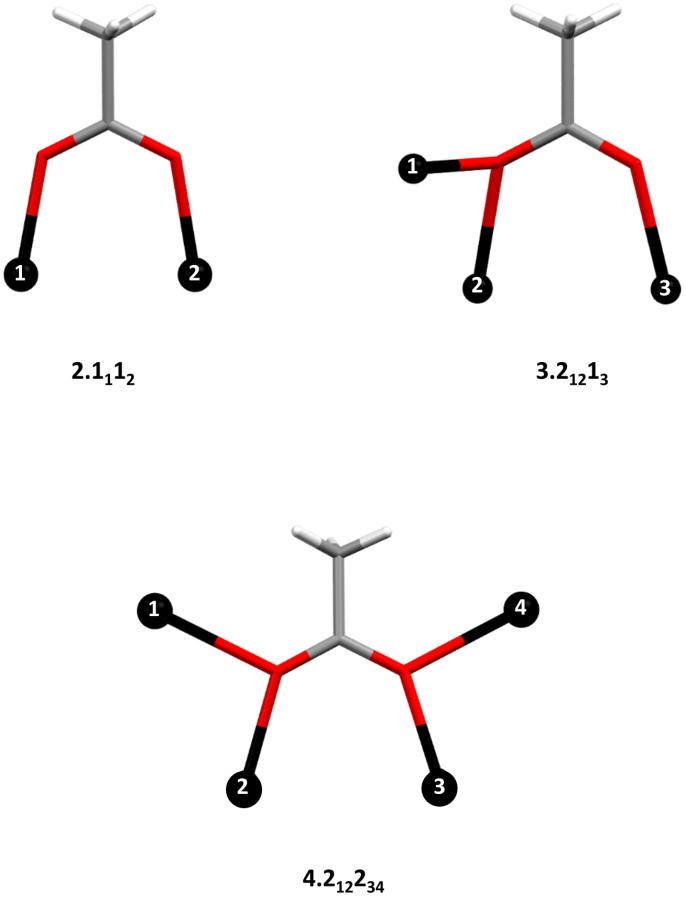

$2.1_1 1_2$ $3.2_{12} 1_3$

$4.2_{12} 2_{34}$

Figure A.17: Schematic representation of the OAc^- coordination modes using the Harris notation.

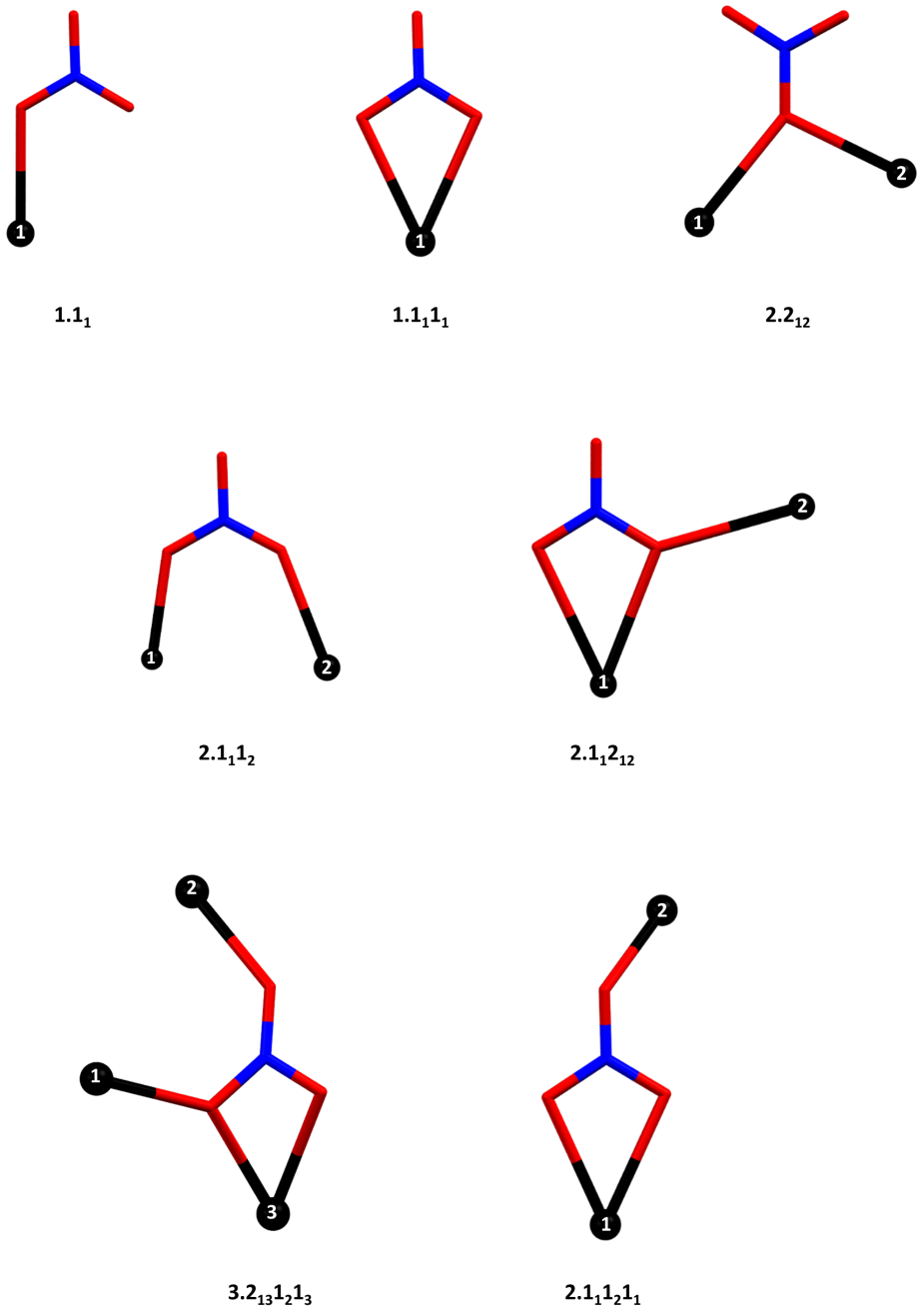

Figure A.18: Schematic representation of the NO_3^- coordination modes using the Harris notation.

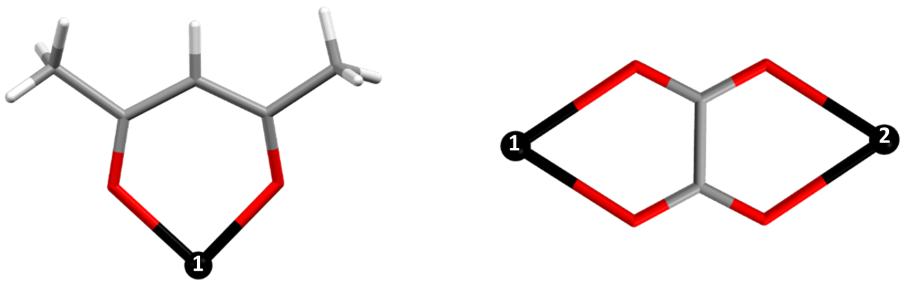

$1.1_1 1_1$ $2.1_1 1_1 1_2 1_2$

Figure A.19: Schematic representation of the $acac^-$ (left) and Ox^{2-} (right) coordination modes using the Harris notation.

A.6.2 CShM Notation

The program SHAPE calculates the geometry of a given set of coordinates by continuous shape measurements relative to the coordinates of ideal polyhedra.[146,147,324] Geometries with no distortion present have a value of one. The geometry codes reported throughout this research correspond to the geometries found in Tables A.1 - A.9.[171,210,267,268,270,274,275,281,283]

Table A.1: CShM notation for four-coordinate metal geometries

Code	Point Group	Geometry
SP-4	D4h	Square
T-4	Td	Tetrahedron
SS-4	C2v	Seesaw
vTBPY-4	C3v	Vacant Trigonal Bipyramid

Table A.2: CShM notation for five-coordinate metal geometries

Code	Point Group	Geometry
PP-5	D5h	Pentagon
vOC-5	C4v	Vacant Octahedron
TBPY-5	D3h	Trigonal Bipyramid
SPY-5	C4v	Spherical Square Pyramid
JTBPY-5	D3h	Johnson Trigonal Bipyramid J12

Table A.3: CShM notation for six-coordinate metal geometries

Code	Point Group	Geometry
HP-6	D6h	Hexagon
PPY-6	C5v	Pentagonal Pyramid
OC-6	Oh	Octahedron
TPR-6	D3h	Trigonal Prism
JPPY-6	C5v	Johnson Pentagonal Pyramid J2

Table A.4: CShM notation for seven-coordinate metal geometries

Code	Point Group	Geometry
PBPY-7	D5h	Pentagonal Bipyramid
COC-7	C3v	Capped Octahedron
CTPR-7	C2v	Capped Trigonal Prism
JPBPY-7	D5h	Johnson Pentagonal Bipyramid J13
JETPY-7	C3v	Johnson Elongated Triangular Pyramid J7

Table A.5: CShM notation for eight-coordinate metal geometries

Code	Point Group	Geometry
SAPR-8	D4d	Square Antiprism
TDD-8	D2d	Triangular Dodecahedron
JBTPR-8	C2v	Biaugmented Trigonal Prism J50
BTPR-8	C2v	Biaugmented Trigonal Prism
JSD-8	D2d	Snub Diphenoid J84

Table A.6: CShM notation for nine-coordinate metal geometries

Code	Point Group	Geometry
JCSAPR-9	C4v	Capped Square Antiprism J10
CSAPR-9	C4v	Spherical Capped Square Antiprism
JTCTPR-9	D3h	Tricapped Trigonal Prism J51
TCTPR-9	D3h	Spherical Tricapped Trigonal Prism
MFF-9	Cs	Muffin

Table A.7: CShM notation for 10-coordinate metal geometries

Code	Point Group	Geometry
JBCSAPR-10	D4d	Bicapped Square Antiprism J17
JSPC-10	C2v	Sphenocorona J87
SDD-10	D2	Staggered Dodecahedron (2:6:2)
TD-10	C2v	Tetradecahedron (2:6:2)

Table A.8: CShM notation for 11-coordinate metal geometries

Code	Point Group	Geometry
JCPPR-11	C5v	Capped Pentagonal Prism J9
JCPAPR-11	C5v	Capped Pentagonal Antiprism J11
JAPPR-11	C2v	Augmented Pentagonal Prism J52
JASPC-11	Cs	Augmented Sphenocorona J87

Table A.9: CShM notation for 12-coordinate metal geometries

Code	Point Group	Geometry
COC-12	Oh	Cuboctahedron
ACOC-12	D3h	Anticuboctahedron J27
IC-12	Ih	Icosahedron
JEPBPY-12	D6h	Johnson Elongated Pentagonal Bipyramid J16

Appendix B

Additional Data for the Defective Dicubanes C1 - C5

B.1 Figures of the X-ray Structures for Complexes, C1 - C5

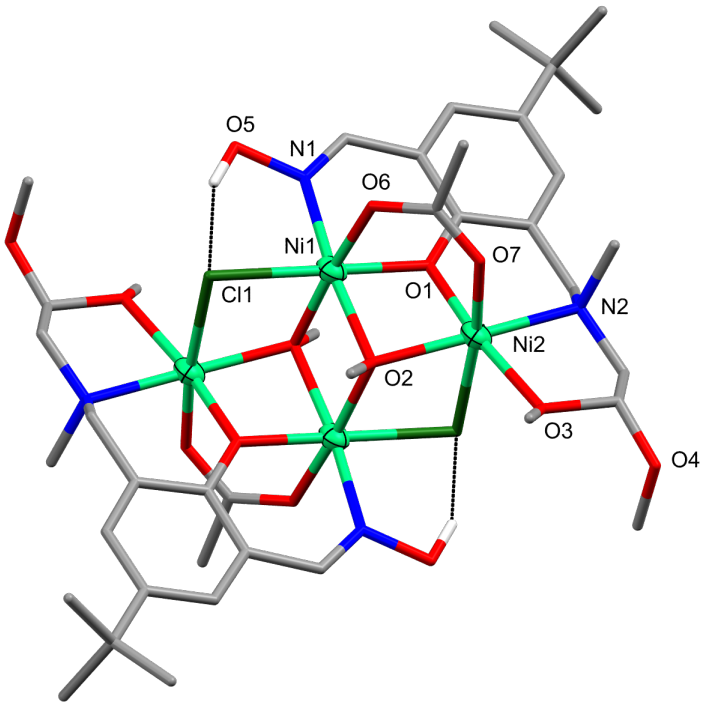

Figure B.1: Full molecular structure of the Ni^{II}_4 defective dicubane $[Ni^{II}_4(HL1)_2(OMe)_2(OAc)_2Cl_2]\cdot 2MeOH$ (**C1**), discussed in Section 3.1.1. Non-interacting hydrogen atoms have been omitted for clarity, hydrogen bonding is represented as black dotted lines, and thermal ellipsoids of the metal ions are shown at 70% probability. Colour code: Ni^{II} = light green, N = blue, O = red, Cl = dark green, C = grey, and H = white.

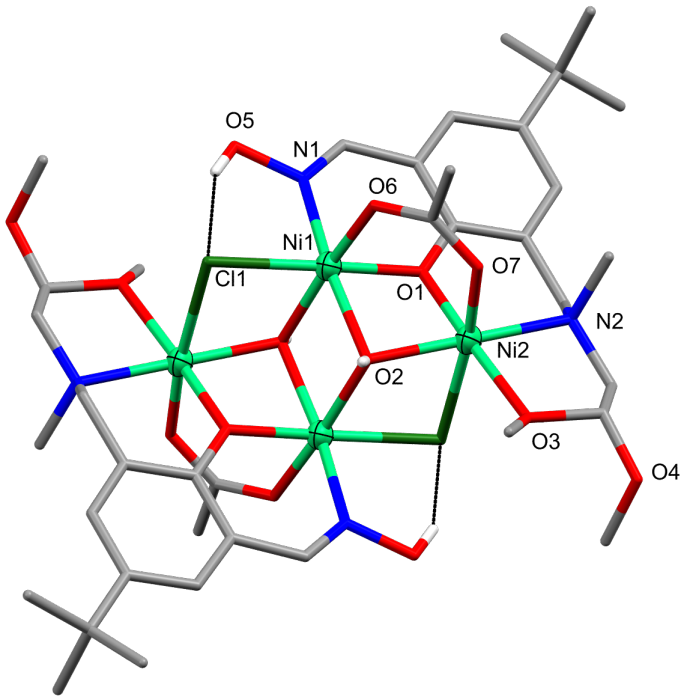

Figure B.2: Full molecular structure of the Ni^{II}_4 defective dicubane $[Ni^{II}_4(H\mathbf{L1})_2(OH)_2(OAc)_2Cl_2]\cdot 2MeCN$ (**C2**), discussed in Section 3.1.1. Non-interacting hydrogen atoms have been omitted for clarity, hydrogen bonding is represented as black dotted lines, and thermal ellipsoids of the metal ions are shown at 70% probability. Colour code: Ni^{II} = light green, N = blue, O = red, Cl = dark green, C = grey, and H = white.

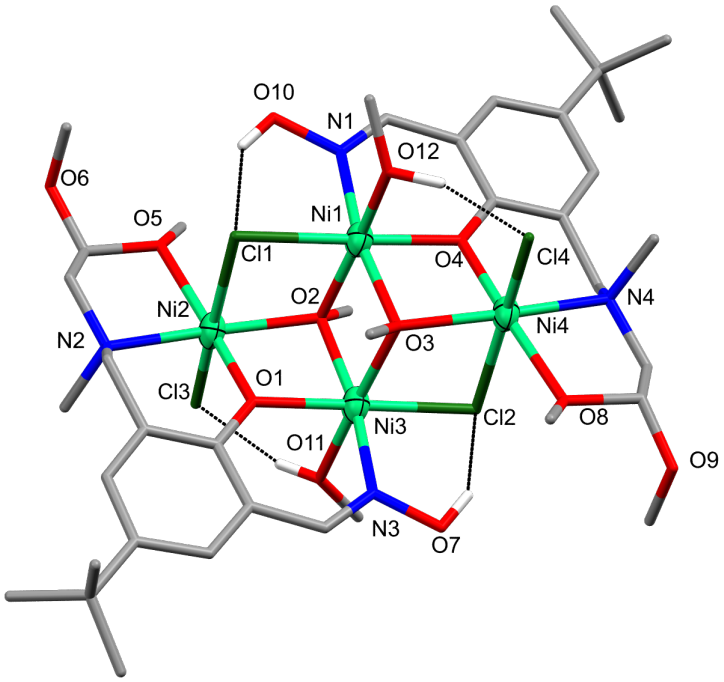

Figure B.3: Full molecular structure of the Ni^{II}_4 defective dicubane $[Ni^{II}_4(HL1)_2(OMe)_2(MeOH)_2Cl_4]\cdot Et_2O$ (**C3**), discussed in Section 3.1.1. Non-interacting hydrogen atoms have been omitted for clarity, hydrogen bonding is represented as black dotted lines, and thermal ellipsoids of the metal ions are shown at 50% probability. Colour code: Ni^{II} = light green, N = blue, O = red, Cl = dark green, C = grey, and H = white.

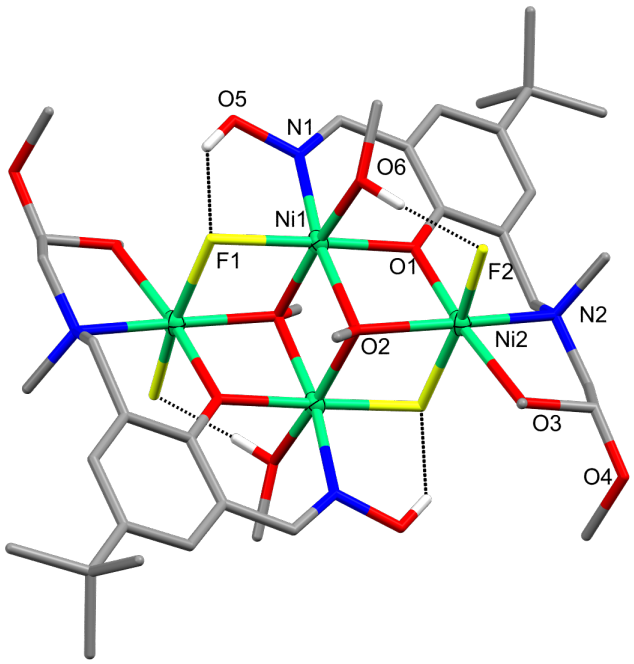

Figure B.4: Full molecular structure of the Ni^{II}_4 defective dicubane $[Ni^{II}_4(HL1)_2(OMe)_2(MeOH)_2F_4]\cdot 4MeOH$ (**C4**), discussed in Section 3.1.1. Non-interacting hydrogen atoms have been omitted for clarity, hydrogen bonding is represented as black dotted lines, and thermal ellipsoids of the metal ions are shown at 70% probability. Colour code: Ni^{II} = light green, N = blue, O = red, F = yellow, C = grey, and H = white.

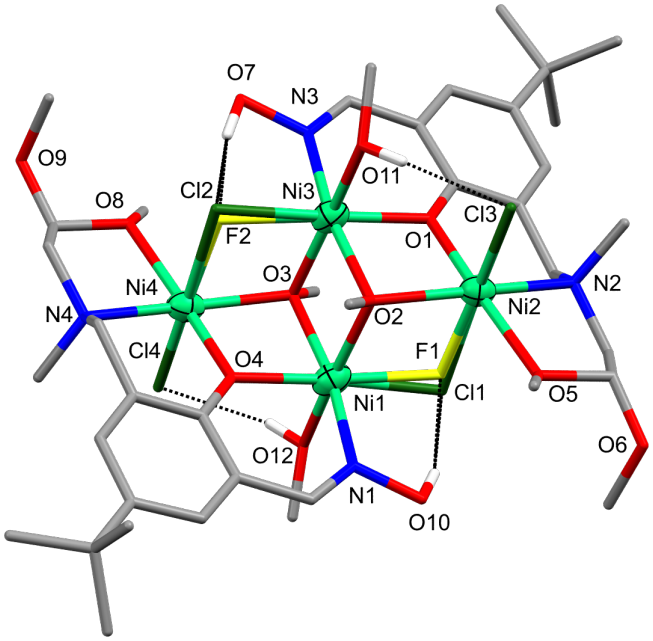

Figure B.5: Full molecular structure of the Ni^{II}_4 defective dicubane $[Ni^{II}_4(HL1)_2(OMe)_2(MeOH)_2Cl_{2.4}F_{1.2}]\cdot Et_2O$ (**C5**), discussed in Section 3.1.1. Non-interacting hydrogen atoms have been omitted for clarity, hydrogen bonding is represented as black dotted lines, and thermal ellipsoids of the metal ions are shown at 50% probability. Colour code: Ni^{II} = light green, N = blue, O = red, Cl = dark green, F = yellow, C = grey, and H = white.

B.2 Additional Structural Data

Table B.1: SHAPE values for complexes **C1 - C5**

	6-Coordinate			
	PPY-6	OC-6	TPR-6	JPPY-6
C1-Ni1	25.196	0.990	13.744	28.493
C1-Ni2	26.463	1.020	13.705	29.325
C2-Ni1	23.857	1.293	13.115	27.285
C2-Ni2	25.993	1.100	12.761	28.907
C3-Ni1	24.242	1.072	12.903	27.503
C3-Ni2	25.346	1.558	11.908	28.315
C3-Ni3	24.724	1.005	14.861	27.907
C3-Ni4	25.438	1.578	12.035	28.417
C4-Ni1	23.821	1.001	11.674	27.142
C4-Ni2	23.189	1.175	11.344	26.763
C5-Ni1^{F}	23.113	1.065	11.523	27.077
C5-Ni2^{F}	22.325	1.726	12.149	27.478
C5-Ni3^{F}	23.376	1.066	11.710	27.366
C5-Ni4^{F}	22.622	1.600	11.993	27.635
C5-Ni1^{Cl}	24.769	0.897	12.719	28.559
C5-Ni2^{Cl}	25.258	1.426	12.942	28.107
C5-Ni3^{Cl}	25.400	0.746	12.993	28.996
C5-Ni4^{Cl}	25.817	1.261	13.345	28.681

Table B.2: Non-averaged bond angles (°) of the complexes **C3** and **C5** from crystal structure determination

	C3	**C5**
Ni1-O2-Ni3	95.51(7)	95.02(11)
Ni1-O3-Ni3	95.77(7)	94.90(11)
Ni1-O4-Ni4	99.96(6)	99.99(13)
Ni2-O1-Ni3	100.75(6)	99.29(12)
Ni1-Cl1-Ni2	86.68(8)	84.29(12)
Ni3-Cl2-Ni4	86.91(8)	85.35(16)
Ni1-F1-Ni2	–	103.1(2)
Ni3-F2-Ni4	–	101.1(3)
Ni1-O2-Ni2	106.95(5)	101.73(10)
Ni3-O3-Ni4	106.84(5)	102.78(11)
Ni2-O2-Ni3	96.38(7)	96.34(11)
Ni4-O3-Ni1	97.25(7)	95.73(12)

Table B.3: Non-averaged bond lengths (Å) of the complexes **C3** and **C5** from crystal structure determination

	C3	**C5**
Ni1-Cl1	2.412(2)	2.283(6)
Ni1-F1	–	2.092(7)
Ni1-O2	2.091(5)	2.058(3)
Ni1-O3	2.056(6)	2.069(3)
Ni1-O4	2.015(5)	2.005(3)
Ni1-O12	2.085(6)	2.088(3)
Ni1-N1	2.054(7)	2.013(4)
Ni2-Cl1	2.473(3)	2.506(5)
Ni2-F1	–	2.017(6)
Ni2-O1	2.020(6)	2.036(3)
Ni2-O2	2.080(5)	2.090(3)
Ni2-O5	2.175(6)	2.173(3)
Ni2-Cl3	2.377(3)	2.369(1)
Ni2-N2	2.087(7)	2.089(3)
Ni3-Cl2	2.401(2)	2.309(7)
Ni3-F2	–	2.122(10)
Ni3-O1	2.000(5)	2.019(3)
Ni3-O2	2.073(6)	2.057(3)
Ni3-O3	2.100(5)	2.051(3)
Ni3-O11	2.095(6)	2.117(3)
Ni3-N3	2.046(7)	2.014(4)
Ni4-Cl2	2.479(3)	2.464(6)
Ni4-Cl4	2.371(3)	2.351(1)
Ni4-F2	–	2.069(9)
Ni4-O3	2.080(5)	2.092(3)
Ni4-O4	2.039(6)	2.024(3)
Ni4-O8	2.182(6)	2.175(3)
Ni4-N4	2.104(7)	2.090(4)
Ni1$\cdots$Ni2	3.103(2)	3.086(1)
Ni3$\cdots$Ni4	3.096(2)	3.090(1)

B.3 Additional Computational Data

Table B.4: Spin configurations for the complexes **C1**, **C3**, and **C5** used to estimating the magnetic exchange parameters

Serial Number	***S***	**Spin Configurations**			
		Ni1	Ni2	Ni3	Ni4
1	4	α	α	α	α
2	2	β	α	α	α
3	2	α	β	α	α
4	2	α	α	β	α
5	2	α	α	α	β
6	0	β	β	α	α
7	0	α	β	β	α
8	0	β	α	β	α

Table B.5: Pertinent structural parameters for the complexes **C1**, **C3**, and **C5**

	Exchange	***avg* Ni-O/F/Cl-Ni angle (°)**	***avg* Ni-O/F/Cl-Ni distance (Å)**
C1	J_1	93.0	2.037
	J_2	96.7	2.256
	J_3	98.2	2.065
C3	J_1	98.6	2.043
	J_2	96.8	2.264
	J_3	95.7	2.080
C5	J_1	97.8	2.051
	J_2	102.4	2.064
	J_3	95.0	2.059

Table B.6: DFT computed overlap integrals for the complexes **C1**, **C3**, and **C5** based off dimeric model complexes

	J_1			J_2			J_3		
C1	**Ni(1)**α**/Ni(2)**β	$\mathbf{d_{z^2}}$	$\mathbf{d_{x^2\text{-}y^2}}$	**Ni(2)**α**/Ni(3)**β	$\mathbf{d_{z^2}}$	$\mathbf{d_{x^2\text{-}y^2}}$	**Ni(1)**α**/Ni(3)**β	$\mathbf{d_{z^2}}$	$\mathbf{d_{x^2\text{-}y^2}}$
	$\mathbf{d_{z^2}}$	0.041^b	0.027^a	$\mathbf{d_{z^2}}$	0.004^a	0.023^a	$\mathbf{d_{z^2}}$	0.011^a	0.009^a
	$\mathbf{d_{x^2\text{-}y^2}}$	0.004^a	0.004^a	$\mathbf{d_{x^2\text{-}y^2}}$	0.019^a	0.055^c	$\mathbf{d_{x^2\text{-}y^2}}$	0.009^a	0.044^b
C3	**Ni(1)**α**/Ni(2)**β	$\mathbf{d_{z^2}}$	$\mathbf{d_{x^2\text{-}y^2}}$	**Ni(2)**α**/Ni(3)**β	$\mathbf{d_{z^2}}$	$\mathbf{d_{x^2\text{-}y^2}}$	**Ni(1)**α**/Ni(3)**β	$\mathbf{d_{z^2}}$	$\mathbf{d_{x^2\text{-}y^2}}$
	$\mathbf{d_{z^2}}$	0.011^a	0.028^a	$\mathbf{d_{z^2}}$	0.001^a	0.022^a	$\mathbf{d_{z^2}}$	0.007^a	0.009^a
	$\mathbf{d_{x^2\text{-}y^2}}$	0.061^c	0.011^a	$\mathbf{d_{x^2\text{-}y^2}}$	0.024^a	0.035^b	$\mathbf{d_{x^2\text{-}y^2}}$	0.013^a	0.019^a
C5	**Ni(1)**α**/Ni(2)**β	$\mathbf{d_{z^2}}$	$\mathbf{d_{x^2\text{-}y^2}}$	**Ni(2)**α**/Ni(3)**β	$\mathbf{d_{z^2}}$	$\mathbf{d_{x^2\text{-}y^2}}$	**Ni(1)**α**/Ni(3)**β	$\mathbf{d_{z^2}}$	$\mathbf{d_{x^2\text{-}y^2}}$
	$\mathbf{d_{z^2}}$	0.024^a	0.016^a	$\mathbf{d_{z^2}}$	0.036^b	0.061^c	$\mathbf{d_{z^2}}$	0.001^a	0.016^a
	$\mathbf{d_{x^2\text{-}y^2}}$	0.012^a	0.050^c	$\mathbf{d_{x^2\text{-}y^2}}$	0.006^a	0.006^a	$\mathbf{d_{x^2\text{-}y^2}}$	0.012^a	0.018^a

^{a} values suggest weak magnetic orbital overlap which - contributes to a F interaction

^{b} values suggest moderate magnetic orbital overlap - contributes to an AF interaction

^{c} values suggest large magnetic orbital overlap - contributes to an AF interaction

Table B.7: DFT computed spin density values of specific atoms for **C1**, **C3**, and **C5**

	C1	**C3**	**C5**
Ni1	1.690	1.689	1.714
Ni2	1.687	1.666	1.701
Ni3	–	1.694	1.717
Ni4	–	1.661	1.697
O1	0.099	0.092	0.090
O2	0.164	0.168	0.165
O3	0.021	0.162	0.162
O4	–	0.099	0.091
O5	–	0.023	0.023
O6	0.042	–	–
O7	0.052	–	–
O8	–	0.023	0.024
O11	–	0.034	0.028
O12	–	0.032	0.029
N1	0.055	0.056	0.058
N2	0.062	0.063	0.065
N3	–	0.054	0.058
N4	–	0.065	0.066
X1	0.099	0.104	0.074
X2	–	0.112	0.068
Cl3	–	0.084	0.068
Cl4	–	0.084	0.073

X = Cl^- (**C1** and **C3**), F^- (**C5**)

Appendix C

Additional Data for the 3*d*3*d*′ Dinuclear Complexes C6 - C13

C.1 FAAS Analysis

Samples were digested with 1.0 mL of conc. nitric acid and diluted with aq. 2M HCl. The standards (0, 1, 2, 4, and 6 ppm) were prepared from BDH standard solutions for atomic absorption spectroscopy. Results are shown in Tables C.1 and C.2 and Figures C.1 - C.4. From the below results it can be seen that **C8**, **CuMn1**, and **CuMn2** have self consistent results indicating a 1 : 1 ratio of Cu^{II} and Mn^{II} ions. For the complexes **C6**, **C10**, and **C12** the experimental concentrations are lower than expected however it can be seen that the Co and Ni results are self consistent with one another and the Cu and Mn results are self consistent with one another, indicating that the ratio of metals are correct, which has been further confirmed by CHN microanalysis. The cause for the low Co and Ni results is not entirely understood, however it could be due to a number of reasons such as poor digestion of the samples, or an interferring substance. Due to limited sample size of **C9** and **C13**, these samples have not been characterised by FAAS, however the 1 : 1 ratio of **C9** and **C13** is indicated by CHN microanalysis and magnetic measurements, which confirmed the presence of a single magnetically active metal centre.

Table C.1: FAAS results for the Co, Cu, Ni, and Mn standard solutions

Conc.	**Abs./St. Dev.**					
	Co	**Cu1**	**Cu2**	**Ni**	**Mn1**	**Mn2**
1.00	0.115/1.41	0.042/1.15	0.07/3.07	0.109/1.11	0.065/0.67	0.065/0.96
2.00	0.178/0.93	0.072/1.09	0.119/1.35	0.154/0.64	0.118/0.91	0.113/0.93
4.00	0.341/0.69	0.145/0.73	0.231/1.15	0.302/0.4	0.246/0.52	0.233/0.46
6.00	0.45/0.63	0.204/0.67	0.319/0.46	0.418/1.38	0.328/0.38	0.309/1.77

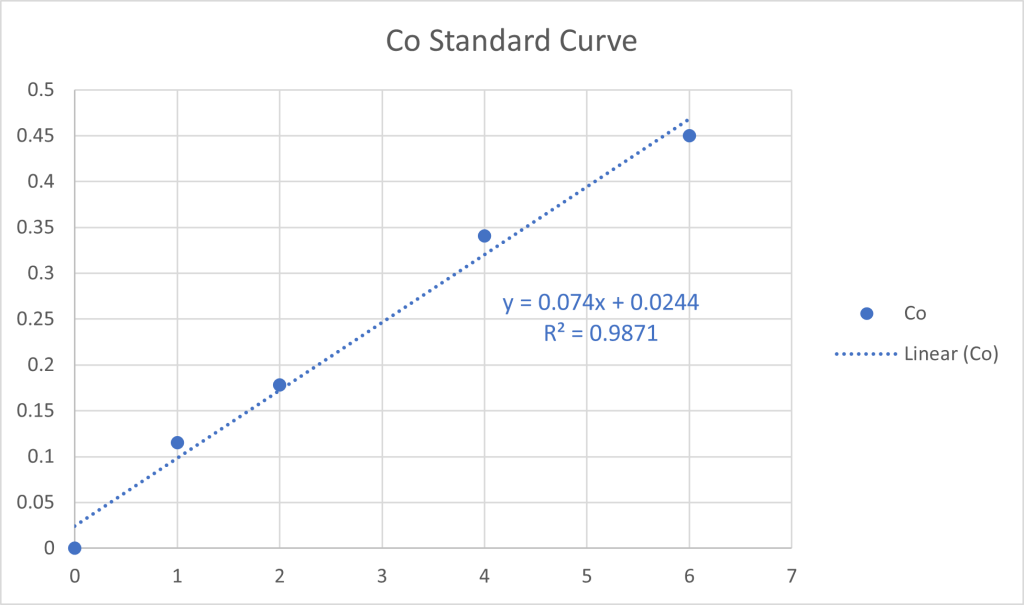

Figure C.1: FAAS standard curve plot for the Co standard solution with the associated trendline equation and R^2 value.

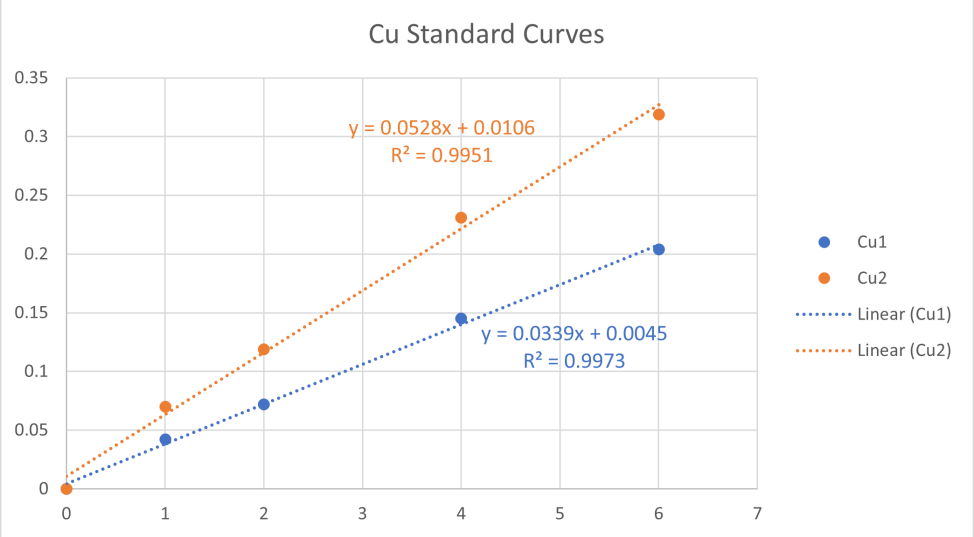

Figure C.2: FAAS standard curve plot for the Cu standard solutions with the associated trendline equations and R^2 values.

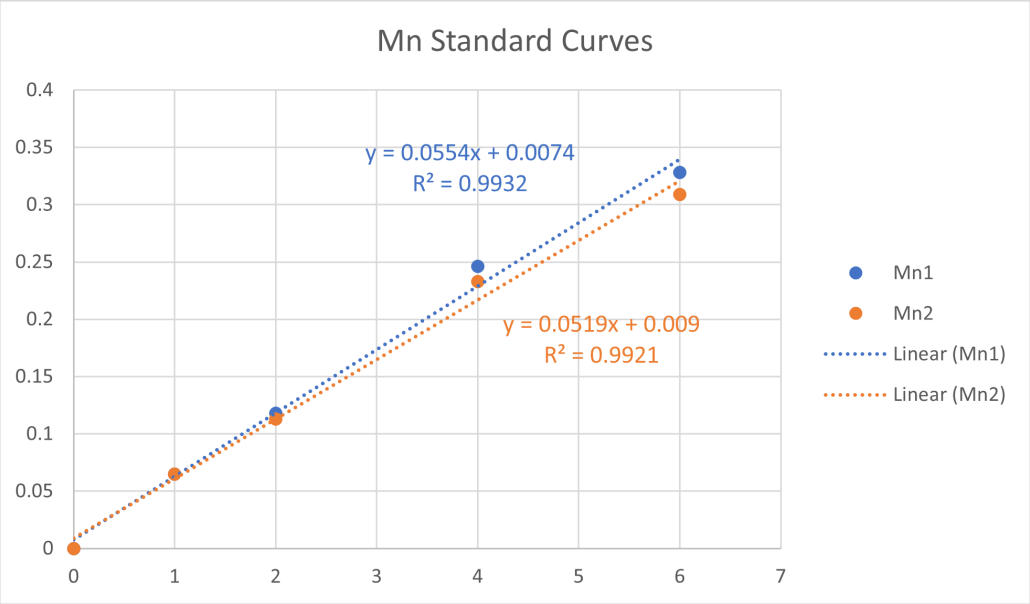

Figure C.3: FAAS standard curve plot for the Mn standard solutions with the associated trendline equations and R^2 values.

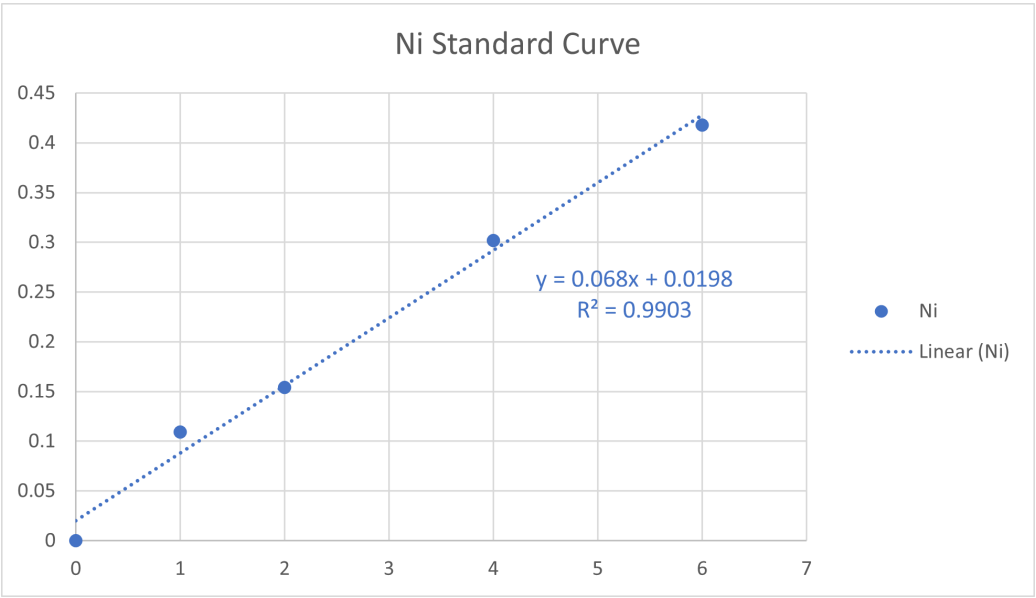

Figure C.4: FAAS standard curve plot for the Ni standard solution with the associated trendline equation and R^2 value.

Table C.2: FAAS results for the complexes, **C6**, **C8**, **C10**, **C12**, **CuMn1**, and **CuMn2**

	M1		M2	
	Conc. (ppm)	**Abs./St. Dev.**	**Conc.** (ppm)	**Abs./St. Dev.**
C6	2.28	0.131/1.61	0.79	0.083/0.27
C8	3.22	0.111/0.81	2.97	0.168/0.11
C10	0.81	0.084/0.99	2.31	0.129/1.05
C12	0.71	0.063/5.26	2.04	0.115/0.58
CuMn1	2.75	0.096/0.52	2.58	0.148/0.64
CuMn2	2.13	0.076/1.06	2.30	0.133/0.37

C.2 Additional Structural Data

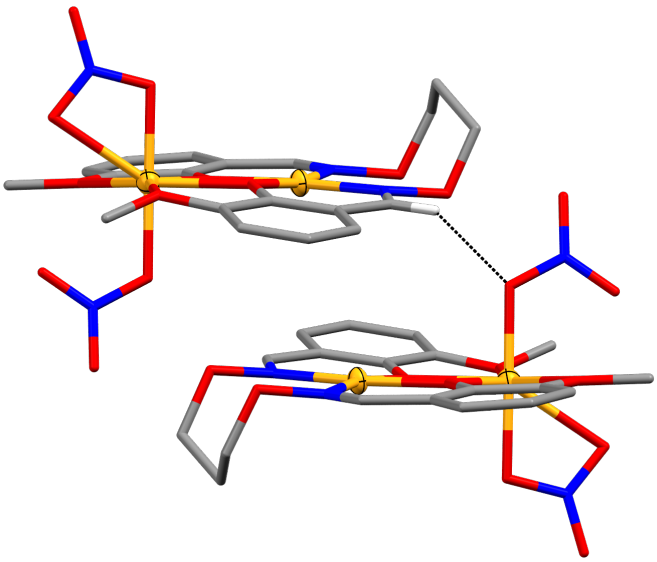

Figure C.5: The close contact, $ONO_3 \cdots (H)C$ (3.160(4) Å), found for **C7**, discussed in Section 4.1.3. Non-interacting hydrogen atoms omitted for clarity, close contact represented as black dotted lines, and the thermal ellipsoids are shown at 70% probability. Colour code: Cu^{II} = yellow, N = blue, O = red, C = grey, and H = white.

Table C.3: SHAPE values of the complexes **C6** - **C13**

	4-Coordinate			
	SP-4	T-4	SS-4	vTBPY-4
C6-Cu1	0.855	30.867	17.463	30.580
C7-Cu1	0.868	29.862	16.794	29.760
C8-Cu1	0.807	30.815	17.457	30.604
C9-Cu1	0.813	30.407	17.186	30.243
	6-Coordinate			
	PPY-6	OC-6	TPR-6	JPPY-6
C10-Co1	23.937	1.498	11.183	27.731
C11-Mn1	23.327	1.939	11.007	27.251
C12-Ni1	24.879	1.224	11.845	28.623
C13-Zn1	23.865	1.722	11.028	27.776
	7-Coordinate			
	PBPY-7	COC-7	CTPR-7	JPBPY-7
C6-Co1	3.652	4.662	3.654	6.827
C7-Cu1	4.427	5.282	4.188	5.396
C8-Mn1	4.815	4.544	3.420	8.399
C9-Zn1	4.073	5.143	3.801	7.771
C10-Mn1	3.855	4.903	3.396	7.477
C11-Mn1	3.928	4.752	3.102	7.443
C12-Mn1	4.264	5.096	3.875	7.880
C13-Mn1	3.943	4.841	3.289	7.595

Table C.4: ESI-MS data for the complexes **C6** - **C13**

	Found *m/z*	Calcd. *m/z*	Calcd. Formula
C6	557.87	557.82	$C_{19}H_{20}N_3O_9CuCo+H^+$
C7	559.98	559.98	$C_{19}H_{20}N_3O_9Cu_2+H^+$
C8	551.75	551.99	$C_{19}H_{20}N_3O_9CuMn+H^+$
C9	564.32	564.85	$C_{19}H_{20}N_3O_9CuZn+H^+$
C10	548.25	548.76	$C_{19}H_{20}N_3O_9CoMn^+$
C11	608.05	608.05	$C_{21}H_{28}N_3O_{11}Mn_2+H^+$
C12	548.25	548.70	$C_{19}H_{20}N_3O_9NiMn^+$
C13	554.70	554.37	$C_{19}H_{20}N_3O_9ZnMn^+$

Table C.5: Common IR stretches for the complexes **C6 - C13**

	$\upsilon_{\text{O-H}}$	$\upsilon_{\text{C=N}}$	$\upsilon_{\text{Ar-O}}$	$\upsilon_{\text{C-O}}$	$\upsilon_{NO_3^-}$			
H_2**L2**	3421	1606	1251	1066	–	–	–	–
C6	–	1607	1246	1098	1462	1288	1038	809
C7	–	1605	1244	1099	1456	1295	1039	821
C8	–	1602	1244	1098	1463	1298	1038	816
C9	–	1606	1249	1105	1464	1290	1036	810
C10	3374	1605	1242	1102	1468	1303	1041	818
C11	3362	1604	1242	1094	1463	1295	1042	809
C12	3374	1605	1242	1102	1467	1301	1042	817
C13	3366	1604	1241	1102	1464	1298	1041	817

C.3 Additional Computational Data

Table C.6: Electronic energy, enthalpy, entropy, and Gibbs free energy values, in Hartree for DFT/B3LYP CPCM(MeOH) TightOpt Freq calculations

Component	*E*(*el*) (Eh)	*H* (Eh)	*T* * *S* (Eh)	*G* (Eh)
$[Cu(H_2O)_5]^{2+}$	-2022.3725	-2022.2326	0.0551	-2022.2878
$[Mn(H_2O)_6]^{2+}$	-1609.4004	-1609.2355	0.0677	-1609.3032
H_2O	-76.4365	-76.4118	0.0214	-76.4332
MeOH	-115.7169	-115.6618	0.0271	-115.6889
NO_3^-	-280.4652	-280.4473	0.0296	-280.4769
L^{2-}	-1296.8102	-1296.4204	0.0815	-1296.4204
C7	-5138.2390	-5137.7978	0.1017	-5137.8995
C8	-4648.8217	-4648.3804	0.1036	-4648.4840
C11	-4390.8195	-4390.2641	0.1235	-4390.3876

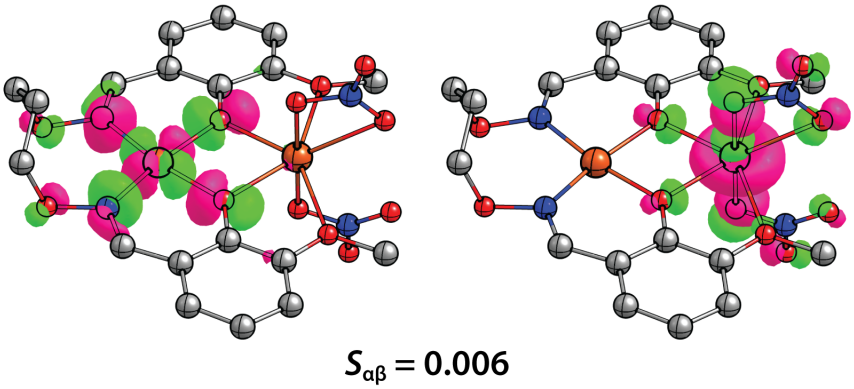

Figure C.6: UCO 157 of **C7**

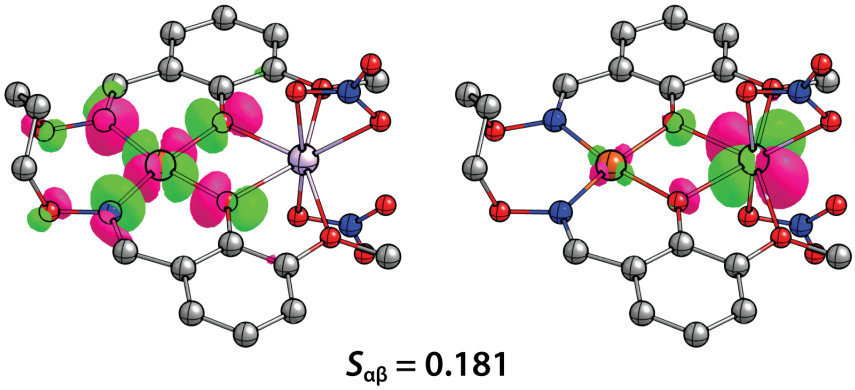

Figure C.7: UCO 153 of **C8**

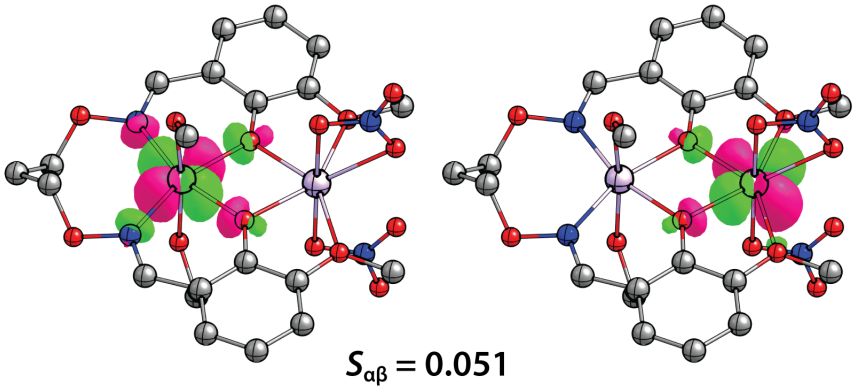

Figure C.8: UCO 167 of **C11**

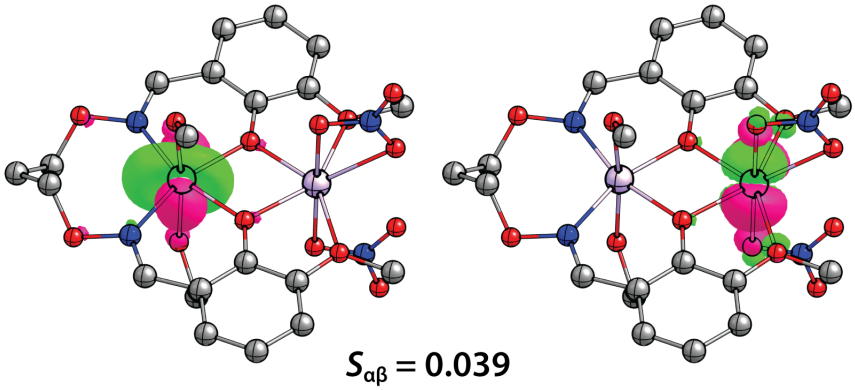

Figure C.9: UCO 168 of **C11**

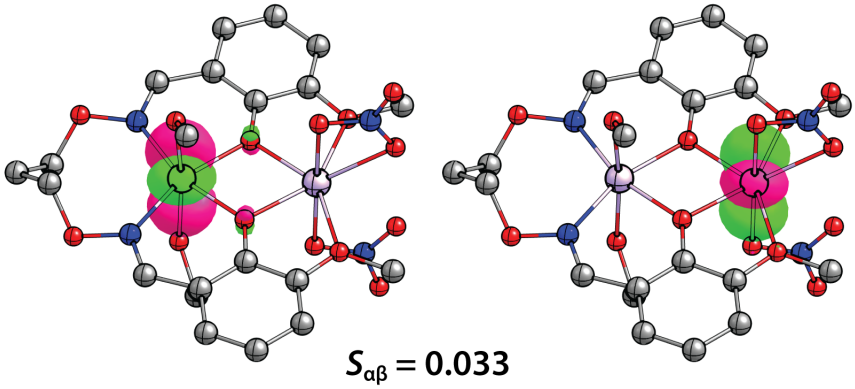

Figure C.10: UCO 169 of **C11**

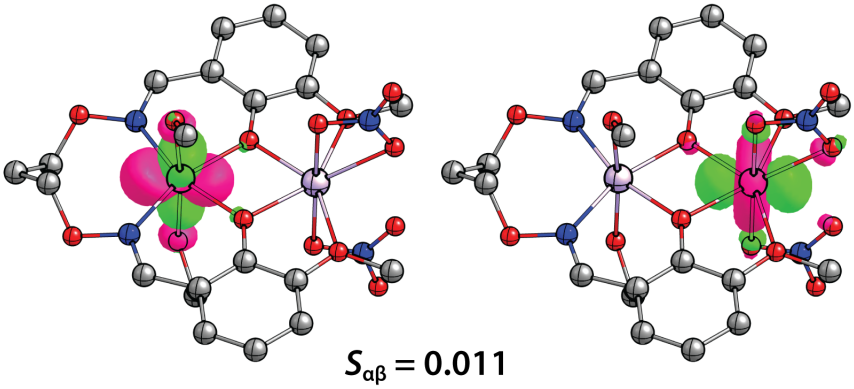

Figure C.11: UCO 170 of **C11**

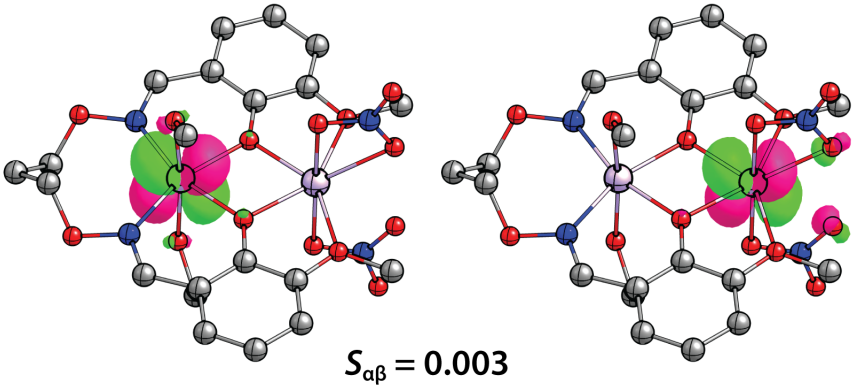

Figure C.12: UCO 171 of **C11**

Appendix D

Additional Data for the 3*d*4*f* Dinuclear Complexes C14 - C49

D.1 Figures of Selected Complexes

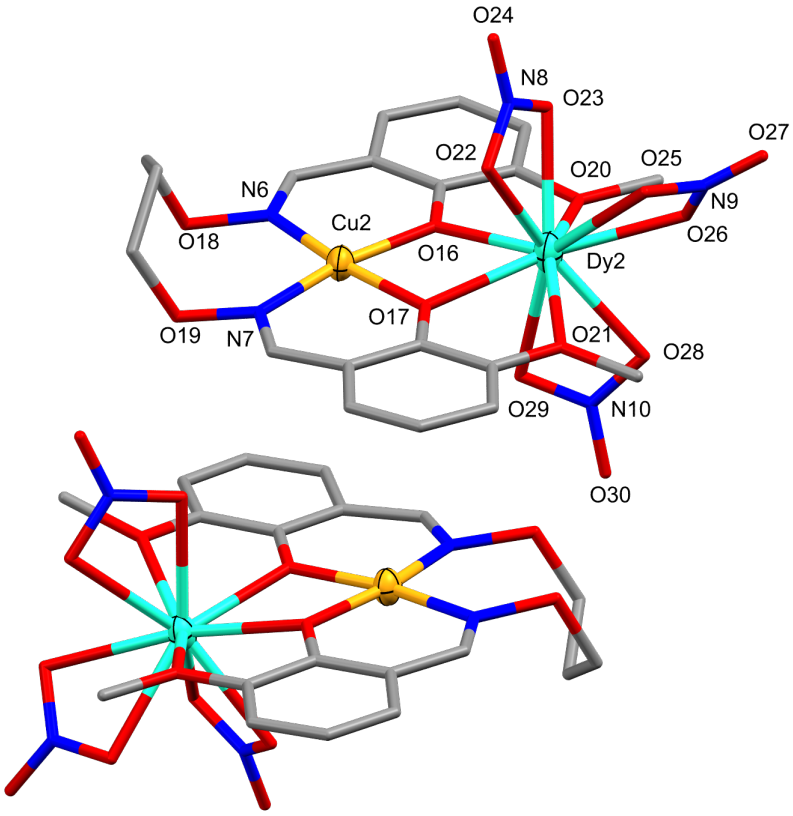

Figure D.1: Representative structure of $[Cu^{II}M2^{III}\mathbf{L2}(NO_3)_3]_2$ (M2 = Dy^{III} (**C21**), Eu^{III} (**C22**), and Gd^{III} (**C23**)) with the second unit labelled (discussed in Section 5.2.1). Hydrogen atoms have been omitted for clarity. Thermal ellipsoids of metal ions are shown at 70% probability. Colour code: Cu^{II} = dark yellow, $M2^{III}$ = aqua, N = blue, O = red, C = grey.

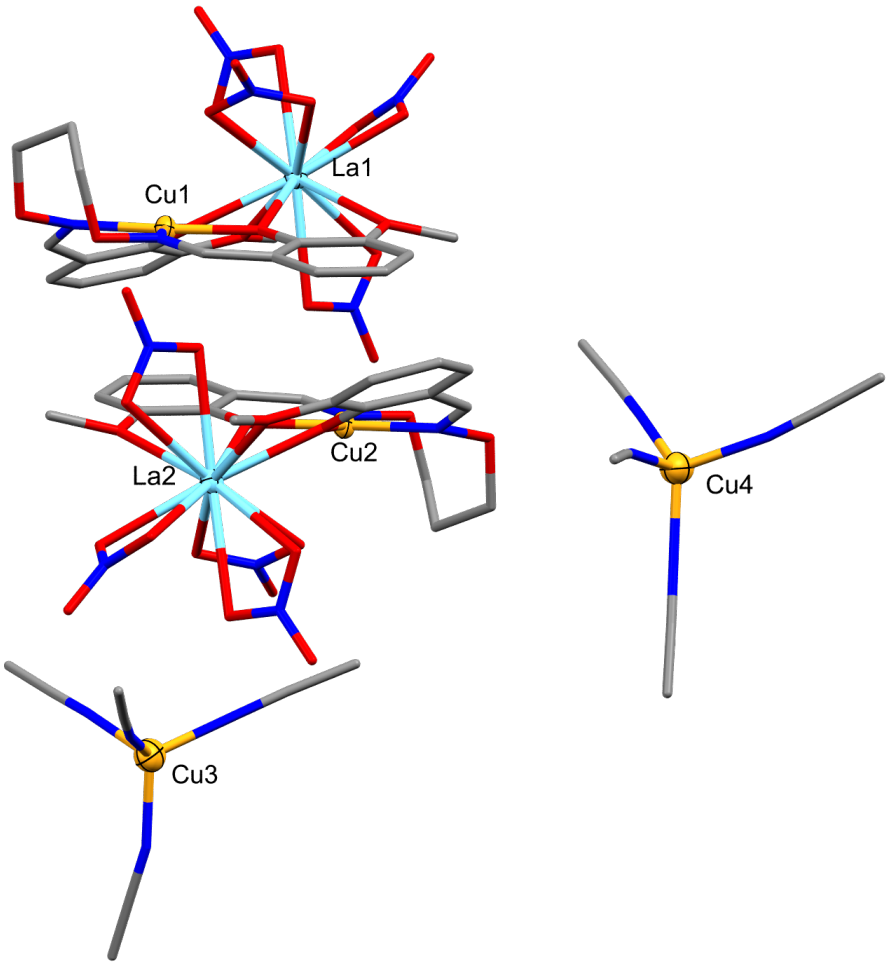

Figure D.2: Asymmetric unit of $[Cu^{I}(MeCN)_4][Cu^{II}La^{III}\mathbf{L2}(NO_3)_4]\cdot MeCN$, **C25**, discussed in Section 5.2.1. Hydrogen atoms and MeCN solvate have been omitted for clarity and thermal ellipsoids of metal ions shown at 50% probability. Colour code: Cu^{II} = dark yellow, La^{III} = aqua, N = blue, O = red, and C = grey.

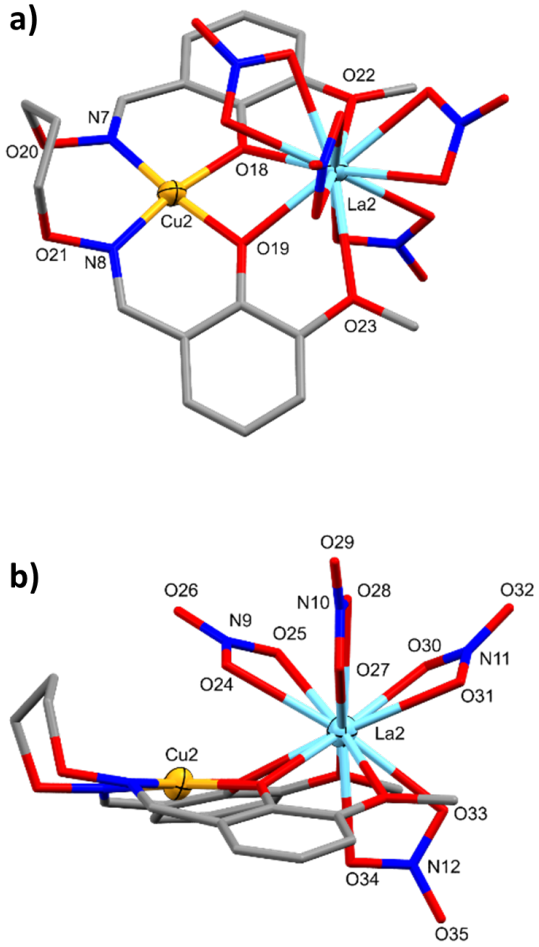

Figure D.3: The second unit of $[Cu^{I}(MeCN)_4][Cu^{II}La^{III}\mathbf{L2}(NO_3)_4]\cdot MeCN$, **C25** with atoms labelled (discussed in Section 5.2.1). Hydrogen atoms, MeCN solvate, first $Cu^{II}La^{III}$ unit and both $[Cu^{I}(MeCN)_4]$ units have been omitted for clarity. The thermal ellipsoids of the metal ions shown at 70% probability. Colour code: Cu^{II} = dark yellow, La^{III} = aqua, N = blue, O = red, and C = grey.

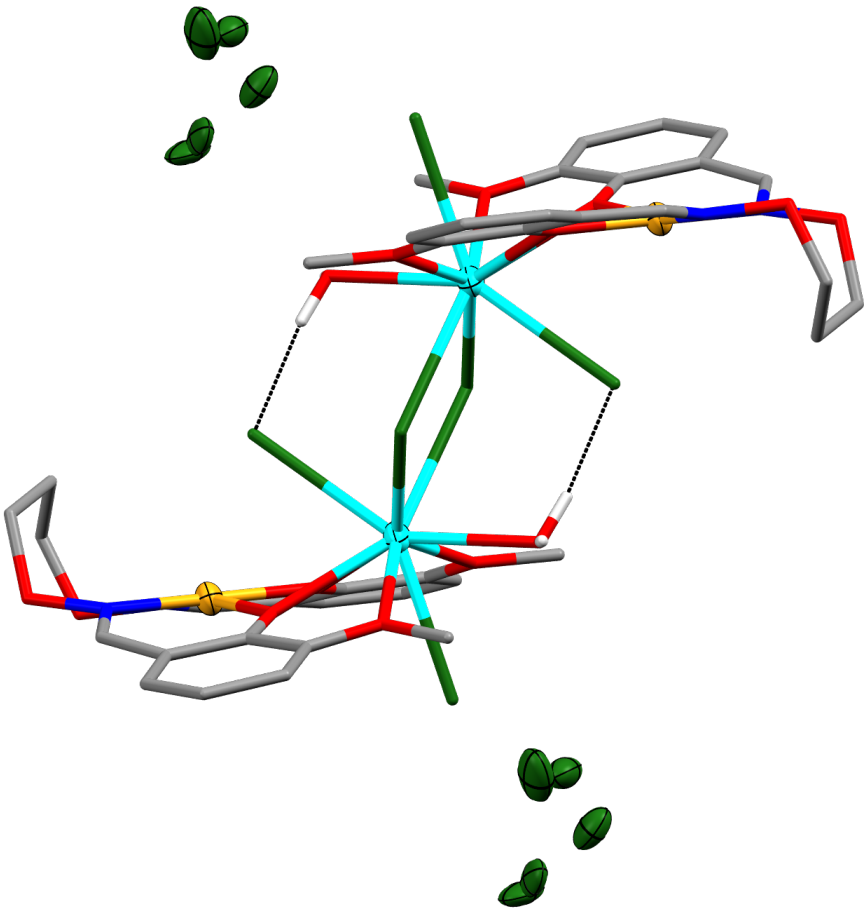

Figure D.4: Full molecular structure of **C40**, discussed in Section 5.2.2. Lattice Cl^- anions represented as ellipsoids for ease of view and non-interacting hydrogen atoms have been omitted for clarity. Hydrogen bonding represented as black dotted lines and thermal ellipsoids of metal ions and lattice Cl^- anions shown at 40% probability. Colour code: Cu^{II} = dark yellow, Ce^{III} = aqua, N = blue, O = red, Cl = green, C = grey, and H = white.

D.2 Additional Structural Data

Table D.1: SHAPE values for the four-coordinate metal ions in the complexes **C14 - C49**

	4-Coordinate			
	SP-4	T-4	SS-4	vTBPY-4
C14-Cu1	0.648	30.757	17.520	30.812
C15-Cu1	0.756	30.407	17.333	30.357
C16-Cu1	0.701	30.609	17.432	30.608
C17-Cu1	0.548	33.141	19.087	33.033
C18-Cu1	0.667	30.508	17.282	30.518
C19-Cu1	0.717	30.338	17.198	30.336
C20-Cu1	0.724	30.663	17.244	30.519
C21-Cu1	0.659	33.075	19.056	32.657
C22-Cu1	0.601	32.641	18.670	32.295
C23-Cu1	0.615	32.770	18.792	32.353
C24-Cu1	2.601	20.690	10.323	21.328
C25-Cu1	0.516	31.685	17.791	31.502
C26-Cu1	0.448	32.697	18.436	32.616
C29-Cu1	2.573	20.878	10.372	21.399
C31-Cu1	0.515	32.829	18.409	32.505
C32-Cu1	1.186	25.859	13.748	26.270
C39-Cu1	1.201	26.950	15.123	26.859
C39-Cu2	1.091	27.554	15.227	27.682
C40-Cu1	1.121	27.299	15.258	27.329

Table D.2: SHAPE values for the five-coordinate metal ions in the complexes **C14 - C49**

	5-Coordinate			
	vOC-5	TBPY-5	SPY-5	JTBPY-5
C27-Cu1	1.376	5.056	1.456	7.973
C28-Cu1	1.402	5.057	1.383	7.968
C30-Cu1	1.350	4.954	1.297	7.694
C33-Cu1	1.410	6.522	1.482	9.290
C34-Cu1	2.773	5.868	1.335	9.600
C35-Cu1	2.804	5.962	1.343	9.763
C36-Cu1	2.967	6.257	1.389	10.094
C37-Cu1	3.239	4.557	1.636	8.379
C38-Cu1	3.247	4.540	1.631	8.382
C42-Co1	1.861	5.331	1.853	7.867
C43-Co1	1.746	5.130	1.745	7.741
C44-Co1	23.951	26.141	23.482	28.303
C45-Co1	1.997	5.589	2.156	8.430
C47-Zn1	2.509	3.836	0.988	6.135
C49-Ni1	1.458	5.388	1.734	8.081

Table D.3: SHAPE values for the six- to nine-coordinate metal ions in the complexes **C14** - **C49**

	6-Coordinate			
	PPY-6	OC-6	TPR-6	JPPY-6
C41-Co1	24.661	1.140	11.429	27.629
C46-Co1	24.258	1.894	10.058	27.075
C48-Ni1	25.200	0.879	13.891	28.232
	7-Coordinate			
	PBPY-7	COC-7	CTPR-7	JPBPY-7
C37-Er2	2.107	5.860	4.496	6.026
C38-Ho2	2.165	5.911	4.519	6.084
	8-Coordinate			
	SAPR-8	TDD-8	JBTPR-8	BTPR-8
C34-Dy2	6.480	3.866	3.785	3.414
C35-Eu2	4.190	3.001	3.842	2.997
C36-Tb2	4.001	2.890	3.672	2.888
C39-Tb1	3.225	2.501	3.288	2.289
C39-Tb2	3.164	1.654	3.387	2.763
C42-Er2	1.706	2.770	2.887	1.748
C43-Eu2	1.878	2.855	3.059	1.953
C44-Er2	3.067	1.277	3.353	2.856
C45-Dy2	3.082	1.334	3.386	2.831
C46-Eu2	7.126	5.742	7.826	6.650
C49-Eu2	1.865	2.809	3.151	2.025
	9-Coordinate			
	JCSAPR-9	CSAPR-9	TCTPR-9	MFF-9
C20-Yb2	2.935	2.028	2.404	2.742
C40-Ce2	3.179	2.362	2.892	1.635
C41-Eu2	3.107	2.250	2.915	2.303
C47-Dy2	3.716	2.354	2.550	2.577
C48-Dy2	3.560	2.711	3.570	1.930

Table D.4: SHAPE values for the 10- to 12-coordinate metal ions in the complexes **C14** - **C49**

	10-Coordinate			
	JBCSAPR-10	JSPC-10	SDD-10	TD-10
C14-Dy2	3.635	3.814	5.647	5.064
C15-Er2	3.366	3.541	5.774	5.143
C16-Ho2	3.577	3.685	5.604	5.012
C17-Gd2	4.884	3.683	4.089	3.395
C18-Eu2	4.117	3.712	5.429	4.922
C19-Tb2	3.891	3.529	5.556	4.986
C21-Dy2	6.711	3.966	5.801	5.870
C22-Eu2	4.794	2.733	5.885	5.407
C23-Gd2	4.745	3.646	5.016	4.136
C24-La2	4.316	3.301	4.091	3.502
C27-La2	4.430	2.583	4.754	3.746
C28-Ce2	4.340	2.630	4.805	3.805
C29-Ce2	4.144	3.269	4.134	3.483
C30-Ce2	3.774	3.571	5.948	4.951
C31-Ce2	9.706	11.309	9.325	9.952
C32-Ce2	4.969	2.198	4.534	3.546
C33-Eu2	5.070	3.126	3.927	2.874
	11-Coordinate			
	JCPPR-11	JCPAPR-11	JAPPR-11	JASPC-11
C26-La2	6.060	3.991	10.979	6.899
	12-Coordinate			
	COC-12	ACOC-12	IC-12	JEPBPY-12
C25-La2	4.679	6.109	1.727	5.408

Table D.5: Non-averaged bond lengths (Å) and bond angles (°) of the complexes **C21** - **C23** and **C25**

	C21	**C22**	**C23**
Cu1-O1	1.952(4)	1.951(4)	1.957(10)
Cu1-O2	1.947(4)	1.955(5)	1.941(10)
Cu1-N1	1.982(5)	1.975(6)	1.970(13)
Cu1-N2	1.979(5)	1.977(6)	1.967(13)
Cu2-O16	1.948(4)	1.955(4)	1.959(10)
Cu2-O17	1.942(4)	1.960(4)	1.949(10)
Cu2-N6	1.972(5)	1.978(6)	1.979(14)
Cu2-N7	1.983(5)	1.974(6)	1.987(13)
M1-O1	2.337(4)	2.416(4)	2.365(10)
M1-O2	2.391(4)	2.373(4)	2.403(10)
M1-O5	2.442(4)	2.502(5)	2.456(10)
M1-O6	2.474(4)	2.464(4)	2.480(10)
M1-O7	2.460(4)	2.502(5)	2.459(12)
M1-O8	2.442(4)	2.484(5)	2.451(12)
M1-O10	2.431(4)	2.458(5)	2.539(11)
M1-O11	2.529(4)	2.544(5)	2.444(11)
M1-O13	2.521(5)	2.550(5)	2.536(11)
M1-O14	2.460(4)	2.515(5)	2.511(11)
M2-O16	2.347(4)	2.434(4)	2.376(9)
M2-O17	2.372(4)	2.397(4)	2.420(10)
M2-O20	2.455(4)	2.499(4)	2.500(10)
M2-O21	2.451(4)	2.500(4)	2.479(10)
M2-O22	2.415(6)	2.453(5)	2.428(11)
M2-O23	2.426(4)	2.470(5)	2.426(11)
M2-O25	2.387(7)	2.532(6)	2.526(13)
M2-O26	2.813(14)	2.547(6)	2.522(12)
M2-O28	2.477(5)	2.515(5)	2.489(12)
M2-O29	2.458(5)	2.493(5)	2.505(11)
Cu1-O1-M1	108.98(16)	107.19(19)	108.6(4)
Cu1-O2-M1	107.08(16)	108.75(19)	107.6(4)
Cu2-O16-M2	108.55(16)	107.56(18)	109.3(4)
Cu2-O17-M2	107.79(17)	108.82(19)	107.9(4)
Cu1···M1	3.499(1)	3.526(1)	3.517(3)
Cu2···M2	3.494(1)	3.552(1)	3.544(3)

Table D.6: Non-averaged bond lengths (Å) and angles (°) of the complex **C31** from crystal structure determination

C31					
Cu1-O1	1.941(6)	Cu1-N2	1.966(8)	Cu2-N7	1.951(8)
Cu1-O2	1.948(6)	Cu2-O18	1.956(6)	Cu2-N8	1.977(8)
Cu1-N1	1.989(8)	Cu2-O19	1.940(6)	La1-O1	2.493(6)
La1-O2	2.550(6)	La1-O8	2.631(7)	La1-O14	2.610(7)
La1-O5	2.745(6)	La1-O10	2.609(7)	La1-O16	2.626(7)
La1-O6	2.761(7)	La1-O11	2.718(7)	La1-O17	2.686(7)
La1-O7	2.731(7)	La1-O13	2.668(7)	La2-O18	2.525(6)
La2-O19	2.494(6)	La2-O25	2.619(7)	La2-O31	2.655(7)
La2-O22	2.765(7)	La2-O27	2.613(7)	La2-O33	2.645(7)
La2-O23	2.758(6)	La2-O28	2.753(7)	La2-O34	2.678(7)
La2-O24	2.723(7)	La2-O30	2.596(7)	Cu1-O1-La1	105.3(3)
Cu1-O2-La1	103.0(2)	Cu2-O18-La2	103.1(3)	Cu2-O19-La2	104.7(3)
Cu1···La1	3.540(1)	Cu2···La2	3.527(1)		

Table D.7: ESI-MS data for selected 3*d*4*f* complexes

	Found *m/z*	**Calcd.** *m/z*	Calcd. Formula
C14	722.43	722.73	$C_{19}H_{20}N_4O_{12}CuDy^+$
C15	666.73	666.20	$C_{19}H_{20}N_3O_9CuEr^+$
C16	725.71	725.86	$C_{19}H_{20}N_4O_{12}CuHo{+}H^+$
C17	718.18	718.71	$C_{19}H_{20}N_4O_{12}CuGd^+$
C18	711.67	711.90	$C_{19}H_{20}N_4O_{12}CuEu^+$
C19	718.86	718.67	$C_{19}H_{20}N_4O_{12}CuTb^+$
C20	733.99	733.75	$C_{19}H_{20}N_4O_{12}CuYb{+}H^+$
C21	722.43	722.70	$C_{19}H_{20}N_4O_{12}CuDy^+$
C22	711.71	711.90	$C_{19}H_{20}N_4O_{12}CuEu^+$
C23	716.78	716.96	$C_{19}H_{20}N_4O_{12}CuGd^+$
C24	697.85	697.94	$C_{19}H_{20}N_4O_{12}CuLa^+$
C26	699.84	699.64	$C_{19}H_{20}N_4O_{12}CuLa{+}H^+$
C28	698.85	698.94	$C_{19}H_{20}N_4O_{12}CuCe^+$
C29	700.05	700.68	$C_{19}H_{20}N_4O_{12}CuCe^+$
C33	641.79	641.80	$C_{15.5}H_{12}N_2O_{11.5}CuEu^+$
C34	668.93	668.81	$C_{19}H_{20}N_2O_6Cl_2CuDy^+$
C35	711.90	711.67	$C_{19}H_{22}N_2O_7Cl_3CuEu^+$
C36	665.82	665.75	$C_{19}H_{20}N_2O_6Cl_2CuTb^+$
C37	674.08	674.82	$C_{19}H_{20}N_2O_6Cl_2CuEr^+$
C38	669.96	669.20	$C_{19}H_{20}N_2O_6ClCuHo^+$
C39	665.82	665.03	$C_{19}H_{28}N_2O_{10}CuTb^+$
C42	758.87	758.96	$C_{19}H_{26}N_2O_9Cl_3CoEr^+$
C43	709.73	709.22	$C_{19}H_{26}N_2O_9Cl_2CoEu{+}H^+$
C44	732.20	732.01	$C_{20}H_{24}N_2O_7Cl_3CoDy^+$
C45	723.94	723.73	$C_{19}H_{22}N_2O_7Cl_3CoEr^+$
C46	771.72	771.14	$C_{21}H_{30}N_2O_9Cl_3CoEu{+}H^+$
C47	436.99	436.06	$C_{19}H_{20}N_2O_6Zn^+$
C48	755.69	755.81	$C_{24}H_{28}N_3O_{11}NiDy{+}H^+$
C49	744.85	744.44	$C_{19}H_{26}N_2O_9Cl_3NiEu{+}H^+$

Table D.8: Common IR stretches for selected 3*d*4*f* complexes

	$\upsilon_{\mathbf{O\text{-}H}}$	$\upsilon_{\mathbf{C{=}N}}$	$\upsilon_{\mathbf{Ar\text{-}O}}$	$\upsilon_{\mathbf{C\text{-}O}}$	$\upsilon_{\mathbf{NO_3^-}}$			
H_2**L2**	3421	1606	1251	1066	–	–	–	–
C14	–	1602	1230	1098	1470	1291	1032	815
C15	–	1607	1225	1093	1463	1286	1027	821
C16	–	1611	1228	1096	1463	1285	1027	817
C17	–	1603	1227	1098	1464	1284	1029	817
C18	–	1603	1226	1099	1464	1283	1028	817
C19	–	1606	1225	1093	1471	1249	1065	835
C20	–	1600	1228	1096	1463	1289	1030	815
C21	–	1601	1229	1098	1468	1290	1031	815
C22	–	1611	1227	1098	1463	1285	1029	817
C23	–	1611	1228	1096	1463	1286	1030	814
C24	3400	1600	1220	1093	1463	1282	1028	816
C26	–	1609	1243	1101	1464	1286	1032	819
C28	3399	1605	1222	1097	1463	1286	1031	818
C29	3352	1600	1244	1093	1463	1281	1028	815
C33	3373	1634	1219	1096	1468	1291	1029	–
C34	3201	1603	1227	1092	–	–	–	–
C35	3349	1608	1249	1093	–	–	–	–
C36	3313	1608	1228	1096	–	–	–	–
C37	3215	1608	1227	1093	–	–	–	–
C38	3228	1602	1228	1095	–	–	–	–
C39	3242	1602	1221	1088	–	–	–	–
C42	3313	1602	1215	1096	–	–	–	–
C43	3394	1602	1215	1096	–	–	–	–
C44	3386	1602	1215	1096	–	–	–	–
C45	3386	1602	1215	1095	–	–	–	–
C46	3374	1606	1251	1093	–	–	–	–
C47	–	1606	1249	1093	–	–	–	–
C48	3255	1611	1238	1096	1467	1290	1035	810
C49	3382	1605	1216	1085	–	–	–	–

Appendix E

Additional Data for the Complexes C50 - C66

E.1 Additional Figures

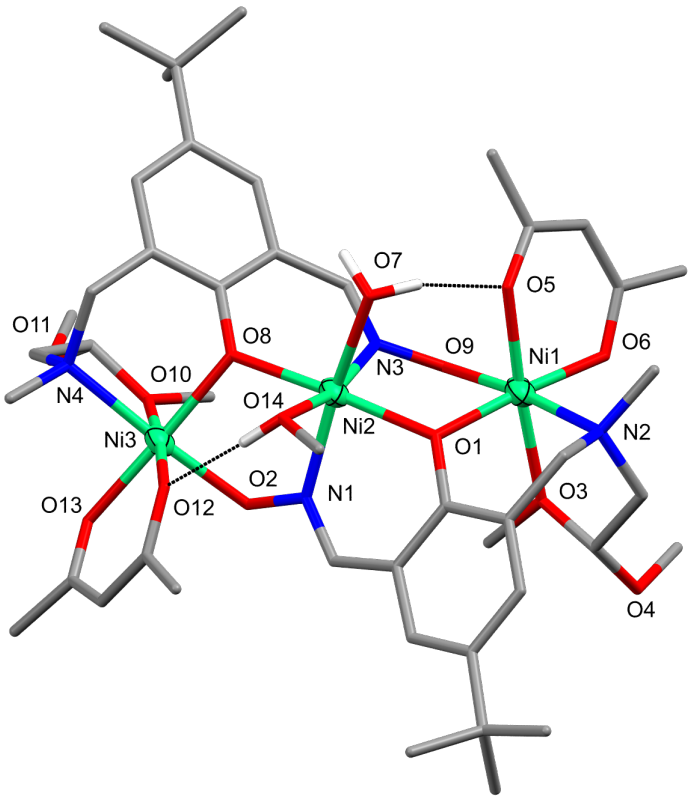

Figure E.1: Full molecular structure of $[Ni^{II}_3(\mathbf{L1})_2(H_2O)(MeOH)(Acac)_2]\cdot 3MeOH$ (**C50**), discussed in Section 6.1.1. Non-interacting hydrogen atoms and lattice MeOH molecules have been omitted for clarity, thermal ellipsoids of metal ions shown at 70% probability, and hydrogen bonding represented as black dotted lines. Colour code: Ni^{II} = light green, N = blue, O = red, C = grey, and H = white.

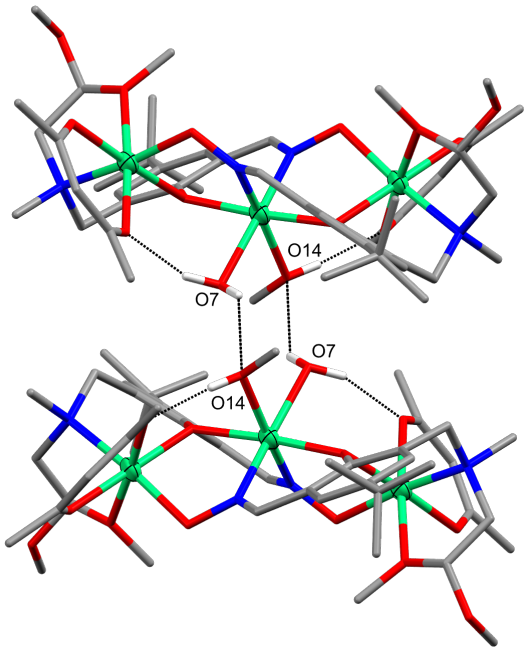

Figure E.2: Intermolecular hydrogen bonding network of **C50**, discussed in Section 6.1.1. Non-interacting hydrogen atoms and lattice MeOH molecules have been omitted for clarity, thermal ellipsoids of metal ions shown at 70% probability, and hydrogen bonding represented as black dotted lines. Colour code: Ni^{II} = light green, N = blue, O = red, C = grey, and H = white.

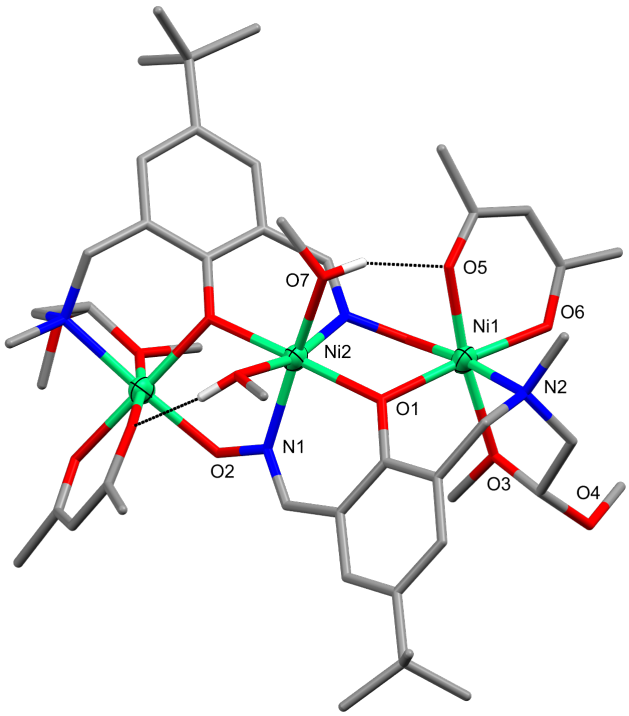

Figure E.3: Full molecular structure of $[Ni^{II}_3(\mathbf{L1})_2(MeOH)_2(acac)_2]\cdot 2MeOH$ (**C51**), discussed in Section 6.1.1. Non-interacting hydrogen atoms and lattice MeOH solvates have been omitted for clarity, thermal ellipsoids of metal ions shown at 70% probability, and hydrogen bonding represented as black dotted lines. Colour code: Ni^{II} = light green, N = blue, O = red, C = grey, and H = white.

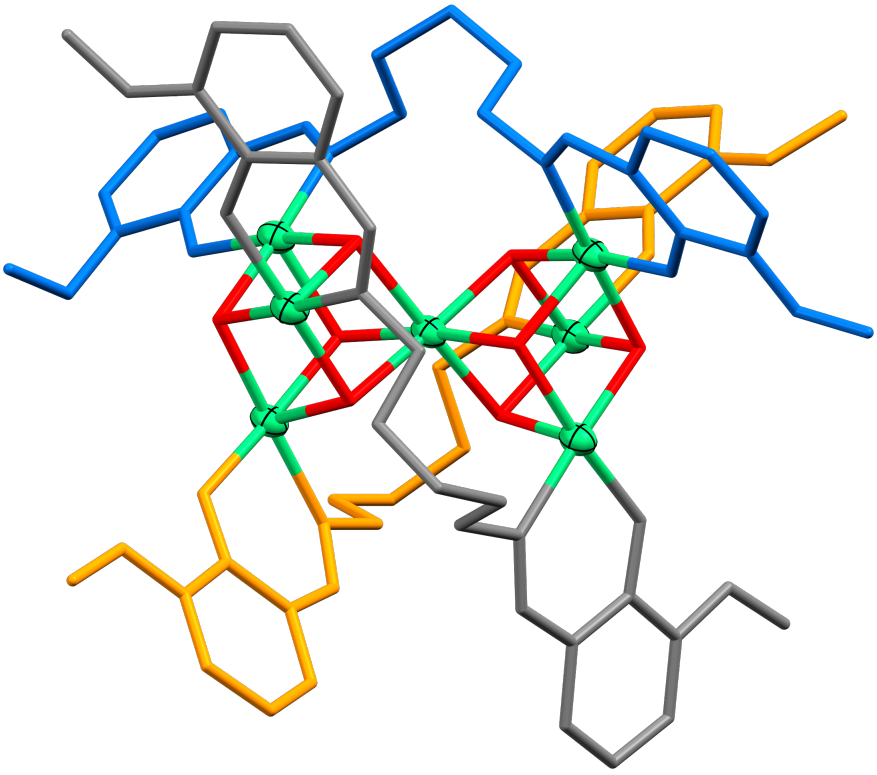

Figure E.4: The ligand arrangement found for the complex **C53**. The ligands have been coloured differently in order to clearly diffrentiate them. Hydrogen atoms, lattice solvates, and peripheral donor groups have been omitted for clarity. The thermal ellipsoids of the metal ions are shown at 70% probability. Colour code: Ni^{II} = light green and O = red.

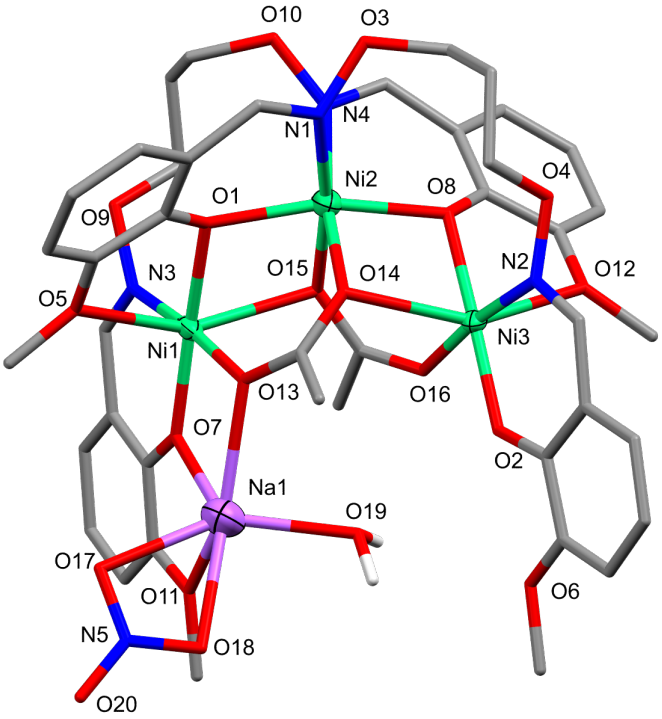

Figure E.5: Full molecular structure of $[Ni^{II}_3Na^{I}(\mathbf{L2})_2(H_2O)(OAc)_2(NO_3)]\cdot 2H_2O$ (**C61**), discussed in Section 6.5.1. Non-interacting hydrogen atoms have been omitted for clarity and thermal ellipsoids of metal ions shown at 60% probability. Colour code: Ni^{II} = light green, Na^{I} = purple, N = blue, O = red, C = grey, and H = white.

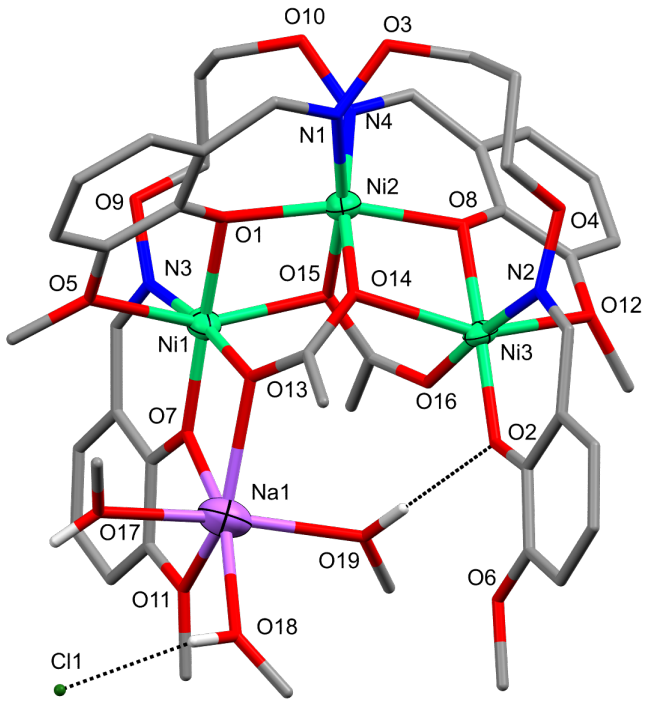

Figure E.6: Full molecular structure of $[Ni^{II}_3Na^{I}(\mathbf{L2})_2(MeOH)_3(OAc)_2][Cl]$ (**C62**), discussed in Section 6.5.1. Non-interacting hydrogen atoms have been omitted for clarity and thermal ellipsoids of metal ions shown at 60% probability. Colour code: Ni^{II} = light green, Na^{I} = purple, N = blue, O = red, Cl = dark green, C = grey, and H = white.

E.2 Additional Structural Data

Table E.1: SHAPE values for the four-coordinate metal ions in the complexes **C50 - C66**

	4-Coordinate			
	SP-4	T-4	SS-4	vTBPY-4
C57-Cu1	0.421	32.539	18.536	32.705
C58-Cu1	2.081	22.463	12.105	23.025
C60-Cu1	1.047	33.654	17.888	32.488
C64-Cu1	0.645	27.409	13.688	27.840
C64-Cu2	0.547	27.608	14.824	28.367
C64-Cu3	0.403	28.634	15.443	29.420
C64-Cu4	0.571	27.969	13.894	28.411
C65-Ni1	0.096	33.388	18.788	34.770

Table E.2: SHAPE values for the five-coordinate metal ions in the complexes **C50 - C66**

	5-Coordinate				
	PP-5	vOC-5	TBPY-5	SPY-5	JTBPY-5
C56-Cu1	31.343	1.140	6.052	1.208	8.821
C59-Cu1	29.942	0.804	6.327	1.085	8.713
C59-Cu2	30.252	0.770	6.069	1.356	8.406
C60-Cu2	31.766	1.553	6.342	1.036	9.278
C60-Cu3	26.837	2.408	4.743	1.975	7.802
C60-Cu4	23.570	3.200	6.127	2.701	9.723
C60-Cu5	25.605	3.049	4.436	2.230	8.383
C60-Cu6	27.056	2.528	4.403	1.847	7.682
C60-Cu7	31.969	1.451	6.347	1.008	9.101
C60-Cu8	31.991	2.074	6.408	1.143	9.381
C63-Na1	8.464	16.530	23.083	19.583	24.123
C63-Na2[a]	32.191	7.936	4.850	5.073	7.593
C63-Na2[b]	19.336	13.855	16.441	12.543	17.914
C64-Na2	27.369	7.227	5.866	4.272	8.898

[a] NO_3; [b] OH

Table E.3: SHAPE values for the six-coordinate metal ions in the complexes **C50 - C66**

	6-Coordinate				
	HP-6	PPY-6	OC-6	TPR-6	JPPY-6
C50-Ni1	31.081	28.185	0.239	15.751	31.586
C50-Ni2	32.498	24.833	0.862	10.796	28.785
C50-Ni3	31.076	27.091	0.410	14.255	30.372
C51-Ni1	31.615	24.177	1.071	10.252	28.133
C51-Ni2	31.358	27.344	0.275	15.295	31.059
C52-Ni1	32.830	25.456	1.221	13.971	29.511
C52-Ni2	31.207	23.758	1.865	13.499	27.598
C53-Ni1	30.600	25.725	1.552	10.322	29.202
C53-Ni2	30.868	27.059	0.598	14.881	29.871
C53-Ni3	30.818	26.774	0.714	14.775	29.446
C53-Ni4	30.862	27.216	0.602	15.231	29.972
C53-Ni5	30.840	27.670	0.619	15.325	30.444
C53-Ni6	30.863	27.039	0.639	15.014	29.779
C53-Ni7	31.338	28.062	0.557	15.639	30.848
C54-Co1	31.178	17.449	6.295	7.088	21.957
C54-Co3	31.609	20.668	4.806	10.670	24.791
C54-Zn2	32.471	20.049	4.814	10.911	23.684
C55-Ni1	31.991	22.174	3.456	11.444	26.363
C55-Ni3	30.334	22.657	3.353	12.150	26.583
C55-Zn1	34.220	20.282	4.989	10.202	24.561
C58-Na1	28.464	4.997	20.595	8.216	8.886
C59-Ni1	30.606	29.106	1.111	14.148	32.327
C59-Ni2	30.515	27.296	1.112	12.659	30.774
C59-Na1	32.269	24.473	1.498	9.177	28.170
C61-Na1	28.553	15.010	11.826	8.231	18.063
C62-Na1	34.469	18.193	6.522	7.128	22.008
C63-Ni1	33.309	24.476	1.662	11.818	28.299
C63-Ni2	31.299	23.794	1.335	11.725	27.396
C63-Ni3	32.599	24.931	1.480	12.205	28.523
C64-Na1	32.914	15.531	7.233	6.229	19.662
C64-Na3	27.435	11.052	15.758	6.043	15.310
C64-Na4	31.521	16.964	8.268	10.760	22.054
C66-Mn1	29.056	27.933	1.386	15.620	30.331

Table E.4: SHAPE values for the seven- to nine-coordinate metal ions in the complexes **C50** - **C66**

	7-Coordinate				
	PBPY-7	COC-7	CTPR-7	JPBPY-7	JETPY-7
C57-Na1	3.073	3.584	3.095	7.386	19.124
C63-Na1	20.212	19.603	18.618	19.360	21.094
	8-Coordinate				
	SAPR-8	TDD-8	JBTPR-8	BTPR-8	JSD-8
C60-Eu1	0.360	2.606	2.823	1.835	5.055
C60-Eu3	1.431	2.093	2.368	1.976	4.507
	9-Coordinate				
	JCSAPR-9	CSAPR-9	TCTPR-9	JTCTPR-9	MFF-9
C56-Gd1	2.104	0.805	1.199	3.440	1.312
C60-Eu2	2.408	1.581	2.493	2.728	1.063

Appendix F

Crystal Data and Structural Refinement Details

The X-ray data for the complexes **C1**, **C3**, and **C5** was collected on a Rigaku Spider diffractometer equipped with a copper rotating anode X-ray source and a curved image plate detector. Crystals were mounted on MiTeGen loops using Fomblin®, transferred into the cold gas stream of the detector and irradiated with graphite monochromated CuKα X-rays (λ = 1.54187 Å). Data was collected using the program Crystal Clear (v. 1.4.0) and processed using FS PROCESS.[325,326] The structures were solved by SHELXT, and refined using SHELXL in the Olex2 crystallographic program.[208,327–329]

The X-ray data for the complexes **C2**, **C4**, and **C6** - **C66** was collected on a Bruker D8 Venture diffractometer equipped with a IμS Diamond, microfocus CuKα X-ray source (λ = 1.54178 Å) and a Photon III detector. Crystals were mounted on MiTeGen loops using Fomblin Y and cooled to 100 K with an Oxford Cryostream 800. Data was collected and processed using APEX3.[330] The structures were solved by SHELXT and refined using either SHELXL (**C2**, **C4**, **C6** - **C33**, and **C35** - **C66**) or Olex2.refine (**C34**) in Olex2.[208,327–329] For **C34**, which was refined using Olex2.refine, the metal ions underwent anharmonic refinement.

For all complexes, non-hydrogen atoms were refined anisotropically and hydrogen atoms were calculated to their ideal positions unless stated otherwise and refined by using a riding model with fixed isotropic U_{iso} values. Disordered lattice regions (details of which can be found in the crystal descriptions) in the complexes **C24**, **C29**, **C39**, **C50** - **C54**, **C56**, **C59** - **C62**, **C64**, and **C66** were treated using the SQUEEZE protocol reported by Spek as implemented in Olex2.[208,273] The SQUEEZE assignments were based off of the reactants used in the complexation reactions. Details of disordered ligand and coordinate regions found in the complexes, **C5**, **C28**, **C34**, **C39**, **C40**, **C48**, **C60**, **C63**, **C64**, and **C66**, can be found in the crystal descriptions and Table F.1.

Table F.1: Disordered regions found in the complexes **C1 - C66**

Complex	Disordered Region	Atoms/Molecule	Treatment	Occupancy
C5	Anion Bridges	F^- & Cl^-	Pos. Disord.	60 : 40
C24	Lattice Solvate	3 H_2O	SQUEEZE	–
C28	Ligand bridge	CH_2	Pos. Disord.	65 : 35
C29	Lattice Solvate	3 H_2O	SQUEEZE	–
C34	Coordinates	Cl2 & Cl3	Pos. Disord.	50 : 50 & 65 : 35
C39	Ligand Bridges	2 CH_2	Pos. Disord.	60 : 40 & 60 : 40
	Lattice Solvate	1 MeOH & 1 H_2O	Pos. Disord.	60 : 40 & 50 : 50
C40	Lattice Anions	2 Cl	Pos. Disord.	
	Coordinate	Cl3	Pos. Disord.	50 : 50
C48	Ligand Bridge	N1-O3-$(CH_2)_3$-O4	Pos. Disord.	50 : 50
C50	Lattice Solvate	2.5 H_2O	SQUEEZE	–
C51	Lattice Solvate	1.5 H_2O	SQUEEZE	–
C52	Lattice Solvate	2 H_2O	SQUEEZE	–
C53	Lattice Solvate	1 MeOH & 1.5 H_2O	SQUEEZE	–
C54	Lattice Solvate	5.5 H_2O	SQUEEZE	–
C56	Lattice Solvate	1 MeOH	SQUEEZE	–
C59	Lattice Solvate	3 MeOH & 1 H_2O	SQUEEZE	–
C60	Lattice Solvate	4 MeOH, 3 Et_2O, & 2 H_2O	SQUEEZE	–
C61	Lattice Solvate	2 H_2O	SQUEEZE	–
C62	Lattice Solvate	1 MeOH & 1 H_2O	SQUEEZE	–
C63	Anion Bridges	NO_3^- & OH^-	Pos. Disord.	75 : 25
C64	Lattice Solvate	4 MeOH, 3 Et_2O, & 1 H_2O	SQUEEZE	–
C66	Coordinates	2 MeOH/H_2O		50 : 50
	Lattice Solvate	2 Et_2O & 1 H_2O	SQUEEZE	–
	Ligand	^{t}Bu	Rot. Disord.	60 : 40

Pos. Disord. = Positionally disordered

Rot. Disord. = Rotationally disordered

F.1 Crystal Data and Structural Refinement Details

H_2L2: $C_{19}H_{22}N_2O_6$ (M =374.38 g/mol): orthorhombic, space group $Fdd2$ (no. 43), a = 23.9841(8) Å, b = 32.4180(11) Å, c = 4.7242(2) Å, V = 3673.1(2) Å^3, Z = 8, T = 215.0 K, μ(CuKα) = 0.848 mm^{-1}, $Dcalc$ = 1.354 g/cm^3, 7224 reflections measured (9.172°$\leq 2\Theta \leq$ 136.38°), 1623 unique (R_{int} = 0.0743, R_{sigma} = 0.0499) which were used in all calculations. The final R_1 was 0.0353 (I > 2σ(I)) and wR_2 was 0.0823 (all data). Largest diff. peak/hole 0.11/-0.14 e Å^3

C1: $C_{42}H_{74}Cl_2N_4Ni_4O_{16}$ (M =1196.79 g/mol): monoclinic, space group $P2_1/a$ (no. 14), a = 10.1468(3) Å, b = 24.8080(6) Å, c = 10.9472(8) Å, β = 109.740(8)°, V = 2593.7(2) Å^3, Z = 2, T = 100.00 K, μ(CuKα) = 3.154 mm^{-1}, $Dcalc$ = 1.532 g/cm^3, 28437 reflections measured (7.126°$\leq 2\Theta \leq$ 136.498°), 4692 unique (R_{int} = 0.1022, R_{sigma} = 0.0825) which were used in all calculations. The final R_1 was 0.0605 (I > 2σ(I)) and wR_2 was 0.1956 (all data). Largest diff. peak/hole 1.04/-1.17 e Å^3

C2: $C_{42}H_{68}Cl_2N_6Ni_4O_{14}$ (M =1186.76 g/mol): triclinic, space group $P\bar{1}$ (no. 2), a = 10.9450(11) Å, b = 11.9399 Å, c = 12.3373 Å, α = 61.800(4)°, β = 77.050(7)°, γ = 66.235(5)°, V = 1299.28(19) Å^3, Z = 1, T = 100.00 K, μ(CuKα) = 3.127 mm^{-1}, $Dcalc$ = 1.517 g/cm^3, 25132 reflections measured (8.138°$\leq 2\Theta \leq$ 136.474°), 4606 unique (R_{int} = 0.0602, R_{sigma} = 0.0427) which were used in all calculations. The final R_1 was 0.0524 (I > 2σ(I)) and wR_2 was 0.1552 (all data). Largest diff. peak/hole 0.67/-0.86 e Å^3

C3: $C_{42}H_{78}Cl_4N_4Ni_4O_{13}$ (M =1223.72 g/mol): monoclinic, space group $P2_1/c$ (no. 14), a = 10.1613(11) Å, b = 20.497(2) Å, c = 25.796(3) Å, β = 91.181(6)°, V = 5371.6(11) Å^3, Z = 4, T = 150.00 K, μ(CuKα) = 3.907 mm^{-1}, $Dcalc$ = 1.513 g/cm^3, 42330 reflections measured (5.508°$\leq 2\Theta \leq$ 136.506°), 9568 unique (R_{int} = 0.2390, R_{sigma} = 0.4551) which were used in all calculations. The final R_1 was 0.0936 (I > 2σ(I)) and wR_2 was 0.2510 (all data). Largest diff. peak/hole 0.86/-0.96 e Å^3

C4: $C_{42}H_{84}F_4N_4Ni_4O_{16}$ (M =1211.97 g/mol): triclinic, space group $P\bar{1}$ (no. 2), a = 9.3027(5) Å, b = 11.0469(6) Å, c = 14.7130(8) Å, α = 101.982(2)°, β = 103.544(2)°, γ = 107.534(2)°, V = 1337.06(13) Å^3, Z = 1, T = 100.00 K, μ(CuKα) = 2.275 mm^{-1}, $Dcalc$ = 1.505 g/cm^3, 23448 reflections measured (8.8°$\leq 2\Theta \leq$ 130.158°), 4525 unique (R_{int} = 0.0602, R_{sigma} = 0.0436) which were used in all calculations. The final R_1 was 0.0395 (I > 2σ(I)) and wR_2 was 0.1077 (all data). Largest diff. peak/hole 0.57/-0.60 e Å^3

C5: $C_{42}H_{78}Cl_{2.8}F_{1.2}N_4Ni_4O_{13}$ (M =1203.98 g/mol): monoclinic, space group $P2_1/c$ (no. 14), a = 9.5697(8) Å, b = 21.0552(14) Å, c = 26.071(2) Å, β = 90.155(6)°, V = 5253.1(7) Å^3, Z = 4, T = 100.00 K, μ(CuKα) = 3.471 mm^{-1}, $Dcalc$ = 1.522 g/cm^3, 37702 reflections measured (9.06°$\leq 2\Theta \leq$ 130.178°), 8926 unique (R_{int} = 0.0727, R_{sigma} = 0.1558) which were used in all calculations. The final R_1 was 0.0581 (I > 2σ(I)) and wR_2 was 0.1904 (all data). Largest diff. peak/hole 1.02/-0.60 e Å^3

C6: $C_{19}H_{20}CoCuN_4O_{12}$ (M =618.86 g/mol): monoclinic, space group $P2_1/n$ (no. 14), a = 14.8377(6) Å, b = 8.3627(3) Å, c = 17.4640(7) Å, β = 90.642(2)°, V = 2166.85(15) Å^3, Z = 4, T = 100.00 K, μ(CuKα) = 7.925 mm^{-1}, $Dcalc$ = 1.897 g/cm^3, 12784 reflections measured (7.776°$\leq 2\Theta \leq$ 133.18°), 3711 unique (R_{int} = 0.0424, R_{sigma} = 0.0424) which were used in all calculations. The final R_1 was 0.0462 (I > 2σ(I)) and wR_2 was 0.1346 (all data). Largest diff. peak/hole 0.88/-0.85 e Å^3

C7: $C_{19}H_{20}Cu_2N_4O_{12}$ (M =623.47 g/mol): monoclinic, space group $P2_1/n$ (no. 14), a = 14.9946(5) Å, b = 8.3429(3) Å, c = 17.5340(6) Å, β = 90.458(2)°, V = 2193.41(13) Å^3, Z = 4, T = 100.00 K, μ(CuKα) = 3.100 mm^{-1}, *Dcalc* = 1.888 g/cm^3, 17617 reflections measured (7.728°$\leq$ 2Θ $\leq$ 152.484°), 4421 unique (R_{int} = 0.0529, R_{sigma} = 0.0389) which were used in all calculations. The final R_1 was 0.0420 (I > 2σ(I)) and wR_2 was 0.1158 (all data). Largest diff. peak/hole 0.67/-0.82 e Å^3

C8: $C_{19}H_{20}CuMnN_4O_{12}$ (M =614.87 g/mol): monoclinic, space group $P2_1/n$ (no. 14), a = 15.0392(6) Å, b = 8.3585(3) Å, c = 17.6313(7) Å, β = 91.462(2)°, V = 2215.62(15) Å^3, Z = 4, T = 110.00 K, μ(CuKα) = 6.523 mm^{-1}, *Dcalc* = 1.843 g/cm^3, 15096 reflections measured (7.63°$\leq$ 2Θ $\leq$ 152.708°), 4475 unique (R_{int} = 0.0457, R_{sigma} = 0.0462) which were used in all calculations. The final R_1 was 0.0496 (I > 2σ(I)) and wR_2 was 0.1367 (all data). Largest diff. peak/hole 0.63/-0.69 e Å^3

C9: $C_{19}H_{20}CuN_4O_{12}Zn$ (M =625.30 g/mol): monoclinic, space group $P2_1/n$ (no. 14), a = 14.9306(12) Å, b = 8.3978(7) Å, c = 17.6667(14) Å, β = 91.012(4)°, V = 2214.8(3) Å^3, Z = 4, T = 100.00 K, μ(CuKα) = 3.219 mm^{-1}, *Dcalc* = 1.875 g/cm^3, 21642 reflections measured (7.686°$\leq$ 2Θ $\leq$ 152.54°), 4516 unique (R_{int} = 0.0401, R_{sigma} = 0.0331) which were used in all calculations. The final R_1 was 0.0565 (I > 2σ(I)) and wR_2 was 0.1379 (all data). Largest diff. peak/hole 1.33/-1.03 e Å^3

C10: $C_{21}H_{28}CoMnN_4O_{14}$ (M =674.34 g/mol): triclinic, space group $P\bar{1}$ (no. 2), a = 9.9747(4) Å, b = 10.5722(4) Å, c = 14.1876(5) Å, α = 107.842(2)°, β = 106.805(2)°, γ = 99.500(2)°, V = 1309.49(9) Å^3, Z = 2, T = 100.00 K, μ(CuKα) = 9.600 mm^{-1}, *Dcalc* = 1.710 g/cm^3, 15240 reflections measured (7.02°$\leq$ 2Θ $\leq$ 140.122°), 4909 unique (R_{int} = 0.0462, R_{sigma} = 0.0460) which were used in all calculations. The final R_1 was 0.0428 (I > 2σ(I)) and wR_2 was 0.1372 (all data). Largest diff. peak/hole 0.77/-0.57 e Å^3

C11: $C_{21}H_{28}Mn_2N_4O_{14}$ (M =670.35 g/mol): triclinic, space group $P\bar{1}$ (no. 2), a = 10.0281(4) Å, b = 10.5626(4) Å, c = 14.3023(5) Å, α = 107.230(2)°, β = 106.643(2)°, γ = 99.870(2)°, V = 1330.88(9) Å^3, Z = 2, T = 100.00 K, μ(CuKα) = 8.424 mm^{-1}, *Dcalc* = 1.673 g/cm^3, 23449 reflections measured (6.93°$\leq$ 2Θ $\leq$ 136.49°), 4762 unique (R_{int} = 0.0441, R_{sigma} = 0.0372) which were used in all calculations. The final R_1 was 0.0377 (I > 2σ(I)) and wR_2 was 0.1078 (all data). Largest diff. peak/hole 0.61/-0.48 e Å^3

C12: $C_{21}H_{28}MnN_4NiO_{14}$ (M =674.12 g/mol): triclinic, space group $P\bar{1}$ (no. 2), a = 9.9564(4) Å, b = 10.5669(5) Å, c = 14.1649(9) Å, α = 108.098(3)°, β = 106.993(2)°, γ = 99.274(2)°, V = 1301.62(12) Å^3, Z = 2, T = 104.00 K, μ(CuKα) = 5.564 mm^{-1}, *Dcalc* = 1.720 g/cm^3, 12001 reflections measured (7.052°$\leq$ 2Θ $\leq$ 136.438°), 4562 unique (R_{int} = 0.0510, R_{sigma} = 0.0603) which were used in all calculations. The final R_1 was 0.0600 (I > 2σ(I)) and wR_2 was 0.1663 (all data). Largest diff. peak/hole 0.59/-0.66 e Å^3

C13: $C_{21}H_{28}MnN_4O_{14}Zn$ (M =680.78 g/mol): triclinic, space group $P\bar{1}$ (no. 2), a = 9.9676(4) Å, b = 10.5660(4) Å, c = 14.2952(5) Å, α = 107.671(2)°, β = 106.679(2)°, γ = 99.696(2)°, V = 1319.19(9) Å^3, Z = 2, T = 100.00 K, μ(CuKα) = 5.722 mm^{-1}, *Dcalc* = 1.714 g/cm^3, 15496 reflections measured (6.956°$\leq$ 2Θ $\leq$ 130.148°), 4379 unique (R_{int} = 0.0542, R_{sigma} = 0.0557) which were used in all calculations. The final R_1 was 0.0611 (I > 2σ(I)) and wR_2 was 0.1769 (all data). Largest diff. peak/hole 0.78/-0.98 e Å^3

C14: $C_{19}H_{20}CuDyN_5O_{15}$ (M =784.438 g/mol): monoclinic, space group $P2_1/n$ (no. 14), a = 9.0414(3) Å, b = 23.8466(7) Å, c = 11.8594(3) Å, β = 96.099(2)°, V = 2542.49(13) Å^3, Z = 4, T =

295.0 K, μ(CuKα) = 17.356 mm^{-1}, *Dcalc* = 2.049 g/cm^3, 22271 reflections measured (7.42° $\leq 2\Theta \leq$ 130.4°), 4198 unique (R_{int} = 0.0665, R_{sigma} = 0.0511) which were used in all calculations. The final R_1 was 0.0553 (I > 2σ(I)) and wR_2 was 0.1194 (all data). Largest diff. peak/hole 0.94/-1.25 e Å^3

C15: $C_{19}H_{20}CuErN_5O_{15}$ (*M* =789.20 g/mol): monoclinic, space group $P2_1/n$ (no. 14), *a* = 8.9640(4) Å, *b* = 23.5775(12) Å, *c* = 11.7460(6) Å, β = 96.561(2)°, *V* = 2466.2(2) Å^3, *Z* = 4, *T* = 100.0 K, μ(CuKα) = 7.999 mm^{-1}, *Dcalc* = 2.125 g/cm^3, 18910 reflections measured (7.498° $\leq 2\Theta \leq$ 136.42°), 4384 unique (R_{int} = 0.0763, R_{sigma} = 0.0673) which were used in all calculations. The final R_1 was 0.0657 (I > 2σ(I)) and wR_2 was 0.1980 (all data). Largest diff. peak/hole 1.81/-1.19 e Å^3

C16: $C_{19}H_{20}CuHoN_5O_{15}$ (*M* =786.87 g/mol): monoclinic, space group $P2_1/n$ (no. 14), *a* = 8.9701(6) Å, *b* = 23.5381(15) Å, *c* = 11.7899(7) Å, β = 96.098(3)°, *V* = 2475.2(3) Å^3, *Z* = 4, *T* = 100.0 K, μ(CuKα) = 7.646 mm^{-1}, *Dcalc* = 2.112 g/cm^3, 35632 reflections measured (7.512° $\leq 2\Theta \leq$ 136.462°), 4446 unique (R_{int} = 0.0469, R_{sigma} = 0.0294) which were used in all calculations. The final R_1 was 0.0352 (I > 2σ(I)) and wR_2 was 0.0886 (all data). Largest diff. peak/hole 0.99/-0.96 e Å^3

C17: $C_{19}H_{20}CuGdN_5O_{15}$ (*M* =779.19 g/mol): triclinic, space group $P\bar{1}$ (no. 2), *a* = 9.0517(3) Å, *b* = 11.7793(4) Å, *c* = 12.6568(4) Å, α = 88.549(2)°, β = 80.923(2)°, γ = 71.8140(10)°, *V* = 1265.63(7) Å^3, *Z* = 2, *T* = 296.0 K, μ(CuKα) = 18.586 mm^{-1}, *Dcalc* = 2.045 g/cm^3, 18461 reflections measured (7.074° $\leq 2\Theta \leq$ 136.484°), 4522 unique (R_{int} = 0.0574, R_{sigma} = 0.0468) which were used in all calculations. The final R_1 was 0.0396 (I > 2σ(I)) and wR_2 was 0.1123 (all data). Largest diff. peak/hole 1.20/-0.74 e Å^3

C18: $C_{19}H_{20}CuEuN_5O_{15}$ (*M* =773.90 g/mol): monoclinic, space group $P2_1/n$ (no. 14), *a* = 8.9377(7) Å, *b* = 23.6278(19) Å, *c* = 11.8881(9) Å, β = 96.527(4)°, *V* = 2494.2(3) Å^3, *Z* = 4, *T* = 100.0 K, μ(CuKα) = 19.664 mm^{-1}, *Dcalc* = 2.061 g/cm^3, 28921 reflections measured (7.482° $\leq 2\Theta \leq$ 136.412°), 4436 unique (R_{int} = 0.0629, R_{sigma} = 0.0424) which were used in all calculations. The final R_1 was 0.0559 (I > 2σ(I)) and wR_2 was 0.1581 (all data). Largest diff. peak/hole 2.28/-1.53 e Å^3

C19: $C_{19}H_{20}CuN_5O_{15}Tb$ (*M* =780.86 g/mol): monoclinic, space group $P2_1/n$ (no. 14), *a* = 8.9290(4) Å, *b* = 23.6257(10) Å, *c* = 11.8429(5) Å, β = 96.862(2)°, *V* = 2480.41(19) Å^3, *Z* = 4, *T* = 100.0 K, μ(CuKα) = 15.694 mm^{-1}, *Dcalc* = 2.091 g/cm^3, 29940 reflections measured (7.484° $\leq 2\Theta \leq$ 133.14°), 4310 unique (R_{int} = 0.0694, R_{sigma} = 0.0423) which were used in all calculations. The final R_1 was 0.0477 (I > 2σ(I)) and wR_2 was 0.1337 (all data). Largest diff. peak/hole 1.71/-1.15 e Å^3

C20: $C_{19}H_{20}CuN_5O_{15}Yb$ (*M* =794.98 g/mol): monoclinic, space group $P2_1/n$ (no. 14), *a* = 9.0635(6) Å, *b* = 23.6137(16) Å, *c* = 11.6796(8) Å, β = 95.070(2)°, *V* = 2489.9(3) Å^3, *Z* = 4, *T* = 100.0 K, μ(CuKα) = 8.613 mm^{-1}, *Dcalc* = 2.121 g/cm^3, 30734 reflections measured (7.488° $\leq 2\Theta \leq$ 144.238°), 4886 unique (R_{int} = 0.0433, R_{sigma} = 0.0246) which were used in all calculations. The final R_1 was 0.0421 (I > 2σ(I)) and wR_2 was 0.0912 (all data). Largest diff. peak/hole 0.92/-0.72 e Å^3

C21: $C_{19}H_{20}CuDyN_5O_{15}$ (*M* =784.44 g/mol): triclinic, space group $P\bar{1}$ (no. 2), *a* = 12.3544(7) Å, *b* = 14.2720(8) Å, *c* = 16.5653(9) Å, α = 111.834(2)°, β = 103.258(2)°, γ = 103.543(2)°, *V* = 2468.6(2) Å^3, *Z* = 4, *T* = 173.0 K, μ(CuKα) = 17.875 mm^{-1}, *Dcalc* = 2.111 g/cm^3, 31688 reflections measured (6.138° $\leq 2\Theta \leq$ 136.49°), 8747 unique (R_{int} = 0.0537, R_{sigma} = 0.0475) which

were used in all calculations. The final R_1 was 0.0441 (I > 2σ(I)) and wR_2 was 0.1231 (all data). Largest diff. peak/hole 1.21/-1.24 e Å^3

C22: $C_{19}H_{20}CuEuN_5O_{15}$ (M =773.90 g/mol): triclinic, space group $P\bar{1}$ (no. 2), a = 12.3855(4) Å, b = 14.2948(6) Å, c = 16.5637(6) Å, α = 111.366(2)°, β = 103.530(2)°, γ = 103.892(2)°, V = 2477.91(16) Å^3, Z = 4, T = 100.0 K, μ(CuKα) = 19.793 mm^{-1}, $Dcalc$ = 2.074 g/cm^3, 25493 reflections measured (6.13°$\leq$ 2Θ $\leq$ 133.188°), 8530 unique (R_{int} = 0.0487, R_{sigma} = 0.0541) which were used in all calculations. The final R_1 was 0.0410 (I > 2σ(I)) and wR_2 was 0.1099 (all data). Largest diff. peak/hole 1.48/-1.39 e Å^3

C23: $C_{19}H_{20}CuGdN_5O_{15}$ (M =779.19 g/mol): triclinic, space group $P\bar{1}$ (no. 2), a = 12.3830(7) Å, b = 14.2857(9) Å, c = 16.5511(10) Å, α = 111.603(3)°, β = 103.365(3)°, γ = 103.867(3)°, V = 2471.9(3) Å^3, Z = 4, T = 100.0 K, μ(CuKα) = 19.032 mm^{-1}, $Dcalc$ = 2.094 g/cm^3, 49176 reflections measured (6.14°$\leq$ 2Θ $\leq$ 136.49°), 8864 unique (R_{int} = 0.0549, R_{sigma} = 0.0429) which were used in all calculations. The final R_1 was 0.0372 (I > 2σ(I)) and wR_2 was 0.0919 (all data). Largest diff. peak/hole 0.76/-0.79 e Å^3

C24: $C_{19}H_{22}CuLaN_5O_{16}$ (M =778.86 g/mol): triclinic, space group $P\bar{1}$ (no. 2), a = 11.5361(4) Å, b = 11.6638(4) Å, c = 11.9374(4) Å, α = 72.284(2)°, β = 65.9240(10)°, γ = 73.045(2)°, V = 1370.81(8) Å^3, Z = 2, T = 100.0 K, μ(CuKα) = 13.601 mm^{-1}, $Dcalc$ = 1.887 g/cm^3, 26106 reflections measured (8.11°$\leq$ 2Θ $\leq$ 133.168°), 4767 unique (R_{int} = 0.0451, R_{sigma} = 0.0334) which were used in all calculations. The final R_1 was 0.0340 (I > 2σ(I)) and wR_2 was 0.0883 (all data). Largest diff. peak/hole 0.85/-0.90 e Å^3

C25: $C_{28}H_{33.5}Cu_2LaN_{10.5}O_{18}$ (M =1071.14 g/mol): triclinic, space group $P\bar{1}$ (no. 2), a = 13.6007(7) Å, b = 17.3919(8) Å, c = 18.4609(9) Å, α = 85.218(3)°, β = 89.461(3)°, γ = 71.512(3)°, V = 4126.3(4) Å^3, Z = 4, T = 100.0 K, μ(CuKα) = 9.797 mm^{-1}, $Dcalc$ = 1.724 g/cm^3, 67885 reflections measured (4.804°$\leq$ 2Θ $\leq$ 136.484°), 14826 unique (R_{int} = 0.0598, R_{sigma} = 0.0554) which were used in all calculations. The final R_1 was 0.0788 (I > 2σ(I)) and wR_2 was 0.2491 (all data). Largest diff. peak/hole 4.78/-2.58 e Å^3

C26: $C_{38}H_{40}Cu_2La_2N_{10}O_{30}$ (M =1521.70 g/mol): triclinic, space group $P\bar{1}$ (no. 2), a = 9.4157(5) Å, b = 11.9077(7) Å, c = 13.0665(7) Å, α = 97.549(2)°, β = 108.070(2)°, γ = 111.523(2)°, V = 1244.85(12) Å^3, Z = 1, T = 100.0 K, μ(CuKα) = 14.928 mm^{-1}, $Dcalc$ = 2.030 g/cm^3, 20843 reflections measured (7.406°$\leq$ 2Θ $\leq$ 136.488°), 4555 unique (R_{int} = 0.0408, R_{sigma} = 0.0301) which were used in all calculations. The final R_1 was 0.0239 (I > 2σ(I)) and wR_2 was 0.0618 (all data). Largest diff. peak/hole 1.41/-1.23 e Å^3

C27: $C_{21}H_{28}CuLaN_5O_{17}$ (M =824.93 g/mol): monoclinic, space group $P2_1/c$ (no. 14), a = 8.5695(6) Å, b = 19.7972(13) Å, c = 17.0919(11) Å, β = 95.571(2)°, V = 2886.0(3) Å^3, Z = 4, T = 100.00 K, μ(CuKα) = 12.988 mm^{-1}, $Dcalc$ = 1.899 g/cm^3, 28564 reflections measured (6.85°$\leq$ 2Θ $\leq$ 144.316°), 5618 unique (R_{int} = 0.0456, R_{sigma} = 0.0391) which were used in all calculations. The final R_1 was 0.0430 (I > 2σ(I)) and wR_2 was 0.1131 (all data). Largest diff. peak/hole 1.39/-1.20 e Å^3

C28: $C_{21}H_{28}CeCuN_5O_{17}$ (M =826.14 g/mol): monoclinic, space group $P2_1/c$ (no. 14), a = 8.6189(2) Å, b = 19.8934(6) Å, c = 17.2010(5) Å, β = 96.2190(10)°, V = 2931.91(14) Å^3, Z = 4, T = 296.0 K, μ(CuKα) = 13.521 mm^{-1}, $Dcalc$ = 1.872 g/cm^3, 23708 reflections measured (6.816°$\leq$ 2Θ $\leq$ 136.492°), 5244 unique (R_{int} = 0.0550, R_{sigma} = 0.0488) which were used in all calculations. The final R_1 was 0.0433 (I > 2σ(I)) and wR_2 was 0.1229 (all data). Largest diff.

peak/hole 1.60/-1.04 e Å^3

C29: $C_{19}H_{22}CeCuN_5O_{16}$ (M =780.07 g/mol): triclinic, space group $P\bar{1}$ (no. 2), a = 11.5151(4) Å, b = 11.6384(4) Å, c = 11.9146(4) Å, α = 72.4950(10)°, β = 65.8790(10)°, γ = 73.1910(10)°, V = 1364.26(8) Å^3, Z = 2, T = 100.0 K, μ(CuKα) = 14.458 mm^{-1}, *Dcalc* = 1.899 g/cm^3, 16311 reflections measured (8.114°$\leq 2\Theta \leq$ 136.456°), 4860 unique (R_{int} = 0.0423, R_{sigma} = 0.0434) which were used in all calculations. The final R_1 was 0.0406 (I > 2σ(I)) and wR_2 was 0.1109 (all data). Largest diff. peak/hole 1.12/-2.17 e Å^3

C30: $C_{21}H_{25}CeCl_3CuN_5O_{16}$ (M =913.47 g/mol): triclinic, space group $P\bar{1}$ (no. 2), a = 9.3678(4) Å, b = 13.0900(6) Å, c = 13.6093(6) Å, α = 74.374(2)°, β = 76.523(2)°, γ = 72.943(2)°, V = 1514.80(12) Å^3, Z = 2, T = 100.0 K, μ(CuKα) = 15.517 mm^{-1}, *Dcalc* = 2.003 g/cm^3, 20873 reflections measured (6.84°$\leq 2\Theta \leq$ 136.472°), 5366 unique (R_{int} = 0.0567, R_{sigma} = 0.0504) which were used in all calculations. The final R_1 was 0.0580 (I > 2σ(I)) and wR_2 was 0.1656 (all data). Largest diff. peak/hole 1.83/-1.63 e Å^3

C31: $C_{40}H_{48}Ce_2Cu_2N_{10}O_{32}$ (M =1588.20 g/mol): triclinic, space group $P\bar{1}$ (no. 2), a = 12.4827(9) Å, b = 14.0842(10) Å, c = 17.3761(12) Å, α = 112.933(3)°, β = 100.117(3)°, γ = 99.657(3)°, V = 2674.0(3) Å^3, Z = 2, T = 100.0 K, μ(CuKα) = 14.766 mm^{-1}, *Dcalc* = 1.973 g/cm^3, 63258 reflections measured (5.728°$\leq 2\Theta \leq$ 136.472°), 9579 unique (R_{int} = 0.0644, R_{sigma} = 0.0409) which were used in all calculations. The final R_1 was 0.0519 (I > 2σ(I)) and wR_2 was 0.1426 (all data). Largest diff. peak/hole 1.29/-2.02 e Å^3

C32: $C_{22}H_{29}CeCuN_5O_{16.5}$ (M =831.16 g/mol): monoclinic, space group $C2/c$ (no. 15), a = 33.4847(12) Å, b = 8.5734(3) Å, c = 20.9609(8) Å, β = 104.579(2)°, V = 5823.7(4) Å^3, Z = 8, T = 100.0 K, μ(CuKα) = 13.606 mm^{-1}, *Dcalc* = 1.896 g/cm^3, 27228 reflections measured (5.454°$\leq 2\Theta \leq$ 136.488°), 5189 unique (R_{int} = 0.0538, R_{sigma} = 0.0416) which were used in all calculations. The final R_1 was 0.0428 (I > 2σ(I)) and wR_2 was 0.1236 (all data). Largest diff. peak/hole 1.71/-1.25 e Å^3

C33: $C_{16.5}H_{16}CuEuN_3O_{15.5}$ (M =719.82 g/mol): orthorhombic, space group $P2_12_12$ (no. 18), a = 15.0007(7) Å, b = 18.6190(8) Å, c = 9.4221(5) Å, V = 2631.6(2) Å^3, Z = 4, T = 100.00 K, μ(CuKα) = 18.574 mm^{-1}, *Dcalc* = 1.817 g/cm^3, 16161 reflections measured (7.568°$\leq 2\Theta \leq$ 130.13°), 4178 unique (R_{int} = 0.0675, R_{sigma} = 0.0702) which were used in all calculations. The final R_1 was 0.0673 (I > 2σ(I)) and wR_2 was 0.1851 (all data). Largest diff. peak/hole 1.75/-0.70 e Å^3

C34: $C_{20}H_{26}Cl_3CuDyN_2O_8$ (M =754.82 g/mol): monoclinic, space group $P2_1/c$ (no. 14), a = 7.3868(6) Å, b = 25.4602(18) Å, c = 13.5479(10) Å, β = 95.937(4)°, V = 2534.3(3) Å^3, Z = 4, T = 100.0 K, μ(CuKα) = 19.964 mm^{-1}, *Dcalc* = 1.978 g/cm^3, 32398 reflections measured (6.944°$\leq 2\Theta \leq$ 136.486°), 4576 unique (R_{int} = 0.0456, R_{sigma} = 0.0301) which were used in all calculations. The final R_1 was 0.0622 (I > 2σ(I)) and wR_2 was 0.1310 (all data). Largest diff. peak/hole 0.96/-0.68 e Å^3

C35: $C_{20}H_{26}Cl_3CuEuN_2O_8$ (M =744.28 g/mol): triclinic, space group $P\bar{1}$ (no. 2), a = 6.9990(3) Å, b = 11.6434(6) Å, c = 15.8285(8) Å, α = 103.380(2)°, β = 90.110(2)°, γ = 102.747(2)°, V = 1222.05(10) Å^3, Z = 2, T = 104.0 K, μ(CuKα) = 22.713 mm^{-1}, *Dcalc* = 2.023 g/cm^3, 13862 reflections measured (5.748°$\leq 2\Theta \leq$ 136.374°), 4331 unique (R_{int} = 0.0536, R_{sigma} = 0.0512) which were used in all calculations. The final R_1 was 0.0489 (I > 2σ(I)) and wR_2 was 0.1406 (all data). Largest diff. peak/hole 1.37/-2.00 e Å^3

C36: $C_{20}H_{26}Cl_3CuN_2O_8Tb$ (M =751.24 g/mol): triclinic, space group $P\bar{1}$ (no. 2), a = 7.0054(6) Å, b = 11.6018(9) Å, c = 15.8063(12) Å, α = 103.424(3)°, β = 90.053(3)°, γ = 102.897(3)°, V = 1216.15(17) Å^3, Z = 2, T = 100.0 K, μ(CuKα) = 18.663 mm^{-1}, $Dcalc$ = 2.051 g/cm^3, 10132 reflections measured (5.758°$\leq 2\Theta \leq$ 130.158°), 4031 unique (R_{int} = 0.0409, R_{sigma} = 0.0542) which were used in all calculations. The final R_1 was 0.0440 (I > 2σ(I)) and wR_2 was 0.1318 (all data). Largest diff. peak/hole 1.16/-1.00 e Å^3

C37: $C_{19}H_{22}Cl_3CuErN_2O_7$ (M =727.53 g/mol): triclinic, space group $P\bar{1}$ (no. 2), a = 9.9238(4) Å, b = 10.9889(4) Å, c = 11.7998(5) Å, α = 102.5220(10)°, β = 97.533(2)°, γ = 107.4490(10)°, V = 1171.50(8) Å^3, Z = 2, T = 295.0 K, μ(CuKα) = 11.112 mm^{-1}, $Dcalc$ = 2.062 g/cm^3, 25059 reflections measured (7.85°$\leq 2\Theta \leq$ 136.472°), 4206 unique (R_{int} = 0.0483, R_{sigma} = 0.0293) which were used in all calculations. The final R_1 was 0.0236 (I > 2σ(I)) and wR_2 was 0.0634 (all data). Largest diff. peak/hole 0.83/-0.58 e Å^3

C38: $C_{19}H_{22}Cl_3CuHoN_2O_7$ (M =725.20 g/mol): triclinic, space group $P\bar{1}$ (no. 2), a = 9.9181(8) Å, b = 10.9845(9) Å, c = 11.7984(10) Å, α = 102.382(5)°, β = 97.565(5)°, γ = 107.485(4)°, V = 1170.65(17) Å^3, Z = 2, T = 293 K, μ(CuKα) = 10.778 mm^{-1}, $Dcalc$ = 2.057 g/cm^3, 19614 reflections measured (7.848°$\leq 2\Theta \leq$ 133.19°), 4054 unique (R_{int} = 0.0525, R_{sigma} = 0.0406) which were used in all calculations. The final R_1 was 0.0395 (I > 2σ(I)) and wR_2 was 0.0897 (all data). Largest diff. peak/hole 1.13/-0.73 e Å^3

C39: $C_{39}H_{60}Cl_8Cu_3N_4O_{21}Tb_2$ (M =1712.97 g/mol): monoclinic, space group $P2_1/c$ (no. 14), a = 19.0380(7) Å, b = 11.3996(4) Å, c = 26.7968(9) Å, β = 94.644(2)°, V = 5796.5(4) Å^3, Z = 4, T = 100.0 K, μ(CuKα) = 17.000 mm^{-1}, $Dcalc$ = 1.963 g/cm^3, 57449 reflections measured (4.656°$\leq 2\Theta \leq$ 144.364°), 11298 unique (R_{int} = 0.0463, R_{sigma} = 0.0350) which were used in all calculations. The final R_1 was 0.0499 (I > 2σ(I)) and wR_2 was 0.1497 (all data). Largest diff. peak/hole 1.81/-1.27 e Å^3

C40: $C_{38}H_{44}Ce_2Cl_8Cu_2N_4O_{14}$ (M =1471.69 g/mol): triclinic, space group $P\bar{1}$ (no. 2), a = 9.7305(5) Å, b = 11.5538(5) Å, c = 13.2766(6) Å, α = 66.135(2)°, β = 69.054(2)°, γ = 76.272(2)°, V = 1267.27(11) Å^3, Z = 1, T = 100.0 K, μ(CuKα) = 18.990 mm^{-1}, $Dcalc$ = 1.928 g/cm^3, 22851 reflections measured (7.618°$\leq 2\Theta \leq$ 136.462°), 4539 unique (R_{int} = 0.0778, R_{sigma} = 0.0486) which were used in all calculations. The final R_1 was 0.0572 (I > 2σ(I)) and wR_2 was 0.1781 (all data). Largest diff. peak/hole 2.05/-1.68 e Å^3

C41: $C_{42}H_{46}Co_2Eu_2N_8O_{28}$ (M =1532.65 g/mol): monoclinic, space group $P2_1/c$ (no. 14), a = 11.4730(3) Å, b = 19.5247(6) Å, c = 12.0945(4) Å, β = 90.671(2)°, V = 2709.07(14) Å^3, Z = 2, T = 120.0 K, μ(CuKα) = 21.890 mm^{-1}, $Dcalc$ = 1.879 g/cm^3, 29624 reflections measured (7.706°$\leq 2\Theta \leq$ 136.464°), 4838 unique (R_{int} = 0.0616, R_{sigma} = 0.0442) which were used in all calculations. The final R_1 was 0.0437 (I > 2σ(I)) and wR_2 was 0.1202 (all data). Largest diff. peak/hole 1.87/-1.37 e Å^3

C42: $C_{19}H_{26}Cl_3CoErN_2O_9$ (M =758.96 g/mol): triclinic, space group $P\bar{1}$ (no. 2), a = 8.3659(6) Å, b = 9.0279(7) Å, c = 17.3044(12) Å, α = 80.596(4)°, β = 84.361(4)°, γ = 74.111(4)°, V = 1238.14(16) Å^3, Z = 2, T = 100.0 K, μ(CuKα) = 14.801 mm^{-1}, $Dcalc$ = 2.036 g/cm^3, 19366 reflections measured (5.184°$\leq 2\Theta \leq$ 133.158°), 4330 unique (R_{int} = 0.1399, R_{sigma} = 0.0787) which were used in all calculations. The final R_1 was 0.0518 (I > 2σ(I)) and wR_2 was 0.1597 (all data). Largest diff. peak/hole 1.75/-3.05 e Å^3

C43: $C_{19}H_{26}Cl_3CoEuN_2O_9$ (M =743.66 g/mol): triclinic, space group $P\bar{1}$ (no. 2), a = 8.4230(5) Å, b = 9.0630(5) Å, c = 17.4354(11) Å, α = 80.808(4)°, β = 84.301(4)°, γ = 73.779(3)°, V =

1259.48(13) Å^3, Z = 2, T = 100.0 K, μ(CuKα) = 26.190 mm^{-1}, *Dcalc* = 1.961 g/cm^3, 48497 reflections measured (5.142°$\leq 2\Theta \leq$ 136.466°), 4521 unique (R_{int} = 0.1030, R_{sigma} = 0.0518) which were used in all calculations. The final R_1 was 0.0443 (I > 2σ(I)) and wR_2 was 0.1083 (all data). Largest diff. peak/hole 0.82/-0.99 e Å^3

C44: $C_{22}H_{35}Cl_3CoDyN_2O_{10.5}$ (M =823.30 g/mol): triclinic, space group $P\bar{1}$ (no. 2), a = 10.4766(6) Å, b = 10.8314(6) Å, c = 14.1186(8) Å, α = 96.838(2)°, β = 109.945(2)°, γ = 104.533(2)°, V = 1420.49(14) Å^3, Z = 2, T = 100.0 K, μ(CuKα) = 21.592 mm^{-1}, *Dcalc* = 1.925 g/cm^3, 13758 reflections measured (6.836°$\leq 2\Theta \leq$ 136.492°), 4994 unique (R_{int} = 0.0972, R_{sigma} = 0.0771) which were used in all calculations. The final R_1 was 0.0536 (I > 2σ(I)) and wR_2 was 0.1505 (all data). Largest diff. peak/hole 2.10/-1.32 e Å^3

C45: $C_{22}H_{34.5}Cl_3CoErN_2O_{10.25}$ (M =823.55 g/mol): triclinic, space group $P\bar{1}$ (no. 2), a = 10.4631(8) Å, b = 10.8332(9) Å, c = 14.0815(11) Å, α = 96.968(3)°, β = 109.923(3)°, γ = 104.477(3)°, V = 1415.1(2) Å^3, Z = 2, T = 100.0 K, μ(CuKα) = 13.043 mm^{-1}, *Dcalc* = 1.933 g/cm^3, 16539 reflections measured (6.856°$\leq 2\Theta \leq$ 136.486°), 5032 unique (R_{int} = 0.0416, R_{sigma} = 0.0417) which were used in all calculations. The final R_1 was 0.0311 (I > 2σ(I)) and wR_2 was 0.0833 (all data). Largest diff. peak/hole 1.08/-1.06 e Å^3

C46: $C_{21}H_{30}Cl_3CoEuN_2O_9$ (M =771.71 g/mol): triclinic, space group $P\bar{1}$ (no. 2), a = 10.5086(7) Å, b = 10.7045(7) Å, c = 14.0682(9) Å, α = 69.299(4)°, β = 68.539(4)°, γ = 75.564(4)°, V = 1364.57(16) Å^3, Z = 2, T = 100.0 K, μ(CuKα) = 24.199 mm^{-1}, *Dcalc* = 1.878 g/cm^3, 16355 reflections measured (7.056°$\leq 2\Theta \leq$ 136.448°), 4848 unique (R_{int} = 0.0553, R_{sigma} = 0.0567) which were used in all calculations. The final R_1 was 0.0414 (I > 2σ(I)) and wR_2 was 0.0990 (all data). Largest diff. peak/hole 0.89/-0.87 e Å^3

C47: $C_{21}H_{23}DyN_4O_{14}Zn$ (M =783.30 g/mol): triclinic, space group $P\bar{1}$ (no. 2), a = 9.5270(6) Å, b = 10.3999(7) Å, c = 13.6149(9) Å, α = 89.667(3)°, β = 83.985(3)°, γ = 82.676(3)°, V = 1330.55(15) Å^3, Z = 2, T = 298.0 K, μ(CuKα) = 16.661 mm^{-1}, *Dcalc* = 1.955 g/cm^3, 27969 reflections measured (6.528°$\leq 2\Theta \leq$ 136.418°), 4783 unique (R_{int} = 0.0689, R_{sigma} = 0.0415) which were used in all calculations. The final R_1 was 0.0365 (I > 2σ(I)) and wR_2 was 0.0957 (all data). Largest diff. peak/hole 1.03/-0.56 e Å^3

C48: $C_{25}H_{33}DyN_4NiO_{16}$ (M =866.76 g/mol): monoclinic, space group $P2_1/n$ (no. 14), a = 10.3941(3) Å, b = 18.9712(6) Å, c = 15.7732(5) Å, β = 98.235(2)°, V = 3078.22(16) Å^3, Z = 4, T = 108.0 K, μ(CuKα) = 14.331 mm^{-1}, *Dcalc* = 1.870 g/cm^3, 40186 reflections measured (7.334°$\leq 2\Theta \leq$ 136.482°), 5562 unique (R_{int} = 0.0438, R_{sigma} = 0.0280) which were used in all calculations. The final R_1 was 0.0325 (I > 2σ(I)) and wR_2 was 0.0879 (all data). Largest diff. peak/hole 0.70/-0.88 e Å^3

C49: $C_{19}H_{26}Cl_3EuN_2NiO_9$ (M =743.44 g/mol): triclinic, space group $P\bar{1}$ (no. 2), a = 8.4117(3) Å, b = 9.0640(3) Å, c = 17.2233(7) Å, α = 80.951(2)°, β = 84.682(2)°, γ = 73.933(2)°, V = 1244.50(8) Å^3, Z = 2, T = 100.0 K, μ(CuKα) = 22.224 mm^{-1}, *Dcalc* = 1.984 g/cm^3, 20287 reflections measured (5.202°$\leq 2\Theta \leq$ 136.46°), 4508 unique (R_{int} = 0.0573, R_{sigma} = 0.0435) which were used in all calculations. The final R_1 was 0.0395 (I > 2σ(I)) and wR_2 was 0.1046 (all data). Largest diff. peak/hole 1.05/-1.64 e Å^3

C50: $C_{48}H_{84}N_4Ni_3O_{17}$ (M =1165.32 g/mol): monoclinic, space group $P2_1/n$ (no. 14), a = 14.639(2) Å, b = 20.587(3) Å, c = 19.569(3) Å, β = 98.902(9)°, V = 5826.7(16) Å^3, Z = 4, T = 100.00 K, μ(CuKα) = 1.683 mm^{-1}, *Dcalc* = 1.328 g/cm^3, 19211 reflections measured (7.47°$\leq 2\Theta \leq$ 130.168°), 9911 unique (R_{int} = 0.1141, R_{sigma} = 0.1127) which were used in all calculations.

The final R_1 was 0.0639 (I > 2σ(I)) and wR_2 was 0.1772 (all data). Largest diff. peak/hole 0.93/-0.74 e Å^3

C51: $C_{46}H_{74}N_4Ni_3O_{14}$ (M =1083.22 g/mol): monoclinic, space group $C2/c$ (no. 15), a = 26.477(2) Å, b = 14.4568(13) Å, c = 14.9455(13) Å, β = 98.341(4)°, V = 5660.1(9) Å^3, Z = 4, T = 100.00 K, μ(CuKα) = 1.655 mm^{-1}, $Dcalc$ = 1.271 g/cm^3, 31233 reflections measured (6.748°$\leq$ 2Θ $\leq$ 136.476°), 5117 unique (R_{int} = 0.0448, R_{sigma} = 0.0343) which were used in all calculations. The final R_1 was 0.0483 (I > 2σ(I)) and wR_2 was 0.1348 (all data). Largest diff. peak/hole 0.82/-0.56 e Å^3

C52: $C_{43}H_{55}Cl_5N_4Ni_4O_{16}$ (M =1296.00 g/mol): triclinic, space group $P\bar{1}$ (no. 2), a = 10.0582(6) Å, b = 12.4867(7) Å, c = 12.9245(9) Å, α = 73.396(3)°, β = 74.171(4)°, γ = 83.227(4)°, V = 1495.16(17) Å^3, Z = 1, T = 108.0 K, μ(CuKα) = 3.993 mm^{-1}, $Dcalc$ = 1.439 g/cm^3, 12286 reflections measured (7.394°$\leq$ 2Θ $\leq$ 130.152°), 4970 unique (R_{int} = 0.0446, R_{sigma} = 0.0597) which were used in all calculations. The final R_1 was 0.0746 (I > 2σ(I)) and wR_2 was 0.2433 (all data). Largest diff. peak/hole 1.84/-0.61 e Å^3

C53: $C_{69}H_{106}N_6Ni_7O_{33}$ (M =1958.56 g/mol): monoclinic, space group $P2_1/n$ (no. 14), a = 14.5091(13) Å, b = 33.698(3) Å, c = 18.4930(17) Å, β = 109.471(5)°, V = 8524.6(13) Å^3, Z = 4, T = 105.0 K, μ(CuKα) = 2.377 mm^{-1}, $Dcalc$ = 1.526 g/cm^3, 106395 reflections measured (5.244°$\leq$ 2Θ $\leq$ 136.49°), 15458 unique (R_{int} = 0.0773, R_{sigma} = 0.0447) which were used in all calculations. The final R_1 was 0.0575 (I > 2σ(I)) and wR_2 was 0.1696 (all data). Largest diff. peak/hole 0.85/-0.74 e Å^3

C54: $C_{38}H_{40}Co_2N_6O_{18}Zn$ (M =1051.99 g/mol): monoclinic, space group $P2_1/c$ (no. 14), a = 10.7688(3) Å, b = 15.3150(4) Å, c = 28.4493(8) Å, β = 97.961(2)°, V = 4646.8(2) Å^3, Z = 4, T = 100.00 K, μ(CuKα) = 6.804 mm^{-1}, $Dcalc$ = 1.504 g/cm^3, 24968 reflections measured (6.274°$\leq$ 2Θ $\leq$ 136.486°), 8448 unique (R_{int} = 0.0574, R_{sigma} = 0.0611) which were used in all calculations. The final R_1 was 0.0456 (I > 2σ(I)) and wR_2 was 0.1216 (all data). Largest diff. peak/hole 0.75/-0.74 e Å^3

C55: $C_{38}H_{40}N_6Ni_2O_{18}Zn$ (M =1051.55 g/mol): triclinic, space group $P\bar{1}$ (no. 2), a = 11.164(2) Å, b = 12.333(3) Å, c = 18.067(4) Å, α = 70.438(7)°, β = 84.642(6)°, γ = 64.728(6)°, V = 2116.1(8) Å^3, Z = 2, T = 100.00 K, μ(CuKα) = 2.435 mm^{-1}, $Dcalc$ = 1.650 g/cm^3, 26644 reflections measured (8.39°$\leq$ 2Θ $\leq$ 140.124°), 7856 unique (R_{int} = 0.0434, R_{sigma} = 0.0474) which were used in all calculations. The final R_1 was 0.0470 (I > 2σ(I)) and wR_2 was 0.1242 (all data). Largest diff. peak/hole 0.64/-0.72 e Å^3

C56: $C_{21.6}H_{22.6}CuGdN_3O_{14}$ (M =769.02 g/mol): monoclinic, space group $P2_1/n$ (no. 14), a = 14.0354(9) Å, b = 11.1833(7) Å, c = 18.0902(12) Å, β = 105.571(5)°, V = 2735.3(3) Å^3, Z = 4, T = 109.0 K, μ(CuKα) = 17.139 mm^{-1}, $Dcalc$ = 1.867 g/cm^3, 34570 reflections measured (7.118°$\leq$ 2Θ $\leq$ 149.302°), 5586 unique (R_{int} = 0.1710, R_{sigma} = 0.1198) which were used in all calculations. The final R_1 was 0.0744 (I > 2σ(I)) and wR_2 was 0.2288 (all data). Largest diff. peak/hole 1.77/-1.54 e Å^3

C57: $C_{20}H_{24}CuN_3NaO_{10}$ (M =552.95 g/mol): triclinic, space group $P\bar{1}$ (no. 2), a = 9.469(3) Å, b = 10.439(3) Å, c = 12.426(4) Å, α = 109.06(2)°, β = 90.859(19)°, γ = 98.755(17)°, V = 1144.7(7) Å^3, Z = 2, T = 100.0 K, μ(CuKα) = 2.094 mm^{-1}, $Dcalc$ = 1.604 g/cm^3, 21567 reflections measured (7.544°$\leq$ 2Θ $\leq$ 130.16°), 3866 unique (R_{int} = 0.0668, R_{sigma} = 0.0424) which were used in all calculations. The final R_1 was 0.0743 (I > 2σ(I)) and wR_2 was 0.2277 (all data). Largest

diff. peak/hole 0.74/-1.26 e Å^3

C58: $C_{19}H_{24}CuN_3NaO_{11}$ (M =556.94 g/mol): monoclinic, space group $P2_1/c$ (no. 14), a = 12.1619(14) Å, b = 12.1925(15) Å, c = 15.3667(18) Å, β = 96.744(4)°, V = 2262.9(5) Å^3, Z = 4, T = 100.0 K, μ(CuKα) = 2.156 mm^{-1}, $Dcalc$ = 1.635 g/cm^3, 25619 reflections measured (10.308°$\leq 2\Theta \leq$ 144.972°), 4427 unique (R_{int} = 0.0582, R_{sigma} = 0.0420) which were used in all calculations. The final R_1 was 0.0479 (I > 2σ(I)) and wR_2 was 0.1367 (all data). Largest diff. peak/hole 0.70/-0.84 e Å^3

C59: $C_4H_{13}Cu_2Na_{0.5}Ni_{1.33}O_{10.5}$ (M =446.00 g/mol): trigonal, space group $R\bar{3}c$ (no. 167), a = 23.9966(8) Å, c = 35.075(2) Å, V = 17491.5(15) Å^3, Z = 36, T = 100.00 K, μ(CuKα) = 4.408 mm^{-1}, $Dcalc$ = 1.524 g/cm^3, 54450 reflections measured (6.594°$\leq 2\Theta \leq$ 136.93°), 3513 unique (R_{int} = 0.0394, R_{sigma} = 0.0203) which were used in all calculations. The final R_1 was 0.0865 (I > 2σ(I)) and wR_2 was 0.2322 (all data). Largest diff. peak/hole 3.65/-1.04 e Å^3

C60: $C_{121.8}H_{144.6}ClCu_{12}Eu_4N_{12}O_{61}$ (M =4199.48 g/mol): monoclinic, space group $C2/m$ (no. 12), a = 24.9451(9) Å, b = 22.8197(8) Å, c = 34.3447(12) Å, β = 102.844(2)°, V = 19061.2(12) Å^3, Z = 4, T = 100.0 K, μ(CuKα) = 11.409 mm^{-1}, $Dcalc$ = 1.463 g/cm^3, 116972 reflections measured (2.638°$\leq 2\Theta \leq$ 136.492°), 17783 unique (R_{int} = 0.0704, R_{sigma} = 0.0417) which were used in all calculations. The final R_1 was 0.0732 (I > 2σ(I)) and wR_2 was 0.2238 (all data). Largest diff. peak/hole 2.18/-1.17 e Å^3

C61: $C_{42}H_{52}N_5NaNi_3O_{22}$ (M =1178.00 g/mol): triclinic, space group $P\bar{1}$ (no. 2), a = 11.4944(4) Å, b = 12.9061(5) Å, c = 18.2728(7) Å, α = 85.403(2)°, β = 84.243(2)°, γ = 72.434(2)°, V = 2567.74(17) Å^3, Z = 2, T = 100.0 K, μ(CuKα) = 2.086 mm^{-1}, $Dcalc$ = 1.524 g/cm^3, 65090 reflections measured (4.868°$\leq 2\Theta \leq$ 136.456°), 9226 unique (R_{int} = 0.0630, R_{sigma} = 0.0399) which were used in all calculations. The final R_1 was 0.0499 (I > 2σ(I)) and wR_2 was 0.1481 (all data). Largest diff. peak/hole 0.92/-0.63 e Å^3

C62: $C_{43.5}H_{53}N_4NaNi_3O_{18}$ (M =1119.02 g/mol): triclinic, space group $P\bar{1}$ (no. 2), a = 11.8848(18) Å, b = 13.030(2) Å, c = 18.131(3) Å, α = 84.908(4)°, β = 75.691(4)°, γ = 75.839(4)°, V = 2636.7(7) Å^3, Z = 2, T = 100.00 K, μ(CuKα) = 1.936 mm^{-1}, $Dcalc$ = 1.409 g/cm^3, 37958 reflections measured (5.032°$\leq 2\Theta \leq$ 136.476°), 9431 unique (R_{int} = 0.0410, R_{sigma} = 0.0430) which were used in all calculations. The final R_1 was 0.0630 (I > 2σ(I)) and wR_2 was 0.1864 (all data). Largest diff. peak/hole 1.47/-0.54 e Å^3

C63: $C_{84}H_{92.5}N_{11.5}Na_4Ni_6O_{43}$ (M =2395.41 g/mol): triclinic, space group $P\bar{1}$ (no. 2), a = 9.8400(3) Å, b = 13.3906(4) Å, c = 19.5859(6) Å, α = 84.133(2)°, β = 81.302(2)°, γ = 72.137(2)°, V = 2423.77(13) Å^3, Z = 1, T = 150.0 K, μ(CuKα) = 2.302 mm^{-1}, $Dcalc$ = 1.641 g/cm^3, 32296 reflections measured (4.572°$\leq 2\Theta \leq$ 136.488°), 8801 unique (R_{int} = 0.0610, R_{sigma} = 0.0595) which were used in all calculations. The final R_1 was 0.0622 (I > 2σ(I)) and wR_2 was 0.1784 (all data). Largest diff. peak/hole 0.88/-0.81 e Å^3

C64: $C_{85.8}H_{107.4}Cu_8N_{15}Na_8O_{64}$ (M =3065.10 g/mol): triclinic, space group $P\bar{1}$ (no. 2), a = 14.9441(6) Å, b = 17.1091(7) Å, c = 17.8360(8) Å, α = 106.898(3)°, β = 106.771(2)°, γ = 99.380(2)°, V = 4023.3(3) Å^3, Z = 1, T = 100 K, μ(CuKα) = 2.056 mm^{-1}, $Dcalc$ = 1.265 g/cm^3, 138537 reflections measured (5.54°$\leq 2\Theta \leq$ 130.142°), 13677 unique (R_{int} = 0.1061, R_{sigma} = 0.0723) which were used in all calculations. The final R_1 was 0.0846 (I > 2σ(I)) and wR_2 was 0.2577 (all data). Largest diff. peak/hole 1.61/-0.58 e Å^3

C65: $C_{16}H_{16}N_2NiO_6$ (M =391.02 g/mol): monoclinic, space group $P2_1/n$ (no. 14), a = 8.3357(7) Å, b = 4.8455(4) Å, c = 18.6854(16) Å, β = 95.298(2)°, V = 751.49(11) Å^3, Z = 2, T = 100.0 K, μ(CuKα) = 2.230 mm^{-1}, *Dcalc* = 1.728 g/cm^3, 8811 reflections measured (9.506°$\leq 2\Theta \leq$ 144.622°), 1471 unique (R_{int} = 0.0225, R_{sigma} = 0.0183) which were used in all calculations. The final R_1 was 0.0256 (I > 2σ(I)) and wR_2 was 0.0699 (all data). Largest diff. peak/hole 0.34/-0.29 e Å^3

C66: $C_{53}H_{78}MnN_5O_{12}$ (M =1032.14 g/mol): monoclinic, space group $P2_1/c$ (no. 14), a = 36.218(9) Å, b = 13.278(3) Å, c = 24.221(5) Å, β = 90.016(10)°, V = 11648(5) Å^3, Z = 8, T = 100.00 K, μ(CuKα) = 2.330 mm^{-1}, *Dcalc* = 1.177 g/cm^3, 117288 reflections measured (2.44°$\leq 2\Theta \leq$ 131.646°), 19832 unique (R_{int} = 0.0879, R_{sigma} = 0.0689) which were used in all calculations. The final R_1 was 0.0810 (I > 2σ(I)) and wR_2 was 0.2320 (all data). Largest diff. peak/hole 0.84/-0.94 e Å^3

Bibliography

(1) Housecroft, C. E.; Sharpe, A. G., *Inorganic Chemistry*, 4th edition; Pearson: Harlow, England; 2012, p 1215.

(2) Rezende, S. M., *Introduction to Electronic Materials and Devices*; Springer Nature Switzerland AG: Cham, Switzerland, 2022.

(3) Sarkar, A.; Dey, S.; Rajaraman, G. Role of Coordination Number and Geometry in Controlling the Magnetic Anisotropy in Fe^{II}, Co^{II}, and Ni^{II} Single-Ion Magnets. *Chem. Eur. J.* **2020**, *26*, 14036–14058.

(4) Vulfson, S. G., *Molecular Magnetochemistry*; Gordon and Breach Science Publishers: Amsterdam, Netherlands, 1998.

(5) Feltham, H. L. C.; Brooker, S. Review of purely 4*f* and mixed-metal n*d*-4*f* single-molecule magnets containing only one lanthanide ion. *Coord. Chem. Rev.* **2014**, *276*, 1–33.

(6) Shriver, D. F.; Atkins, P. W., *Inorganic Chemistry*, Third; Oxford University Press: Oxford, United Kingdom, 1999.

(7) Milios, C. J.; Piligkos, S.; Brechin, E. K. Ground state spin-switching via targeted structural distortion: Twisted single-molecule magnets from derivatised salicylaldoximes. *Dalton Trans.* **2008**, 1809–1817.

(8) Han, T.; Shi, W.; Niu, Z.; Na, B.; Cheng, P. Magnetic blocking from exchange interactions: Slow relaxation of the magnetization and hysteresis loop observed in a dysprosium-nitronyl nitroxide chain compound with an antiferromagnetic ground state. *Chem. Eur. J.* **2013**, *19*, 994–1001.

(9) Dey, A.; Acharya, J.; Chandrasekhar, V. Heterometallic 3d-4f Complexes as Single-Molecule Magnets. *Chem. Asian J.* **2019**, *14*, 4433–4453.

(10) Swain, A.; Sarkar, A.; Rajaraman, G. Role of Ab Initio Calculations in the Design and Development of Organometallic Lanthanide-Based Single-Molecule Magnets. *Chem. Asian J.* **2019**, *14*, 4056–4073.

(11) Bogani, L.; Wernsdorfer, W. Molecular spintronics using single-molecule magnets. *Nat. Mat.* **2008**, *7*, 179–186.

(12) Leuenberger, M. N.; Loss, D. Quantum computing in molecular magnets. *Nature* **2001**, *410*, 789–793.

(13) Mason, K.; Chang, J.; Garlatti, E.; Prescimone, A.; Yoshii, S.; Nojiri, H.; Schnack, J.; Tasker, P. A.; Carretta, S.; Brechin, E. K. Linking [$Fe(III)_3$] triangles with "double-headed" phenolic oximes. *Chem. Commun.* **2011**, *47*, 6018–6020.

(14) Mason, K.; Chang, J.; Prescimone, A.; Garlatti, E.; Carretta, S.; Tasker, P. A.; Brechin, E. K. Linking [$M(III)_3$] triangles with "double-headed" phenolic oximes. *Dalton Trans.* **2012**, *41*, 8777–8785.

(15) Wenzel, M.; Forgan, R. S.; Faure, A.; Mason, K.; Tasker, P. A.; Piligkos, S.; Brechin, E. K.; Plieger, P. G. A New Polynuclear Coordination Type for (Salicylaldoxime)copper(II) Complexes: Structure and Magnetic Properties of an (Oxime)Cu_6 Cluster. *Eur. J. Inorg. Chem.* **2009**, *2009*, 4613–4617.

(16) Woodruff, D. N.; Winpenny, R. E. P.; Layfield, R. A. Lanthanide Single-Molecule Magnets. *Chem. Rev.* **2013**, *113*, 5110–5148.

(17) Piquer, L. R.; Sanudo, E. C. Heterometallic 3d-4f single-molecule magnets. *Dalton Trans.* **2015**, *44*, 8771–8780.

(18) Atanasov, M.; Aravena, D.; Suturina, E.; Bill, E.; Maganas, D.; Neese, F. First principles approach to the electronic structure, magnetic anisotropy and spin relaxation in mononuclear 3d-transition metal single molecule magnets. *Coord. Chem. Rev.* **2015**, *289-290*, 177–214.

(19) Guo, F. S.; Day, B. M.; Chen, Y. C.; Tong, M. L.; Mansikkamaki, A.; Layfield, R. A. Magnetic hysteresis up to 80 kelvin in a dysprosium metallocene single-molecule magnet. *Science* **2018**, *362*, 1400–1403.

(20) Benelli, C.; Gatteschi, D., *Introduction to Molecular Magnetism: From Transition Metals to Lanthanides*; Wiley-VCH: Weinheim, 2015.

(21) Zabala-Lekuona, A.; Seco, J. M.; Colacio, E. Single-Molecule Magnets: From Mn_{12}-ac to dysprosium metallocenes, a travel in time. *Coord. Chem. Rev.* **2021**, *441*, 213984–214021.

(22) Goodwin, C. A. P. Blocking like it's hot: A synthetic chemists' path to high-temperature lanthanide single molecule magnets. *Dalton Trans.* **2020**, *49*, 14320–14337.

(23) Dey, A.; Bag, P.; Kalita, P.; Chandrasekhar, V. Heterometallic Cu^{II}-Ln^{III} complexes: Single molecule magnets and magnetic refrigerants. *Coord. Chem. Rev.* **2021**, *432*, 213707–213775.

(24) Castro-Alvarez, A.; Gil, Y.; Llanos, L.; Aravena, D. High performance single-molecule magnets, Orbach or Raman relaxation suppression? *Inorg. Chem. Front.* **2020**, *7*, 2478–2486.

(25) Weihe, H.; Gudel, H. U. Quantitative Interpretation of the Goodenough-Kanamori Rules: A Critical Analysis. *Inorg. Chem.* **1997**, *36*, 3632–3639.

(26) Kanamori, J. Superexchange interaction and symmetry properties of electron orbitals. *J. Phys. Chem. Solids* **1959**, *10*, 87–98.

(27) Climova, A.; Pivovarova, E.; Szczesio, M.; Gobis, K.; Ziembicka, D.; Korga-Plewko, A.; Kubik, J.; Iwan, M.; Antos-Bielska, M.; Krzyżowska, M.; Czylkowska, A. Anticancer and antimicrobial activity of new copper (II) complexes. *J. Inorg. Biochem.* **2023**, *240*, 112108.

(28) Bonke, S. A.; Risse, T.; Schnegg, A.; Brückner, A. In situ electron paramagnetic resonance spectroscopy for catalysis. *Nat. Rev. Methods Primers* **2021**, *1*, 33.

(29) Toida, H.; Matsuzaki, Y.; Kakuyanagi, K.; Zhu, X.; Munro, W. J.; Yamaguchi, H.; Saito, S. Electron paramagnetic resonance spectroscopy using a single artificial atom. *Commun. Phys.* **2019**, *2*, 33.

(30) Mibu, K.; Tanaka, M.; Hamaya, K. In *Heusler Alloys*; Springer International Publishing: Switzerland, 2016; Chapter 14, pp 341–351.

(31) Nakashima, S. In *Hyperfine Interactions*; Springer International Publishing: Switzerland, 2017.

(32) Dyar, M. D.; Agresti, D. G.; Schaefer, M. W.; Grant, C. A.; Sklute, E. C. Mössbauer spectroscopy of earth and planetary materials. *Annu. Rev. Earth Planet. Sci.* **2006**, *34*, 83–125.

(33) Cowtan, K. In *Encyclopedia of Life Sciences*; John Wiley & Sons, Ltd.: Hoboken, New Jersey, U.S., 2001.

(34) Taylor, G. The phase problem. *Acta Crystallogr. Sect. D* **2003**, *59*, 1881–1890.

(35) Clegg, W., *Crystal Structure Determination*; Oxford Chemistry Primer; Oxford University Press: Oxford, United Kingdom, 1998.

(36) Clegg, W., *Crystal Structure Determination*; Oxford University Press Inc., New York: United States, 1998.

(37) Atkins, P.; Overton, T.; Rourke, J.; Weller, M.; Armstrong, F., *Shriver and Atkins' Inorganic Chemistry*, Fourth; Oxford University Press: Oxford, United Kingdom, 2006.

(38) Carlin, R. L., *Magnetochemistry*, First; Springer-Verlag Berlin Heidelberg: 1986.

(39) Gallop, J.; Hao, L. Nanoscale Superconducting Quantum Interference Devices Add Another Dimension. *ACS Nano* **2016**, *10*, 8128–8132.

(40) Levenson-Falk, E. M.; Antler, N.; Siddiqi, I. Dispersive nanoSQUID magnetometry. *Supercond. Sci. Technol.* **2016**, *29*, 113003–113014.

(41) Sawicki, M.; Stefanowicz, W. Sensitive SQUID magnetometry for studying nano-magnetism. *Semicond. Sci. Technol.* **2011**, *26*, 1–16.

(42) Wernsdorfer, W. From micro- to nano-SQUIDs: applications to nanomagnetism. *Supercond. Sci. Technol.* **2009**, *22*, 064013–064026.

(43) Koch, W.; Holthausen, M. C., *A Chemist's Guide to Density Functional Theory*, Second; Wiley-VCH Verlag GmbH: Weinheim, Germany, 2001, p 306.

(44) Parr, R. G.; Weitao, Y., *Density functional theory of atoms and molecules*; Oxford University Press: New York, 1989.

(45) Beal, N. J. Broken Symmetry Density Functional Theory Studies of Multinuclear Manganese Metalloproteins, Thesis, University of Manchester, UK, 2017.

(46) Ruiz, E.; Cano, J.; Alvarez, S.; Alemany, P. Broken Symmetry Approach to Calculation of Exchange Coupling Constants for Homobinuclear and Heterobinuclear Transition Metal Complexes. *J. Comput. Chem.* **1999**, *20*, 1391–1400.

(47) Soda, T.; Kitagawa, Y.; Onishi, T.; Takano, Y.; Shigeta, Y.; Nagao, H.; Yoshioka, Y.; Yamaguchi, K. Ab initio computations of effective exchange integrals for H–H, H–He–H and Mn_2O_2 complex: comparison of broken-symmetry approaches. *Chem. Phys. Lett.* **2000**, *319*, 223–230.

(48) Noodleman, L. Valence bond description of antiferromagnetic coupling in transition metal dimers. *J. Chem. Phys.* **1981**, *74*, 5737–5743.

(49) Ruiz, E.; Rodriguez-Fortea, A.; Cano, J.; Alvarez, S.; Alemany, P. About the Calculation of Exchange Coupling Constants in Polynuclear Transition Metal Complexes. *J. Comput. Chem.* **2003**, *24*, 982–989.

(50) Yamanaka, S.; Kawakami, T.; Nagao, H.; Yamaguchi, K. Effective exchange integrals for open-shell species by density functional methods. *Chem. Phys. Lett.* **1994**, *231*, 25–33.

(51) Anson, C. E.; Eichhöfer, A.; Issac, I.; Fenske, D.; Fuhr, O.; Sevillano, P.; Persau, C.; Stalke, D.; Zhang, J. Synthesis and Crystal Structures of the Ligand-Stabilized Silver Chalcogenide Clusters $[Ag_{154}Se_{77}(dppxy)_{18}]$, $[Ag_{320}(StBu)_{60}S_{130}(dppp)_{12}]$, $[Ag_{352}S_{128}(StC_5H_{11})_{96}]$, and $[Ag_{490}S_{188}(StC_5H_{11})_{114}]$. *Angew. Chem. Int. Ed.* **2008**, *47*, 1326–1331.

(52) Kumar, P.; Griffiths, K.; Anson, C. E.; Powell, A. K.; Kostakis, G. E. A tetranuclear $Cu^{II}_2Dy^{III}_2$ coordination cluster as a Suzuki (C–C) coupling reaction promoter. *Dalton Trans.* **2018**, *47*, 17202–17205.

(53) Aime, S.; Baranyai, Z. How the catalysis of the prototropic exchange affects the properties of lanthanide(III) complexes in their applications as MRI contrast agents. *Inorg. Chim. Acta* **2022**, *532*, 120730–120744.

(54) Zhou, J.-J.; Mei, Y.; Pan, Z.; Zhou, H. Structure, DNA binding and cleavage of a new Zn(II)Mn(II) macrocyclic complex. *Spectrochim. Acta A* **2012**, *99*, 329–334.

(55) Bai, H.; Ai, J.; Sun, P. A new lanthanide–Schiff base ligand complex: Structural characterization and biological effect on children nosocomial infection. *Inorg. Nano-Met. Chem.* **2022**, 1–5.

(56) Coxall, R. A.; Lindloy, L. F.; Miller, H. A.; Parkin, A.; Parsons, S.; Tasker, P. A.; White, D. J. Solvent extraction of metal sulfates by zwitterionic forms of ditopic ligands. *Dalton Trans.* **2003**, *1*, 55–64.

(57) Ning, Y.; Jin, G.-Q.; Wang, M.-X.; Gao, S.; Zhang, J.-L. Recent progress in metal-based molecular probes for optical bioimaging and biosensing. *Curr. Opin. Chem. Biol.* **2022**, *66*, 102097–102108.

(58) Jia, R.; Gao, T.; Yang, Y.; Sun, W.; Chen, R.; Yan, P.; Hou, G. Luminescence of Salen Lanthanide Bimetallic Complexes: Dual Emission and Energy Transfer. *Z. Anorg. Allg. Chem.* **2015**, *641*, 1974–1979.

(59) Sessoli, R.; Gatteschi, D.; Caneschi, A.; Novak, M. A. Magnetic bistability in a metal-ion cluster. *Nature* **1993**, *365*, 141–143.

(60) Barber, J. Mn_4Ca Cluster of Photosynthetic Oxygen-Evolving Center: Structure, Function and Evolution. *Biochemistry* **2016**, *55*, 5901–5906.

(61) Lis, T. Preparation, Structure, and Magnetic Properties of a Dodecanuclear Mixed-Valence Manganese Carboxylate. *Acta Crystallogr.* **1980**, *B36*, 2042–2046.

(62) Sessoli, R.; Tsai, H.-L.; Schake, A. R.; Wang, S.; Vincent, J. B.; Folting, K.; Gatteschi, D.; Christou, G.; Hendrickson, D. N. High-Spin Molecules: $[Mn_{12}O_{12}(O_2CR)_{16}(H_2O)_4]$. *J. Am. Chem. Soc.* **1993**, *115*, 1804–1816.

(63) Fang, X.; McCallum, K.; Pratt, H. D.; Anderson, T. M.; Dennis, K.; Luban, M. A co-crystal of polyoxometalates exhibiting single-molecule magnet behavior: The structural origin of a large magnetic anisotropy. *Dalton Trans.* **2012**, *41*, 9867–9870.

(64) Halcrow, M. A. Jahn-Teller distortions in transition metal compounds, and their importance in functional molecular and inorganic materials. *Chem. Soc. Rev.* **2013**, *42*, 1784–1795.

(65) Milios, C. J.; Vinslava, A.; Wernsdorfer, W.; Moggach, S.; Parsons, S.; Perlepes, S. P.; Christou, G.; Brechin, E. K. A Record Anisotropy Barrier for a Single-Molecule Magnet. *J. Am. Chem. Soc.* **2007**, *129*, 2754–2755.

(66) Banerjee, A.; Gómez García, C. J.; Benmansour, S.; Gomlia, R. M.; Frontera, A.; Chattopadhyay, S. Field-induced single-molecule magnet behaviour in a series of dinuclear cobalt(III,II) complexes. *Polyhedron* **2022**, *220*, 115802.

(67) Chandrasekhar, V.; Dey, A.; Mota, A. J.; Colacio, E. Slow Magnetic Relaxation in Co(III)–Co(II) Mixed-Valence Dinuclear Complexes with a $Co^{II}O_5X$ (X = Cl, Br, NO_3) Distorted-Octahedral Coordination Sphere. *Inorg. Chem.* **2013**, *52*, 4554–4561.

(68) Zhu, Y.-Y.; Cui, C.; Zhang, Y.-Q.; Jia, J.-H.; Guo, X.; Gao, C.; Qian, K.; Jiang, S.-D.; Wang, B.-W.; Wang, Z.-M.; Gao, S. Zero-field slow magnetic relaxation from single Co(II) ion: A transition metal single-molecule magnet with high anisotropy barrier. *Chem. Sci.* **2013**, *4*, 1802–1806.

(69) Buvaylo, E. A.; Kokozay, V. N.; Vassilyeva, O. Y.; Skelton, B. W.; Ozarowski, A.; Titiš, J.; Vranovičová, B.; Boča, R. Field-Assisted Slow Magnetic Relaxation in a Six-Coordinate Co(II)–Co(III) Complex with Large Negative Anisotropy. *Inorg. Chem.* **2017**, *56*, 6999–7009.

(70) Banerjee, A.; Banerjee, S.; Gómez García, C. J.; Benmansour, S.; Chattopadhyay, S. Field-induced single molecule magnet behavior of a dinuclear cobalt(II) complex: A combined experimental and theoretical study. *Dalton Trans.* **2020**, *49*, 16778–16790.

(71) Plyuta, N.; Petrusenko, S.; Kokozay, V. N.; Cauchy, T.; Lloret, F.; Julve, M.; Cano, J.; Avarvari, N. Field-induced mononuclear cobalt(II) single-molecule magnet (SMM) based on a benzothiadiazole-ortho-vanillin ligand. *Dalton Trans.* **2022**, *51*, 4760–4771.

(72) Dos Santos, C. M. G.; Harte, A. J.; Quinn, S. J.; Gunnlaugsson, T. Recent developments in the field of supramolecular lanthanide luminescent sensors and self-assemblies. *Coord. Chem. Rev.* **2008**, *252*, 2512–2527.

(73) Ishikawa, N.; Sugita, M.; Ishikawa, T.; Koshihara, S.-Y.; Kaizu, Y. Lanthanide Double-Decker Complexes Functioning as Magnets at the Single-Molecular Level. *J. Am. Chem. Soc.* **2003**, *125*, 8694–8695.

(74) Zhao, X.; Zhao, T.; Wang, Y.; Zhou, J. Two heterometallic $[Co^{II}{}_6Ln^{III}{}_2]$ (Ln=Dy, Ho) clusters with local symmetry exhibiting single-molecule magnet behaviours. *Appl. Organomet. Chem.* **2023**, *37*, e7104.

(75) Guo, F. S.; Day, B. M.; Chen, Y. C.; Tong, M. L.; Mansikkamaki, A.; Layfield, R. A. A Dysprosium Metallocene Single-Molecule Magnet Functioning at the Axial Limit. *Angew. Chem. Int. Ed. Engl.* **2017**, *56*, 11445–11449.

(76) Buchwalter, P.; Rosé, J.; Braunstein, P. Multimetallic Catalysis Based on Heterometallic Complexes and Clusters. *Chem. Rev.* **2015**, *115*, 28–126.

(77) Mata, J. A.; Hahn, F. E.; Peris, E. Heterometallic complexes, tandem catalysis and catalytic cooperativity. *Chem. Sci.* **2014**, *5*, 1723–1732.

(78) Zhang, S.; Cheng, P. Coordination-Cluster-Based Molecular Magnetic Refrigerants. *Chem. Rec.* **2016**, *16*, 2077–2126.

(79) Van Niekerk, A.; Chellan, P.; Mapolie, S. F. Heterometallic Multinuclear Complexes as Anti-Cancer Agents-An Overview of Recent Developments. *Eur. J. Inorg. Chem.* **2019**, *2019*, 3432–3455.

(80) Osa, S.; Kido, T.; Matsumoto, N.; Re, N.; Pochaba, A.; Mrozinski, J. A Tetranuclear 3d-4f Single Molecule Magnet: $[Cu^{II}LTb^{III}(hfac)_2]_2$. *J. Am. Chem. Soc.* **2004**, *126*, 420–421.

(81) Chakraborty, A.; Goura, J.; Bag, P.; Chandrasekhar, V. Ni^{II}-Ln^{III} Heterometallic Complexes as Single-Molecule Magnets. *Eur. J. Inorg. Chem.* **2019**, *2019*, 1180–1200.

(82) Bao, D.-X.; Xiang, S.; Wang, J.; Li, Y.-C.; Zhao, X.-Q. Review: Single-molecule magnets based on pyridine alcohol ligands. *J. Coord. Chem.* **2016**, *69*, 3131–3147.

(83) Murugesu, M.; Mishra, A.; Wernsdorfer, W.; Abboud, K. A.; Christou, G. Mixed 3d/4d and 3d/4f metal clusters: Tetranuclear $Fe_2^{III}M_2^{III}$ (M^{III}=Ln,Y) and $Mn_2^{IV}M_2^{III}$ (M=Yb,Y) complexes, and the first Fe/4f single-molecule magnets. *Polyhedron* **2006**, *25*, 613–625.

(84) Chakraborty, A.; Goura, J.; Kalita, P.; Swain, A.; Rajaraman, G.; Chandrasekhar, V. Heterometallic 3d–4f single molecule magnets containing diamagnetic metal ions. *Dalton Trans.* **2018**, *47*, 8841–8864.

(85) Andruh, M.; Costes, J.-P.; Diaz, C.; Gao, S. 3d4f Combined Chemistry: Synthetic Strategies and Magnetic Properties. *Inorg. Chem.* **2009**, *48*, 3342–3359.

(86) Shukla, P.; Ezhava, M.; Roy, S.; Mallick, A.; Das, S. In *Tailored Functional Materials*, ed. by Mukherjee, K.; Layek, R. K.; De, D., Springer Nature Singapore, pp 199–208.

(87) Liu, K.; Shi, W.; Cheng, P. Toward heterometallic single-molecule magnets: Synthetic strategy, structures and properties of 3d–4f discrete complexes. *Coord. Chem. Rev.* **2015**, *289-290*, 74–122.

(88) Liu, J.-L.; Wu, J.-Y.; Huang, G.-Z.; Chen, Y.-C.; Jia, J.-H.; Ungur, L.; Chibotaru, L. F.; Chen, X.-M.; Tong, M.-L. Desolvation-Driven 100-Fold Slow-down of Tunneling Relaxation Rate in Co(II)-Dy(III) Single-Molecule Magnets through a Single-Crystal-to-Single-Crystal Process. *Sci. Rep.* **2015**, *5*, 16621–16629.

(89) Pichon, C.; Suaud, N.; Jubault, V.; Duhayon, C.; Guihëry, N.; Sutter, J.-P. Trinuclear Cyanido-Bridged [Cr_2Fe] Complexes: To Be or not to Be a Single-Molecule Magnet, a Matter of Straightness. *Chem. Eur. J.* **2021**, *27*, 15484–15495.

(90) Frisch, H. L.; Wasserman, E. Chemical Topology. *J. Am. Chem. Soc.* **1961**, *83*, 3789–3795.

(91) Beves, J. E.; Blight, B. A.; Campbell, C. J.; Leigh, D. A.; McBurney, R. T. Strategies and Tactics for the Metal-Directed Synthesis of Rotaxanes, Knots, Catenanes, and Higher Order Links. *Angew. Chem. Int. Ed.* **2011**, *50*, 9260–9327.

(92) Greedan, J. E. Geometrically frustrated magnetic materials. *J. Mater. Chem.* **2001**, *11*, 37–53.

(93) Pavlovic, G.; Majer, M.; Cindric, M. A tetranuclear cubane-like nickel(II) complex with a tridentate salicylideneimine Schiff base ligand: Tetrakis[[μ]3-4-methyl-*N*-(2-oxidophenyl)salicylideneiminato]tetrakis[methanolnickel(II)]methanol 0.8-solvate. *Acta Crystallogr. E* **2016**, *72*, 1776–1779.

(94) Richers, C. P.; Bertke, J. A.; Gray, D. L.; Rauchfuss, T. B. Crystal structure of tetrakis-(acetyl-acetonato)di-chloridodi-μ_3-methano-lato-tetra-μ_2-methano-lato-tetra-iron(III). *Acta Crystallogr. E* **2015**, *71*, 976–979.

(95) Glaser, T.; Lugger, T. A new tetranuclear iron complex with a $[Fe_4O_6]_6$ core: Synthesis, structure, spectroscopic and magnetic properties. *Inorg. Chim. Acta* **2002**, *337*, 103–112.

(96) Ako, A. M.; Mereacre, V.; Hewitt, I. J.; Clérac, R.; Lecren, L.; Anson, C. E.; Powell, A. K. Enhancing single molecule magnet parameters: Synthesis, crystal structures and magnetic properties of mixed-valent Mn_4 SMMs. *J. Mater. Chem.* **2006**, *16*, 2579–2586.

(97) Abbas, G.; Ibrahim, M.; Schmidt, S. F. M.; Moreno-Pineda, E.; Anson, C. E.; Powell, A. K. Synthesis of five isostructural tetranuclear Fe_2Ln_2 (Ln=Gd, Tb, Dy, Ho, Er) complexes with an "inverse butterfly" core. *Polyhedron* **2019**, *158*, 255–261.

(98) Baniodeh, A.; Lan, Y.; Novitchi, G.; Mereacre, V.; Sukhanov, A.; Ferbinteanu, M.; Voronkova, V.; Anson, C. E.; Powell, A. K. Magnetic anisotropy and exchange coupling in a family of isostructural $Fe^{III}{}_2Ln^{III}{}_2$ complexes. *Dalton Trans.* **2013**, *42*, 8926–8938.

(99) Peng, G.; Kostakis, G. E.; Lan, Y.; Powell, A. K. Body-wing swapping in butterfly $Fe(III)_2Ln(III)_2$ coordination clusters with triethylene glycol as ligand. *Dalton Trans.* **2013**, *42*, 46–49.

(100) Griffiths, K.; Dokorou, V. N.; Spencer, J.; Abdul-Sada, A.; Vargas, A.; Kostakis, G. E. Isoskeletal Schiff base polynuclear coordination clusters: synthetic and theoretical aspects. *Cryst. Eng. Comm.* **2016**, *18*, 704–713.

(101) Jiang, L.; Zhang, D. Y.; Suo, J. J.; Gu, W.; Tian, J. L.; Liu, X.; Yan, S. P. Synthesis, magnetism and spectral studies of six defective dicubane tetranuclear M_4O_6 (M = Ni(II), Co(II), Zn(II)) and three trinuclear Cd(II) complexes with polydentate Schiff base ligands. *Dalton Trans.* **2016**, *45*, 10233–10248.

(102) Liu, F.; Yang, F.; Chen, H.; Chen, Q.; Yan, P.; Li, G. Salen Type Homo-multinuclear Yb_3 and Yb_4 Complexes and Their NIR Luminescence. *J. Inorg. Organomet. Polym. Mater.* **2014**, *24*, 259–266.

(103) Peng, Y.; Mereacre, V.; Anson, C. E.; Powell, A. K. The role of coordinated solvent on Co(II) ions in tuning the single molecule magnet properties in a CoDy system. *Dalton Trans.* **2017**, *46*, 5337–5343.

(104) Peng, Y.; Powell, A. K. What do 3d-4f butterflies tell us? *Coord. Chem. Rev.* **2021**, *426*, 213490.

(105) Peng, Y.; Singh, M. K.; Mereacre, V.; Anson, C. E.; Rajaraman, G.; Powell, A. K. Mechanism of magnetisation relaxation in $M^{III}{}_2Dy^{III}{}_2$ (M = Cr, Mn, Fe, Al) "Butterfly" complexes: how important are the transition metal ions here? *Chem. Sci.* **2019**, *10*, 5528–5538.

(106) Rinck, J.; Lan, Y.; Anson, C. E.; Powell, A. K. Coordination cluster nuclearity decreases with decreasing rare earth ionic radius in 1:1 Cr/Ln *N*-butyldiethanolamine compounds: A journey across the lanthanide series from $Cr_4(III)La_4Cr_4(III)Tb_4$ via $Cr_3(III)Dy_3$ and $Cr_3(III)Ho_3$ to $Cr_2(III)Er_2Cr_2(III)Lu_2$. *Inorg. Chem.* **2015**, *54*, 3107–3117.

(107) Das, C.; Upadhyay, A.; Shanmugam, M. Influence of Radicals on Magnetization Relaxation Dynamics of Pseudo-Octahedral Lanthanide Iminopyridyl Complexes. *Inorg. Chem.* **2018**, *57*, 9002–9011.

(108) Demir, S.; Zadrozny, J. M.; Nippe, M.; Long, J. R. Exchange Coupling and Magnetic Blocking in Bipyrimidyl Radical-Bridged Dilanthanide Complexes. *J. Am. Chem. Soc.* **2012**, *134*, 18546–18549.

(109) Griffiths, K.; Tsipis, A. C.; Kumar, P.; Townrow, O. P. E.; Abdul-Sada, A.; Akien, G. R.; Baldansuren, A.; Spivey, A. C.; Kostakis, G. E. 3d/4f Coordination Clusters as Cooperative Catalysts for Highly Diastereoselective Michael Addition Reactions. *Inorg. Chem.* **2017**, *56*, 9563–9573.

(110) Griffiths, K.; Kumar, P.; Akien, G. R.; Chilton, N. F.; Abdul-Sada, A.; Tizzard, G. J.; Coles, S. J.; Kostakis, G. E. Tetranuclear Zn/4f coordination clusters as highly efficient catalysts for Friedel–Crafts alkylation. *Chem. Commun.* **2016**, *52*, 7866–7869.

(111) Lan, T.-X.; Gao, W.-S.; Chen, C.-N.; Wang, H.-S.; Wang, M.; Fan, Y.-H. Two tetranuclear 3d–4f heterometal complexes Mn_2Ln_2 (Ln = Dy, Gd): Synthesis, structure, magnetism, and electrocatalytic reactivity for water oxidation. *New J. Chem.* **2018**, *42*, 5798–5805.

(112) Rasmussen, S. C. Transmetalation: a fundamental organometallic reaction critical to synthesis and catalysis. *ChemTexts* **2020**, *7*, 1–8.

(113) Davies, G.; El-Sayed, M. A.; El-Toukhy, A. Transmetallation and its applications. *Chem. Soc. Rev.* **1992**, *21*, 101–104.

(114) Osakada, K. In *Fundamentals of Molecular Catalysis*, Kurosawa, H., Yamamoto, A., Eds.; Elsevier: Amsterdam, Netherlands, 2003.

(115) Liu, C.; Szostak, M. Decarbonylative Sonogashira cross-coupling: a fruitful marriage of alkynes with carboxylic acid electrophiles. *Org. Chem. Front.* **2022**, *9*, 216–222.

(116) Escudero-Adán, E. C.; Benet-Buchholz, J.; Kleij, A. W. Expedient Method for the Transmetalation of Zn(II)-Centered Salphen Complexes. *Inorg. Chem.* **2007**, *46*, 7265–7267.

(117) Kumar, R.; Kaur, R.; Rana, S.; Kataria, R.; Sahoo, S. C. Single-crystal-to-single-crystal mediated metal exchange from Zn(II) to Cu(II) and diverse structures in Zn/Cu coordination polymers using pyridylmethionine ligand. *J. Mol. Struct.* **2021**, *1227*, 129527.

(118) Irving, H.; Williams, R. J. P. The stability of transition-metal complexes. *J. Chem. Soc.* **1953**, 3192–3210.

(119) Costa, J.; Delgado, R. Metal complexes of macrocyclic ligands containing pyridine. *Inorg. Chem.* **1993**, *32*, 5257–5265.

(120) Singh, M.; Sinha, S.; Krishna, V. Computed Distribution of Quaternary Complexes of Cu(II), Zn(II) Co(II) and Ni(II) with Citrulline and Tryphtophan as Primary Ligand and Thymine as Secondary Ligand. *P. Natl. A. Sci. India A* **2021**, *91*, 1–7.

(121) Cieslik, P.; Comba, P.; Dittmar, B.; Ndiaye, D.; Tóth, É.; Velmurugan, G.; Wadepohl, H. Exceptional Manganese(II) Stability and Manganese(II)/Zinc(II) Selectivity with Rigid Polydentate Ligands. *Angew. Chem. Int. Ed.* **2022**, *61*, 1–8.

(122) Ephraim, F. Uber ein neues Reagens zur qualitativen and quantitativen Bestimmung des Kupfers. *Ber. Dtsch. Chem. Ges.* **1930**, *63*, 1928–1930.

(123) Zhu, H. L.; Qu, Y.; You, Z. L.; Tan, M. Y.; Liu, W. S.; Ma, J. L. Crystal structure of trans-diaqua-bis(salicylaldehydato-O,O) chromium(III) chloride, $[Cr(C_7H_5O_2)_2(H_2O)_2]Cl$. *Z. Krist. New Cryst. St.* **2003**, *218*, 519–520.

(124) Li, X.-L.; Tang, J. CCDC 1036017. *CSD Communication* **2016**, DOI: 10.5517/ccdc.csd.cc13s1xv.

(125) Andruh, M. The exceptionally rich coordination chemistry generated by Schiff-base ligands derived from *o*-vanillin. *Dalton Trans.* **2015**, *44*, 16633–16653.

(126) Costes, J.-P.; Dahan, F.; Vendier, L.; Shova, S.; Lorusso, G.; Evangelisti, M. Ni_6^{II}–Ln^{III} complexes with *o*-vanillin as the main ligand: Syntheses, structures, magnetic and magnetocaloric properties. *Dalton Trans.* **2018**, *47*, 1106–1116.

(127) Tang, J.; Hewitt, I. J.; Madhu, N. T.; Chastanet, G.; Wernsdorfer, W.; Anson, C. E.; Benelli, C.; Sessoli, R.; Powell, A. K. Dysprosium Triangles Showing Single-Molecule Magnet Behavior of Thermally Excited Spin States. *Angew. Chem. Int. Ed.* **2006**, *45*, 1729–1733.

(128) Costes, J.-P.; Dahan, F.; Dupuis, A.; Laurent, J.-P. A Genuine Example of a Discrete Bimetallic (Cu, Gd) Complex: Structural Determination and Magnetic Properties. *Inorg. Chem.* **1996**, *35*, 2400–2402.

(129) Enamullah, M.; Chamayou, A.-C.; Banu, K. S.; Kautz, A. C.; Janiak, C. Copper-(II)-salicylaldehydate/-methoxy(pyridine-2-yl)methanolate complexes via in-situ hydrolysis of Schiff bases. *Inorg. Chim. Acta* **2017**, *464*, 186–194.

(130) Forgan, R. S.; Davidson, J. E.; Galbraith, S. G.; Henderson, D. K.; Parsons, S.; Tasker, P. A.; White, F. J. Transport of metal salts by zwitterionic ligands; simple but highly efficient salicylaldoxime extractants. *Chem. Commun.* **2008**, 4049–51.

(131) Bates, G. W.; Davidson, J. E.; Forgan, R. S.; Gale, P. A.; Henderson, D. K.; King, M. G.; Light, M. E.; Moore, S. J.; Tasker, P. A.; Tong, C. C. A dual host approach to $NiSO_4$ extraction. *Supramol. Chem.* **2012**, *24*, 117–126.

(132) Wenzel, M.; Jameson, G. B.; Ferguson, L. A.; Knapp, Q. W.; Forgan, R. S.; White, F. J.; Parsons, S.; Tasker, P. A.; Plieger, P. G. Anion-induced contraction of helical receptors. *Chem. Commun.* **2009**, 3606–3608.

(133) Dong, W.-K.; Zhang, X.-Y.; Sun, Y.-X.; Dong, X.-Y.; Li, G.; Wang, J. A 2D Supramolecular Copper(II) Complex With an Asymmetric Salamo-Type Ligand: Synthesis, Crystal Structure, and Fluorescent Property. *Synth. React. Inorg. Me.* **2015**, *45*, 956–962.

(134) Yang, Y.-H.; Zhang, L.-S.; Zhang, Y.-J.; Zhao, M.-M.; Li, G.; Dong, X.-Y. Synthesis and Crystal Structure of Supramolecular Copper(II) Dimer with Asymmetric Salamo-Type Ligand. *Asian J. Chem.* **2014**, *26*, 1116–1118.

(135) Dong, W.-K.; Li, X.-L.; Wang, L.; Zhang, Y.; Ding, Y.-J. A new application of Salamo-type bisoximes: As a relay–sensor for Zn^{2+}/Cu^{2+} and its novel complexes for successive sensing of H^+/OH^-. *Sensor. Actuat. B Chem.* **2016**, *229*, 370–378.

(136) Dong, W.-K.; Zhang, J.; Zhang, Y.; Li, N. Novel multinuclear transition metal(II) complexes based on an asymmetric Salamo-type ligand: Syntheses, structure characterizations and fluorescent properties. *Inorg. Chim. Acta* **2016**, *444*, 95–102.

(137) Jasim, S. A.; Ansari, M. J.; Majdi, H. S.; Opulencia, M. J. C.; Uktamov, K. F. Nanomagnetic Salamo-based-Pd(0) Complex: an efficient heterogeneous catalyst for Suzuki–Miyaura and Heck cross-coupling reactions in aqueous medium. *J. Mol. Struct.* **2022**, *1261*, 132930.

(138) Bian, R.-N.; Wang, J.-F.; Xu, X.; Dong, X.-Y.; Ding, Y.-J. Investigation of mononuclear, dinuclear, and trinuclear transition metal (II) complexes derived from an asymmetric Salamo-based ligand possessing three different coordination modes. *Appl. Organomet. Chem.* **2021**, *35*, e6040.

(139) Dalal, D. S.; Pawar, N. S.; Mahulikar, P. P. Simple and rapid synthesis of biologically active phthalemide and N-hydroxyphthalimide dimers using polymer-supported anions. *Org. Prep. Proced. Int.* **2007**, *39*, 81–85.

(140) Dong, W.-K.; Ma, J.-C.; Zhu, L.-C.; Zhang, Y. Nine self-assembled nickel(II)–lanthanide(III) heterometallic complexes constructed from a Salamo-type bisoxime and bearing a N- or O-donor auxiliary ligand: syntheses, structures and magnetic properties. *New J. Chem.* **2016**, *40*, 6998–7010.

(141) Li, P.; Li, S.-Z.; Wei, Y.-X.; Dong, W. K. A family of salamo-type trinuclear Co(II) and Ni(II) complexes: Structural characterization, Hirshfeld surface analysis and fluorescent properties. *Polyhedron* **2021**, *204*, 115267.

(142) Yao, M.-X.; Lu, X.-Y.; Zhu, Z.-X.; Deng, X.-W.; Jing, S. Synthesis, structures and magnetism of a series of dinuclear and one-dimensional Ni–Ln complexes: Single-molecule magnetic behavior in one-dimensional nitrate-bridged Dy analogue. *New J. Chem.* **2015**, *39*, 8356–8363.

(143) Lund, H.; Bjerrum, J. Eine einfache Methode zur Darstellung wasser-freier Alkohole. *Ber. Dtsch. Chem. Ges.* **1931**, *64*, 210–213.

(144) Armarego, W. L. F., *Purification of Laboratory Chemicals*, 8th; Butterworth-Heinemann: Waltham, Massachusetts, 2016.

(145) Harris, S. G. Crystallographic and modelling studies of organic ligands on metal surfaces, Thesis, University of Edinburgh, UK, 1999.

(146) Pinsky, M.; Avnir, D. Continuous Symmetry Measures. 5. The Classical Polyhedra. *Inorg. Chem.* **1998**, *37*, 5575–5582.

(147) Casanova, D.; Cirera, J.; Llunell, M.; Alemany, P.; Avnir, D.; Alvarez, S. Minimal Distortion Pathways in Polyhedral Rearrangements. *J. Am. Chem. Soc.* **2004**, *126*, 1755–1763.

(148) Woodhouse, S. S. Salicylaldoxime Derivatives for New Magnetic Materials, Thesis, Massey University, NZ, 2019.

(149) Woodhouse, S. S.; Dais, T. N.; Payne, E. H.; Singh, M. K.; Brechin, E. K.; Plieger, P. G. The structural manipulation of a series of Ni_4 defective dicubanes: Synthesis, X-ray Structures, Magnetic and Computational analyses. *Dalton Trans.* **2021**, *50*, 5318–5326.

(150) Meier, P.; Broghammer, F.; Latendorf, K.; Rauhut, G.; Peters, R. Cooperative Al(Salen)-Pyridinium Catalysts for the Asymmetric Synthesis of trans-Configured β-Lactones by [2+2]-Cyclocondensation of Acylbromides and Aldehydes: Investigation of Pyridinium Substituent Effects. *Molecules* **2012**, *17*, 7121–7150.

(151) Woodhouse, S. S.; Dais, T. N.; Etcheverry-Berríos, A.; Brechin, E. K.; Lane, J. R.; Plieger, P. G. Against the Norm: Non Irving–Williams Transmetalation in Transition Metal Dimers. *Inorg. Chem.* **2022**, *61*, 17819–17827.

(152) Tao, C.-H.; Ma, J.-C.; Zhu, L.-C.; Zhang, Y.; Dong, W.-K. Heterobimetallic 3d–4f Zn(II)–Ln(III) (Ln=Sm, Eu, Tb and Dy) complexes with a N_2O_4 bisoxime chelate ligand and a simple auxiliary ligand Py: Syntheses, structures and luminescence properties. *Polyhedron* **2017**, *128*, 38–45.

(153) Dong, W.-K.; He, X.-N.; Yan, H.-B.; Lv, Z.-W.; Chen, X.; Zhao, C.-Y.; Tang, X.-L. Synthesis, structural characterization and solvent effect of copper(II) complexes with a variational multidentate Salen-type ligand with bisoxime groups. *Polyhedron* **2009**, *28*, 1419–1428.

(154) Covaci, I. C.; Ionita, P.; Caproiu, M. T.; Socoteanu, R.; Constantinescu, T.; Balaban, A. T. 1,3-bis(2,4,6-trinitrophenylaminooxy)propane and its 4-cyano-2,6-dinitrophenyl Congener: Synthesis and Properties. *Central Eur. J. Chem.* **2003**, *1*, 53–64.

(155) Bauer, L.; Suresh, K. S. S[ω-(Aminooxy)alkyl]isothiuronium Salts, ω,ω'-Bis(aminooxy)alkanes and Related Compounds. *J. Org. Chem.* **1962**, *28*, 1604–1608.

(156) Shirayev, A.; Lin, P. K. T.; Moiseev, I. K. Synthesis of Novel Adamantylalkoxyurea Derivatives from 2-(1-Adamantylimino)-1,3-oxathiolane. *Synthesis* **1997**, 38–40.

(157) Ren, Z.-L.; Gao, S.-X.; Zhang, Y.; Wang, L.; Dong, X.-Y. Synthesis and Characterization of Methoxy-Substituted Salamo-Type Bisoximes Based on Bis(aminooxy)alkane and 3-Methoxy-2-hydroxybenzaldehyde. *Asian J. Chem.* **2014**, *26*, 6940–6942.

(158) Steiner, T. The Hydrogen Bond in the Solid State. *Angew. Chem. Int. Ed.* **2002**, *41*, 48–76.

(159) Smith, J. G.; Dibble, P. W.; Sandborn, R. E. The Preparation and Reactions of Naphtho[1,2-c]furan and Naphtho[2,3-c]furan. *J. Org. Chem.* **1986**, *51*, 3762–3768.

(160) Jeong, K.-S.; Hahn, K.-M.; Cho, Y. L. Molecular receptor for binding quaternary ammonium salts and a large anion effect on the complexation. *Tetrahedron Lett.* **1998**, *39*, 3779–3782.

(161) Baker, M. V.; Bosnich, M. J.; Brown, D. H.; Byrne, L. T.; Hesler, V. J.; Skelton, B. W.; White, A. H.; Williams, C. C. Azolium-Linked Cyclophanes: A Comprehensive Examination of Conformations by ^{1}H NMR Spectroscopy and Structural Studies. *J. Org. Chem.* **2004**, *69*, 7640–7652.

(162) Welch, J. T.; Seper, K. W. Synthesis, Regioselective Deprotonation, and Stereoselective Alkylation of Fluoro Ketimines. *J. Org. Chem.* **1988**, *53*, 2991–2999.

(163) Liu, B.; Chen, H.; Li, X.; Zhao, C.; Liu, Y.; Zhu, L.; Deng, H.; Li, J.; Li, G.; Guo, F.; Zhu, X. pH-responsive flower-like micelles constructed via oxime linkage for anticancer drug delivery. *RSC Adv.* **2014**, *4*, 48943–48951.

(164) Pan, Y.-Q.; Zhang, Y.; Yu, M.; Zhang, Y.; Wang, L. Newly synthesized homo-multinuclear Co (II) and Cu (II) bissalamo-like complexes: Structural characterizations, Hirshfeld analyses, fluorescence and antibacterial properties. *Appl. Organomet. Chem.* **2020**, *34*, e5441–5454.

(165) Guo, W.-T.; Dou, L.; Yan, Y.-J.; Li, R.-Y.; Dong, W.-K. A naphthol-functionalized bis(salamo)-like chromogenic and fluorogenic probe for monitoring hydrogen sulfide and application in water samples. *Phosphorus Sulfur* **2022**, 1–10.

(166) Akine, S.; Taniguchi, T.; Nabeshima, T. Acyclic Bis(N_2O_2 chelate) Ligand for Trinuclear d-Block Homo- and Heterometal Complexes. *Inorg. Chem.* **2008**, *47*, 3255–3264.

(167) Kulchat, S.; Chaur, M. N.; Lehn, J.-M. Kinetic Selectivity and Thermodynamic Features of Competitive Imine Formation in Dynamic Covalent Chemistry. *Chem. Eur. J.* **2017**, *23*, 11108–11118.

(168) Nanda, K.; Thompson, L. K.; Bridson, J.; Nag, K. Linear dependence of spin exchange coupling constant on bridge angle in phenoxy-bridged dinickel(II) complexes. *J. Chem. Soc., Chem. Commun.* **1994**, 1337–1338.

(169) Mandal, S.; Majumder, S.; Mohanta, S. Syntheses, Crystal Structures and Experimental/Theoretical Magnetic Properties of Two Butterfly $Ni^{II}_2Y^{III}_2$ Compounds. *ChemistrySelect* **2019**, *4*, 8074–8081.

(170) Palacios, M. A.; Mota, A. J.; Perea-Buceta, J. E.; White, F. J.; Brechin, E. K.; Colacio, E. Antiferromagnetic versus ferromagnetic exchange interactions in bis(μ-O(oximate))dinickel(II) units for a series of closely related cube shaped carboxamideoximate-bridged Ni(4) complexes. A combined experimental and theoretical magneto-structural study. *Inorg. Chem.* **2010**, *49*, 10156–10165.

(171) Alvarez, S.; Avnir, D.; Llunell, M.; Pinsky, M. Continuous symmetry maps and shape classification. The case of six-coordinated metal compounds. *New J. Chem.* **2002**, *26*, 996–1009.

(172) Chilton, N. F.; Anderson, R. P.; Turner, L. D.; Soncini, A.; Murray, K. S. PHI: A powerful new program for the analysis of anisotropic monomeric and exchange-coupled polynuclear *d*- and *f*-block complexes. *J. Comput. Chem.* **2013**, *34*, 1164–1175.

(173) Rogez, G.; Rebilly, J. N.; Barra, A. L.; Sorace, L.; Blondin, G.; Kirchner, N.; Duran, M.; van Slageren, J.; Parsons, S.; Ricard, L.; Marvilliers, A.; Mallah, T. Very Large Ising-Type Magnetic Anisotropy in a Mononuclear Ni^{II} Complex. *Angew. Chem.* **2005**, *117*, 1910–1913.

(174) Titiš, J.; Boča, R. Magnetostructural D Correlation in Nickel(II) Complexes: Reinvestigation of the Zero-Field Splitting. *Inorg. Chem.* **2010**, *49*, 3971–3973.

(175) Singh, S. K.; Gupta, T.; Badkur, P.; Rajaraman, G. Magnetic Anisotropy of Mononuclear Ni^{II} Complexes: On the Importance of Structural Diversity and the Structural Distortions. *Chem. Eur. J.* **2014**, *20*, 10305–10313.

(176) Titiš, J.; Boča, R.; Dlháň, Ľ.; Ďurčeková, T.; Fuess, H.; Ivaniková, R.; Mrázová, V.; Papánková, B.; Svoboda, I. Magnetostructural correlations in heteroleptic nickel(II) complexes. *Polyhedron* **2007**, *26*, 1523–1530.

(177) Ballester, L.; Coronado, E.; Gutierrez, A.; Monge, A.; Perpinan, M. F.; Pinilla, E.; Rico, T. Studies on the reactivity of S,N-derivatives of nickel with N-donor bases. Crystal structure and magnetic properties of the cubane cluster tetrakis(μ-hydroxo)tetrakis(μ-1,3-thiazolidine-2-thionato)tetrakis(pyridine)tetranickel(II)-dipyridine. *Inorg. Chem.* **1992**, *31*, 2053–2056.

(178) Halcrow, M. A.; Sun, J.-S.; Huffman, J. C.; Christou, G. Structural and Magnetic Properties of $[Ni_4(\mu_3\text{-}OMe)_4(dbm)_4(MeOH)_4]$ and $[Ni_4(\eta_1, \mu_3\text{-}N_3)_4(dbm)_4(EtOH)_4]$ Magnetostructural Correlations for $[Ni_4X_4]^{4+}$ Cubane Complexes. *Inorg. Chem.* **1995**, *34*, 4167–4177.

(179) Serna, Z. E.; Barandika, M. G.; Cortés, R.; Urtiaga, M. K.; Barberis, G. E.; Rojo, T. Structural analysis and magnetic properties of the dicubane-like tetramer $[Ni(dpk{\cdot}OH)(N_3)]_4{\cdot}2H_2O$ (dpk = di-2-pyridyl ketone). *J. Chem. Soc., Dalton Trans.* **2000**, 29–34.

(180) Yang, P.-P.; Shao, C.-Y.; Xu, Y.; Zhu, L.-L. A Tetranuclear Defective Dicubane-like Nickel Complex: Synthesis, Crystal Structure, and Magnetic Properties. *Z. Anorg. Allg. Chem.* **2013**, *639*, 548–551.

(181) Modak, R.; Sikdar, Y.; Mandal, S.; Gómez-García, C. J.; Benmansour, S.; Chatterjee, S.; Goswami, S. Homo and heterometallic rhomb-like Ni_4 and Mn_2Ni_2 complexes. *Polyhedron* **2014**, *70*, 155–163.

(182) Das, D.; Mahata, G.; Adhikary, A.; Konar, S.; Biradha, K. Structural Adaptation of Ni_4O_4 Units To Form Cubane, Open Dicubane, Dimeric Cubane, and One-Dimensional Polymeric Cubanes: Magnetostructural Correlation of Ni_4 Clusters. *Cryst. Growth Des.* **2015**, *15*, 4132–4141.

(183) Singh, M. K.; Rajaraman, G. Theoretical Studies on Hexanuclear $[M_3(\mu_3\text{-O/OH})]_2$ (M = Fe(III), Mn(III), and Ni(II)) Clusters: Magnetic Exchange, Magnetic Anisotropy, and Magneto-Structural Correlations. *Inorg. Chem.* **2019**, *58*, 3175–3188.

(184) Atakol, O.; Boa, R.; Ercan, I.; Ercan, F.; Fuess, H.; Haase, W.; Herchel, R. Magnetic properties of trinuclear Ni–M–Ni complexes, M=Mn, Co and Ni. *Chem. Phys. Lett.* **2006**, *423*, 192–196.

(185) Sharma, A. K.; Lloret, F.; Mukherjee, R. Phenolate- and Acetate (Both μ_2-1,1 and μ_2-1,3 Mode)-Bridged Face-Shared Trioctahedral Linear $Ni^{II}{}_3$, $Ni^{II}{}_2M^{II}$ (M = Mn, Co) Complexes: Ferro- and Antiferromagnetic Coupling. *Inorg. Chem.* **2007**, *46*, 5128–5130.

(186) Serna, Z.; De la Pinta, N.; Urtiaga, M. K.; Lezama, L.; Madariaga, G.; Clemente-Juan, J. M.; Coronado, E.; Cortés, R. Defective Dicubane-like Tetranuclear Nickel(II) Cyanate and Azide Nanoscale Magnets. *Inorg. Chem.* **2010**, *49*, 11541–11549.

(187) Mahapatra, P.; Drew, M. G. B.; Ghosh, A. Ni(II) Complex of N_2O_3 Donor Unsymmetrical Ligand and Its Use for the Synthesis of Ni^{II}–Mn^{II} Complexes of Diverse Nuclearity: Structures, Magnetic Properties, and Catalytic Oxidase Activities. *Inorg. Chem.* **2018**, *57*, 8338–8353.

(188) Maity, S.; Mahapatra, P.; Ghosh, T. K.; Gomila, R. M.; Frontera, A.; Ghosh, A. Synthesis of Ni(II)–Mn(II) complexes using a new mononuclear Ni(II) complex of an unsymmetrical N_2O_3 donor ligand: structures, magnetic properties and catalytic oxidase activity. *Dalton Trans.* **2021**, *50*, 4686–4699.

(189) Zenno, H.; Kobayashi, F.; Nakamura, M.; Sekine, Y.; Lindoy, L. F.; Hayami, S. Hydrogen bond-induced abrupt spin crossover behaviour in 1-D cobalt(II) complexes – the key role of solvate water molecules. *Dalton Trans.* **2021**, *50*, 7843–7853.

(190) Ge, J.-Y.; Cui, L.; Li, J.; Yu, F.; Song, Y.; Zhang, Y.-Q.; Zuo, J.-L.; Kurmoo, M. Modulating Single-Molecule Magnetic Behavior of a Dinuclear Erbium(III) Complex by Solvent Exchange. *Inorg. Chem.* **2017**, *56*, 336–343.

(191) Frisch, M. J. et al. Gaussian 16 Revision C.01, Computer Program, Gaussian Inc. Wallingford CT, 2016.

(192) Noodleman, L.; Norman Jr., J. G. The $\chi\alpha$ valence bond theory of weak electronic coupling. Application to the low-lying states of $Mo_2Cl_{84}{}^-$. *J. Chem. Phys.* **1979**, *70*, 4903–4906.

(193) Noodleman, L.; Davidson, E. R. Ligand spin polarization and antiferromagnetic coupling in transition metal dimers. *Chem. Phys.* **1986**, *109*, 131–143.

(194) Noodleman, L.; Case, D. A. In *Advances in Inorganic Chemistry*, Cammack, R., Ed.; Academic Press: Cambridge, Massachusetts, 1992, pp 423–470.

(195) Lee, C.; Yang, W.; Parr, R. G. Development of the Colle-Salvetti correlation-energy formula into a functional of the electron density. *Phys. Rev. B* **1988**, *37*, 785–789.

(196) Becke, A. D. A new mixing of Hartree–Fock and local density-functional theories. *J. Chem. Phys.* **1993**, *98*, 1372–1377.

(197) Stephens, P. J.; Devlin, F. J.; Chabalowski, C. F.; Frisch, M. J. Ab Initio Calculation of Vibrational Absorption and Circular Dichroism Spectra Using Density Functional Force Fields. *J. Phys. Chem.* **1994**, *98*, 11623–11627.

(198) Schäfer, A.; Horn, H.; Ahlrichs, R. Fully optimized contracted Gaussian basis sets for atoms Li to Kr. *J. Chem. Phys.* **1992**, *97*, 2571–2577.

(199) Schäfer, A.; Huber, C.; Ahlrichs, R. Fully optimized contracted Gaussian basis sets of triple zeta valence quality for atoms Li to Kr. *J. Chem. Phys.* **1994**, *100*, 5829–5835.

(200) Scuseria, G. E.; Schaefer III, H. F. Is coupled cluster singles and doubles (CCSD) more computationally intensive than quadratic configuration interaction (QCISD)? *J. Chem. Phys.* **1989**, *90*, 3700–3703.

(201) Hariharan, P. C.; Pople, J. A. The influence of polarization functions on molecular orbital hydrogenation energies. *Theoret. chim. acta* **1973**, *28*, 213–222.

(202) Van Vleck, J. H., *The theory of electric and magnetic susceptibilies*; Oxford University Press: Oxford, United Kingdom, 1930.

(203) Borrás-Almenar, J. J.; Clemente-Juan, J. M.; Coronado, E.; Tsukerblat, B. S. MAGPACK1 A package to calculate the energy levels, bulk magnetic properties, and inelastic neutron scattering spectra of high nuclearity spin clusters. *J. Comput. Chem.* **2001**, *22*, 985–991.

(204) Hazra, S.; Bhattacharya, S.; Singh, M. K.; Carrella, L.; Rentschler, E.; Weyhermueller, T.; Rajaraman, G.; Mohanta, S. Syntheses, Structures, Magnetic Properties, and Density Functional Theory Magneto-Structural Correlations of Bis(μ-phenoxo) and Bis(μ-phenoxo)-μ-acetate/Bis(μ-phenoxo)-bis(μ-acetate) Dinuclear $Fe^{III}Ni^{II}$ Compounds. *Inorg. Chem.* **2013**, *52*, 12881–12892.

(205) Singh, M. K.; Rajaraman, G. Can CH$\cdots\pi$ Interactions Be Used To Design Single-Chain Magnets? *Chem. Eur. J.* **2015**, *21*, 980–983.

(206) Cano, J.; Ruiz, E.; Alvarez, S.; Verdaguer, M. Spin Density Distribution in Transition Metal Complexes: Some Thoughts and Hints. *Comment. Inorg. Chem.* **1998**, *20*, 27–56.

(207) Oyarzabal, I.; Ruiz, J.; Mota, A. J.; Rodríguez-Diéguez, A.; Seco, J. M.; Colacio, E. An experimental and theoretical magnetostructural study of polynuclear Ni^{II} complexes assembled from a versatile bis(salicylaldehyde)-diamine polytopic ligand. *Dalton Trans.* **2015**, *44*, 6825–6838.

(208) Dolomanov, O. V.; Bourhis, L. J.; Gildea, R. J.; Howard, J. A. K.; Puschmann, H. OLEX2: A complete structure solution, refinement and analysis program. *J. Appl. Cryst.* **2009**, *42*, 339–341.

(209) Yang, L.; Powell, D. R.; Houser, R. P. Structural variation in copper(I) complexes with pyridylmethylamide ligands: structural analysis with a new four-coordinate geometry index, τ_4. *Dalton Trans.* **2007**, 955–964.

(210) Casanova, D.; Alemany, P.; Bofill, J. M.; Alvarez, S. Shape and Symmetry of Heptacoordinate Transition-Metal Complexes: Structural Trends. *Chem. Eur. J.* **2003**, *9*, 1281–1295.

(211) McLellan, R.; Palacios, M. A.; Sanz, S.; Brechin, E. K.; Dalgarno, S. J. Importance of Steric Influences in the Construction of Multicomponent Hybrid Polymetallic Clusters. *Inorg. Chem.* **2017**, *56*, 10044–10053.

(212) Costes, J.-P.; Garcia-Tojal, J.; Tuchagues, J.-P.; Vendier, L. Structural and Magnetic Study of a Trinuclear Mn^{II}–Gd^{III}–Mn^{II} Complex. *Eur. J. Inorg. Chem.* **2009**, *2009*, 3801–3806.

(213) Branzea, D. G.; Madalan, A. M.; Ciattini, S.; Avarvari, N.; Caneschi, A.; Andruh, M. New heterometallic coordination polymers constructed from 3d–3d' binuclear nodes. *New J. Chem.* **2010**, *34*, 2479–2490.

(214) Wong, W.-K.; Liang, H.; Wong, W.-Y.; Cai, Z.; Li, K.-F.; Cheah, K.-W. Synthesis and near-infrared luminescence of 3d-4f bi-metallic Schiff base complexes. *New J. Chem.* **2002**, *26*, 275–278.

(215) Pu, L.-M.; An, X.-X.; Liu, C.; Long, H.-T.; Zhao, L. Insights into crystal structures, supramolecular architectures and antioxidant activities of self-assembled fluorescent hetero-multinuclear [Cu(II)-Ln(III)] (Ln = La, Ce, Pr and Nd) salamo-like complexes. *Appl. Organomet. Chem.* **2020**, *34*, e5980–5998.

(216) Dong, Y.-J.; Ma, J.-C.; Zhu, L.-C.; Dong, W.-K.; Zhang, Y. Four 3d–4f hetero-multinuclear zinc(II)–lanthanide(III) complexes constructed from a distinct hexadentate N_2O_2-type ligand: syntheses, structures and luminescence properties. *J. Coord. Chem.* **2017**, *70*, 103–115.

(217) Song, X.-Q.; Cheng, G.-Q.; Wang, X.-R.; Xu, W.-Y.; Liu, P.-P. Structure-based description of a step-by-step synthesis of heterodinuclear $Zn^{II}Ln^{III}$ complexes and their luminescence properties. *Inorg. Chim. Acta* **2015**, *425*, 145–153.

(218) Song, X.-Q.; Wang, L.; Zheng, Q.-F.; Liu, W.-S. Synthesis, crystal structure and luminescence properties of lanthanide complexes with a new semirigid bridging furfurylsalicylamide ligand. *Inorg. Chim. Acta* **2012**, *391*, 171–178.

(219) Crawford, V. H.; Richardson, H. W.; Wasson, J. R.; Hodgson, D. J.; Hatfield, W. E. Relationship Between the Singlet-Triplet Splitting and the Cu-O-Cu Bridge Angle in Hydroxo-Bridged Copper Dimers. *Inorg. Chem.* **1976**, *15*, 2107–2110.

(220) Thompson, L. K.; Mandal, S. K.; Tandon, S. S.; Bridson, J. N.; Park, M. K. Magnetostructural Correlations in Bis(μ_2-phenoxide)-Bridged Macrocyclic Dinuclear Copper(II) Complexes. Influence of Electron-Withdrawing Substituents on Exchange Coupling. *Inorg. Chem.* **1996**, *35*, 3117–3125.

(221) Black, D.; Blake, A. J.; Dancey, K. P.; Harrison, A.; McPartlin, M.; Parsons, S.; Tasker, P. A.; Whittaker, G.; Schröder, M. Synthesis, structures and magnetochemistry of binuclear cobalt(II), nickel(II) and copper(II) complexes of 2,6-diformyl-4-methylphenol dioxime. *J. Chem. Soc., Dalton Trans.* **1998**, 3953–3960.

(222) Venegas-Yazigi, D.; Aravena, D.; Spodine, E.; Ruiz, E.; Alvarez, S. Structural and electronic effects on the exchange interactions in dinuclear bis(phenoxo)-bridged copper(II) complexes. *Coord. Chem. Rev.* **2010**, *254*, 2086–2095.

(223) Mondal, D.; Majee, M. C.; Bhattacharya, K.; Long, J.; Larionova, J.; Khusniyarov, M. M.; Chaudhury, M. Crossover from Antiferromagnetic to Ferromagnetic Exchange Coupling in a New Family of Bis-(μ-phenoxido)dicopper(II) Complexes: A Comprehensive Magneto–Structural Correlation by Experimental and Theoretical Study. *ACS Omega* **2019**, *4*, 10558–10570.

(224) Costes, J.-P.; Duhayon, C.; Vendier, L.; Mota, A. J. Reactions of a series of ZnL, CuL and NiL Schiff base and non-Schiff base complexes with MCl_2 salts (M = Cu, Ni, Mn): Syntheses, structures, magnetic properties and DFT calculations. *New J. Chem.* **2018**, *42*, 3683–3691.

(225) O'Connor, C. J.; Freyberg, D. P.; Sinn, E. Relation between structure and magnetic exchange interactions in bis(hexafluoroacetylacetonato)*N*,*N*′-ethylenebis-[2-hydroxypropiophenone iminato-*N*,*O*]copper(II)M′(II), Cu((prp)$_2$en)M, where M′ = Cu, Ni, and Mn. Crystal structures of the complexes (M((prp)$_2$en)M, where M = Cu and Ni and M′ = Cu, Co, and Mn. *Inorg. Chem.* **1979**, *18*, 1077–1088.

(226) Lucas, C. R.; Byrne, J. M. D.; Collins, J. L.; Dawe, L. N.; Miller, D. O. Copper(II) complexes of open-chain thioether ligands terminated by salicylaldimine functionality. *Can. J. Chem.* **2011**, *89*, 1190–1201.

(227) Maity, D.; Drew, M. G. B.; Godsell, J. F.; Roy, S.; Mukhopadhyay, G. Synthesis and characterization of Cu(II) complexes of tetradentate and tridentate symmetrical Schiff base ligands involving *o*-phenelenediamine, salicylaldehyde and diacetylmonoxime. *Transition Met. Chem.* **2010**, *35*, 197–204.

(228) Ruiz, E.; Alemany, P.; Alvarez, S.; Cano, J. Structural Modelling and Magneto-Structural Correlations for Hydroxo-Bridged Copper(II) Binuclear Complexes. *Inorg. Chem.* **1997**, *36*, 3683–3688.

(229) Sutter, J.-P.; Béreau, V.; Jubault, V.; Bretosh, K.; Pichon, C.; Duhayon, C. Magnetic anisotropy of transition metal and lanthanide ions in pentagonal bipyramidal geometry. *Chem. Soc. Rev.* **2022**, *51*, 3280–3313.

(230) Dutta, S.; Mayans, J.; Ghosh, A. Facile synthesis of a new Cu(II) complex with an unsymmetrical ligand and its use as an O_3 donor metalloligand in the synthesis of Cu(II)–Mn(II) complexes: structures, magnetic properties, and catalytic oxidase activities. *Dalton Trans.* **2020**, *49*, 1276–1291.

(231) Luo, S.; Sun, X.; Zeng, B.; Zheng, P. From antiferromagnetic to ferromagnetic exchange in a family of phenoxido-bridged heterodinuclear Cu(II)-Mn(II) complexes: A magneto-structural theoretical study. *Polyhedron* **2021**, *194*, 114955.

(232) Birkelbach, F.; Winter, M.; Floerke, U.; Haupt, H.-J.; Butzlaff, C.; Lengen, M.; Bill, E.; Trautwein, A. X.; Wieghardt, K.; Chaudhuri, P. Exchange Coupling in Homo- and Heterodinuclear Complexes $Cu^{II}M$ [M = Cr(III), Mn(III), Mn(II), Fe(III), Co(III), Co(II), Ni(II), Cu(II), Zn(II)]. Synthesis, Structures, and Spectroscopic Properties. *Inorg. Chem.* **1994**, *33*, 3990–4001.

(233) Golombek, A. P.; Hendrich, M. P. Quantitative analysis of dinuclear manganese(II) EPR spectra. *J. Magn. Reson.* **2003**, *165*, 33–48.

(234) Gultneh, Y.; Tesema, Y. T.; Yisgedu, T. B.; Butcher, R. J.; Wang, G.; Yee, G. T. Studies of a Dinuclear Manganese Complex with Phenoxo and Bis-acetato Bridging in the Mn_2(II,II) and Mn_2(II,III) States: Coordination Structural Shifts and Oxidation State Control in Bridged Dinuclear Complexes. *Inorg. Chem.* **2006**, *45*, 3023–3033.

(235) Arora, H.; Barman, S. K.; Lloret, F.; Mukherjee, R. Isostructural Dinuclear Phenoxo-/Acetato-Bridged Manganese(II), Cobalt(II), and Zinc(II) Complexes with Labile Sites: Kinetics of Transesterification of 2-Hydroxypropyl-*p*-nitrophenylphosphate. *Inorg. Chem.* **2012**, *51*, 5539–5553.

(236) Comba, P.; Rajaraman, G.; Sarkar, A.; Velmurugan, G. What controls the magnetic anisotropy in heptacoordinate high-spin cobalt(II) complexes? A theoretical perspective. *Dalton Trans.* **2022**, *51*, 5175–5183.

(237) Dais, T. N.; Takano, R.; Ishida, T.; Plieger, P. G. Lanthanide induced variability in localised Co^{II} geometries of four triangular $L_3Co_3{}^{II}Ln^{III}$ complexes. *RSC Adv.* **2022**, *12*, 4828–4835.

(238) Seth, P.; Figuerola, A.; Jover, J.; Ruiz, E.; Ghosh, A. Ferro- to Antiferromagnetic Crossover Angle in Diphenoxido- and Carboxylato-Bridged Trinuclear $Ni^{II}{}_2$–Mn^{II} Complexes: Experimental Observations and Theoretical Rationalization. *Inorg. Chem.* **2014**, *53*, 9296–9305.

(239) Bain, G. A.; Berry, J. F. Diamagnetic Corrections and Pascal's Constants. *J. Chem. Ed.* **2008**, *85*, 532.

(240) Malik, W. U.; Deo Sharma, K.; Sharma, R. D.; S., U. J. Complexes of Co(II), Cu(II), Cd(II) & Hg(II) with 2-Amino-4-methyl-benzothiazoles. *Indian J. Chem.* **1976**, *15A*, 152–153.

(241) Joshi, S. R.; Habib, S. I. Synthesis, Spectral study of Ni(II) and Cu(II) metal ions with Heterocyclic Ligands. *Int. J. Drug Dev. Res.* **2014**, *6*, 32–38.

(242) Enamullah, M.; Al-moktadir Zaman, M.; Bindu, M. M.; Woschko, D.; Islam, M. K.; Janiak, C. Pseudotetrahedral high-spin manganese(II)-complexes with (*S* or *R*)-*N*-1-(Ar)ethyl-salicylaldimine: Chiroptical property, chirality induction at-metal, paramagnetism, redox-potential, PXRD structures and DFT/T-DDFT. *J. Mol. Struct.* **2021**, *1239*, 130455.

(243) El-Sonbati, A. Z.; El-Mogazy, M. A.; Nozha, S. G.; Diab, M. A.; Abou-Dobara, M. I.; Eldesoky, A. M.; Morgan, S. M. Mixed ligand transition metal(II) complexes: Characterization, spectral, electrochemical studies, molecular docking and bacteriological application. *J. Mol. Struct.* **2022**, *1248*, 131498.

(244) Neese, F. The ORCA program package. *Wiley Interdiscip. Rev.-Comput. Mol. Sci* **2012**, *2*, 73–78.

(245) Neese, F.; Wennmohs, F.; Becker, U.; Riplinger, C. The ORCA quantum chemistry program package. *J. Chem. Phys.* **2020**, *152*, 224108–224126.

(246) Perdew, J. P.; Burke, K.; Ernzerhof, M. Generalized Gradient Approximation Made Simple. *Phys. Rev. Lett.* **1996**, *77*, 3865–3868.

(247) Perdew, J. P. Density-functional approximation for the correlation energy of the inhomogeneous electron gas. *Phys. Rev. B* **1986**, *33*, 8822–8824.

(248) Perdew, J. P. Erratum: Density-functional approximation for the correlation energy of the inhomogeneous electron gas. *Phys. Rev. B* **1986**, *34*, 7406–7406.

(249) Becke, A. D. Density-functional exchange-energy approximation with correct asymptotic behavior. *Phys. Rev. A* **1988**, *38*, 3098–3100.

(250) Staroverov, V. N.; Scuseria, G. E.; Tao, J.; Perdew, J. P. Deviations of calculated properties from experiment for species of the G3/99, T-96R, and T-82F test sets. Properties of hydrogen-bonded complexes. *J. Chem. Phys.* **2003**, *119*, 12129–12137.

(251) Wang, Y.; Verma, P.; Jin, X.; Truhlar, D. G.; He, X. Revised M06 density functional for main-group and transition-metal chemistry. *P. Natl. Acad. Sci.* **2018**, *115*, 10257–10262.

(252) Ehrlich, S.; Moellmann, J.; Reckien, W.; Bredow, T.; Grimme, S. System-Dependent Dispersion Coefficients for the DFT-D3 Treatment of Adsorption Processes on Ionic Surfaces. *ChemPhysChem* **2011**, *12*, 3414–3420.

(253) Grimme, S.; Ehrlich, S.; Goerigk, L. Effect of the damping function in dispersion corrected density functional theory. *J. Comput. Chem.* **2011**, *32*, 1456–1465.

(254) Weigend, F.; Ahlrichs, R. Balanced basis sets of split valence, triple zeta valence and quadruple zeta valence quality for H to Rn: Design and assessment of accuracy. *Phys. Chem. Chem. Phys.* **2005**, *7*, 3297–3305.

(255) Weigend, F. Accurate Coulomb-fitting basis sets for H to Rn. *Phys. Chem. Chem. Phys.* **2006**, *8*, 1057–1065.

(256) Barone, V.; Cossi, M. Quantum Calculation of Molecular Energies and Energy Gradients in Solution by a Conductor Solvent Model. *J. Phys. Chem. A* **1998**, *102*, 1995–2001.

(257) Stevens, J. R.; Plieger, P. G. Anion-driven conformation control and enhanced sulfate binding utilising aryl linked salicylaldoxime dicopper helicates. *Dalton Trans.* **2011**, *40*, 12235–12241.

(258) Wenzel, M.; Bruere, S. R.; Knapp, Q. W.; Tasker, P. A.; Plieger, P. G. Zwitterionic dicopper helicates: Anion encapsulation and binding studies. *Dalton Trans.* **2010**, *39*, 2936–2941.

(259) Wenzel, M.; Knapp, Q. W.; Plieger, P. G. A bis-salicylaldoximato-copper(II) receptor for selective sulfate uptake. *Chem. Commun.* **2011**, *47*, 499–501.

(260) Yamaguchi, K.; Takahara, Y.; Fueno, T. In *Applied Quantum Chemistry*, ed. by Smith, V. H.; Schaefer, H. F.; Morokuma, K., Springer: Dordrecht, Netherlands, pp 155–184.

(261) Sun, Y.-X.; Gao, X.-H. Synthesis, Characterization, and Crystal Structure of a New Cu^{II} Complex with Salen-Type Ligand. *Synth. React. Inorg. Me.* **2011**, *41*, 973–978.

(262) Pu, L.-M.; Akogun, S. F.; Li, X.-L.; Long, H.-T.; Dong, W.-K.; Zhang, Y. A Salamo-type fluorescent sensor for selective detection of Zn^{2+}/Cu^{2+} and its novel Cd^{2+} complex with triangular prism geometry. *Polyhedron* **2017**, *134*, 356–364.

(263) Dong, Y.-J.; Li, X.-L.; Zhang, Y.; Dong, W.-K. A highly selective visual and fluorescent sensor for Pb^{2+} and Zn^{2+} and crystal structure of Cu^{2+} complex based-on a novel single-armed Salamo-type bisoxime. *Supramol. Chem.* **2017**, *29*, 518–527.

(264) Akine, S.; Taniguchi, T.; Nabeshima, T. Helical Metallohost-Guest Complexes via Site-Selective Transmetalation of Homotrinuclear Complexes. *J. Am. Chem. Soc.* **2006**, *128*, 15765–15774.

(265) Ren, Z.-L.; Li, X.-Y.; Hao, J.; Zhang, Y.; Dong, W.-K. Syntheses, structural characterizations, and electrochemical and fluorescent properties of homo- and hetero-polynuclear transition metal(II) complexes. *Appl. Organomet. Chem.* **2018**, *32*, e4614.

(266) Branzea, D. G.; Guerri, A.; Fabelo, O.; Ruiz-Pérez, C.; Chamoreau, L.-M.; Sangregorio, C.; Caneschi, A.; Andruh, M. Heterobinuclear Complexes as Tectons in Designing Coordination Polymers. *Cryst. Growth Des.* **2008**, *8*, 941–949.

(267) Cirera, J.; Alemany, P.; Alvarez, S. Mapping the Stereochemistry and Symmetry of Tetracoordinate Transition-Metal Complexes. *Chem. Eur. J.* **2004**, *10*, 190–207.

(268) Ruiz-Martínez, A.; Alvarez, S. Stereochemistry of Compounds with Coordination Number Ten. *Chem. Eur. J.* **2009**, *15*, 7470–7480.

(269) Hartshorn, R. M.; Hey-Hawkins, E.; Kalio, R.; Leigh, G. J. Representation of configuration in coordination polyhedra and the extension of current methodology to coordination numbers greater than six. *Pure Appl. Chem.* **2007**, *79*, 1779–1799.

(270) Ruiz-Martínez, A.; Casanova, D.; Alvarez, S. Polyhedral Structures with an Odd Number of Vertices: Nine-Coordinate Metal Compounds. *Chem. Eur. J.* **2008**, *14*, 1291–1303.

(271) Mattei, C. A.; Lefeuvre, B.; Dorcet, V.; Argouarch, G.; Cador, O.; Lalli, C.; Pointillart, F. Counterintuitive Single-Molecule Magnet Behaviour in Two Polymorphs of One-Dimensional Compounds Involving Chiral BINOL-Derived Bisphosphate Ligands. *Magnetochemistry* **2021**, *7*.

(272) Schnitzer, T.; Preuss, M. D.; van Basten, J.; Schoenmakers, S. M. C.; Spiering, A. J. H.; Vantomme, G.; Meijer, E. W. How Subtle Changes Can Make a Difference: Reproducibility in Complex Supramolecular Systems. *Angew. Chem. Int. Ed.* **2022**, e202206738.

(273) Spek, A. PLATON SQUEEZE: A tool for the calculation of the disordered solvent contribution to the calculated structure factors. *Acta Crystallogr. C.* **2015**, *71*, 9–18.

(274) Echeverría, J.; Casanova, D.; Llunell, M.; Alemany, P.; Alvarez, S. Molecules and crystals with both icosahedral and cubic symmetry. *Chem. Commun.* **2008**, 2717–2725.

(275) Alvarez, S. How icosahedral are icosahedral clusters? *Inorg. Chim. Acta* **2010**, *363*, 4392–4398.

(276) Lopez-Dellamary, T.; Sampedro, J. A.; Carlos, G.; Fontes, M.; Ogura, T. Copper(I) nitrile complexes, part IV. Mechanism of copper(II) acetate and trifluoroacetate reduction by copper in acetonitrile in the presence of free carboxylic acid. *Transit. Metal Chem.* **1978**, *3*, 342–344.

(277) Moreno Pineda, E.; Heesing, C.; Tuna, F.; Zheng, Y.-Z.; McInnes, E. J. L.; Schnack, J.; Winpenny, R. E. P. Copper Lanthanide Phosphonate Cages: Highly Symmetric $[Cu_3Ln_9P_6]$ and $[Cu_6Ln_6P_6]$ Clusters with C_3v and D_3h Symmetry. *Inorg. Chem.* **2015**, *54*, 6331–6337.

(278) Tahli, A.; Elshaarawy, R. F. M.; Köc, Ü.; Kautz, A. C.; Janiak, C. A HKUST-1 MOF inclusion compound with in-situ reduced copper(I) as $[Cu(NCCH_3)_4]^+$ cation complex in the octahedral A-type pore. *Polyhedron* **2016**, *117*, 579–584.

(279) Fielden, J.; Quasdorf, K.; Cronin, L.; Kögerler, P. A fluorophosphate-based inverse Keggin structure. *Dalton Trans.* **2012**, *41*, 9876–9878.

(280) Dais, T. N.; Takano, R.; Ishida, T.; Plieger, P. G. Self-assembly of non-macrocyclic triangular Ni_3Ln clusters. *Dalton Trans.* **2022**, *51*, 1446–1453.

(281) Alvarez, S.; Llunell, M. Continuous symmetry measures of penta-coordinate molecules: Berry and non-Berry distortions of the trigonal bipyramid. *J. Chem. Soc., Dalton Trans.* **2000**, 3288–3303.

(282) Guo, S.-Z.; Wang, J.-F.; Feng, S.-S.; Zhao, L. Co(II) and Ni(II) bis(salamo)-based tetraoxime complexes: Syntheses, structural characterizations, fluorescence properties, and Hirshfeld analyses. *J. Coord. Chem.* **2021**, *74*, 1181–1195.

(283) Casanova, D.; Llunell, M.; Alemany, P.; Alvarez, S. The Rich Stereochemistry of Eight-Vertex Polyhedra: A Continuous Shape Measures Study. *Chem. Eur. J.* **2005**, *11*, 1479–1494.

(284) Al Damen, M. A.; Haddad, S. F. The nonclassical noncovalent interactions control: A case study of the crystal structure of 3,5-dibromo-2-amino-4,6-dimethylpyridinium tetrahalocuprate [3,5-DBr-2-A-4,6-DMPH]$_2$CuX$_4$ (X = Cl, and Br). *J. Mol. Struct.* **2011**, *985*, 27–33.

(285) Bhattacharya, R.; Chanda, S.; Bocelli, G.; Cantoni, A.; Ghosh, A. Synthesis and crystal structure of bis(2-methylbenzimidazolium) tetrahalocuprate(II). *J. Chem. Crystallogr.* **2004**, *34*, 393–400.

(286) Miecznikowski, J. R.; Lynn, M. A.; Jasinski, J. P.; Reinheimer, E.; Bak, D. W.; Pati, M.; Butrick, E. E.; Drozdoski, A. E. R.; Archer, K. A.; Villa, C. E.; Lemons, E. G.; Powers, E.; Siu, M.; Gomes, C. D.; Morio, K. N. Synthesis, characterization, and computational study of three-coordinate SNS-copper(I) complexes based on bis-thione precursors. *J. Coord. Chem.* **2014**, *67*, 29–44.

(287) Towatari, M.; Nishi, K.; Fujinami, T.; Matsumoto, N.; Sunatsuki, Y.; Kojima, M.; Mochida, N.; Ishida, T.; Re, N.; Mrozinski, J. Syntheses, Structures, and Magnetic Properties of Acetato- and Diphenolato-Bridged 3d–4f Binuclear Complexes [M(3-MeOsaltn)(MeOH)$_x$(ac)Ln(hfac)$_2$] (M = Zn^{II}, Cu^{II}, Ni^{II}, Co^{II}; Ln = La^{III}, Gd^{III}, Tb^{III}, Dy^{III}; 3-MeOsaltn = N,N-Bis(3-methoxy-2-oxybenzylidene)-1,3-propanediaminato; ac = Acetato; hfac = Hexafluoroacetylacetonato; x = 0 or 1). *Inorg. Chem.* **2013**, *52*, 6160–6178.

(288) Wen, H.-R.; Bao, J.; Liu, S.-J.; Liu, C.-M.; Zhang, C.-W.; Tang, Y.-Z. Temperature-controlled polymorphism of chiral Cu^{II}–Ln^{III} dinuclear complexes exhibiting slow magnetic relaxation. *Dalton Trans.* **2015**, *44*, 11191–11201.

(289) Zhang, P.; Zhang, L.; Lin, S.-Y.; Tang, J. Tetranuclear [MDy]$_2$ Compounds and Their Dinuclear [MDy] (M = Zn/Cu) Building Units: Their Assembly, Structures, and Magnetic Properties. *Inorg. Chem.* **2013**, *52*, 6595–6602.

(290) Chiboub Fellah, F. Z.; Boulefred, S.; Chiboub Fellah, A.; El Rez, B.; Duhayon, C.; Sutter, J.-P. Binuclear CuLn complexes (Ln^{III}=Gd, Tb, Dy) of alcohol-functionalized bicompartmental Schiff-base ligand. Hydrogen bonding and magnetic behaviors. *Inorg. Chim. Acta* **2016**, *439*, 24–29.

(291) Ishida, T.; Watanabe, R.; Fujiwara, K.; Okazawa, A.; Kojima, N.; Tanaka, G.; Yoshii, S.; Nojiri, H. Exchange coupling in TbCu and DyCu single-molecule magnets and related lanthanide and vanadium analogs. *Dalton Trans.* **2012**, *41*, 13609–13619.

(292) Upadhyay, A.; Singh, S. K.; Das, C.; Mondol, R.; Langley, S. K.; Murray, K. S.; Rajaraman, G.; Shanmugam, M. Enhancing the effective energy barrier of a Dy(III) SMM using a bridged diamagnetic Zn(II) ion. *Chem. Commun.* **2014**, *50*, 8838–8841.

(293) Panja, A.; Jaglicic, Z.; Herchel, R.; Brandão, P.; Jana, N. C. Influence of bridging and chelating co-ligands on the distinct single-molecule magnetic behaviours in ZnDy complexes. *New J. Chem.* **2022**, *Accepted Mnuscript*.

(294) Mahapatra, P.; Koizumi, N.; Kanetomo, T.; Ishida, T.; Ghosh, A. A series of Cu^{II}–Ln^{III} complexes of an N_2O_3 donor asymmetric ligand and a possible Cu^{II}–Tb^{III} SMM candidate in no bias field. *New J. Chem.* **2019**, *43*, 634–643.

(295) Jana, A.; Majumder, S.; Carrella, L.; Nayak, M.; Weyhermueller, T.; Dutta, S.; Schollmeyer, D.; Rentschler, E.; Koner, R.; Mohanta, S. Syntheses, Structures, and Magnetic Properties of Diphenoxo-Bridged $Cu^{II}Ln^{III}$ and Ni^{II}(Low-Spin) Ln^{III} Compounds Derived from a Compartmental Ligand (Ln = CeYb). *Inorg. Chem.* **2010**, *49*, 9012–9025.

(296) Kajiwara, T.; Nakano, M.; Takahashi, K.; Takaishi, S.; Yamashita, M. Structural Design of Easy-Axis Magnetic Anisotropy and Determination of Anisotropic Parameters of Ln^{III}-Cu^{II} Single-Molecule Magnets. *Chem. Eur. J.* **2011**, *17*, 196–205.

(297) Meiklejohn, W. H.; Bean, C. P. New Magnetic Anisotropy. *Phys. Rev.* **1957**, *105*, 904–913.

(298) Yang, J.-W.; Tian, Y.-M.; Tao, J.; Chen, P.; Li, H.-F.; Zhang, Y.-Q.; Yan, P.-F.; Sun, W.-B. Modulation of the Coordination Environment around the Magnetic Easy Axis Leads to Significant Magnetic Relaxations in a Series of 3d-4f Schiff Complexes. *Inorg. Chem.* **2018**, *57*, 8065–8077.

(299) Qin, Q.-P.; Qin, J.-L.; Meng, T.; Lin, W.-H.; Zhang, C.-H.; Wei, Z.-Z.; Chen, J.-N.; Liu, Y.-C.; Liang, H.; Chen, Z.-F. High in vivo antitumor activity of cobalt oxoisoaporphine complexes by targeting G-quadruplex DNA, telomerase and disrupting mitochondrial functions. *Eur. J. Med. Chem.* **2016**, *124*, 380–392.

(300) Wang, J.; Wu, J.; Tang, N. Synthesis, characterization of a new bicobalt complex $[Co_2L_2(C_2H_5OH)_2Cl_2]$ and application in cyclic carbonate synthesis. *Inorg. Chem. Commun.* **2007**, *10*, 1493–1495.

(301) Hołyńska, M.; Gawryszewska, P.; Lisowski, J. Tetranuclear Eu(III)-Co(II) complex of an N_4O_4 macrocycle. *Inorg. Chem. Commun.* **2016**, *71*, 27–31.

(302) Siega, P.; Dreos, R.; Brancatelli, G.; Demitri, N.; Geremia, S. Formation and Structure of a Cobalt(III) Complex Containing a Nonstabilized Pyridinium Ylide Ligand. *Organometallics* **2014**, *33*, 6076–6080.

(303) Basak, D.; Leusen, J. v.; Gupta, T.; Kögerler, P.; Bertolasi, V.; Ray, D. Unusually Distorted Pseudo-Octahedral Coordination Environment Around CoII from Thioether Schiff Base Ligands in Dinuclear [CoLn] (Ln = La, Gd, Tb, Dy, Ho) Complexes: Synthesis, Structure, and Understanding of Magnetic Behavior. *Inorg. Chem.* **2020**, *59*, 2387–2405.

(304) Landart-Gereka, A.; Quesada-Moreno, M. M.; DÍaz-Ortega, I. F.; Nojiri, H.; Ozerov, M.; Krzystek, J.; Palacios, M. A.; Colacio, E. Large easy-axis magnetic anisotropy in a series of trigonal prismatic mononuclear cobalt(II) complexes with zero-field hidden single-molecule magnet behaviour: The important role of the distortion of the coordination sphere and intermolecular interactions in the slow relaxation. *Inorg. Chem. Front.* **2022**, *9*, 2810–2831.

(305) Xie, Q.-W.; Wu, S.-Q.; Shi, W.-B.; Liu, C.-M.; Cui, A.-L.; Kou, H.-Z. Heterodinuclear M^{II}–Ln^{III} single molecule magnets constructed from exchange-coupled single ion magnets. *Dalton Trans.* **2014**, *43*, 11309–11316.

(306) Shao, D.; Xu, F.-X.; Yin, L.; Li, H.-Q.; Sun, Y.-C.; Ouyang, Z.-W.; Wang, Z.-X.; Zhang, Y.-Q.; Wang, X.-Y. Fine-Tuning of Structural Distortion and Magnetic Anisotropy by Organosulfonates in Octahedral Cobalt(II) Complexes. *Chin. J. Chem.* **2022**, *40*, 2193–2202.

(307) Plyuta, N.; Petrusenko, S.; Kokozay, V. N.; Cauchy, T.; Lloret, F.; Julve, M.; Cano, J.; Avarvari, N. Field-induced mononuclear cobalt(II) single-molecule magnet (SMM) based on a benzothiadiazole-ortho-vanillin ligand. *Dalton Trans.* **2022**, *51*, 4760–4771.

(308) Zheng, S.-S.; Dong, W.-K.; Zhang, Y.; Chen, L.; Ding, Y.-J. Four Salamo-type 3d–4f hetero-bimetallic [$Zn^{II}Ln^{III}$] complexes: Syntheses, crystal structures, and luminescent and magnetic properties. *New J. Chem.* **2017**, *41*, 4966–4973.

(309) Lu, X.-Y.; Liu, Y.-Q.; Deng, X.-W.; Zhu, Z.-X.; Yao, M.-X.; Jing, S. Synthesis, structures and magnetism of heterodinuclear Ni–Ln complexes: Field-induced single-molecule magnet behavior in the dysprosium analogue. *New J. Chem.* **2015**, *39*, 3467–3473.

(310) Jiang, L.; Liu, Y.; Liu, X.; Tian, J.; Yan, S. Three series of heterometallic Ni^{II}–Ln^{III} Schiff base complexes: Synthesis, crystal structures and magnetic characterization. *Dalton Trans.* **2017**, *46*, 12558–12573.

(311) Costes, J.-P.; Mallet-Ladeira, S.; Vendier, L.; Maurice, R.; Wernsdorfer, W. Influence of ancillary ligands and solvents on the nuclearity of Ni–Ln complexes. *Dalton Trans.* **2019**, *48*, 3404–3414.

(312) Yardan, A.; Hopa, C.; Yahsi, Y.; Karahan, A.; Kara, H.; Kurtaran, R. Two new heterodinuclear Schiff base complexes: Synthesis, crystal structure and thermal studies. *Spectrochim. Acta A* **2015**, *137*, 351–356.

(313) Duckworth, P. A.; Stephens, F. S.; Wainwright, K. P.; Weerasuria, K. D. V.; Wild, S. B. Synthesis and structural studies of nickel(II) complexes of 14-membered *trans*-N_2O_2 and *trans*-N_2S_2 quadridentate macrocycles. *Inorg. Chem.* **1989**, *28*, 4531–4535.

(314) Akine, S.; Matsumoto, T.; Taniguchi, T.; Nabeshima, T. Synthesis, Structures, and Magnetic Properties of Tri- and Dinuclear Copper(II)-Gadolinium(III) Complexes of Linear Oligooxime Ligands. *Inorg. Chem.* **2005**, *44*, 3270–3274.

(315) Yang, Y.-H.; Zhang, Y.; Yu, M.; Zheng, S.-S.; Dong, W. K. *Wuji Huaxue Xuebao* **2018**, *34*, 997.

(316) Kajiwara, T.; Nakano, M.; Takaishi, S.; Yamashita, M. Coordination-Tuned Single-Molecule-Magnet Behaviour of Tb^{III}-Cu^{II} Dinuclear Systems. *Inorg. Chem.* **2008**, *47*, 8604–8606.

(317) Dong, W.-K.; Zhu, L.-C.; Dong, Y.-J.; Ma, J.-C.; Zhang, Y. Mono, di and heptanuclear metal(II) complexes based on symmetric and asymmetric tetradentate Salamo-type ligands: Syntheses, structures and spectroscopic properties. *Polyhedron* **2016**, *117*, 148–154.

(318) Sheikh, J. A.; Goswami, S.; Konar, S. Modulating the magnetic properties by structural modification in a family of Co-Ln (Ln = Gd, Dy) molecular aggregates. *Dalton Trans.* **2014**, *43*, 14577–14585.

(319) Coxall, R. A.; Harris, S. G.; Henderson, D. K.; Parsons, S.; Tasker, P. A.; Winpenny, R. E. Inter-ligand reactions: *in situ* formation of new polydentate ligands. *J. Chem. Soc., Dalton Trans.* **2000**, *2000*, 2349–2356.

(320) Lada, Z. G.; Katsoulakou, E.; Polyzou, C. D.; Raptopoulou, C. P.; Psycharis, V. A missing nuclearity in the Co(III)/Ln(III)2-Pyridyladoxime chemistry: Tetranuclear compounds using the "assisted self-assembly" approach (Ln = rare earth metals). *Chemistry* **2023**, *5*, 996–1005.

(321) Konar, S.; Bhuvanesh, N.; Clearfield, A. Oxo-, Hydroxo-, and Peroxo-Bridged Fe(III) Phosphonate Cages. *J. Am. Chem. Soc.* **2006**, *128*, 9604–9605.

(322) Sheikh, J. A.; Jena, H. S.; Clearfield, A.; Konar, S. Phosphonate based high nuclearity magnetic cages. *Acc. Chem. Res.* **2016**, *49*, 1093–1103.

(323) Hermer, N.; Reinsch, H.; Mayer, P.; Stock, N. Synthesis and characterisation of the porous zinc phosphonate $[Zn_2(H_2PPB)(H_2O)_2]\cdot xH_2O$. *CrystEngComm* **2016**, *18*, 8147–8150.

(324) Cirera, J.; Ruiz, E.; Alvarez, S. Shape and Spin State in Four-Coordinate Transition-Metal Complexes: The Case of the d^6 Configuration. *Chem. Eur. J.* **2006**, *12*, 3162–3167.

(325) PROCESS-AUTO, Computer Program, Tokyo, 1998.

(326) Crystal Clear, Computer Program, The Woodlands, Texas, 2005.

(327) Sheldrick, G. M. Crystal structure refinement with SHELXL. *Acta Crystallogr. C* **2015**, *71*, 3–8.

(328) Sheldrick, G. M. SHELXT - Integrated space-group and crystal-structure determination. *Acta Crystallogr. A* **2015**, *71*, 3–8.

(329) Sheldrick, G. A short history of SHELX. *Acta Crystallogr. A* **2008**, *64*, 112–122.

(330) APEX3 and SAINT, Computer Program, Madison, Wisconsin, USA, 2019.

MASSEY UNIVERSITY
TE KUNENGA KI PŪREHUROA
UNIVERSITY OF NEW ZEALAND

GRADUATE RESEARCH SCHOOL

STATEMENT OF CONTRIBUTION
DOCTORATE WITH PUBLICATIONS/MANUSCRIPTS

We, the student and the student's main supervisor, certify that all co-authors have consented to their work being included in the thesis and they have accepted the student's contribution as indicated below in the Statement of Originality.

Student name:	Sidney Woodhouse
Name and title of main supervisor:	Prof. Paul Plieger
In which chapter is the manuscript/published work?	Chapter 3 : Defective Dicubanes
What percentage of the manuscript/published work was contributed by the student?	60%

Describe the contribution that the student has made to the manuscript/published work:

Drafting of the manuscript, and the synthetic efforts were completed by the student.

Please select one of the following three options:

- (●) **The manuscript/published work is published or in press**

  Please provide the full reference of the research output:

  S. S. Woodhouse, T. N. Dais, E.H. Payne, M. K. Singh, E. K, Brechin and P. G. Plieger. The structural manipulation of a series of Ni4 defective dicubanes: Synthesis, X-ray structures, magnetic and computational analyses. Dalton Trans., 2021, 50(15), 5318-5326.

- ( ) **The manuscript is currently under review for publication**

  Please provide the name of the journal:

- ( ) **It is intended that the manuscript will be published, but it has not yet been submitted to a journal**

Student's signature:	Sidneyn	Main supervisor's signature:	Digitally signed by Paul Plieger DN: cn=Paul Plieger, c=NZ, o=Massey University, ou=School of Natural Sciences, email=p.g.plieger@massey.ac.nz Date: 2022.12.09 13:28:02 +13'00'

This form should be placed at the beginning of each relevant thesis chapter.

MASSEY UNIVERSITY
TE KUNENGA KI PŪREHUROA
UNIVERSITY OF NEW ZEALAND

GRADUATE RESEARCH SCHOOL

STATEMENT OF CONTRIBUTION
DOCTORATE WITH PUBLICATIONS/MANUSCRIPTS

We, the student and the student's main supervisor, certify that all co-authors have consented to their work being included in the thesis and they have accepted the student's contribution as indicated below in the Statement of Originality.

Student name:	Sidney Woodhouse
Name and title of main supervisor:	Prof. Paul Plieger
In which chapter is the manuscript/published work?	Chapter 4: 3d3d' Dimers
What percentage of the manuscript/published work was contributed by the student?	60%

Describe the contribution that the student has made to the manuscript/published work:

Drafting of the manuscript, the synthetic efforts, and the crystallographic analysis were completed by the student.

Please select one of the following three options:

- (●) **The manuscript/published work is published or in press**

  Please provide the full reference of the research output:

  S. S. Woodhouse, T. N. Dais, A. Etcheverry-Berrios, E. K. Brechin, J. R. Lane, P. G. Plieger. Against the Norm: Non Irving-Williams Transmetalation in Transition Metal Dimers. Inorg. Chem., 2022, 61(44), 17819-17827.

- ( ) **The manuscript is currently under review for publication**

  Please provide the name of the journal:

- ( ) **It is intended that the manuscript will be published, but it has not yet been submitted to a journal**

Student's signature:	Sidneym	Main supervisor's signature:	Digitally signed by Paul Plieger DN: cn=Paul Plieger, c=NZ, o=Massey University, ou=School of Natural Sciences, email=p.g.plieger@massey.ac.nz Date: 2022.12.09 13:27:16 +13'00'

This form should be placed at the beginning of each relevant thesis chapter.